RARE NUCLEAR PROCESSES
IN
LOW ENERGY HEAVY ION PHYSICS

Indian Academy of Sciences
Bangalore

Digitized by the Internet Archive
in 2018 with funding from
Public.Resource.Org

https://archive.org/details/rarenuclearproce00unse

RARE NUCLEAR PROCESSES
IN
LOW ENERGY HEAVY ION PHYSICS

Host Institution:

Nuclear Science Centre
Post Box No. 10502
Aruna Asaf Ali Marg
New Delhi 110 067, India

Venue:

Auditorium: International Centre for Genetic Engineering and Bio-technology (ICGEB)

Supported by:

- Department of Science and Technology, Government of India
- Board of Research in Nuclear Sciences, India
- Council of Scientific and Industrial Research, India
- Indian National Science Academy, India

© 1999 Indian Academy of Sciences

Reprinted from *Pramana – J. Phys.*
Vol. 53, No. 3, September 1999

Edited by P. Sugathan, N. Madhavan, A.K. Sinha and R. Singh and printed for
the Indian Academy of Sciences by Tholasi Prints India, Bangalore

INTERNATIONAL ADVISORY COMMITTEE

Y. ABE, *Kyoto Univ., Japan*
Y.K. AGARWAL, *TIFR, Mumbai, India*
C.V.K. BABA, *Hyderabad, India*
B.B. BACK, *ANL, USA*
R.K. BHOWMIK, *NSC, India*
R. CASTEN, *Yale Univ., USA*
E. CHEREPANOV, *DUBNA, Russia*
S.N. CHINTALAPUDI, *IUC-DAEF, Calcutta, India*
C.H. DASSO, *NBI, Denmark and ECT, Trento*
C.N. DAVIDS, *ANL, USA*
G.DRACOULIS, *ANU, Australia*
I.M.GOVIL, *Panjab Univ., Chandigarh, India*
J.H. HAMILTON, *Vanderbilt Univ., USA*
XU JINCHENG, *CIAE, China*
S.S. KAPOOR, *BARC, Mumbai, India*
G.K. MEHTA (Chairman), *NSC, India*
T. MOTOBAYASHI, *Rikkyo Univ., Japan*
G. MUNZENBERG, *GSI, Germany*
J.B.NATOWITZ, *Texas A&M Univ., USA*
V. NINOV, *Berkeley , USA*
S.B. PATEL, *Bombay Univ., Mumbai, India*
V.S. RAMAMURTHY, *DST, New Delhi, India*
R. SINGH, *Delhi Univ., New Delhi, India*
B. SINHA, *VECC/SINP, Calcutta, India*
A.M. STEFANINI, *LNL, Italy*
M.THOENNESSEN, *MSU, USA*
R. VANDENBOSCH, *Univ. of Washington, USA*
A.H. WUOSMAA, *ANL, USA*

ORGANISING COMMITTEE

K. ASOKAN, *NSC, India*
LAGY T. BABY, *NSC, India*
J.J. DAS, *NSC, India*
S.K. HUI, *Calcutta Univ., India*
AKHIL JHINGAN, *NSC, India*
P. JOSHI, *NSC, India*
N. MADHAVAN, *NSC, India*
P.V. MADHUSUDHANA RAO, *Andhra Univ., India*
I. MAJUMDAR, *SUNY, USA*
S. MURALITHAR, *NSC, India*
N.V.S.V. PRASAD, *I.K.S, K.U. Leuven, Belgium*
M.C. RADHAKRISHNA, *Bangalore Univ., India*
D.L. SASTRY, *Andhra Univ., India*
R. SINGH, *Delhi Univ., India*
A.K. SINHA, *NSC, India*
P. SUGATHAN, *NSC, India*
VANDANA TRIPATHI, *NSC, India*
A.M. VINODKUMAR, *Calicut University, India*
K.M. VARIER, *Calicut University, India*
THOMAS VARUGHESE, *NSC, India*

Contents

Preface 1

Nuclear structure and dynamics

Nuclear structure studies on halo nuclei by direct reactions with radioactive beams . . . . *Peter Egelhof* 3

Alpha particle evaporation as a probe for dynamical deformations . . . . *I M Govil* 19

Experimental investigations of the nuclear level density by using heavy ion reactions . . . . *G Viesti, M Lunardon, D Fabris, G Nebbia, M Cinausero, E Fioretto, G Prete, J B Natowitz, K Hagel and R Wada* 33

Extremes of nuclear structure . . . . *S B Patel* 43

$M1$ and $E2$ band structures in the Sn–Xe–Ba region . . . . *R Srinivasa Chakrawarthy* 45

Fusion–fission dynamics in the superheavy nucleus production . . . . *G Giardina, P D'Agostino, G Fazio, M Herman, A I Muninov, A Nasirov, G Oliva, R Palamara and R Ruggeri* 47

Fluctuations of the second order observables for dissipative processes in ^{19}F + ^{27}Al system . . . . *I Berceanu, A Andronic, M Duma, D Moisa, M Petrovici, A Pop, V Simion, A Del Zoppo, G d'Erasmo, G Immé, G Lanzanò, A Pagano, A Pantaleo and G Raciti* 57

Transition strengths and shapes of 2-qp bands in ^{74}Se and ^{76}Kr . . . . *G Mukherjee, P Joshi, S N Roy, S Datta, R P Singh, S Muralithar and R K Bhowmik* 63

Structure of neutron-rich nuclei around $A \cong 100$ . . . . *Maitreyee Saha Sarkar* 69

Dissipative processes in light heavy ion collisions . . . . . *A Pop, A Andronic, I Berceanu, M Duma, D Moisă, M Petrovici, V Simion, G Immé, G Lanzanò, A Pagano, G Raciti, R Coniglione, A Del Zoppo, P Piatelli, P Sapienza, N Colonna, G d'Erasmo and A Pantaleo* 75

Distinction between pre-formed cluster emission and heavy ion decay by fission . . . . *G Shanmugam and G M Carmel Vigila Bai* 81

Nuclear structure studies of nuclei near $N = 80$ . . . . *E Dragulescu, G Semenescu and I Iftimia* 85

The simulations of Ca–Ca collisions: Binary break-up, onset of multifragmentation and vaporization . . . . *Rajeev K Puri and Suneel Kumar* 91

Rotational co-existence in selenium isotopes . . . . *G Shanmugam, V Ramasubramanian and P Arumugam* 95

Signature splitting in magnetic rotational bands . . . . *Amita, Ashok K Jain, Alpana Goel and Balraj Singh* 101

Relevance of thermally populated first excited state of ^{44}Ti to the abundance problem of Cassiopiea A: A model study . . . . *Sukhendusekhar Sarkar* 107

Nuclear Reactions at Near and Sub-Barrier Energies

Multinucleon transfer reactions . . . . *G Pollarolo* 111

Fusion–fission of light nuclear systems . . . . *A Szanto de Toledo, N Carlin, N Added, E M Szanto, M G Munhoz, J Takahashi, A Suaide and M M de Moura* 121

Heavy-ion induced fission reactions at near-barrier energies – what have we learnt? . . . . *S Kailas* 123

Heavy-ion fusion at low energies . . . . *Neil Rowley* 133

Dynamics of low-energy heavy-ion fusion . . . . *A M Stefanini* 143

Exploiting barrier distributions to investigate break up effects in the fusion of ^{9}Be + ^{208}Pb . . . . *M Dasgupta, D J Hinde, R D Butt, A C Berriman, C R Morton, J O Newton and K Hagino* 151

Some aspects of heavy ion fusion–fission dynamics . . . . *D V Shetty, R K Choudhury, B K Nayak, D M Nadkarni and S S Kapoor* 159

Transfer measurements for the Ti + Ni systems at near barrier energies . . . . *K M Varier, A M Vinodkumar, N V S V Prasad, P V Madhusudhana Rao, D L Sastry, Lagy T Baby, M C Radhakrishna, N G Puttaswamy, J J Das, P Sugathan, N Madhavan, A K Sinha and D O Kataria* 167

Measurement of the ground state $2n$ pickup probability for ^{28}Si + ^{68}Zn and its role in sub-barrier fusion enhancement . . . . . . *Vandana Tripathi, Lagy T Baby, P V Madhusudhana Rao, S K Hui, R Singh, J J Das, P Sugathan, N Madhavan and A K Sinha* 173

Inclusive and exclusive measurements in the projectile break up of ^{7}Li . . . . . . *T Madhusoodhanan, Samit Mandal, M P Sathyavathiamma, Ramani, N G Puttaswamy, T S Mudhole, A Mandal, D K Avasthi, R Shyam and S K Datta* 179

Asymmetric barrier model for heavy ion fusion and its relation to channel coupling . . . .*Basudeb Sahu and C S Shastry* 183

Nuclear orbiting and anomalies in nuclear reactions . . . . *A De, A Mitra, A Ray, S R Banerjee, M Sengupta, A Chatterjee, S Kailas, H S Patel, M G Betigiri and S K Datta* 187

Quasielastic reactions around the Coulomb barrier in ^{16}O + ^{118}Sn . . . . *S Saha, Samit K Mandal, M B Chatterjee, B K Sinha and S K Datta* 191

Coupled channels calculations for ^{18}O and ^{16}O break-up reaction . . . . *Samit K Mandal and R K Bhowmik* 197

Fission fragment angular distributions in ^{16}O + ^{181}Ta . . . .*Bivash R Behera, Subinit Roy, P Basu, M K Sharan, S Jena, M Satpathy, S K Datta, L Satpathy and M L Chatterjee* 201

Nuclei at Extreme Conditions

A three body approach to study the structural properties of 2-n halo nuclei and the search for Efimov states . . . . *V S Bhasin* 205

Rare cold nuclear processes – A review and some new results . . . .*Raj K Gupta* 215

Astrophysical S-factors from asymptotic normalization coefficients . . . .*R E Tribble, A Azhari, H L Clark, C A Gagliardi, Y-W Lui, A M Mukhamedzhanov, A Sattaroy, X Tang, L Trache, V Burjan, J Cejpek, V Kroha, Š Piskoř, J Vincour and F Cârstoiu* 223

Break up of ^{8}B and the ^{7}Be(p, γ)^{8}B reaction . . . . *R Shyam and I J Thompson* 233

Perspectives from above and beyond the proton drip-line . . . . *P J Woods* 245

Mass measurements of relativistic projectile fragments in the storage ring ESR . . . . . . *T Radon, H Geissel, F Attallah, K Beckert, F Bosch, A Dolinskiy, H Eickhoff, M Falch, B Franczak, B Franzke, Y Fujita, M Hausmann, M Hellström, F Herfurth, Th Kerscher, O Klepper, H-J Kluge, C Kozhuharov, Yu Litvinov, K E G Löbner, G Münzenberg, F Nolden, Yu Novikov, Z Patyk, W Quint, H Reich, C Scheidenberger, B Schlitt, J Stadlmann, M Steck, K Sümmerer, L Vermeeren, M Winkler, Th Winkler and H Wollnik* 247

The analysis of reactions leading to synthesis of super heavy elements within the dinuclear system concept . . . .*E A Cherepanov* 257

Proton radioactivity – spherical and deformed . . . . *C N Davids, P J Woods, D Seweryniak, A A Sonzogni, J C Batchelder, C R Bingham, T Davinson, D J Henderson, R J Irvine, G L Poli, J Uusitalo and W B Walters* 269

A rare nuclear decay process: The internal conversion between bound atomic states . . . . *J F Chemin, T Carreyre, M Aiche, F Attallah, G Bogaert, J P Grandin, M Harston, W E Meyerhof and J N Scheurer* 271

Cubic potential models for cluster radioactivity . . . .*G Shanmugam* 273

Fission experiments with secondary beams . . . . *J Benlliure, S Steinhäuser, C Böckstiegel, A Grewe, H-G Clerc, A Heinz, M de Jong, A R Junghans, J Müller, K-H Schmidt and M Pfützner* 275

Statistical fluctuations in hot rotating nuclei . . . .*M Rajasekaran and D Caleb Chanthi Raj* 285

List of participants 291

FOREWORD

There has been a revival in nuclear physics studies using low/medium energy heavy ion beams. This interest has come about with the possibility of carrying out measurements involving channels with low probabilities. With the advent of new techniques in ion beam production and particle/photon detection it is now possible to carry out exclusive measurements of rare/exotic nuclear processes with relative ease though they were earlier considered to be rare and difficult to study. Such studies demand sophisticated instrumentation and devices which need continuous upgradation and more importantly new design concepts. Therefore, it is important to periodically review the current trends and future directions in this field. With this objective, an International Workshop on Rare Nuclear Processes in Low Energy Heavy Ion Physics (IWRNP-98) was held at Nuclear Science Centre (NSC)*, New Delhi, India from November 16–20, 1998.

At IWRNP-98, there were about one hundred participants from India and abroad who presented the results of their latest research work in the frontier areas of nuclear physics. This workshop provided an opportunity to the participants to exchange ideas related to the present achievements and future plans spanning experimental facilities, experimental plans and theoretical approaches.

In his welcome address, Prof. G K Mehta, Director, NSC made introductory remarks about the accelerator and the associated experimental facilities including the accelerator upgradation programme of the Centre. Prof. V S Ramamurthy of the Department of Science and Technology, New Delhi inaugurated the Workshop and Dr. S S Kapoor of Bhabha Atomic Research Centre, Mumbai delivered the keynote address on “Emerging Frontiers in Heavy Ion Nuclear Physics” thereby setting the tone of the Workshop. The programme consisted of 23 invited talks and several contributed papers in the form of short talks and posters. Dr. S Kailas and Prof. S C Pancholi summarised the talks and discussions.

This proceedings consists of invited talks and refereed contributed papers. We thank all the experts who agreed to be referees in spite of their tight schedule and also did a wonderful job of evaluation in a short time.

We are grateful to Prof. G K Mehta for his guidance, encouragement and continuous support in organising this International Workshop. We thank the distinguished members of the International Advisory Committee for their valuable suggestions and recommendations which helped immensely in the finalisation of the programme. Apart from the University Grants Commission (through Nuclear Science Centre), the financial support for organising the Workshop was provided by the Department of Science and Technology (Govt. of India, New Delhi), Board of Research in Nuclear Sciences (Dept. of Atomic Energy, Govt. of India, Mumbai), Council of Scientific and Industrial Research (New Delhi) and Indian National Science Academy (New Delhi). The talks were held at the auditorium of International Centre for Genetic Engineering and Biotechnology (ICGEB).

Keen interest of Prof. H R Krishnamurthy, Prof. Rohini M Godbole and Dr. S Kailas in our efforts to have the proceedings of the Workshop published in *Pramana* in the form of a special issue is very much appreciated. The editorial office of *Pramana* rendered immense help in organising electronic mail transmission/acceptance of the manuscripts and proofs, etc.

Dr. P B Tripathi needs special mention for his help in getting necessary approvals and completion of visa formalities for foreign participants. In addition to the local organising committee members, help received from N J Jose, Ms Neelaveni, Maurya, Prakash and Rajpal Sharma (all from NSC) is acknowledged.

P Sugathan
N Madhavan
A K Sinha
R Singh
(*Guest Editors*)

* About NSC: (http://www.nsc.ernet.in)

Nuclear Science Centre, an Inter-University research centre of University Grants Commission (UGC), provides front-ranking experimental facilities for University users to carry out accelerator based research. The centre is equipped with a 15 MV Tandem accelerator and experimental facilities such as Recoil Mass Spectrometer and Gamma and Charged Particle Detector Arrays for nuclear physics studies. A low energy RIB facility has been made operational recently. There is an ongoing process to augument the energy and beam intensity by building a Superconducting LINAC and a high current injector using ECR source. Among future experimental facilities, a Hybrid Recoil Mass Spectrometer and a Large Gamma Detector Array are planned.

Nuclear structure studies on halo nuclei by direct reactions with radioactive beams

PETER EGELHOF
Gesellschaft für Schwerionenforschung (GSI), D-64291 Darmstadt, Germany

Abstract. The investigation of direct reactions with exotic beams in inverse kinematics gives access to a wide field of nuclear structure studies in the region far off stability. The basic concept and the methods involved are briefly discussed. The present contribution will focus on the investigation of light neutron-rich halo nuclei. Such nuclei reveal a new type of nuclear structure, namely an extended neutron distribution surrounding a nuclear core. An overview on this phenomenon, and on the various methods which gave first evidence and qualitative confirmation of our present picture of halo nuclei, is given.

To obtain more quantitative information on the radial shape of halo nuclei, elastic proton scattering on neutron-rich light nuclei at intermediate energies was recently investigated for the first time. This method is demonstrated to be an effective means for studying the nuclear matter distributions of such nuclei. The results on the nuclear matter radii of ^{6}He and ^{8}He, the deduced nuclear matter density distributions, and the significance of the data on the halo structure is discussed. The present data allow also a sensitive test of theoretical model calculations on the structure of neutron-rich helium isotopes. A few examples are presented.

The investigation of few-nucleon transfer reactions in inverse kinematics may provide new and complementary information on nuclear structure, as well as astrophysical questions. The physics motivation and the experimental concept for such experiments, to be performed due to momentum matching reasons at low incident energies around 5 – 20 MeV/u at the new generation low energy radioactive beam facilities SPIRAL, PIAFE, etc., is briefly discussed.

Keywords. Halo nuclei; direct reactions with radioactive beams; nuclear matter radii.

PACS Nos **21.10.Gv; 25.40.Cm; 25.60.-t; 25.60.Dz; 25.60.Gc; 27.20.+n**

1. Introduction

One of the most powerful classical methods for obtaining spectroscopic information on the structure of nuclei is the investigation of light-ion induced direct reactions, i.e. elastic or inelastic scattering, or one- and few-nucleon transfer reactions. A lot of what we know about the structure of stable nuclei was obtained from such investigations. Of course, before the availability of radioactive ion beams, this method was limited to stable or very long-lived nuclei for which targets could be prepared. The use of good-quality secondary exotic beams now enables to study such reactions on exotic nuclei using the method of inverse kinematics, which is sketched in figure 1 for the example of a (d,p) reaction.

In principle, a large variety of light-ion induced reactions with various physics motivations may be investigated. One- and few-nucleon transfer reactions, such as (d,p), (p,d),

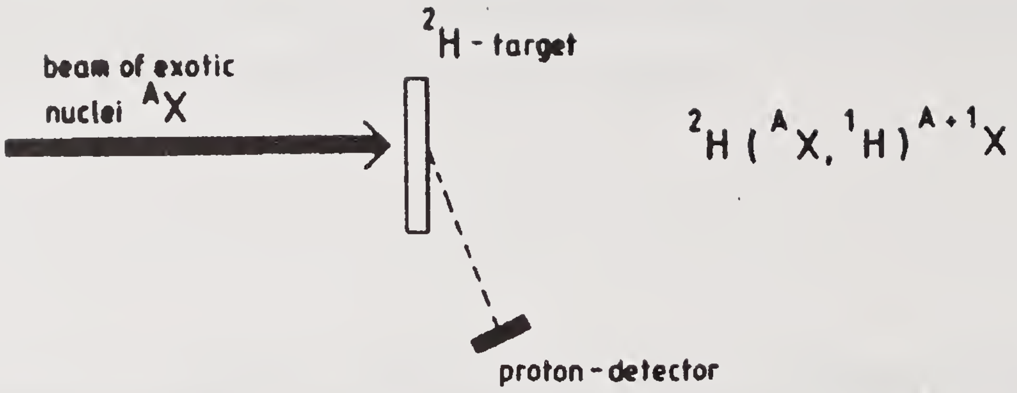

Figure 1. The method of inverse kinematics is sketched for the example of a (d,p)-reaction on the nucleus ^{A}X.

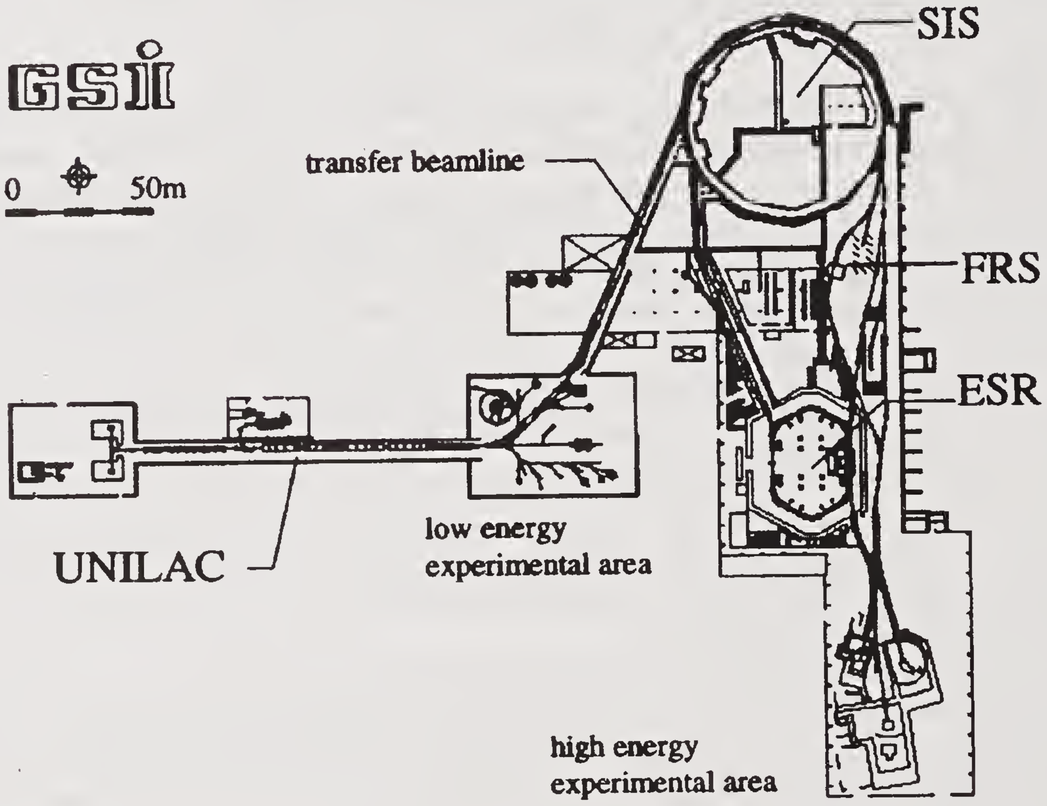

Figure 2. Schematic view of the accelerator facilities at GSI, Darmstadt. Heavy-ion beams of all ion species up to ^{238}U from the linear accelerator UNILAC ($E\leq 20$ MeV/u) are post-accelerated by the heavy-ion synchrotron SIS ($E\leq 2$ GeV/u), and may be injected into the fragment separator FRS and (or) into the experimental storage ring ESR.

(d,t), $(d,{}^3\text{He})$, $({}^3\text{He},\alpha)$, etc., allow to populate single-particle (hole) states or two-particle (two-hole) states, whereas inelastic (p,p'), (α,α'), etc. scattering leads to the population of collective states, and (p,p), (α,α), etc. elastic scattering allows to deduce information on the nuclear matter distribution of nuclei. Of particular physics interest are, for example, the nuclear shell model in the region far off stability, the two-body residual interaction in nuclei, as well as astrophysical questions, transition densities and deformation parameters, the radial shape of nuclei, etc.

The new heavy-ion accelerator facilities at GSI Darmstadt (see figure 2), which came into operation in 1990, opened new opportunities for a variety of nuclear physics studies. With respect to exotic nuclei the combination of the heavy-ion synchrotron SIS, the fragment separator FRS and, for selected cases, the experimental storage ring ESR provides good-quality beams of relatively short-lived nuclei, extending to isotopes far off stability, in the energy range from the Coulomb barrier up to intermediate energies around 1 GeV/u.

The present contribution will focus on nuclear structure studies on light neutron-rich halo nuclei. Such nuclei, located near or at the neutron drip line, in particular ^{6}He, ^{8}He, ^{11}Li, ^{14}Be, etc., have attracted much attention in the recent years since there is clear experimental evidence that these nuclei reveal a qualitatively new type of nuclear structure, namely an extended neutron distribution surrounding a nuclear core.

A brief overview on this phenomenon and on some of the experimental methods which gave first evidence, and which were used for further experimental access to the halo structure of nuclei, is given in the following section. The third section is dedicated to the investigation of nuclear matter distributions of halo nuclei by intermediate-energy elastic proton scattering, a method which was applied on exotic nuclei for the first time in recent experiments at GSI. Finally, the investigation of few-nucleon transfer reactions in inverse kinematics is discussed which may in future provide complementary information on the structure of halo nuclei.

2. Halo nuclei – A new phenomenon of the structure of nuclei

The discovery and the interpretation of the phenomenon of halo nuclei was initiated in the mid-eighties by the pioneering work of Tanihata and coworkers [1–3]. In these experiments the total interaction cross section σ_I was determined for the interaction of light neutron-rich isotopes with various targets. σ_I was deduced from the change of intensity of a beam of exotic nuclei before and after hitting a target. From the measured interaction cross sections the nuclear matter radii $R_I(\text{proj.})$ of the projectile nuclei may be estimated by simple geometrical considerations using the relation

$$\sigma_I = \pi[R_I(\text{proj.}) + R_I(\text{tar.})]^2, \tag{1}$$

$R_I(\text{tar.})$ being the matter radius of the target nucleus (it should be noted that for a quantitative determination of the matter radii a more sophisticated analysis taking into account the reaction dynamics was used).

The surprisingly steep rise of σ_I for ^{11}Li in the chain of the Li-isotopes, and less pronounced, for ^{6}He and ^{8}He for the He-isotopes, was therefore interpreted as due to a pronounced increase of the nuclear matter radius. In figure 3 a compilation of such data [3] measured for a larger number of neutron-rich isotopes is displayed. In almost all of the isotope chains we observe for the most neutron-rich nuclei a deviation from the $A^{(1/3)}$-law (see dotted line in figure 3), which is well established for stable and less exotic nuclei. These findings were at that time interpreted in terms of the following picture (see also figure 4): For the case of ‘normal’ nuclei, which are stable or are situated close to the valley of stability, and which therefore possess only a small excess of neutrons, the neutrons and protons are equally distributed (left part of figure 4), and the addition of one neutron will not drastically change the spatial extension of the nucleus. In contrast, a new phenomenon of nuclear structure appears for some nuclei which are close to the drip line, and for which the binding energy of additional valence nuclei is consequently very low, usually of the order of a few hundred keV only. Adding one or more neutrons to such an already very neutron-rich nucleus will produce in certain cases a so-called ‘halo’ around a nuclear core, consisting of an extremely spatially extended, low-density aureole in which the additional neutrons are located (right part of figure 4). Thus, in special cases, a significant

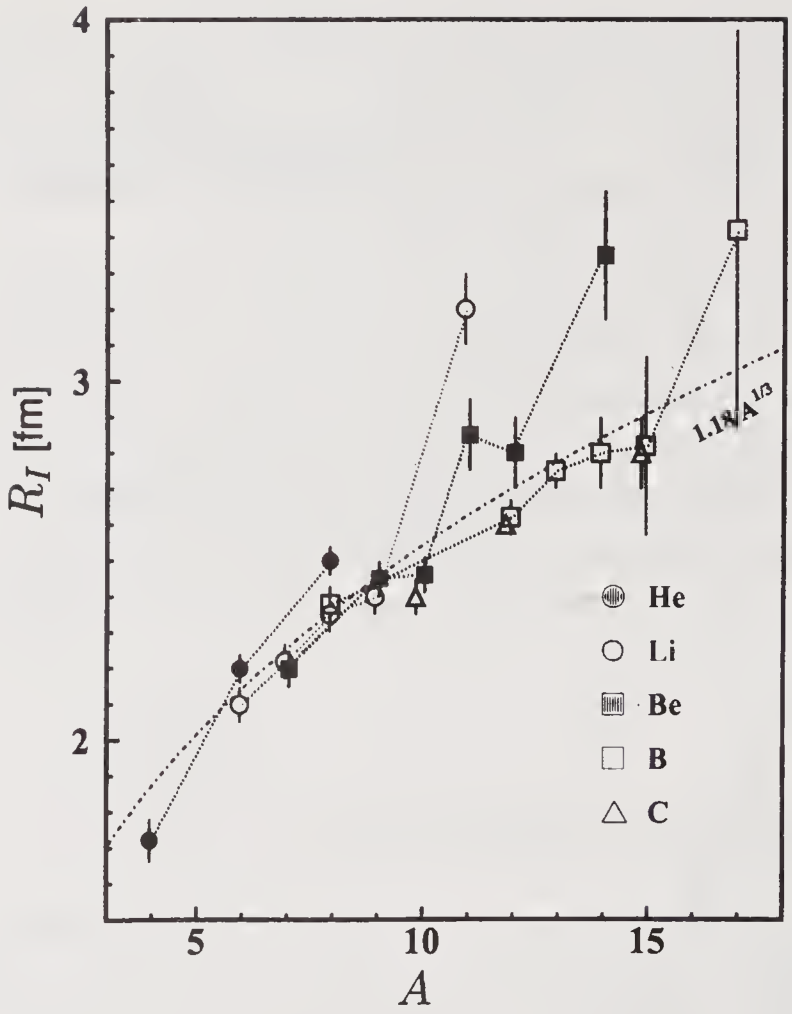

Figure 3. Nuclear matter radii R_I deduced from measured total interaction cross sections for several isotope chains of light neutron-rich nuclei (from ref. [3].

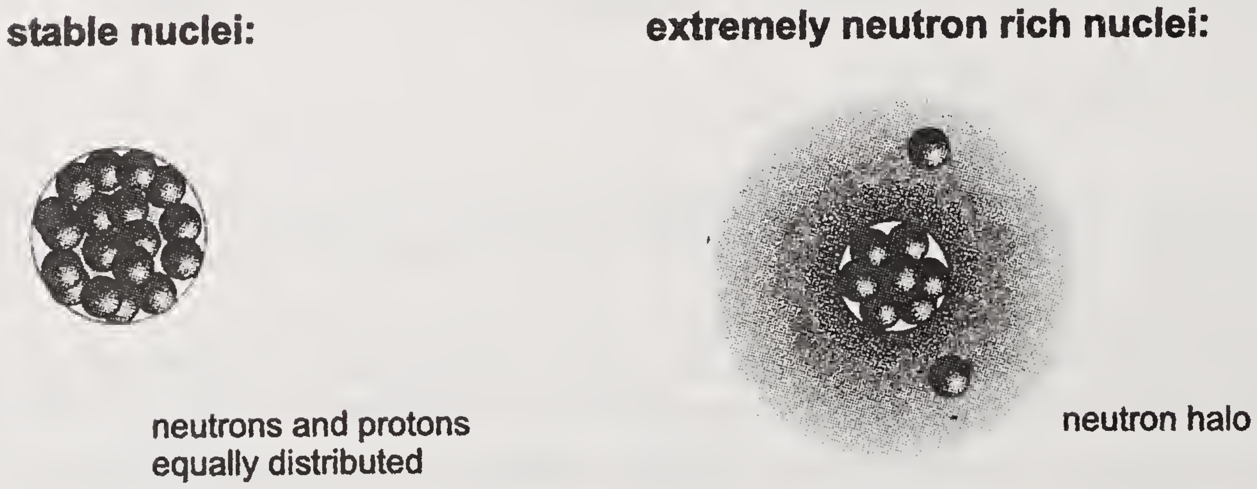
stable nuclei:
extremely neutron rich nuclei:
neutrons and protons equally distributed
neutron halo

Figure 4. Density distributions of nuclear matter for stable nuclei and extremely neutron-rich nuclei.

fraction of more than 90% of the valence neutron wave function can be outside the central part of the nucleus, leading to an extended radius of the nuclear matter distribution. So, for example, the nuclear radius determined for ^{11}Li is similar to that of the stable ^{32}S, which consists of approximately three times the number of nucleons. It turns out that the phenomenon of halo nuclei is always closely connected to a very low binding energy of the valence nucleons.

In order to confirm the present picture of halo nuclei, and to get a deeper insight into the structure of such nuclei, halo nuclei were subjected to numerous studies during the last decade, using various methods. For a detailed overview over this field the reader may be referred to recent review articles [4–7]. Experiments performed at the on-line mass separator ISOLDE at CERN focused on the electric and magnetic moments of halo nuclei

[8,9]. Beta-decay measurements following in-beam polarization by optical pumping on ^{9}Li and ^{11}Li showed that the electric and magnetic properties of both nuclei are very similar. This finding is a clear confirmation that the large interaction cross section obtained for ^{11}Li is only due to the spatial distribution of the valence neutrons, and not created by core deformation or core polarization effects.

Another frequently used method is the investigation of momentum distributions of the reaction products after fragmentation of the halo nucleus following the interaction with a target. Experiments were performed using beams produced by heavy ion projectile fragmentation and in-flight separation at GANIL, MSU, RIKEN in the energy range 20–80 MeV/u, and at BEVALAC and GSI for higher incident energies of about 200–1000 MeV/u. Thus, a large variety of data on longitudinal and transverse momentum distributions of the heavy 'core'-fragment, and of the valence neutrons, and, in kinematically complete experiments, of both have been taken for various exotic nuclei, and for various targets and incident energies (for an overview see [4–7,10], and references therein).

It follows from relatively simple considerations that the momentum distributions of the fragments reflect the intrinsic distribution of the constituents, and thus the spatial structure of the fragmenting nucleus. The momentum distribution of the valence neutrons of the nucleus being the Fourier transform of its wave function, the size of the spatial distribution of the nucleus is – due to the uncertainty principle – expected to be inversely proportional to the width Γ of the momentum distribution. Hence we obtain for the root mean square matter radius:

$$\langle R_m^2\rangle^{1/2} \sim 1/\Gamma. \tag{2}$$

Indeed, narrow momentum distributions were obtained for practically all candidates for halo nuclei, as established from the data on the total interaction cross section. As an example, recent data [11] on longitudinal momentum distributions of ^{18}C (^{16}C)-fragments after one-neutron removal from ^{19}C (^{17}C)-projectiles are displayed in figure 5. Both projectile nuclei are assumed to have an extended neutron distribution due to the small binding energy of the valence neutron. Consequently both momentum distributions are found to be narrower by factors of about 2 and 3 compared to the corresponding momentum

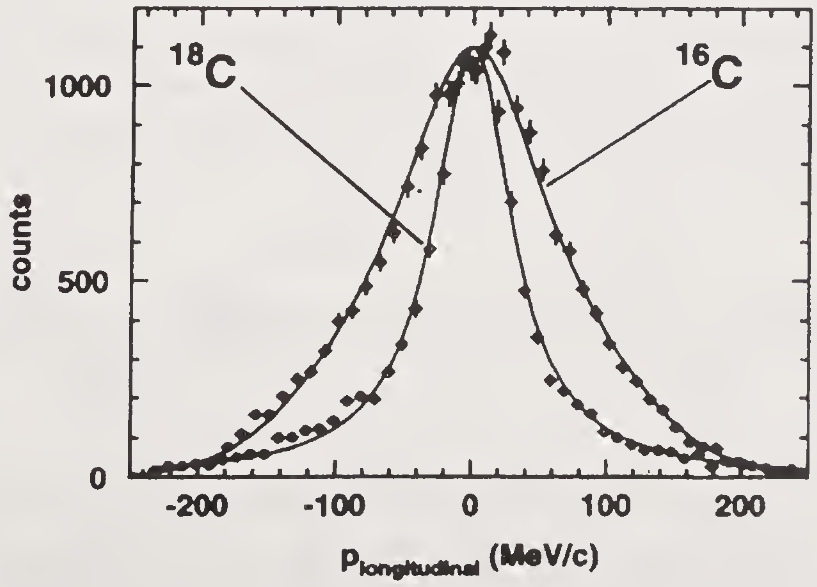

Figure 5. Longitudinal momentum distributions of ^{18}C, and ^{16}C after one-neutron removal from ^{19}C, and ^{17}C, respectively (from ref. [11].

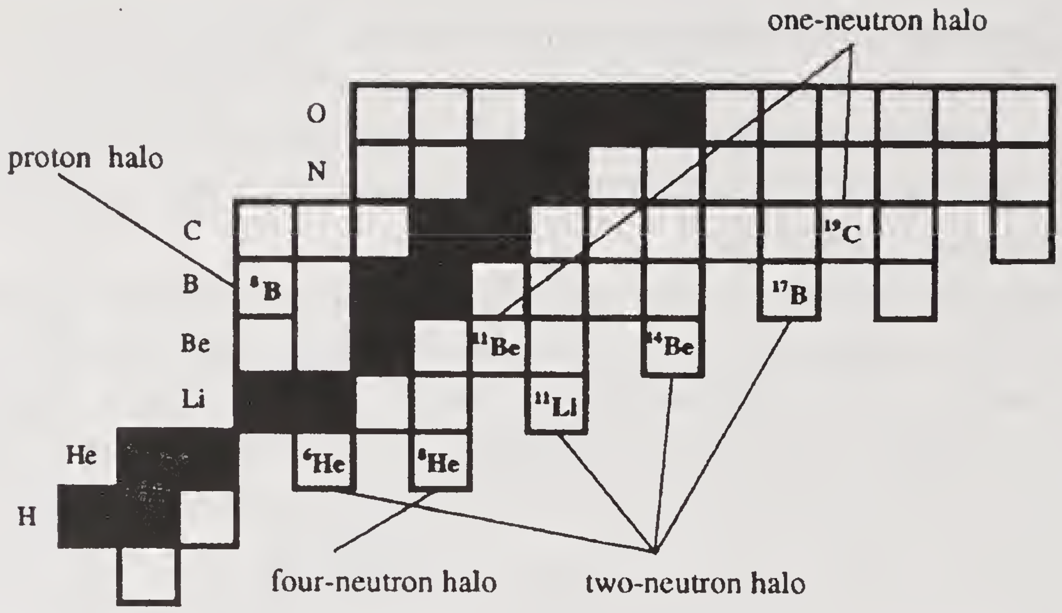

Figure 6. Chart of isotopes up to element $Z = 8$. Nuclei for which a halo structure was confirmed experimentally are indicated.

distributions of tightly bound nuclei, thus confirming an extended neutron distribution in both nuclei. The significant difference in the width of the distributions is attributed to the difference in the separation energies of the valence neutron, and thus a pronounced halo structure is established for the ^{19}C nucleus. Figure 6 displays the latest compilation of nuclei for which the halo structure has been confirmed by the various experimental information. Besides one-, two-, and four-neutron halos on the neutron-rich side, there is meanwhile also evidence for proton halos.

In summary we conclude that the assumed picture on the structure of halo nuclei, established after the finding of the large interaction radii (see above), was qualitatively confirmed by various experiments. Halo nuclei are thus characterized by large interaction cross sections, weak binding of the valence nucleon(s), and narrow momentum distributions of the reaction products after fragmentation. On the other hand it should be pointed out, that a more quantitative information on the radial structure and the size of halo nuclei from such experiments is to a considerable extent limited by the limited knowledge of the underlying reaction mechanism and dynamics of the reactions used. Hence, systematic uncertainties in the determination of the matter radii appear due to uncertainties created by effects like the interaction of the target with the nuclear constituents, by the final state interaction of the knocked-out fragments with the remaining system, etc.. Thus, in order to obtain more quantitative information on the radial shape of halo nuclei and the nuclear matter radii, the method of elastic proton scattering at intermediate energy was recently applied, as will be discussed in the following section.

3. Nuclear matter distributions of halo nuclei from elastic proton scattering at intermediate energy

Proton nucleus elastic scattering at intermediate energies was proved (for the case of stable nuclei) to be a well suited method for obtaining accurate and detailed information on nuclear matter distributions of nuclei [12]. This method was recently applied at GSI Darmstadt for the first time for the investigation of exotic nuclei. The advantage of such experiments as compared to investigations at considerably lower incident energies (see for example [13,14]) is, that for intermediate energies, available for exotic beams at GSI, proton-nucleus elastic scattering can be described accurately by the diffractive multiple scattering theory which relates the measured cross section to the nuclear matter distribution in a rather unambiguous way [12]. Furthermore, as theoretical considerations have shown [15,16], proton scattering in the region of small momentum transfer is sensitive to the halo structure of nuclei. Thus, besides the precise determination of the nuclear matter radius, information on the shape of the radial distribution of nuclear matter of halo nuclei can be obtained. Both quantities are fundamental quantities of nuclei, and therefore of large interest for our understanding of the structure of halo nuclei, and for an effective test of respective theoretical model calculations.

Differential cross sections for elastic proton scattering at small scattering angles were measured at GSI Darmstadt at energies around 700 MeV/u in inverse kinematics for the neutron-rich helium isotopes ^{6}He, ^{8}He [17,18], and recently also for the neutron-rich lithium isotopes ^{8}Li, ^{9}Li, and ^{11}Li. The present contribution will mainly concentrate on data on the helium isotopes for which the data analysis was completed recently [16]. Secondary ^{4,6,8}He beams (the p ^{4}He cross section was measured for a consistency check of the method) were produced with incident energies of 699 MeV/u, 717 MeV/u, and 674 MeV/u, respectively, by fragmentation of ^{18}O ions from the heavy-ion synchrotron SIS (see figure 2), impinging on a beryllium target, and were isotopically separated by the fragment separator FRS [19]. The separation method is displayed schematically in figure 7 for the production of a ^{6}He beam as an example. In the first section of the FRS the produced isotopes are separated according to their magnetic rigidity, resulting in a selection

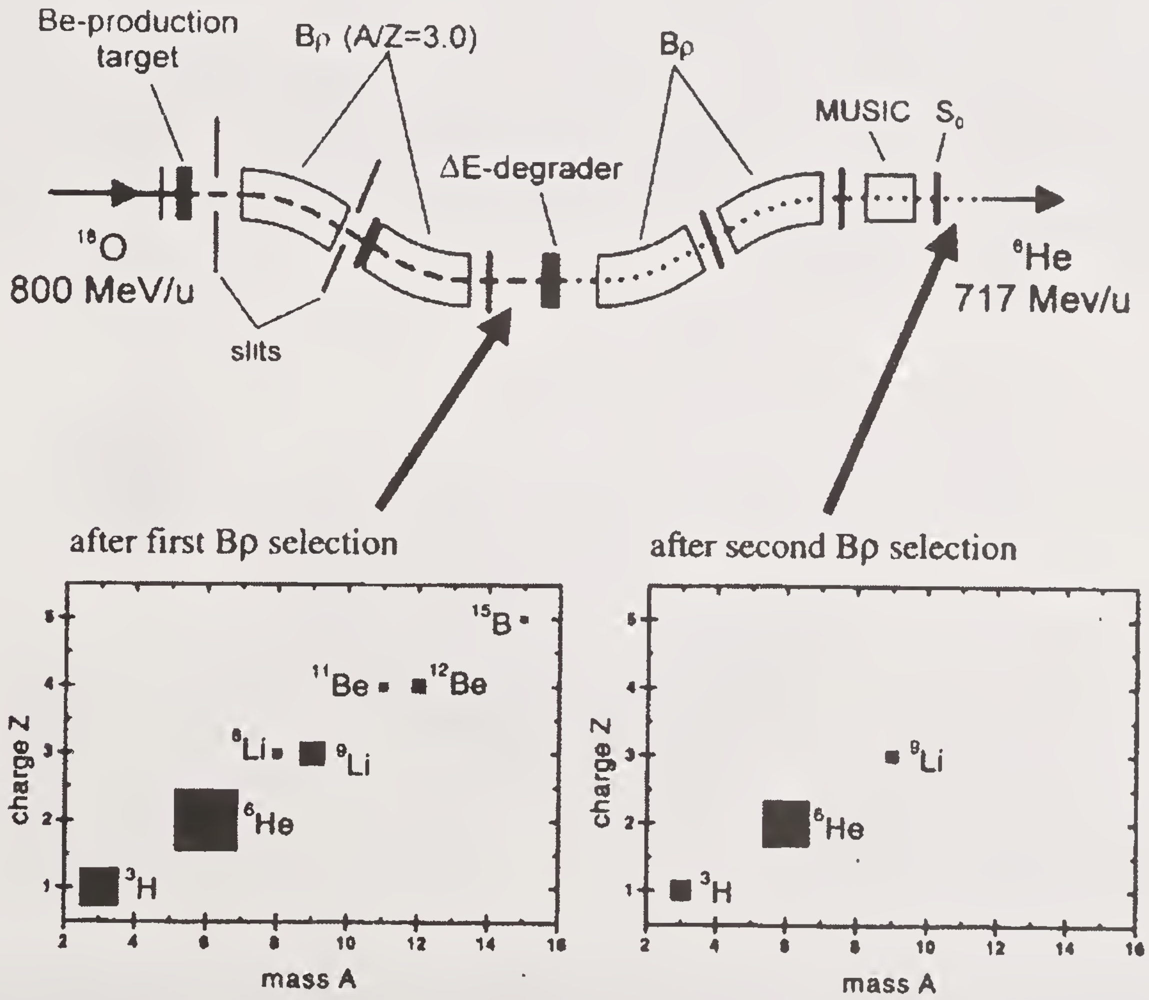

Figure 7. The operation principle of the fragment separator FRS is displayed for the example of the separation of a ^{6}He beam after bombardment of a Be production target with a ^{18}O beam (upper part). The resulting isotope distributions after the first and the second $B\rho$ selection are shown in the lower part of the figure.

of all isotopes with $A/Z \approx 3.0$ (see lower part of figure 7). The separation power was considerably enhanced by inserting an achromatic energy degrader at the dispersive focal plane. The thickness of the degrader in terms of the range of the beam particles was about 0.05, resulting in a rather clean ^{6}He beam after the second separator stage. The intensity of the secondary beams was about 10^3 sec^{-1} in all cases.

The experimental setup is displayed in figure 8 (for more details on the technical design and experimental procedure see also refs [18,20]). The relatively low secondary beam intensities for isotopes close to the drip line demand for a thick effective hydrogen target, and for a large solid angle detector for the recoil protons. In order to meet these experimental conditions the hydrogen filled time-projection ionization chamber IKAR was used, which serves simultaneously as a gas target and a detector. It was developed at the St. Petersburg Nuclear Physics Institute (PNPI), Gatchina, and was originally used for studying small angle hadron elastic scattering [21]. IKAR ensures a high H_2 target thickness (about 3×10^{22} protons/cm^2), and has a 2π acceptance in azimuthal angle for recoil proton registration. It operates at 10 bar pressure of hydrogen and consists of 6 identical modules. One of these modules is shown schematically in figure 9, together with an illustration of a typical scattering event between a projectile nucleus and a proton from the chamber gas. Each module contains an anode plate, divided into two rings (A and B), a cathode plate and a grid, the whole setup being rotationally symmetric with respect to the beam axis. The amplitude and the drift time analysis of the signals from the electrodes, registered by flash ADCs, provide the energy T_R of the recoil proton, or its energy loss ΔT_R in case it leaves the active volume, the scattering angle Θ_R of the recoil proton, and the coordinate z of the interaction point in the grid–cathode space. The obtained energy and angular resolutions are $\Delta E \leq 90$ keV, and $\Delta\Theta_R \leq 0.6°$, respectively, and the coordinate z is determined with an accuracy of $\Delta z \leq 100$ μm. The detector is able to operate at secondary beam intensities up to about 10^4 sec^{-1}. The scattering angle Θ_s for the helium projectiles was determined by a tracking detector consisting of 4 two-dimensional multiwire-proportional chambers (see figure 8). In addition, the scintillation counters S1, S2, S3, and VETO were

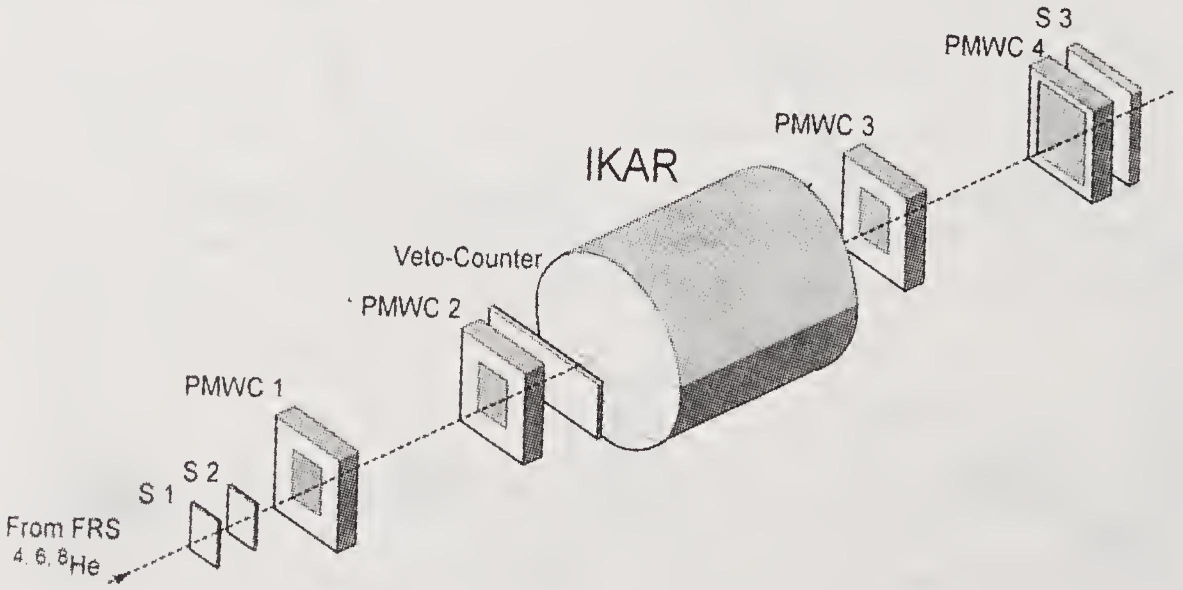

Figure 8. Schematic view of the experimental setup. The central part shows the hydrogen filled ionization chamber IKAR which serves simultaneously as a gas target and a detector system for recoil protons. Four multiwire proportional chambers (PMWC 1-4) determine the scattering angle of the projectile. Scintillation counters (S1-S3, VETO) were used for trigger and for particle identification.

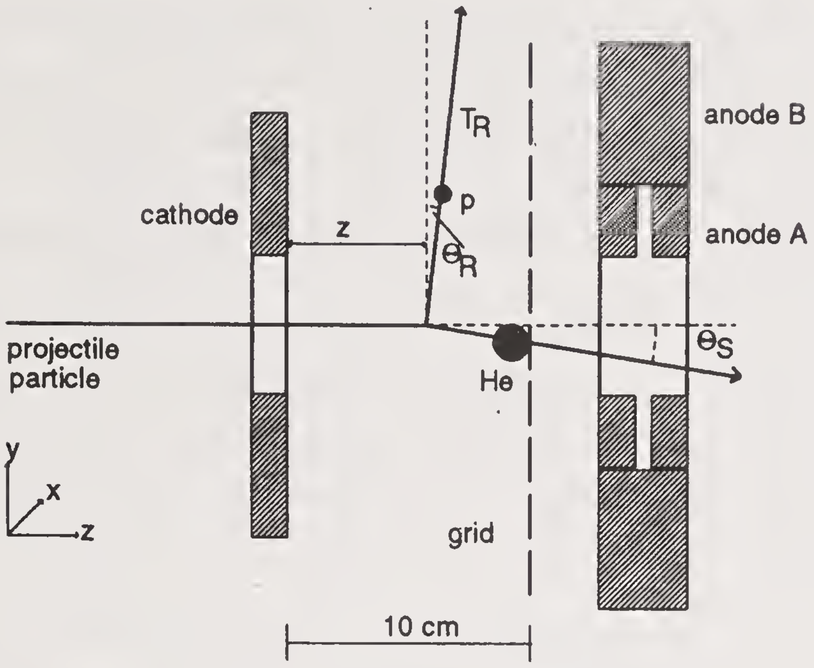

Figure 9. Schematic view of one of the six ionization chamber modules of IKAR.

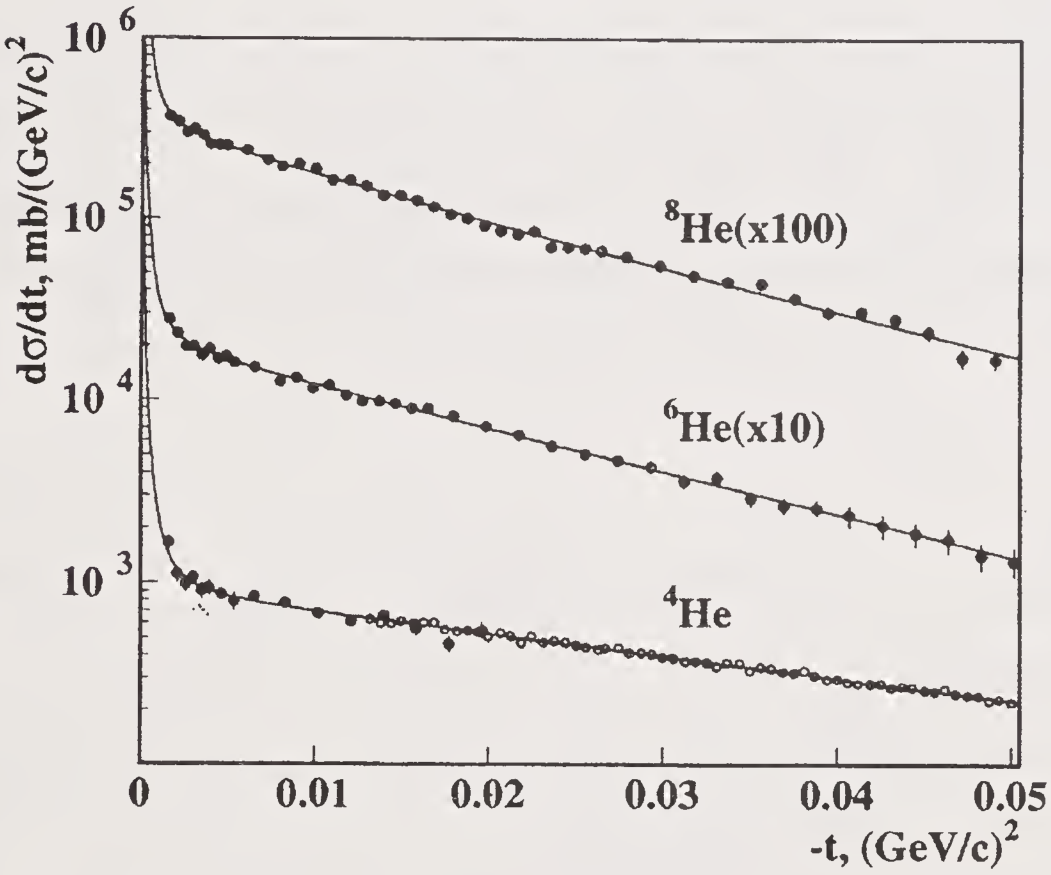

Figure 10. Absolute differential cross sections $d\sigma/dt$ versus the four momentum transfer squared $-t$ for p^4He, p^6He and p^8He elastic scattering at incident energies of 699 MeV/u, 717 MeV/u, and 674 MeV/u, respectively, obtained from the present experiment (full dots). Open dots show the data of ref. [22]. Full lines are the result of fits using the GH parametrization for the nuclear density distributions.

used for triggering, and for the identification of the incident and scattered beam particles via time-of-flight and dE/dx measurements.

The resulting cross sections are displayed in figure 10. Plotted error bars denote statistical errors only. The absolute normalization obtained is estimated to be accurate within ± 3%. The measured p^4He cross section is in excellent agreement with previous data [22], which were obtained in direct kinematics.

To derive information on the nuclear density distributions of ^{6}He and ^{8}He from the measured cross sections the Glauber multiple scattering theory was applied. Calculations were performed using the basic Glauber formula [12] for proton–nucleus elastic scattering, and taking experimental data on proton–proton and proton–neutron scattering as an input. For the analysis of the present experiment [16,17] various parametrizations of the nuclear density distributions of ^{4}He, ^{6}He and ^{8}He were used as an input for the Glauber calculations, and the parameters were varied in order to obtain a best fit to the experimental cross sections. All nucleon distributions deduced, as well as the resulting root mean square radii R_m, refer to point nucleon distributions. Two parametrizations of the total matter distribution $\rho_m(r)$ were used which do not make a difference between core and valence nucleons, namely a symmetrized Fermi (SF) distribution, and a Gaussian with a 'halo' (GH) (for details see ref. [16]). Furthermore two parametrizations were applied which assume that the ^{6,8}He nuclei consist of an α core and of 2(4) valence neutrons for ^{6}He (^{8}He). Here, a Gaussian distribution for the core, and either a Gaussian (GG) or a $1p$-shell harmonic oscillator-type density (GO) for the valence neutrons were used.

The experimental data are equally well described independent of the density parametrization used, with a reduced χ^2 around unity. Solid lines in figure 10 show the GH case as an example. The deduced nuclear matter density distributions $\rho_m(r)$ for ^{6}He and ^{8}He are displayed in figure 11 in comparison with the one for ^{4}He. The results for all four parametrizations used agree reasonably well within small errors (for a detailed discussion see ref. [16]) over a wide range of the radius parameter r. For both neutron-rich He isotopes, ^{6}He and ^{8}He, rather extended matter distributions were obtained, the matter densities decreasing much slower with the radius than the one for ^{4}He. This result is interpreted as a clear evidence for the existence of a significant neutron halo in ^{6}He and ^{8}He.

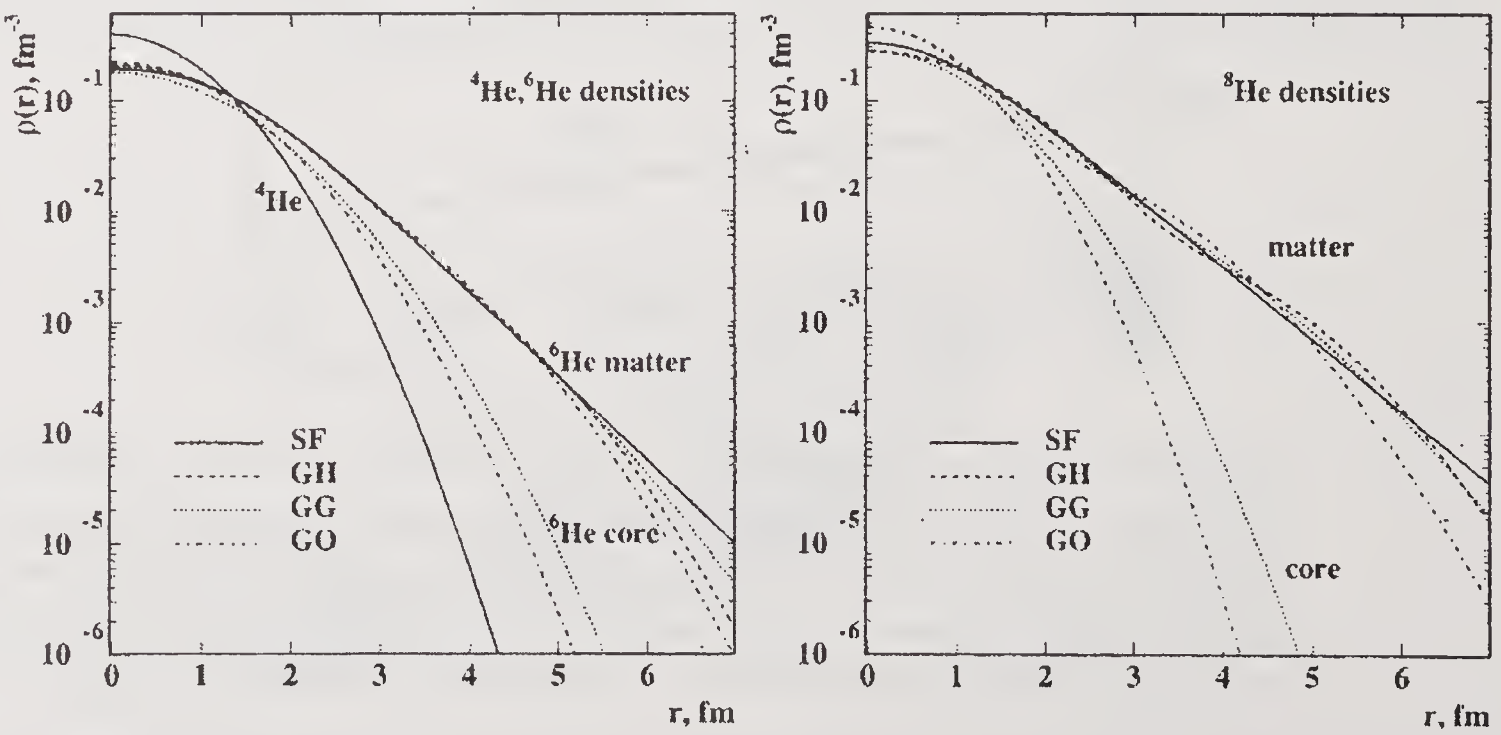

Figure 11. Nuclear core and nuclear matter density distributions $\rho(r)$ for ^{6}He (left side) and for ^{8}He (right side) obtained for the different parametrizations applied (for notations see text). For a comparison the nuclear matter density distribution for ^{4}He is also plotted (left side). Curves are normalized to the number of nucleons.

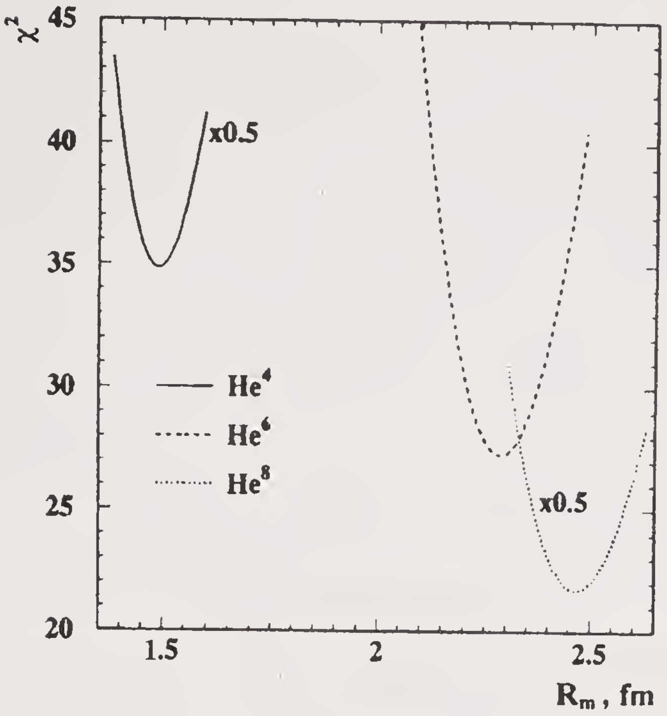

Figure 12. x^2 values versus the matter radius R_m, obtained from a fit to the data for ^{4}He, ^{6}He and ^{8}He using the parametrization GH.

To demonstrate the sensitivity of the data on the matter radius R_m the χ^2 dependence of the fitting parameter R_m is displayed in figure 12 for the example of the analysis with the parametrization GH. Both parametrizations (SF and GH) applied for ^{4}He have yielded identical values R_m = 1.49 ± 0.03 fm. In the case of ^{6}He and ^{8}He the values obtained for the matter radii R_m from the four parametrizations mutually agree within small errors (±0.02 fm). This demonstrates that the results of the radii are quite independent of the model assumptions considered. The final average values are R_m = 2.30 ± 0.07 fm for ^{6}He, and R_m = 2.45 ± 0.07 fm for ^{8}He (with total errors including systematical uncertainties). The values determined for the core radii are R_c = 1.88 ± 0.12 fm for ^{6}He, and R_c = 1.55 ± 0.15 fm for ^{8}He.

The present data on nuclear matter radii from elastic proton scattering cross sections may be compared to corresponding data deduced from the total interaction cross sections, a method which was discussed in §2 of this contribution. Such a comparison is of special interest, as both methods to determine nuclear matter radii are independent. The results from the present experiment are in close agreement with the accepted values R_m = 2.33 ± 0.04 fm for ^{6}He and R_m = 2.49 ± 0.04 fm for ^{8}He from Tanihata *et al* [25]. However, the data on the ^{6}He matter radius from the total interaction cross sections were again under discussion recently, as a re-analysis [26,27] of the data from ref. [2] resulted in two new values for R_m, which both disagree with the radius from the present experiment. In figure 13 the results on the matter radius of ^{6}He from various analysis [23–27] over the years, which were all based on the same experimental data set from Tanihata *et al* [2], are displayed (black dots). For comparison the result of the present experiment is also shown in figure 13 (open square). It may be concluded from figure 13 that the error bars given for the various values deduced from analysing the data on the total interaction cross section do in some cases not include, or underestimate the systematical uncertainties. At present this topic is still under discussion.

Besides the determination of phenomenological nucleon density distributions and their parameters, the present data allow also a sensitive test of theoretical model calculations on the structure of neutron-rich nuclei. As an example, the results of microscopic calculations performed in the framework of the refined resonating group model (RRGM) [28], using as

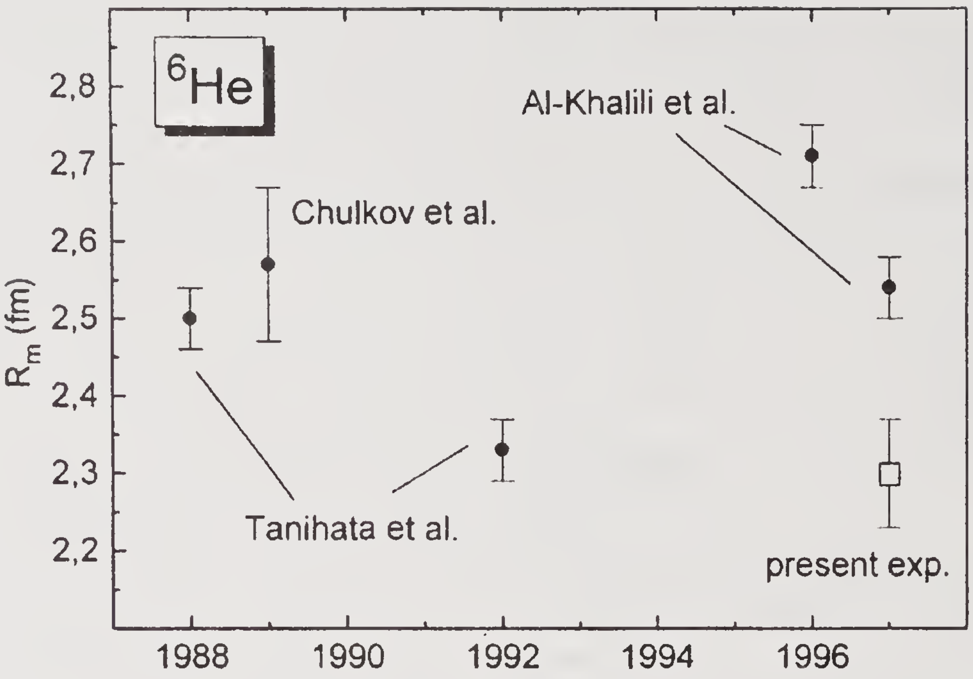

Figure 13. Compilation of values for the nuclear matter radius of ^{6}He, deduced from various analysis [23–27], which were all based on the same data set on the total interaction cross sections [2] (black dots). For comparison the value obtained from the present experiment is also shown (open square).

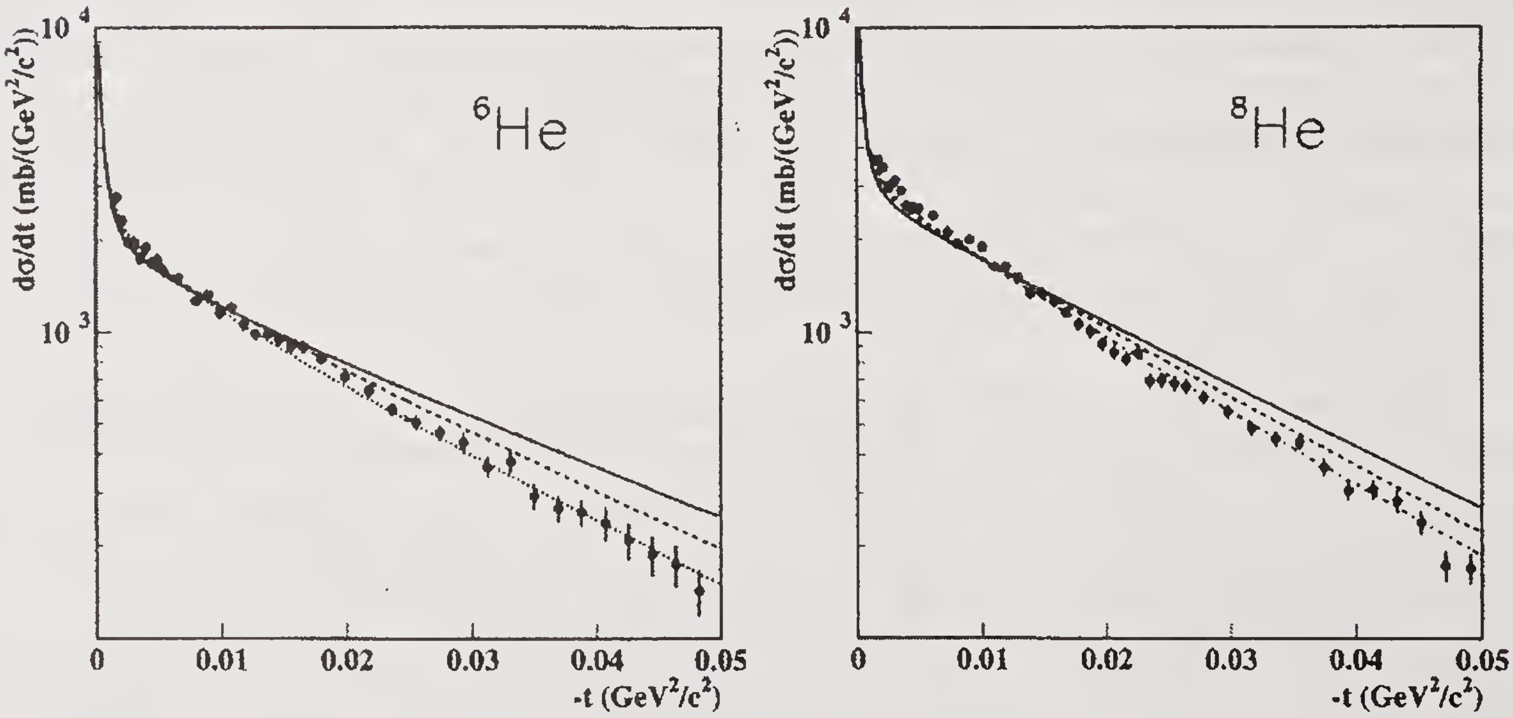

Figure 14. Differential cross sections for p^6He scattering (left side) and p^8He scattering (right side) obtained from the present experiment are compared with calculated cross sections on the basis of nuclear matter distributions resulting from microscopic RRGM calculations with various effective nucleon–nucleon forces, namely CS (solid lines), SZ (dashed lines), SZ-V2 (dotted line), modified SZ-V2 (dashed-dotted line). For notations see text.

an input various effective nucleon–nucleon forces without additional free parameters, are compared with the experimental data. For that purpose, the nucleon density distributions obtained from the theoretical RRGM calculations [29,30] for the different helium isotopes investigated were used as an input for Glauber calculations, as described above. Finally the obtained 'theoretical cross sections' were compared with the experimental data, thus allowing for a test of the nucleon–nucleon force used. In figure 14 the experimental data on ^{6}He and ^{8}He are displayed in comparison with the corresponding results of RRGM calculations [29,30] performed with the effective nucleon–nucleon force introduced by Csoto (CS), and various modifications of the effective nucleon–nucleon force introduced by Stöwe and Zahn (SZ) (for details see refs [20,29,30]). For both isotopes, the SZ-V2 force, which includes (as compared to the original version SZ-2) the central force in the odd-parity singlet and triplet states of the nucleon–nucleon two-body force, yields the best description of the experimental data. In the case of ^{8}He the SZ-V2 force had to be modified [30] (inclusion of a realistic hard core) to obtain a reasonable agreement with the experimental data.

In figure 15 (left side) the corresponding theoretical nuclear matter densitiy distributions are, for the case of ^{6}He, compared with the distribution deduced from the present experiment for the GG parametrization (see above). For $r < 5$ fm, the best agreement is obtained for the SZ-V2 force which gave also the best agreement for the cross sections. There seems to be a general trend of these calculations to exhibit, as compared to the experimental result, an enhanced tail for very large radii ($r > 5$ fm). This trend is in agreement with calculations from ref. [26], but in disagreement with a recent calculation using the boson dynamic-correlation model [31]. The result of this calculation is also shown in figure 15 (right side). A remarkably good agreement with the experimentally determined density distribution over the whole range of the radius parameter r is obtained.

In an experiment performed very recently at GSI Darmstadt data on elastic proton scattering from neutron-rich lithium isotopes ^{8}Li, ^{9}Li and ^{11}Li were taken using the same experimental method. At present the data analysis is in progress. From the statistics

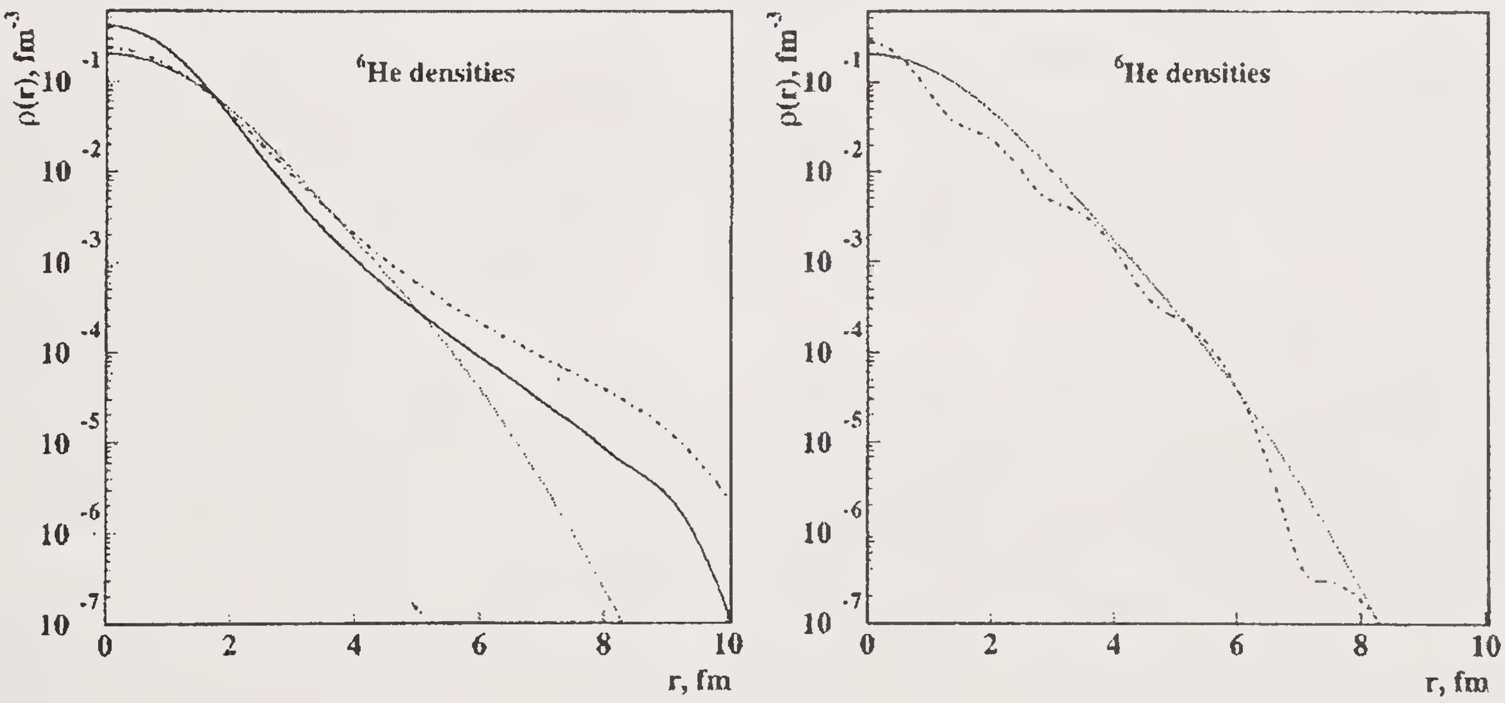

Figure 15. On the left side the nuclear matter density distribution for ^{6}He, obtained from microscopic RRGM calculations with the effective nucleon–nucleon forces CS (solid line) and SZ-V2 (dashed-dotted line), are compared with the density distribution deduced from the present experiment for the GG parametrization (dotted line). On the right side of the figure, again the distribution deduced from the present experiment (dotted line) is compared with the result of a calculation using the boson dynamic-correlation model [31] (dashed-dotted line).

obtained we expect a similar, or even better sensitivity on the nuclear matter distributions of ^{8,9,11}Li as compared to the case of the helium isotopes.

4. Investigation of few-nucleon transfer reactions

The investigation of light ion induced few-nucleon transfer reactions with exotic beams in inverse kinematics opens potentially a large spectrum of physics interest. The experimental scenario for such measurements is essentially different from the one for elastic and inelastic scattering. This is mainly due to the fact that incident energies of the order of 5 – 20 MeV/u are required to fulfill the momentum matching criterion for the transferred particle(s). For much higher energies the momentum mismatch for the transferred nucleon in projectile and target will lead to a loss of cross section and l-selectivity, the latter needed for an unambiguous identification of the populated states. Such experiments are most favourably performed at the new generation of radioactive beam facilities presently under construction or just starting operation (for example: SPIRAL at GANIL, France, REX-ISOLDE at CERN, Switzerland, or PIAFE at Munich, Germany, etc.), which provide good quality low energy exotic beams. Therefore the present contribution mainly concentrates on the future perspectives and possibilities (for a more detailed discussion of this topic see also [32]).

The investigation of few-nucleon transfer reactions (for example (d,p), (p,d), (p,t), etc.) allows the population and spectroscopy of single particle- and single hole-states, as well as two particle (hole)-states, which is of particular interest in the region near closed shells. The location and identification of such states and the determination of their spectroscopic strength provides a sensitive test of the nuclear shell model in the region far off stability. It should be pointed out, that such studies are complementary to decay spectroscopy, which does not allow to determine spectroscopic factors. The investigation of two particle (hole)-states in the vicinity of doubly closed-shell nuclei opens the possibility to deduce matrix elements of the two-body residual interaction, which is an important input for microscopic calculations. Many new combinations of shell model orbits become available by investigating nuclei near the doubly magic ^{132}Sn nucleus. Moreover the spectroscopy (identification of energy levels and determination of spectroscopic factors) of neutron resonances by the (d,p)-reaction on r-process nuclei in the $A \approx 80$ and $A \approx 130$ regions (near the neutron shell-closures) may yield important data, necessary to explain the observed solar isotopic abundance pattern and to give constraints on neutron density and temperature for the astrophysical scenario.

With respect to neutron-rich light halo nuclei information on neutron pair-correlations may be obtained from the comparison of cross sections for one- and two-neutron pickup reactions, whereas neutron-stripping reactions may allow spectroscopy at or even beyond the drip line.

As the intensities of secondary exotic beams are limited, all these experiments require thick effective targets and large solid angle detector systems. Therefore we propose to use the concept of a time-projection ionization chamber as active target, similar to the one discussed in §3, also for experiments with low-energy exotic beams. Of course such a design has to be adjusted to the specific experimental conditions. In figure 16 a design for such a device is displayed together with the experimental situation for the example of a (p,t) reaction on ^{11}Li. Due to the relatively high specific energy loss of the beam particles in the entrance window, its thickness, and therefore the operating pressure, has

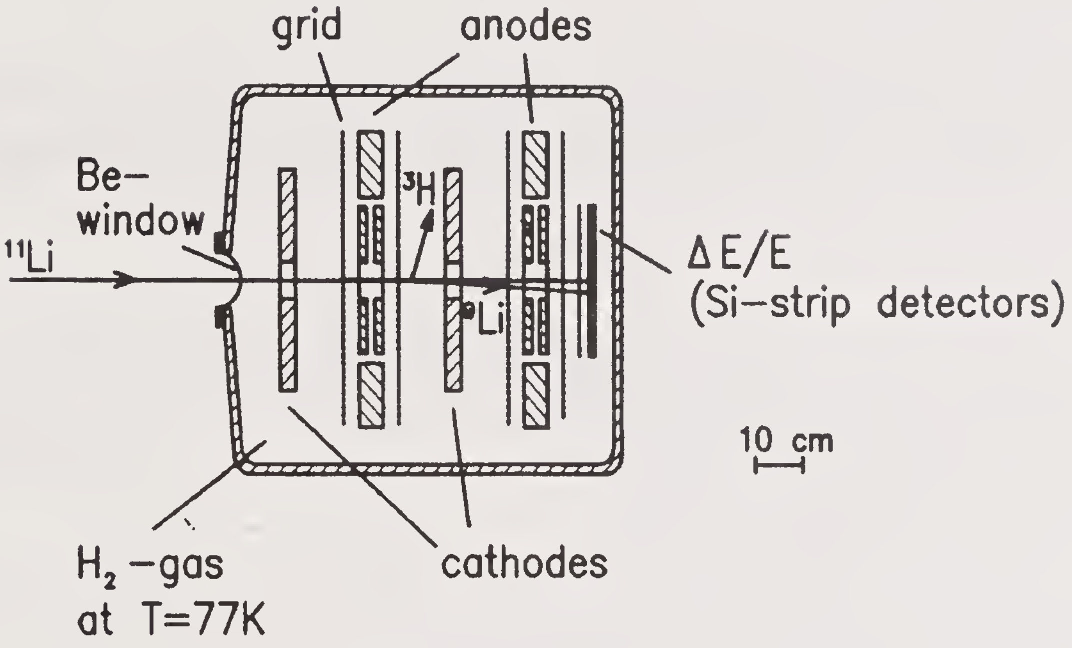

Figure 16. Schematic view of a design for a time-projection ionization chamber as active target for the investigation of direct reactions with exotic beams at low incident energies around 5–20 MeV/u.

to be limited to about 1–2 bar. In order to ensure sufficient target thickness and stopping power to stop the target like particles, the whole setup is operated at LN_2 temperature. The operating principle and the readout procedure will be similar to that discussed in §3 (see also figure 9). In summary, such a device will provide a high target thickness up to 10–20 $\mathrm{mg/cm^2}$ of pure hydrogen, a large detector solid angle (angular acceptance: $20° < \Theta < 160°$ over the whole azimuthal angle), and good energy and angular resolution (see §3). Particle identification is provided by $\Delta E/E$ techniques due to a separated anode (for the target-like particles), and a forward $\Delta E/E$ silicon strip telescope (for the projectile-like particles). This setup may be used for all kinds of direct reactions with low energy secondary beams and with H_2, D_2, ^{3}He, ^{4}He targets. Due to the increase of energy loss in the entrance window and the gas for very heavy ions its application will be limited to light beams up to $Z \approx 15 - 20$.

For experiments with heavier beams more conventional setups using large solid angle arrays of silicon strip detectors or PIN-diodes and solid targets (for example CH_n, CD_n or deuterated Ti-foils) may be used. It has been demonstrated in a prototype experiment [33], where the $d(^{136}\mathrm{Xe}, p)^{137}\mathrm{Xe}^*$ reaction was investigated at $E = 5.9$ MeV/u with stable beam in inverse kinematics, that such an experimental setup will be well suited, and will provide sufficient energy resolution ($\Delta E < 80$ keV) for such measurements with exotic beams.

For the identification of heavy projectile-like reaction products in the outgoing channel the concept of calorimetric low temperature detectors provides considerable advantage over conventional detection schemes, and is therefore foreseen, for example, for the VAMOS spectrometer, presently under construction for the SPIRAL facility at GANIL, France. For such detectors, operated at temperatures around $T \approx 1.5$–2 K, excellent energy resolutions of $\Delta E/E \approx 1 - 2 \cdot 10^{-3}$ were achieved [34,35] even for very heavy ions like ^{238}U. Thus their use for the isotope mass identification via a TOF/energy measurement may allow the separation of masses up to the heaviest isotopes, and replace the standard TOF/$B \cdot \rho$ method with solid angle limiting magnet spectrometers.

Acknowledgements

The author is indebted to G D Alkhazov, M Mutterer and S R Neumaier for many stimulating discussions, and to W Falkenberg for the help in preparing the manuscript.

References

[1] I Tanihata *et al*, *Phys. Rev. Lett.* **55**, 2676 (1985)
[2] I Tanihata *et al*, *Phys. Lett.* **B160**, 380 (1985)
[3] I Tanihata, *Nucl. Phys.* **A488**, 113c (1988)
[4] K Riisager, *Rev. Mod. Phys.* **66**, 1105 (1994)
[5] P G Hansen *et al*, *Ann. Rev. Nucl. Part. Sci.* **45**, 591 (1995)
[6] I Tanihata, *Prog. Part. Nucl. Phys.* **35**, 505 (1995)
[7] I Tanihata, *J. Phys.* **G22**, 157 (1996)
[8] E Arnold *et al*, *Phys. Lett.* **B197**, 311 (1987)
[9] E Arnold *et al*, *Phys. Lett.* **B281**, 16 (1992)
[10] H Emling, *J. Phys.* **G24**, 1561 (1998)
[11] T Baumann *et al*, *Phys. Lett.* **B439**, 256 (1998)
[12] G D Alkhazov *et al*, *Phys. Rep.* **42**, 89 (1978)
[13] A A Korsheninnikov *et al*, *Nucl. Phys.* **A617**, 45 (1997)
[14] M D Cortina-Gil *et al*, *Phys. Lett.* **B401**, 9 (1997)
[15] G D Alkhazov *et al*, *Pisma ZhETF* **55**, 377 (1992); *JETP Lett.* **55**, 379 (1992)
[16] G D Alkhazov *et al*, *Nucl. Phys.* (1999) to be published
[17] G D Alkhazov *et al*, *Phys. Rev. Lett.* **78**, 2313 (1997)
[18] S R Neumaier *et al*, *Nucl. Phys.* (1999) to be published
[19] H Geissel *et al*, *Nucl. Instr. Meth.* **B70**, 286 (1992)
[20] S R Neumaier *et al*, Proc. Int. Conf. on Exotic Nuclei and Atomic Masses, ENAM, Arles, France, *Edit. Front.* **227** (1995)
[21] A A Vorobyov *et al*, *Nucl. Instr. Meth.* **119**, 509 (1974)
[22] O G Grebenjuk *et al*, *Nucl. Phys.* **A500**, 637 (1989)
[23] I Tanihata *et al*, *Phys. Lett.* **B206**, 592 (1988)
[24] L V Chulkov *et al*, *Europhys. Lett.* **8**, 245 (1989)
[25] I Tanihata *et al*, *Phys. Lett.* **B289**, 261 (1992)
[26] J S Al-Khalili *et al*, *Phys. Rev.* **C54**, 1843 (1996)
[27] J S Al-Khalili *et al*, *Nucl. Phys.* **A616**, 418c (1997)
[28] H M Hofmann, *Lecture Notes in Physics* **273**, 243 (1987)
[29] J Wurzer *et al*, *Phys. Rev.* **C55**, 688 (1997) and references therein
[30] J Wurzer, PhD thesis, University of Erlangen (1997)
[31] M Tomaselli *et al*, (1999) to be published: GSI scientific report 1998
[32] P Egelhof, *Proc. of the Int. Workshop on Research with Fission Fragments*, Benediktbeuren, 1996, World Scientific, ISBN 981-02-3140-7, p. 178 (1997)
[33] G Kraus *et al*, *Z. Phys.* **A340**, 339 (1991)
[34] A V Kienlin *et al*, *Nucl. Instr. Meth.* **A368**, 815 (1996)
[35] H J Meier *et al*, *Nucl. Phys.* **A626**, 451c (1997)

Alpha particle evaporation as a probe for dynamical deformations

I M GOVIL
Department of Physics, Panjab University, Chandigarh 160 014, India

Abstract. Evaporation of alpha particles in heavy ion reactions followed by fusion has proved to be a powerful probe for the properties of emitting nuclei. Detailed experimental data and different model calculations allow us to probe whether the foundation of the statistical model holds for the compound nucleus populated in these reactions. It has been observed that in the case of composite nuclei at moderate energies and angular momenta, evaporation spectra are well explained in terms of the standard statistical model CASCADE code employing optical model transmission coefficients in the description of particle evaporation. However, it has been observed that experimental particle spectra from heavy ion induced fusion reactions are no longer consistent with the predictions of such models. It has been predicted by some authors that in these systems the emission barriers are lower than those expected from optical model transmission coefficients calculated for the respective inverse absorption channels. Some authors claim that these spectra may be well explained in terms of the statistical model incorporating only spin dependent level density and without lowering the emission barriers. The field is not yet free from the controversies. Furthermore, the assumption of the very short formation time in statistical model analysis is one extreme of the general evolution process which in fact is a continuous relaxation process, leading to the composite system from the entrance channel to the equilibrated configuration. Recent dynamical description of heavy ion collisions do not support this assumption in many cases. In symmetric entrance channels and for collisions where centre of mass energy is well above the Coulomb barrier, formation time can be even larger than decay time of the resulting composite system. In such cases realistic approach will be to couple the dynamical evolution of the intrinsic excitation of the composite system to a time dependent statistical model calculation. The above question has been addressed in the light of the alpha particle spectra taken in coincidence with the evaporation residues for the asymmetric ^{28}Si + ^{51}V and the symmetric ^{28}Si + ^{27}Al systems. The experimental data have been interpreted in the framework of dynamical trajectory model calculations.

Keywords. Proton and alpha spectra; dynamical deformations; statistical model.

PACS Nos 25.70.Gh; 24.60.Dr

1. Introduction

Heavy ion reactions are routinely used to produce composite nuclei with large angular momenta and excitation energies. Over the past few years, there has been a strong interest directed towards inferring the statistical properties of these hot, rapidly rotating nuclei. Statistical-model reaction simulations are used in conjunction with experimental data in order to infer these properties. High excitation energy implies that the nucleus de-excite by emitting several particles and gamma rays so that the decay pattern involves a number of different paths. High spins are expected to favor the emission of complex clusters which are more effective than nucleons in removing the angular momentum. While the statistical model has been used for many decades to analyse a variety of observables related to compound nucleus decay [1], the successful description of light particle emission remains essential for evaluating the validity of the model and the choice of parameters within it. Studies of evaporated particle energy spectra yield direct information about the main statistical model ingredients, the nuclear level densities, and barrier penetration probabilities. Determination of these properties has applications to current research into fusion and fission dynamics which often depends on the statistical model in some form for comparison to data.

Over the past decade, there have been several claims of serious discrepancies between standard statistical model predictions and measured light charged particle energy spectra [2–13]. Measured light charged particles have been characterised as having lower average energies than predicted. Several papers reported that these nuclei are subjected to lower emission barriers as compared to inverse absorption channels due to large deformations at these higher excitation energy and angular momentum [2–10]. Some other authors claim that these spectra may be well explained in terms of a statistical model incorporating only a spin dependent level density and without lowering the emission barriers [10–13]. Possible deficiencies of an ‘average’ one step [6,7] or two step decay [12] approximation employed in some statistical model codes were pointed out, as well as the need for proper treatment of level density for expected rotating liquid drop model (RLDM) deformations [5,8,13,14].

Furthermore, the assumption of a very short formation time in statistical model is one extreme of the general evolution process which in fact is a continuous relaxation process, leading to the composite system from the entrance channel to the equilibrated configuration. Recent dynamical descriptions of heavy ion collisions do not support this assumption in many cases [15,16]. In symmetric entrance channels and for collisions where center of mass energy is well above the Coulomb barrier, formation time can be even larger than decay time of the resulting composite system. In such cases a realistic approach will be to couple the dynamical evolution of the intrinsic excitation of the composite system to a time dependent statistical model calculation. Such calculations have been reported where the dynamical part is calculated using a realistic macroscopic description of the nucleus-nucleus collision based on the concept of one body dissipation [17–19]. However in these calculations the structure or shape of the forming compound nucleus at each time stage in terms of its level density, and transmission coefficients for particle emissions have not been considered adequately. This can result in a major discrepancy in prediction for all particle channels, if the formation time is comparable to or longer than the decay time of the eventually formed compound nucleus. Recently some authors have suggested the possibility of the dynamical effects on the de-excitation process [20,21].

A simplistic attempt to describe the collision has been based on the schematic picture of the collision process in terms of the topology of the entrance channel potential. If the resultant force is attractive, the collision will lead to fusion. Calculations become elaborate if the dynamics of the process is considered explicitly along the whole reaction path, through the multi-dimensional space of relevant collective degrees of freedom of the nuclear system by incorporating dissipation [22]. A more correct approach will be to divide the total decay time into two parts: (i) decay during the formation of the equilibrated system, and (ii) decay of the equilibrated compound nucleus. However, results from this approach also become qualitative as noted by Thoennessen *et al* [19], since the statistical model is being applied to the non-equilibrated system also.

In the present work, we have measured the alpha particle energy spectra in coincidence with evaporation residues for the ^{79}Rb* compound system, produced in the heavy ion fusion reaction with great experimental care. Statistical model and dynamical calculations have been used in an attempt to interpret the experimental data.

2. Experiment

The experiment was performed with the 15UD Pelletron at NSC, New Delhi, India. The 140 MeV ^{28}Si beam was used to bombard a 1000μg/cm^2 spectroscopically pure ^{51}V foil as target. The experiment was done using the Heavy Ion Reaction Analyser (HIRA) (recoil mass separator). The evaporation residues were separated from the beam and were detected by the focal plane detector at different angles of HIRA to take into account the recoil due to the α-particle emission. Figure 1 shows the experimental set-up. High quality particle spectra were obtained at different laboratory angles using $\Delta E - E$ (40 μm–5mm) detector telescopes (T_1 and T_2) with proper precautions regarding the energy calibration, and a very good vacuum of roughly 10^{-7} Torr in the scattering chamber so as to avoid oxygen and carbon built-up on the target. Light charged particle spectra were taken in coincidence with the evaporation residues in order to discriminate the particle evaporation from various mechanisms viz. evaporation from projectile-like nuclei. The compound nucleus ^{79}Rb* was formed at an excitation energy of 85 MeV with $l_{\max} = 56\hbar$.

3. Analysis

3.1 Statistical model calculations

The statistical computer code CASCADE [23] was used to perform the theoretical calculations, which assumes the reaction to occur in two steps. First the formation of the compound nucleus and second the statistical decay of the equilibrated system. There are two aspects of the physics which govern the flow of an evaporation cascade, the spin dependent level density defining the available phase space and the

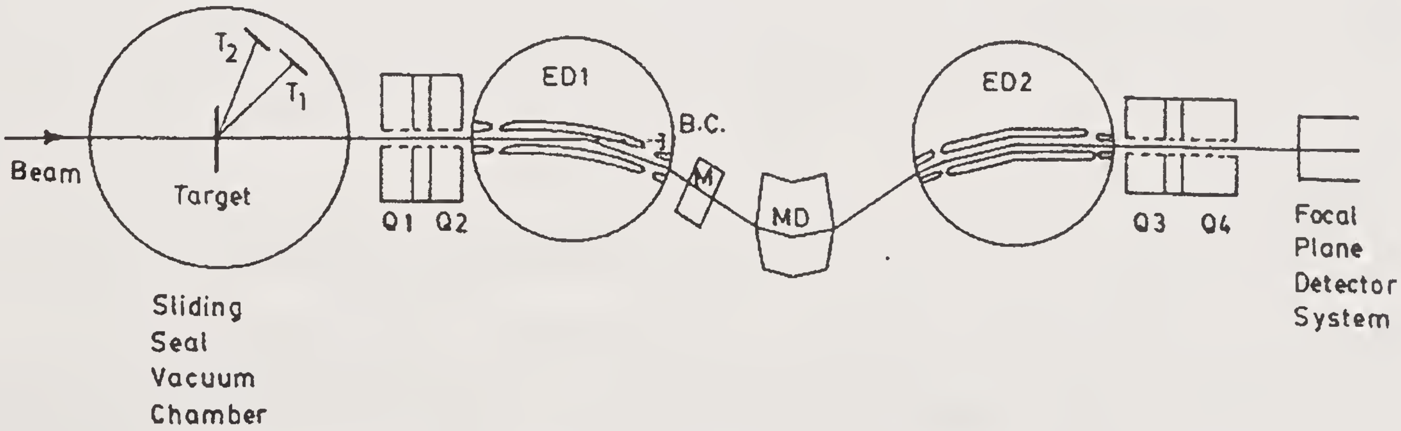

Figure 1. The schematic layout of the scattering chamber and HIRA. B.C. is the beam catcher; Q_1, Q_2, Q_3, Q_4, the quadrupoles; ED1, ED2, the electric dipoles; M the multipole; MD the magnetic dipole and T_1, T_2 are the two telescopes.

transmission coefficients that control access to this space. The transmission coefficients mainly effect the lower energy part of the particle spectrum. In heavy ion induced fusion reactions, high excitation and in particular the levels at high angular momentum have an essential influence on the deexcitation cascade. The level density formula, for a given angular momentum I and both parities $\pm\pi$, can be written as

$$\rho(E,I) = \frac{2I+1}{12}\, a^{1/2} \left(\frac{\hbar^2}{2J}\right)^{3/2} \frac{1}{(E-\Delta-t-E_I)^2} \times \exp\left\{2\left[a\left(E-\Delta-t-E_I\right)\right]^{1/2}\right\},$$

where a is the level density parameter, t is the thermodynamic temperature, Δ is the pairing correction and E_I is the rotational energy. The rotational energy in terms of rigid body moment of inertia J_0 is given by

$$E_I = \frac{\hbar^2}{2J} I(I+1) = \frac{\hbar^2}{2J_o} \frac{I(I+1)}{(1+\delta_1 I^2 + \delta_2 I^4)},$$

where δ_1 and δ_2 are the input parameters providing a range of choices for the spin dependence of the level density.

Figure 2 compares the experimental data with the cumulative alpha and proton spectra from cascade calculations using rotating liquid drop model (RLDM) moment of inertia and the optical model transmission coefficients for the respective inverse absorption channels. The experimental data are presented for singles as well as in coincidence with the residues. The coincidence measurements are done by rotating HIRA set up from 0° to 15° to account for the recoil of the residual nucleus. The coincidence data at different angles of HIRA is then normalized by the total charge on the target and then intergrated. It can be seen that the experimental spectra differ from the theoretical calculations. In order to fit these spectra, we introduced a spin dependent level density with E_I values generated with increased values of δ_1 and δ_2 and without changing the optical model transmission coefficients. The spin dependence of the level density, effected by the variation of E_I produces a noticeable change in the slope of high energy tail of the spectrum. However, the peak position and lower energy part of the spectrum remain unchanged. Increasing the values of δ_1 and δ_2 parameters and thus reducing the value of E_I, enhances the available phase space for low l-wave emission of neutrons and protons from high spin compound nuclear states relative to the higher l-wave emission of alpha particles from these states. As a result the more strongly competing neutron and proton emission suppresses the early emission of alpha particles from high spin states. The suppression of first chance alpha particle emission leads to the softening of the high energy part of the alpha spectrum. However, the lower energy part of the spectrum remains uneffected due to this change of level density.

The present results were compared with ^{28}Si + ^{27}Al system studied by us earlier [10]. It is found that the experimental spectra in the present case of ^{28}Si + ^{51}V system may be explained by the statistical model calculations taking into account much less deformation of the compound nucleus as compared to the ^{28}Si + ^{27}Al system, though the average angular momentum of $\approx 40\hbar$ in the ^{28}Si + ^{51}V asymmetric system is higher as compared to $\approx 30\hbar$

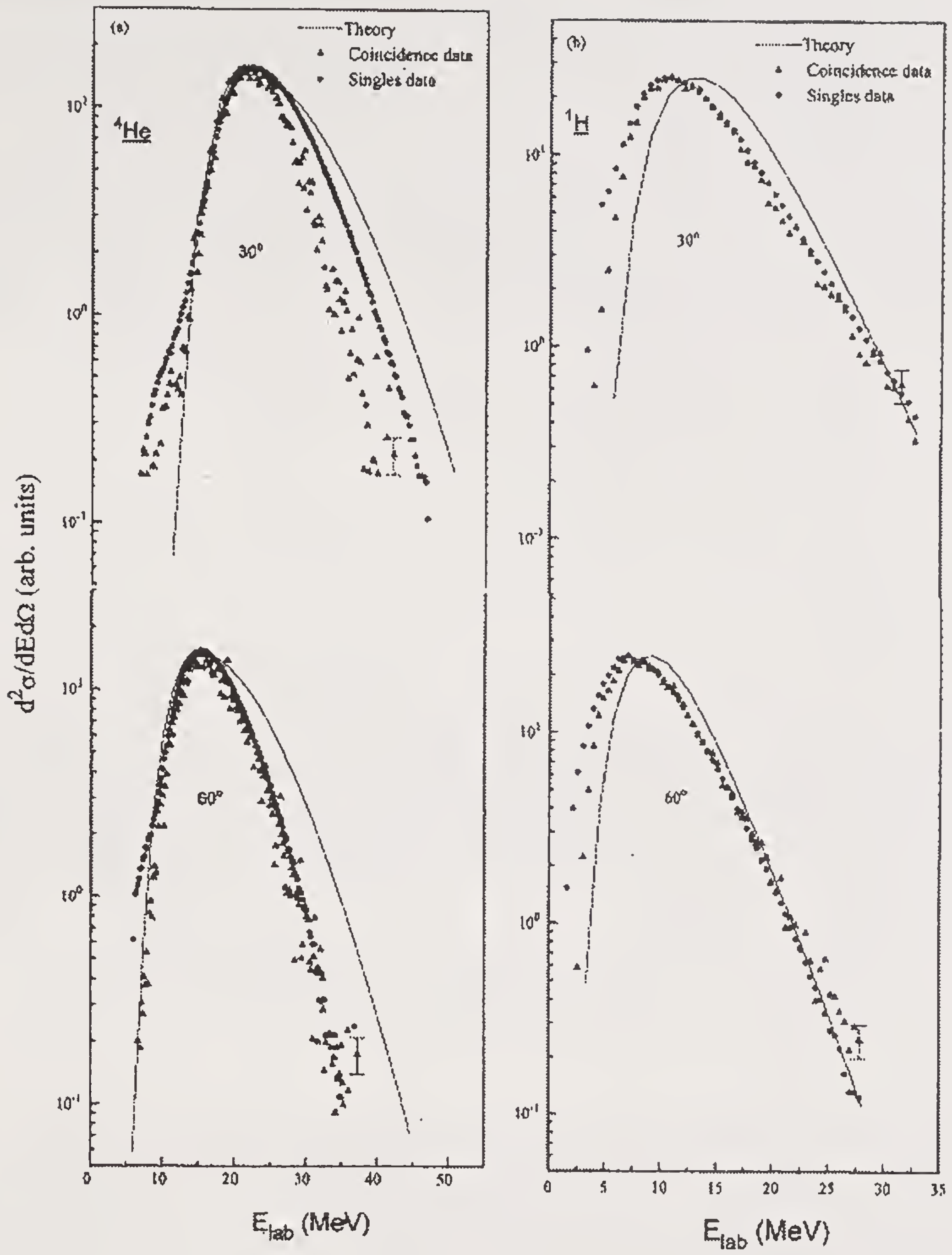

Figure 2. Comparison of the experimental spectra (triangles for coincidence with ER and circles for singles) with the statistical model (solid line) using transmission coefficients for the spherical nuclei and the RLDM moment of inertia with $l_{\text{max}} = 56\hbar$ for the reaction ^{28}Si + ^{51}V. (**a**) α-spectra at angles 30° and 60°. (**b**) Same for the proton spectra.

in ^{28}Si + ^{27}Al symmetric system. To understand the above behaviour, we did dynamical analysis in order to verify the symmetric and asymmetric entrance channel effects on the formation of the compound nucleus.

3.2 Dynamical trajectory model calculations

In the model developed by Feldmeier [24], various aspects of dissipative heavy-ion collision are brought out for center of mass energies ranging from the Coulomb barrier up to several MeV per nucleon above the barrier. The lower limit is for treating classical trajectories and the upper limit to ensure that the mean field assumption is valid. The macroscopic properties of large scale nuclear motion are obtained, where the coupling between the intrinsic and collective degrees of freedom is treated in a microscopic picture of particle exchange [25], which provide the friction and the diffusion tensor. The dynamical evolution of the two colliding nuclei is described by a sequence of shapes which basically consist of two spheres connected by a conical neck. Throughout the collision the volume of the shape is conserved so that the uniform mass and charge densities remain the same. The macroscopic shapes of the nuclear system are represented by axially symmetric configurations with sharp surfaces. These shapes are uniquely determined by three macroscopic degrees of freedom: the distance between the nuclei s (elongation), the neck-coordinate (σ), and the asymmetry coordinate (Δ), defined as

$$
\begin{aligned}
s &= \text{distance between two spheres,}\\
\sigma &= \frac{V_0 - (4\pi/3)R_1^3 - (4\pi/3)R_2^3}{V_0},\\
\Delta &= \frac{R_1 - R_2}{R_1 + R_2}
\end{aligned}
$$

where V_0 is the total volume of the system and is independent of the s, σ and Δ. R_1 and R_2 are the radii of the two interacting nuclei. In addition there are three rotational degrees of freedom for the intrinsic and relative rotation of the di-nuclear complex. Denoting the six macroscopic co-ordinates and their momenta by $(q(t), p(t))$, the Langevin dynamical equations of motion can be written as

$$
\begin{aligned}
\mathrm{d}\mathbf{p}/dt &= -\mathrm{d}T/\mathrm{d}q - \mathrm{d}V/\mathrm{d}q + X(t)\\
\mathrm{d}\mathbf{q}/\mathrm{d}t &= M^{-1}p
\end{aligned}
$$

where T is the collective kinetic energy and M is the mass tensor, V is the conservative potential and $X(t)$ is the fluctuating force due to coupling of the collective degrees of freedom to the intrinsic degrees of freedom. The mass tensor is calculated from the profile function by assuming incompressible and irrotational flow of mass during the shape evolution in the collision. The potential energy V is calculated by associating with each shape the nuclear and Coulomb energies; the nuclear potential is obtained as a double volume integral of a Yukawa plus exponential folding function, the Coulomb potential is calculated assuming a uniform charge distribution with a sharp surface. The motion of the system is governed by strong dissipative force $X(t)$, which is related to the friction and the diffusion terms obtained from particle exchange model [25]. One-body dissipation is assumed to be predominant as it has been found to be more relevant for these type of reactions [26]. This model gives a realistic macroscopic description of the nucleus–nucleus collision, based on the concept of one-body dissipation. It does not contain free parameters and consistently describes the dynamical evolution of various composite systems formed in nucleus–nucleus collisions in a wide range of impact parameters.

The results of HICOL calculations are given in figures 3 and 4. In figure 3, the elongation of the fusing nuclei is plotted as a function of time. The calculations were done for the whole range of l values and these values are given in the plot. It can be observed that for high l-values, trajectories do not lead to a spherical compound nucleus but remained elongated for long times and it is a general feature of both the systems studied. The dashed lines in the figure show the radii $(R = R_0 A^{1/3})$ of the compound nuclei ^{79}Rb(^{28}Si + ^{51}V) and ^{55}Co(^{28}Si + ^{27}Al). This line indicates that the l-values with separation greater than

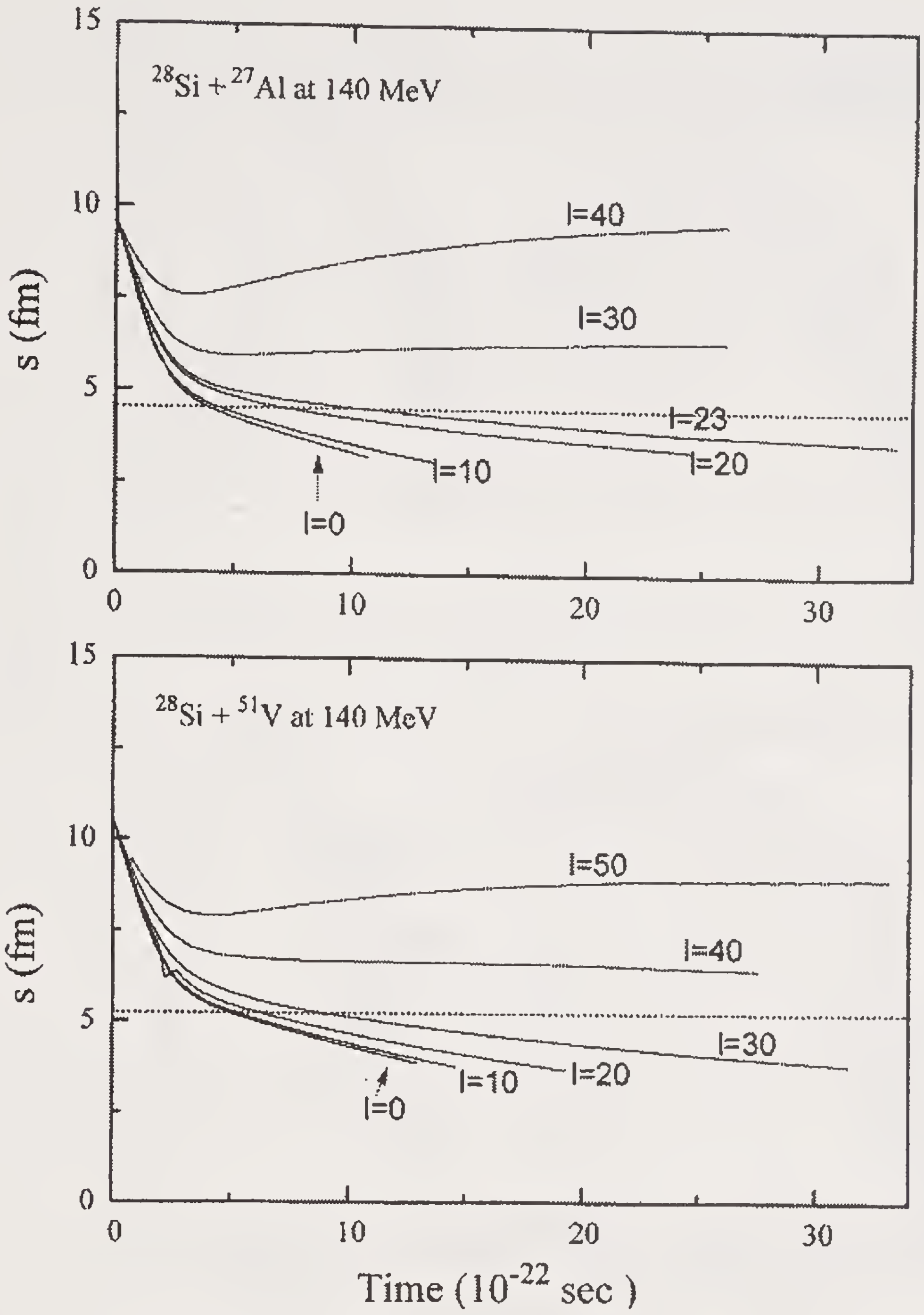

Figure 3. Calculated evolution of the separation (s) of the colliding nuclei as a function of time for the reactions ^{28}Si + ^{51}V and ^{28}Si + ^{27}Al at 140 MeV. Dashed line (- -) corresponds to the radius $R = R_0\ A^{1/3}$ for the compound nuclei ^{79}Rb and ^{55}Co for the two systems (see text).

this value do not lead to the fusion. The thermal excitation energy as a function of time is plotted in figure 4. It can be seen that the excitation energy available for particle emission achieves its final value roughly in 5×10^{-22} sec after the zero time. (Zero time is defined as the time when the participating nuclei begin to feel the nuclear force and deviate from the earlier Coulomb trajectories.) Furthermore, the excitation energy available for particle emission decreases as the angular momentum increases.

Decay times were estimated using the computer code PACE2 [27]. These times were compared with the formation times of the compound nuclei in order to see whether evaporation is significant during the formation process. The decay times for ^{28}Si + ^{51}V and ^{28}Si + ^{27}Al systems are 3.1×10^{-21} sec and 1.78×10^{-21} sec respectively. The average formation times for ^{28}Si + ^{51}V and ^{28}Si + ^{27}Al systems are 2.5×10^{-21} sec and 2.09×10^{-21} sec respectively. The formation times for both the systems are comparable to the decay times, therefore the influence on particle decay during the formation process of compound nucleus will be significant in both the cases. The α-particles emitted due to the fragments

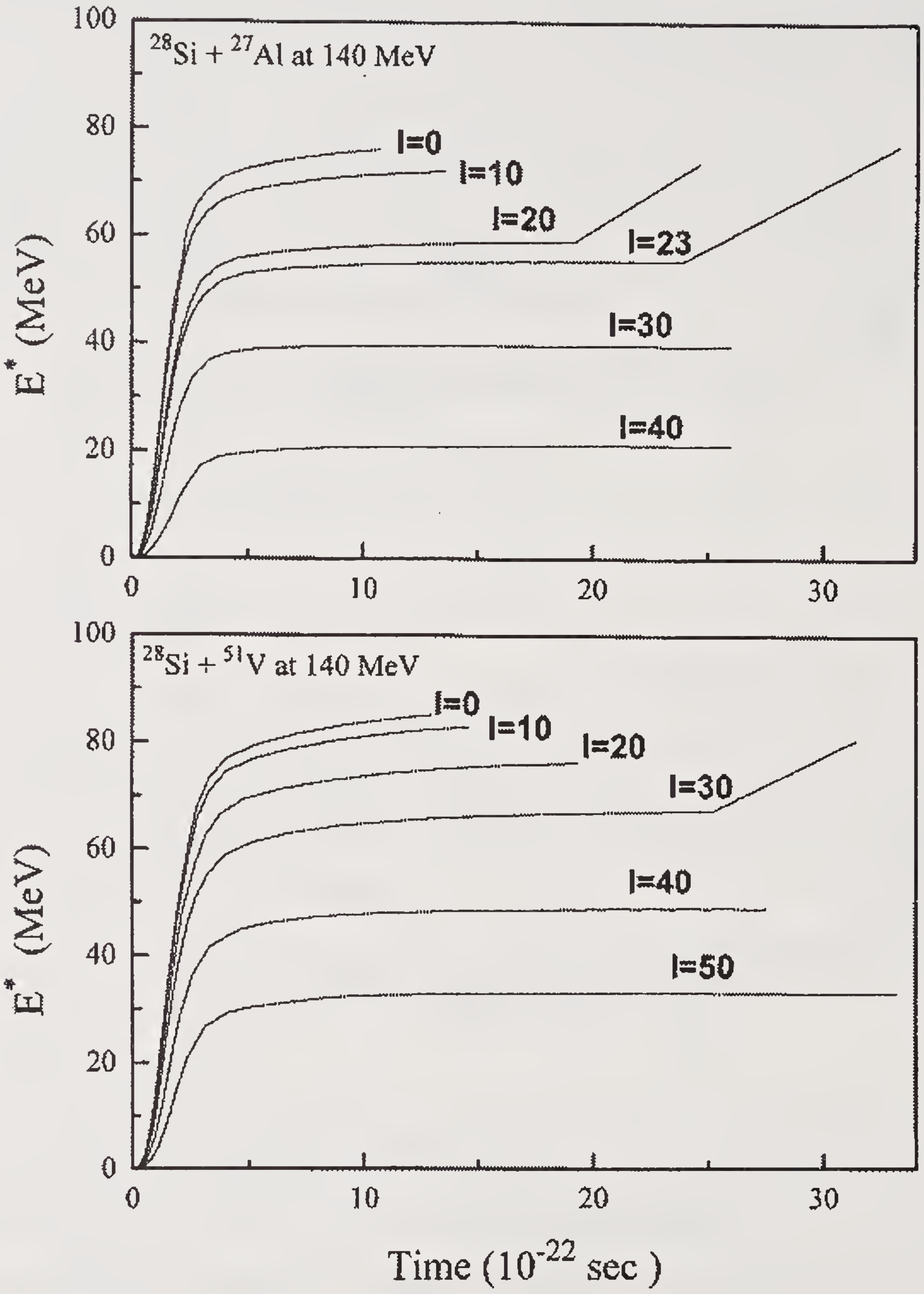

Figure 4. Calculated evolution of the excitation energy of the colliding nuclei (E^*) as a function of time for the reactions ^{28}Si + ^{51}V and ^{28}Si + ^{27}Al at 140 MeV.

in the pre-compound process are focussed in the forward direction and hence, the spectra for $\theta > 30°$ will be mainly dominated by the statistical decay of the compound equilibrated system. As is evident from figure 2, at 30° the singles and the coincidence spectra do not coincide with each other. However, at 60° they completely overlap, indicating that there is no contribution from the fragment like or pre-compound emission.

The semiclassical code HICOL does not predict fusion to occur for ^{28}Si+^{51}V system for angular momentum larger than $30\hbar$, instead the system remains in a rotating configuration for long times. In this case the maximum value of angular momentum for which the system fuses is $30\hbar$. In the case of ^{28}Si+^{27}Al system the maximum value of angular momentum for which the code HICOL predicts the fusion to occur is $23\hbar$. Taking these values of $l_{\max}$, we did the statistical model calculations for both the systems. Figure 5 shows the experimental data for the α-particles and the protons compared with the theoretical predictions for the ^{28}Si + ^{51}V system with $l_{\max} = 30\hbar$ and the RLDM moment of inertia. It is evident from the figure that the statistical model predictions are in agreement with the experimental data with the HICOL predicted l-values without taking into account the deformation of the

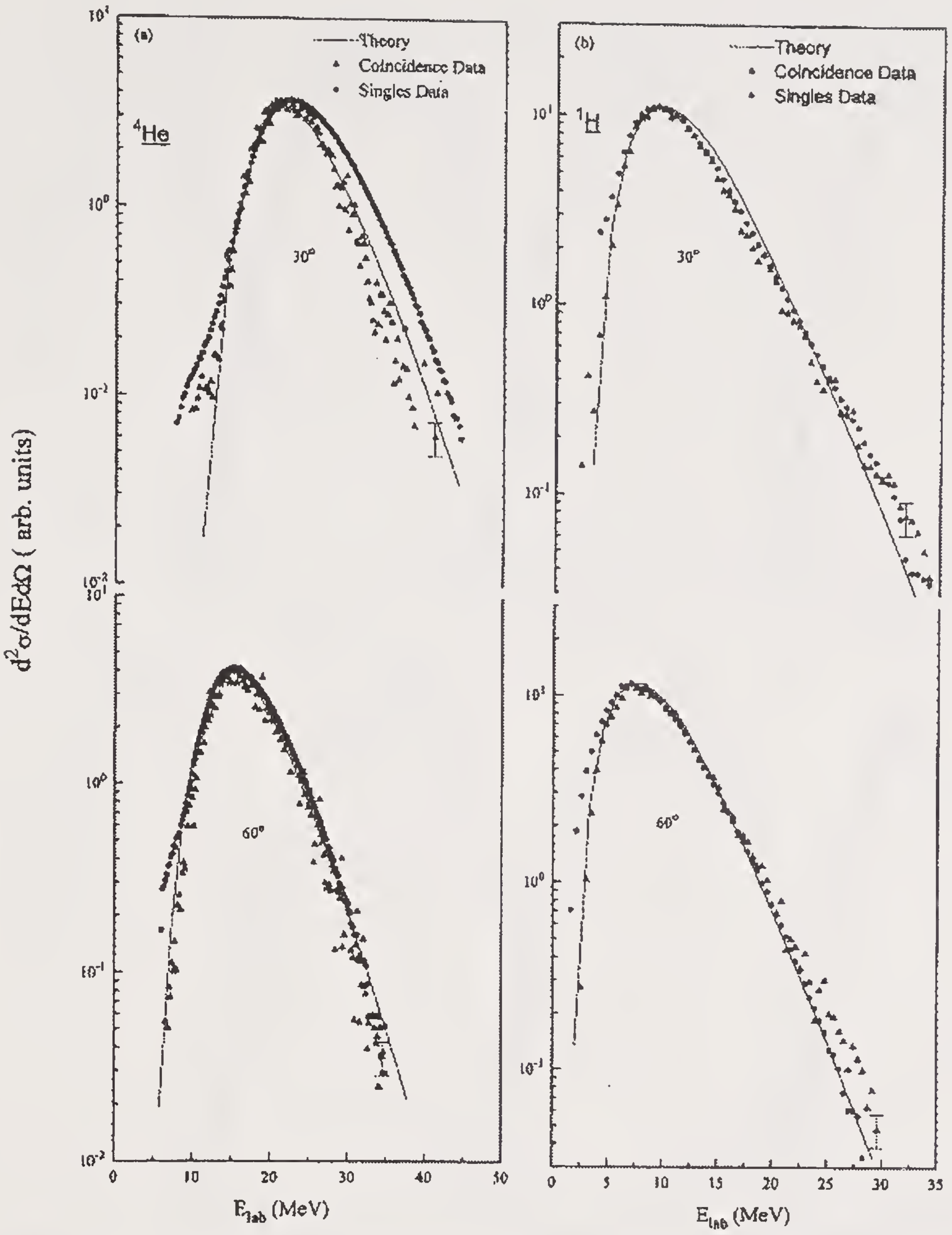

Figure 5. Comparison of the experimental spectra (triangles for coincidence with ER and circles for singles) with the statistical model (solid line) using the transmission coefficients for the spherical nuclei and the RLDM moment of inertia with $l_{\rm max} = 30\hbar$ as predicted by the dynamical model (HICOL) for the reaction ^{28}Si + ^{51}V. (**a**) α-spectra at angles 30° and 60°. (**b**) Same for the proton spectra.

compound nucleus. It is remarkable to note that the theoretical calculations agree well for both the alphas and the protons. Figure 6a shows the experimental data for the α-particles compared with the theoretical predictions for the ^{28}Si + ^{27}Al system with $l_{\rm max} = 23\hbar$ and RLDM moment of inertia. It can be seen that the high energy part of the α-spectrum can be well fitted but the lower energy part of the spectrum remains unexplained by taking the low l-values in this case. The lower energy part of the spectrum is therefore fitted by changing the effective radius of the compound nucleus. This change is about 20% larger than the half density radius of the Woods–Saxon potential assumed in the calculation of the transmission coefficients for the inverse absorption channel. With the changed transmission coefficients and using the same value of $l_{\rm max}$ i.e. $l_{\rm max} = 23\hbar$, the alpha spectra are obtained as shown in figure 6b which are in agreement with the experimental data. However, the observed proton spectra in figure 7a for the symmetric system ^{28}Si + ^{27}Al have such low energies

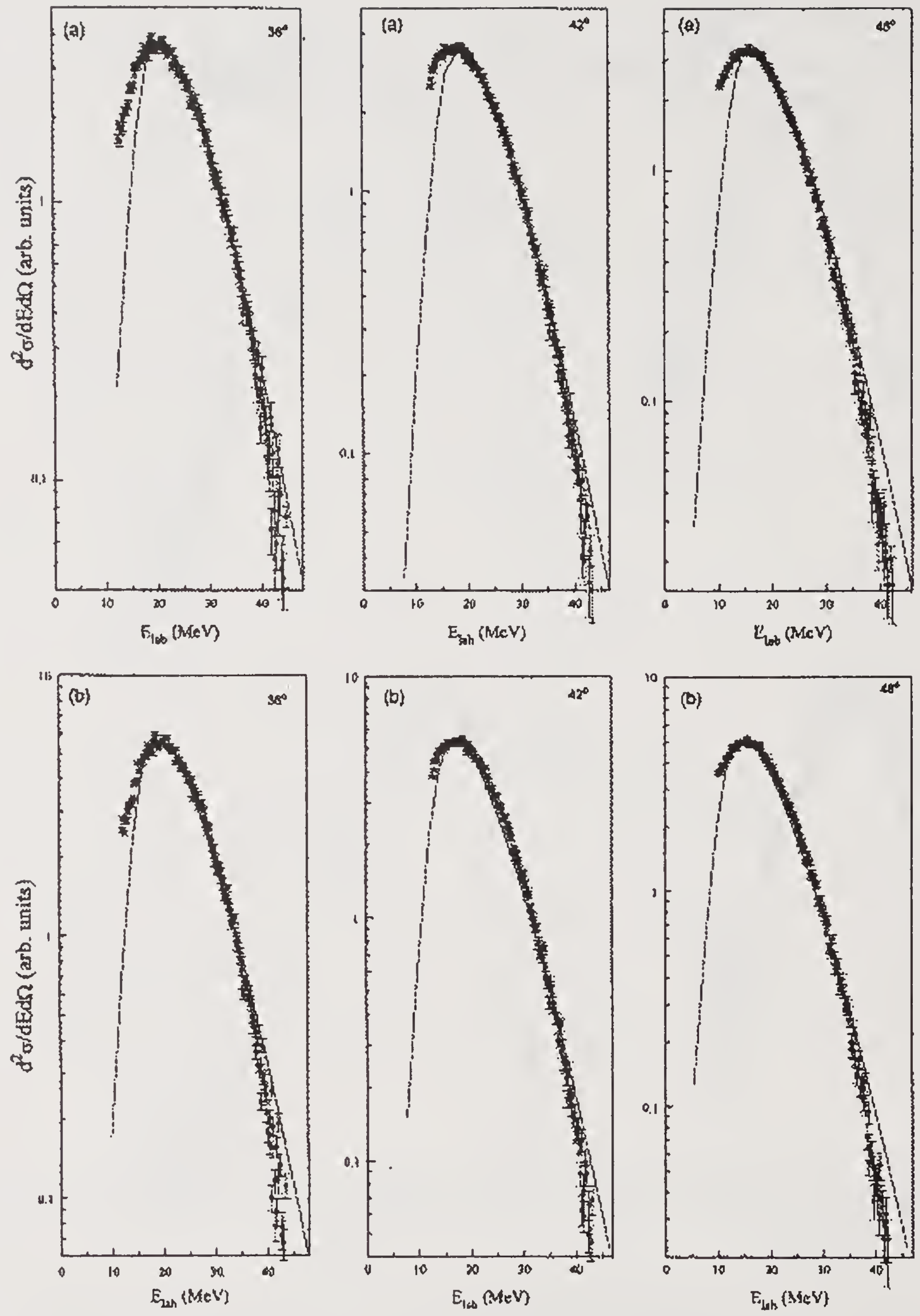

Figure 6. (**a**) Comparison of the experimental α-spectra (circles) at different angles with the statistical model (solid line) using the transmission coefficients for the spherical nuclei and the RLDM moment of inertia with $l_{\max} = 23\hbar$ as predicted by the dynamical model (HICOL) for the reaction ^{28}Si + ^{27}Al. (**b**) Same with the transmission coefficient changed for deformed nuclei having the average radius increased by 20%.

that it deviates at the lower as well as at the higher energy part of the spectrum with the statistical model calculations using RLDM moment of inertia and $l_{\max} = 23\hbar$ as predicted by the dynamical model (HICOL). The change of the radius parameter by 20% in figure 7b, as was done in the case of α- spectrum, also fall short of representing the experimental data. It indicates that a reasonable nuclear deformation may not account for the measured very low proton energies as reported by Parker *et al* [9]. It seems that in the symmetric systems the collisions in the early stages of the nuclear reaction excite particularly those nucleons which are near to the surface of the nucleus. In the outer fringes of the reacting system, the emission barriers would be lower than in the central region resulting in the unexpectedly low average particle energies for the protons.

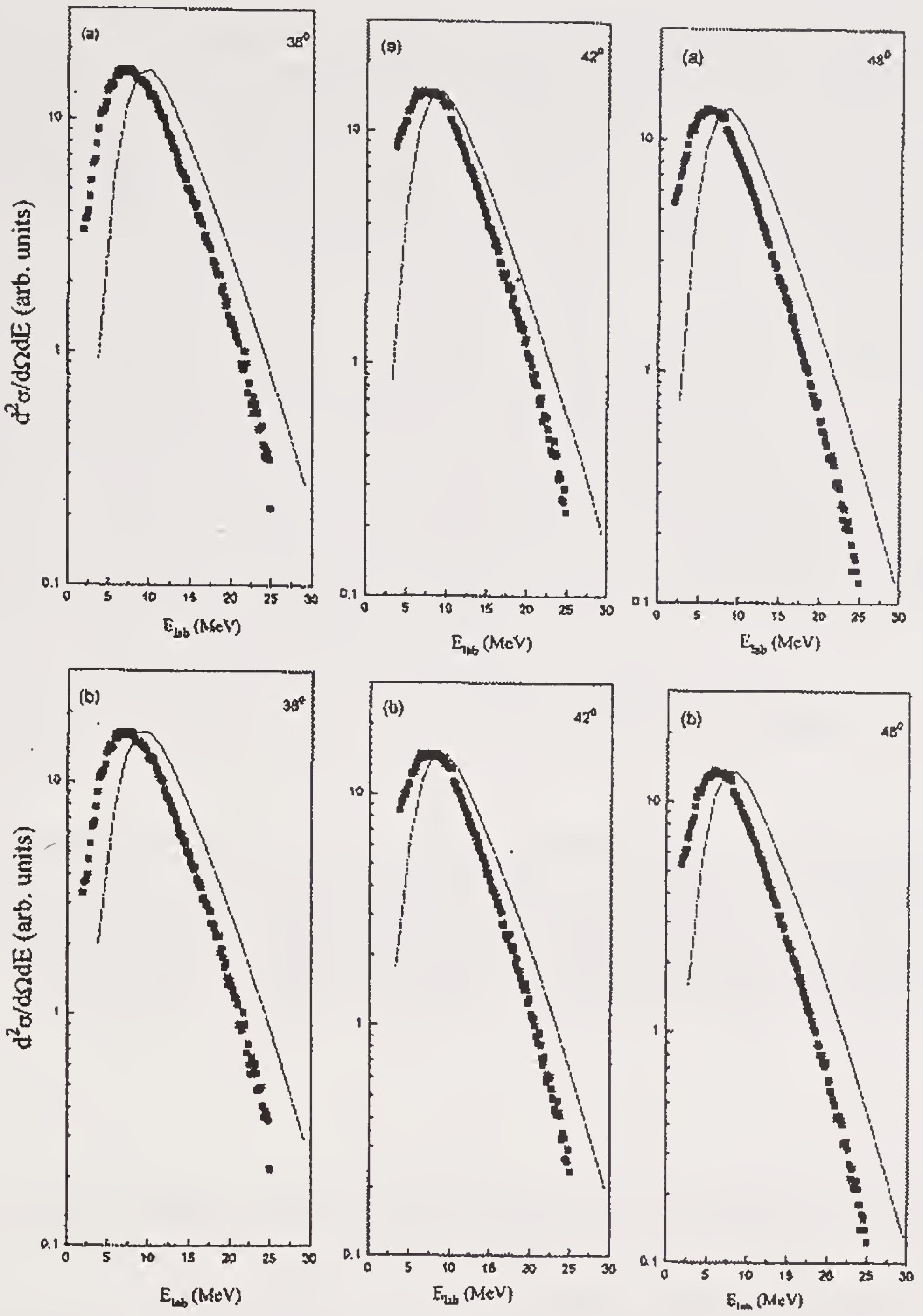

Figure 7. (**a**) Comparison of the experimental proton spectra (circles) with the statistical model using the transmission coefficients for the spherical nuclei and RLDM moment of inertia, with $l_{\text{max}} = 23\hbar$ as predicted by the dynamical model (HICOL) for the reaction ^{28}Si +^{27}Al. (**b**) Same with the changed transmission coefficients for the deformed nuclei with the average radius increased by 20%.

4. Summary

We have measured the evaporation residue-gated alpha spectra from the ^{79}Rb* composite nuclei. The measured spectra are softer than those predicted by standard statistical model calculations. A satisfactory description of data can be obtained by varying the level density parameters and invoking deformation in the transmission coefficient calculations considering that most α -emission comes from the tips of the nucleus. However, when considering the symmetric ^{28}Si + ^{27}Al and the asymmetric ^{28}Si + ^{51}V system, it was noted that the deformation in the former system having a lower average angular momentum of $30\hbar$ was larger than the latter system having a greater average angular momentum of $40\hbar$ which indicates that the deformation of the compound system depends not only on its angular momentum but also on the entrance channel. The dynamical effects prior to the formation of the compound system, therefore, seem to play an important role in deciding the final l-values and excitation energy of the compound nucleus. Dynamical trajectory model (HICOL) calculations predicted lower l-values for fusion in both cases and were found to be responsible for the higher energy part of the α-spectrum of the two systems. The deformation of the system plays a role in describing the lower energy part of the α-spectrum and was found to be present in ^{28}Si + ^{27}Al system. However, the observed proton spectra for this symmetric system have such low energies that it is impossible to fit the statistical model calculations with RLDM moment of inertia and HICOL predicted l-values with a reasonable deformation. This indicates that in the symmetric systems probably the collisions in the early stages of the equilibration, predominantly excite the nucleons near the surface of the nucleus resulting in the unexpectedly low emission barrier and thus the low average particle energies. The present study gives a new insight regarding the role of the dynamics of the nuclear reaction in the evaporation of α-particles from hot nuclei.

Acknowledgement

The author acknowledges with thanks the discussion and useful suggestions made by Dr S S Kapoor and Prof V S Ramamurthy on the manuscript of this paper. The author also thank the Accelerator crew of the Nuclear Science Centre, New Delhi for providing an excellent beam. This work has been supported by the UGC–NSC project.

References

[1] R G Stokstad, in *Treatise on Heavy-Ion Science* edited by D A Bromley (Plenum, New York, 1985) vol. **3**, p. 83

[2] B Fornal, G Prete, G Nebbia, F Trotti, G Viesti, D Fabris, K Hagel and J B Notwitz, *Phys. Rev.* **C37**, 2624 (1988)

[3] B Fornal *et al*, *Phys. Rev.* **C41**, 127 (1990)

[4] R K Choudhury, P L Gonthier, K Hagel, M N Namboodiri, J B Natowitz, L Adler, S Simon, S Kniffen and G Berkowitz, *Phys. Lett.* **B143**, 74 (1989)

[5] G Viesti, B Fornal, D Fabris, K Hagel, J B Natowitz, G Nebbia, G Prete, and F Trotti, *Phys. Rev.* **C38**, 2640 (1988)

[6] G L Rana, David J Moses, Winifred E Parker, Morton Kaplan, Douglas Logan, Roy Lacey, John Alexander and Robert J Welberry, *Phys. Rev.* **C35**, 373 (1987)

[7] G L Rana, R Moro, A Brondi, P Cuzzocrea, A D'Onofrio, E Perilo, M Romano, F Terrasi, E Vardaci and H Dumont, *Phys. Rev.* **C37**, 1920 (1988)

[8] Z Majka, M E Brandan, D Fabris, K Hagel, A Menchaca-Rocha, J B Natowitz, G Nebbia, G Prete and G Viesti, *Phys. Rev.* **C35**, 2125 (1987)

[9] W E Parker *et al*, *Phys. Rev.* **C44**, 774 (1991)

[10] D K Agnihotri, A Kumar, K C Jain, K P Singh, G Singh, D Kabiraj, D K Avasthi and I M Govil, *Phys. Lett.* **B307**, 283 (1993)

[11] I M Govil, J R Huizenga, W U Schroder and J Toke, *Phys. Lett.* **197**, 515 (1987)

[12] B Fornal, G Viesti, G Nebbia, G Prete and J B Natowitz, *Phys. Rev.* **C40**, 664 (1989)

[13] J R Huizenga, A N Behkami, I M Govil, W U Schroder and J Toke, *Phys. Rev.* **C40**, 668 (1989)

[14] S Cohen, F Plasil and W J Swiatecki, *Ann. Phys. (NY)* **82**, 557 (1974)

[15] M Thoennessen, J R Beene, F E Bertrand, C Baktash, M L Halbert, D J Horen, D G Sarantites, W Spang and D W Stracener, *Phys. Rev. Lett.* **70**, 1055 (1993)
[16] Kiran Kumar, R K Choudhary and A Saxena, *Pramana – J. Phys.* **42**, 123 (1994)
[17] P Frobrich, I I Gontchar and N D Mavlitov, *Nucl Phys.* **A556**, 281 (1993)
[18] K Siwek-Wilczynska, J Wilczynski, R H Siemssen and H W Wilschut *Phys. Rev.* **C51**, 2054 (1995)
[19] M Thoennessen, E Ramakrishnan, J R Beene, F E Bertrand, M L Halbert, D J Horen, P F Mueller and R L Varner, *Phys. Rev.* **C51**, 3148 (1995)
[20] M Gonin *et al*, *Phys. Rev.* **C42**, 2125 (1990)
[21] B J Fineman, K-T Brinkmann, A L Caraley, N Gan, W J Kernan, R L McGrath and T A Savas, *Phys. Rev.* **C50**, 1991 (1994)
[22] W J Swiatecki, *Phys. Scr.* **24**, 113 (1981)
[23] F Puhlhofer, *Nucl. Phys.* **A280**, 267 (1977)
[24] H Feldmeier, *Rep. Prog. Phys.* **50**, 915 (1987)
[25] H Feldmeier and H Spangenberger, *Nucl. Phys.* **A435**, 229 (1985)
[26] J Blocki, R Planeta, J Brzychczyk and K Grotowski, *Z. Phys.* **A341**, 307 (1992)
[27] A Gavron, *Phys. Rev.* **C21**, 230 (1980)

Experimental investigations of the nuclear level density by using heavy ion reactions

G VIESTI, M LUNARDON, D FABRIS, G NEBBIA, M CINAUSERO*, E FIORETTO*, G PRETE*, J B NATOWITZ†, K HAGEL† and R WADA†
Dipartimento di Fisica dell' Universitá di Padova and I.N.F.N., I-35131 Padova, Italy
*I.N.F.N., Laboratori Nazionali di Legnaro, I-35020 Legnaro, Italy
†Cyclotron Institute, Texas A&M University, College Station, Texas 77843, USA

Abstract. The transition of the level density parameter a_{eff} from the low excitation energy value $a_{\text{eff}}=A/8\ \text{MeV}^{-1}$ to the Fermi gas value $a_{\text{FG}}\sim A/15\ \text{MeV}^{-1}$ was discovered a few years ago studying particle spectra evaporated from hot compound systems of $A\sim160$. A number of experiments have been recently performed to confirm the earlier findings and extend the investigation to other mass regions and to higher excitation energies. Furthermore, precision coincidence experiments have been done in the lead region in which evaporation residues are tagged by low energy gamma-rays. Those experiments open the possibility of a detailed study of the level densities in nuclei where the shell effects are important.

Keywords. Heavy-ion reactions; measured light-charged-particle multiplicity and energy spectra; deduced level density parameter mass dependence features.

PACS Nos 21.10.Ma; 25.70.Gh; 25.70.Jj; 27.80.+w

1. Introduction

The level density in excited nuclei is a topic of current interest in nuclear physics from the experimental as well as from the theoretical point of view [1].

It is well known that at low excitation energies the level density is strongly influenced by the shell structure of the nucleus. Such effects, which are particularly important for nuclei having proton and neutron numbers at the shell closures, are predicted to disappear with increasing excitation energy [2].

In the Fermi gas (FG) approach, a key quantity is the level-density parameter a, which is simply related to the density of single-particle levels $g(\epsilon_{\text{F}})$ at the Fermi energy ϵ_{F} and reflects the properties of the single-particle potential. In the simplest approach, the excitation energy E_x is related to the nuclear temperature T by the relation $E_x = aT^2$. Therefore, the experimental knowledge of E_x and T allows the definition of an effective level-density parameter a_{eff}. It is well known that for excitation energies of the order of the neutron separation energy, $E_x\sim8$ MeV, the average empirical value of the level-density parameter is $a_{\text{eff}} \approx A/8\ \text{MeV}^{-1}$, where A is the mass number. This has to be compared with the expected value from the FG model $a_{\text{FG}} \approx A/15\ \text{MeV}^{-1}$. The disagreement between the

FG value and the one at low excitation energy is well understood as an effect of the finite size of the nucleus and of the increase of the nucleon effective mass at the Fermi energy produced by the coupling of the single-particle motion to other degrees of freedom. This last correlation is predicted [3,4] to disappear for temperatures larger than that associated to the low-lying excited states, so that a transition to the FG value of the level density parameter a_{eff} is expected.

The knowledge of the level density parameter a_{eff} as a function of excitation energy and mass of the nucleus is not only interesting in itself, but also of crucial importance in modelling heavy ion reactions designed to determine whether equilibration takes place and in nuclear astrophysics [5].

Results of experiments devoted to explore the excitation energy dependence of the level density, from tepid to hot nuclei, are reported and discussed in this paper.

2. Experiments on hot nuclei

The transition of the level density parameter to the FG value was discovered few years ago in the study of the alpha particles emitted at backward angles in the reactions of 19 and 35 MeV/nucleon ^{14}N+^{154}Sm [6], which are characterized by a wide distribution in the transferred linear momentum, producing a continuum of sources of different mass and excitation energies. Several points of those earlier measurements have been verified in successive investigations using the ^{60}Ni+^{100}Mo reactions at 9–17 MeV/nucleon [7]. Such reactions were chosen because of the nearly complete momentum transferred, which better define the emitting source. In this case p, d, t, ^{4}He and neutron spectra were measured.

The quantity experimentally determined is the slope of the particle spectra, i.e. the apparent temperature T_{app}. Because of the length of the deexcitation chain, the measured T_{app} is determined not only by the first-chance particles emitted in the decay of the nucleus A at the excitation energy E_x, but also by those particles emitted in later steps of the cascade, corresponding to lower excitation energies and masses. The derivation of T, the temperature of the nucleus after the first chance emission, is achieved by unfolding slopes (T_{app}) with the measured multiplicity (M) at two excitation energies $E_{x,1} \leq E_{x,2}$:

$$T = (T_{\mathrm{app},2} \times M_2 - T_{\mathrm{app},1} \times M_1)/(M_2 - M_1).$$

In few cases 'quasi-first chance' spectra of the emitted particles have been obtained directly by a subtraction procedure. The assumption, in both cases, is that the cascade originating at $E_{x,2}$ includes also that at $E_{x,1}$.

An increase of the inverse level density parameter $K = A/a$ in increasing the excitation energy of the composite system was clearly evidenced. The transition to the FG value is located at an excitation energy of $\epsilon \sim 1.3$ MeV/nucleon (note that ϵ is the excitation energy in the daughter nucleus after the particle emission).

Furthermore, the initial temperature was found to be the same ($T = 4.6$ MeV) at an average total excitation energy of $E_x = 290$ MeV regardless of the type of particle considered, demonstrating that the thermal equilibrium was achieved.

In a second set of measurements, $A \sim 110$ nuclei were studied by coincidences between heavy residues and alpha particles from the reactions of 30 MeV/nucleon ^{16}O and ^{32}S on Ag [8]. Successive measurements were performed by using low energy fusion reactions (^{32}S + ^{74}Ge at beam energies between 5 and 13.6 MeV/nucleon delivered from the XTU

Tandem in Legnaro and the SARA facility in Grenoble [9]). The corresponding $A = 106$ compound system was populated at excitation energies $\epsilon = 0.5 - 2.2$ MeV/nucleon. After combining the data from the different experiments, a transition to the FG value was detected at $\epsilon \sim 2$ MeV/nucleon, an excitation energy larger than that in the $A \sim 160$ case, as expected from theoretical predictions [10].

Some experimental information is also available in case of lighter nuclei. The ^{32}S + ^{27}Al reaction has been extensively investigated in the past at the XTU Tandem up to 190 MeV bombarding energy. Light particles spectra [11], as well as hard γ-ray [12], were measured. Furthermore, particle spectra emitted in the decay of hot ^{40}Ca nuclei were studied at the XTU Tandem, by using the reaction 130 MeV ^{16}O+^{24}Mg [13].

Generally, the slopes of the particle spectra in light systems are strongly determined by the angular momentum dependence of the phase space (i.e. by the position of the yrast line). Up to now, only average level density parameters $\langle K \rangle$ have been derived by comparing the experimental spectra with those predicted by statistical model calculations. In all cases, a rather accurate description of the experimental data has been achieved by using the parameter $\langle K \rangle \doteq 8$ MeV.

3. Level density of excited nuclei in the lead region

We have then considered the nuclei in the region of ^{208}Pb, where the shell corrections are very large, with the aim of experimentally mapping out the two transitions in the level density parameter as a function of the excitation energy: the disappearance of the shell effects and then the transition to the fermi-gas model value.

As a part of this investigation we have studied the fusion reactions $^{11}\text{B} + {}^{198}\text{Pt} \rightarrow {}^{209}\text{Bi}^*$ and $^{10}\text{B} + {}^{198}\text{Pt} \rightarrow {}^{208}\text{Bi}^*$ at bombarding energies $E_{\text{beam}} = 55 - 90$ MeV. The experiment was performed at the XTU Tandem accelerator in Legnaro. Low energy γ-rays were detected with the GASP spectrometer [14] up-graded with two large BGO crystals (10 cm × 10 cm) to detect high energy γ-rays. A complete description of the operation of the large BGO detectors in coincidence with the GASP spectrometer is given in ref. [15]. The charged particles detector array ISIS (Italian Silicon Sphere) was used [16], up-graded by some CsI(Tl) scintillators to stop energetic protons. We collect 200×10^6 events in the case of the ^{11}B irradiation at 75 MeV for coincidences between ISIS and GASP (trigger conditions: 2 HPGe and 3 inner ball elements). The corresponding coincidences between energetic protons hitting the CsI(Tl) scintillators were in this case only 2.6×10^6 events. The statistics collected in the ^{10}B irradiation at 60 MeV was 150×10^6 events and 0.9×10^6 events, respectively.

The experiment was specifically designed to track down the disappearance of shell effects in the nucleus ^{208}Pb from the proton evaporation feeding directly the excited ^{208}Pb in the first step of the deexcitation cascade. In fact, the ^{11}B + ^{198}Pt reaction at 75 MeV bombarding energy populates the ^{209}Bi compound nucleus at an excitation energy of $E_x = 68.1$ MeV when a complete fusion reaction is considered [17]. In this case, the average angular momentum is estimated from the systematics to be $\langle J \rangle \sim 20\hbar$. The bombarding energy for the ^{10}B irradiation was selected to be $E_{\text{beam}} = 60$ MeV, so that the ^{208}Bi compound nucleus is populated at an excitation energy of $E_x = 58.1$ MeV. The difference in the excitation energies obtained with the two beams is supposed to correspond to the emission of the first neutron from the decay of the ^{209}Bi CN. The proton spectrum

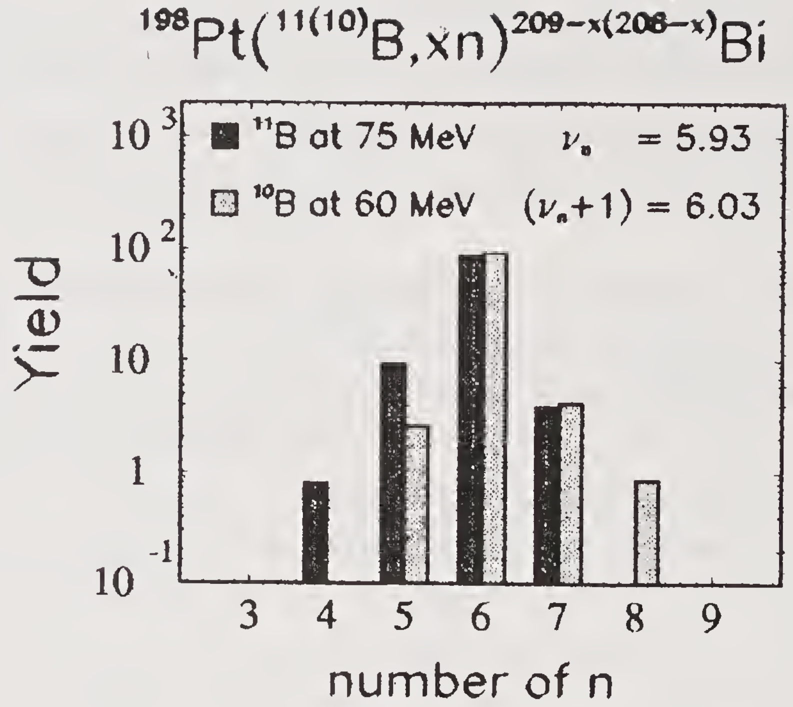

Figure 1. Relative yield distribution of the Bi isotopes produced in the ^{11}B- and ^{10}B-induced reactions.

measured in the ^{10}B induced reaction accounts for the emission of protons in the deexcitation chain of the ^{209}Bi compound nucleus when the particle emitted in the first step is a neutron, i.e. for protons emitted in the second or latest steps of the decay. Consequently, the difference between the proton spectra obtained in the two reactions is due only to the particles which populate the ^{208}Pb excited nucleus in the ^{209}Bi decay. It is, however, worth mentioning that the average angular momentum for the ^{10}B induced reaction is estimated to be $\langle J\rangle \sim 15\hbar$, which is lower than the one associated with the ^{11}B beam. The mismatch in the angular momenta distributions between the two reactions cannot be avoided. However, their effect on the proton emission can be disregarded, as predicted by statistical model calculations.

A direct test of the assumptions made in selecting the two reactions can be obtained by looking directly to the distribution of the Bi evaporation residue in the xn channels which are strongly populated in the two reactions. Results are reported in figure 1. It appears that the relative yields of the ^{202}Bi and ^{203}Bi nuclei are the same in the two reactions, as expected. A difference in yield is evident in the case of the ^{204}Bi nucleus which is sensitive to the angular momentum mismatch discussed above.

The average numbers of evaporated neutrons derived from the residues distribution are $\nu_n^{^{11}\mathrm{B}} = 5.93$ and $\nu_n^{^{10}\mathrm{B}} = 5.03$, giving a difference $\Delta\nu_n = 0.9$, very close to the expected difference of one unit between the two reactions. The result is even better ($\nu_n^{^{11}\mathrm{B}} = 6.04$ and $\nu_n^{^{10}\mathrm{B}} = 5.06$, $\Delta\nu_n$=0.98) if the data relative to the ^{204}Bi and ^{205}Bi nuclei are excluded, that is equivalent to cut the higher partial waves in the CN decay reducing the angular momentum mismatch.

The energy spectra of the protons in coincidences with transitions in final Pb evaporation residues are reported in figure 2. In the same figures it is reported the sum spectrum obtained by using as weighting factors the experimental yield derived from the discrete γ-ray spectra.

The high energy tails of proton spectra in coincidence with the ^{204}Pb nucleus were fitted with Maxwellian distributions deriving the apparent nuclear temperatures $T_{\mathrm{app}}^{^{11}\mathrm{B}} =$ 1.24 ± 0.09 MeV and $T_{\mathrm{app}}^{^{10}\mathrm{B}} = 0.99 \pm 0.09$ MeV. The reported uncertainties take also

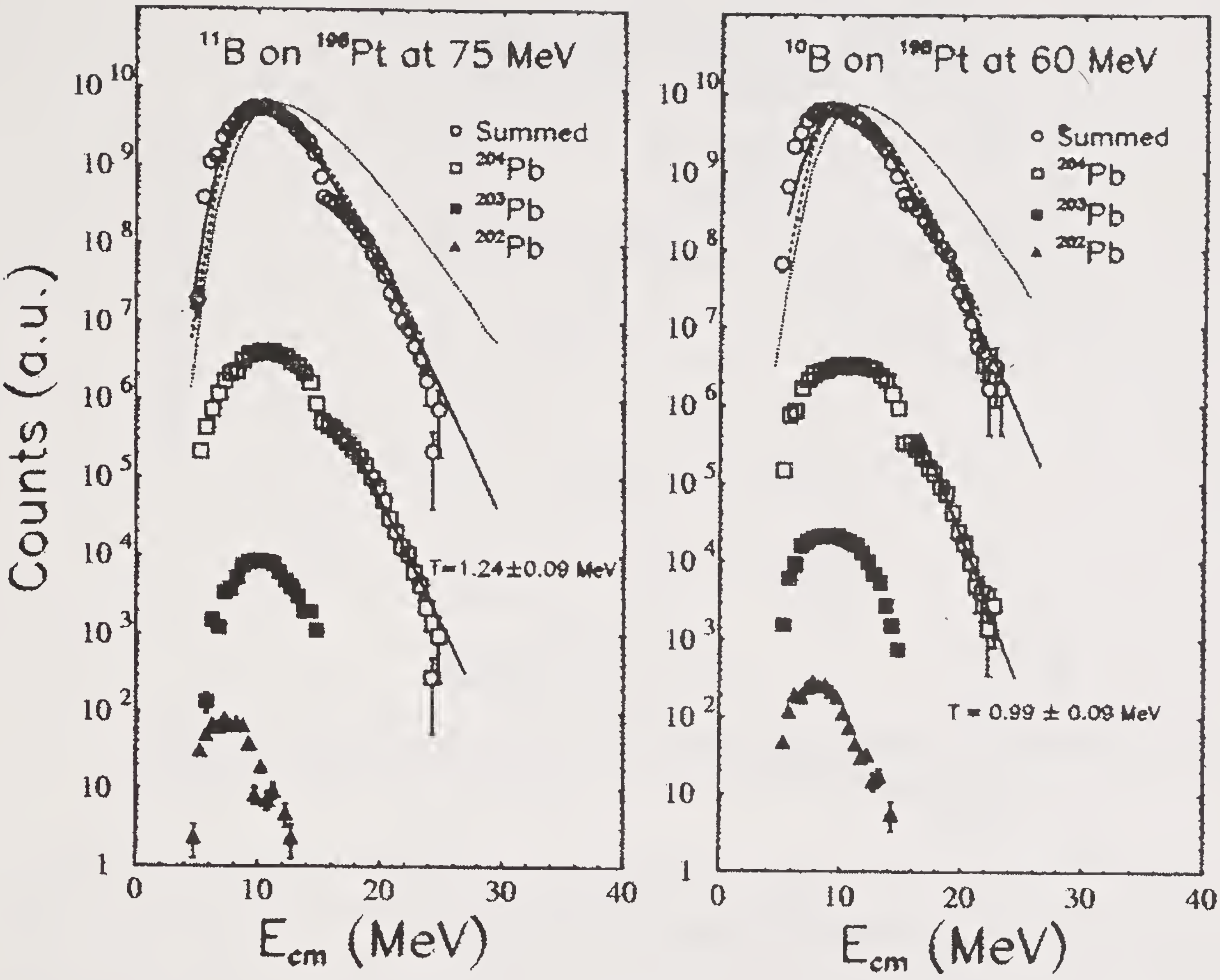

Figure 2. Energy spectra of the protons emitted in coincidence with the different Pb isotopes in the reactions induced by ^{11}B (left) and ^{10}B (right). Statistical model calculations are also shown for different level densities: Reisdorf (dashed lines), $a = A/10$ MeV^{-1} (solid line) and $a = A/21$ MeV^{-1} (dotted line).

into account the small dependences of the best-fit T_{app} parameter on the assumed average barrier ($B_c = 9.5 \pm 0.5$ MeV) and on the fitting region. The multiplicity of the decay channel ending in the ^{204}Pb nucleus was obtained for both reactions from the $\gamma-\gamma$ matrix, relative to the sum of the ER yields in the xn channel which accounts for the bulk of the fusion-evaporation cross section.

Consequently, the temperature associated to the decay from the ^{209}Bi initial compound nucleus to the ^{208}Pb in the first step of the $p4n$ deexcitation chain is obtained from the measured apparent temperatures and relative multiplicities as

$$T(^{208}\mathrm{Pb}) = (\mathrm{M}^{^{11}\mathrm{B}} \times \mathrm{T}_{\mathrm{app}}^{^{11}\mathrm{B}} - \mathrm{M}^{^{10}\mathrm{B}} \times \mathrm{T}_{\mathrm{app}}^{^{10}\mathrm{B}})/(\mathrm{M}^{^{11}\mathrm{B}} - \mathrm{M}^{^{10}\mathrm{B}}) = 1.63 \pm 0.28\ \mathrm{MeV}.$$

This temperature is associated to a thermal excitation energy E_{th} in the daughter ^{208}Pb nucleus $E_{\mathrm{th}} = E^{*}_{^{209}\mathrm{Bi}} - E^{\mathrm{rot}}_{^{208}\mathrm{Pb}} - S_p - E_p^{\mathrm{kin}} = 49.5$ MeV.

It is possible to compare the result obtained in the present work with predictions from the excitation energy dependent parameterization of the level density given by Reisdorf [18] and with the two limiting values corresponding to a cold nucleus where the shell corrections dominate and to an highly excited nucleus where such corrections disappeared. The comparison, presented in figure 3, shows that at the excitation energy of

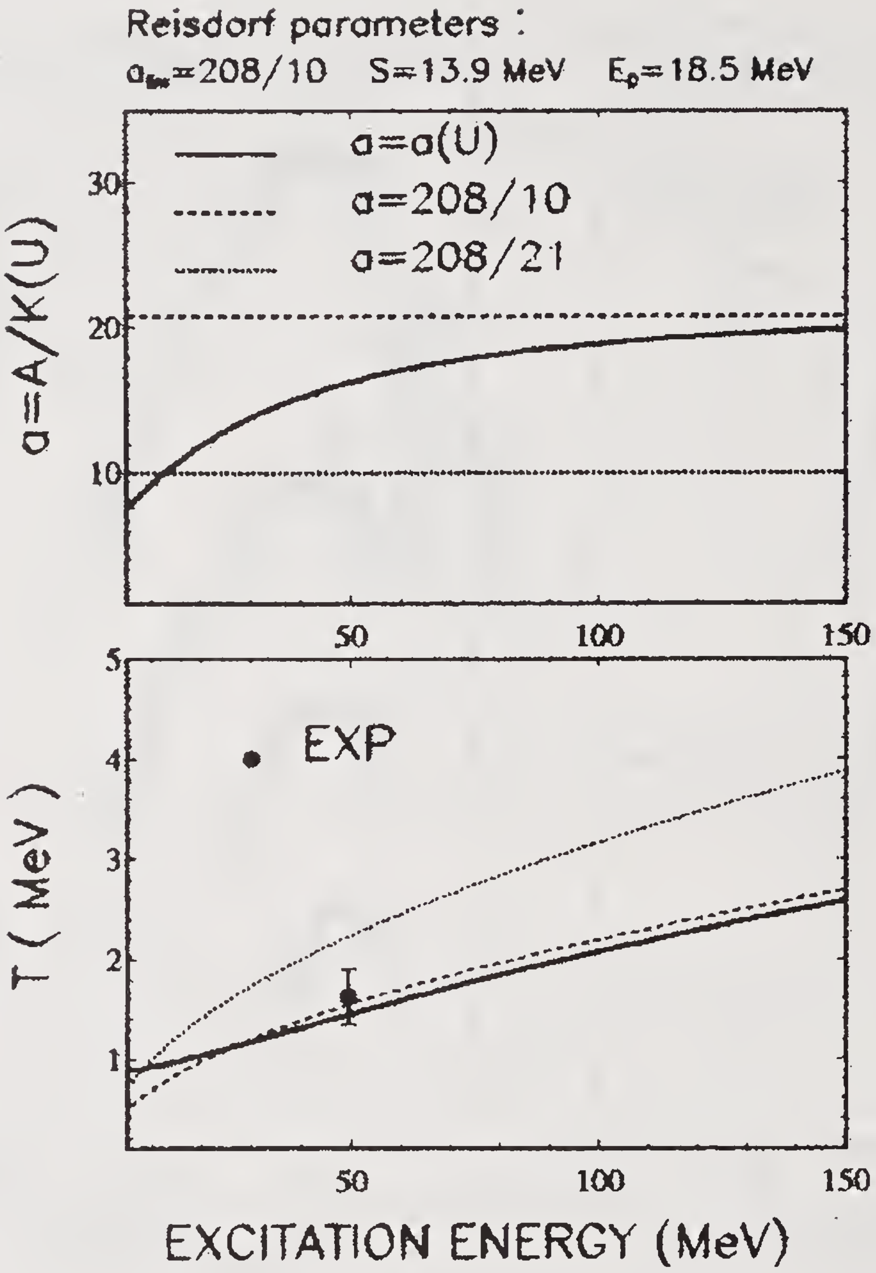

Figure 3. Comparison between the temperature value determined in this work and predictions from different level density prescriptions.

$E_{\text{th}} \sim 50$ MeV in the ^{208}Pb nucleus the nuclear temperature is very far from the value associated to the level density parameter $a \sim A/21$ MeV^{-1}, which characterizes the cold nucleus. On the contrary, the experimental nuclear temperature is in agreement with the values associated to the Reisdorf parameterization and to the asymptotic value $a \sim A/10$ MeV^{-1}. The result reported in figure 3 is in agreement with the findings of a recent work on the reactions ^{207,208}Pb$(n, xn\gamma)$ for neutron energies from 3 to 200 MeV [19].

We note that, despite in the Reisdorf approach the level density parameter is not yet in its asymptotic value, there is a rather reduced difference between the temperatures associated with the excitation dependent level density parameter $a = a(U)$ and the asymptotic value at high excitation. The uncertainty of our temperature measurement does not allow to distinguish between the two temperature predictions.

To further test the level density of the nuclei around ^{208}Pb we have also compared the experimental data with the predictions from complete statistical model calculations. Since the deexcitation chains involve several nuclei, the model calculations cannot be used to study specifically the level density in a given nucleus. The comparison between model predictions and experimental data offer, however, the opportunity of testing in a global way the level density in the mass region around the ^{208}Pb as defined by the limiting values $a \sim A/10$ MeV^{-1} or $a \sim A/21$ MeV^{-1} or as parameterized as a function of the excitation energy and of the shell corrections by Reisdorf.

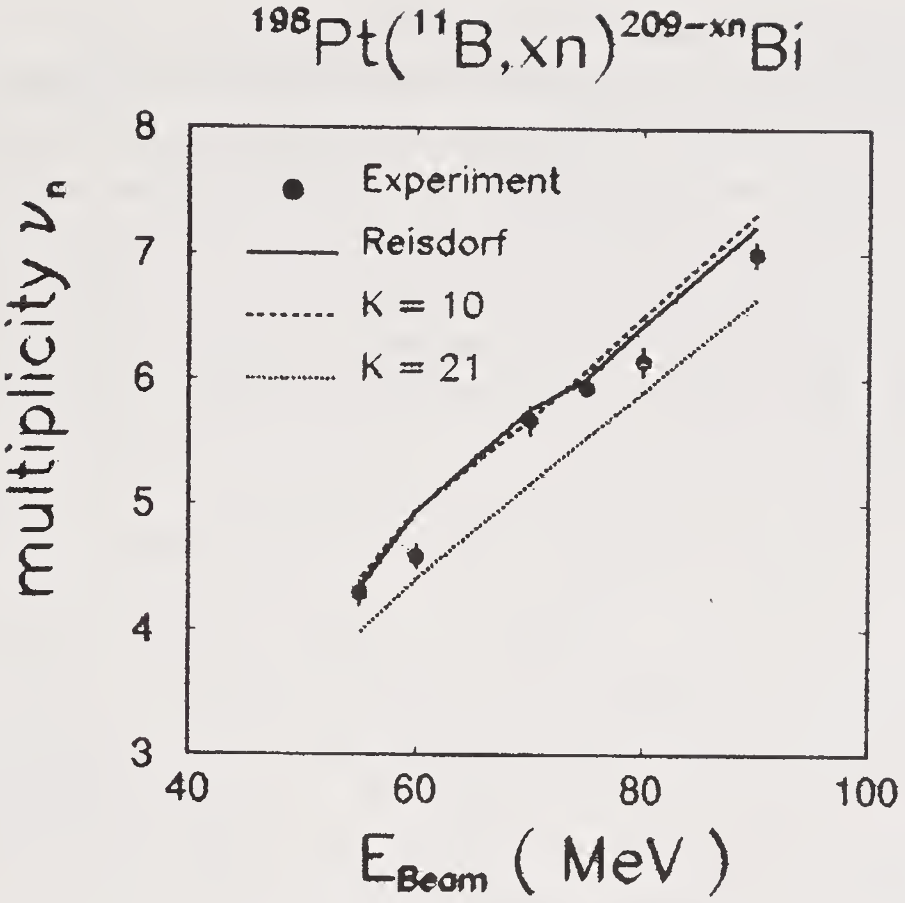

Figure 4. Comparison between the measured neutron multiplicities and the predictions from statistical model calculations using different level density parameters.

To this end the CASCADE code was used, using either the constant level density parameter $a = A/K$ or the Reisdorf parameterization. We first compare in figure 4 the average neutron multiplicity ν_n as derived from the distribution of the Bi isotopes produced in the xn decay with the SM predictions. It appears that the calculations employing the Reisdorf parameterization give a very precise account of the experimental ν_n in the range of bombarding energies explored in this work. The good reproduction of ν_n reflects the capability of the model of predicting well the relative distribution of the Bi isotopes at all bombarding energies.

The same good descriptions were also obtained by looking at the experimental ν_n in coincidence with one proton, i.e. associated to the Pb isotope distributions. Because neutrons are certainly emitted all the way down during the decay, they are sampling also the level density of the more neutron deficient, cold Bi (or Pb) isotopes. Those nuclei are supposed to be characterized by shell effects which are lower than those in the ^{208}Pb nuclei.

In figure 4 the experimental data is also compared with the predictions from calculations employing a constant level density parameter $a = A/K$ using the extreme values of $K =$ 10 and 21 MeV. It is well known that the average kinetic energy of the evaporated neutrons increases by increasing the K value and therefore the predicted average number of the neutrons is lower, when the $K = 21$ MeV value is used. The relevant fact in figure 4 is that the calculations employing the constant level density parameter $K = 10$ also reproduce well the experimental ν_n.

To understand the low sensitivity of the statistical model calculations to the details of the level density, we have computed the average temperature T associated to each neutron emission in the 75 MeV ^{11}B+^{198}Pt reaction when the two parameterizations of the level density are considered. It is found that the difference of the temperature estimates (and then the difference in the average kinetic energy of the neutrons) is generally very small, with the exception of last neutron which is emitted in the region of low excitation energy where the effects due to the shell corrections are magnified.

Equivalent results are obtained by comparing the experimental ‘summed’ proton spectra with the predictions from statistical model calculations, as shown in figure 2. The calculated spectra using the Reisdorf parameterization as well as the constant value $a = A/10$ MeV^{-1} fit well the experimental spectra. On the contrary the level density parameter $a = A/21$ MeV^{-1} predicts unrealistic shapes for the proton spectra. We note that, following the statistical model predictions, the ‘summed’ proton spectra contain in large part particles which are emitted at the higher excitation energies, being therefore far from the region where shell effects dominate.

High energy γ-rays have been measured in the present experiment at all bombarding energies in both ^{11}B- and ^{10}B induced reactions by using the two, large volume BGO detectors. The high energy gamma-rays are in this case of special interest. In fact it is well known [20] that the statistical tail at $E_\gamma \leq 8$ MeV, is sensitive to the level density of the nuclei in the latest steps of the decay cascade, for which we expect a very large influence of the shell corrections. It is therefore expected that the ratio between the statistical tail ($E_\gamma \leq 8$ MeV) and the giant dipole resonance region ($E_\gamma \geq 8$ MeV) should be a sensitive probe for the level density parameterization used in the statistical model calculations. Furthermore, high energy gamma-ray spectra emitted in the decay of the neutron deficient ^{200}Pb compound nucleus have been extensively studied in the past giving the opportunity of comparing two systems (^{200}Pb and ^{209}Bi) quite different from the point of view of the shell corrections.

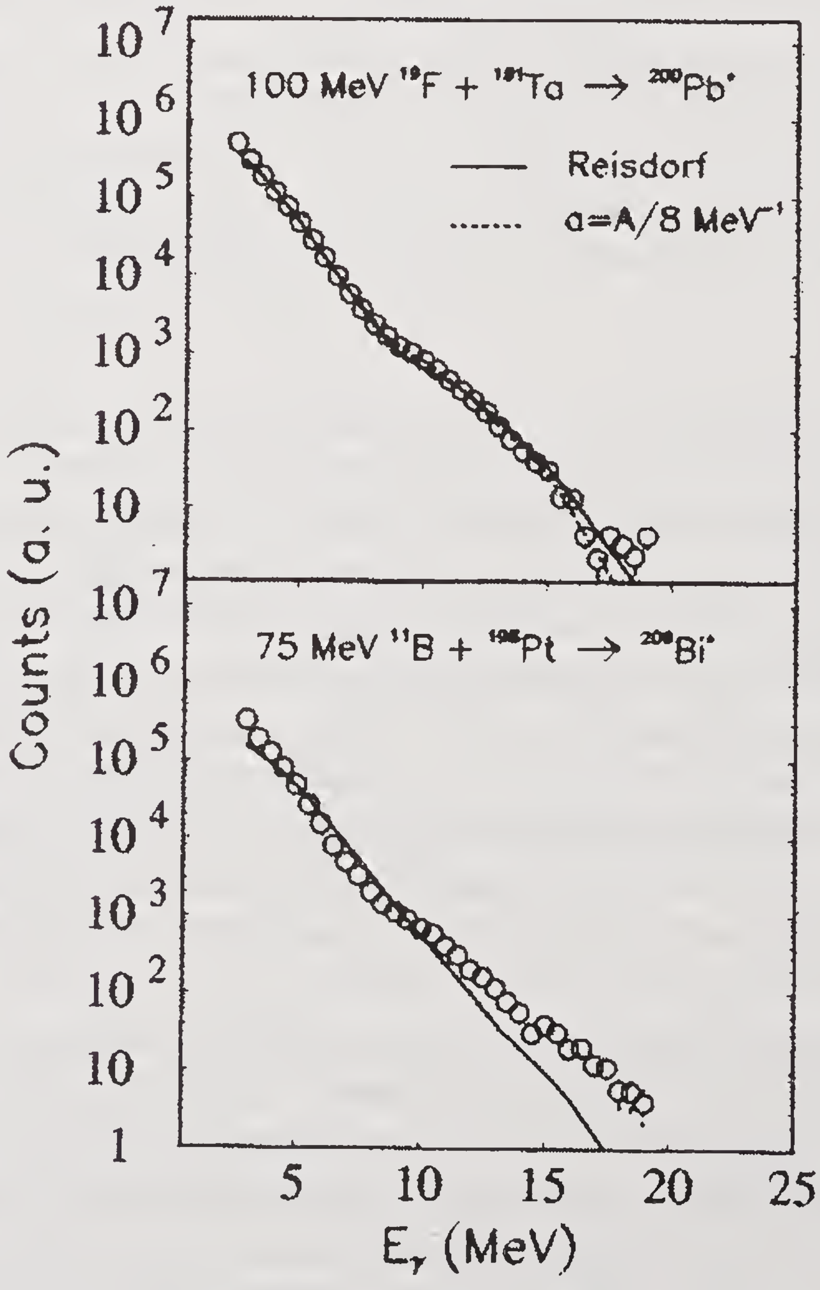

Figure 5. High energy γ-ray spectra measured in the present work.

In figure 5 spectra are reported from the two reactions ^{19}F+^{181}Ta at 100 MeV and ^{11}B+^{198}Pt at 75 MeV, which are populating compound nuclei at a rather equivalent excitation energy. The high energy spectrum from the first reaction is rather well accounted for by using constant parameter $a = A/8$ MeV^{-1} as well as the Reisdorf level density parameters and published GDR parameters [21]. Results are different when the ^{11}B+^{198}Pt is considered. In this case the description of the experimental spectra is rather poor and the deviations between experiment and model predictions increases by decreasing the bombarding energy. This means that the statistical model fails in giving a sufficiently good description of the phase space at low excitation energies even if the more detailed parameterization of the level densities available is used.

4. Conclusions

The study of the excitation energy dependence of the level density is a topic of continuous interest in nuclear physics.

Transition from the low energy level density parameter $a_{\text{eff}} = A/8$ MeV^{-1} towards the FG value $a = A/15$ MeV^{-1} have been evidenced in different mass regions ($A \sim 110, 160$).

In the mass region $A \sim 200$ we are presently investigating the diminishing of the effects due to the shell structure in increasing the excitation energy. Experimental results about 50 MeV excitation energy in the ^{208}Pb confirm that the bulk of the shell effects are already washed out. Nevertheless, the level density parameter seems still far from its predicted asymptotic value. High energy γ-rays seems to be a very important tool to study the level density at excitation energies of few tens of MeV. Furthermore we would also like to explore, increasing the bombarding energy, the second transition from the asymptotic average level density parameter towards the FG value, as suggested from earlier investigations [22,23]. In this attempt extreme care has to be taken due to the onset of the incomplete fusion already below 10 MeV/nucleon bombarding energy, as already reported from γ-ray particle correlation studies.

Further experimental work aimed to extend the present knowledge of the level density, should carefully solve the problem of determining the probe and/or the experimental technique most suitable for measuring the nuclear temperature and the excitation energy in hot nuclear systems.

Acknowledgement

The experimental works described here have been part of collaborations between Padova, Legnaro and the Texas A&M University and several other groups. Special thanks are due to the members of the GASP collaboration for the experiments performed at this facility.

References

[1] A Bohr and B R Mottelson, *Nuclear Structure* (Benjamin, Reading, MA, 1969 and 1975) vols I and II

[2] A V Ignatuk *et al*, *Sov. J. Nucl. Phys.* **21**, 255 (1975)
[3] P F Bortignon and C Dasso, *Phys. Lett.* **B189**, 381 (1987) and references therein
[4] A K Kerman and S Levit, *Phys. Rev.* **C24**, 1029 (1981)
B Lauritzen, G Puddu, P F Bortignon and R A Broglia, *Phys. Lett.* **B246**, 329 (1990)
[5] P Donati *et al*, *Phys. Rev. Lett.* **72**, 2835 (1994)
[6] K Hagel *et al*, *Nucl. Phys.* **A486**, 429 (1988)
[7] M Gonin *et al*, *Phys. Lett.* **B217**, 406 (1989); *Phys. Rev.* **C42**, 2125 (1990)
[8] R Wada *et al*, *Phys. Rev.* **C39**, 497 (1989)
[9] G Nebbia *et al*, *Nucl. Phys.* **A578**, 285 (1994)
[10] S Shlomo and J B Natowitz, *Phys. Rev.* **C44**, 2878 (1991)
[11] B Fornal *et al*, *Phys. Lett.* **B255**, 325 (1991) and references therein
[12] B Fornal *et al*, *Z. Phys.* **A340**, 59 (1991)
[13] B Fornal *et al*, *Phys. Rev.* **C44**, 2588 (1991)
[14] D Bazzacco *et al*, *Phys. Lett.* **B309**, 235 (1993)
[15] G Viesti *et al*, *Nucl. Phys.* **A604**, 81 (1996)
[16] E Farnea *et al*, *Nucl. Inst. Meth.* **A400**, 87 (1997)
[17] M Lunardon, PhD Thesis, (University of Padova 1998) to be published
[18] W Reisdorf, *Z. Phys.* **A300**, 227 (1981)
[19] H Vonach *et al*, *Phys. Rev.* **C50**, 1952 (1994)
[20] M Kicinska-Habior *et al*, *Phys. Rev.* **C41**, 2075 (1990)
[21] R Butsch *et al*, *Phys. Rev.* **C41**, 1530 (1990) and references therein
[22] D Fabris *et al*, *Phys. Rev.* **C50**, R1261 (1994)
[23] B J Fineman *et al*, *Phys. Rev.* **C50**, 1991 (1994)

Extremes of nuclear structure

S B PATEL
Physics Department, University of Mumbai, Vidyanagari, Mumbai 400 098, India

Abstract. With the advent of medium and large gamma detector arrays, it is now possible to look at nuclear structure at high rotational forces. The role of pairing correlations and their eventual breakdown, along with the shell effects have showed us the interesting physics for nuclei at high spins – superdeformation, shape co-existence, yrast traps, alignments and their dramatic effects on nuclear structure and so on. Nuclear structure studies have recently become even more exciting, due to efforts and possibilities to reach nuclei far off from the stability valley. Coupling of gamma ray arrays with ‘filters’, like neutron wall, charged particle detector array, gamma ray total energy and multiplicity castles, conversion electron spectrometers etc gives a great handle to study nuclei produced online with ‘low’ cross-sections. Recently we studied, nuclei in mass region 80 using an array of 8 germanium detectors in conjunction with the recoil mass analyser, HIRA at the Nuclear Science Centre and, most unexpectedly came across the phenomenon of identical bands, with two quasi-particle difference. The discovery of magnetic rotation is another highlight. Our study of light In nucleus, 107In brought us face to face with the ‘dipole’ bands. I plan to discuss some of these aspects. There is also an immensely important development — that of the ‘radioactive ion beams’. The availability of RIB, will probably very dramatically influence our ‘conventional’ concept of nuclear structure. The exotic shapes of these exotic nuclei and some of their expected properties will also be touched upon.

Keywords. Nuclear structure; high spin spectroscopy; gamma detector arrays.

PACS Nos 21.10.Tg; 23.20.Lv

$M1$ and $E2$ band structures in the Sn–Xe–Ba region

R SRINIVASA CHAKRAWARTHY*
Institut für Kernphysik, Universität zu Köln, Zülpicher Str. 77, 50937 Köln, Germany

Abstract. In the present talk I will discuss some 'rare' aspects of the $E2$ band structures and the novel features concerning the dipole bands in this mass region. Reliable and accurate lifetimes have been measured using coincidence recoil distance method. The results of ^{129,130}Ba will be discussed. In contrast to the predictions of the tilted axis cranking model, the dipole bands in Sb–Xe–Ba nuclei can be nicely described as high-K prolate bands. New data from multi-detector arrays has established extended bands structure, their decay to low lying states have been established and the angular correlation supports the predominant, $\Delta I = 1$ character. Finally the sensitive measures, i.e. $B(M1)$ rates of the tilted axis model are compared with the high-K formula based on 1-dim cranking model.

Keywords. Nuclear structure; recoil distance method; cranking model.

PACS Nos 21.10.Tg; 23.20.Lv

---

*For the Köln Group and Collaborators in Italy, Heidelberg, Riso.

Fusion–fission dynamics in the superheavy nucleus production

G GIARDINA[1], P D'AGOSTINO[1], G FAZIO[1], M HERMAN[2], A I MUNINOV[3], A NASIROV[3,4], G OLIVA[1], R PALAMARA[5] and R RUGGERI[1]

[1]Istituto Nazionale di Fisica Nucleare, Sezione di Catania, Dipartimento di Fisica dell'Università di Messina, 98166 Messina, Italy
[2]IAEA, A-1400 Vienna, Austria
[3]Institute of Nuclear Physics, 702132 Ulugbek, Tashkent, Uzbekistan
[4]Bogoliubov Laboratory of Theoretical Physics, JINR, 141980 Dubna, Russia
[5]Dipartimento PAU dell'Universitá di Reggio Calabria, 89100 Reggio Calabria, Italy

Abstract. The fusion–fission reaction mechanism leading to the massive nucleus formation is studied. We investigate the superheavy nucleus formation in heavy-ion induced reactions by analysing the evaporation residue (ER) production in order to study the fusion dynamics and the decay properties of nuclei close to the stability island at $Z = 114$. We consider the ^{64}Ni + ^{208}Pb, ^{48}Ca + ^{238}U and ^{48}Ca + ^{244}Pu reactions that lead to the $Z = 110, 112$ and 114 superheavy elements respectively.

By using the dinuclear system (DNS) concept of the two interacting nuclei we calculate the quasifission–fusion competition in the entrance channel and the fission–evaporation competition along the de-excitation cascade of the compound nucleus. The dynamics of the entrance channel allows us to determine the beam energy window which is favorable to the fusion, while the dynamic evolution of the compound nucleus on the shell correction to the fission barrier and the dissipative effects influence the fission–evaporation competition in order to obtain the residue nuclei from the superheavy nucleus formation. We also calculate the $\Gamma_n/\Gamma_{\rm tot}$ ratio at each step of the de-excitation cascade of the compound nucleus and we present a systematics of $\Gamma_n/\Gamma_{\rm tot}$ (at first step of the cascade) for many reactions that lead to nuclei with $Z = 102$–114.

Keywords. Quasifission; fusion; fission; evaporation residues; superheavy elements.

PACS Nos 25.70.-z; 25.70.Jj; 27.90.+b

1. Introduction

The synthesis of superheavy nuclei is an interesting and present research field [1–6] but the cross section for the formation of heavy elements by fusion reaction (using Pb, U and Pu targets) decreases down to a very low value that the evaporation residue (ER) production is about few pb or lower. According to the dinuclear system (DNS)-concept the fusion of nuclei is considered as a two stage process: the first stage is the capture (the formation of the DNS after dissipation of some part of the relative kinetic energy and orbital angular momentum); the second stage is the fusion (the transformation of the dinuclear system in the compound nucleus by a continuous multinucleon transfer from a light nucleus to a heavy one retaining the individuality of nuclei having a shell structure). In this second stage, fusion is in competition with quasifission which is the decay of the dinuclear system in two fragments before the formation of the compound nucleus. Thus, fusion is treated as a motion in the charge (mass) asymmetry variable, and capture and quasifission are a consequence of the relative motion of nuclei in DNS. The energy window for the capture was revealed. If there is no capture, nuclei cannot be fused due to the smallness of the interaction time and the excitation energy generated from the relative kinetic energy. Therefore, the used model [7] is required to analyse the fusion of light nuclei at high energies and the fusion of massive nuclei at all collision energies where quasifission plays a decisive role in decreasing the fusion cross section [8,9]. As a result of the calculation we find that: (i) a number of partial waves with angular momentum lead to capture (i.e., those partial waves which have been trapped in a potential minimum of the entrance channel; the critical value of angular momentum l_{cr} for a given collision energy can be calculated dynamically); (ii) an amount of the excitation energy is available before the complete fusion at given collision energy and impact parameter or orbital angular momentum; (iii) a beam energy window is favorable to the fusion: the low limit (E_{min}) of this window is defined by the dynamical barrier in the entrance channel before the capture. The upper limit (E_{max}) appears because friction forces cannot provide an intense loss of the initial kinetic energy in order to trap the dinuclear system into a pocket.

After fusion, the de-excitation cascade of the compound nucleus was analysed in detail in the framework of the advanced statistical model (ASM) approximation [10]. With this model it is possible to trace the $\Gamma_n/\Gamma_{\mathrm{tot}}$ values at each step of the de-excitation cascade and to have information on the consequences for the fission process dynamics. The model allows us to consider the influence of the nuclear viscosity and the dynamical dependence of the shell correction to the fission barrier on the calculated ER cross sections.

2. General remarks on the formalism

We study the precompound nucleus dynamics through the evolution of DNS (after capture) to complete fusion (that is in competition with the quasifission process). The excited compound nucleus can undergo fission or emit particles before detecting the reaction products (evaporation residues, or fission fragments, or light particles).

In the suggested model [7], the relevant variables are energies and occupation numbers of single-particle states of nucleons in nuclei (the intrinsic degrees of freedom) and relative motion of nuclei at the first-capture stage, and the mass (charge) asymmetry degrees of freedom at the second stage of fusion. The competition between complete fusion and quasifission of the dinuclear system formed after capture as its further evolution is taken into account by the statistical theory of level densities on the intrinsic fusion barrier which is on the charge asymmetry axis and quasifission barrier which is on the relative distance axis as in [11]. In contrast to [11], the capture probability $T_l^{\mathrm{capture}}(E, l)$ is estimated in a dynamic approach, considering the evolution of the coupling between the relative motion of nuclei and intrinsic motion of their nucleons. In the capture stage the system is trapped in a potential wall due to the dissipation of the initial kinetic energy. The formed DNS lives long enough (several 10^{-21} s) to evolute from the projectile-and target-like configuration to become mononucleus (compound nucleus). This evolution corresponds to the motion on the mass (charge) asymmetry axis.

The evaporation residue cross section is related to the partial fusion cross section $\sigma_l^{\mathrm{fus}}(E,l)$, as well as to the probability $W_{\mathrm{sur}}(E,l)$ that the compound nucleus survives fission during the de-excitation cascade at the bombarding energy E:

$$\sigma_{\mathrm{er}}(E) = \sum_{l=0}^{\infty} \sigma_l^{\mathrm{cap}}(E) P_{CN}(E,l) W_{\mathrm{sur}}(E,l), \tag{1}$$

where the partial fusion cross section is $\sigma_l^{\mathrm{fus}} = \sigma_l^{\mathrm{cap}}(E) P_{CN}(E,l)$ and the partial capture cross section is $\sigma_l^{\mathrm{cap}}(E) = \lambda^2/4\pi(2l+1)T_l^{\mathrm{capture}}(E,l)$. The factor $P_{CN}(E,l)$ is used to take into account the decrease of the fusion probability due to dinuclear system break-up competing with fusion. At first this factor was determined in [11].

The calculation of competition between fusion and quasifission processes can be made according to principles of the statistical theory by comparing the level density at the top point (after which the dinuclear system goes to the fusion through smaller mass asymmetry values) of the $U(Z,A;l,R_m)$ driving potential (see figure 1) with the level density at the bottom of the exit barrier pocket in the $V(Z,A;l,\mathbf{R})$ internuclear potential (see figure 2). The driving potential, playing the main role in fusion dynamics, was calculated as follows:

$$\begin{aligned} U(Z,A;l,R_m) = {} & B_1(Z;A) + B_2(Z_P+Z_T-Z;A_P+A_T-A) \\ & + V(Z,A;l,R_m) - B_0, \end{aligned} \tag{2}$$

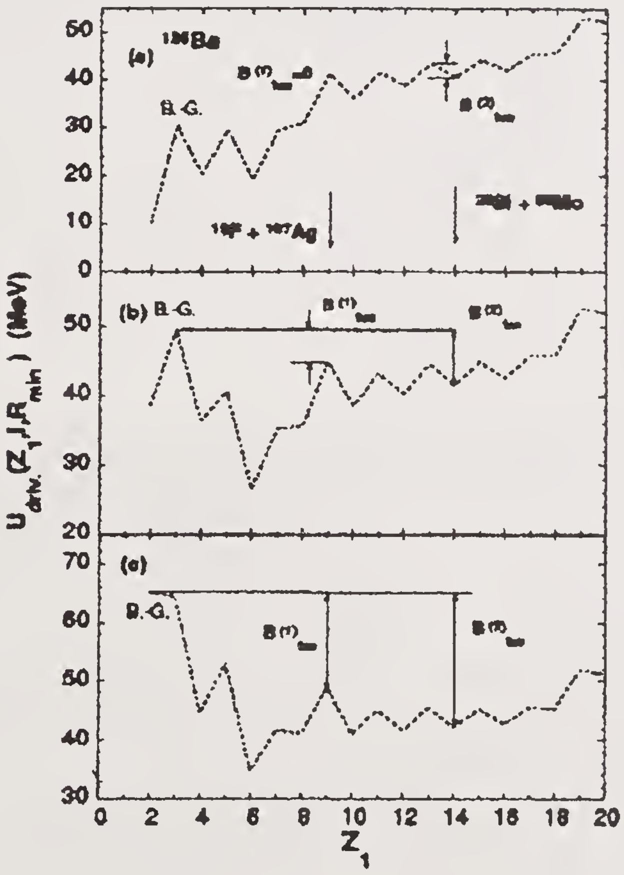

Figure 1. The driving potential (dashed curves) of compound nucleus ^{126}Ba calculated for different values of angular momentum: $l = 0$ (**a**), $l = 20\hbar$ (**b**), and $l = 30\hbar$ (**c**). The different values of the entrance mass asymmetry are shown by arrows ($Z_1 = 9$ and 14). $B_{\mathrm{fus}}^{(1)}$ and $B_{\mathrm{fus}}^{(2)}$ are intrinsic barriers in the way to fusion for the ^{19}F + ^{107}Ag and ^{28}Si + ^{98}Mo reactions, respectively.

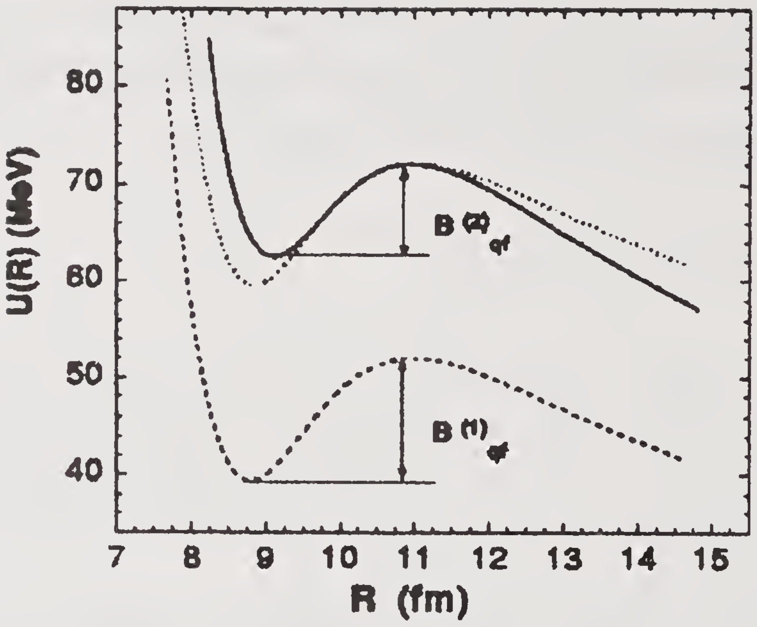

Figure 2. The nucleus–nucleus potential $U(R)$ calculated for the ^{28}Si + ^{98}Mo (solid curve) and ^{19}F + ^{107}Ag (dashed curve) reactions as a function of internuclear distance. For an easier comparison of two pockets (in width and depth) the dashed curve is shifted (dotted curve) up to overlapping with the solid curve. $B_{\mathrm{qf}}^{(1)}$ and $B_{\mathrm{qf}}^{(2)}$ are quasifission barriers for the corresponding reactions.

where B_1 and B_2 are the binding energies of the nuclei in a dinuclear system, $V(R_m) = V(Z,A,R_m)$ is the minimum value of the nucleus–nucleus interaction potential at the bottom of the pocket; B_0 is the binding energy of the compound nucleus. For the given total charge and mass numbers, $Z_{\mathrm{tot}} = Z_1 + Z_2$ and $A_{\mathrm{tot}} = A_1 + A_2$, the A/Z ratio of the considered fragment was determined from the minimum value of $U(Z,A;l,R_m)$.

The $T_l^{\mathrm{capture}}(E,l)$ factor is connected with the relative kinetic energy and angular momentum losses which were determined from the equations of motion

$$\mu(\mathbf{R}(t))\ddot{\mathbf{R}} + \gamma_R[\mathbf{R}(t)]\dot{\mathbf{R}}(t) = -\frac{\partial V[\mathbf{R}(t)]}{\partial \mathbf{R}}, \tag{3}$$

$$\frac{\mathrm{d}L}{\mathrm{d}t} = \gamma_\theta[\mathbf{R}(t)]\left(\dot{\theta}R_{\mathrm{eff}}^2 - \dot{\theta}_1 R_{1\mathrm{eff}}^2 - \dot{\theta}_2 R_{2\mathrm{eff}}^2\right), \tag{4}$$

where $\mathbf{R}(t)$ is the relative motion coordinate, $\dot{\mathbf{R}}(t)$ is the corresponding velocity; $\dot{\theta}, \dot{\theta}_1$ and $\dot{\theta}_2$ are angular velocities of the dinuclear system and its two fragments, respectively, while R_1 and R_2 are the fragment radii. The γ_R and γ_θ friction coefficients, a change of the nucleus–nucleus potential during interaction of nuclei, $V[\mathbf{R}(t)] = V_0[\mathbf{R}(t)] + \delta\hat{V}(\mathbf{R})$, and the dynamic contribution $\delta\mu(\mathbf{R})$ to the reduced mass $\mu(\mathbf{R}) = mA_TA_P/(A_T + A_P) + \delta\mu(\mathbf{R})$ are calculated from the estimation of the coupling term between the relative motion of nuclei and intrinsic excitation of nucleons in them [12].

The dynamics of the capture is sensitive to the nucleus–nucleus potential

$$V_0(\mathbf{R}) = V_C(\mathbf{R}) + V_{\mathrm{nucl}}(\mathbf{R}) + V_{\mathrm{rot}}(\mathbf{R}), \tag{5}$$

where $V_C(\mathbf{R}), V_{\mathrm{nucl}}(\mathbf{R})$, and $V_{\mathrm{rot}}(\mathbf{R})$ are the Coulomb, nuclear and rotational potentials, respectively. The nuclear shape is important to calculate the Coulomb and nuclear interaction between colliding nuclei.

By our AMS it was possible to take into account the dynamical aspect of the compound nucleus evolution on the fission–evaporation competition along the de-excitation cascade.

As far as the fission barriers are concerned, we use the rotating droplet model predictions (angular momentum dependent) as parameterized by Sierk [13] and allow for angular momentum and temperature fade-out of the shell corrections [14]. It is expressed by the formula for the actual fission barrier used in our calculations:

$$B_{\mathrm{f}}(J,T) = cB_{\mathrm{f}}^{\mathrm{m}}(J) - f(T)g(J)\delta W, \tag{6}$$

with

$$f(T) = \begin{cases} 1 & T \leq 1.65\,\mathrm{MeV} \\ k\exp(-mT) & T > 1.65\,\mathrm{MeV} \end{cases}$$

and

$$g(J) = \left\{1 + \exp[(J - J_{1/2})/\Delta J]\right\}^{-1},$$

where $B_{\mathrm{f}}^{\mathrm{m}}(J)$ is the parameterized macroscopic fission barrier [13] depending on J angular momentum, $\delta W = \delta W_{\mathrm{sad}} - \delta W_{\mathrm{gs}} \simeq -\delta W_{\mathrm{gs}}$ is the microscopic (shell) correction to the fission barrier taken from the tables [15] and the constants for the macroscopic fission barrier scaling, temperature and angular momentum dependencies of the microscopic correction are chosen to be as follows: $c = 1.0, k = 5.809$, $m = 1.066\,\mathrm{MeV}^{-1}$, $J_{1/2} = 24\hbar$ (for nuclei with an A mass number of about 210) and $\Delta J = 3\hbar$. These constants were obtained as the result of analysis of a large set of the data on the fissility of nuclei in the Lu–At range obtained in the reactions induced by light (p, t and α) and heavy (^{12}C and ^{18}O) projectiles [14]. This makes our shell corrections become dynamical quantities too. The $J_{1/2}$ parameter slowly decreases increasing the A mass number. For nuclei with $A > 250$ we use $J_{1/2} = 20\hbar$.

The systematics obtained by Bhattacharya *et al* [16] gives the possibility of taking into account the incident energy per nucleon ϵ and compound nucleus mass A_{cn} dependencies of the reduced dissipation coefficient β (the ratio between the γ friction coefficient describing the coupling to the fission degree of freedom and the m reduced mass of the system.

We use the same set of parameters for all superheavy nuclei and there are no free parameters in our calculations. By this model it is possible to trace the $\Gamma_n/\Gamma_{\mathrm{tot}}$ values at each step of the de-excitation cascade.

3. Results and discussion

We present the results of the investigation on massive systems that lead to the formation of the $Z = 110, 112$ and 114 superheavy elements, and we compare our calculation with the available experimental data.

Figure 3 shows the fusion cross section (full line) for the ^{64}Ni + ^{208}Pb reaction that forms the ^{272}110 excited compound nucleus by a *cold fusion reaction*. In the same figure we report the quasifission contribution (dotted-dashed line), the evaporation residue cross-section (dashed line) after 1 neutron emission from the excited compound nucleus, and the fission barrier (dotted line). In this figure we also report the experimental data of the

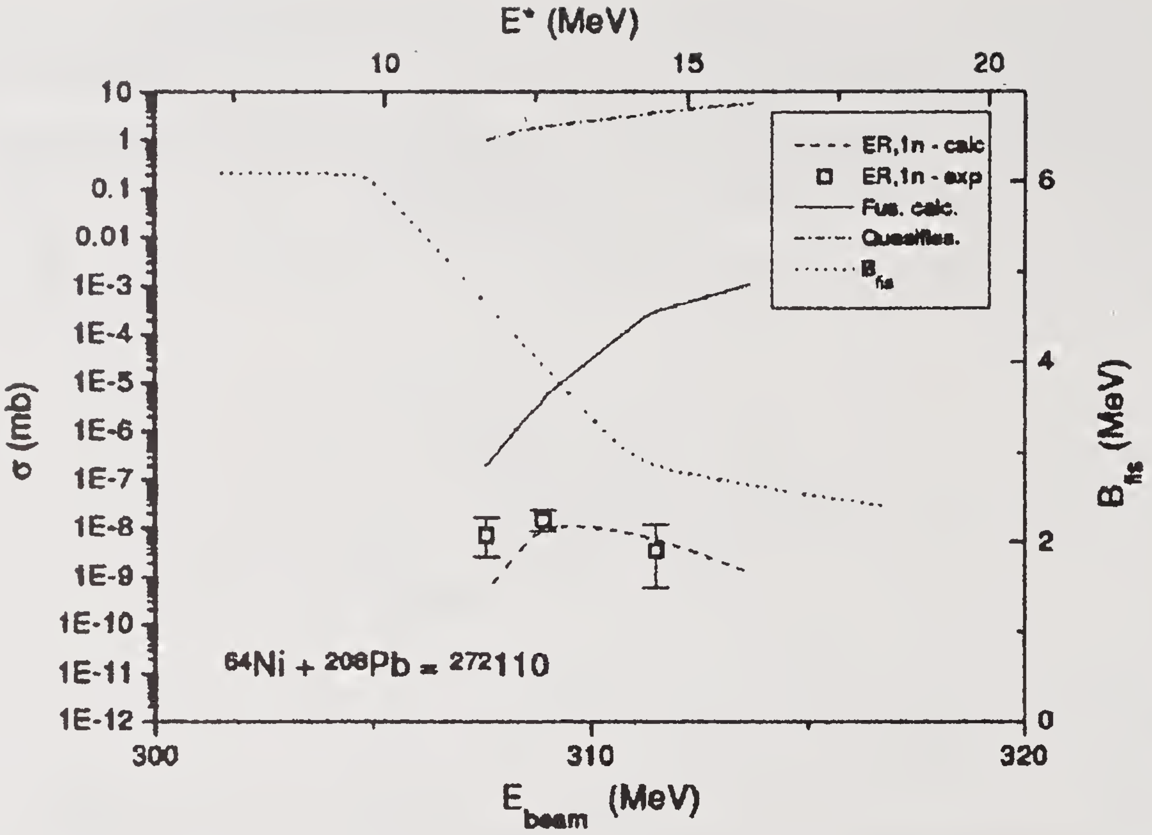

Figure 3. Fusion cross section for reaction ^{64}Ni + ^{208}Pb ⇒ ^{272}110.

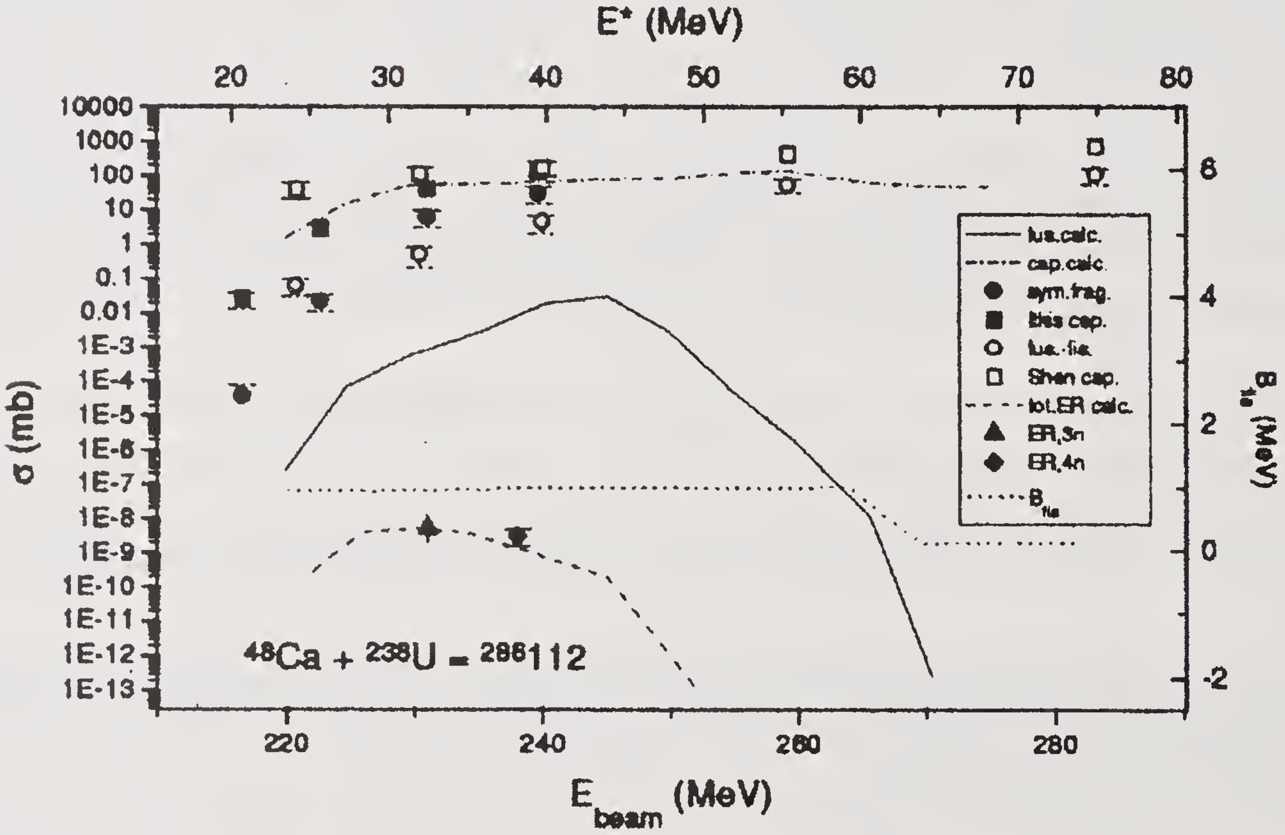

Figure 4. Fusion cross section for reaction ^{48}Ca + ^{238}U ⇒ ^{286}112.

evaporation residues [1]. We can observe the full agreement between experimental data and calculation. It is possible to analyse the ratio (10^{-7}–2×10^{-4}) between the complete fusion and quasifission, and the ratio (2×10^{-3}–10^{-5}) between the evaporation residue production and fusion. At low beam energies (lower than 307 MeV) the ER cross section is limited by the low value of the fusion formation. At high beam energies (higher than 313 MeV) the ER production decreases because the fission process strongly increases. This last effect is related to the fade-out of the fission barrier, due to the damping of the shell correction.

Figure 4 shows the results obtained for the ^{48}Ca + ^{238}U reaction that lead to the ^{286}112 excited compound nucleus. From this figure one can observe the beam energy window

($E_{\mathrm{beam}} \simeq$ 218–262 MeV, corresponding to about $E^* = 21$–58 MeV) that allows for the complete fusion formation (> 1 nb). In this energy interval and for the above-mentioned *hot fusion reaction*, the ratio between fusion and quasifission is about 10^{-8}–2×10^{-4} and the ratio between the ER cross section and complete fusion is about 10^{-4}–5×10^{-8}. At lower beam energies the ER production is limited by the fusion formation, at higher beam energies the ER cross section is limited by both the low fusion formation and the fade-out of the fission barrier ($B_{\mathrm{fis}} < 0.12$ MeV) that strongly increases the fission process.

In figure 5 we report the excitation functions for the ^{48}Ca (^{238}U, xn) $^{286-xn}112$ reaction after the x ($x = 2, 3, 4$) neutron emission from the excited compound nucleus. In this figure we also report the experimental ER cross section [17] obtained by the $^{286-3n}112$ (triangle) spontaneous fission events. For the $^{286-4n}112$ residual nucleus (diamond) the experimental estimation of the upper limit is reported. The agreement between the calculation and experimental data is very good, even if until now only partial experimental measurements are known. Dotted line is the fission barrier for the compound nucleus (see figures 4 and 5).

In figure 4 the experimental data of capture cross section [17] (full squares) and [18] (open squares), the symmetric fragment cross section [17] (full circles), the ER production [17] after $3n$ (triangle) and $4n$ (diamond) emission and the fusion–fission production [18] (open circles) for the reaction induced by ^{48}Ca (where an intrinsic fusion farrier $B_{\mathrm{f}} \simeq 13.5$ MeV exists) are also reported. In the same figure we report, for comparison, our capture cross section calculation (dashed-dotted line), fusion cross section (full line) and the total ER production (dashed line) after 2, 3 and 4 neutron emission from the excited $^{286}112$ compound nucleus. As one can see, the capture cross section calculation and the total ER calculation are in agreement with the experimental data of [17,18], whereas the fusion cross section calculation is lower than the symmetric fragment production [17] and the fusion cross section [18] extracted from the experimental fragment production. Therefore, the fragment production should be mainly contributed from the quasifission process, whereas the fission products after fusion at the various beam energies can reach the fusion cross section value. In fact, for the beam energy range corresponding to the experimental data of

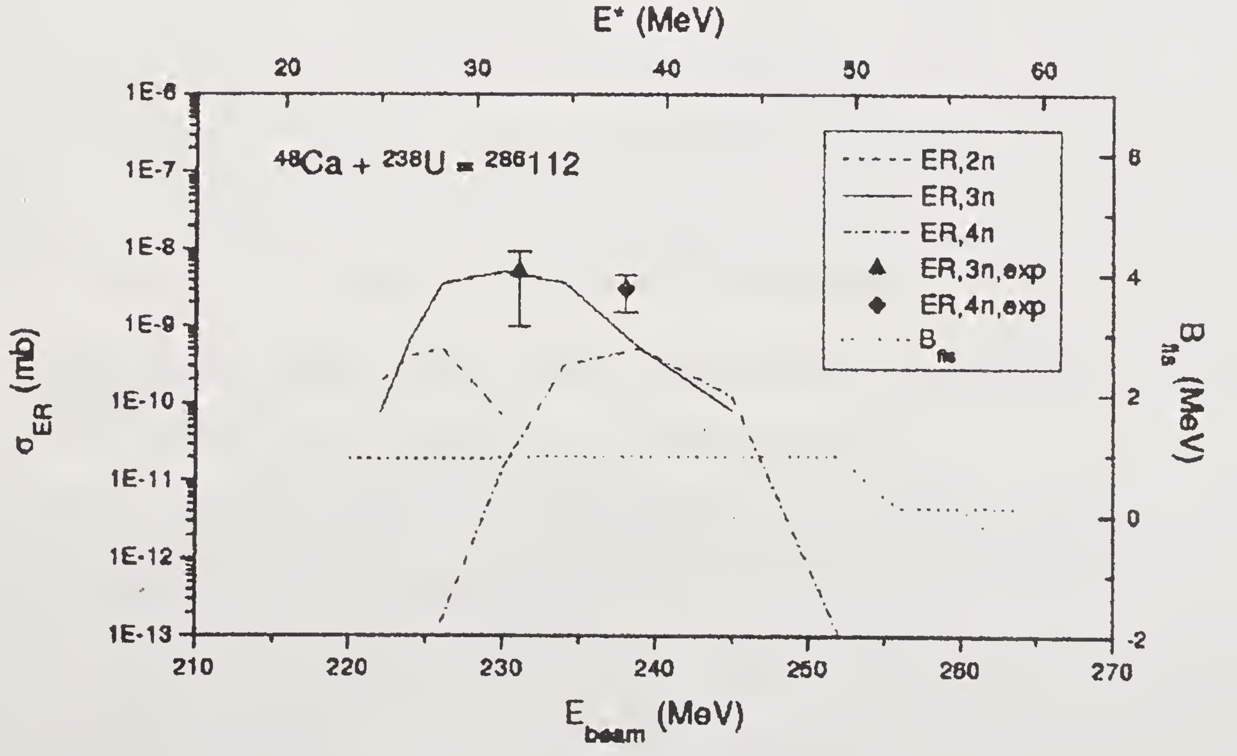

Figure 5. Excitation functions for the ^{48}Ca (^{238}U, xn) $^{286-xn}112$ reactions.

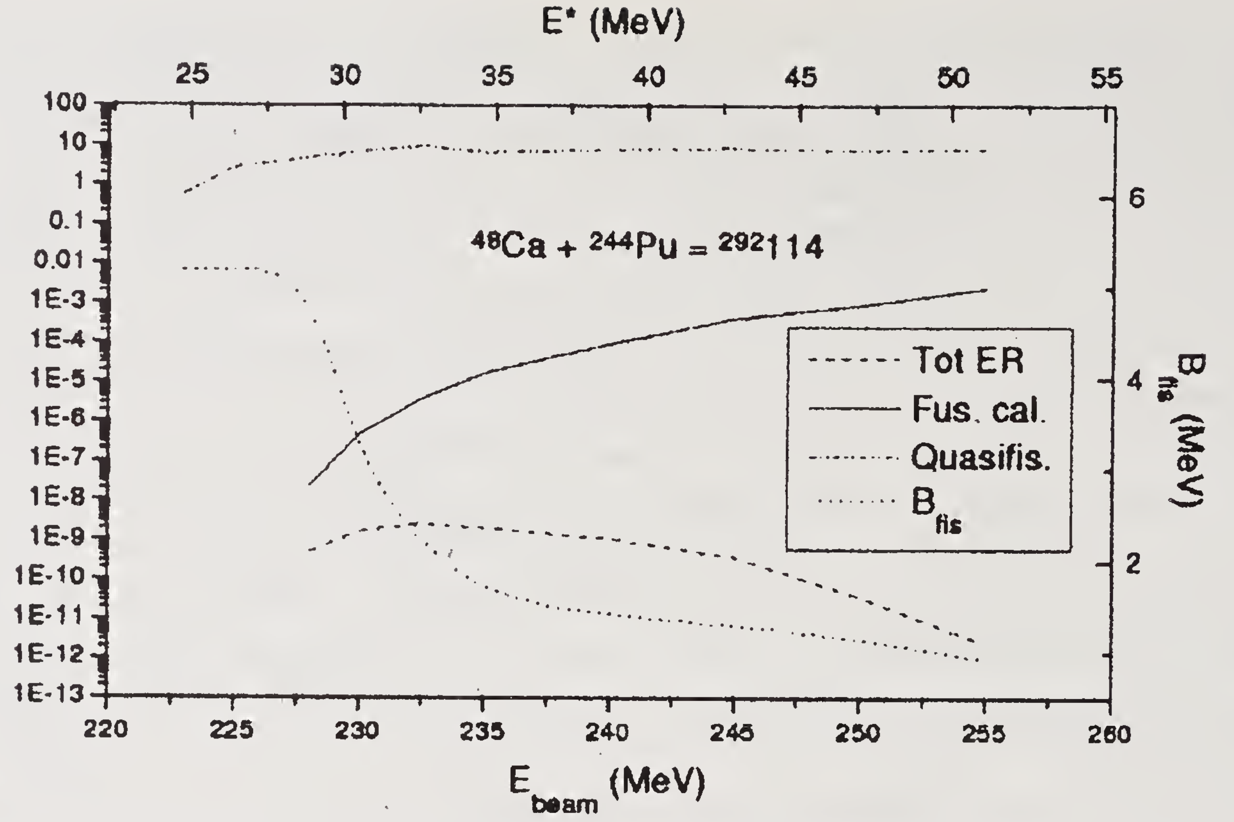

Figure 6. Calculated cross sections for the reaction ^{48}Ca + ^{244}Pu.

ER, the ratio between our ER calculation and the fusion cross section calculation is about 10^{-5}–10^{-6}, whereas the ratio between the experimental ER production and the experimental symmetric fragment production is about 5×10^{-8}–5×10^{-9} (corresponding to a very small ER value, considering that the B_{fis} fission barrier is about 1 MeV).

From these considerations it is possible to affirm that by *cold fusion reactions* it is very difficult to synthesize superheavy elements (and to observe the evaporation residue products) because the E^*_{DNS} excitation energy of the dinuclear system (after capture) is generally lower than (or close to) the B_{f} intrinsic fusion barrier, whereas by *hot fusion reactions* the E^*_{DNS} energy is higher than B_{f}.

In figure 6 we report the calculation for the ^{48}Ca + ^{244}Pu reaction that lead to the ^{292}114 compound nucleus at beam energies of 228–255 MeV, corresponding to excitation energies lower than 52 MeV and the $^{287-290}$114 residue nucleus production. Full line represents the fusion cross section, dashed-dotted line is the quasifission contribution, dashed line is the total ER production after x neutron emission. Dotted line represents the fission barrier against the excitation energy of the compound nucleus. In figure 7 we report the excitation functions for the ^{48}Ca (^{244}Pu, xn) $^{292-xn}$144 reaction after the x ($x = 2, 3, 4$ and 5) neutron emission from the compound nucleus. The ER to fusion ratio is included in the 10^{-2}–10^{-8} range while the fusion to quasifission ratio changes between 10^{-4}–10^{-7} in the considered energy range.

In figure 8 we present the systematics of the $\Gamma_n/\Gamma_{\text{tot}}$ ratio, at first step of the de-excitation cascade of the compound nucleus, for reactions that lead to heavy and superheavy nuclei with $Z = 102$–114. This figure shows the trend of the $\Gamma_n/\Gamma_{\text{tot}}$ ratio against E^*/B_{fis} for many reactions at different energies. As one can see the $\Gamma_n/\Gamma_{\text{tot}}$ ratio is strongly correlated (within a factor 2) to the E^*/B_{fis} ratio. It is to be noted that the emission of the gamma rays, neutrons, protons and alpha particles is not considered in the present model. This effect (that will be the subject of a future work) can be relevant at higher energies, and can significantly change the $\Gamma_n/\Gamma_{\text{tot}}$ trend at higher E^*/B_{fis} values. Therefore, the trend of the ER production versus the excitation energy (in comparison with the effective fission barrier) has the same behaviour for all investigated reactions.

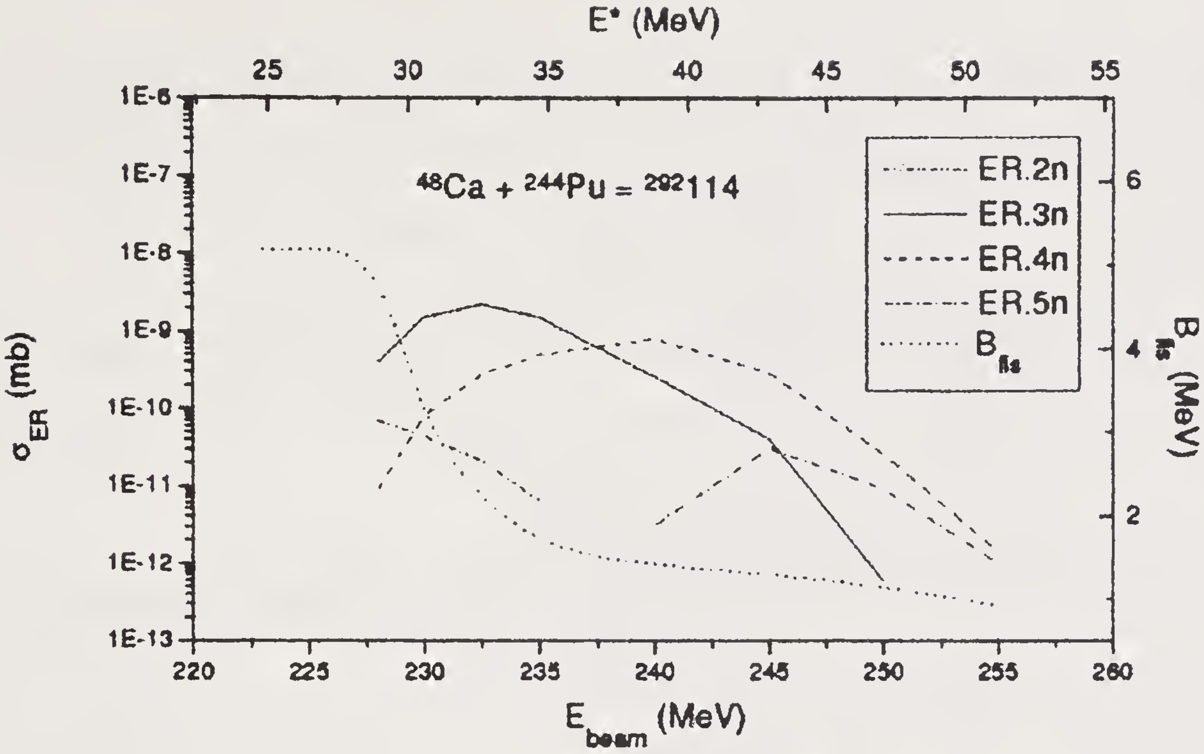

Figure 7. Excitation functions for the ^{48}Ca (^{244}Pu, xn) $^{292-xn}$144 reaction.

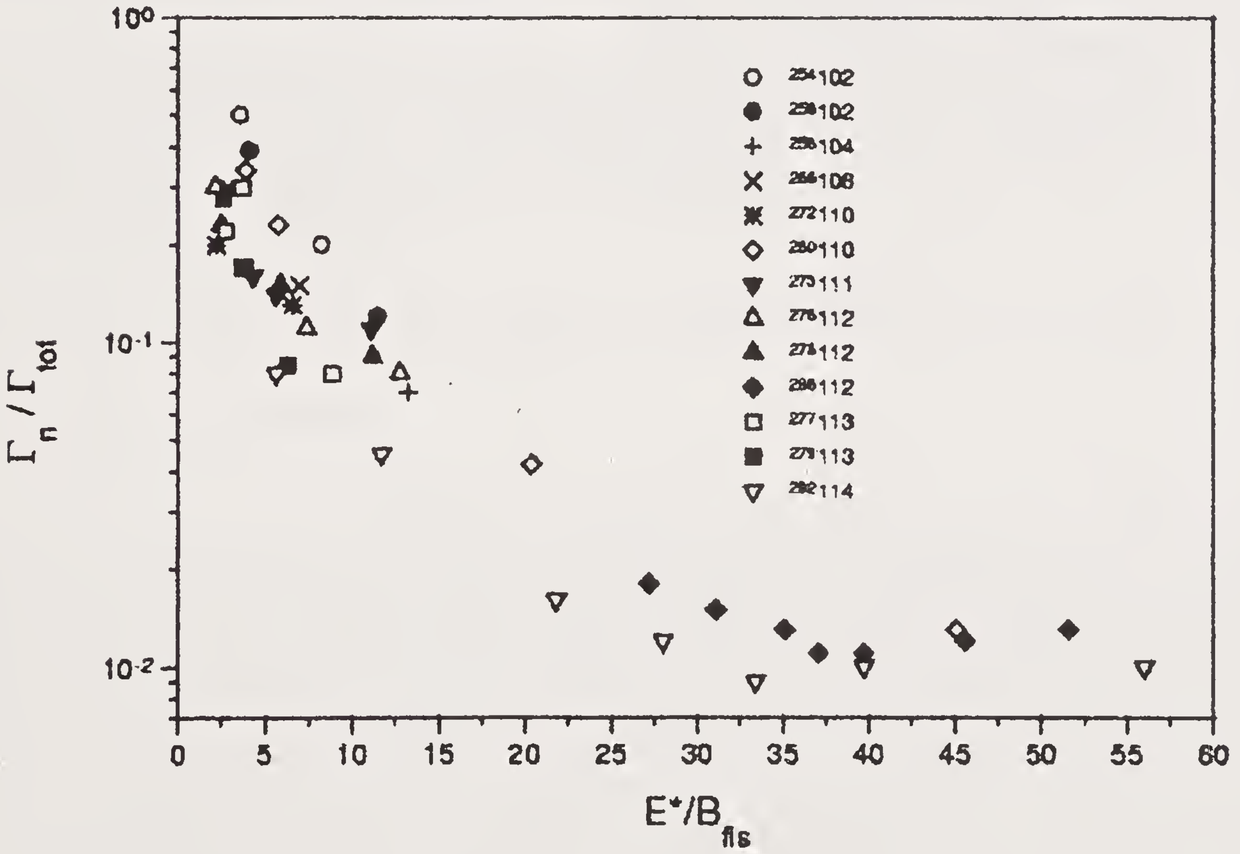

Figure 8. Systematics of the $\Gamma_n/\Gamma_{\text{tot}}$ ratio for the reaction leading to heavy nuclei with $Z = 102$–114.

This means that the ratio between the ER production and fusion cross section is mainly related (for all reactions) to the E^*/B_{fis} value, while the absolute ER value is related to the competition between the fusion and quasifission during the evolution of the dinuclear system (after capture) in the entrance channel. Therefore, the ER production (normalized to the fusion cross section) for the heavy and superheavy nuclei is mainly dependent on the E^*/B_{fis}, while the fusion process is related to the dynamic effect (the ratio between the intrinsic fusion barrier and the quasifission barrier) in the entrance channel.

References

[1] S Hofmann, GSI-Preprint-98-16, Darmstadt, March 1998, and references therein

[2] Yu Ts Oganessian, *Proc. of Int. Conf. Nucl. Phys. at the Turn of the Millenium* (Wilderness, South Africa, World Scientific, Singapore, 1996) p.11

[3] A Ghiorso *et al*, *Nucl. Phys.* **A583**, 861 (1995); *Phys. Rev.* **C51**, R2293 (1995)

[4] Yu A Lazarev *et al*, *Phys. Rev.* **C54**, 620 (1996)

[5] G Giardina, *J. Phys.* **G23**, 1285 (1997)

[6] Y Abe *et al*, *J. Phys.* **G23**, 1275 (1997)

[7] G Giardina *et al*, submitted to *Nucl. Phys.*

[8] R V Jolos *et al*, *JINR* Preprint E4-97-302, Dubna, 1997

[9] G G Adamian *et al*, *Nucl. Phys.* **A633**, 409 (1998)

[10] A D' Arrigo *et al*, *Phys. Lett.* **B34**, 1 (1994)

[11] N V Antonenko *et al*, *Phys. Lett.* **B319**, 425 (1993); *Phys. Rev.* **C51**, 2635 (1995)

[12] G G Adamian *et al*, *Phys. Rev.* **C56**, 373 (1997)

[13] A J Sierk, *Phys. Rev.* **C33**, 2039 (1986)

[14] A D' Arrigo *et al*, *J. Phys.* **G20**, 365 (1994)

[15] P Möller and J R Nix, *At. Data Nucl. Data Tables* **26**, 165 (1981)

[16] C Bhattacharya *et al*, *Phys. Rev.* **C53**, 1012 (1996)

[17] M Itkis *et al*, to be published in *Proc. of the Int. Conf. INPC98* (Parigi, 1998)

[18] W Q Shen *et al*, *Phys. Rev.* **C36**, 115 (1987)

Fluctuations of the second order observables for dissipative processes in ^{19}F + ^{27}Al system

I BERCEANU[1], A ANDRONIC[1], M DUMA[1], D MOISĂ[1], M PETROVICI[1], A POP[1], V SIMION[1], A DEL ZOPPO[2], G D'ERASMO[4,5], G IMMÉ[2,3], G LANZANÒ[2,3], A PAGANO[2,3], A PANTALEO[4] and G RACITI[2,3]
[1]National Institute for Physics and Nuclear Engineering, MG-6, Bucharest, Romania
[2]INFN, LNS-Catania, v. S. Sofia 44, I-95100, Catania, Italy
[3]Dipartimento di Fisica, Univ. di Catania, I-95129 Catania, Italy
[4]INFN, Sezione di Bari, v. Amendola 173, 70125 Bari, Italy
[5]Dipartimento di Fisica, Univ. di Bari, Italy

Abstract. The excitation function (EF) data for dissipative processes in ^{19}F + ^{27}Al system in the incident energy interval from 113.5 to 130 MeV are used to obtain the dependence of the charge variance and of the interaction time as a function of the incident energy. Fluctuations are observed in the EFs of both these secondary observables. Their correlation is supported by a mechanism based on stochastic exchange of nucleons.

Keywords. Deep inelastic processes; excitation function; non-statistical fluctuations.

PACS Nos 25.70.Lm; 24.60.Ky

Non-statistical fluctuations in the EFs of dissipative heavy ion collisions (DHIC) was rather unexpected due to the fact that cross sections are always obtained on a 'coarse cell' of total kinetic energy loss (TKEL) and center of mass angle of observation (ϑ_{cm}) [1]. The contribution of a large number of microchannels to the measured cross section is expected to attenuate the fluctuation amplitude. The partially overlapping molecular levels model (POMLM) introduces, besides the angular momentum correlation, the hypothesis that the dinuclear system (DNS) formed in the first stage of a dissipative process is excited in a region of low level density situated in the vicinity of the yrast line in order to describe such fluctuation phenomena [2].

A detailed experimental study of the ^{19}F on ^{27}Al and ^{19}F on ^{12}C collisions at 111.4, 125.0 and 136.9 MeV has been realized. The correlations between different observables evidenced that even for such light combinations, in this energy range, a full dynamics specific for deep inelastic processes from quasielastic down to complete damping is present [3,4]. This systematic study of dissipative processes in light systems was completed with experiments dedicated to the measurement of the excitation functions in ^{19}F + ^{27}Al and ^{27}Al + ^{27}Al systems in order to obtain deeper insight on DNS configuration and its time evolution.

The excitation function for ^{19}F + ^{27}Al system has been measured between 113.5

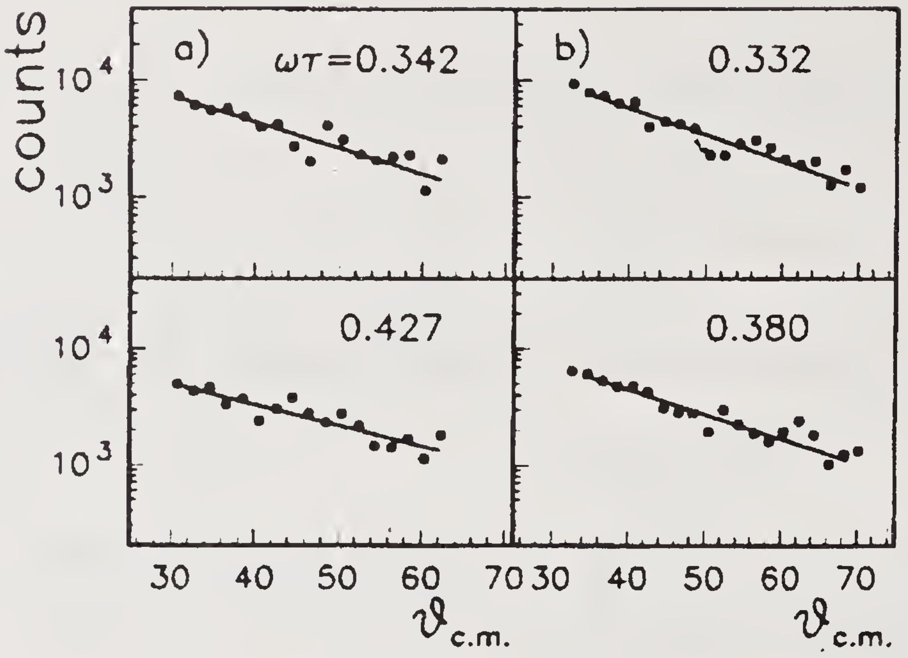

Figure 1. Angular distributions at incident energies 121 and 123 MeV for (**a**) $Z = 6$ fragment and (**b**) $Z = 8$ fragments for W4 window.

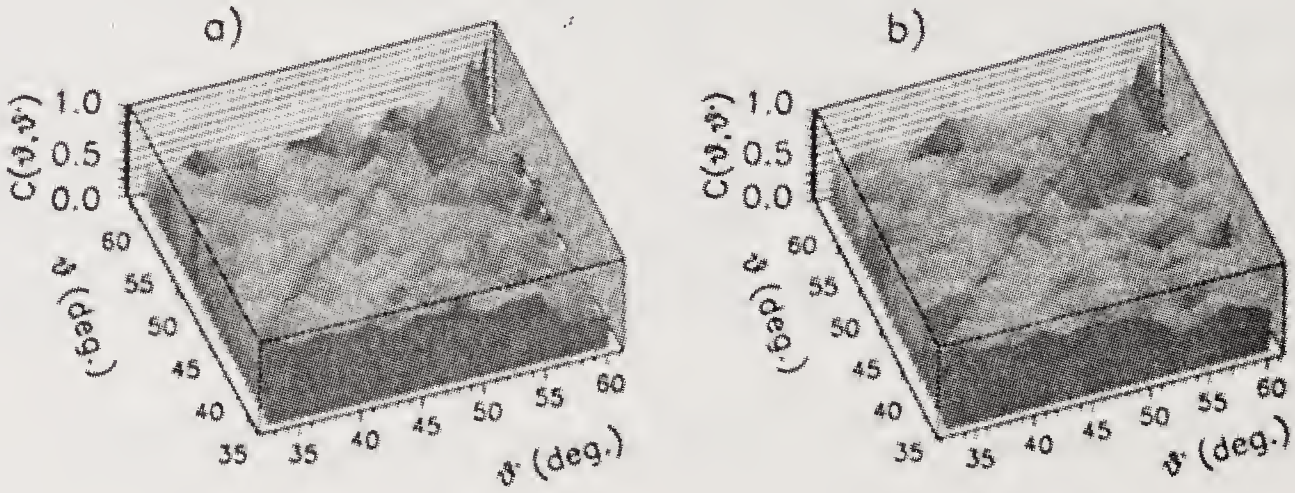

Figure 2. Angular correlation coefficients for (**a**) $Z = 7$ and (**b**) $Z = 8$ fragments for W4 window.

and 130.0 MeV with a 250 keV energy step [5]. The EF for ^{27}Al + ^{27}Al collision has been measured with the same step on the incident energy interval from 120.0 to 130.0 MeV and some preliminary results are presented in this communication. The experiments were performed at the SMP tandem accelerator from LNS, Catania. The outgoing fragments were detected using experimental device DRACULA having as a main component two large area position sensitive ionization chambers [6].

The EFs for $Z = 6-12$ fragments from ^{19}F + ^{27}Al collision having TKEL and $\vartheta_{\rm cm}$ in the W1–W5 windows given in figure 3 were obtained. The windows have been chosen in order to select dissipative processes which take place in this interaction but to avoid the complete energy dissipation. Fluctuations with amplitude larger than the statistical errors were observed. Large Z and angular cross correlation coefficients show their non-statistical nature.

For angular correlation analysis, the angular distributions with a 2° bin for bombarding energy from 116.75 to 122.25 MeV have been obtained for windows W2, W4 and W5. As an example angular distributions for $Z = 6$ and 8 for W4 window are given in figure 1. The angular correlation coefficients $C(\vartheta, \vartheta')$ have large values as can be seen in figure 2. An oscillating pattern could be seen. The minima are filled as predicted for the case of deep inelastic reactions in contrast with the case of compound elastic and

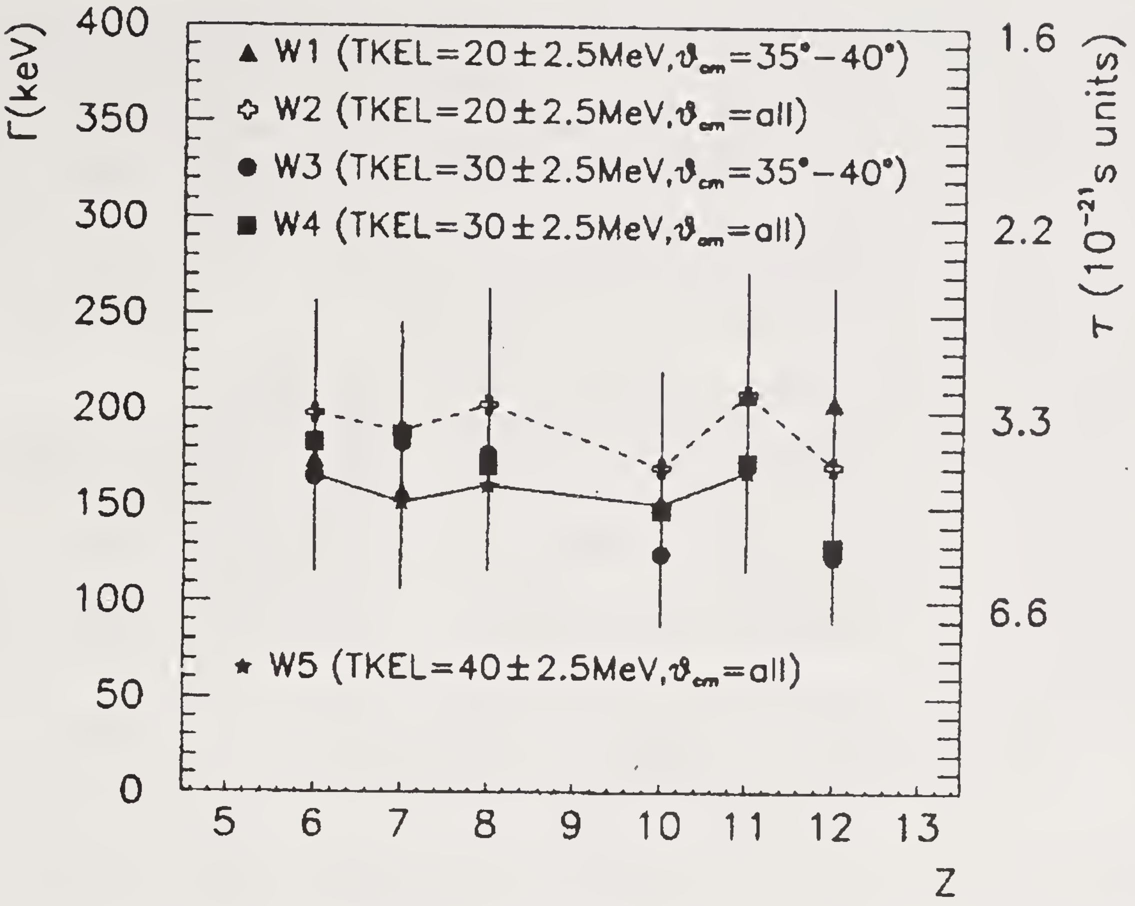

Figure 3. The dependence of the energy correlation width Γ on fragment charge.

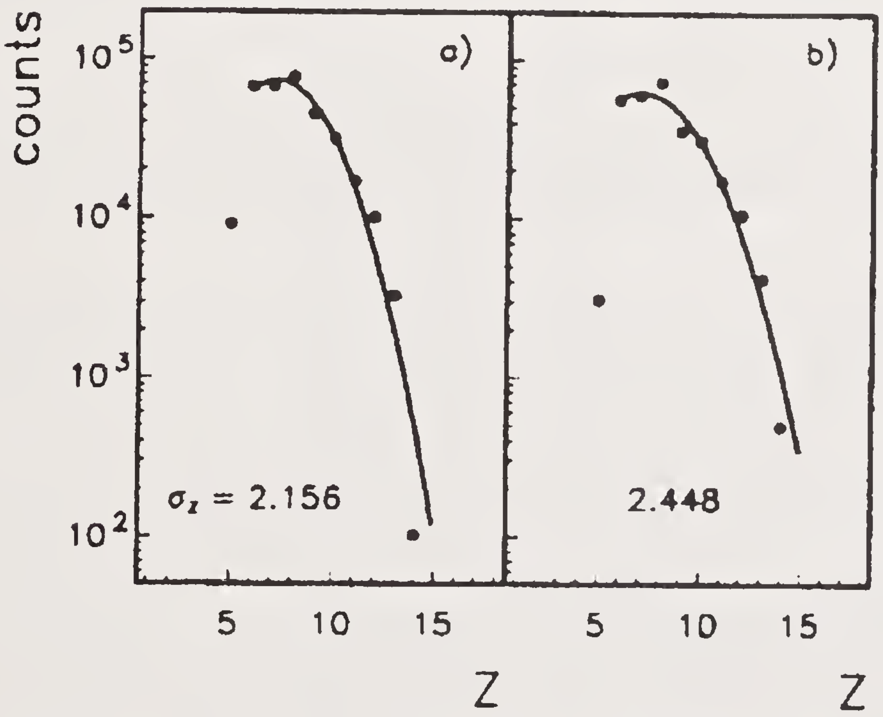

Figure 4. Charge distributions for TKEL = 30±2.5 MeV at incident energy: (**a**) 121 MeV and (**b**) 123 MeV.

inelastic scattering when minima are close to zero [7].

The energy correlation width Γ of the fluctuations was determined by energy autocorrelation function (EAF) method. The results are represented as a function of fragment charge number Z for all (TKEL, ϑ_{cm}) windows in figure 3. Within the errors, the Γ values do not show any clear dependence on ϑ_{cm}, Z or TKEL. An average Γ value of 170 ± 65 keV was calculated. The corresponding DNS lifetime $\tau = (3.9 \pm 1.1) \cdot 10^{-21}$s is almost equal to its rotation period. Secondary structures were observed in the experimental EAF as predicted in ref. [8] for this case. Their period ($\approx$ 1 MeV) agrees with the predicted one considering deformed fragments.

In this work the dependence of second order observables, namely the second moment of the charge distribution and the product $\omega \cdot \tau$ (ω is the angular velocity of the DNS and τ its mean lifetime) extracted from the angular distributions, on the incident energy was studied. The fluctuations observed in the cross section EFs should propagate in the second order observable excitation functions if their origin is due to the relatively simple structure of the DNS levels as proposed by POMLM. The above data for $^{19}F + ^{27}Al$ system were used. The statistics allowed the analysis of the charge distributions and angular distributions for W2 and W4 windows on the incident energy from 120 to 130 MeV.

The charge distributions corresponding to W4 window for incident energy E_{lab} = 121 and 123 MeV are given in figure 4(a) and (b). The variance of the charge distribution, σ_Z, was obtained by the fit of the charge distribution with a Gaussian. In the panel (a) of the figure 5 is represented the dependence of σ_Z values as a function of E_{lab}. Fluctuations with quite large amplitude can be seen. The product $\omega \cdot \tau$ was extracted from the angular distributions described by the expression [9]: $d\sigma/d\vartheta_{cm} \propto \exp(-\vartheta_{cm}/\omega \cdot \tau) + \exp(-(2\pi - \vartheta_{cm})/\omega \cdot \tau)$. The continuous lines on figure 2 represent the result of the fit. The EFs of $\omega \cdot \tau$ for Z = 6 – 8 fragments with TKEL in W4 window can be followed in panels (b)–(d) of figure 5. The fluctuations with amplitude larger than statistical errors are present and some of them are nicely correlated with those from σ_Z excitation function. Also a correlation of the second order observable fluctuations with those from cross section EF could be observed. The cross section EF for $Z = 8$ fragment is represented in the last panel of figure 5 in order to follow this.

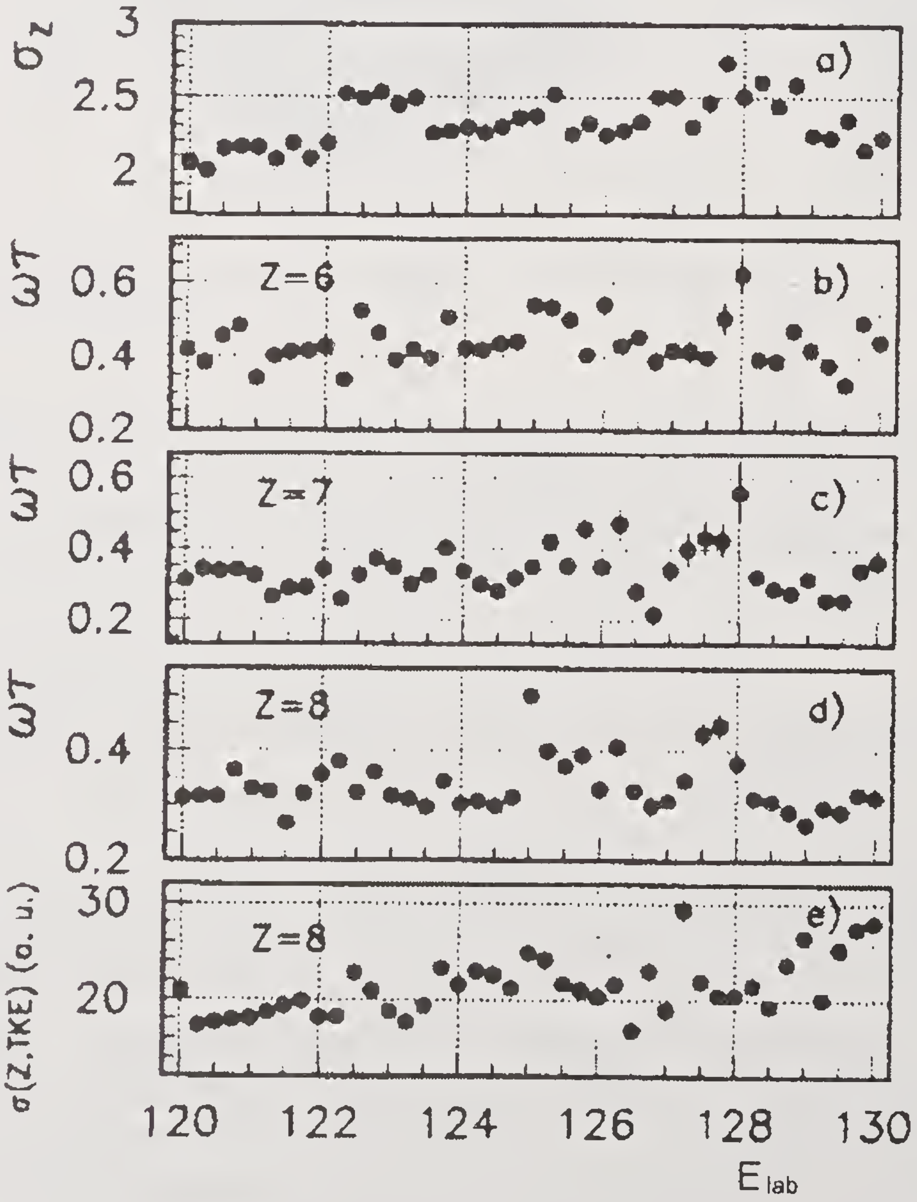

Figure 5. Excitation functions of (**a**) charge variance and $\omega \cdot \tau$ for (**b**) $Z = 6$, (**c**) $Z = 7$, (**d, e**) $Z = 8$ from $^{19}F + ^{27}Al$ system for W4 window.

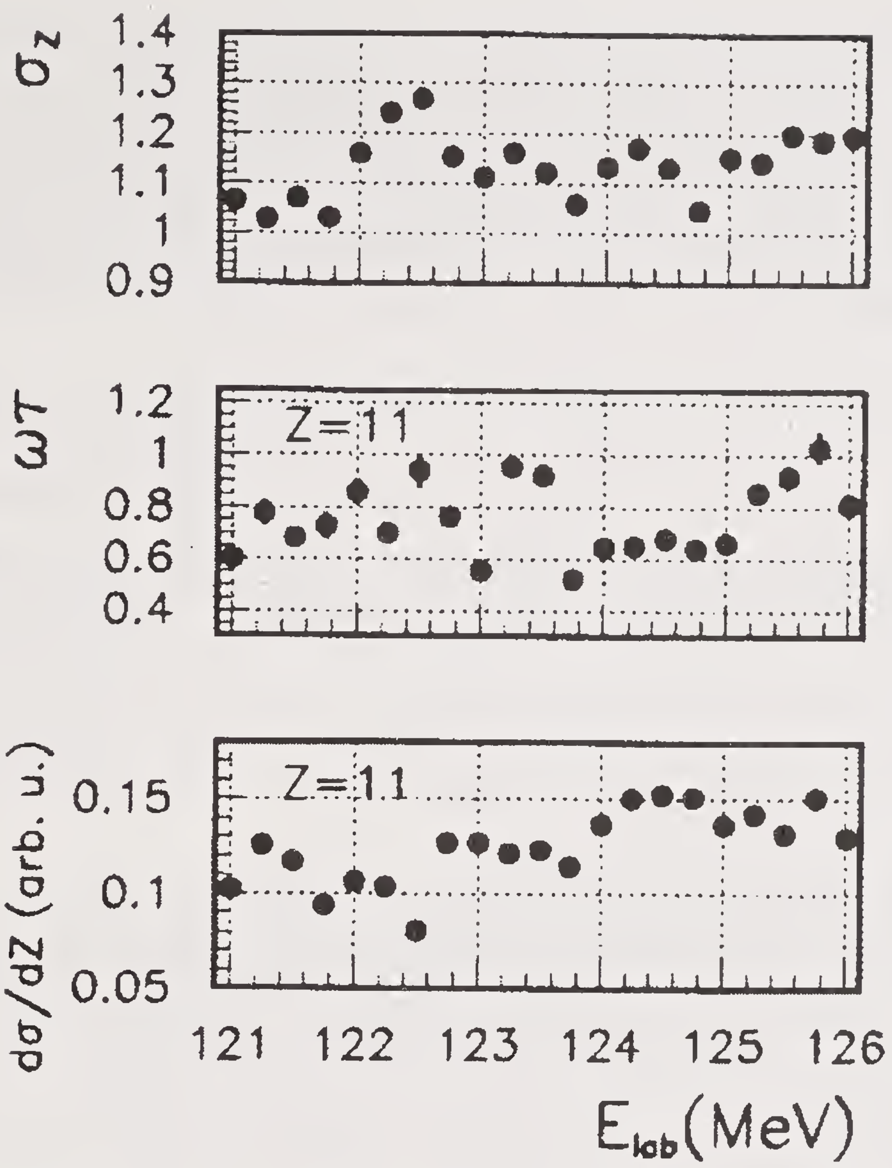

Figure 6. Excitation functions for fragments having TKEL from 20 to 32 MeV from ^{27}Al + ^{27}Al collision; (**a**) charge variance, (**b**) $\omega \cdot \tau$, (**c**) cross section.

The above results are confirmed by a preliminary analysis of the EF data for ^{27}Al + ^{27}Al system. Fluctuations correlated in the final channels corresponding to different charge numbers could be observed in the EFs obtained for $Z = 10-12$ and 14 fragments having TKEL in the range from 20 to 32 MeV. The charge variance was obtained by the fit with a Gaussian of the peak centered at $Z = 13$. For the fragment with $Z = 11$ the product $\omega \cdot \tau$ was extracted from the angular distribution. The charge variance, $\omega \cdot \tau$ and cross section excitation functions for $Z = 11$ fragment are represented in figure 6. A correlation of the fluctuations from the excitation functions of these three observables could also be noticed.

One has to mention that the data for ^{27}Al + ^{27}Al system are not corrected for particle evaporation processes. In the case of ^{19}F + ^{27}Al system evaporation corrections have been evaluated by an iterative procedure similar to that from ref. [10] which takes into account evaporation of neutrons and protons.

For ^{27}Al + ^{27}Al system an evaluation of the evaporation corrections was done using a Monte Carlo simulation. The excitation functions for ^{27}Al + ^{27}Al system for primary fragments and after giving them the possibility to evaporate particle were simulated. No structures in the EFs due to particle evaporation were observed.

The observed correlation of the fluctuations from the cross section and $\omega \cdot \tau$ EFs could be interpreted as an evidence of the excitation of simple states of rotational nature in the DNS as proposed by POMLM. In a diffusion approach of deep inelastic processes the charge distribution and DNS lifetime are related by the expression: $\sigma_Z^2 = 2D_Z \cdot \tau$, where D_Z represents charge diffusion coefficient. As it is known the diffusion models have been elaborated for describing the dissipative processes in heavier systems [11]. The observed correlated fluctuations in σ_Z and $\omega \cdot \tau$ EFs support a mechanism based on a stochastic exchange of nucleons. This speaks in favour of a common reaction mechanism of dissipative processes in light systems and in medium and heavy ones. The same conclusion is sustained by the fact that the correlation $\ln(\sigma_Z^2)$ as a function of TKEL/l_{gr} for light systems could be comprised in the same systematics with medium and heavy systems [4].

Acknowledgement

Part of this work and the participation of I Berceanu at the workshop were supported by Grant No. 3028 of the Romanian Academy.

References

[1] D M Brink and K Dietrich, *Z. Phys.* **A326**, 7 (1987)

[2] M Papa, G Cardella, A Di Pietro, S L Li, A Musumarra, G Pappalardo, F Rizzo, A De Rosa, G Inglima, M La Comarra, D Pierroutsakou and M Romoli, *Z. Phys.* **A353**, 205 (1995)

[3] M Petrovici, A Andronic, I Berceanu, A Buţă, M Duma, D Moisă, A Pop, V Simion, A Bonasera, G Immé, G Lanzanò, A Pagano, G Raciti, N Colonna, G d'Erasmo and A Pantaleo, *Z. Phys.* **A354**, 11 (1996)

[4] A Pop, A Andronic, I Berceanu, A Buţă, M Duma, D Moisă, M Petrovici, V Simion, A Bonasera, G Immé, G Lanzanò, A Pagano, G Raciti, N Colonna, G d'Erasmo and A Pantaleo, *Phys. Lett.* **B397**, 25 (1997)

[5] I Berceanu, A Andronic, M Duma, D Moisă, M Petrovici, A Pop, V Simion, G D'Erasmo, A Del Zoppo, G Immé, G Lanzanò, A Pagano, A Pantaleo and G Raciti, *Phys. Rev.* **C57**, 2359 (1998)

[6] V Simion, *Rom. J. Phys.* **38**, 513 (1993)

[7] K M Hartman, W Dünweber and W E Frahn, *Nucl. Phys.* **A380**, 170 (1982)

[8] Yu S Kun, *Phys. Lett.* **B257**, 247 (1991)

[9] C K Gelbke, C Olmer, M Buenerd, D L Hendrie, J Mahoney, M C Mermay and D K Scott, *Phys. Rep.* **42**, 311 (1978)

[10] H Breuer, N R Yoder, A C Mignerey, V E Viola Jr, K Kwiatotkowski and K L Wolf, *NIM* **204**, 418 (1983)

[11] W Nörenberg, *Phys. Lett.* **B52**, 289 (1977)

[12] G Wollschin and W Nörenberg, *Z. Phys.* **A284**, 209 (1979)

Transition strengths and shapes of 2-qp bands in ^{74}Se and ^{76}Kr

G MUKHERJEE[1,2], P JOSHI[1], S N ROY[2], S DATTA[3], R P SINGH[1],
S MURALITHAR[1] and R K BHOWMIK[1]
[1]Nuclear Science Centre, Post Box 10502, New Delhi 110 067, India
[2]Department of Physics, Visva-Bharati University, Santiniketan 731 235, India
[3]Department of Physics, University of Calcutta, Calcutta 700 009, India

Abstract. The lifetimes of the states of −ve parity 2-qp bands of $N = 40$ nuclei ^{74}Se and ^{76}Kr were measured. The transition strengths and quadrupole moments, obtained from the lifetimes, show a large collectivity of such bands in both the nuclei. The alignment frequencies were calculated from Woods–Saxon cranking model. Previously suggested quasi proton nature of band 5 and 6 of ^{74}Se were argued to be based on quasi neutron excitations. The total Routhian surface calculations suggest triaxial shapes with large +ve and −ve values of triaxiality parameter γ after proton and neutron alignments in these bands respectively.

Keywords. Heavy ion; $\gamma - \gamma$ coincidence; DSAM; Woods–Saxon cranking; TRS.

PACS Nos 23.30.Lv; 21.10.Tg; 27.50.+e

1. Introduction

The even–even $N = 40$ nuclei ^{74}Se and ^{76}Kr show interesting structure properties including shape coexistence in the yrast bands [1,2]. In addition to the +ve parity yrast bands, other −ve parity bands with strong E2 transitions have recently been observed in both the nuclei [2–4]. These were interpreted as two quasi particle (2-qp) bands. In ^{76}Kr, two such signature partner bands (band 3 and band 6) were interpreted as two quasi-proton in character [2] and other two signature partner bands (band 4 and band 5) are two quasi-neutron in character [4]. These bands are predicted to have larger deformation than the yrast S-band [2]. Lifetime measurements of these states can test these predictions. Moreover, the quasi particle configuration assigned to these bands can be tested if the deformation is known for these bands. In ^{74}Se, the nature of such two quasi particle bands are not resolved. The close proximity of proton and neutron crossing frequencies makes the interpretation, of whether the bands (band 5 and band 6) are based on two quasi protons or two quasi neutrons, very ambiguous [3]. If the deformation of such bands are known then it might be easier to resolve this ambiguity. This again needs the lifetime measurements of these 2-qp bands.

In the present work, our aim was to study the 2-qp bands of ^{74}Se and ^{76}Kr in detail with lifetime measurements to determine the deformations. The cranking calculations were performed for these bands to interpret the results.

2. Experimental details and data analysis

The nuclei ^{76}Kr and ^{74}Se were populated by heavy ion fusion evaporation reaction, ^{51}V(^{28}Si, $p2n(\alpha,p)$)^{76}Kr (^{74}Se) at 115 MeV of beam energy. The beam was delivered from 15UD Pelletron at Nuclear Science Centre (NSC), New Delhi. The target was a self supporting thick (~ 76 mg/cm^2) vanadium foil. The recoils were stopped in the target itself for the line shape analysis. The maximum recoil velocity of the recoiling nuclei was $\sim$ 3% of the velocity of light. Gamma–gamma coincidence data were taken in the list mode using the gamma detector array (GDA) set up at NSC. GDA consists of 12 Compton suppressed HPGe detectors with 14 element BGO multiplicity filter. The detectors were at three rings at 144°, 98° and 50° angles. There were 4 detectors in each ring. The set up for the similar measurements can been seen in ref. [5].

In the analysis, two 4 K×4 K $\gamma\gamma$-coincidence matrices were constructed separately for forward and backward angle detectors. Most of the transitions in ^{76}Kr reported in refs [2] and [4] and in ^{74}Se reported in refs [1] and [3] have been observed in our experiment. The sum gated spectra were used for line shape analysis. For ^{76}Kr gated spectra with gates put on 424 keV, 611 keV and 825 keV, yrast transitions were added while for ^{74}Se, 635 keV, 728 keV and 868 keV gated spectra were summed up. The computer program LINESHAPE [6] was used to fit the Doppler line shapes. Wherever possible, the lifetimes were obtained by fitting the data from forward and backward matrices separately and the averages were taken. The errors associated with the measured lifetimes were calculated by the MINOS routine in the LINESHAPE program [6]. These were obtained for both backward and forward data. The reported error values are the larger values found between these two measurements.

3. Results

The results are summarized in table 1. It contains the lifetimes (τ) of the levels of band 3 (even spin) and band 6 (odd spin) in ^{76}Kr and band 4 and band 6 of ^{74}Se along with the transition strengths B(E2) and transition quadrupole moments Q_t obtained from the lifetimes. Here we are using the band nomenclatures as given in ref. [4] for ^{76}Kr and in ref. [3] for ^{74}Se. The band 3 and band 6 are the signature partners of the quasi proton band of ^{76}Kr while band 5 and band 6 are the signature partners of quasi proton band of ^{74}Se as interpreted in ref. [3]. However, in the present study it is argued that later bands are quasi neutron in character. The lifetimes of the levels of band 5 of ^{74}Se were previously measured by Cottle *et al* [1] and are not shown in table 1. The measured lifetimes for few levels match quite well with the previous measurements except for the 9^- state of ^{76}Kr. The value obtained by Piercey *et al* for this state was very low compared to our value and this gives an exceptionally high value of Q_t and consequently very large axial deformation. It may be noted, however, that the lifetimes were not known for most of the levels in these bands. The large B(E2) values obtained for these bands indicate highly collective nature of the bands. The quadrupole moments Q_t for both the nuclei remain almost constant at a value of ≈ 2.5 eb for ^{74}Se and ≈ 3.0 eb for ^{76}Kr. These correspond to an axial deformation of $\beta_2 \approx 0.33$ and ≈ 0.38 for ^{74}Se and ^{76}Kr respectively. In the yrast band of ^{76}Kr, it was found that the Q_t decreases from $\sim$ 3 eb for the g-band to $\sim$ 2.2 eb for the S-band [8].

Table 1. Lifetime (τ) for the +ve and −ve parity states in ^{76}Kr and ^{74}Se from previous [7] and present works. 1 w.u = 19.13 and 18.46 e^{2}fm^4 for ^{76}Kr and ^{74}Se respectively.

I_i^π	E_γ (keV)	τ (ps) (previous)	τ (ps) (present)	τ (ps) (adopted)	B(E2) (w.u)	Q_t (eb)
^{76}Kr						
8^-	725		$1.61^{.41}_{.27}$	$1.61^{.41}_{.27}$	132^{27}_{27}	$2.99^{.29}_{.32}$
10^-	905		$0.80^{.17}_{.23}$	$0.80^{.17}_{.23}$	88^{35}_{16}	$2.34^{.43}_{.22}$
12^-	1066		$0.25^{.05}_{.04}$	$0.25^{.05}_{.04}$	124^{23}_{21}	$2.71^{.25}_{.23}$
14^-	1234		< 0.28	< 0.28	> 53	> 1.75
7^-	604		$2.60^{1.1}_{.64}$	$2.60^{1.1}_{.64}$	204^{67}_{61}	$4.45^{.68}_{.72}$
9^-	784	0.16(6)	$0.81^{.13}_{.11}$	$0.81^{.13}_{.11}$	178^{27}_{25}	$3.66^{.27}_{.27}$
11^-	978	0.18(7)	$0.26^{.05}_{.04}$	$0.22^{.05}_{.04}$	217^{48}_{41}	$3.80^{.41}_{.37}$
13^-	1169	0.34(8)	$0.13^{.04}_{.04}$	$0.13^{.04}_{.04}$	150^{67}_{35}	$3.06^{.62}_{.38}$
15^-	1356		< 0.20	< 0.20	> 46	> 1.67
^{74}Se						
8^-	816		$1.89^{.66}_{.55}$	$1.89^{.66}_{.55}$	65^{26}_{18}	2.28^{43}_{32}
10^-	1011		$0.44^{.17}_{.13}$	$0.44^{.17}_{.13}$	$95^{.40}_{.26}$	$2.55^{.49}_{.40}$
12^-	1044		< 1.07	< 1.07	> 33	>1.43
9^-	1007		$0.57^{.19}_{.16}$	$0.57^{.19}_{.16}$	75^{29}_{18}	$2.32^{.43}_{.30}$
11^-	1080		$0.38^{.10}_{.10}$	$0.38^{.10}_{.10}$	79^{28}_{16}	$2.26^{.38}_{.26}$
13^-	1135		< 1.10	< 1.10	> 21	> 1.11

This indicates that the deformation of the 2-qp band of ^{76}Kr is more deformed than the proton S-band, as conjectured by Gross *et al* [2].

4. Discussion

The results are discussed in the frame work of the cranking model. The protons and neutrons crossing frequencies for different values of deformation parameters β_2 and γ were calculated. These are plotted in figure 1.

Quasi neutron nature of bands 5 *and* 6 *of* ^{74}Se: The bands 5 and 6 were interpreted as quasi proton in nature by Doring *et al* [3]. The band crossing frequencies corresponding to particle alignments in these bands were observed at $\hbar\omega_c \approx 0.5$ MeV. If these bands were quasi proton in nature then this corresponds to neutron crossing frequency, since proton crossing is blocked. The calculated neutron crossing frequency in figure 1(a) shows a value of ≈ 0.5 MeV for $\beta_2 \simeq 0.23$ which is much less than the value obtained from lifetime measurements. In figure 1(b), it can be seen that the neutron crossing frequency never comes closer to 0.5 MeV for any value of triaxiality parameter γ, if the observed deformation of $\beta_2 \approx 0.3$ is assumed. Thus it is very unlikely that the bands 5 and 6 of ^{74}Se are quasi proton bands. However, if quasi neutron nature is assigned to these bands, then the observed crossing frequency

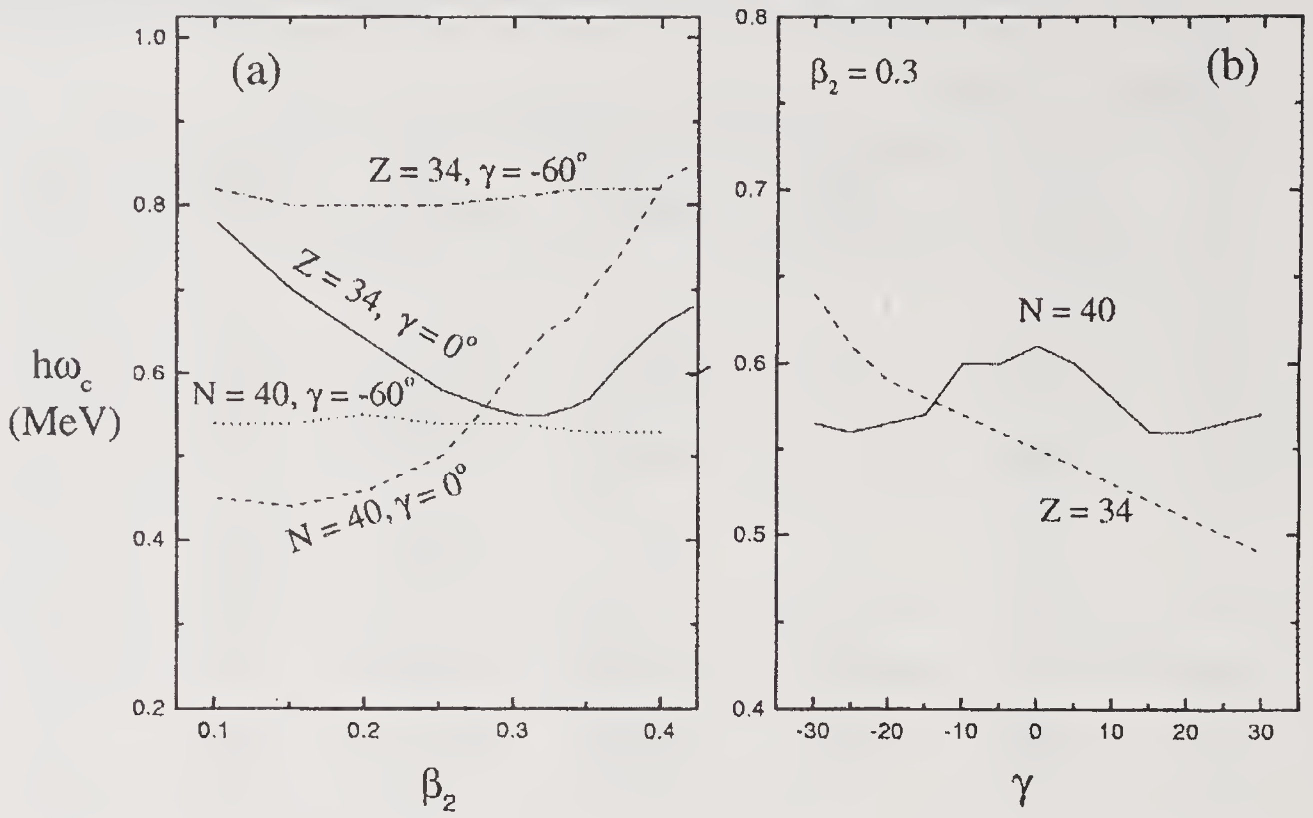

Figure 1. The calculated proton and neutron crossing frequencies for proton and neutrons as a function of β_2 (**a**) and γ (**b**).

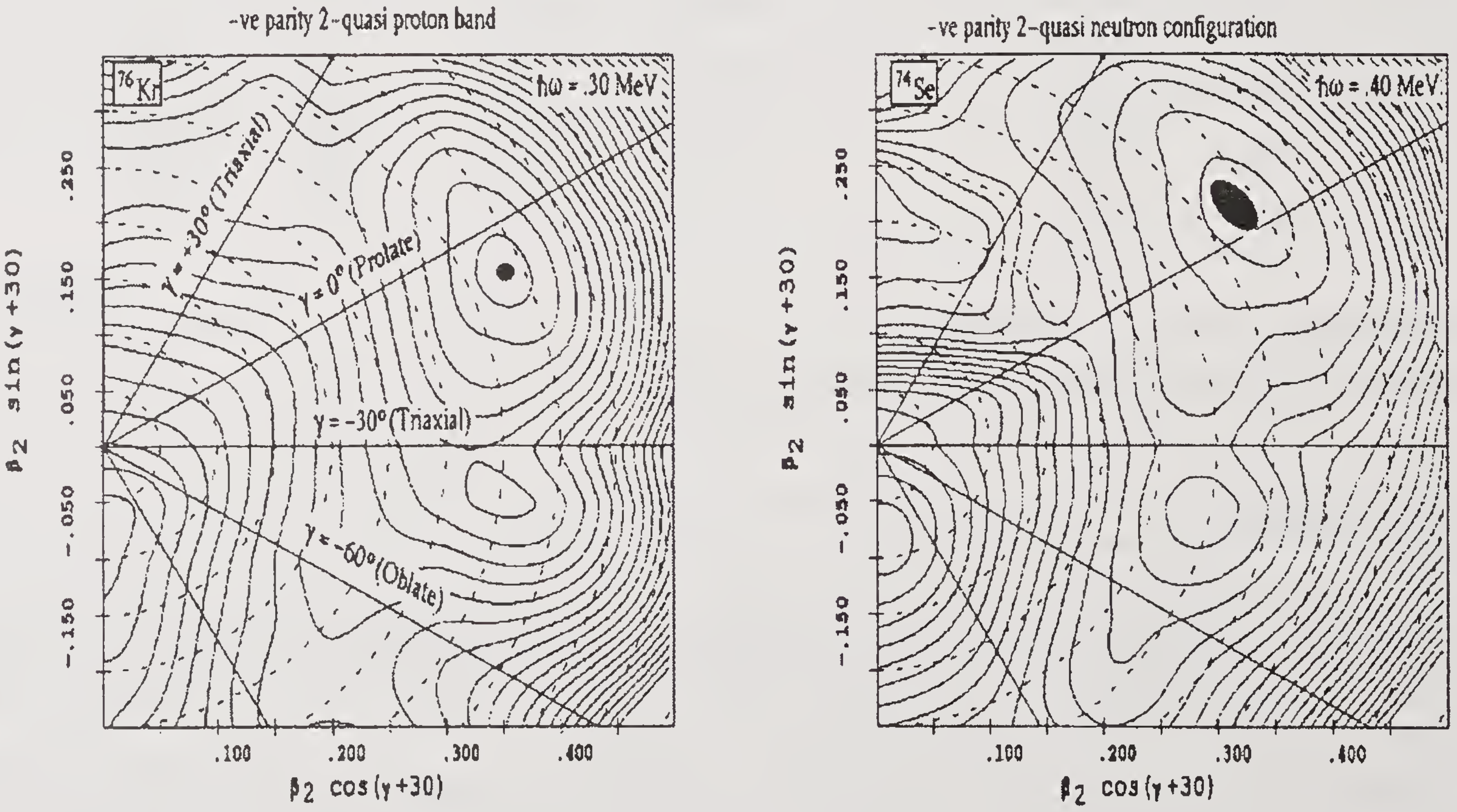

Figure 2. TRS plots for the −ve parity 2-qp bands in ^{76}Kr (left) and ^{74}Se (right) calculated at $\hbar\omega = 0.3$ and 0.4 MeV respectively.

agrees well with calculated proton crossing frequency for the deformation $\beta_2 \approx 0.3$, close to the value obtained from lifetimes, with slightly +ve γ (see figure 1(a) and (b)).

4.1 Shape calculation

To investigate the shape of the −ve parity two quasi particle bands in ^{76}Kr and ^{74}Se, we have carried out the theoretical calculations of total Routhian surfaces in Hartree–Fock–

Bogoliubov cranking model with Woods–Saxon potential and monopole pairing [9]. The total Routhian surfaces (TRS) calculated for the quasi particle bands of ^{76}Kr and ^{74}Se at rotational frequencies $\hbar\omega = 0.3$ and 0.4 MeV respectively are shown in figure 2.

The minimum in the potential energy for ^{76}Kr occurs at $\beta_2 \approx 0.38$ and $\gamma \approx -6°$. The quadrupole moment calculated from these deformation paremeters comes out to be $Q_{\rm th} \approx 3.2$ eb. This is in fair agreement with the experimental values for the even-spin $-$ve parity band (see table 1).

The TRS plot for the two quasi neutron band of ^{74}Se shows a minimum at $\beta_2 \approx 0.36$ and at +ve triaxiality $\gamma \approx 7°$. These values are in very good agreement with the values obtained from the experimental observations of crossing frequencies and lifetime data. This provides further support to the quasi neutron nature of the $-$ve parity bands of ^{74}Se, as discussed earlier. The TRS plots calculated at frequencies after the band crossings indicate (not shown) that the alignment of a pair of protons drives the shape towards +ve γ value while the neutron pair alignments drives it towards $-$ve γ value.

5. Conclusions

The lifetimes of the $-$ve parity 2-qp bands of ^{76}Kr and ^{74}Se were measured by DSAM. The predicted larger deformation of the 2-qp bands of ^{76}Kr than the proton S-band was confirmed in the present study. The bands 5 and 6 of ^{74}Se were argued to be based on 2 quasi neutron excitations. The TRS calculations were performed with Woods–Saxon potential for these bands in both the nuclei. The results of such calculations are in fair agreement with the measured deformations. The calculations predict a shape change towards +ve ($-$ve) γ after proton (neutron) pair alignments.

References

[1] P D Cottle, J W Holcomb, T D Johnson, K A Stuckey, S L Tabor, P C Womble, S G Buccino and F E Durham, *Phys. Rev.* **C42**, 1254 (1990)

[2] C J Gross, J Heese, K P Lieb, S Ulbig, W Nazarewicz, C J Lister, B J Varley, J Billowes, A A Chishti, J H McNeill and W Gelletly, *Nucl. Phys.* **A501**, 367 (1989)

[3] J Döring, G D Johns, M A Riley, S L Tabor, Y Sun and J A Sheikh, *Phys. Rev.* **C57**, 2912 (1998)

[4] J Döring, G D Johns, R A Kaye, M A Riley, S L Tabor, P C Womble and J X Saladin, *Phys. Rev.* **C52**, R2284 (1995)

[5] G Mukherjee, P Joshi, S N Roy, S Datta, R P Singh, S Muralithar and R K Bhowmik, *Z. Phys.* **A359**, 111 (1997)

[6] N R Johnson, J C Wells, Y Akovali, C Baktash, R Bengtsson, M J Brinkman, D M Cullen, C J Gross, H-Q Jin, I-Y Lee, A O Macchiavelli, F K McGowan, W T Milner and C-H Yu, *Phys. Rev.* **C55**, 652 (1997)

[7] R B Piercey, A V Ramayya, J H Hamilton, X J Sun, Z Z Zhao, R L Robinson and H J Kim, *Phys. Rev.* **C25**, 1941 (1982)

[8] G Mukherjee, P Joshi, S N Roy, S Datta, R P Singh, S Muralithar and R K Bhowmik, *Proc. DAE-NP Symp. India* **B41** (1998)

[9] W Nazarewicz, J Dudek, R Bengtsson, T Bengtsson and I Ragnarsson, *Nucl. Phys.* **A435**, 397 (1985)

Structure of neutron-rich nuclei around $A \simeq 100$

MAITREYEE SAHA SARKAR
Saha Institute of Nuclear Physics, 1/AF, Bidhan Nagar, Calcutta 700 064, India

Abstract. Neutron-rich isotopes of Mo ($Z = 42$) around $A \simeq 100$ have been investigated within the formalisms of cranked Nilsson Strutinsky and CHFB, to study several interesting features of nuclear structure in this mass region. The total energy/routhian surfaces have been generated for the isotopes of Mo ranging from $A \simeq 96 - 112$, as a function of deformation (β_2 and γ) for ground state and higher angular momentum states. Results of calculations using two different formalisms have been compared and combined to have a better understanding of the underlying mechanism of shape evolution.

Keywords. Nuclear structure; CHFB; Nilsson Strutinsky calculations; ${}^{96-112}_{42}$Mo.

PACS Nos 21.10.Re; 21.60.Jz; 27.60.+j

1. Introduction

Information [1–3] obtained so far indicate that the nuclei in the Sr–Zr–Mo region around $A \simeq 100$ have several appealing features in their nuclear structure. These nuclei show rapid changes in structure-dramatic variation in quadrupole collectivity has been observed in isotopes of Sr–Zr nuclei. For $Z > 40$ (Mo, Ru, Pd) nuclei, the shape transition is less dramatic but they show softening of the nuclear energy surface to triaxiality. The rapidity in shape change results in shape coexistence in these nuclei. Moreover these nuclei have shown a richness of various structural effects at high angular momentum (ω). There is also evidence of pairing collapse evident through the moment of inertia value which is almost equal to the rigid body value. So in the $A \simeq 100$ region, there is an extremely favourable condition to study many different nuclear structural characteristics in a narrow range of isotopes and isotones. This is a fertile territory for testing various theoretical models.

Most of these nuclei are neutron rich and despite different experimental efforts [1,2], detailed experimental information on high-spin properties of $A \simeq 100$ nuclei are still scarce.

We plan to systematically study neutron rich ${}_{42}$Mo isotopes ($N = 54-70$) within Nilsson Strutinsky formalism [4] to study the equilibrium deformations in their ground states and their evolution with spin. Similar calculations have been started within CHFB with pairing plus quadrupole interaction [5,6], for studying the microscopic origin of the onset of deformation and self-consistent determination of the evolution of pairing gap and deformation with spin. Total energy surfaces have been generated for these nuclei within

HFB and higher angular momentum states for ^{96}Mo and ^{104}Mo have been calculated using CHFB. Detailed microscopic calculation of higher angular momentum states of other nuclei is in progress.

2. Formalism

The main assumption of Nilsson-Strutinsky approach [4] is that the total energy of a nucleus can be decomposed into two parts,

$$E = E_{\text{macro}} + E_{\text{micro}}, \tag{1}$$

where E_{macro} is the macroscopic energy and E_{micro} is the microscopic shell correction energy calculated from a non-self-consistent average deformed potential (modified harmonic oscillator potential). Pairing is included only for $I = 0$. Rotation is introduced in cranking approximation corresponding to rotation around one principal axis.

In the cranked HFB model, the hamiltonian H_ω is cranked about an axis (here, x axis) perpendicular to the symmetry axis (here, z axis) of the nucleus

$$H_\omega = H - \omega \hat{I}_x - \lambda \hat{N}, \tag{2}$$

where the different terms have their usual meanings [6]. H is given by the pairing plus quadrupole model hamiltonian of Baranger and Kumar [5]. Evolution of pairing gap and deformation with spin is calculated self-consistently in this model.

The oscillator shells $N = 4$ and 5 are included in the basis states for both protons and neutrons. The inert core is therefore, $^{80}_{40}\text{Zr}_{40}$. The single particle parameter sets (μ, κ values) are used as suggested by Nilsson *et al* [7] to obtain spherical single particle energies. The pairing and quadrupole force constants are given by

$$G_p = 30/\text{A MeV}, \quad G_n = 22/\text{A MeV}, \quad \chi_2 = 80\,\text{A}^{-1.4}\,\text{MeV}. \tag{3}$$

3. Results and discussion

Table 1 contains the comparison of our results using two different approaches with previous experimental [8] and theoretical results with extended Thomas Fermi Strutinsky integral method (ETFSI) [9] and finite range droplet model (FRDM) [10].

Figure 1 shows the total energy surface plots for the ground states of $^{96-112}$Mo isotopes as a function of β and γ, within Nilsson Strutinsky approach. The changes in deformation with increasing neutron number is evident from the figure. ^{96}Mo ($N = 54$) with only 4 neutrons outside the closed $N = 50$ shell shows small β deformation (table 1). Its total energy surface (TES) is flat against triaxiality indicating extreme γ-softness. As neutron number increases the minimum becomes more confined in the γ-axis, and the β value increases reaching a maximum ($\approx$ 0.26) for $N = 64$. As N increases from $N = 62$, a second minimum develops for oblate deformation and shape coexistence is predicted for $N = 66$. For higher N isotopes, the first minimum shifts to an oblate shape ($\beta \approx -0.20$).

Table 1. Comparison of present results with previous results.

		Theory			
A	Expt. [8]	Previous		Present	
		FRDM [10]	ETFSI [9]	Nil. Strut.	CHFB
		ϵ_2	β	ϵ_2	β
96	0.1720(16)	0.08	0.02	0.08	0.06
98	0.1684(16)	0.180	0.20	0.10	0.08
100	0.2309(22)	0.244	−0.27	0.15	0.10
102	0.326(19)	0.329	−0.27	0.20	0.15
104	0.325(12)	0.349	0.36	0.25	0.18
106	0.353(10)	0.361	0.37	0.26	0.20
108	0.354(41)	0.333	0.37	−0.20	0.20
				0.25	
110	-	0.335	−0.31	−0.20	−0.20
			1	0.25	0.20
112	-	0.337	−0.31	−0.20	−0.15

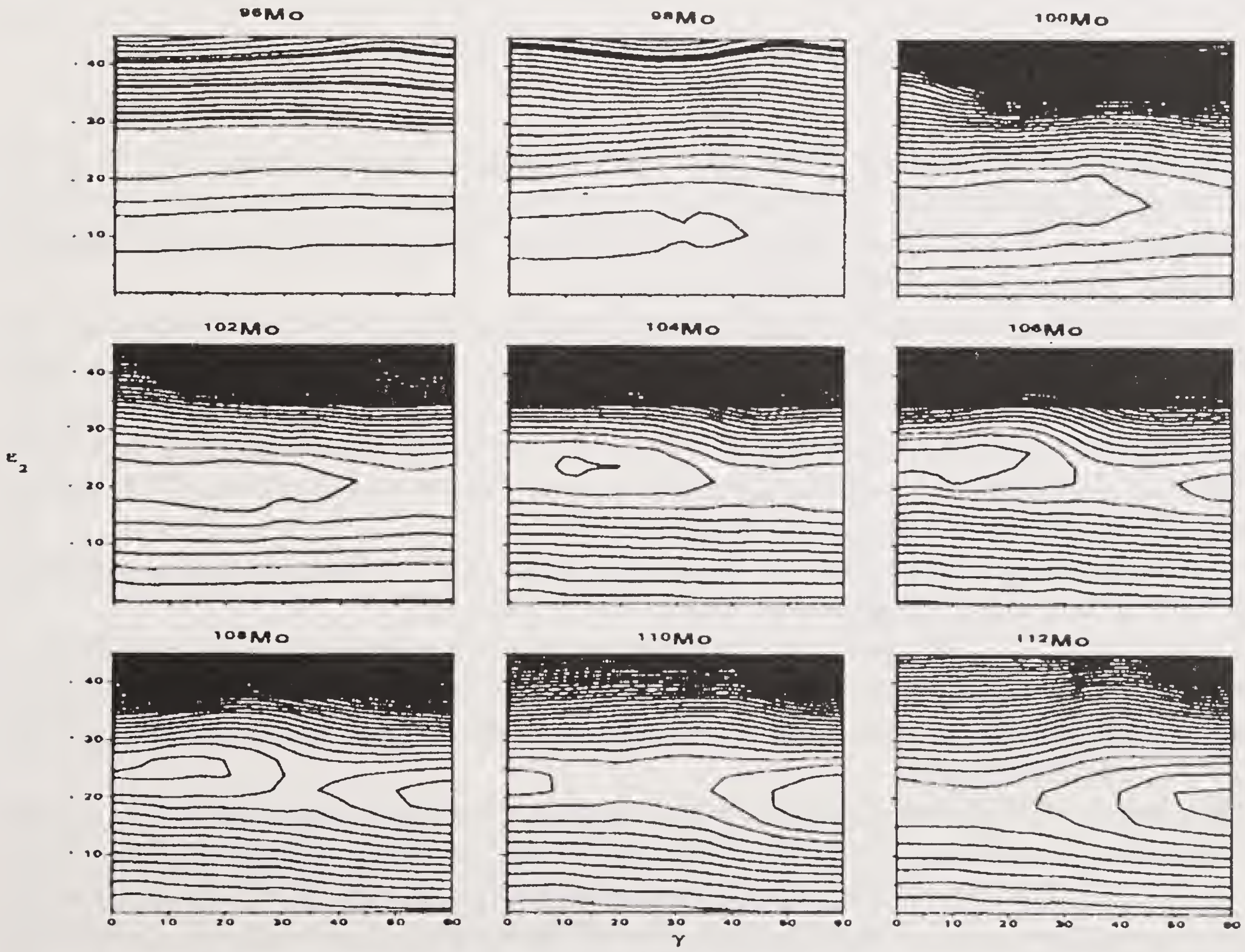

Figure 1. TES plots within Nilsson Strutinsky approach.

For $N = 70$, ^{112}Mo isotope, there is a single minimum for an oblate deformation ≈ -0.20, which agrees with previous theoretical result [9].

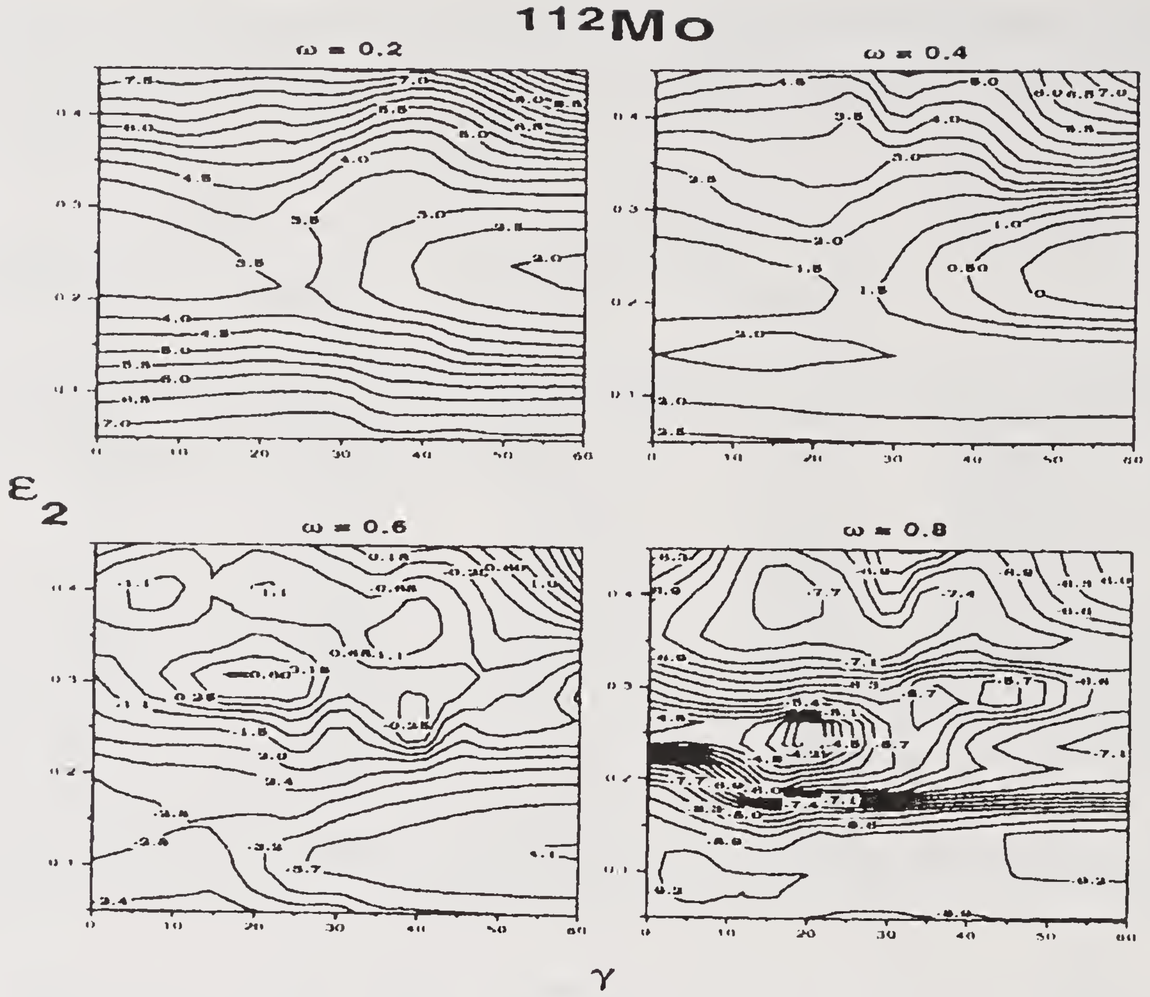

Figure 2. TRS plots within Nilsson Strutinsky approach.

The total routhian surface (TRS) plots for Mo isotopes with $N < 64$, for $\omega = 0.2$ to 0.8 show that the extreme γ-soft minimum at ground state shifts towards definite triaxial minimum at $\omega = 0.2$ with an increase in the β value. But then with increasing rotational frequency the equilibrium shape shifts to oblate.

But for heavier isotopes, the trend in shape evolution changes. Figure 2 shows the TRS plot for $A = 112$, Mo isotope. Although the ground state equilibrium shape is oblate (figure 1), the higher rotational frequency generates a second minimum for prolate shape. This shape coexistence prevails until at ω about 0.6, the prolate minimum shifts to $\beta \approx 0.4$. This is an indication of non-yrast superdeformation. This feature is seen for $N > 64$. The spin values associated with the SD shape is ≈ 50.

The total energy surface plots for the ground states of $^{96-112}$Mo isotopes as a function of β and γ have also been generated within CHFB approach.

The changes in deformation with increasing neutron number is similar to figure 1. Smaller values of deformation obtained in the present work compared to the previous results, shown in table 1, indicates that a readjustment of the quadrupole–quadrupole interaction strength is needed.

Preliminary CHFB calculation for higher angular momentum states (up to $I \simeq 8$) show the following interesting results for ^{96}Mo and ^{104}Mo. In ^{96}Mo, neutron alignment takes place ($\nu g_{7/2}$). Neutron pairing gap decreases drastically with spin. In ^{104}Mo, proton alignment takes place ($\pi g_{9/2}$). Proton pairing gap decreases drastically with spin. Preliminary CHFB results indicate that the rapid onset of deformation in this mass region is a result of strong $n - p$ interaction in the orbitals with large spatial overlap. The overlapping orbitals are $\pi g_{9/2} - \nu g_{7/2}$. The decrease in pairing gap may also be an indication of the pairing collapse predicted in this mass region [3] resulting from a relatively low single particle level density.

References

[1] T Kutsarova *et al*, *Phys. Rev.* **C58**, 1966 (1998)
[2] J Skalski, S Mizutori and W Nazarewicz, *Nucl. Phys.* **A617**, 282 (1997)
[3] K Sistemich, in *International Conference on Contemporary Topics in Nuclear Structure Physics* edited by R Casten, A Frank, M Moshinsky and S Pittel (World Scientific, 1988) p. 207
[4] T Bengtsson *et al*, in *Computational Nuclear Physics* edited by K Langanke *et al* (Berlin: Springer-Verlag, 1991) vol.1
[5] K Kumar and M Baranger, *Nucl. Phys.* **A110**, 490, 529 (1968)
[6] M Saha Sarkar and S Sen, *Phys. Rev.* **C56**, 3140 (1997)
[7] S G Nilsson, C F Tsang, A Sobiczewski, Z Szymanski, S Wycech, C Gustafson, I L Lamm, P Moller and B Nilsson, *Nucl. Phys.* **A131**, 1 (1969)
[8] S Raman *et al*, *At. Data Nucl. Data Tables* **36**, 1 (1987)
[9] Y Aboussir *et al*, *At. Data Nucl. Data Tables* **61**, 127 (1995)
[10] P Möller *et al*, *At. Data Nucl. Data Tables* **59**, 185 (1995)

Dissipative processes in light heavy ion collisions

A POP[1], A ANDRONIC[1], I BERCEANU[1], M DUMA[1], D MOISĂ[1], M PETROVICI[1], V SIMION[1], G IMMÉ[2], G LANZANÒ[2], A PAGANO[2], G RACITI[2], R CONIGLIONE[2], A DEL ZOPPO[2], P PIATELLI[2], P SAPIENZA[2], N COLONNA[3], G d'ERASMO[3,4] and A PANTALEO[3]
[1]National Institute for Physics and Nuclear Engineering, P.O. Box MG-6, RO-76900, Bucharest-Măgurele, Romania
[2]Istituto Nazionale di Fisica Nucleare, Laboratorio Nazionale del Sud and Dipartimento di Fisica, Università di Catania, I-95129 Catania, Italy
[3]Istituto Nazionale di Fisica Nucleare, Sezione di Bari, via Amendola, 173-70125, Bari, Italy
[4]Dipartimento di Fisica, Università di Bari, Bari, Italy

Abstract. The characteristics of the dissipative processes in the collisions of light heavy ion systems at incident energies below 10 MeV/nucleon have been studied. The correlations between different experimental observables show similar trends as those known at much heavier systems and semiempirical relationships are established starting from assumptions on the nature of the microscopic mechanisms. The charge equilibration process in light systems is also studied.

Keywords. Multinucleon transfer reactions.

PACS Nos 25.70

The idea of the formation of the dinuclear system, seen as a doorway to deep inelastic collisions, is supported by the experimental study of the statistical consequences of its presence, through the analysis of fluctuations in the excitation functions of the products formed in the collision of the systems with masses $A_1 + A_2 \leq 100$ [1]. While statistical concepts are more or less accepted to be valid for heavy nuclear systems, for those with a small number of nucleons involved, the situation is not so clear, as the existence of deep inelastic processes for light systems remained still insufficiently studied. In view of these considerations, it would be of interest to see, to what extent experimental data really show differences or, on the contrary, a noticeable similitude between these two extremes.

Continuous measurements in energy and angle for the projectile-like fragments identified in the reactions: ^{19}F (111.4, 125, 136.9 MeV) + ^{27}Al, ^{19}F (111.4, 136.9 MeV) + ^{12}C and ^{27}Al (140.14 MeV) + ^{12}C, ^{27}Al have been carried out using the experimental device DRACULA [2], mounted at an extension of the 15 MV SMP Tandem from LNS, Catania, whose main components are two large area position sensitive ionization chambers, placed up and down relative to the horizontal reaction plane. Start and stop PPADs allowed to perform mass measurements too.

The double differential cross sections as a function of different experimental observables, show similar trends with those observed for much heavier systems. Thus, a complete dynamics from quasielastic to complete dissipation regime is evidenced even in the case of such light systems and microscopic models were able to describe it [3,4]. The double differential cross section as a function of the atomic number (Z) of the reaction product and the total kinetic energy (TKE) shows a continuous broadening of the charge distribution with increasing total kinetic energy loss (TKEL). Maxima centered approximately at the projectile and target Z values are present up to large TKEL. This shows that the interacting nuclei did not completely lose their identity, suggesting a statistically not equilibrated process.

The experimental angular distributions of the reaction products depend on the nature and time scale of the reaction. An estimate of the interaction time, for different degrees of inelasticity of the reaction process (windows of TKE), can be done from the angular distributions for any reaction product, in the frame of a Regge-pole model [5]. The representation of the interaction time as a function of Z and TKEL in figure 1 shows that, it is possible to populate more and more different Z values from that corresponding to the projectile, as the interaction time increases. Thus, the energy integrated angular distributions usually presented in the literature, becoming flatter as the atomic number difference between the detected product and the projectile increases, reflect the necessity of a longer interaction time in order to reach Z values far off from the projectile atomic number, but for the same degree of inelasticity of the reaction, the value of the average lifetime is independent of the specific fragment in the exit channel whose angular distribution has been used to deduce it. This behaviour is characteristic to a diffusion type process.

The natural logarithm of the charge distribution variance (σ_Z^2) obtained from a two-gaussian fit, in windows of TKE, as a function of the ratio of the total kinetic energy loss to the grazing angular momentum (TKEL/l_{gr}), follows a systematics which has been established for light, medium and heavy mass systems in [6], namely:

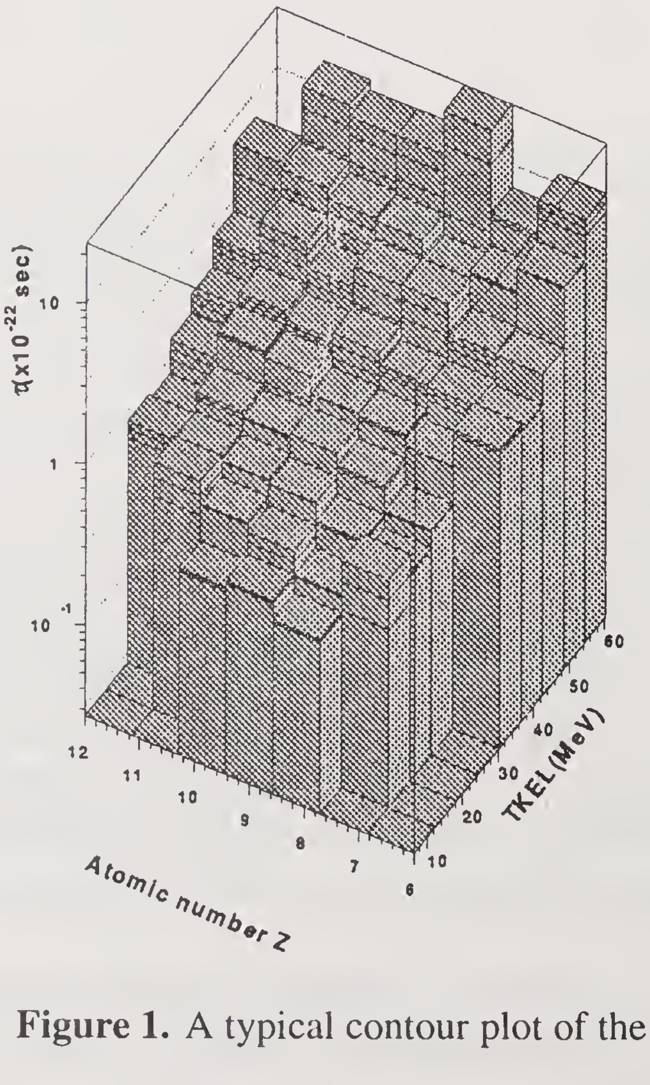

Figure 1. A typical contour plot of the interaction time as a function of Z and TKEL.

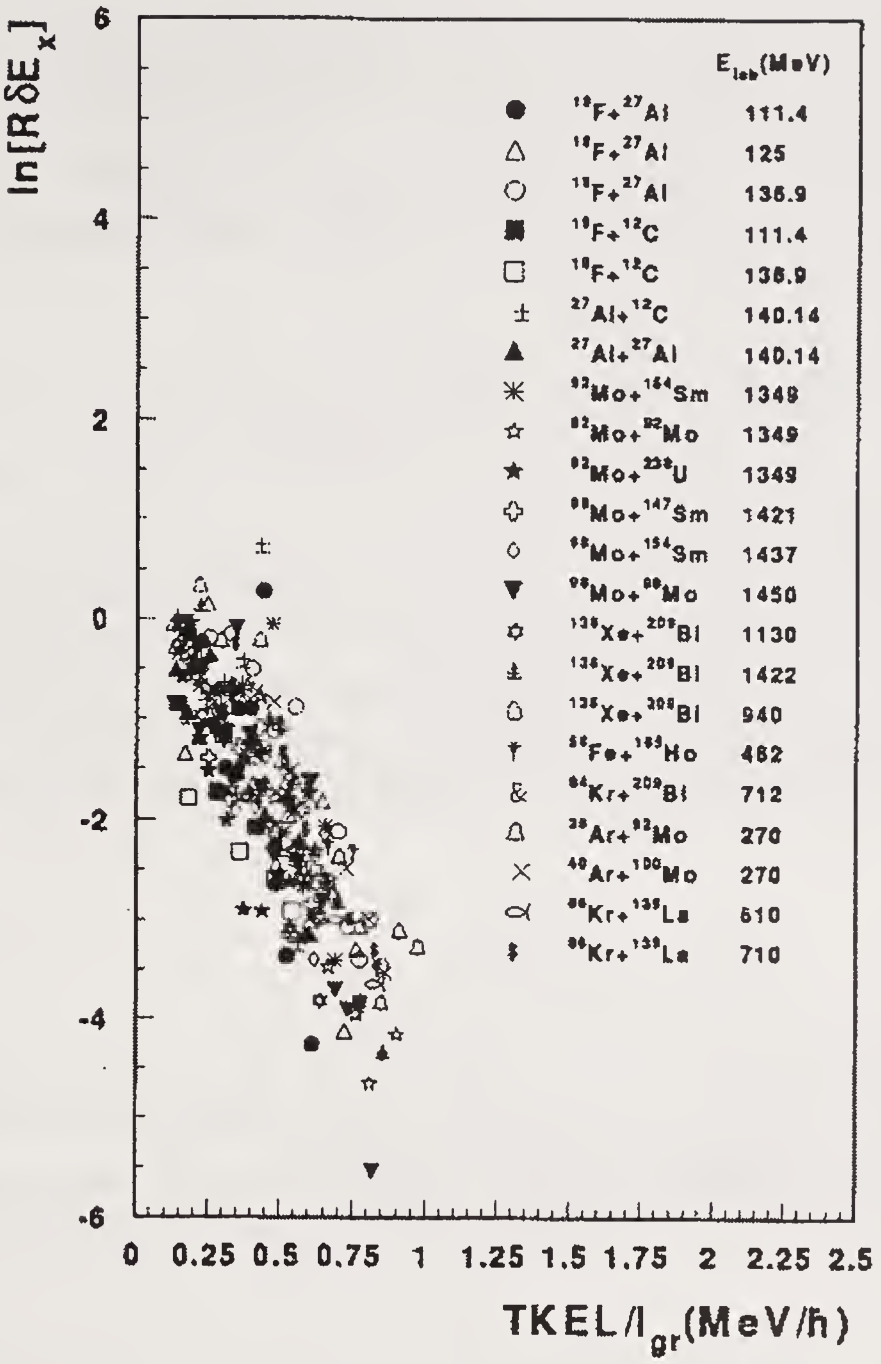

Figure 2. Dependence of energy dissipated per transferred nucleon on TKEL and l_{gr} for various systems.

$$\ln[F\sigma_Z^2] = s\left[\frac{\mathrm{TKEL}}{l_{\mathrm{gr}}} - \frac{\Delta}{l_{\mathrm{gr}}}\right], \qquad F = s\frac{m}{\mu}\alpha\frac{E_0}{l_{\mathrm{gr}}}\left(\frac{A}{Z}\right)^2. \tag{1}$$

This corresponds to an energy dissipation time rate assumed to be of the form [6]:

$$\frac{\mathrm{d}E}{\mathrm{d}\tau} = -2D_A\frac{m}{\mu}\alpha E_0\frac{\tau_0}{\tau}. \tag{2}$$

m is the nucleon mass; μ is the reduced mass of the system; $E_0 = E_{\mathrm{cm}} - V_{\mathrm{coul}}$ is the initial kinetic energy available over the Coulomb barrier; V_{coul} is the Coulomb potential evaluated at the interaction radius; α takes into account the Pauli exclusion principle in the process of nucleon exchange. D_A is the mass diffusion coefficient; A and Z refer to the composite system. A correlated exchange of nucleons is assumed: $\sigma_A^2 = (A/Z)^2\sigma_Z^2$. τ_0 represents the time when the statistical exchange of nucleons shows up and Δ the corresponding value of TKEL, which can be correlated to the change of slope more clearly observed in the experimental data from [7]. s is the universal value of the slope experimentally established for heavy (6.07 ħ/MeV) [8], medium (5.27 ħ/MeV) [7] and light (5.93 ħ/MeV) [6] systems.

Thus, the width of the charge distribution, measured experimentally as a function of TKEL, is limited by the size and incident energy of the system, as the expression of the abscissa in eq. (1) behaves like a system independent quantity. The relationship (2), the linear dependence of σ_Z^2 on the interaction time in a simple diffusion model and the exponential dependence of τ on TKEL [6], lead to the following expression for the amount of energy dissipated per transferred nucleon (δE_x):

$$\ln[R\delta E_x] = -s\left[\frac{\mathrm{TKEL}}{l_{\mathrm{gr}}} - \frac{\Delta}{l_{\mathrm{gr}}}\right], \qquad R = \frac{1}{\frac{m}{\mu}\alpha E_0}, \tag{3}$$

which can be followed in figure 2.

By considering in the TKEL range from 0 up to Δ, a mechanism of collective exchange of nucleons (corresponding to charge equilibration) and under the assumption that the number of exchanged nucleons is equal to the mass distribution variance, related to σ_Z^2 by a continuous evolution from uncorrelated to correlated exchange of nucleons, one obtains that the charge distribution variance scaled with a factor which depends on the system, follows the dependence:

$$F_\Delta \sigma_Z^2 = \mathrm{TKEL}, \qquad F_\Delta = f\frac{A}{Z}\frac{m}{\mu}\alpha E_0, \tag{4}$$

with $f = 1 + ((A/Z) - 1)\cdot\mathrm{TKEL}/\Delta$.

If it is assumed that at time τ_0, the charge distribution variance reaches the value of the plateau predicted by the one-dimensional oscillator model in the charge asymmetry degree of freedom [9] : $\sigma_Z^2 = \hbar\omega/2K$ (K is the stiffness parameter), the following expression is obtained for the slope:

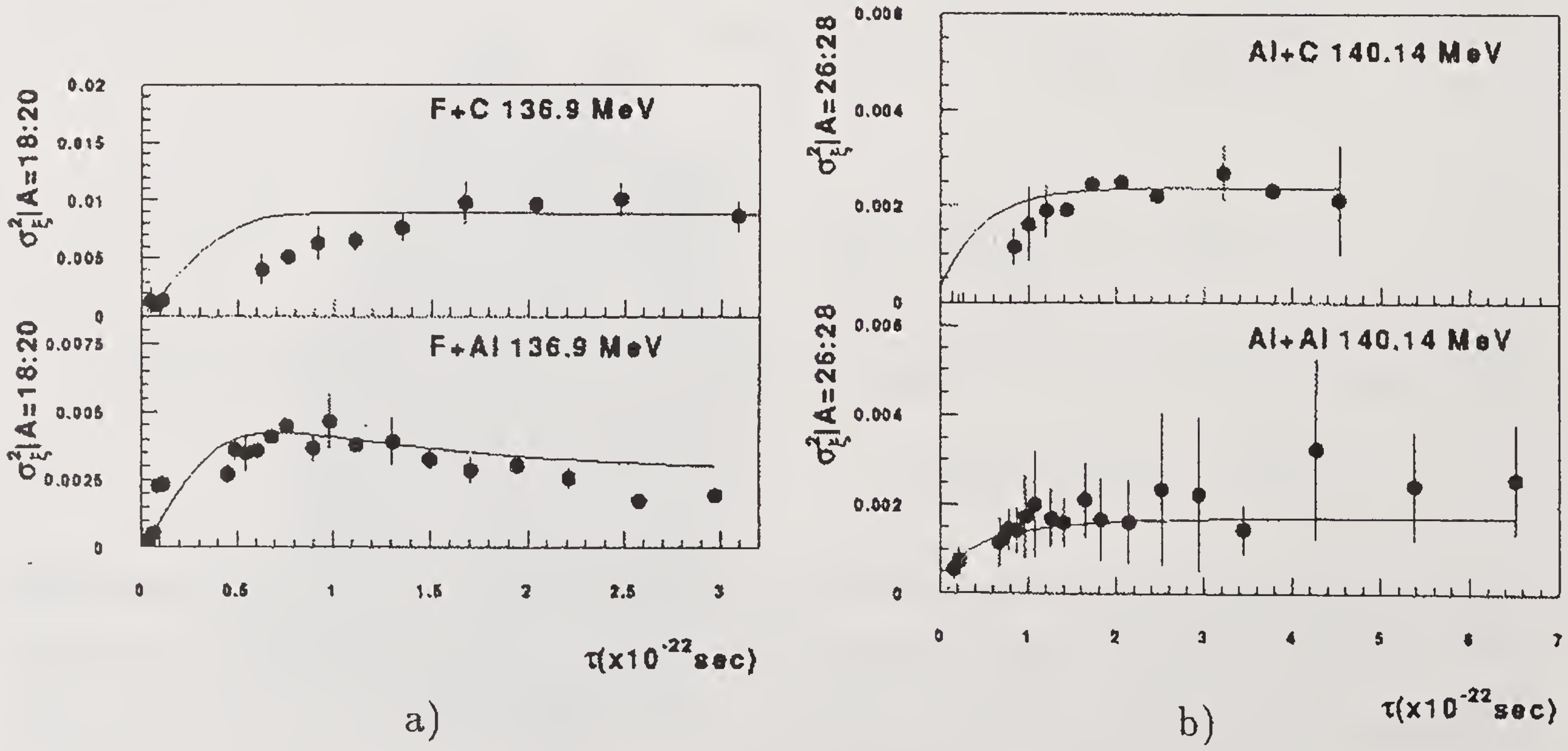

a) b)

Figure 3. Comparison of experimental data for conditional charge variance with predictions of damped quantum oscillator model for (**a**) fluorine induced reactions Al and (**b**) aluminium induced reactions on C and Al.

$$s = \frac{1}{\frac{m}{\mu}\alpha\frac{E_0}{l_{\mathrm{gr}}}\frac{\hbar\omega}{2K}\left(\frac{A}{Z}\right)^2}. \tag{5}$$

In spite of the very simple hypotheses, the relationship (5) is valid in the limit of a factor 1.5 for all the systems included in the systematics.

In figures 3(a), (b) one can see the comparison between the experimental data for the conditional charge variance and the predictions of the model for the damped quantum oscillator in the charge asymmetry degree of freedom, treated as an open quantum system, with the same parameters used for heavier systems [10].

The elastic scattering data have been analysed within the Frahn formalism and reaction and non-fusion processes cross sections have been estimated.

From the experimental results presented in this work one can conclude that, the deep inelastic reaction mechanism is also present in the interaction of light systems at energies below 10 MeV/nucleon. The presence of the same types of correlations as those established for medium and heavy systems, suggests the existence of similar underlying microscopic mechanisms, which could be a challenge to the new generation of microscopic models.

References

[1] I Berceanu *et al*, *Phys. Rev.* **C57**, 2359 (1998) and contribution to IWRNP-98
[2] V Simion, *Rom. J. Phys.* **38**, 513 (1993)
[3] M Petrovici *et al*, *Z. Phys.* **A354**, 11 (1996)
[4] H Feldmeier and J Schnack, *Prog. Part. Nucl. Phys.* **39**, 393 (1997)
[5] C K Gelbke *et al*, *Phys. Rep.* **42**, 31 (1978)
[6] A Pop *et al*, *Phys. Lett.* **B397**, 25 (1997)
[7] M Petrovici *et al*, *Nucl. Phys.* **A477**, 277 (1988)
[8] H J Wollerscheim *et al*, *Phys. Rev.* **C25**, 338 (1982)
[9] M Berlanger *et al*, *Z. Phys.* **A291**, 133 (1979)
[10] A Pop *et al*, *Z. Phys.* **A329**, 357 (1988)

Distinction between pre-formed cluster emission and heavy ion decay by fission

G SHANMUGAM and G M CARMEL VIGILA BAI
Department of Physics, Manonmanian Sundaranar University, Tirunelveli 627 012, India

Abstract. For studying cluster radioactivity in the actinide region as well as trans-tin region two types of models are used: the pre-cluster formation model and the unified fission model. In the case of the actinide region, the cluster-like shapes are preferred for very high asymmetry while fissioning shapes are more suitable for less asymmetry and symmetry (the line of demarcation being around $A_e = 31$). In this work this line of demarcation is studied in the case of the trans-tin region. The results of this study show that the transition from cluster mode to fission mode takes place at $A_e = 16$.

Keywords. Cluster radioactivity; pre-formed cluster emission; heavy ion decay by fission; comparison.

PACS Nos **23.70+j; 23.60+e; 21.60.Gx**

1. Introduction

The spontaneous emission of fragments heavier than alpha particle termed as cluster radioactivity has now become an experimentally confirmed reality. Theoretically, such emissions were first predicted by Sandulescu, Poenaru and Greiner [1]. The first experimental observation was made by Rose and Jones [2]. Encouraged by this, researchers tried to detect other novel modes of radioactive decay in which heavy nuclei disintegrate by emission of intermediate mass fragments. Theoretically, the interest in such decays lies in the estimation of lifetimes and branching ratios with respect to alpha decays. The lifetimes for the observed cluster radioactivity of radioactive nuclei have been estimated using various models and compared with the experimental data. These models can be classified as the fission models, where only the barrier penetrabilities are calculated, and the preformed cluster models, where the cluster is assumed to be formed before it penetrates the barrier and its preformation probability is also included in the calculations. The physics of the two approaches is apparently different, though it has been possible to look for some similarities between them [3].

The purpose of this work is to compare the cluster mode and fission mode of cluster radioactivity to find the transition point from one mode to the other in the case of trans-tin region using our model. In section two, we give the description of our model applicable for treating cluster radioactivity from trans-tin region. The transition from the cluster mode to fission mode in actinide region is discussed in the third section. Extension to trans-tin region is discussed in §4. Finally §5 contains conclusion.

2. Our model

In order to study such cluster radioactivity, we have developed a model (CYEM) [4] in two sphere approximation in which the zero-point vibration energy is explicitly included without violating the conservation of energy and the nuclear inertial mass coefficient dependent on the centre of mass distance has been used. We have already demonstrated the success of this model by applying it to the cases of ^{14}C, ^{24}Ne [4] and also extended [5] this model for the emission of fragments heavier than ^{24}Ne from uranic and trans-uranic nuclei. Recently, we have also extended [6,7] this model for the newly predicted trans-tin region incorporating the most important cluster deformation. In the case of newly discovered trans-tin cluster radioactivity the daughter nuclei are formed around the doubly magic ^{100}Sn, the deformations of the clusters are very large and hence they have to be incorporated in the lifetime calculations.

In our earlier version of the model [8], we have treated the parent and the daughter nuclei spheroid, keeping the cluster as spherical. But in this work the parent and the emitted cluster are considered to be spheroid, keeping the daughter as spherical. If the emitted cluster has a deformation, say quadrupole deformation only, while the daughter nucleus is spherical and if the Q-value of the reaction is taken as the origin, the potential for the post-scission region as a function of the centre of mass distance r of the fragments is given by

$$V(r) = V_c(r) + V_n(r) - V_{df}(r) - Q. \tag{1}$$

Here, V_c is the Coulomb potential between a spheroidal emitted cluster and spherical daughter, V_n is the nuclear interaction energy due to finite range effects of Krappe *et al*; and V_{df} is the change in the nuclear interaction energy due to quadrupole deformation β_2 of the emitted cluster.

The Coulomb potential between the emitted fragments is taken as the interaction of a spheroidal emitted cluster and a spherical daughter. For a prolate spheroidal emitted cluster with longer axis along the fission direction, Pik-Pichak obtained

$$V_c(r) = \frac{3}{2}\frac{Z_d Z_e e^2 \nu}{r}\left(\frac{1-\nu^2}{2}\ln\frac{\nu+1}{\nu-1} + \nu\right) \tag{2}$$

and for an oblate spheroidal emitted cluster with shorter axis along the fission direction,

$$V_c(r) = \frac{3}{2}\frac{Z_d Z_e e^2}{r}\left(\nu(1+\nu^2)\arctan\nu^{-1} - \nu^2\right). \tag{3}$$

For the overlapping region, we approximate the potential barrier by a third-order polynomial in r having the form [4]

$$V(r) = -E_v + [V(r_t) + E_v]\left\{s_d\left(\frac{r-r_i}{r_t-r_i}\right)^2 - s_e\left(\frac{r-r_i}{r_t-r_i}\right)^3\right\}, \quad r_i \le r \le r_t \tag{4}$$

where

$$r_t = a_e + R_d. \tag{5}$$

Here, a_e is the semi-major or minor axis of the spheroidal cluster depending on the prolate or oblate shape of the emitted cluster; and ri is the distance between the centres of mass of the daughter and the emitted particle portions in the spheroidal parent nucleus.

Expressing the energies in MeV, lengths in fm and time in seconds, for calculating the lifetime of the decay system we use the formula

$$T = \frac{1.433 \times 10^{-21}}{E_v}[1 + \exp(K)]. \tag{6}$$

The action integral K is given by

$$K = K_L + K_R, \tag{7}$$

where

$$K_L = \frac{2}{\hbar} \int_{r_a}^{r_t} [2B_r(r)V(r)]^{1/2}\, \mathrm{d}r \tag{8}$$

and

$$K_R = \frac{2}{\hbar} \int_{r_t}^{r_b} [2B_r(r)V(r)]^{1/2}\, \mathrm{d}r. \tag{9}$$

The limits of integration r_a and r_b are the two appropriate zeros of the integrand which are found numerically.

3. Transition from cluster mode to fission mode in actinide region

Poenaru *et al* have discussed the applicability of the cluster mode or the fission mode for studying cluster radioactivity in the actinide region and have found out that the transition from one mode to other takes place around $A_e = 31$. They have considered the parametrisation of two intersecting spheres with constant radius R_e of the light fragment (cluster mode) or with constant volume V_e of the light fragment (fission mode). They have concluded that cluster mode is preferred for studying cluster radioactivity for $A_e < 31$, the fission mode is more suitable for $A_e > 31$ [9].

4. Extension to trans-tin region

We have applied our model to study the emission of ^{12}C, ^{16}O, ^{20}Ne, ^{24}Mg, ^{28}Si [10] etc from the trans-tin region and compared with that of Poenaru *et al* [11]. In the figures 1–3, we give the life times for the decay of lighter to heavier clusters where the deviation of the results obtained by our fission model and the cluster model is found to become large after ^{16}O emission.

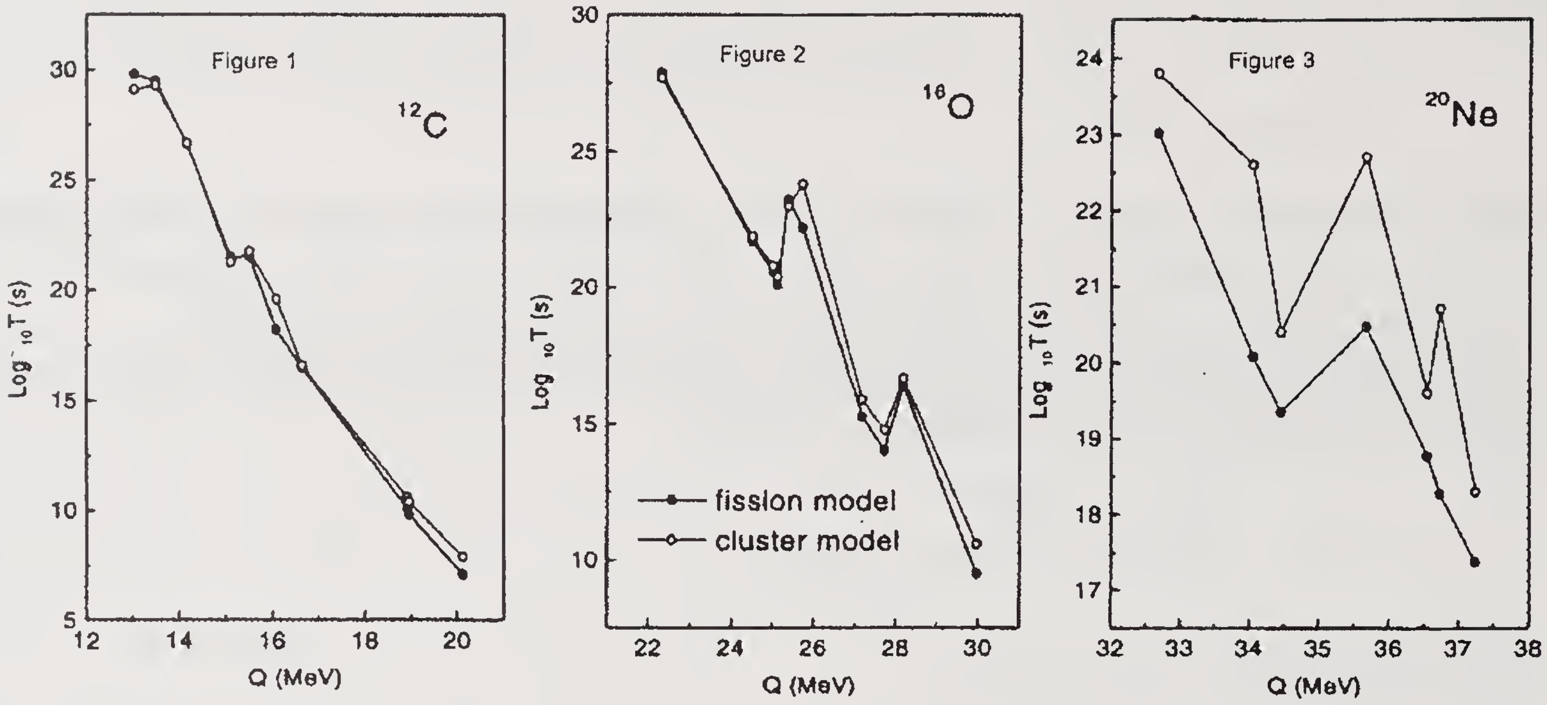

Figures 1–3. Lifetimes for the decay of lighter to heavier clusters.

5. Conclusion

Even though the preformed cluster model can be used for cluster radioactivity, still there is a distinction between cluster mode and fission mode. Thus we conclude that fission model is more apt for all cluster decays while the pre-cluster model is quite applicable for the lighter clusters.

References

[1] A Sandulescu, D N Poenaru and W Greiner, *Fiz. Elem. Chastits At. Yadra* **11**, 1334 (1980) [*Sov. J. Part. Nucl.* **11**, 528 (1980)]
[2] H J Rose amd G A Jones, *Nature (London)* **307**, 245 (1984)
[3] D N Poenaru, D Schnabel, W Greiner, D Mazilu and R Gherghescu, *Atomic Data Nucl. Tables* **48**, 231 (1991)
[4] G Shanmugam and B Kamalaharan, *Phys. Rev.* **C38**, 1377 (1988)
[5] G Shanmugam and B Kamalaharan, *Proc. of Int. Conf. on Nucl. Reaction Mechanisms*, Calcutta, India (1989) p.73
[6] G Shanmugam, G M Carmel Vigila Bai and G Suresh, *Nucl. Phys. Symp. (India)* **B36**, 108 (1993)
[7] G Shanmugam, G M Carmel Vigila Bai and B Kamalaharan, *Phys. Rev.* **C51**, 2616 (1995)
[8] G Shanmugam and B Kamalaharan, *Phys. Rev.* **C41**, 1184 (1990)
[9] G M Carmel Vigila Bai, Ph.D Thesis (Manonmanian Sundaranar University, Tirunelveli, 1997)
[10] D N Poenaru, W Greiner and R Gherghescu, *Phys. Rev.* **C47**, 2030 (1993)
[11] D N Poenaru, J A Maruhn, W Greiner, M Ivascu, D Mazilu and I Ivascu, *Z. Phys.* **A333**, 291 (1989)

Nuclear structure studies of nuclei near $N = 80$

E DRAGULESCU, G SEMENESCU and I IFTIMIA*
Department of Atomic and Nuclear Physics, National Institute for Physics and Nuclear Engineering, P.O. Box MG-6, RO-76900, Bucharest, Romania
*Technical Military Academy, Bucharest, Romania

Abstract. High-spin states in ^{135,136}Ba, ^{136}La, ^{137}Ce, ^{139}Nd were populated following (HI, χn) reactions and subsequent radiation was studied using in-beam γ-ray spectroscopy methods. Level schemes with new states belonging to the above mentioned nuclei are given.

These nuclei situated near $N = 80$ have been analysed within the framework of the interacting-boson model (IBM), applied to the description of even–even, odd–even and odd–odd nuclei to calculate excitation energies and electromagnetic properties for the above mentioned nuclei.

Keywords. Nuclear structure; interacting boson model.

PACS Nos 21.10.Tg; 23.20.Lv

1. Introduction

The nuclei situated near $N = 80$ are in a mass region of transitional nuclei, where they show a gradual change from a nearly vibrational structure to one with similarity to a rotational band structure. In the study of nuclei near closed shell configurations, one can expect the interplay between collective degrees of freedom and specific shell-model excitations (two, or three particle clusters) to determine the experimental spectra.

This study as part to a program [1–3] to study the nuclear structure near $N = 80$ reports our results on ^{135,136}Ba, ^{136}La, ^{137}Ce, and ^{139}Nd nuclei. The previous experimental information on ^{135,136}Ba nuclei is very limited, it comes from β-decay, $(n, n\gamma)$ and Coulomb excitation [1,2,4].

2. Experimental procedures and results

The high-spin states in the above mentioned nuclei have been studied using the nuclear reactions induced by ^{9}Be, ^{10,11}B, ^{12}C and ^{16}O ions. The heavy ions were delivered by FN-Tandem accelerator of the NINPE, Bucharest with energies in the range of 30–64 MeV. The experimental information was deduced from γ-ray singles spectra as well as from excitation functions, $\gamma - \gamma(t)$ coincidences and angular distributions. The placement of γ-ray in the level scheme was based on coincidence relationship and relative transition

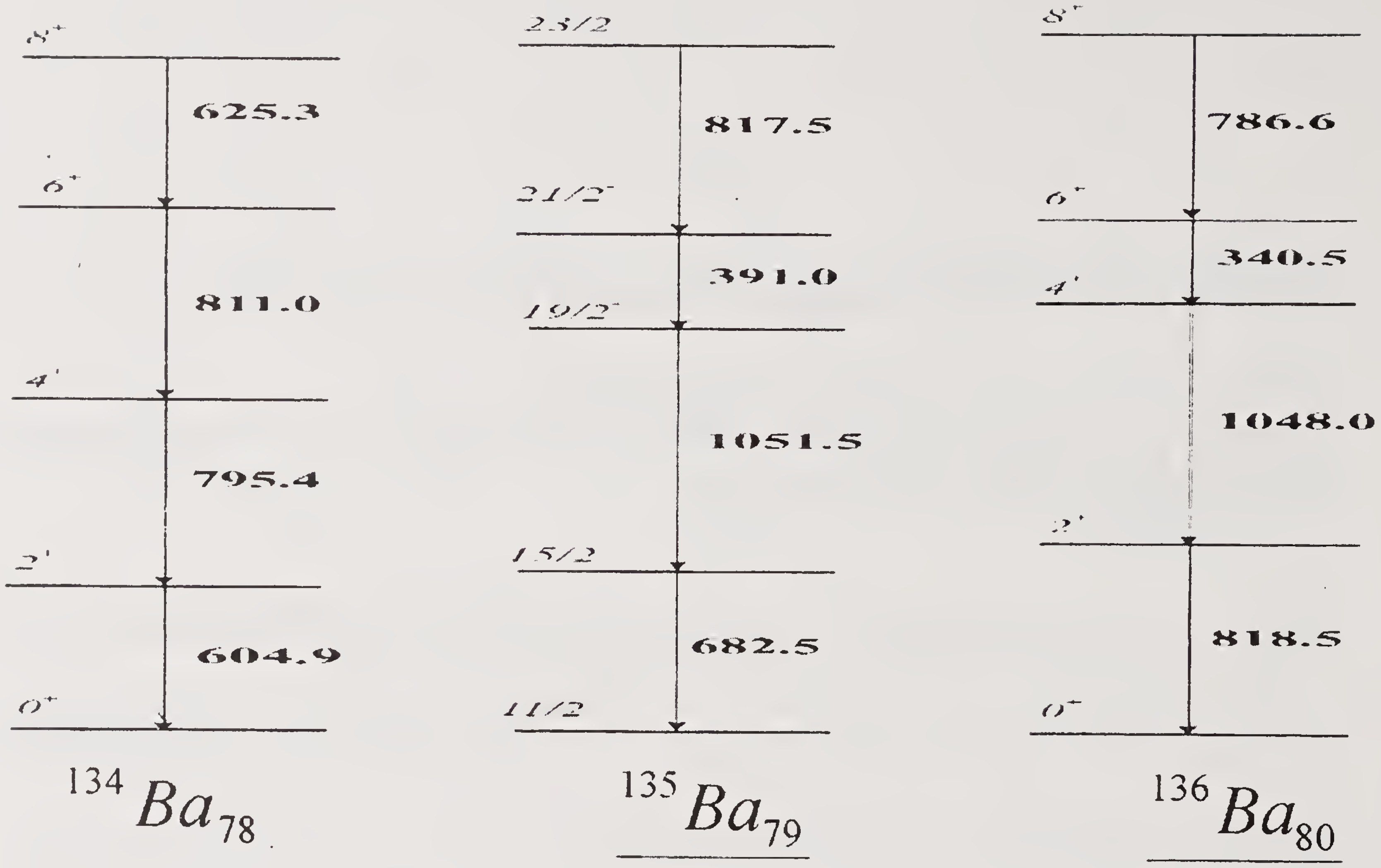

Figure 1. The systematics of the ground-state band in ^{134,135,136}Ba nuclei.

intensities. The spin and parity assignments, the multipole mixing ratios δ were deduced from the angular distribution analysis.

Our results confirmed most of the previously known levels in above-mentioned nuclei [4–8] and level schemes were extended with the spin and the excitation energy, many new levels and bands were observed.

New experimental information is obtained for the ground band in ^{136}Ba which is extended from 6^+ state to 12^+ state and yrast band built on $11/2^-$ in ^{135}Ba (figure 1). A new band $\Delta J = 1$ built on the 204 transition was observed in ^{135}Ba as well as in other $N = 79$ isotones: ^{137}Ce and ^{139}Nd in the present work (figure 2).

3. Discussion

3.1 Level structure of the ^{135,136}Ba nuclei

The ground state in ^{136}Ba is very similar to those of $N = 80$ isotones: ^{138}Ce, ^{140}Nd, ^{142}Sm and ^{144}Gd. From figure 1, the band built on $h_{11/2^-}$ has energy spacings very similar with the ground state band in ^{136}Ba and not with ^{134}Ba nucleus, leading to the conclusion that ^{135}Ba nucleus can be interpreted as neutron hole coupled to ^{136}Ba core.

3.2 $\Delta J = 1$ bands in $N = 79$ nuclei: ^{135}Ba, ^{137}Ce, ^{139}Nd

We observed for the first time a $\Delta J = 1$ band on the $23/2^-$ state in ^{135}Ba, ^{137}Ce, ^{139}Nd ($N = 79$) and also observed previously in ^{141}Sm, ^{143}Gd and ^{145}Dy [6,8]. The excitation

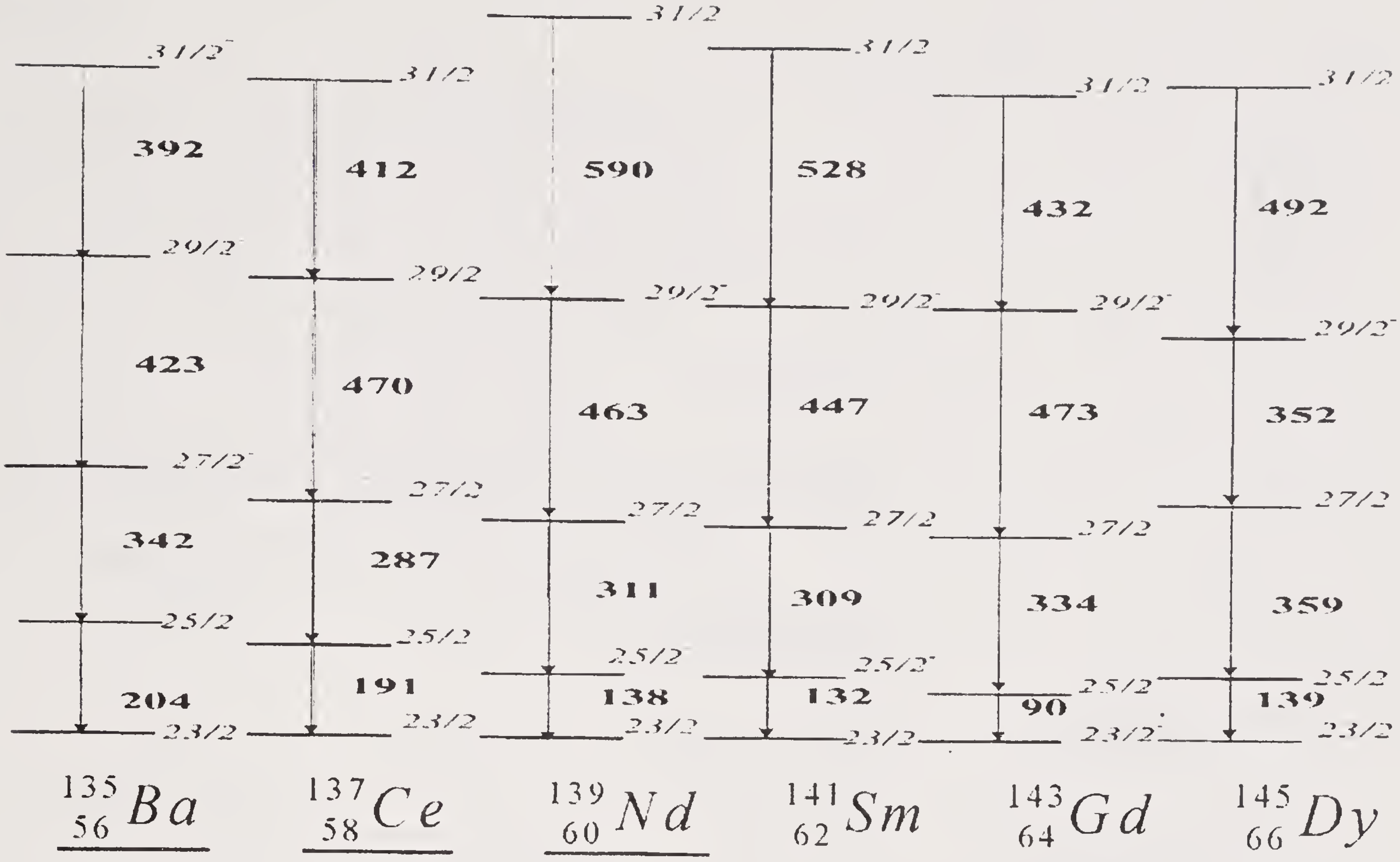

Figure 2. The systematics of the $\Delta J = 1$ band $(\pi h^2_{11/2}\nu h^{-1}_{11/2})$ in the $N = 79$ nuclei.

energy of $23/2^-$ states in $N = 79$ isotones follows the same trend of the experimentally known $(\pi h_{11/2})^2 10^+$ excitation at $N = 78$ and $N = 80$. These bands probably involve core excitations coupled to the $(\pi h^2_{11/2}\nu h^{-1}_{11/2})$, 1 hole-2 particle states (see figure 2).

3.3 *IBM calculations for the* ^{135,136}Ba, ^{137}La *and* ^{136}La *nuclei*

In the last decade the interacting boson model (IBM) was extensively applied to the description of even–even nuclei. Its extension to boson–fermion systems, the interacting boson–fermion model (IBFM) [9,12] was applied to odd–even nuclei. Recently, the model was extended to odd–odd nuclei [10,11] and referred to as interacting boson–fermion–fermion model (IBFFM).

The calculation of ^{135}Ba and ^{137}La is performed within the framework of IBFM by the coupling of valence-shell neutron quasiparticles and proton quasiparticles, respectively to the IBM core ^{136}Ba. The core nucleus ^{136}Ba was fitted by using a boson parameterization, which is an interplay between U(5) and O(6) symmetries. The nuclear structure of odd–odd $N = 79$ isotone ^{136}La is described within the framework of IBFFM by coupling of proton and neutron quasiparticles to even–even core ^{136}Ba. The proton orbitals: $1g_{7/2}, 2d_{5/2}$ and $1h_{11/2}$ describe the structure of ^{137}La and the neutron orbitals: $2d_{3/2}, 3s_{1/2}$ and $1h_{11/2}$ describe the structure of ^{135}Ba nucleus. We performed IBFFM calculations for ^{136}La with the residual proton–neutron parameterization [10], $V_\delta = -0.3$ and $V_{\sigma\sigma\delta} = 0.01$. We have calculated the positive and negative parities and compared them with experimental levels in figure 3. The observed level energy spectra are reasonably well described by the

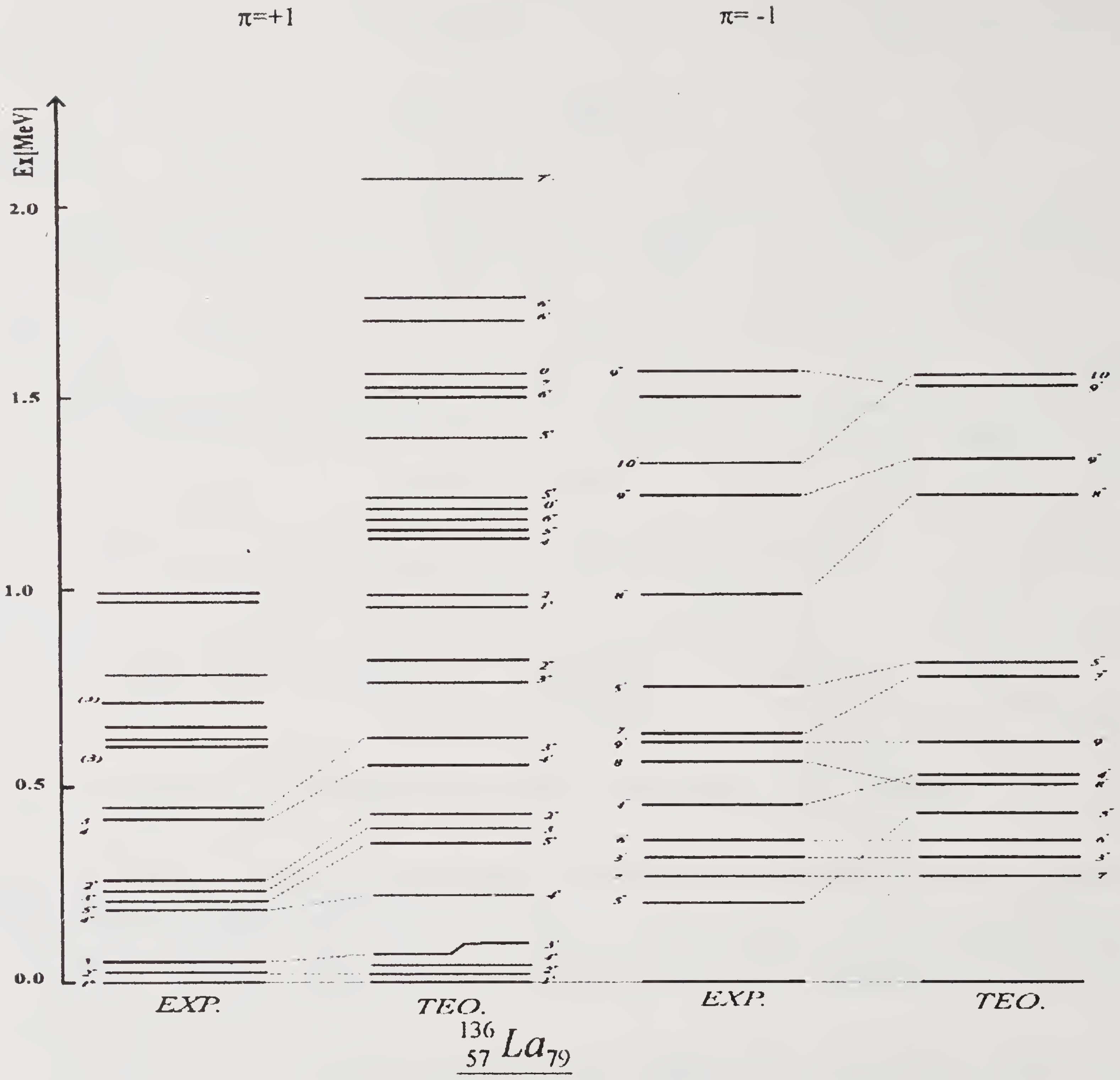

Figure 3. The experimental and the calculated energy spectra for ^{136}La.

IBFFM. The calculated E2 and M1 electromagnetic properties are also in agreement with the observed ones.

4. Conclusions

This paper describes a part of an extensive work to investigate the experimental and theoretical properties of the transitional nuclei, situated near $N = 80$. New bands have been established in all nuclei following (HI, χn) reactions.

The experimental energy level spectra electromagnetic properties were compared with the calculations using the interacting boson model (IBM) with its versions for even–even, odd–even and odd–odd nuclei.

References

[1] E Dragulescu *et al*, *J. Phys.* **G10**, 1099 (1984)
[2] E Dragulescu *et al*, *Rev. Roum. Phys.* **32**, 743 (1987)
[3] E Dragulescu *et al*, *Nucl. Phys.* **A548**, 435 (1992)
[4] Yu V Sergeenkov, *Nucl. Data Sheets* **52**, 205 (1987)
[5] M Muller-Veggian *et al*, *Nucl. Phys.* **A344**, 89 (1980)
[6] M A Cardonna *et al*, *Z. Phys.* **A340**, 345 (1991)
[7] M Lach *et al*, *Z. Phys.* **A345**, 427 (1993)
[8] M Sferraza *et al*, *Z. Phys.* **A350**, 5 (1994)
[9] V Paar *et al*, *Nucl. Phys.* **A378**, 42 (1982)
[10] S Brant and V Paar, *Z. Phys.* **A329**, 151 (1988)
[11] S Brant *et al*, *Phys. Rev.* **C37**, 830 (1988)
[12] R Aryaeinejead *et al*, *Phys. Rev.* **C40**, 142 (1989)

The simulations of Ca–Ca collisions: Binary break-up, onset of multifragmentation and vaporization

RAJEEV K PURI and SUNEEL KUMAR
Physics Department, Panjab University, Chandigarh 160 014, India

Abstract. The incomplete fusion, onset of multifragmentation and vaporization is studied in Ca–Ca collisions at bombarding energies between 20–1000 A MeV and at impact parameters between $b = 0$ to $b_{\max}$ using quantum molecular dynamics model. We find incomplete fusion events at $E/A = 20$ MeV. The light mass fragment production at a given incident energy does not show any rise and fall with a change in the impact parameter. Whereas, the IMF production at higher energies (≥ 150 A MeV) has a clear rise and fall.

Keywords. Quantum molecular dynamics; multifragmentation; rapidity; flow.

PACS Nos 25.70Jj; 25.70 Mn; 25.70Pq

1. Introduction

The most interesting domain of the incident energy in heavy ion collisions is between 20 A MeV to 1000 A MeV where one can have incomplete fusion, fusion–fission, multifragmentation or a complete disassembly of the excited nuclear matter [1]. The new experimental studies of the multifragmentation have revealed that it is a very complicated phenomenon which depends crucially on the bombarding energy and on the impact parameter. Here we plan to understand the complex dependence of the light mass and intermediate mass fragments on bombarding energy and impact parameter by carrying a systematic study of the formation of fragments and their properties in Ca–Ca collision using quantum molecular dynamics (QMD) model [2].

2. The model

The simulations of Ca–Ca collisions are performed using QMD model [2], where each nucleon is described by a Gaussian in momentum and coordinate space and the centroid of each nucleon propagates using the Hamiltonian equations of motion:

$$\frac{\mathrm{d}\vec{r}_i}{\mathrm{d}t} = \frac{\partial H}{\partial \vec{p}_i}; \qquad \frac{\mathrm{d}\vec{p}_i}{\mathrm{d}t} = \frac{\partial H}{\partial \vec{r}_i} \tag{1}$$

with Hamiltonian

$$H = \sum_{i}^{A} \frac{\vec{p_i}^2}{2m} + \frac{1}{2} \sum_{i=1}^{A} \sum_{j \neq i}^{A} (u_{sk}^{ij} + u_{yk}^{ij} + u_{c}^{ij}). \tag{2}$$

The u_{yk}, u_{sk} and u_c appearing in eq. (2) are, respectively, the Yukawa, Skyrme and Coulomb interactions. For details, the reader is referred to ref. [2].

3. Results and discussion

In the present study, a hard equation of state with energy dependent cross-section is used. We follow the time evolution of nucleons till 200 fm/c and then construct the fragments using the minimum spanning tree method which allows two nucleons to share the same fragment if their centroids are closer than 4 fm.

In figure 1, we display the final multiplicities (at 200 fm/c) as a function of the scaled impact parameter $\hat{b} = b/b_{\max}$. The displayed quantities are: the largest fragment $A^{\max}$, emitted nucleons, light mass fragments (LMFs) $(2 \leq A \leq 4)$ and intermediate mass fragments (IMF's) $(5 \leq A \leq 25)$. The A^{max} will give us possibility to look for fusion in Ca–Ca collisions. Whereas the emission of nucleons will show the disassembly (and hence the vaporization) of the matter. At low energies, few nucleons are emitted from the excited compound system which is followed by the emission of the LMFs. In some cases (specially at non-central collisions), the excited system decays in two steps: (i) it fissions into two parts (the binary break-up) and (ii) these fissioned products emit nucleons/LMFs. The $A^{\max}$ yields several interesting points: (i) One clearly sees a partial fusion at 20 A MeV for $\hat{b}$ $(= b/b_{\max}) = 0.45$–0.75. (ii) The $A^{\max}$ at low energies is nearly independent of the impact parameter. Whereas a stronger impact parameter dependence is observed at higher energies. This can be understood on the ground that at low energies, the available phase-space is too small to allow the frequent nucleon–nucleon collisions. Therefore, the variation in the impact parameter at low energies has a least effect on $A^{\max}$. At higher bombarding energies ($\geq$ 100 A MeV), the dynamics is dominated by the frequent nucleon–nucleon collisions which depend strongly on the impact parameter.

The emission of nucleons increases with increase in the bombarding energy for central and semi-central collisions. In central collisions at 1000 A MeV, nearly 90% of the nuclear matter ends emitted nucleons. If we label the phenomenon with $\approx$ 60% matter emitted nucleons as 'vaporization', we see the vaporization for central collisions above 200 A MeV.

The LMFs production in central collisions peaks around 150–200 A MeV. This peak vanishes for peripheral collisions. The IMFs show a clear transition from multifragmentation to complete disassembly of the nuclear matter at central collision. We notice a rise and fall in IMFs production with increase in the bombarding energy in central collisions. The peak/plateau in IMFs production has also been observed recently [1]. The variation of LMFs and IMFs with impact parameter yields different results: (i) There is no rise and fall in the LMFs production with a change in the impact parameter. (ii) The IMFs clearly show a rise and fall for bombarding energies $\geq$ 150 A MeV. The plateau of the peak in the multiplicity decreases with increase in the bombarding energy till 400 A MeV and remains the same for further change in the incident energy. This is simply due to the fact that the mass of the system is very small. Therefore, after certain excitation energy, the final structure will no longer change. We also see the onset of the multifragmentation around 60 A MeV where the IMF production is maximum.

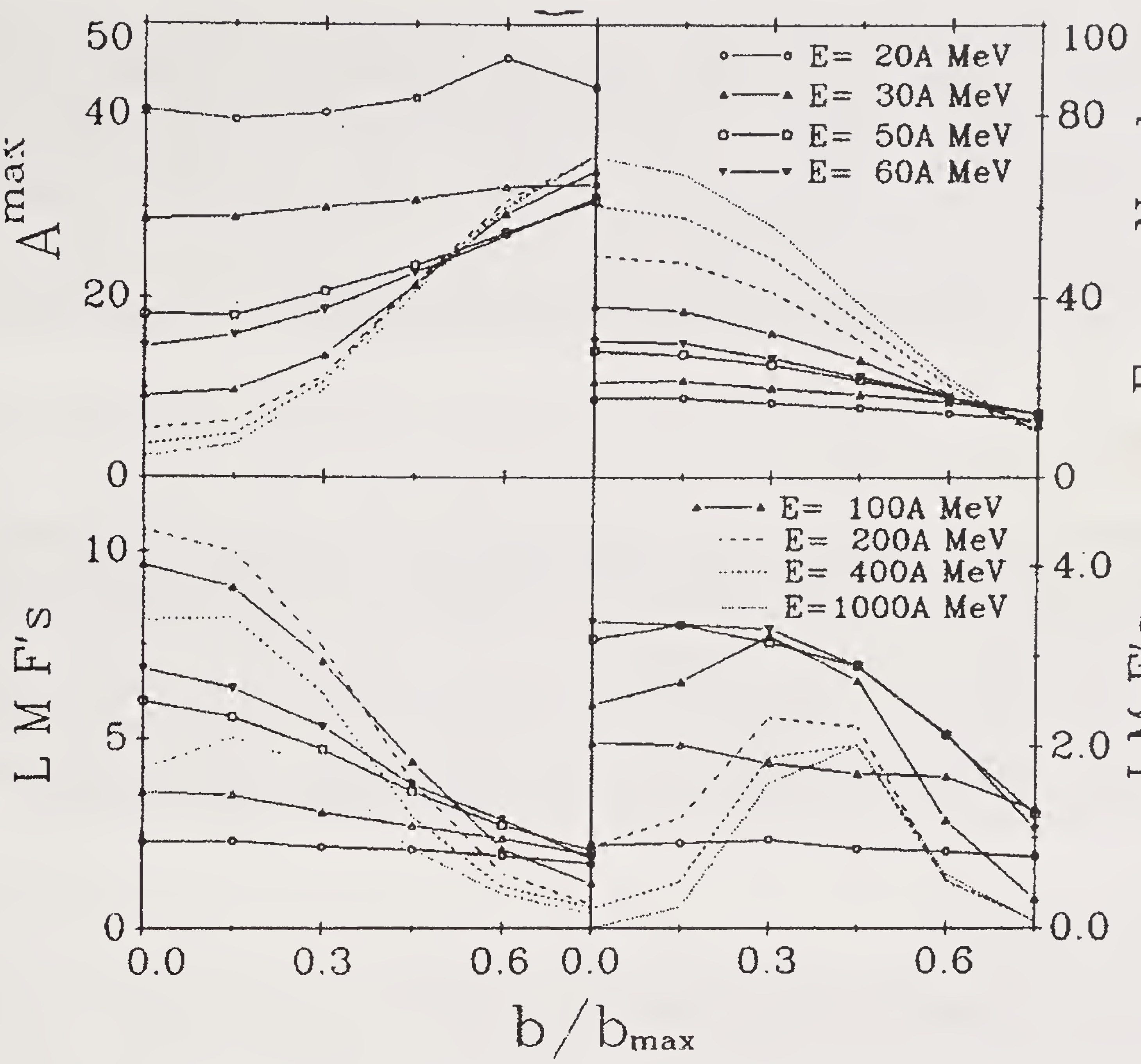

Figure 1. Different fragment multiplicities as a function of the scaled impact parameter $\hat{b} = b/b_{\text{max}}$. Here we simulate Ca–Ca reaction for 500 events.

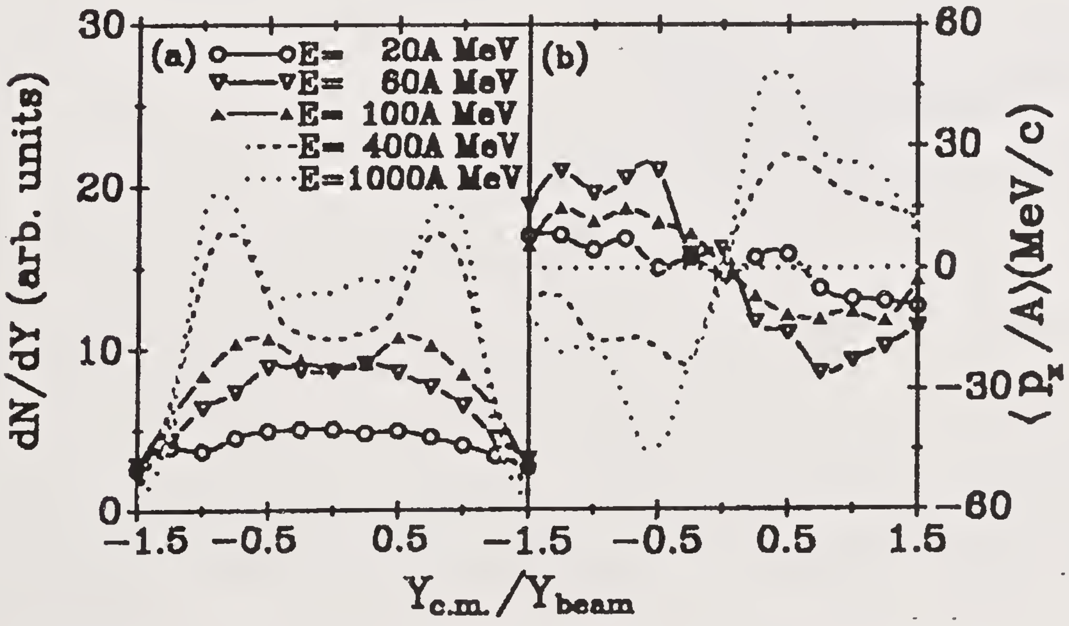

Figure 2. (**a**) The rapidity distribution of nucleons emitted in Ca–Ca collisions. (**b**) The nuclear flow as a function of rapidity.

In figure 2(a) and (b), we display the rapidity distribution ($\mathrm{d}N/\mathrm{d}Y$) and the flow (p_x/A) of nucleons at $b = 4.5$ fm. Here different curves display the results at various incident energies. We notice that at low energies ($\leq$ 60 MeV/A) nucleons overlap in momentum space and as a result one sees a peak at mid-rapidity region. On the other hand, peaks at target and projectile rapidities occur at higher incident energies indicating non-equilibrium situation. Note that the rapidity distribution depends strongly on the number of nucleons emitted. The flow (p_x/A) depicts well-known behavior. The nuclear flow is negative at lower incident energies which becomes repulsive (+ve) at higher incident energies.

We also see an increase in the slope of flow with increase in the incident energies. Note that at some incident energy, the nucleonic flow will disappear.

4. Summary

We have carried out a systematic study of the formation of fragments and their properties in Ca–Ca collisions. Our results clearly indicate that (i) the simulations at 20 A MeV show several events of partial fusion. (ii) A rise and fall in the fragment production in central collisions with an increase in the bombarding energy. (iii) The IMF multiplicity is maximum at central collision and it decreases with increase in the impact parameter at lower energies whereas it has a clear rise and fall at higher energies. The rapidity distribution of nucleons indicates non-equilibrium at higher incident energies. The nucleonic flow is negative at low incident energies which becomes positive at higher incident energies.

Acknowledgement

The work is supported by DAE research grant.

References

[1] M B Tsang *et al*, *Phys. Rev. Lett.* **71**, 1502 (1993)
M Begemann-Blaich *et al*, *Phys. Rev.* **C56**, 610 (1993)
[2] J Aichelin, *Phys. Rep.* **202**, 233 (1991)
R K Puri and S Kumar, *Phys. Rev.* **C57**, 2744 (1998)

Rotational co-existence in selenium isotopes

G SHANMUGAM, V RAMASUBRAMANIAN and P ARUMUGAM
Physics Department, Manonmanian Sundaranar University, Tirunelveli 627 012, India

Abstract. High spin states of ^{72,73,74}Se nuclei are discussed using calculations from the cranked Nilsson Strutinsky method with tuning to fixed spins. The low spin anomaly in the yrast bands of these nuclei is interpreted in a rotational co-existence picture. High K rotational isomers are proposed for $I^{\pi} = 4^+$ in ^{72}Se and 6^+ in ^{74}Se.

Keywords. Rotational co-existence; Se isotopes; CNSM; K-isomers.

PACS Nos 21.10.Re; 21.60.Ev; 27.30.+t

1. Introduction

Rotational co-existence can be defined as the situation in which a nucleus having the same spin and shape but with axis of rotation coinciding with or perpendicular to the axis of symmetry. Nuclei exhibiting such property may give rise to rotational isomers (or K-isomers). Large non-axial fluctuations can carry such nuclei from axially symmetric prolate or oblate shapes with $K = I$ to the same shapes with $K = 0$, penetrating a barrier in the $\beta - \gamma$ space [1]. Such a mechanism is referred to as γ-tunneling, which may give rise to high K-isomers. The main aim of this work is to construct the potential energy surfaces of the selenium isotopes, ^{72,73,74}Se at various spins to look for the occurrence of rotational co-existence. This is done using the cranked Nilsson Strutinsky method (CNSM) with tuning to fixed spins [2]. The effectiveness of the CNSM in interpreting the spectra of nuclei at high spins and in predicting the occurrence of such rotational isomers has been explicitly discussed in [1,3,4]. In this paper we will focus on the theoretical study of the competition between aligned and collective configurations and look at overall trends within the yrast bands of ^{72,73,74}Se. Irregularities observed along the yrast positive parity bands of ^{70,72,74}Se nuclei are well known and have been so far interpreted in a shape co-existence picture [5]. Besides a varying collectivity reflected by the $B(E2)$ values, they exhibit pronounced single-particle and shell effects [6]. Experimental studies have been recently pursued at the Nuclear Science Centre, New Delhi to obtain the high spin states of these nuclei [7].

2. Theoretical framework

The shell energy calculation for non-rotating case $(I = 0)$ assumes a triaxial Nilsson single particle field [2].

The Strutinsky shell correction method is adapted to $I \neq 0$ case by suitably tuning the angular velocities to yield fixed spins. For unsmoothened single particle level distribution we have

$$I = \int_{-\infty}^{\lambda} g_2 \mathrm{d}e^{\omega} = \sum_i \langle m_i \rangle \tag{1}$$

and

$$E_{\mathrm{sp}} = \int_{-\infty}^{\lambda} g_1 e^{\omega} \mathrm{d}e^{\omega} + \hbar\omega I = \sum_i e_i^{\omega} + \hbar\omega I, \tag{2}$$

where m_is are the spin projections and e_i^{ω}s are the single particle energies of the cranked Nilsson Hamiltonian.

For the Strutinsky smeared single particle level distribution, (1) and (2) transform into

$$\widetilde{I} = \int_{-\infty}^{\lambda} \widetilde{g_2} \mathrm{d}e^{\omega} = \sum_i \langle \widetilde{m_i} \rangle \tag{3}$$

and

$$\widetilde{E}_{\mathrm{SP}} = \int_{-\infty}^{\lambda} \widetilde{g_1} e^{\omega} \mathrm{d}e^{\omega} + \hbar\omega \widetilde{I} = \sum_i \widetilde{e_i^{\omega}} + \hbar\omega \widetilde{I}. \tag{4}$$

In the tuning method we have adapted [2], the total spin is calculated as

$$I = \widetilde{I}_z = \sum_{\nu=1}^{N} \left\langle \widetilde{j}_z \right\rangle_{\nu}^{\omega} + \sum_{\pi=1}^{Z} \left\langle \widetilde{j}_z \right\rangle_{\pi}^{\omega}. \tag{5}$$

The above relation allows us to select numerically the ω values that correspond to the chosen integer or half integer spins. Obviously the corresponding frequency values $\omega(I)$ change from one deformation point to another and the corresponding calculation have to be repeated accordingly.

The total energy is given by

$$E_{\mathrm{TOT}} = E_{\mathrm{RLDM}} + (E_{\mathrm{SP}} - \widetilde{E}_{\mathrm{SP}}) \tag{6}$$

where the rotating liquid drop energy at constant spin

$$E_{\mathrm{RLDM}} = E_{\mathrm{LDM}} - \frac{1}{2}\Im_{\mathrm{rig}}\omega^2 + \hbar\omega\widetilde{I}. \tag{7}$$

Here the liquid drop energy E_{LDM} is given by the sum of Coulomb and surface energies and $\Im_{\mathrm{rig}}$, the rigid body moment of inertia defined by β and γ including the surface diffuseness correction.

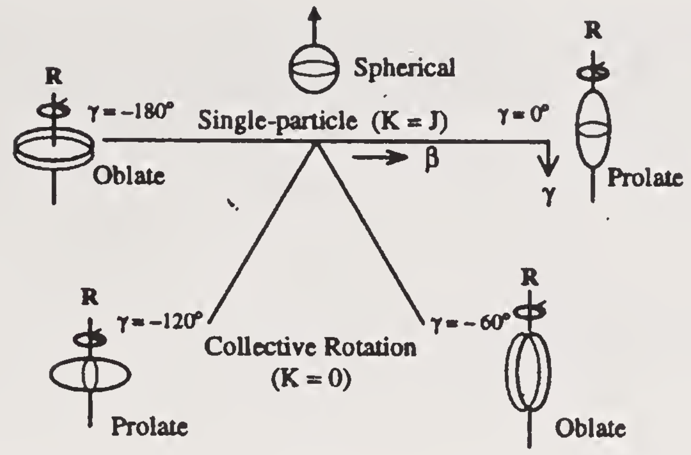

Figure 1. The relation between shape of nuclei rotating around the z-axis and various values of deformation parameter γ.

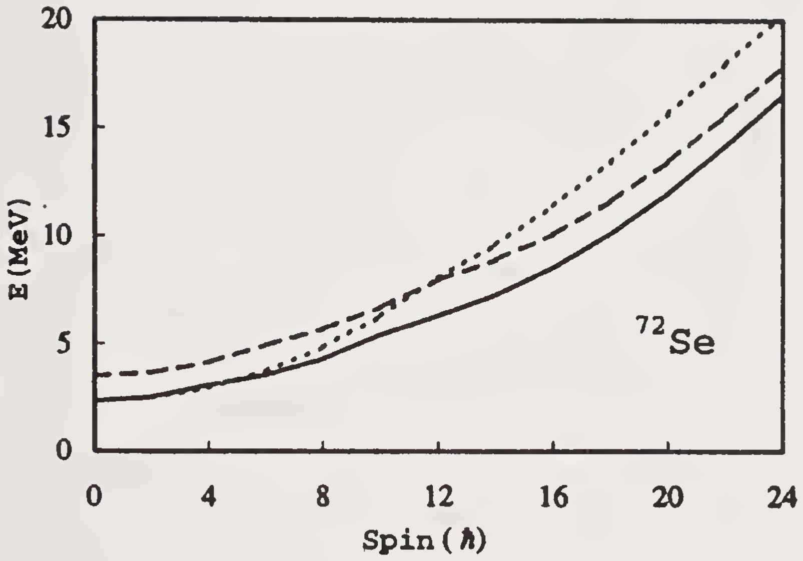

Figure 2.

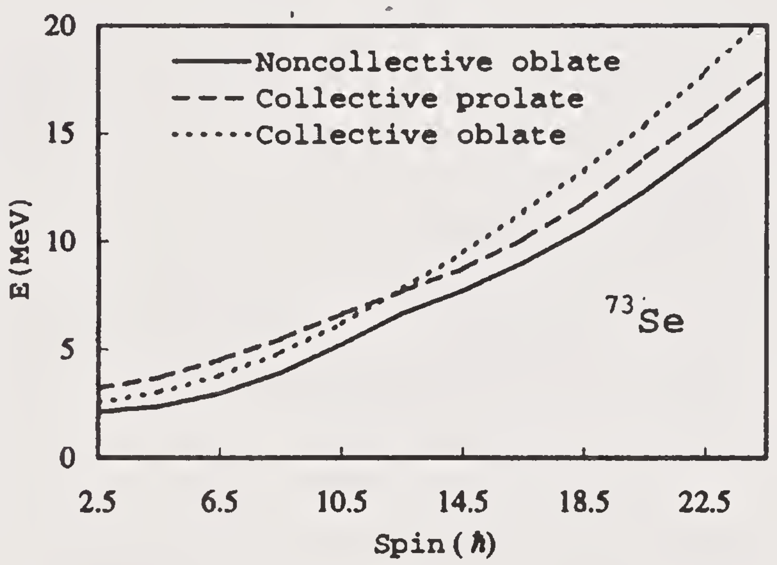

Figure 3.

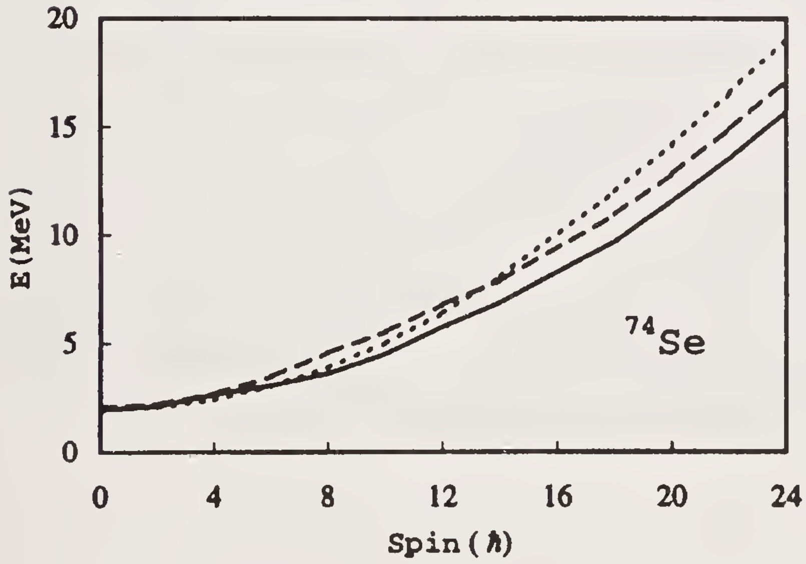

Figure 4.

Figures 2–4. Energy vs. spin plots for the nuclei ^{72,73,74}Se.

The resulting energies are normalized according to the Strutinsky prescription and then the minimum at fixed spin over different deformations is searched for.

3. Details of calculations

The calculations are carried out by varying ω values in steps of 0.02 ω_0 from $\omega = 0$ to $\omega = 0.16\omega_0$, ω_0 being the oscillator frequency. Since we are interested in non-collective oblate ($\gamma = -180°$), collective prolate ($\gamma = -120°$) and collective oblate ($\gamma = -60°$)

shapes, γ is varied from $-180°$ to $-60°$ in steps of 10°. The β values are varied from $\beta = 0.0$ to $\beta = 1$ in steps of 0.1. The κ and μ values are taken as the same for all the shells and are given below as

$$\kappa(\mathrm{P}) = 0.068, \qquad \mu(\mathrm{P}) = 0.48$$
$$\kappa(\mathrm{N}) = 0.071, \qquad \mu(\mathrm{N}) = 0.36.$$

In these first calculations pairing has been omitted.

4. Rotational co-existence in ^{72,73,74}Se nuclei

Within a given axially deformed nucleus, we define the term ‘rotational isomers’ as two (or more) states of the same spin and similar gross shape but with the spin vector in different directions [3]. In this work, only oblate isomers have been proposed. These correspond to collective rotation with the spin vector perpendicular to the symmetry axis and to aligned coupling along the symmetry axis. The aligned isomers, often referred to as ‘rotating around the symmetry axis’ need not possess a long lifetime (e.g., nano-seconds or longer). The γ-tunneling framework provides a natural explanation for the rotational co-existence. The γ-tunneling path is assumed to be the path of steepest ascent to the saddle point and steepest descent from the saddle point. In order to detect the rotational co-existence and to pin point the spins at which it occurs, energy vs. spin plots are constructed for the nuclei ^{72,73,74}Se, which are shown in figures 2, 3 and 4 respectively. The potential energy surfaces for all the three nuclei are found to be looking very similar at fixed spins. The ground state shapes of these nuclei are clearly oblate with $\beta \approx 0.2$, which is preserved to high spins up to $24\hbar$. The yrast state is found to be non-collective oblate. The γ-softness of these nuclei is clearly observed. Competing minima are found to occur along non-collective oblate, collective oblate and collective prolate lines. At lower spins, the competition between the non-collective oblate and collective oblate states is significant which may cause rotational isomers. In the case of ^{72,74}Se nuclei, one interesting feature we observe is that at a spin of $4\hbar$ and $6\hbar$ respectively, the collective oblate and non-collective shapes coexist. This can be clearly seen in figures 2 and 4. Thus there is a strong indication of the existence of rotational isomers at the spin of $4\hbar$ where the competition between the collective and single particle states occurs. Such a crossing-over of non-collective and collective oblate lines is not observed in the case of ^{73}Se, which has an odd number of neutrons.

5. Conclusion

It is thus to be concluded that the ^{72,74}Se isotopes are good candidates to look for rotational coexistence and K-isomers.

References

[1] B Crowell, P Chowdhury, D J Blumenthal, S J Freeman, C J Lister, M P Carpenter, R G Henry, R V F Janssens, T L Khoo, T Lauritsen, Y Liang, F Soramel and I G Bearden, *Phys. Rev.* **C53**, 1173 (1996)

[2] G Shanmugam, V Ramasubramanian and S N Chintalapudi, revised manuscript submitted to *Phys. Rev.* (1998)

[3] D M Headly, R K Sheline and Ingemar Ragnarsson, *Phys. Rev.* **C49**, 222 (1994)

[4] G Shanmugam and V Ramasubramanian, *DAE Symposium on Nucl. Phys.* **B40** (1997)

[5] J Döring, G D Johns, M A Riley, S L Tabor, Y Sun and J A Sheik, *Phys. Rev.* **C57**, 2912 (1998)

[6] K H Speidel, N Benezer-Koller, G Kumbartzki, C Barton, A Gelberg, J Holden, G Jakob, N Matt, R H Mayer, M Satteson, R Taneczyn and L Weissman, *Phys. Rev.* **C57**, 2181 (1998)

[7] R K Bhowmik and G Mukherjee, *DAE Symposium on Nucl. Phys.* **A40**, 204 (1997)

Signature splitting in magnetic rotational bands

AMITA, ASHOK K JAIN, ALPANA GOEL* and BALRAJ SINGH†
Department of Physics, University of Roorkee, Roorkee 247 667, India
*Career Institute of Technology and Management, Faridabad, India
†Department of Physics and Astronomy, McMaster University, Hamilton, Ontario, Canada L8S 4M1, Canada

Abstract. Nearly-spherical nuclei in three mass regions have recently been observed to exhibit rotational-like features. We have identified almost 80 such bands; largest number (43) lie in the lead region. Most of these bands are assigned oblate multi-quasiparticle configurations. Their interpretation in terms of 'magnetic rotation' does not allow for signature splitting in these bands. We have however found signature splitting as well as signature inversion in many bands. We apply the two-quasiparticle plus rotor model to understand the occurrence of signature splitting vis-a-vis the role of 'shears mechanism' in these bands.

Keywords. Magnetic rotation; shears mechanism; nearly spherical nuclei; signature splitting; Pb isotopes; particle rotor model.

PACS Nos 21.60; 27.80+w

1. Introduction

Nuclear structure physics has been witness to the discovery of some very rare phenomena like superdeformation [1] and halo structure in select groups of nuclei. One such phenomenon which has recently been identified is the occurrence of rotational bands in nearly-spherical nuclei. It has been suggested that these bands arise out of the rotation of a magnetic dipole formed out of two or more high-j proton particles (holes) and high-j neutron holes (particles), which make up a resultant vector inclined at an angle to the axis of symmetry. The total angular momentum formed out of the resultant j and a small rotational angular momentum, is also tilted to the axis of symmetry. It was suggested by Frauendorf [2] that further angular momentum is generated by the closing of the particle angular momenta towards the total angular momentum giving rise to the name 'shears mechanism'. The rotational angular momentum thus plays a minor role in generating the higher spin states. The several particles generate a net magnetic dipole leading to the name 'magnetic rotation' (MR).

In this paper, we present evidence of strong signature splitting in many bands identified as MR bands; signature inversion is also present in some cases. We use the two-quasiparticle plus rotor model (TQPRM) to simulate the conditions of 'shears mechanism' at small oblate deformation and analyse the results to study the compatibility of signature splitting with the 'shears' explanation of these bands.

2. Properties of magnetic rotational bands and TAC

The magnetic rotational bands are expected to display the following properties:

1. A $\Delta I = 1$ structure rather than a $\Delta I = 2$ structure.
2. Intraband transitions are predominantly M1 in nature. Crossover E2 transitions are very weak or, absent. The ratio $B(\mathrm{M1})/B(\mathrm{E2})$ is therefore quite large $\sim$10–100 $(\mu_N/\mathrm{eb})^2$.
3. The bandhead lies at a high excitation energy (few MeV) and has a high spin $I \sim$ 10–15 $\hbar$.

Keeping these criteria in mind, we have been able to identify from the published literature on the experimentally observed level structures, about 80 MR bands. These are spread in three mass regions namely A = 105–110, 130–140 and 191–202 [3]. While most of these bands have been assigned an oblate many-quasiparticle configuration, several prolate configurations have also been assigned to bands in the lighter mass regions.

We find that in addition to the above mentioned features, the experimentally observed bands also exhibit the following features:

1. Many of these cascades do not display a regular $I(I+1)$ behaviour and are quite irregular in their structure.
2. Large number of MR bands display a signature splitting.
3. Backbending is observed in a large number of cases.

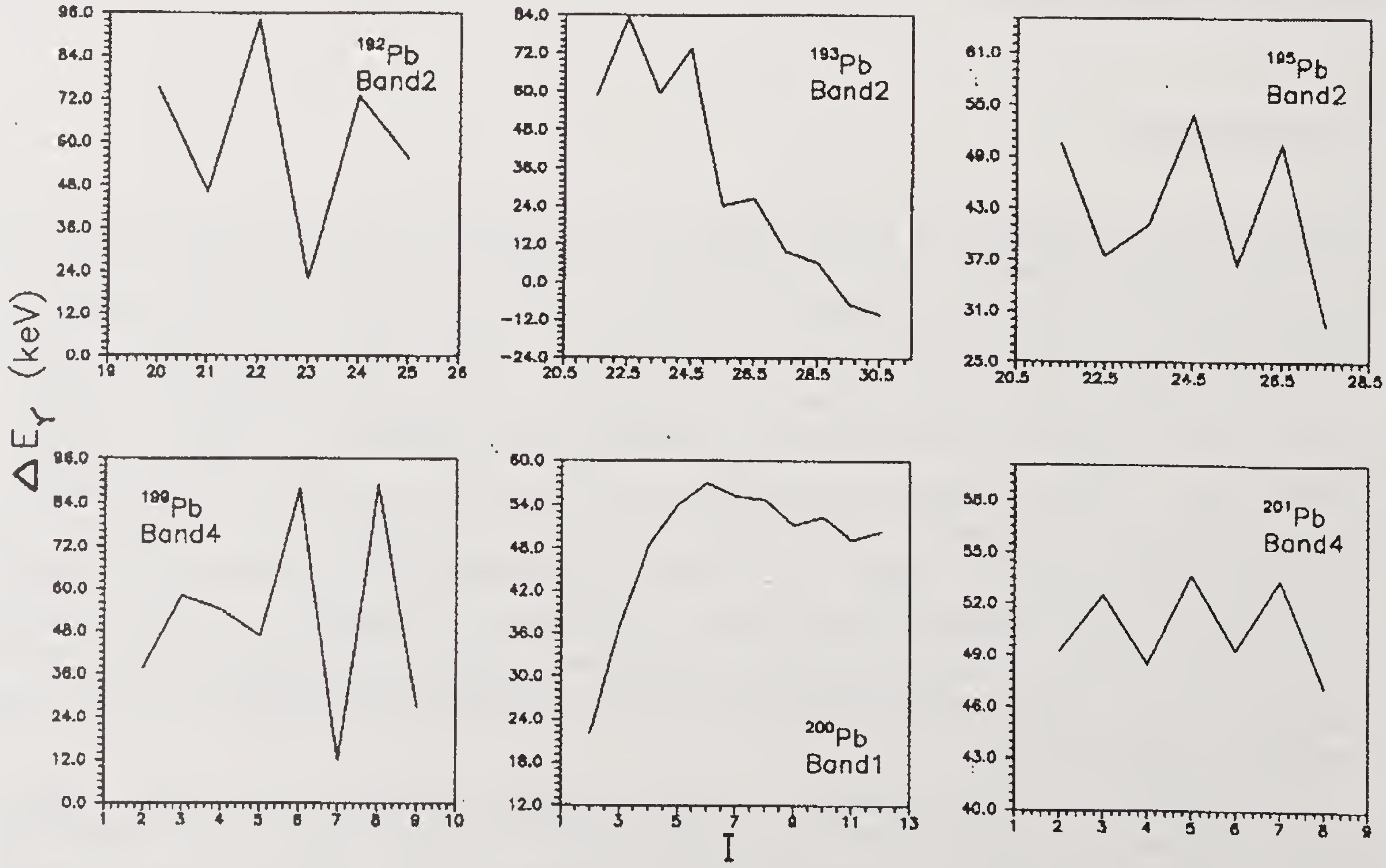

Figure 1. Signature splitting in some of the MR bands in Pb isotopes as observed in the experimental data. The spins are not known in the three cases in the bottom panels.

The rotational motion is usually studied in terms of the principal axis cranking (PAC) model and the particle rotor model (PRM). However, to explain the unusual features of these bands, Frauendorf suggested a tilted axis version of the cranking model (TAC) which is able to take care of the 'shears mechanism' of generating high spin states [4,5]. One of the most important consequences of the TAC is to mix the signature quantum numbers. It is therefore expected that MR bands will not display any significant signature splitting and give rise to a predominantly $\Delta I = 1$ like structure with enhanced B(M1) rates.

3. Signature splitting in MR bands of lead isotopes

Contrary to the expectations of the TAC, we find that a large number of MR bands do display a signature splitting. Since largest set of data on these bands exists in lead isotopes, we will concentrate our attention on signature splitting in lead isotopes only. We find that out of 43 bands classified as MR bands, as many as 14 display evidence of signature splitting. No judgement on the presence or absence of splitting could however be made in many cases where only 4–5 levels have been observed. In figure 1, we show the plots of $\Delta E_\gamma(I)$ vs. I for six cases. Here $\Delta E_\gamma(I) = E_\gamma(I \to I-1) - E_\gamma(I-1 \to I-2)$. We find that two of the cases shown here namely, ^{195}Pb, band 2 and ^{199}Pb, band 4 also exhibit a signature inversion. Observation of such features therefore raises questions about the explanation of these bands in terms of TAC model.

4. Signature splitting from the particle-rotor model

It is well-known that the PRM is quite successful in explaining the rotational spectra, and such features as odd–even staggering and signature inversion in odd-A and odd–odd nuclei [6,7]. This model treats the angular momentum coupling and its dynamics explicitly and is quite suited to describe such phenomena. However, the MR bands are based on many-quasiparticles and therefore the PRM must be extended to include many-particles which makes this approach more complex. Keeping this in mind, we decided to use the TQPRM for calculating the energies and to plot the geometry of the angular momenta as most of the basic features of tilted-axis can be simulated here. Frauendorf and Meng [5] recently compared the TQPRM with TAC results and found the two compatible with each other. The TQPRM Hamiltonian for an axially symmetric rotor is given by [8],

$$H = H_{\mathrm{intr}} + H_{\mathrm{rot}}. \tag{1}$$

The rotational part of the Hamiltonian may be further written as

$$H_{\mathrm{rot}} = \frac{\hbar^2}{2\Im}(I^2 - I_3^2) + H_{\mathrm{rpc}} + H_{\mathrm{ppc}} + H_{\mathrm{irrot}}, \tag{2}$$

where the rotation–particle coupling (or, the Coriolis term), particle–particle coupling and the irrotational terms are given by

$$H_{\mathrm{rpc}} = -\frac{\hbar^2}{2\Im}(I_+ j_- + I_- j_+), \tag{3a}$$

$$H_{\mathrm{ppc}} = \frac{\hbar^2}{2\Im}(j_{p+}j_{n-} + j_{p-}j_{n+}), \tag{3b}$$

$$H_{\mathrm{irrot}} = \frac{\hbar^2}{2\Im}[(j_p^2 - j_{p3}^2) + (j_n^2 - j_{n3}^2)]. \tag{3c}$$

Here I_3 is the component of I along the symmetry axis. The operators $I_\pm = I_1 \pm iI_2$, $j_\pm = j_1 \pm ij_2$, $j_{n\pm} = j_{n_1} \pm ij_{n_2}$, and $j_{p\pm} = j_{p_1} \pm ij_{p_2}$ are the usual shifting operators. $\Im$ is the moment of inertia with respect to the rotation axis. Hamiltonian (1) is diagonalized within the basis

$$|IMK\alpha_\rho\rangle = \left[\frac{2I+1}{16\pi^2(1+\delta_{K0})}\right]^{1/2} \times [D^I_{MK}|K\alpha_\rho\rangle + (-1)^{I+K} D^I_{M-K} R_i |K\alpha_\rho\rangle], \tag{4}$$

where the index α_ρ characterizes the 2qp configuration ($\alpha_\rho \equiv \rho_p\rho_n$) of the odd proton and the odd neutron. To explain the observed signature splitting in MR bands, we considered a complete basis space of $h_{11/2} \otimes i_{13/2}$ and proper choices of Fermi energy for proton–neutron configuration which may give rise to the shears mechanism.

5. Results and discussion

In figure 2, we show the staggering patterns for a deformation aligned (DAL) proton particle in 9/2[514] and rotation aligned and mid-shell neutron hole in 1/2[600], 5/2[602]

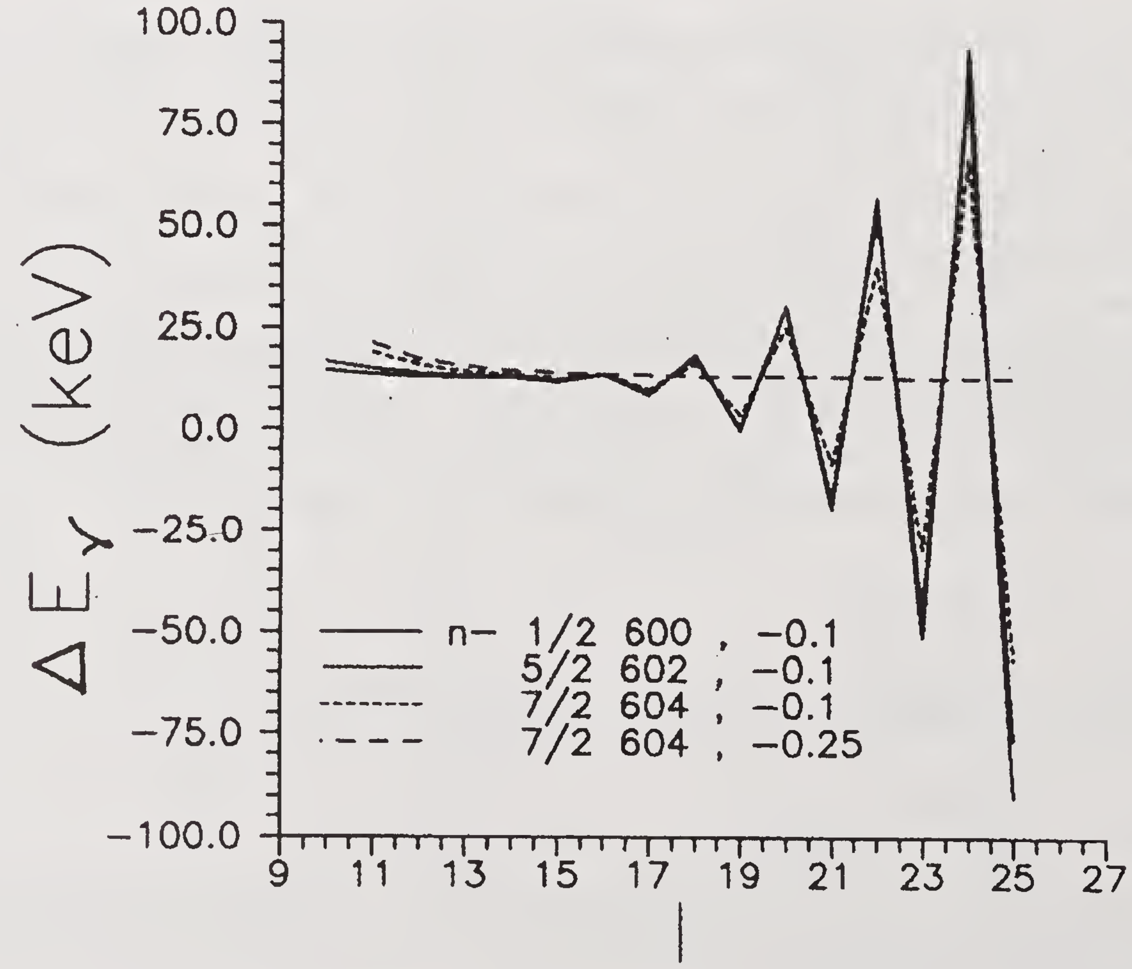

Figure 2. Staggering patterns for a DAL proton particle in 9/2[514] and RAL and mid-shell neutron hole in 1/2[600], 5/2[602] and 7/2[604] for a small oblate deformation $\epsilon_2 = -0.1$ and also the result for a DAL proton particle in 9/2[514] and a neutron hole in 7/2[604] for deformation $\epsilon_2 = -0.25$.

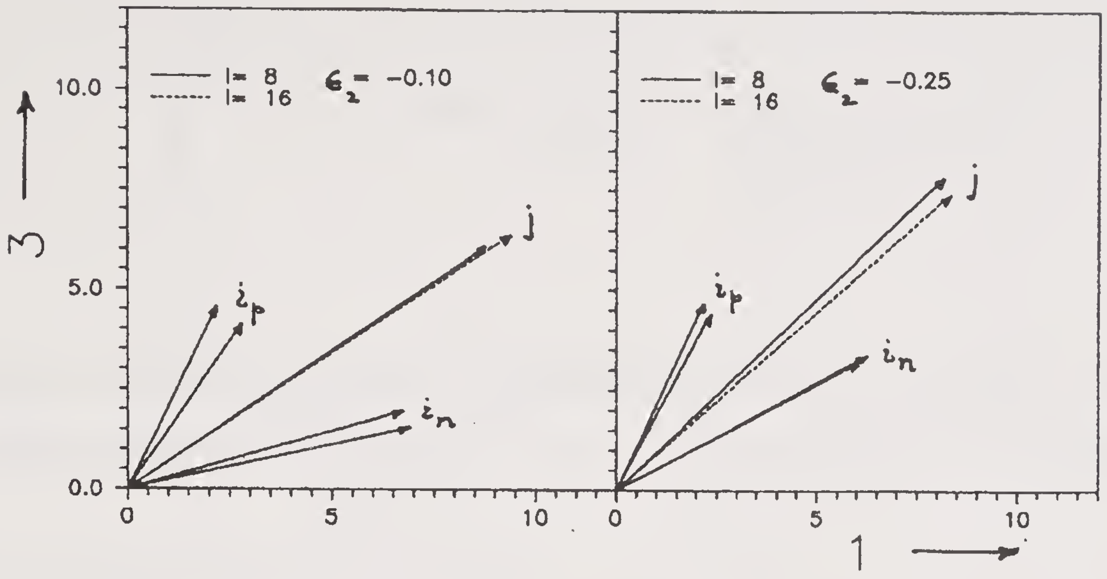

Figure 3. Geometry of particle angular momenta at $I = 8$ and 16 for small oblate deformation $\epsilon_2 = -0.1$ (left panel) and for large oblate deformation $\epsilon_2 = -0.25$ (right panel).

and 7/2[604] for a small oblate deformation ($\epsilon_2 = -0.1$). We also show the results for a deformation aligned (DAL) proton particle in 9/2[514] and a neutron hole in 7/2[604] for deformation ($\epsilon_2 = -0.25$); we find no signature splitting in the case of normal deformation as shown by long dashed line in figure 2. However, for ($\epsilon_2 = -0.1$), a strong signature splitting develops at $I > 15$ in all the cases. This is clearly an effect of enhanced Coriolis mixing due to small deformation. It is therefore not surprising that many bands in Pb nuclei exhibit signature splitting. The bands however remain quite regular from $I = 9$ to 15.

In figure 3, we show the geometry of angular momenta at $I = 8$ and 16 for both small as well as large oblate deformations. It may be noted that signature splitting just sets in at $I = 16$ and therefore both the angular momenta correspond to situations where splitting is minimum. We show the proton and neutron alignments and their resultant vectors. The 1- and 3-axis correspond to rotation and symmetry axis respectively. The resultant $\vec{j}$ combines with a small rotational angular momentum along 1-axis to give the total angular momentum $\vec{I}$. The tilt angle of the total angular momentum is therefore basically decided by the tilting of $\vec{j}$. In case of small oblate deformation (left panel) we find that as I increases along a band, the proton and neutron alignments tilt towards their resultant $\vec{j}$ thereby increasing its magnitude and there is no appreciable change in the tilt angle which the resultant $\vec{j}$ makes with the 3-axis. This is as expected in the 'shears mechanism'. On the other hand in case of large deformation (right panel), the tilting of the proton and neutron alignments with increasing I ceases and the resultant $\vec{j}$ does not increase with I and therefore the angular momentum is generated by the rotational angular momentum R. It may therefore be concluded that a small deformation is necessary for shears mechanism to occur and particle rotor model can describe this mechanism quite well.

In figure 4, we show similar results for three consecutive angular momenta $I = 20$, 21 and 22 which lie in the region of signature splitting. The angular momenta $I = 20$ and 22 correspond to signature $\alpha = 0$ and $I = 21$ corresponds to signature α=1. We find that the tilt angle of the resultant $\vec{j}$ is significantly different for the two signatures. Further, only proton alignment appears to be closing with no change in the neutron alignment. The 'shears mechanism' is therefore not active that strongly once the signature splitting sets in.

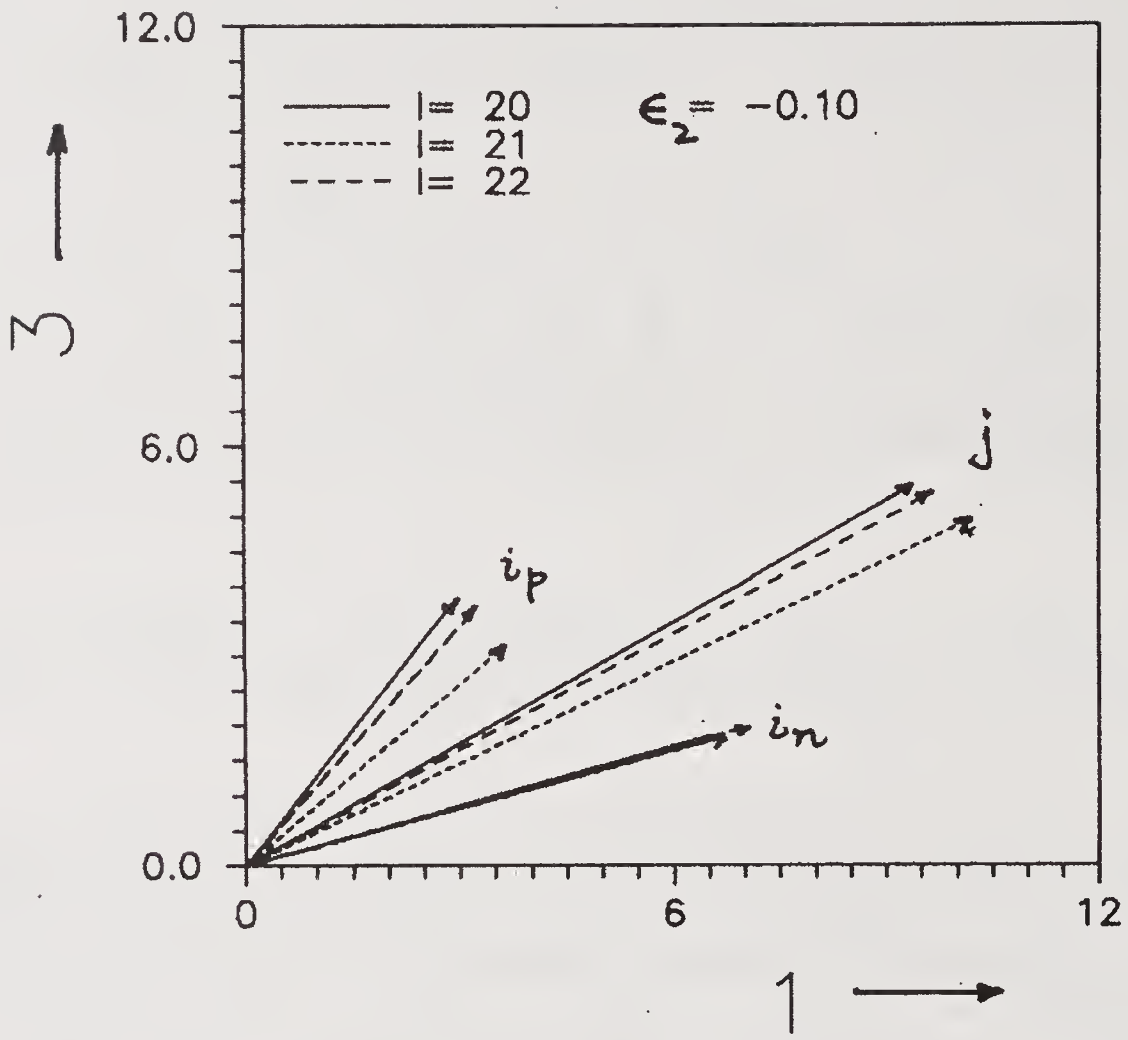

Figure 4. Geometry of particle angular momenta for three consecutive angular momenta $I = 20$, 21 and 22 which lie in the region of signature splitting for small oblate deformation $\epsilon_2 = -0.1$.

6. Conclusions

We therefore conclude that the observation of signature splitting in many bands identified as MR bands is in line with the results of TQPRM calculations. The shears mechanism appears to be valid only for small deformation and weakens significantly after the signature splitting sets in the bands. More detailed calculations along these lines including the calculation of transition probabilities are in progress.

Acknowledgement

We thank Department of Science and Technology (Govt. of India) for financial support.

References

[1] B Singh, R B Firestone and S Y Frank Chu, *Nucl. Data Sheets* **78**, 1 (1996)
[2] S Frauendorf, Invited talk at 'Gammasphere' Conference (1995)
[3] Amita, A K Jain and B Singh, *At. Data Nucl. Data Tables* (to be published)
[4] G Baldsiefen *et al*, *Nucl. Phys.* **A574**, 521 (1994)
[5] S Frauendorf and J Meng, *Z. Phys.* **A356**, 263 (1996)
[6] A K Jain *et al*, *Rev. Mod. Phys.* **70**, 843 (1998) and references therein
[7] A Goel and A K Jain, *Pramana – J. Phys.* **46**, 51 (1996)
[8] A K Jain, J Krasil, R K Sheline and R W Hoff, *Phys. Rev.* **C40**, 432 (1989)

Relevance of thermally populated first excited state of ^{44}Ti to the abundance problem of Cassiopiea A: A model study

SUKHENDUSEKHAR SARKAR
Ananda Mohan College, 102/1, Raja Rammohan Sarani, Calcutta 700 009, India

Abstract. We examine the possible role of electron-capture on the thermally populated first 2^+ excited state of ^{44}Ti in hot astrophysical environments pertaining to post explosive nucleosynthesis supernova debris. We find in a simple schematic model that the astrophysical weak interaction rate for electron-capture decay of ^{44}Ti can depend considerably on temperature and hence on time. We propose a time varying decay rate for the evolving supernova debris and demonstrate its consequence for the ^{44}Ti mass yield of the supernova Cas A, observed through the measured 1.157 MeV γ-ray flux from the electron-capture decay of ^{44}Ti.

Keywords. Nuclear structure; electron capture; nucleosynthesis; supernova.

PACS Nos 26.50.+x; 23.40.-s; 95.85.Pw; 27.40.+z

1. Introduction

Recent measurement [1] of 1.157 MeV γ-ray flux following the decay of ^{44}Ti by the space-borne instrument aboard Compton Gamma Ray Observatory (CGRO) leads to an estimate of the amount of ^{44}Ti produced in explosive nucleosynthesis in supernova Cassiopiea A (Cas A). It is believed that ^{44}Ti yield can be used to test and calibrate the supernova models. The measurement shows a large absolute amount of ^{44}Ti mass ($M_{^{44}\mathrm{Ti}} > 1 \times 10^{-4} M_\odot$) and a high $M_{^{44}\mathrm{Ti}}/M_{^{56}\mathrm{Ni}}$ abundance ratio [2,3], when compared with theoretical predictions of spherically symmetric collapse-driven supernova nucleosynthesis models. Recently Nagataki *et al* [3] proposed axisymmetric models for the Cas A and obtained larger ^{44}Ti yield. Thus the observed ^{44}Ti yield should be known as accurately as possible before it can be used as a probe for supernova models.

In calculating the total ^{44}Ti yield of the supernova using the measured line flux of CGRO one needs also the distance, explosion date of the supernova and the half-life of ^{44}Ti. Uncertainty in the measured terrestrial half-life of ^{44}Ti was very large, ranging from 39 to 66.6 years and the results of all the three recent measurements with higher precision suggest a half-life of 59.2±0.6 y for ^{44}Ti [2,4].

An accurate determination of terrestrial half-life of ^{44}Ti will reduce the uncertainty of the observed yield but actual half-life of ^{44}Ti may be different in the astrophysical environments. When nuclear statistical equilibrium prevail, electron-capture (EC) or β-decay may occur on thermally populated states as well [5].

Contribution of these excited states to the total decay rate may sometimes dominate over that from the ground state depending upon the value of lepton-fraction Y_e (lepton/baryon), density (ρ) and temperature (T) [5]. Explosive nucleosynthesis occurs in a time scale of $\simeq 1$ s and the synthesized nuclei are left in sufficiently hot environment for the next 10–16 sec in expanding debris. However, the debris cools over a very long time and thins out when γ-rays can escape. ^{44}Ti is believed to be synthesized during α-rich freeze-out and the peak temperature may be around 5.5×10^9 K (0.474 MeV) and density in the range 10^6–10^8 gm/cc [6,3]. Around the temperature 0.474 MeV the thermally populated first 2^+ excited state at 1.08299 MeV of ^{44}Ti in nuclear statistical equilibrium may decay by electron-capture to 2^+ ground state of ^{44}Sc. This decay may even occur through an allowed Gamow-Teller electron-capture transition with log *ft* value less than the two non-unique first forbidden transitions from the ground state of ^{44}Ti to the $1^-(E_x = 0.0679$ MeV, $I^\epsilon = 0.7\%)$ and $0^-(E_x = 0.1463$ MeV, $I^\epsilon = 99.3\%)$ excited states of ^{44}Sc. These two non-unique first forbidden transitions occur via orbital electron-capture and the corresponding log *ft* values too can be different from the terrestrial ones in astrophysical environments [5]. In this work we examine in a schematic model, the role of continuum electron-capture on the first excited state and find its consequence for the ^{44}Ti yield of the explosion.

2. Formulation

In deriving a relation between the measured γ-flux and the ^{44}Ti yield one assumes the decay rate of the ^{44}Ti nucleus independent of time (always equal to its terrestrial value, $\log\lambda_L = -9.431, \lambda_L$ in sec^{-1}) during the evolution of the debris for a period of t_a y, the age of the supernova. This appears quite surprising and we expect that in most general situation the decay rate at time t of ^{44}Ti synthesized in the explosion and decaying via weak interaction should be given by

$$-\frac{\mathrm{d}N}{\mathrm{d}t} = 4\pi D^2 F_\gamma(t) = \int_V n(\vec{r},t)\lambda'[Y_e(\vec{r},t),\rho(\vec{r},t),T(\vec{r},t)]\mathrm{d}V, \qquad (1)$$

where N is the total number of ^{44}Ti nuclei at time t in the supernova debris, D is the distance of the supernova from the detector in Kpc, $F_\gamma(t)$ is the flux of characteristic γ-line following decay of ^{44}Ti detected in cm^{-2} sec^{-1}, n is the number density of the ^{44}Ti nucleus at a distance $\vec{r}$ from the centre of the supernova at time t, λ' is the decay rate in dV. The decay rate λ' is a function of (Y_e, ρ, T) at $(\vec{r}, t)$. The volume integral may be taken over the whole volume V of the debris. Evaluation of the integral on the right hand side of eq. (1) requires knowledge of stellar evolution trajectory of the debris at time t. Here we replace $\lambda'[Y_e(\vec{r},t),\rho(\vec{r},t),T(\vec{r},t)]$ in eq. (1) by the value $\lambda(t)$, same throughout the volume of the layer in the debris, where ^{44}Ti was synthesized during explosion (Si-shell) and obtain,

$$-\frac{\mathrm{d}N}{\mathrm{d}t} = 4\pi D^2 F_\gamma(t) = N(t)\lambda(t). \qquad (2)$$

From eq. (2) we obtain for ^{44}Ti the final expression for the mass yield as

$$M_{^{44}\mathrm{Ti}} = 1.39 \times 10^{-4} F_\gamma(t_a) D^2 \lambda^{-1}(t_a) \mathrm{e}^{\int_0^{t_a} \lambda(t)\mathrm{d}t}, \qquad (3)$$

where $M_{^{44}\mathrm{Ti}}$ is in solar masses $M_\odot$, and the decay rate $\lambda(t)$ of ^{44}Ti at time t is in y^{-1}.

In the post explosive nucleosynthesis expansion of the supernova, temperature in any volume element changes with time. So the time dependence of the astrophysical decay rate may come from its temperature dependence ($T = T(\vec{r}, t)$). Assuming nuclear statistical equilibrium the expression for the decay rate of ^{44}Ti at temperature T (in MeV) is

$$\lambda(t) \simeq \lambda(T(\vec{r},t)) = \frac{\ln(2)}{G(T(\vec{r},t))}\left[\frac{1}{t_{1/2}(\mathrm{gs})} + \frac{5f(Q_{\mathrm{gs}}+1.08299, \epsilon(\vec{r},t), T(\vec{r},t))}{\langle ft_{1/2}(2^+\to 2^+)\rangle}\mathrm{e}^{-1.08299/T(\vec{r},t)}\right]. \tag{4}$$

In eq. (4) the nuclear partition function $G(T(\vec{r},t)) = 1 + 5\mathrm{e}^{-1.08299/T(\vec{r},t)}$, $t_{1/2}(\mathrm{gs})$ is the terrestrial half-life, $f(Q_{\mathrm{gs}} + 1.08299, \cdots)$ is the f-factor for the transition from the first 2^+ excited state of ^{44}Ti to the 2^+ ground state of ^{44}Sc, with Q_{gs} (= 0.2645 MeV), the Q-value for the decay from the ground state and $\langle ft_{1/2}(2^+ \to 2^+)\rangle$ is the ft-value for this transition. An estimate of the continuum electron capture (cec) rate on the first 2^+ state of ^{44}Ti, using the allowed Gamow-Teller nuclear matrix element corresponding to log $ft = 4$ and 5, suggest that λ_{cec} can take drastically very low value (10^{-2}–10^{-3} sec^{-1}) around the peak temperature 0.474 MeV and then quickly falls off with temperature.

If the actual log ft value fall within the allowed GT range, the $t_{1/2}(T)$ may be reduced considerably for $T > 0.10$ MeV. Consequently a non-negligible fraction of the ^{44}Ti produced in the explosion will decay, even if the duration of this finite temperature situation is small, and will contribute to the early phase of the supernova light-curve. This implies more ^{44}Ti yield than calculated from eq. (3) with $\lambda(t) = \lambda_L$, the terrestrial decay rate.

We now use a simple model for the proposed time dependence of the astrophysical decay rate $\lambda(t)$ to calculate analytically the ^{44}Ti mass using eq. (3). This is based on the behaviour of $t_{1/2}(T)$ we study using eq. (4) and is given by

$$\lambda(t) = 1 + (\lambda_0 - 1)\mathrm{e}^{-t/\Delta}, \tag{5}$$

where decay rates are expressed in units of the terrestrial decay rate λ_L. λ_0 is the value of the astrophysical rate $\lambda(\vec{r}, t = 0)$ just after the explosive nucleosynthesis is over, chosen as the origin of time ($t = 0$) for the evolution of the debris. The parameters Δ, can be viewed as a time constant with which the astrophysical decay rate drops from the peak value λ_0 to the terrestrial value during the expansion phase of the debris.

3. Results and discussion

We choose the peak values of $\lambda_0 = 10^{6.431}, 10^{7.431}$ in unit of terrestrial rate corresponding to an effective astrophysical rate 10^{-3} and 10^{-2} sec^{-1}.

With eq. (5) for the $\lambda(t)$ we calculate $(\mathrm{e}^{\lambda_L\int_0^{t_a}\lambda(t)\mathrm{d}t} - \mathrm{e}^{\lambda_L t_a})/\mathrm{e}^{\lambda_L t_a}$ and obtain from eq. (3) an expression for the change of the ^{44}Ti yield only due to the proposed time dependence,

$$\frac{\Delta M_{^{44}\mathrm{Ti}}}{M_{^{44}\mathrm{Ti}}} = \left[\mathrm{e}^{(\lambda_0-1)(\Delta/t_m)(1-\mathrm{e}^{-t_a/\Delta})} - 1\right]. \tag{6}$$

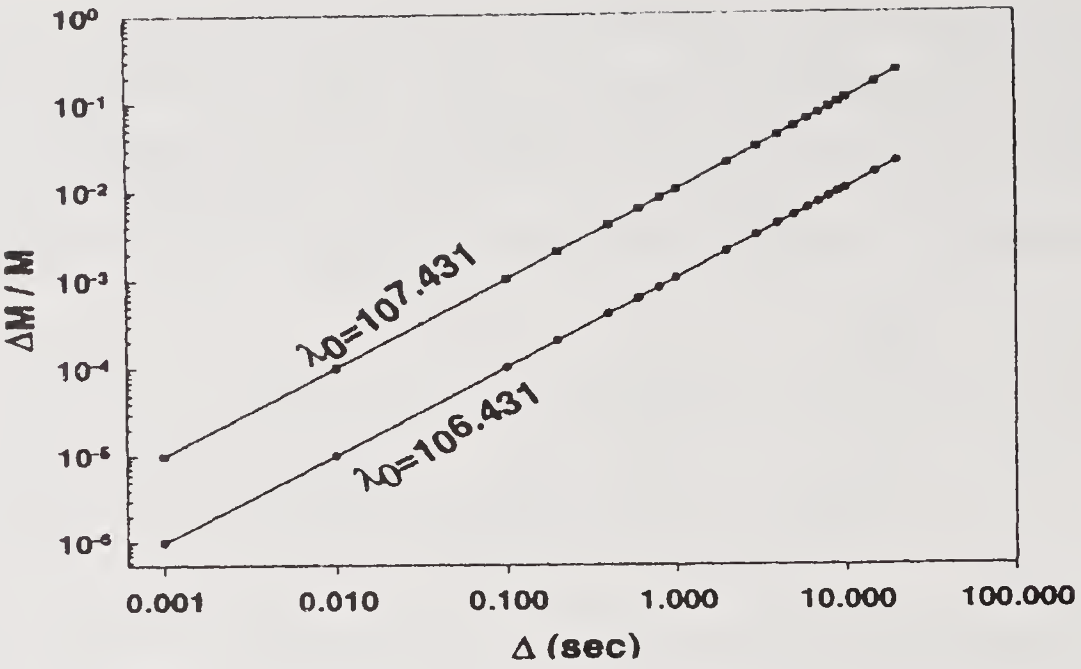

Figure 1. Variation of $\Delta M_{^{44}\mathrm{Ti}}/M_{^{44}\mathrm{Ti}}$ with Δ. λ_0 is in unit of terrestrial rate λ_L and is obtained from eq. (4).

Here $t_m = 1/\lambda_L$ is the terrestrial mean life of ^{44}Ti in y. We have also tried with $\lambda(t) = \lambda_0 - (\lambda_0 - 1)\tanh(t/\Delta)$, with results qualitatively similar to that of the above model.

In figure 1 we show the variation of $\Delta M_{^{44}\mathrm{Ti}}/M_{^{44}\mathrm{Ti}}$ as a function of Δ for the supernova Cas A for different values of λ_0 corresponding to log *ft* = 4, 5. We take $t_a = 312$ y for the age of the supernova Cas A. The figure demonstrates that if there is EC at all on the first 2^+ state of ^{44}Ti, and unless the decay rate from the ground state is reduced due to stellar environmental effects, the value of $M_{^{44}\mathrm{Ti}}$, will be larger than the value estimated using constant terrestrial decay rate and 1.157 MeV γ-flux. It may be necessary therefore to pay attention to this aspect of the Cas A abundance problem before using the observed ^{44}Ti mass as a probe for supernova models.

Acknowledgement

The author thanks Prof. B Dasmahapatra, Dr M Saha Sarkar and Prof. K Kar of Saha Institute of Nuclear Physics, Calcutta, for useful discussions.

References

[1] A F Iyudin *et al*, *Astron. Astrophys.* **284**, L1 (1994)
C Dupraz *et al*, *Astron. Astrophys.* **324**, 683 (1997)
[2] J Görres *et al*, *Phys. Rev. Lett.* **80**, 2554 (1998)
[3] S Nagataki *et al*, *Astrophys. J.* **492**, L45 (1998)
S Nagataki *et al*, *Astrophys. J.* **486**, 1026 (1997)
[4] I Ahmed *et al*, *Phys. Rev. Lett.* **80**, 2550 (1998)
E B Norman *et al*, *Phys. Rev.* **C57**, 2010 (1998)
[5] G M Fuller, W A Fowler and M J Newman, *Astrophys. J. Suppl.* **48**, 279 (1982)
K Kar, A Ray and S Sarkar, *Astrophys. J.* **434**, 662 (1994)
M B Aufderheide *et al*, *Astrophys. J.* **424**, 257 (1994)
[6] S E Woosley and R D Hoffman, *Astrophys. J.* **368**, L31 (1991)

Multinucleon transfer reactions

G POLLAROLO
Dipartimento di Fisica Teorica, Universitá di Torino and INFN Sezione di Torino,
Via Pietro Giuria 1, 10125 Torino, Italy

Abstract. In this talk I will discuss transfer reactions between heavy ions with special emphasis to multinucleon transfer. I will use a semi-classical model that incorporates, in an independent description, both inelastic excitation to collective states and one-particle transfer channels. The importance of evaporation in determining the isotope distribution of the final yields of the reaction will be discussed.

Keywords. Transfer; multi-nucleon; neutron evaporation.

PACS No. 25.70.Jj

1. Introduction

The outstanding characteristic of heavy ion collisions at energy close, and even below, the Coulomb barrier is the interplay between several channels (or if you prefer several degrees of freedom). The coupling among these degrees of freedom results in important multi-step contributions to some specific channels. The number of channels (degrees of freedom) involved in a given situation depend upon the chosen representation. We invoke the standard degrees of freedom corresponding to the separated ions, viz., collective variables and single particle states. In this way we can calculate the yields for those channels that can be accessed by the experiments.

One has to keep in mind that in special situations the number of channels one has to include in the calculation may be very large so that they cannot be treated explicitly. In such a situation a macroscopic description that involves the degrees of freedom of the combined system (neck, neutron flow,...) may be more appropriate. One has however to keep in mind that in this macroscopic description, one misses the asymptotic channels so that one can only describe inclusive experiments.

The presence of multi-step contributions to specific reaction channel shows itself in several cases: elastic scattering via the polarization potential, inelastic scattering via the energy dependence of the form-factors, fusion enhancement, multiple particle transfer. In this talk I will be mostly concerned with single particle degrees of freedom, in particular I will discuss particle transfer reactions with special attention to the multinucleon transfer channels. In doing so I will make use of a model GRAZING [1–4] developed, over many years, at the Niels Bohr Institute (Copenhagen) and that has been used very successfully in the description of grazing reactions. In particular one has been able to elucidate the importance of one-particle transfer channels in the imaginary part of the optical potential [5,6] and also in the polarization potential [7].

This talk will be organized as follows, I will introduce first a very brief summary of the theoretical concepts avoiding all the technical details but just listing the different ingredients that define it, then I will concentrate on the comparison with the data. These were taken at the Laboratori Nazionali di Legnaro (Italy), with a new time-of-flight spectrometer with good mass and charge resolution that allowed the identification of the individual nuclei produced in the reactions. And then I will discuss the importance of the evaporation in determining the final yields of the different isotopes produced in the collision.

2. The theory

In the semiclassical description of grazing reactions one uses a basis that is a product of the eigenstates of the two separated ions. The relative motion is treated classically and the time dependence amplitude c_β of the product eigenstates $\psi_\beta = \psi^b(\xi_b)\psi^B(\xi_B)$ is given by the following system of coupled equations

$$i\hbar\dot{c}_\beta(t) = \sum_\gamma \langle\beta|(V_\gamma - U_\gamma)|\gamma\rangle c_\gamma(t)\mathrm{e}^{i(E_\beta - E_\gamma)t/\hbar} \tag{1}$$

that has to be solved with the initial condition $c_\beta = \delta_{\alpha\beta}$, α being the entrance channels. The potential U_γ is the expectation value of the interaction V_γ (i.e. the folding potential in the appropriate channel) and determines the classical trajectory along which the two ions move (for more details cfr. [8]). The quantity $Q_{\beta\gamma} = E_\beta - E_\gamma$ defines the Q-value of the transition. To calculate the physical observable one has to solve the above system of coupled equations for each impact parameter ρ and to use the familiar formulae of the semiclassical approximation.

In an heavy ion reaction beside the excitation of few inelastic collective modes one should include also the transfer channels namely the stripping and pick-up of neutrons and protons. Since we want to deal with the transfer of many nucleons we must rely on multistep transition. In this case the number of channels becomes immediately very large so that the direct solution of eq. (1) becomes impossible. We must thus resort to a simplified solution.

We are interested, for all impact parameters, to know the probability

$$P(E_a^*, M_a, N_a, Z_a, \cdots) = \langle\bar{\Psi}(t)|(\delta(E_a - \hat{H}_a)\delta(E_a - \hat{H}_a), \cdots|\Psi(t)\rangle \tag{2}$$

to have a final state with products of mass $A_i = N_i + Z_i$, excitation energy E_i^* and angular momentum M_i ($i \equiv a, A$). Following refs [1–3] the calculation of the above probability is done by introducing the characteristic function

$$Z(\beta_a, \beta_A, \cdots) = \langle\bar{\Psi}(t)|\mathrm{e}^{i(\hat{H}_a\beta_a + \hat{H}_A\beta_A) + \cdots}|\Psi(t)\rangle \tag{3}$$

once this function is calculated the above probabilities are obtained via Fourier transforms.

The single particle operators that enter in the definition of the probability introduced above are the intrinsic Hamiltonians $\hat{H}_i$, the intrinsic angular momentum $\hat{M}_i$ the numbers operators $\hat{N}_i$ for neutrons and $\hat{Z}_i$ protons. In term of the usual creation operators, for the projectile system, they are defined

$$\begin{aligned}
\hat{H}_a &= \sum_{i=\pi,\nu} \epsilon_i a_i^\dagger a_i + \sum_n \hbar\omega_n \alpha_n^\dagger \alpha_n, \\
\hat{M}_a &= \sum_{i=\pi,\nu} m_i a_i^\dagger a_i + \sum_n \mu_n \alpha_n^\dagger \alpha_n, \\
\hat{N}_a &= \sum_{i=\nu} a_i^\dagger a_i, \\
\hat{Z}_a &= \sum_{i=\pi} a_i^\dagger a_i,
\end{aligned} \tag{4}$$

with i we have indicated the single-particle quantum number of energy ϵ_i and with n the quantum number of the collective modes of energy $\hbar\omega_n$. Similar expressions hold for the target system.

The quantity $|\Psi(t)\rangle$ is the time dependent state vector of the system. It may be calculated from the expression:

$$|\Psi(t)\rangle = \mathcal{T} \exp\left\{ -\frac{1}{\hbar} \int_{-\infty}^{t} \tilde{V}^{\alpha}(t')\mathrm{d}t' \right\} |0\rangle, \tag{5}$$

where $|0\rangle$ is the entrance channel, $\mathcal{T}$ is the time ordering operator and $\tilde{V}^{\alpha}(t)$ is the coupling term written in the interaction representation.

To be able to calculate the characteristic function I still have to introduce the interaction that governs the exchange of mass and charge between the two ions and the exchange of energy and angular momentum from the relative motion to the intrinsic states. This interaction term has two components, one responsible for the exchange of mass and charge and a second responsible for the excitation of the collective states. We thus write

$$\hat{V}_\alpha = \hat{V}_{\mathrm{tr}} + \hat{V}_{\mathrm{in}}, \tag{6}$$

where

$$\hat{V}_{\mathrm{in}} = \sum_n f^n(\mathbf{r}) \left(\alpha_n^\dagger \mathrm{e}^{i\omega_n t} + \alpha_n \mathrm{e}^{-i\omega_n t} \right) + (\text{target system}). \tag{7}$$

$f^n(\mathbf{r})$ is the collective form factors, proportional to the derivative of the ion–ion potential, for the excitation of the collective state with energy $\hbar\omega_n$ and quantum number n. The interaction responsible for the transfer of particles may be written as

$$\hat{V}_{\mathrm{tr}} = \sum_{i,j} \left[f^{ij}(\mathbf{r}) a_j^\dagger a_i \mathrm{e}^{i/\hbar((\epsilon_j - \epsilon_i)t)} + f^{ji}(\mathbf{r}) a_i^\dagger a_j \mathrm{e}^{i/\hbar(\epsilon_i - \epsilon_j)t} \right], \tag{8}$$

where $f^{ij}(\mathbf{r})$ are the single particle form factors for stripping from the single particle state i in the projectile to the single particle j in the target and where $f^{ji}(\mathbf{r})$ are the corresponding form factors for pick-up reactions [5,8]. Of course they are function of the relative distance $\mathbf{r}$ and of the momentum transfer. The sum has to be extended over all neutrons and protons single particle states.

With the definition of all the operators, one is in a condition, with standard technique, to calculate the characteristic function and thus the probabilities of eq. (2), for more details cfr. [2, 3].

Summarizing, in this model the collision between two heavy ions has been reduced to the study of the redistribution in time of nucleons among two single particle density distributions that move along classical trajectories. This approximation is justified, a posteriori, by the fact that the change in population of the different single particle states in projectile and target is quite small. At last I want here to remind that the outcome of the reaction is determined by the well known form factors for one-particle transfer and the excitation of collective states, from the actual binding energies of the two nuclei and by the average single particle level density. The actual values of the cross sections for the different channels are determined by the width of the Q-value windows that is centered at the optimum Q-value.

3. Comparison with the data

In the last few years at the Laboratori Nazionali di Legnaro (INFN Italy) a systematic study of transfer reactions has been undertaken in the hope to elucidate the importance of transfer degrees of freedom in the enhancement of fusion below the Coulomb barrier and in understanding the transition from the quasi-elastic to the deep-inelastic regimes. With this perspective in mind a new ‘time of flight spectrometer’ (PISOLO) [15] has been built with a mass and charge resolution such that all the individual fragments produced in the reaction could be identified. The acceptance of the spectrometer is quite large so that very weak channels and accurate angular distributions and excitation functions can be measured.

Let me start with the last measurement concerning the ^{64}Ni + ^{238}U collision at a bombarding energy of 390 MeV where transitions up to 6 protons and 6 neutrons have been clearly identified [9]. To have an overview of the results, figure 1 shows the total cross sections, obtained after integration of the angular and Q-value distributions for all the channels where statistics is reasonable together with calculations.

First of all let me remark how well theory reproduces the data for pure neutron transfer channels demonstrating the correct treatment of neutron transfer (0p) on the basis of independent single neutron transfer modes (cfr. also ref. [10,11]). Also well predicted are

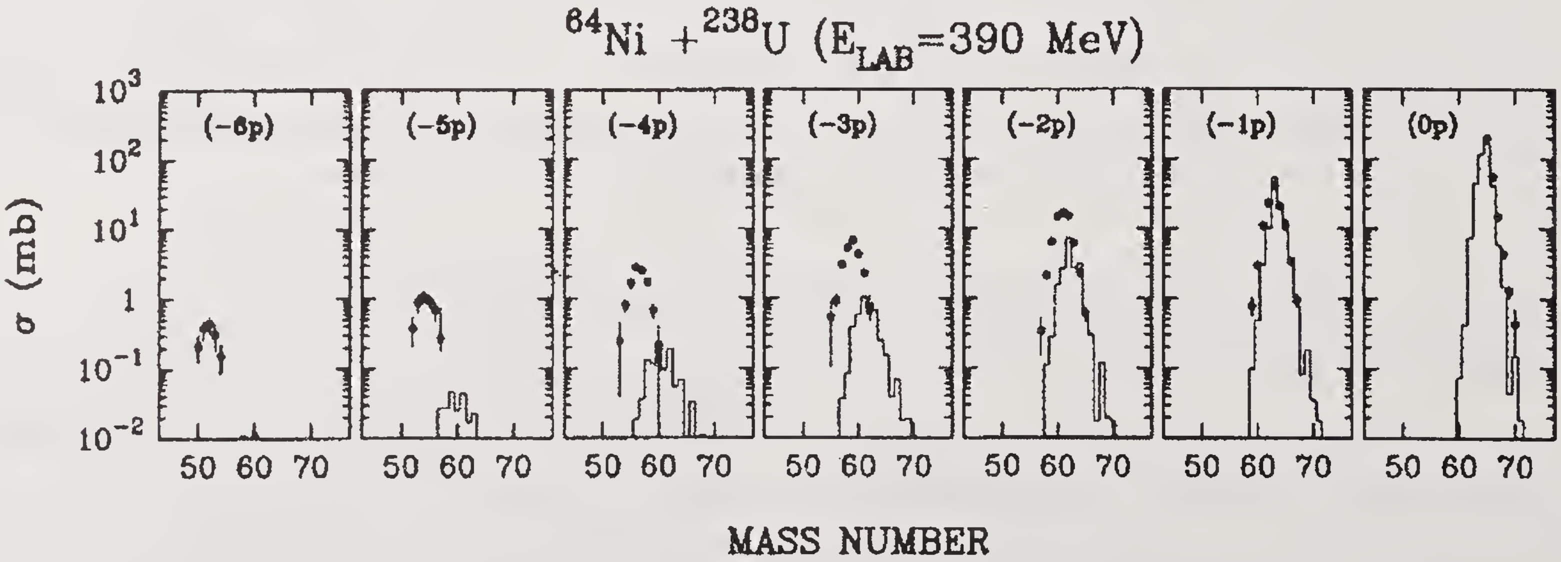

Figure 1. Experimental (points) and calculated (histograms) angle- and Q-value integrated cross sections for the indicated transfer products.

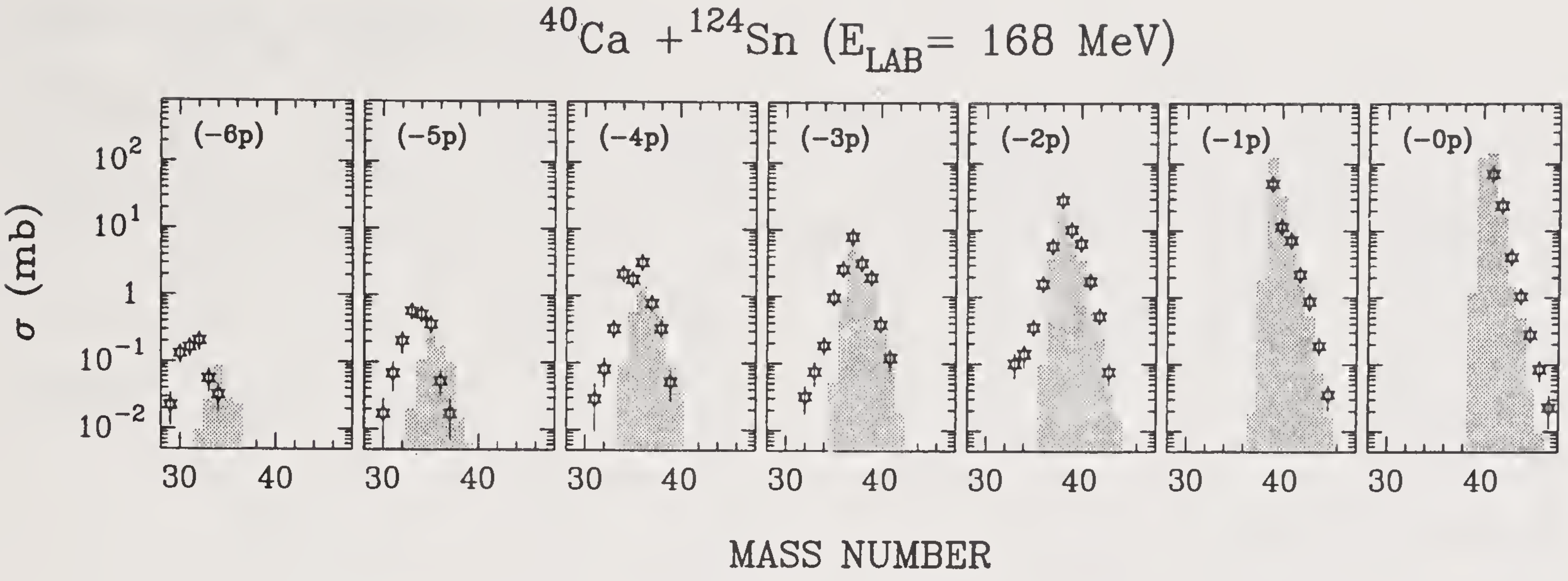

Figure 2. Experimental (points) and calculated (histograms) angle- and Q-value integrated cross sections for the indicated transfer products.

the isotope distributions for the $(-1p)$ case, but, as one moves along the proton stripping direction, one sees that the theory under predicts the population of the light isotopes despite maintaining a good agreement in the neutron pick-up side (heavy isotopes). These discrepancies become more and more evident moving toward channels with more transferred protons. Always from figure 1 one notices that for the $-2p$, $-4p$ and $-6p$ channels the maxima of the isotope distribution peak at channels corresponding to the transfer of $-2n$, $-4n$ and $-6n$ pointing to a possible evidence of multiple α-transfer channels. This is however not the case since no odd-even staggering is present in the data, the isotope distributions evolve, as a function of the number of transferred protons, in a very smooth and regular way suggesting that also the protons behave as independent objects in the transfer process.

Very similar results were observed in other reaction [12–14], here I show just the isotope distribution for the ^{40}Ca + ^{124}Sn collision at a bombarding energy of 186 MeV [12]. From figure 2, one can draw the same consideration as discussed for the ^{238}U case.

The theory, outlined above, not only allows the calculation of inclusive isotope distributions but also the calculation of angular distributions and excitation energy spectra. In figure 3, in comparison with the data, are shown the angular distribution of several channels. The continuous line corresponds to the calculation performed with the program GRAZING [4]. The agreement is quite good in all the angular range. When many nucleons are transferred the theory under predicts the cross section at forward angle where contributions from more complicated reactions (deep-inelastic) may be important. The theory is not in a condition to calculate the angular distribution of channels with neutron stripping. As it is well known for stable nuclei the only open channels are proton stripping and neutron pick-up since the other, neutron stripping and proton pick-up, are strongly hindered by optimum Q-value considerations. One is thus led to conclude that these channels are populated in the experiment by more complicated processes (see below).

At last, let me show in figure 4 for some selected channels the total kinetic energy loss (TKEL) spectra. As it is apparent, the theory gives a good description for the average energy-loss but has the tendency to underestimate the long tail of the distributions. It is important also to notice that the transfer processes populate channels at high excitation energy. This, via evaporation, may influence the final yields of the fragment distributions.

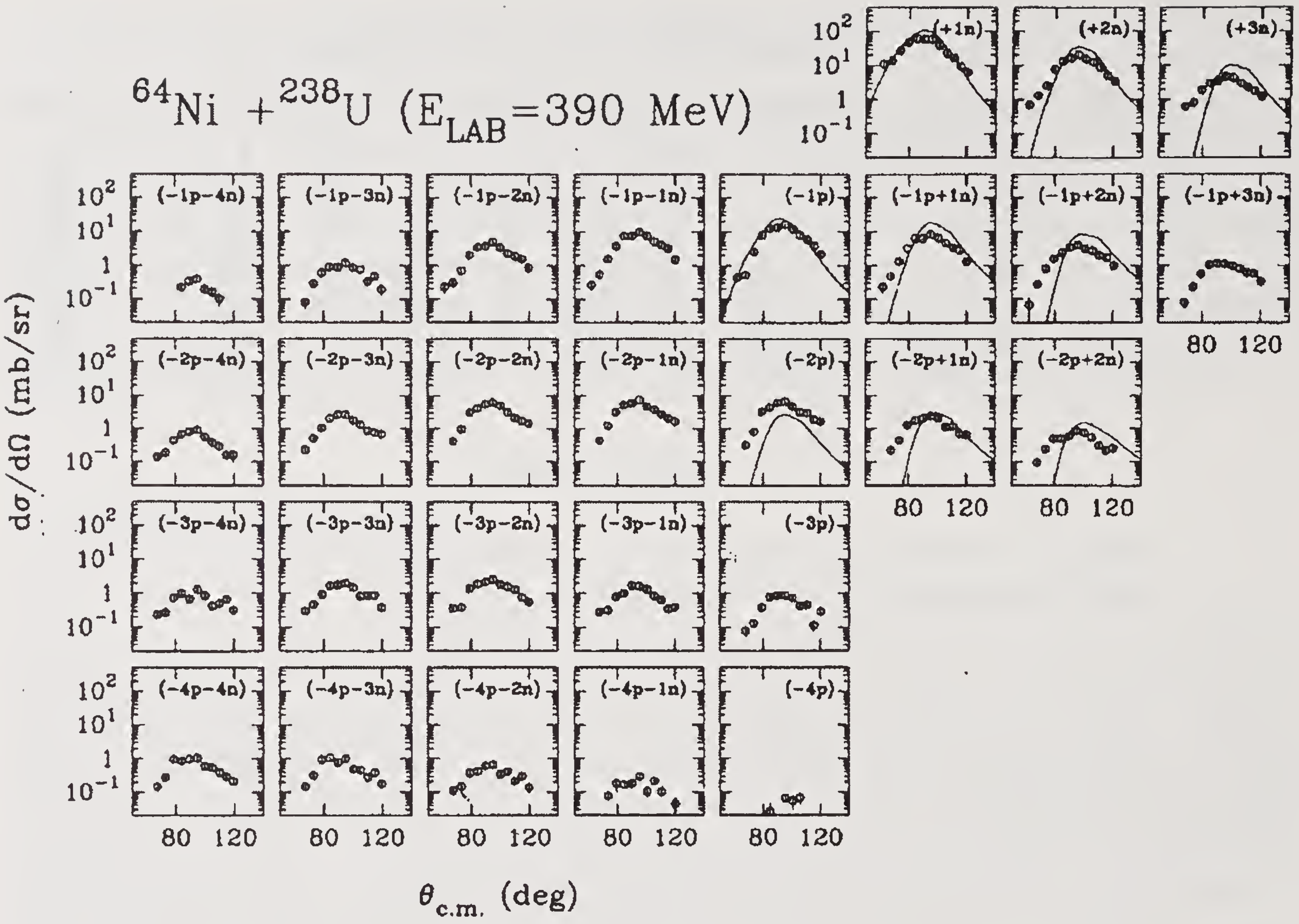

Figure 3. Experimental (points) and theoretical (lines) Q-value integrated angular distributions for the indicated transfer channels.

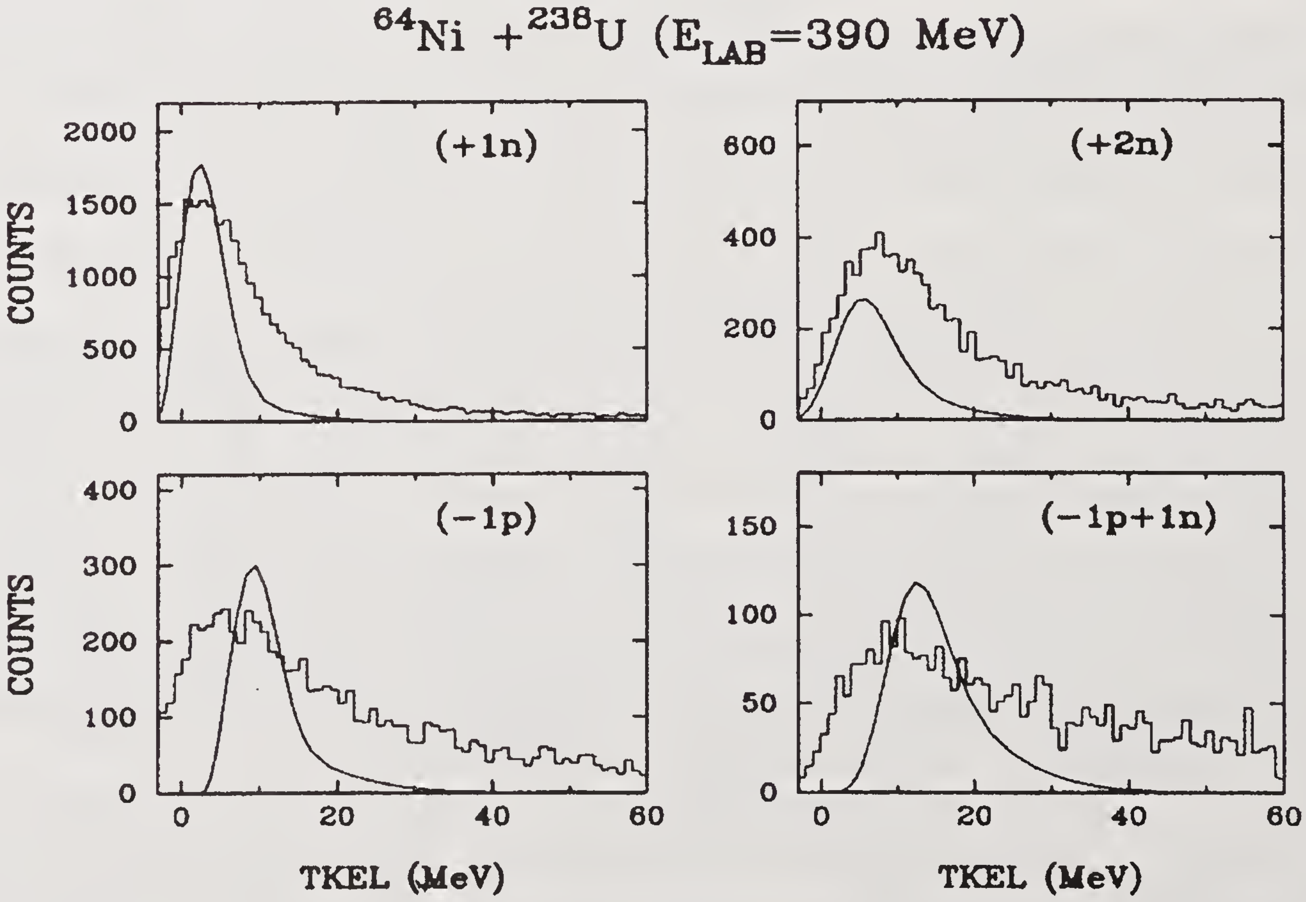

Figure 4. Experimental (histograms) and theoretical (lines) total kinetic energy loss (TKEL) distributions for the indicated transfer channels.

4. Neutron evaporation

To get a deeper insight into the behavior of the experimental yields in figure 5 we plot, again, the total cross sections for the ^{64}Ni + ^{238}U, this time not as a function of the mass number (as in figure 1) but as a function of the number of transferred protons (ΔZ). In the left-hand side we display the cross sections involving neutron pick-up while in the right-hand side the ones involving neutron stripping (notice that the neutron stripping side reaches the $-6p$ while the neutron pick-up side stop at $-4p$). As it is apparent from this kind of plot the neutron pick-up and neutron stripping reactions have a very different behavior. The neutron pick-up decrease in a very smooth way as the number of transferred protons increase, while neutron stripping reactions have a maxima when the number of transferred protons is almost equal to the number of transferred neutrons. This is a clear indication that the two kinds of reactions are populated by different mechanism. While the neutron pick-up side indicates a direct population in terms of independent transfer of neutrons (pick-up) and protons (stripping) the neutron stripping side shows that the yield of these reactions have to depend on more complicated mechanism.

From optimum Q-value arguments one knows that neutron stripping reactions are strongly hindered in collisions among stable nuclei so the channels involving neutron stripping cannot be populated via this mechanism. The first alternative mechanism that came in mind is the neutron evaporation (we know from figure 4 that transfer reactions populate

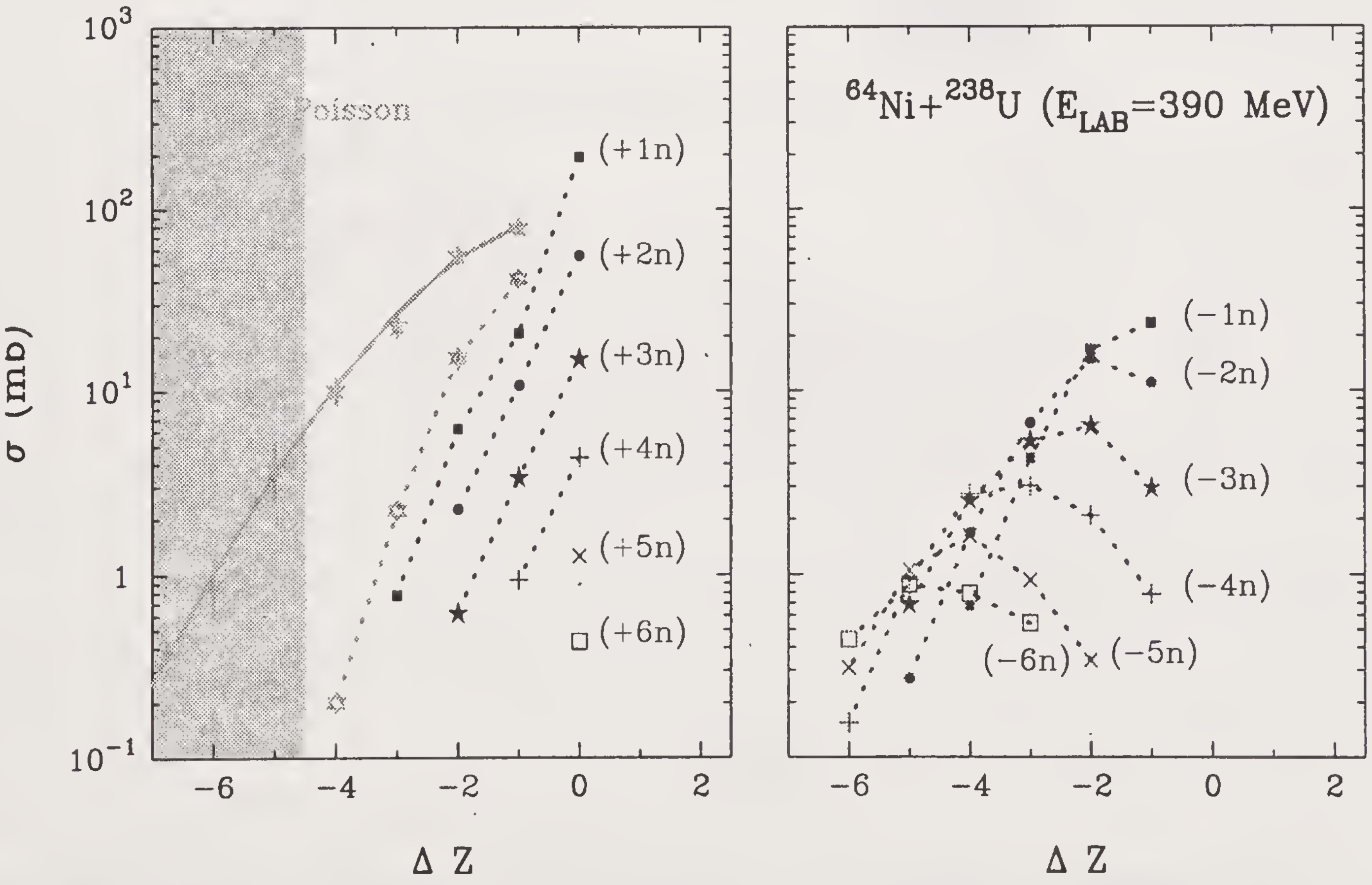

Figure 5. Experimental total cross sections as a function of the number of transferred protons ΔZ for channels involving neutron pick-up (left side) and neutron stripping (right side). To guide the eye we connected, with a dash line, the different proton transfer channels corresponding to the equal number of neutron. The symbol with no label corresponds to the $(0n)$ channels. The full line is a Poisson distribution, normalized to the data. The point close to this line are obtained by adding to each pure proton transfer $(0n)$ channels all those corresponding to neutron stripping.

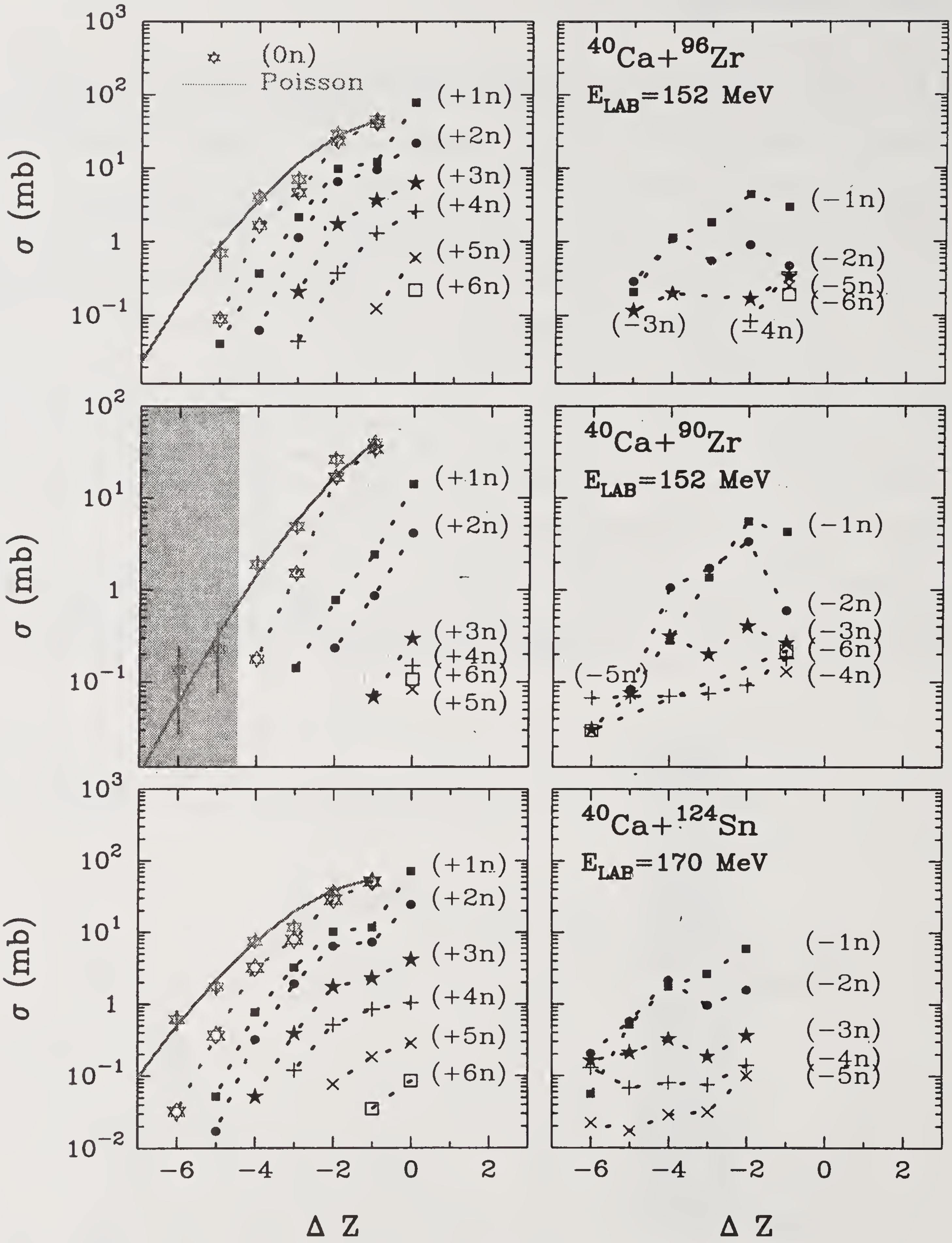

Figure 6. Experimental total cross sections as a function of the number of transferred protons ΔZ for channels involving neutron pick-up (left side) and neutron stripping (right side) for the indicated reactions. Cfr. figure 5 for more details.

predominantly at highest excitation energy and we remind that in the experiment only the light fragment is identified). It is thus tempting to add, for each ΔZ, the cross section of all the neutron stripping channels. In doing so one obtains the points labelled with stars on the left-hand side of figure 5.

These can be nicely fitted (full line) with a Poisson distribution defined by an average number of 2. Since the Poisson distribution describes the transfer of independent modes, it is clear that this finding points into the direction that also protons are transferred independently.

It is clear that if evaporation influences the isotope distribution this must be a common feature of the multinucleon transfer reactions. We thus apply the same reasoning to all the reactions for which multinucleon transfer reactions have been measured. In figure 6 we display for the indicated reaction the isotope distribution. In all cases the cross section obtained by adding to the pure $-0p$ channels all the one involving neutron stripping are all nicely fitted by Poisson distribution with an average number ranging 1.8 for the ^{40}Ca + ^{90}Zr to 2.2 for the ^{40}Ca + ^{124}Sn reactions. It is quite likely that this systematic behavior of the inclusive cross section indicate that also protons behave like independent particle in a transfer process.

5. Conclusion

In this talk I discussed transfer reaction among heavy ions. I hope I convince you that the main features of these reactions can be understood in term of independent single particle transfer. I also discussed the importance of neutron evaporation in determining the final isotope distribution.

References

[1] A Winther, *Fisika* **22**, 41 (1990)

[2] A Winther, *Nucl. Phys.* **A572**, 191 (1994)

[3] A Winther, *Nucl. Phys.* **A594**, 203 (1995)

[4] A Winther, *Program GRAZING*, unpublished

[5] R A Broglia, G Pollarolo and A Winther, *Nucl. Phys.* **A361**, 307 (1981)

[6] G Pollarolo, R A Broglia and A Winther, *Nucl. Phys.* **A406**, 369 (1983)

[7] C H Dasso, S Landowne, G Pollarolo and A Winther, *Nucl. Phys.* **A459**, 134 (1986)

[8] R A Broglia and A Winther, *Heavy Ion Reactions*, Part I and II, Frontiers in Physics, vol. 84 (Addison-Wesley, 1991)

[9] L Corradi, A M Stefanini, C J Lin, S Beghini, G Montagnoli, F Scarlassara, G Pollarolo and A Winther *Phys. Rev.* **C59**, 261 (1998)

[10] C L Jiang, K E Rehm, J Gehring, B Glagola, W Kutschera, M Rhein and A H Wuosmaa, *Phys. Lett.* **B337**, 59 (1994)

[11] C L Jiang, K E Rehm, H Esbensen, D J Blumenthal, B Crowell, J Gehring, B Glagola, J P Schiffer and A H Wuosmaa, *Phys. Rev.* **C57**, 2393 (1998)

[12] L Corradi, J H He, D Ackermann, A M Stefanini, A Pisent, S Beghini, G Montagnoli, F Scarlassara, G F Segato, G Pollarolo, C H Dasso and A Winther, *Phys. Rev.* **C54**, 201 (1996)

[13] L Corradi, A M Stefanini, J H He, S Beghini, G Montagnoli, F Scarlassara, G F Segato, G Pollarolo and C H Dasso, *Phys. Rev.* **C56**, 938 (1997)

[14] G Montagnoli and A Stefanini, private communication

[15] G Montagnoli, F Scarlassara, S Beghini, G F Segato, D Ackermann, L Corradi, He Jian-Hua, A Pisent and A M Stefanini, Legnaro Annual Report 1994, Report LNL-INFN (Rep)-095/95, 1995, p. 205

Fusion–fission of light nuclear systems

A SZANTO DE TOLEDO, N CARLIN, N ADDED, E M SZANTO, M G MUNHOZ, J TAKAHASHI, A SUAIDE and M M DE MOURA
Instituto de Física da Universidade de São Paulo, Departamento de Física Nuclear, Caixa Postal 66318, CEP 05315-970, São Paulo, Brazil

Abstract. Considerable interest has been devoted to fusion reactions between light heavy ions specially between weakly bound ones, due to the anomalous decrease of the fusion cross sections when compared to the total reaction cross section in the energy region around the barrier [1–4].

While the exact nature of the process responsible for the fusion cross section limitation at barrier energies is still unclear, this study shows an inhibition of the yield as the system mass decreases, resulting from the progressive increase of the barrier height and decrease of the effective barrier radius [3]. Furthermore, extensive efforts have been made recently in the study of energy-damped binary yields from light heavy-ion collisions [2,4]. Based on the substantial amount of data accumulated so far, it is now generally accepted and supported by the transition state model [4], that the observed yields arise mostly from a fusion–fission process. Data on complete fusion, fusion–fission and 'elastic fission' for the ^{9}Be, ^{10,11}B + ^{10,11}B; ^{16,17,18}O + ^{10,11}B; ^{19}F + ^{12}C; ^{6,7}Li + ^{9}Be, ^{12}C reactions among others, are presented. For the loosely bound nuclei it was found that the severe fusion cross section limitation is due to a low survival probability of the weakly bound nuclei until the instant of the collision [1].

Keywords. Nuclear reactions; complete fusion; fusion–fission.

PACS Nos 25.70.Jj; 25.70.Gh; 25.70.Lm; 27.30.+t

References

[1] J Takahashi, M Munhoz, E M Szanto, N Carlin, N Added, A A P Suaide, M M Moura, R Liguori Neto, A Szanto de Toledo and L F Canto, *Phys. Rev. Lett.* **78**, 30 (1997)

[2] R M Anjos, N Added, N Carlin, L Fante Jr, M C S Figueira, R Matheus, H Schelin, E M Szanto, C Tenreiro and A Szanto de Toledo, *Phys. Rev.* **C48**, R2154 (1993)

[3] L Fante Jr, N Added, R M Anjos, N Carlin, M M Coimbra, M C S Figueira, R Matheus, E M Szanto and A Szanto de Toledo, *Nucl. Phys.* **A552**, 82 (1993)

[4] R M Anjos, N Added, N Carlin, L Fante Jr, M C S Figueira, R Matheus, E M Szanto, C Tenreiro, A Szanto de Toledo and S J Sanders, *Phys. Rev.* **C49**, 2918 (1994)

Heavy-ion induced fission reactions at near-barrier energies – what have we learnt ?

S KAILAS
Nuclear Physics Division, Bhabha Atomic Research Centre, Mumbai 400085, India

Abstract. Systematic studies of heavy-ion induced fission reactions at near-barrier energies carried out in the last decade have brought out many interesting aspects of fission process in general. The recent experimental findings which show dependence of fission fragment angular distributions on entrance channel, shape, size and spin of the interacting nuclei and shell closure of the intermediate compound nucleus are summarised in the present paper.

Keywords. Heavy-ion fission reactions; near-barrier energies; fission fragment anisotropies; Th, U, Np, Pt, Pb, W, Bi targets; B, C, O projectiles.

PACS Nos 25.70.Jj

1. Introduction

Heavy-ion induced fission reactions at near Coulomb barrier energies performed during the last decade have provided many new interesting features of fission phenomena [1]. These studies suggest [1–5] dependence of fission fragment anisotropy (A) on the entrance channel of the colliding nuclei, size, spin and shape of the target/projectile, bombarding energy with respect to the fusion barrier and compound nucleus shell closure. In this review some of the recent results, their implications and the new puzzles in this area are summarized.

2. Saddle-point statistical model (SPSM)

In the present work, the saddle-point statistical model (SPSM) [6] has been taken as the reference model whose predictions are compared with the experimental data of fission anisotropies. If the fission data for a target plus projectile system are in agreement with the SPSM calculations, then the system is considered to exhibit 'normal' values of anisotropies. However, the system whose anisotropy values are significantly larger than the SPSM predictions, is considered to show 'anomalous' values of anisotropies. According to SPSM, the fission anisotropy is written as $A = 1 + \langle l^2 \rangle / 4K_0^2$ where $\langle l^2 \rangle$ is the second moment of the compound nucleus spin distribution and K_0^2 is the variance of the K distribution at the saddle-point where the orientation of the fission axis with respect to the angular momentum vector is determined. The quantity K_0^2 is defined as $K_0^2 = I_{\text{eff}}T$, with I_{eff} as the effective moment of inertia of the configuration of the fissioning nucleus and T as the effective temperature, both evaluated at the saddle-point. The value of T is calculated from the expression $T = \sqrt{E_x/a}$, where E_x is the excitation energy and 'a' is the level density parameter. The excitation energy E_x at the saddle is computed using the following expression $E_x = E_{c.m} + Q - B_f - E_R - E_n$ where B_f and E_R are the ℓ dependent fission barrier and rotational energy respectively. E_n is defined as the energy removed by the pre-scission (pre-saddle) neutrons. The ℓ distribution of the fissioning compound system is obtained by fitting the fission excitation function (or fusion excitation function) and the B_f, I_{eff} and E_R values have been taken from the Sierk prescription [7].

3. Fission data at near-barrier energies

3.1 Fission data for $E/V_B > 1$

In the last few years systematic measurements of fission angular distribution data have been carried out by different groups to bring out interesting features of fission dynamics [1,8–16]. The fission data for both deformed actinide targets having small B_f/T values and spherical targets like Pb, Bi having large B_f/T values have been measured for a range of projectiles (Li, Be, B, C, O and F). It has been observed that the anisotropies for actinide targets are well accounted for by SPSM for the lighter projectiles such as Li, Be, B and C but are larger than expected for the heavier projectiles such as O and F [1,8,9]. These observations have been interpreted as an entrance channel effect arising from contributions of fission like events from preequilibrium fission [17] expected only in the case of heavier projectiles such as ^{16}O and ^{19}F, on the basis of the variation of the liquid drop model driving force at the saddle in the mass asymmetry degree of freedom. The mass asymmetry value where the driving force changes direction is called the Businaro-Gallone critical asymmetry(α_{BG}). For values of entrance channel mass asymmetry (α) greater than α_{BG}, the driving force favours amalgamation of the nascent partners, whereas for smaller values the smaller partner gains in mass at the expense of the heavier, and the dinuclear system may re-separate as a fissionlike event without K equilibration and formation of a compound nucleus. In the latter case the fission events will consist of both K equilibrated and non-equilibrated (pre-equilibrium) components and hence systems with entrance channel mass asymmetry values less than the BG critical value will exhibit anomalous anisotropies. The above study, however, involved formation of different compound nuclei. Thus, a definitive test of entrance channel mechanism requires making the same compound nucleus at the same excitation energies and if possible, even with similar angular momenta. With this motivation, fission data have been measured [3] for three entrance channels that lead to the same compound nucleus (^{248}Cf). Two of these entrance channels ^{11}B + ^{237}Np ($\alpha = 0.911$) and ^{12}C + ^{236}U ($\alpha = 0.903$) have alpha greater than $\alpha_{\text{BG}} = 0.9$ and the third, ^{16}O + ^{232}Th ($\alpha = 0.871$), has alpha smaller than the critical asymmetry. The fission anisotropy data are plotted in figure 1 as a function of E/V_B. In figure 1 the data of Liu *et al* [18], Back *et al* [19], Ramamurthy *et al* [8] and Vandenbosch *et al* [20] are also shown along with the data from ref. [3].

It is found that although the anisotropies differ at lower excitation energies (E_x = 45–60 MeV and energies upto 20% above the fusion barrier) for the three systems, this

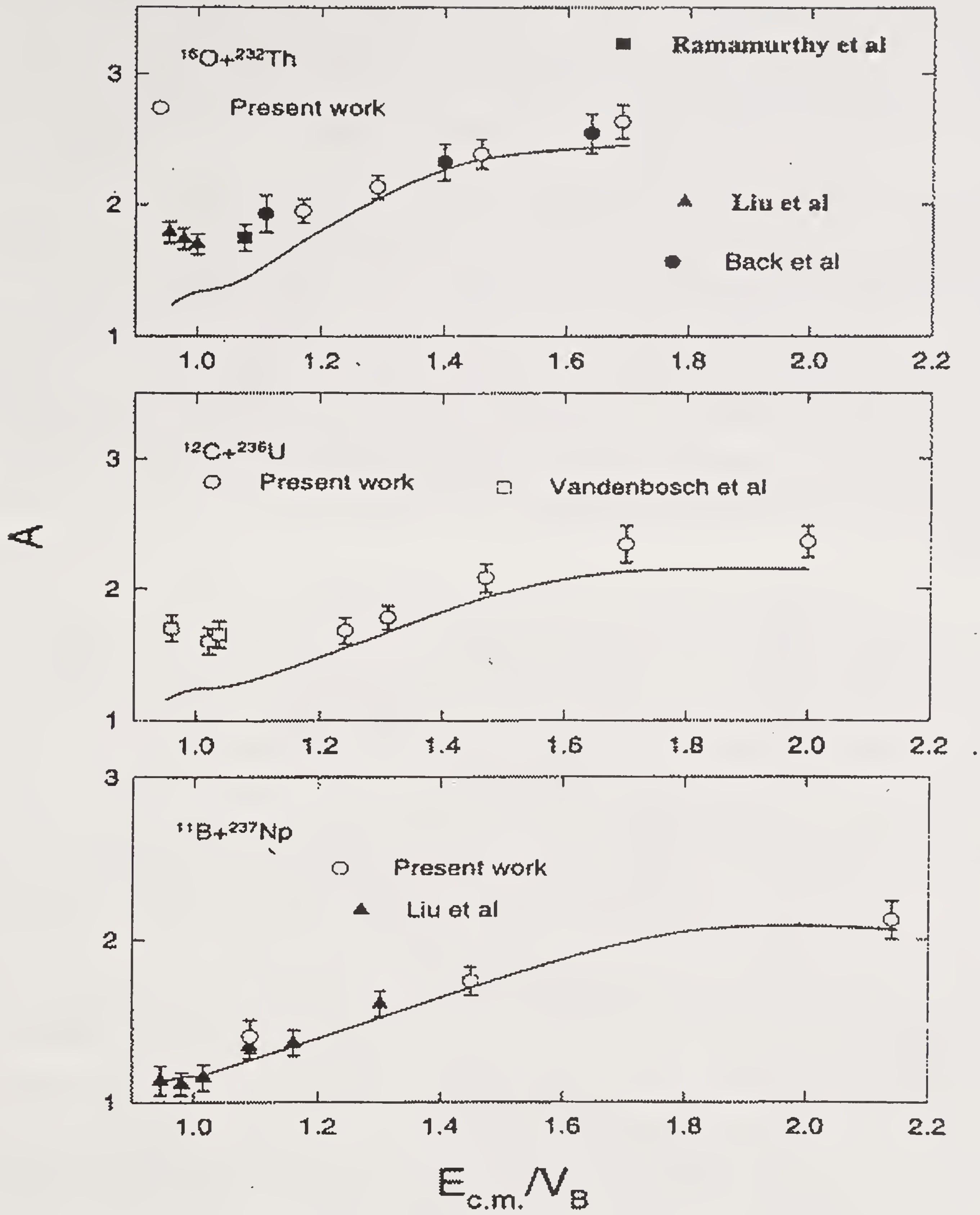

Figure 1. Fission anisotropies measured for ^{11}B + ^{237}Np, ^{12}C + ^{236}U and ^{16}O + ^{232}Th systems plotted as a function of E/V_B. The continuous lines are the SPSM calculations.

entrance channel dependence is washed out at higher energies. In order to compare the measured data with the SPSM calculations, the fission events were arbitrarily divided [3] into two types: (1) $\ell < l_c$, for which $B_f > T$, (2) $\ell > l_c$ for which $B_f < T$, where l_c is the angular momentum for which $B_f = T$. The anisotropy A_{exp} is defined as $A_{\text{exp}} = (\sigma_1/\sigma_f)A_1 + (\sigma_2/\sigma_f)A_2$ where A_1 and A_2 are the anisotropy values for the two components respectively. The corresponding cross sections are σ_1, σ_2 and σ_f is the measured fission (fusion) cross section. For component (1), the anisotropy values have been calculated using the SPSM. The Sierk prescription has been used to obtain the ℓ-dependent B_f,

E_R and $I_{\rm eff}$ values. The pre-saddle neutron corrections have been applied starting from the systematics of Saxena *et al* [21]. From the above analysis, the A_2 values have been deduced. Knowing $\langle l^2 \rangle$ values from calculation, the corresponding K_0^2 values have been obtained starting from the expression for A_2. It was interesting to note that the $I_{\rm eff}$ values deduced from the corresponding K_0^2 values for the region $B_f < T$, are consistent with the ones expected from the SPSM, implying that the SPSM works even for cases where $B_f < T$. The reason for this surprising result is not very clear. One reason could be that the fission barriers are actually much larger than predicted by Sierk. A similar conclusion was recently reached [22] in another observation involving evaporation residues for ^{12}C + ^{236}U system. In view of the above findings, the SPSM calculations have been performed without any restriction on ℓ values for both the components mentioned above. In figure 1, the calculations are shown as continuous curves. For $E/V_B > 1$, they adequately represent the data except for ^{16}O + ^{232}Th at energies above but close to the barrier, implying entrance channel dependence at these energies. At higher energies, the SPSM calculations are in good accord with the data for all the three systems and no entrance channel dependence is indicated.

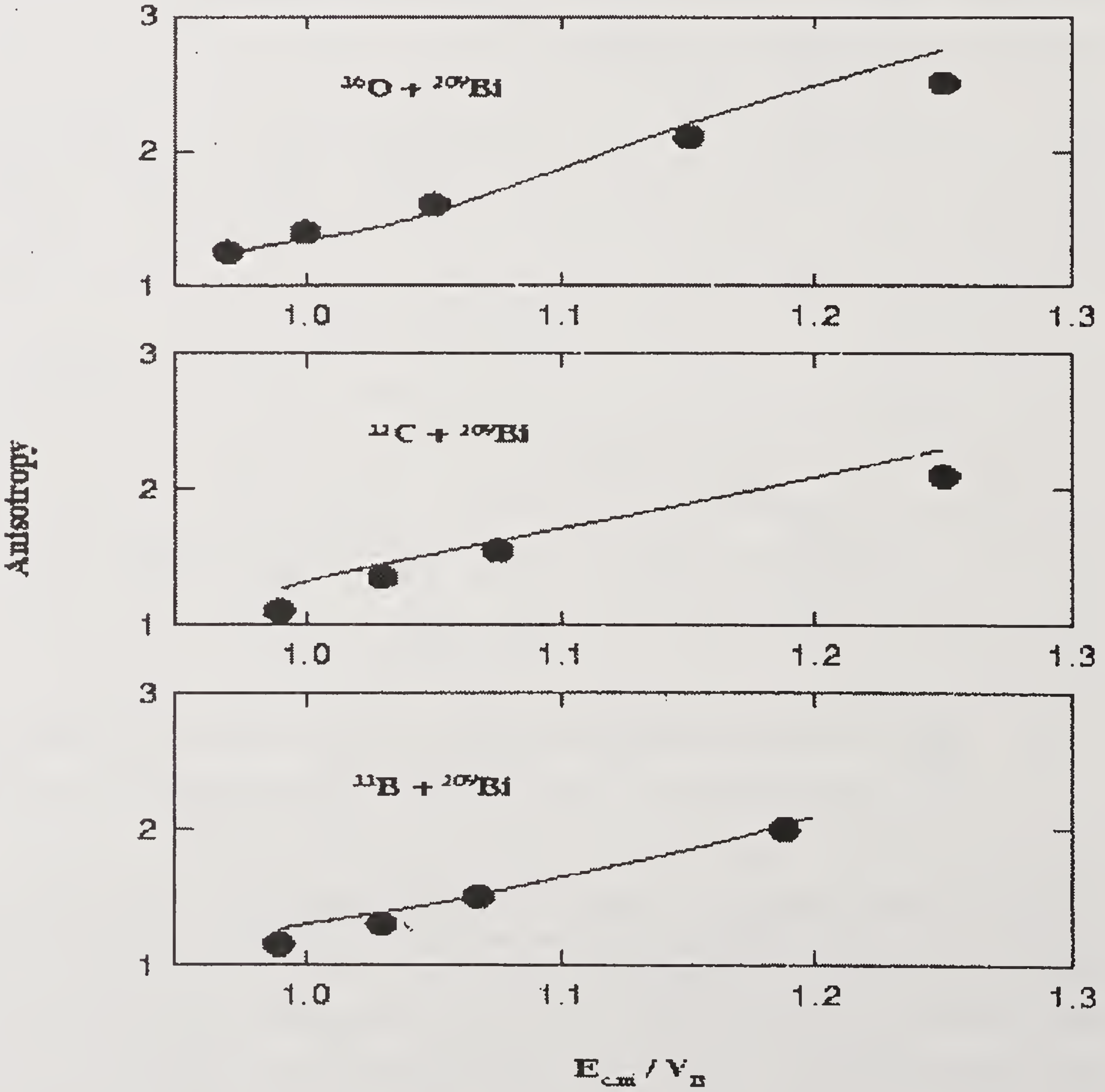

Figure 2. Fission anisotropies for ^{11}B, ^{12}C and ^{16}O + ^{209}Bi systems. The measured data are compared with the SPSM calculations.

The fission anisotropy data measured for the spherical systems at energies above the barrier are all consistent with the SPSM calculations which take into account corrections for pre-saddle neutron emission. No entrance channel dependence has been observed [1,11,23] in varying the projectile mass from ^{11}B to ^{19}F interacting with ^{209}Bi target. In figure 2 the anisotropy values measured for ^{11}B, ^{12}C and ^{16}O + ^{209}Bi systems are compared with the SPSM calculations.

It is seen from the figure that SPSM theory is consistent with the data over the entire energy range. As per the pre-equilibrium fission model [17], the contribution of K non-equilibrated fission events will be smaller for systems with larger B_f/T values. Hence the mechanism which leads to observation of 'anomalous' anisotropies (and entrance channel dependence of fission anisotropies) is not expected to play a significant role for systems having large B_f/T. Thus the observation of 'normal' anisotropies is consistent with the above expectation for the spherical systems which have relatively larger values of B_f/T compared to the ones of the deformed actinides.

3.2 Fission data for $E/V_B < 1$

The fission data for deformed actinide targets when extended to lower energies exhibit very interesting features quite unanticipated. It was observed that the fission anisotropies for essentially all target-projectile combinations involving an actinide target do not decrease when energy is lowered (up to 10% below barrier) in the sub-barrier region [18,24–26]. Several plausible explanations have been suggested to understand this feature [24]. However, the spherical targets do not exhibit this 'anomalous' feature. This clearly points to the fact that deformation (shape) of the target has a strong role to play in influencing this behaviour. Hinde *et al* [25] have proposed a 'quasi-fission' mechanism to explain this observation. According to this model, while collisions of the incoming projectile with the tips of the deformed target lead to quasi-fission, collisions with the sides lead to compound nucleus fission. Recently, Lestone *et al* [2] have reported anisotropy data for ^{12}C + ^{235,236,238}U systems. They found that while the even U targets exhibited 'anomalous' anisotropies,the odd U target (having spin 7/2) showed almost normal anisotropies at sub-barrier energies. This is taken as strong evidence for an influence of target spin on sub-barrier fission anisotropies. The same feature is observed in the case of data for B+Np, C+U and O+Th systems (figure 1) for $E/V_B < 1$. While the zero spin O + Th and C + U systems show anomalous values of anisotropies at energies below the barrier, the B+Np system involving large spin values for both projectile and target shows near normal anisotropies, confirming the influence of (projectile/target) spin on the measured anisotropies. However, the anisotropy data measured for the spherical systems, ^{16}O,^{19}F + ^{208}Pb (spin = 0) or ^{209}Bi (spin = 9/2) do not show noticeable effect due to target spin [23] and both are in agreement with the SPSM calculations. Hence it can be concluded that both shape and spin together are important factors in influencing the fission data at sub-barrier energies.

In figure 3 the deviation of measured anisotropies from the SPSM calculations at near-barrier energies, $(A_{\text{exp}} - 1)/(A_{\text{cal}} - 1)$, are plotted for O + Th (deformed) and O + Pb (spherical) systems to bring out the features discussed above. While the deformed system exhibits anomalous values of A, the spherical system shows normal values. In addition Lestone *et al* [2] have also shown that observed anomaly for even mass number actinide

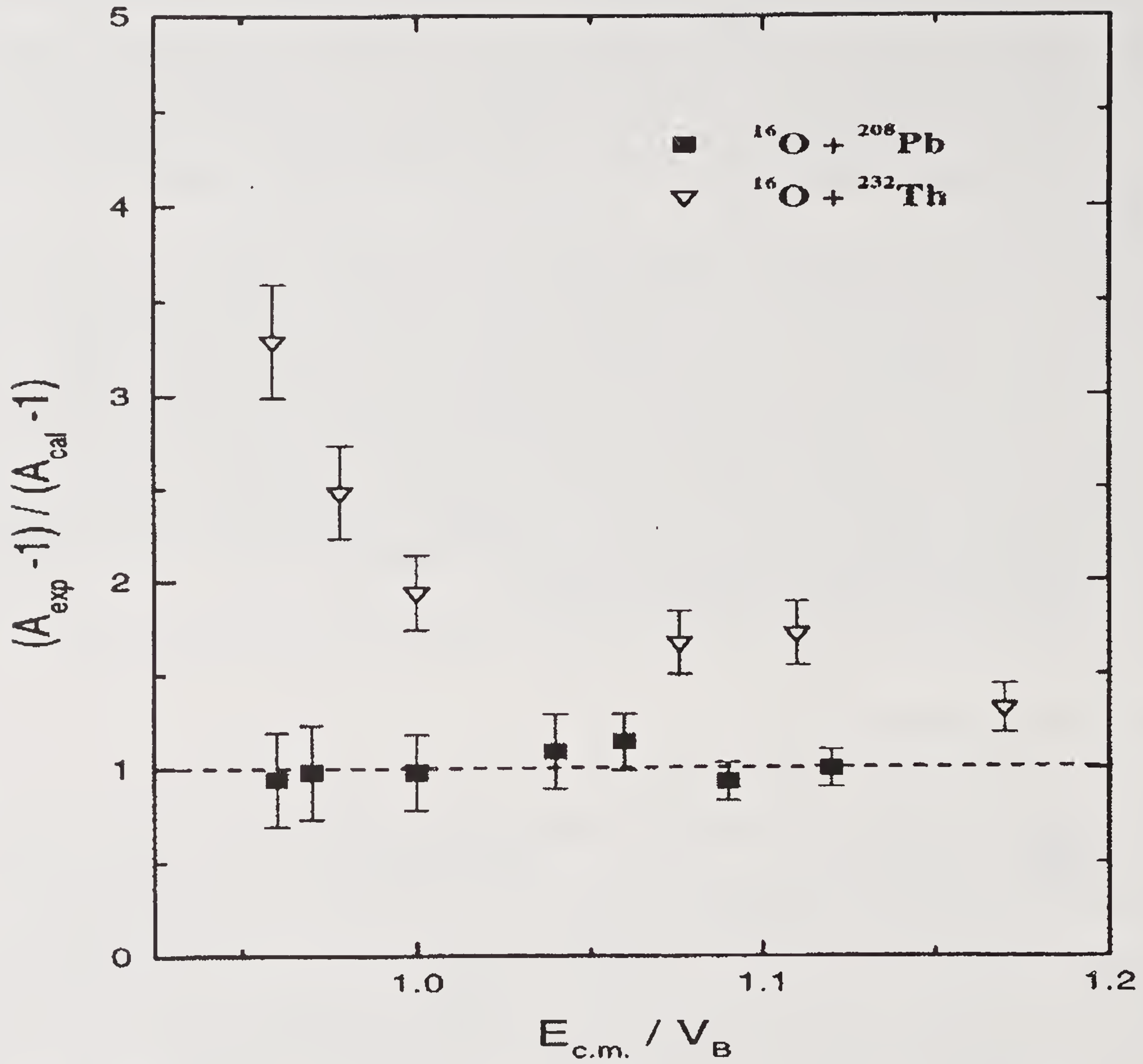

Figure 3. The $(A_{\rm exp} - 1)/(A_{\rm cal} - 1)$ values are plotted as a function of E/V_B for ^{16}O + ^{208}Pb and ^{232}Th systems.

targets, decreases with decrease of projectile mass number. This feature might imply some kind of entrance channel or fissility dependence of fission anisotropies.

3.3 Influence of shell closure on fission anisotropies

It is of interest to investigate the role of nuclear shell closure on fission anisotropies as shell effects are known to influence the potential energy surface in general. With this in view systematic measurements of fission fragment anisotropies and evaporation residue cross sections have been measured spanning a range of energies for two systems ^{12}C + $^{194,198}Pt$ [4].

It may be mentioned that the latter system forms a compound nucleus with $N = 126$. Detailed statistical model analysis of the fission and the evaporation residue cross section data yielded satisfactory fits to the data. The compound nucleus spin distribution and the l distribution related to fission decay have been determined from the above statistical model analysis. The Sierk parametrization has been used for the calculation of l-dependent $I_{\rm eff}, B_f$ and E_R values. The SPSM has been used to calculate the fission anisotorpies. While the anisotropy data for ^{12}C + ^{194}Pt system could be explained by the SPSM calculations, the ones for ^{12}C + ^{198}Pt are found to be significantly larger than the theoretical predictions.

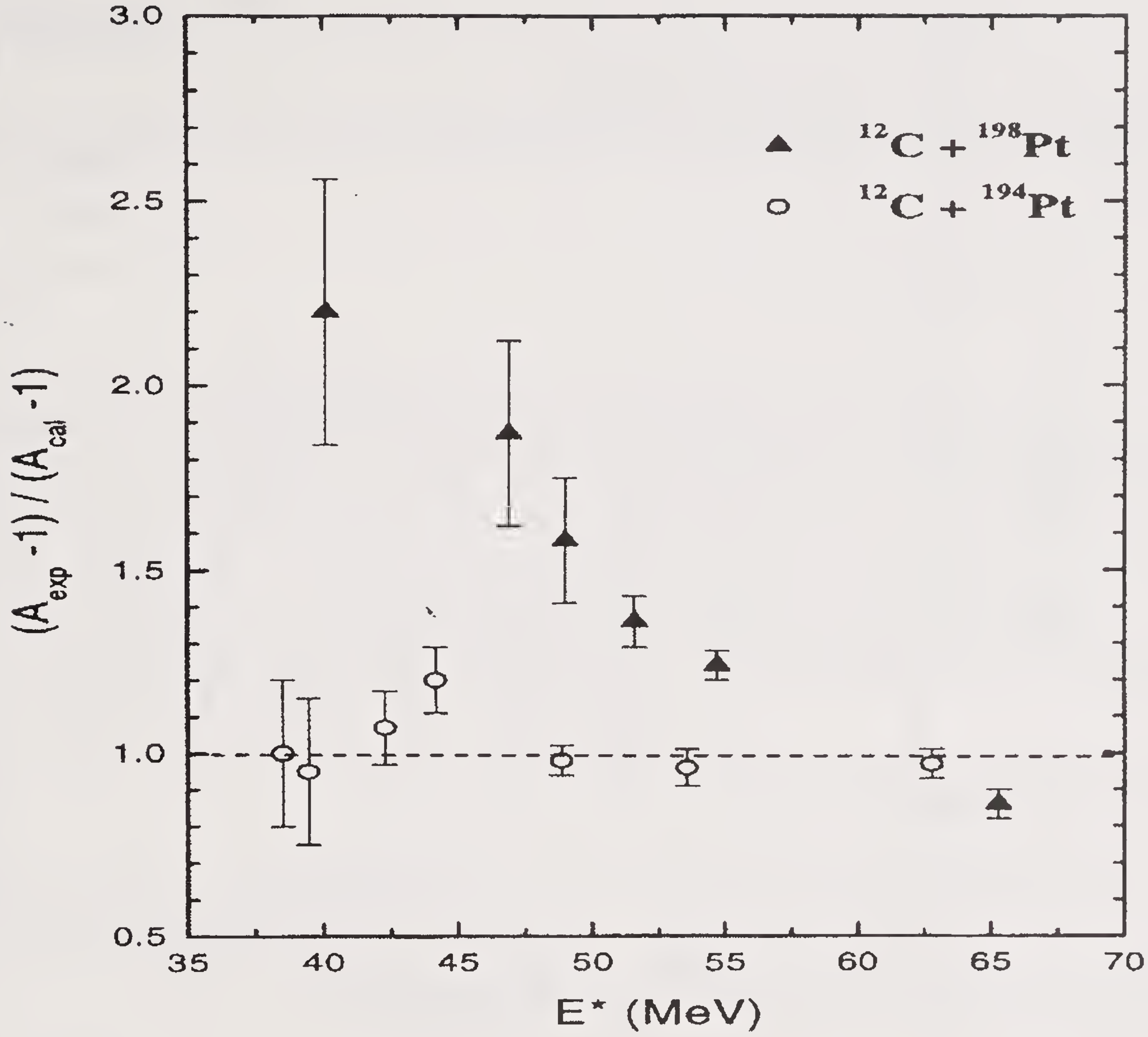

Figure 4. The $(A_{\rm exp} - 1)/(A_{\rm cal} - 1)$ values are plotted as a function of compound nucleus excitation energy, E^* for ^{12}C + ^{194,198}Pt.

The deviation from theory is represented as $(A_{\rm exp} - 1)/(A_{\rm cal} - 1)$ plotted as a function of the compound nucleus excitation energy (figure 4). It is found that the deviation from theory decreases as the excitation energy is increased. From the observation that the anomalous anisotropies are found only for ^{12}C + ^{198}Pt system (^{210}Po, $N = 126$) and that the discrepancy between measurement and calculations decreases at higher energies, it is conjectured that shell effect in the potential energy surface is responsible for this behaviour. The target isotope dependence as a plausible reason for this anomalous behaviour is ruled out as SPSM analysis of ^{12}C + ^{182,184,186}W fission anisotropy data [27] do not show any abnormal effect due to target isotope variation (figure 5).

Further, recently measurements have been extended to ^{19}F + ^{194,198}Pt systems. In this case the former system has $N = 126$ for the compound nucleus. If our earlier conjecture, that $N = 126$ is responsible for anomalous anisotropies is correct, then ^{19}F + ^{194}Pt should exhibit anomalous anisotropy and not ^{19}F + ^{198}Pt. Indeed the fission anisotropies measured for the above two systems are consistent with the above expectation [28]. Even though a complete description of this puzzle is not available at present, a definite correlation between the anomaly and the neutron shell closure ($N = 126$) has been clearly demonstrated in these measurements.

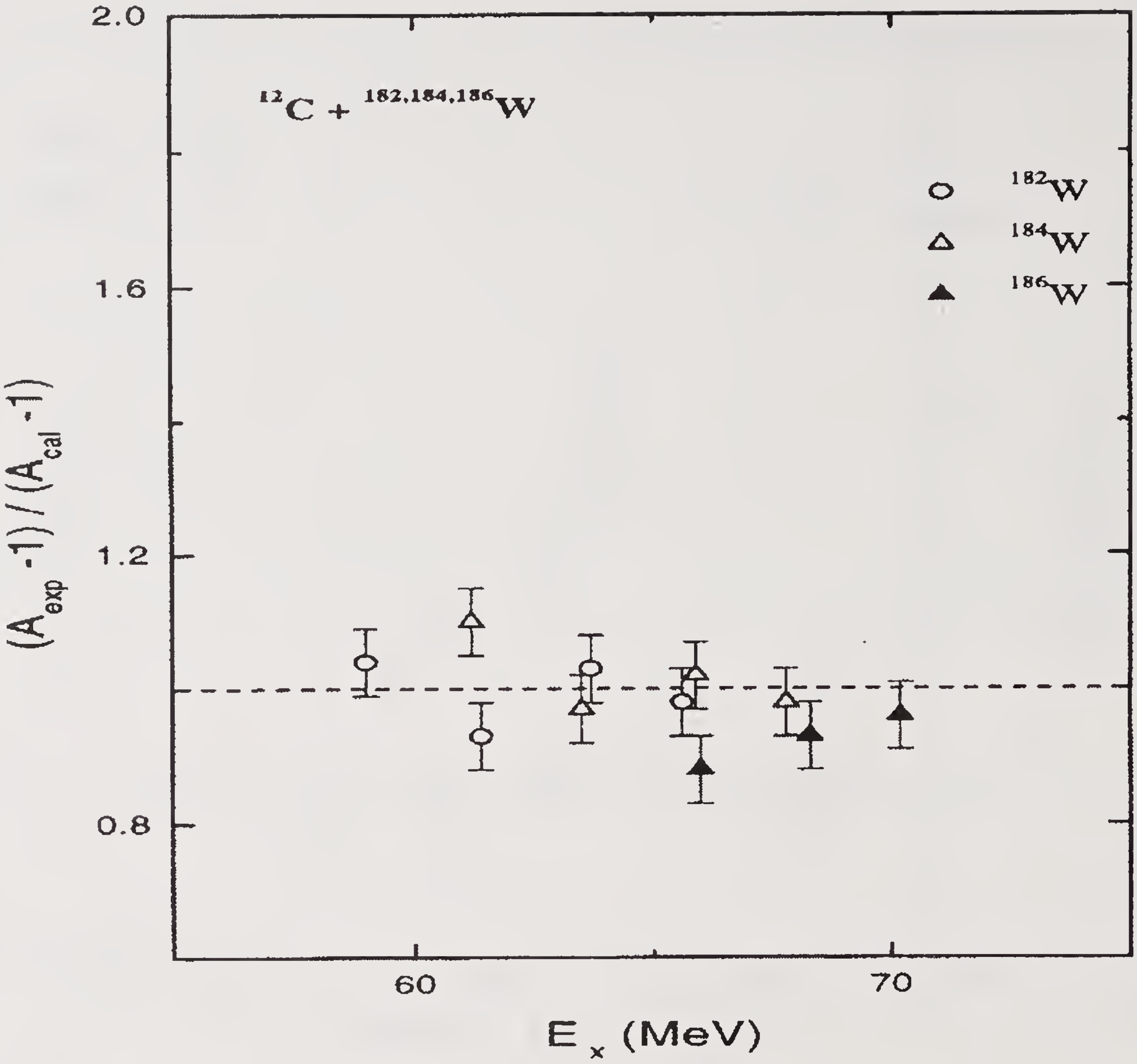

Figure 5. The deviations from SPSM calculations are plotted as a function E_x for $^{12}C + ^{182,184,186}W$ systems.

4. Conclusion

From a systematic study of heavy-ion induced fission reactions at near-barrier energies, the following conclusions can be drawn: For $E > V_B$, the fission fragment angular distributions measured for deformed actinides with low B_f/T values, are dependent on the entrance channel. However, the spherical target systems with large B_f/T values do not exhibit entrance channel dependence of fission anisotropies. Both these observations are consistent with the predictions of preequilibrium model. For well matched channels, having different entrance channels but leading to the same compound at similar excitation energies and angular momenta, entrance channel dependence of the measured anisotorpies is found only at lower E_x (up to 20% above the barrier) but not at energies well above the barrier. It is interesting that the fission anisotropy data for these systems could be described by SPSM calculations even in energy regions where $B_f < T$. For E/V_B <1, while the deformed actinide targets exhibit anomalous anisotropies, the spherical systems do not show this feature. Besides target shape, the role of target spin and size in influencing the fission anisotropy data has also been brought out. Lastly, interesting correlation has been observed between the anomalous anisotropy and the neutron shell closure, implying possible influence of shell effects on fission data.

Acknowledgement

The author is thankful to H S Patel, K Mahata and D Shetty for their help in the preparation of the manuscript.

References

[1] S Kailas, *Phys. Rep.* **284**, 381 (1997); *J. Phys. G. Nucl. Phys.* **23**, 1227 (1997)

[2] J P Lestone, A A Sonzogni, M P Kelly and R Vandenbosch, *Phys. Rev.* **C56**, 2907 (1997)

[3] R Vandenbosch, J D Bierman, J P Lestone, J F Liang, D J Prindle, A A Sonzogni, S Kailas, D M Nadkarni and S S Kapoor, *Phys. Rev.* **C54**, R977 (1996)
S Kailas, D M Nadkarni, A Chatterjee, A Saxena, S S Kapoor, R Vandenbosch, J P Lestone, J F Liang, D J Prindle, A A Sonzogni and J D Bierman, *Phys. Rev.* (1999) (in press)

[4] A Shrivastava, S Kailas, A Chatterjee, A M Samant, A Navin, P Singh and B S Tomar, *Phys. Rev. Lett.* **82**, 699 (1999)

[5] R K Choudhury, *Proc. Indian Nat. Sci.Acad.* **64**, 67 (1998)

[6] I Halpern and V M Strutinsky, *Proc Int. Conf. Peaceful uses of Atomic Energy, Geneva*, **15**, 408 (1958)
R Vandenbosch and J R Huizenga, *Nuclear Fission* (Academic Press, New York, 1973)

[7] A J Sierk, *Phys. Rev.* **C33**, 2039 (1986)

[8] V S Ramamurthy, S S Kapoor, R K Choudhury, A Saxena, D M Nadkarni, A K Mohanty, B K Nayak, S V Sastry, S Kailas, A Chatterjee, P Singh and A Navin, *Phys. Rev. Lett.* **65**, 25 (1990)

[9] A Karnik, S Kailas, A Chatterjee, A Navin, A Shrivastava, P Singh and M S Samant, *Phys. Rev.* **C52**, 3189 (1995)

[10] H Zhang, Z Liu, J Xu, X Qian, Y Qiao, C Lin and K Xu, *Phys. Rev.* **C49**, 926 (1994)

[11] G Ravi Prasad, A M Samant, A Shrivastava, A Navin, A Chatterjee, P Singh, S Kailas and V S Ramamurthy, *Phys. Rev.* **C57**, 971 (1998)

[12] C R Morton, D J Hinde, J R Leigh, J P Lestone, M Dasgupta, J C Mein, J O Newton and H Timmers, *Phys Rev.* **C52**, 243 (1995)

[13] N Majumdar, P Bhattacharya, D C Biswas, A Saxena, R K Choudhury, D M Nadkarni and A Saxena, *Phys. Rev.* **C51**, 3109 (1995)

[14] B John, A Nijasure, S K Kataria, A Goswami, B S Tomar, A V R Reddy and S B Manohar, *Phys. Rev.* **C51**, 165 (1995)

[15] D J Hinde and M Dasgupta, Australian National University ANU-P/1340, October 1997 (unpublished)

[16] S Kailas and P Singh, *Z. Phys.* **A347**, 267 (1994)
E Vulgaris, L Grodzins, R Ledoux and S Steadman, *Phys. Rev.* **C33**, 2017 (1986)

[17] V S Ramamurthy and S S Kapoor, *Phys. Rev. Lett.* **54**, 178 (1985); *Proc. Int. Conf. on Nucl. Phys., Harrogate, U.K.*, edited by J L Durell, J M Irvine and G C Morrison, IOP Conf. Proc. No. **86** (Institute of Physics, Bristol, 1986) vol.1, p.292

[18] Z Lui, H Zhang, J Xu, Y Qian and C Lin, *Phys. Lett.* **B353**, 173 (1995)

[19] B B Back, R R Betts, J E Gindler, B D Wilkins, S S Saini, M B Tsang, C K Gelbke, W G Lynch, M A McMahan and P A Baisden, *Phys. Rev.* **C32**, 195 (1985)

[20] R Vandenbosch, T Murakami, C C Sahm, D D Leach, A Ray and M J Murphy, *Phys. Rev. Lett.* **56**, 1234 (1986)

[21] A Saxena, A Chatterjee, R K Choudhury, D M Nadkarni and S S Kapoor, *Phys. Rev.* **C54**, 932 (1994)

[22] A A Sonzogni, R Vandenbosch, A L Caraley and J P Lestone, *Phys. Rev.* **C58**, R1873 (1998)
[23] A M Samant, S Kailas, A Chatterjee, A Shrivastava, A Navin and P Singh (to be published)
[24] A M Samant and S Kailas, *Z. Phys.* **A356**, 309 (1996)
[25] D J Hinde, M Dasgupta, J R Leigh, J P Lestone, J C Mein, C R Morton, J O Newton and H Timmers, *Phys. Rev. Lett.* **74**, 1295 (1995)
[26] N Majumdar, P Bhattacharya, D C Biswas, R K Choudhury, D M Nadkarni and A Saxena, *Phys. Rev. Lett.* **77**, 25 (1996)
[27] J U Anderson, A S Jensen, E Laegsgeard, K Nielsen, J S Forster, I V Mitchell, D Ward and W M Gibson, IAE -SM-241/**C7**, 387 (1979)
[28] A Shrivastava, S Kailas, A Chatterjee, K Mahata, S Santra, P Singh and B S Tomar, *DAE Symposium on Nucl. Phys.* **B41**, 158 (1998)

Heavy-ion fusion at low energies

NEIL ROWLEY
Institut de Recherches Subatomiques, 23 rue du Loess, F67037 Strasbourg Cedex 2, France

Abstract. Through precision measurements of fusion cross sections at energies close to the Coulomb barrier and through the application of the method of "experimental barrier distributions" which these permit, many recent advances have been made in our understanding of the dynamical processes occuring during a heavy-ion collision. It is now clear that the target and projectile reach one another in superpositions of states which correspond to different orientations for rotational nuclei or to different induced deformations for vibrational nuclei. The creation of a neck of neutron matter has also long been postulated and by studying the isotopic dependence of the fusion reaction, some recent results in the ^{40}Ca + ^{90,96}Zr systems appear to confirm this result. For large Z_1Z_2 a type of extra-push effect can arise from the same inelastic entrance-channel effects which enhance the fusion of lighter systems, though this will be absent in cases where the enhancement arises from neutron transfers.

The existence of different barriers will of course influence all other reaction channels. Fusion simply allows one to visualise the barriers most easily, since for this process, the total cross section is an *incoherent* sum of the contributions from all relevant eigenchannels. Some effects in other channels have already been observed. Other possible effects will be discussed. These include; the exploitation of the lowest-energy barrier to produce exotic evaporation residues and strongly deformed high-spin states at low excitation energy.

Keywords. Fusion barrier-distributions; exotic nuclei; deformed high-spin states.

PACS Nos 25.70.Jj; 25.70.Bc; 25.70.De; 25.70.Gh; 25.70.Hi; 21.60

1. Introduction

The fusion of two heavy-ions is not in itself a rare nuclear process, cross sections above the Coulomb barrier being of the order of the geometrical limit πR^2 i.e. of the order of barns. However, many interesting phenomena do oblige us to study situations with much smaller cross sections, for example:

1) The dynamics of the entrance channel lead to a distribution of Coulomb barriers and a full understanding of this process can be obtained only by measuring the fusion cross section σ_f over a wide range of energies E both above and below the conventional barrier. If these data are sufficiently good, the 'experimental barrier distribution' $D(E)$ can be obtained from [1]:

$$D(E) = \frac{\mathrm{d}^2(E\sigma_f)}{\mathrm{d}E^2}. \tag{1}$$

2) The existence of barriers lowered in energy leads to the possibility of a small but significant compound-nucleus (CN) formation at lower excitation energies than one might

have expected, while still populating relatively high-spin states. The lower excitation energy may lead to reduced particle evaporation and thus to the formation of some relatively exotic nuclei which are not populated at higher $E^*_{\rm CN}$.
3) It is well known that to form very heavy compound systems, in particular new elements, one is limited by the phenomenon of fission. The cross section for the formation of these high Z systems is the product of the fusion (passage to a compound nucleus) and the probability that they will survive fission. The latter probability increases with decreasing excitation energy and so taking advantage of entrance-channel effects may be of paramount importance here.

The first point outlined above i.e. the existence of a range of barriers, has been known for some time and over recent years the use of eq. (1) has given us significant insights into reaction dynamics. Figure 1 shows a representative selection of structures of fusion barriers which provide ‘fingerprints’ of different types of inelastic coupling which can intervene in sub-barrier fusion enhancement.

One sees in (1a) that for the system ^{40}Ca + ^{40}Ca [2], where both target and projectile are

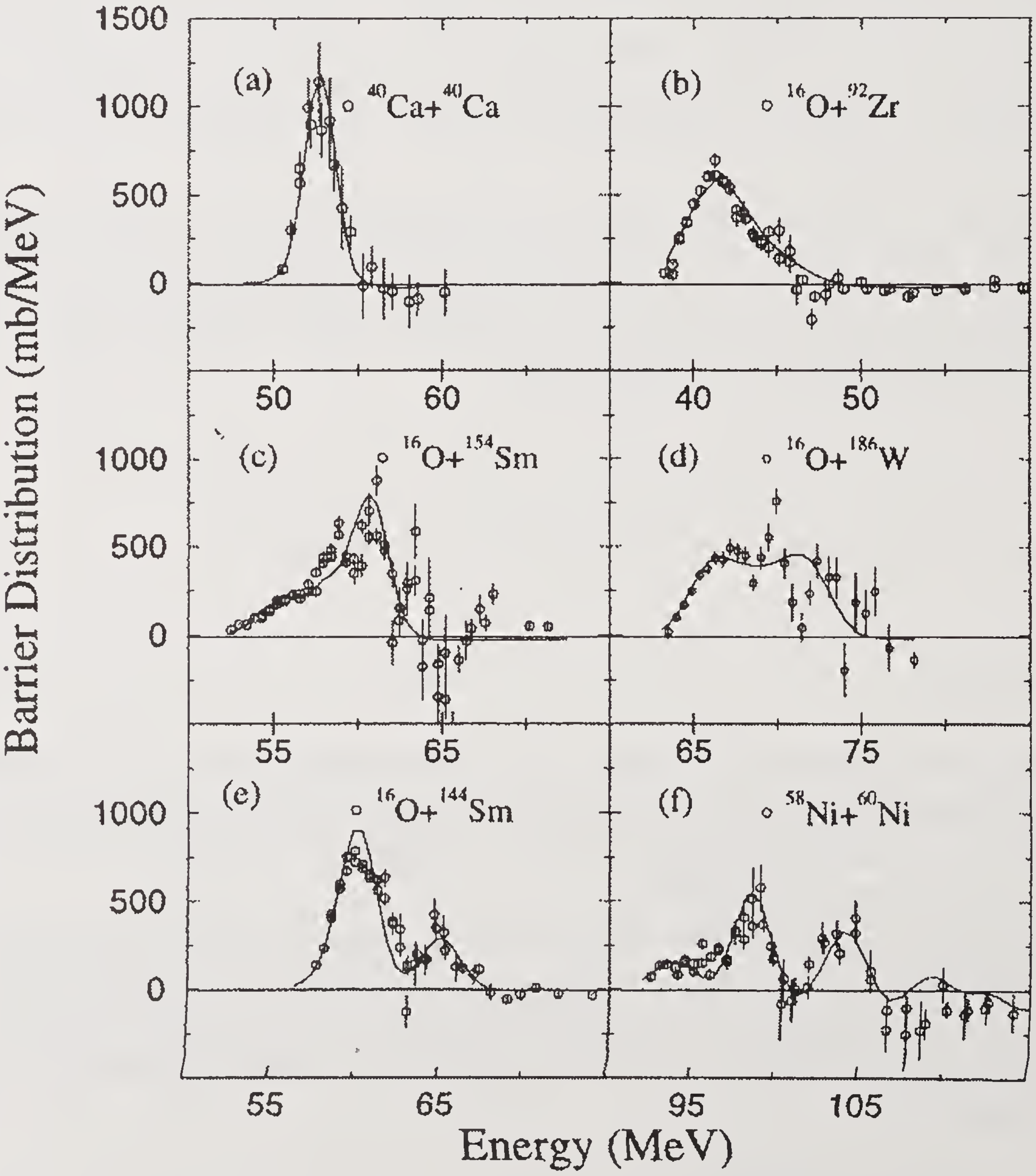

Figure 1. The great variety of experimental barriers distributions is demonstrated even when coupling is confined to inelastic excitations. Solid lines are theoretical results. See text.

double-closed-shell nuclei, a single peak is obtained with the width of around 3 MeV expected for a single Coulomb barrier. In (b), (c) and (d) essentially continuous distributions are seen. The latter two, corresponding to the spherical ^{16}O on two different deformed systems [3,4], can be reproduced by summing the fusion from barriers corresponding to all possible orientations of the targets. However, the significant differences in $D(E)$ can be related to a detail of the nuclear deformation; although ^{154}Sm and ^{186}W are both prolate rotors with large β_2, the former has a small positive hexadecapole moment whereas the latter has a small *negative* β_4. Frame (e) shows the double-peaked structure expected for strong coupling to a single-phonon state (3^- in ^{144}Sm) [5], while (f) shows a spectacular three-barrier structure due to complex surface vibrations induced by coupling to multiphonon states in the ^{58}Ni + ^{60}Ni system [6]. In frame (b), ^{16}O + ^{92}Zr [7] should display similar structures to the ^{58}Ni + ^{60}Ni case. However, since the different Coulomb barriers correspond to variations of the nuclear radius, these effects scale as $\bar{\beta} Z_1 Z_2$. The relatively low $Z_1 Z_2$ value for this system causes the structures to overlap. They are thus 'unresolved' and the overall distribution appears continuous.

These experiments and many others have led to a deeper understanding of nuclear reaction mechanisms and shown quite unambiguously that the fusion cross section carries an enormous amount of information if only one looks carefully enough. Other results and consequences have been recently reviewed in detail in ref. [8].

In earlier studies of barrier distributions, Stelson and co-workers [9] claimed an important role for neutron transfer channels. However, for none of the above systems was it necessary to invoke such effects. Indeed for ^{58}Ni + ^{60}Ni, it was expected that the elastic 2-neutron-transfer channel would have a strong effect but a comparison with an earlier experiment of Beckerman [10] showed that the structures for ^{58}Ni + ^{58}Ni were practically identical to those in the present system. Since transfer Q-values are all rather different but the collectivity and excitation energies of the relevant phonon states are very similar, it was concluded that transfer played only a minor role.

Since it is clear that one cannot find systems where inelastic excitations do not come into play, it is necessary to look for isotopic effects in order to study neutron degrees of freedom. An ideal case would be a heavy double-closed-shell nucleus impinging on different isotopes of the same element (same $Z_1 Z_2$), one having a closed neutron shell and the other having several neutrons outside the closed shell.

2. The ^{40}Ca + ^{90,96}Zr systems: Neutron necking

With the above considerations in mind, the ^{40}Ca + ^{90,96}Zr systems were studied in detail at Legnaro [11]. The former target has a closed $N = 50$ neutron shell, whereas the second has 6 neutrons outside that shell, all with positive Q values for transfer to the projectile.

Figure 2 compares the cross sections for these two systems. The dashed line shows the results of a calculation with no couplings to the ^{90}Zr target. For the same system the solid curve shows that a good fit can be obtained by including inelastic excitations. Such a calculation fails, however, for the heavier target which has a further significant enhancement, apparently due to $Q > 0$ neutron-transfer channels. Figure 3 shows the corresponding experimental barrier distributions and the fits arising from the calculations including inelastic excitations only. The failure to predict the low-energy barrier strength for ^{96}Zr is manifest.

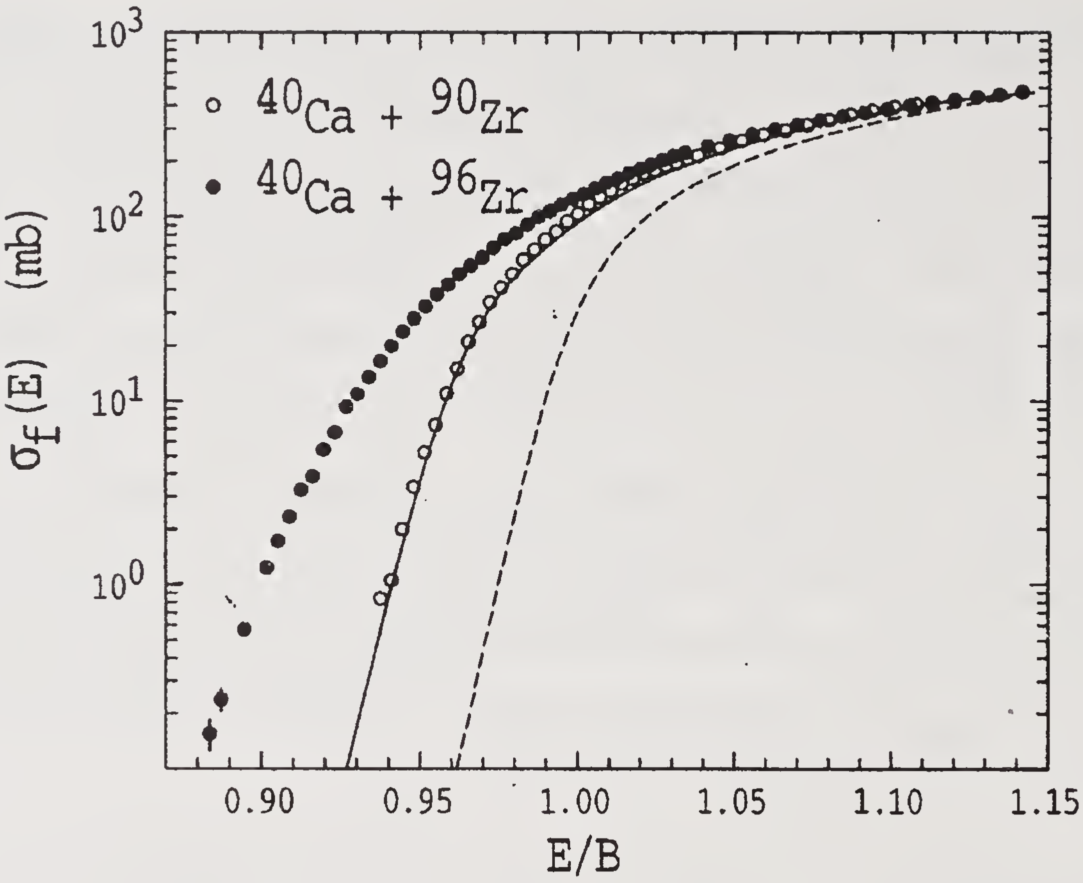

Figure 2. Fusion excitation functions for $^{40}\mathrm{Ca} + {}^{90,96}\mathrm{Zr}$ around the average barrier B. The dashed line shows the results of a calculation with no couplings for the former system. For the same reaction the solid curve shows that a good fit can be obtained by including inelastic excitations. Such a calculation fails for the latter case which has a further significant enhancement due to neutron-transfer channels. See text and figure 3.

An important consideration in fusing heavy systems is that at high $Z_1 Z_2$, Coulomb effects become more important. Of course the nuclear coupling is also proportional to $Z_1 Z_2$ since it is determined by the changes in barrier height associated with changes in the nuclear radius. For systems with low excitation energy, where the initial configuration is essentially frozen, the relative importance of nuclear and Coulomb effects remains constant. However, for systems with high excitation energy, the long-range Coulomb interaction can polarise the nuclei well before the barrier is reached. Such a long-range polarization will always give a configuration unfavourable to fusion. These considerations are valid for inelastic excitations but of course for neutron-transfers, the Coulomb force has no effect. Thus the fusion of heavy systems might be facilitated by use of neutron-rich projectiles with many nucleons outside the closed shell available for transfer[1].

3. Effects in other channels

The existence of different Coulomb barriers has been sought in other final channels with varying degrees of success. Both elastic [13] and quasi-elastic [14] channels do display

---

[1] Since this talk was presented, the possible creation of element $Z = 114$ has been announced at Dubna [12]. The neutron excess of the ^{48}Ca projectile used leads to a compound nucleus closer to the predicted island of stability but it is likely that it also plays the role discussed above of enhancing the fusion probability itself.

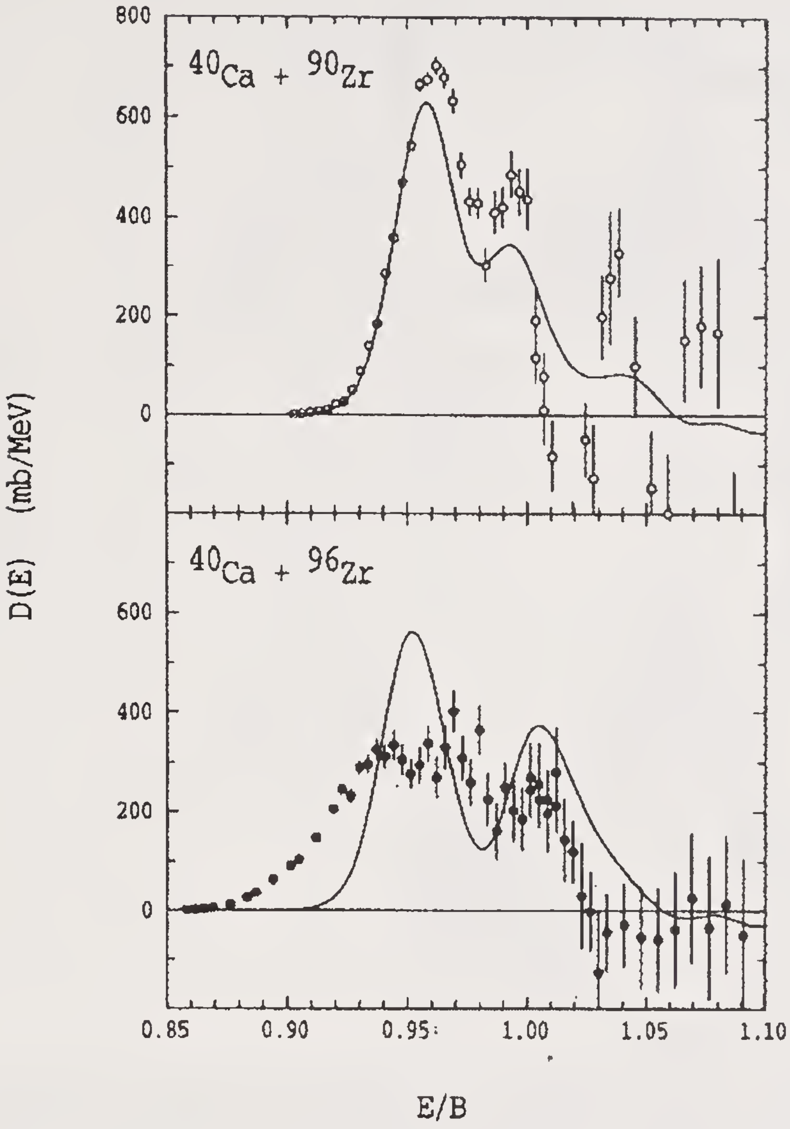

Figure 3. Experimental barrier distributions for ^{40}Ca + ^{90,96}Zr along with the results of theoretical calculations including only inelastic excitations. These produce reasonable results for the former system but fail to give the low-energy strength in the latter case. Results are shown with respect to the corresponding average barrier B.

some evidence of the same gross structures observed in fusion (i.e. the overall width and shape of the distribution), however, the details of the individual peaks is often lost due to the fact that the relevant barrier amplitudes do not add incoherently thus giving rise to interference effects and dephasing.

Another important observation is that some dynamics of the fission channel may equally be related to entrance-channel effects, with the compactness of the formed compound nucleus depending on the orientation of a fusing deformed target, and leading to an energy-dependent fission anisotropy around the barrier region, which disagrees with the predictions of the statistical saddle-point method [15].

A recent experiment performed at the ANU [16] also suggests an important effect arising from the breakup channel. The system studied was ^{9}Be + ^{208}Pb, which is of particular interest due to the *borromean* nature of the projectile. The results show what is effectively an overall renormalisation of the excitation function (hence the barrier distribution) due to the strong break-up channel.

An important consideration in fusion studies is how the different barriers may affect the properties of the compound nucleus formed i.e. how will the spin distribution be affected and will certain evaporation residues be favoured. We shall discuss these topics in the context of the ^{58}Ni + ^{60}Ni system where additional experiments have been performed and are planned.

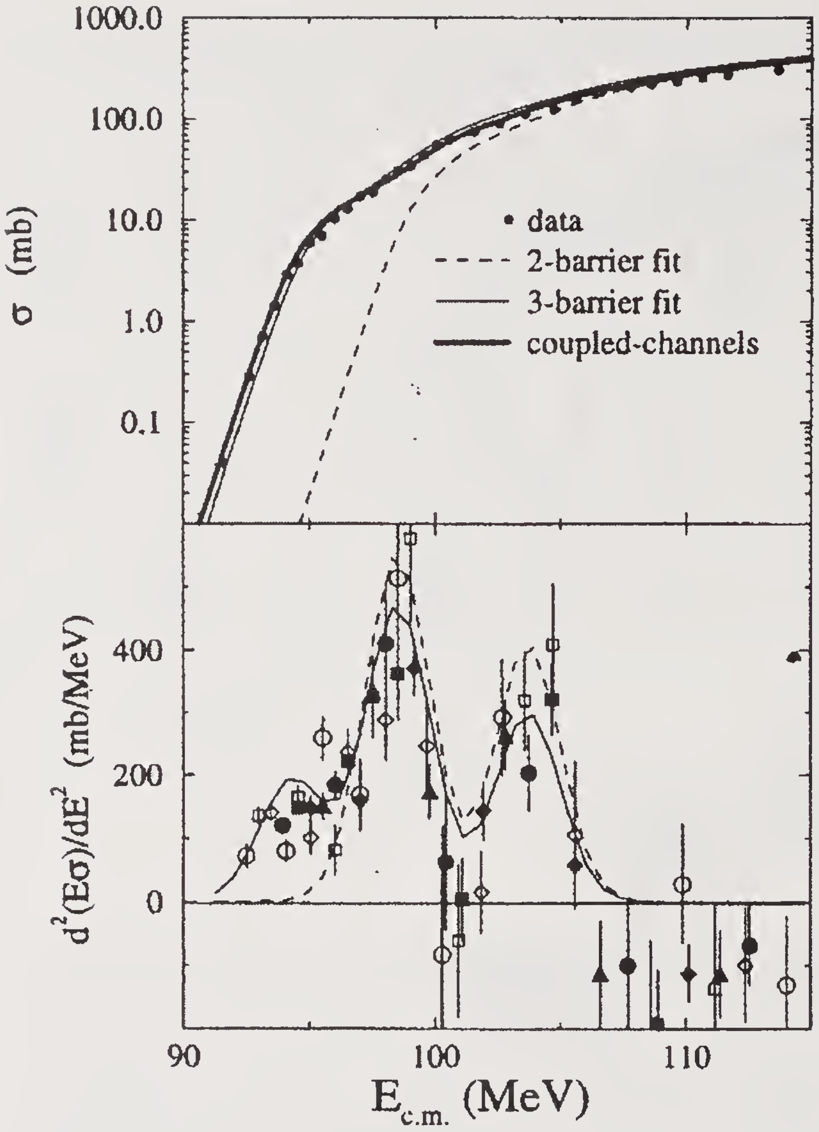

Figure 4. Experimental excitation function and barrier distribution for ^{58}Ni + ^{60}Ni. The results of simple parametrized 2- and 3-barrier fits are shown along with the results of a full coupled-channels calculation.

4. The ^{58}Ni + ^{60}Ni system: Feeding the compound nucleus

This reaction is of particular interest since the barrier distribution has three distinct peaks, as shown in more detail in figure 4. Reproducing this structure demands a rather full coupled-channels calculation, both from the point of view of which channels are included and how the dynamics are treated.

This is demonstrated in figures 5 and 6. Figure 5 shows the effects of the successive inclusion of higher-phonon channels. A good fit to the data is obtained only when one goes as far as the 4-phonon channel i.e. the double-mutual excitation of the quadrupole phonon vibrations in these nickel nuclei. Interestingly, the fit worsens if one supposes the existence of (unobserved) 3-phonon states in each nucleus, perhaps indicating a strong depletion of the collectivity as the single-particle space becomes blocked. This is an interesting example of a problem where the barrier fingerprint may give new information on the target and projectile internal structure.

Figure 6 shows the danger of approximations. A good fit is obtained only by taking account of couplings to all orders, finite excitation energies and Coulomb excitation at large r. This last effect suppresses the low-energy strength, increases the barrier centroid and, for high $Z_1 Z_2$ may give rise to an effective extra-push energy.

The solid curves in figure 7 show the calculated spin distribution for the compound nucleus at three energies, each just above one of the three barriers of figure 4. The complex

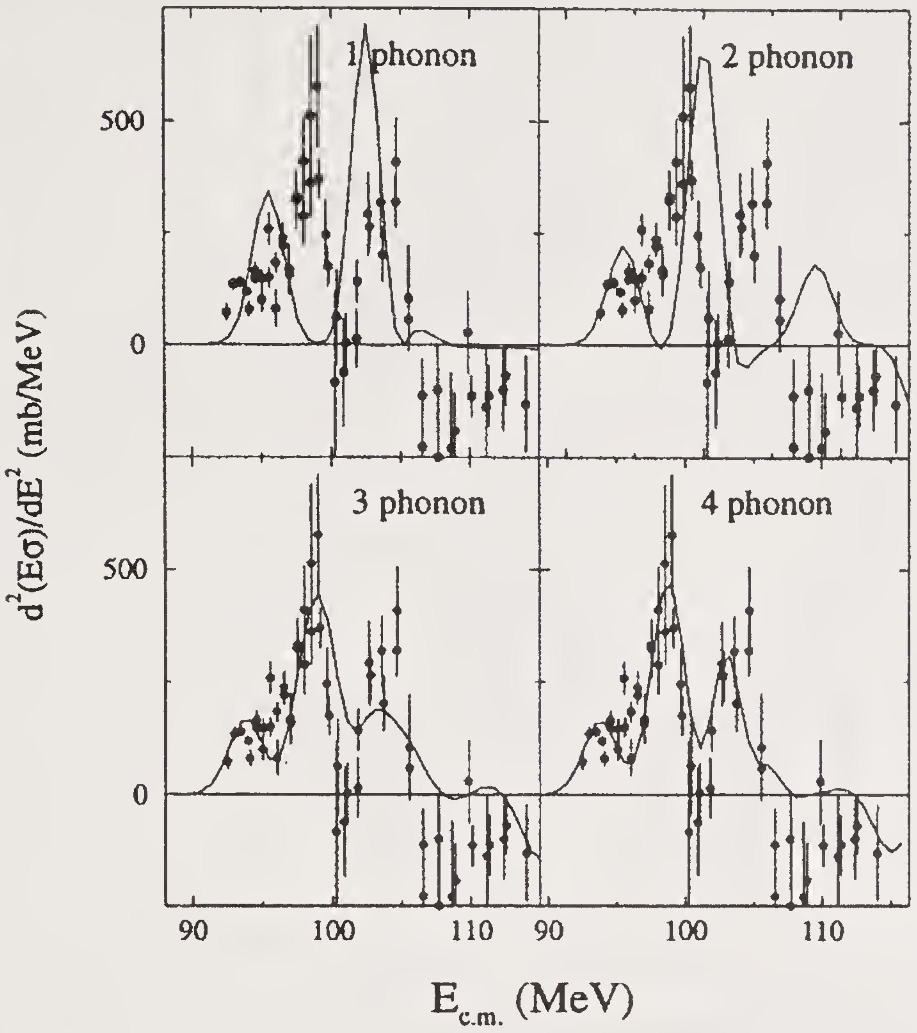

Figure 5. Results are shown for full coupled-channels calculations including from one to four phonons. In the one-phonon channel, the quadrupole phonon may be in either nucleus i.e. $|1,0\rangle$ or $|0,1\rangle$. The four-phonon channel includes everything up to mutual-double excitation i.e. $|2,2\rangle$ but does not exceed two phonons in either nucleus.

structures are surprisingly simple to understand in terms of a smoothed triangular $(2l+1)$ distribution from each individual barrier, though the results shown emerge naturally from a full coupled-channels calculation. The great advantage of this system is that one can have considerable confidence in the predicted spin distributions since the same calculations fit a rather complex and highly enhanced fusion excitation function extremely well.

This was taken advantage of in a recent GAREL+ experiment at the Strasbourg Vivitron [17]. At each of the three energies, the discrete γ-ray transitions (near-yrast) were observed in order to see if the complexity of the initial distribution carried through to the yrast line. The rather remarkable result is that this is not the case, as shown by the data in figure 7. Indeed the shape of the spin population cuts off at around 20 $\hbar$ for both the lower energies despite the much higher spin put into the compound nucleus. At the third energy a slight increase in $\langle l\rangle$ is observed but nowhere near in proportion to the additional spin put into the compound nucleus.

This may be due to a relatively small spreading width Γ of states well above the yrast line at high spin, preventing the percolation down to the region of discrete decays. Such effects would of course strongly inhibit the population of super-deformed and hyper-deformed configurations at high spins. Thus understanding this phenomenon is of considerable importance. The fact that the flux starts to fall down rapidly at around spin 20 $\hbar$, may indicate a rapidly increasing Γ in this region and could be indicative of an order/chaos transition.

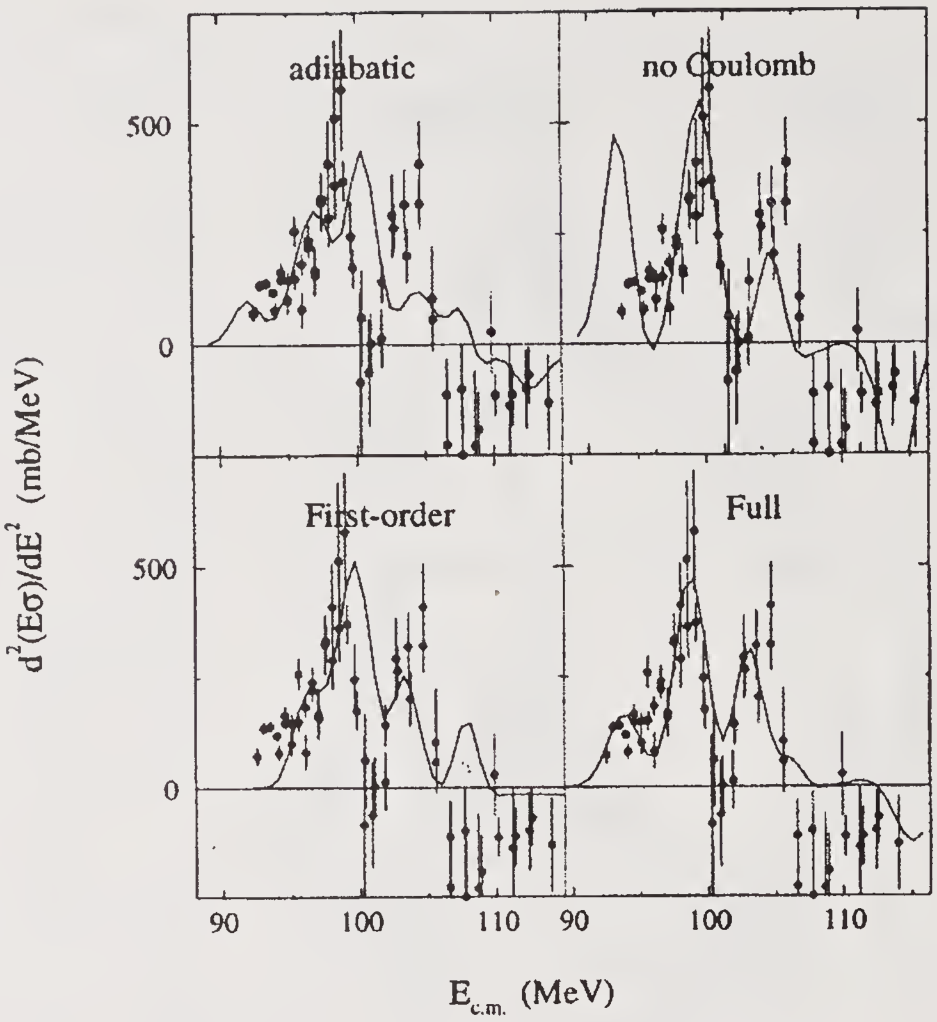

Figure 6. The four-phonon calculation of figure 5 is shown with various approximations: adiabatic (ignoring excitation energies), ignoring Coulomb excitation (note how Coulex suppresses the lowest barrier) and finally the effect of coupling only to first-order.

Other interesting features arising from the lowest barrier are:

1) The compound nucleus formed by fusion through the lowest barrier is created with a large prolate deformation due to the initial distortion of the target and projectile. If this shape survives sufficiently long, it should lead to enhanced charged-particle emission. Indeed a significant enhancement of proton emission, relative to evaporation-code predictions, is observed at the lowest energy [17].

2) The possibility of fusion at energies below the conventional Coulomb barrier could lead to the survival of some exotic neutron-deficient nuclei. Indeed at the lowest energy, ^{116}Cs is predicted. This nucleus is 17 neutrons away from β-stability and lies very close to the proton-drip line. It has no known γ-rays.

The ^{58}Ni + ^{60}Ni experiment will be repeated at Legnaro using GASP and the recoil mass spectrometer. The GASP inner ball will allow us to extract the total γ-ray spin distribution i.e. that prevailing after particle evaporation. This will give greater insight into where the entrance-channel angular momentum is lost and will also provide invaluable information for the calculation of the ensuing continuum γ-decays, thus enabling a better evaluation of the spreading width Γ. The use of the RMS will also allow a gating on ^{116}Cs to test whether one can exploit entrance-channel effects to populate very proton-rich nuclei at relatively high spins.

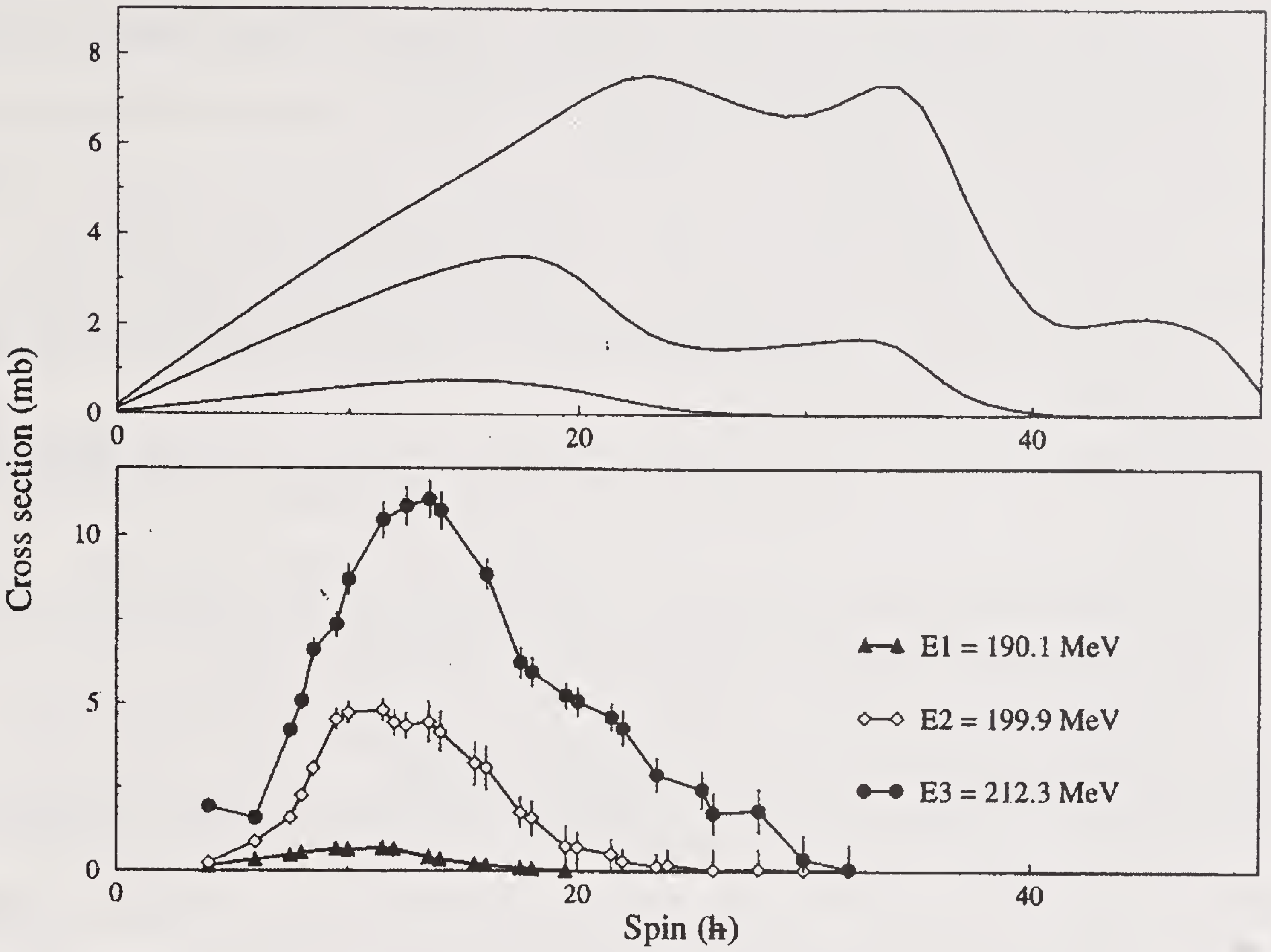

Figure 7. The angular momentum of the compound nucleus at formation is compared with the measured spin distribution for near-yrast (discrete) γ-decays at various energies.

5. Conclusions

The extraction of a fusion barrier distribution from experimental data is now very well established, as are many of its experimental consequences [8]. The demands for good statistics are well rewarded by the ensuing information which frequently gives enormous insights into nuclear reaction dynamics and presents a real challenge to theoretical analysis.

We have already seen the reflection of these barriers in other reaction channels; elastic, inelastic and even fission and are beginning to learn how to exploit their influence on the formation of the compound nucleus both in the spin and isospin degrees of freedom, and possibly ultimately in the creation of systems of higher mass and charge. Of course studies of fusion with radioactive beams have also started (see e.g. refs [18,19]) and we also look forward to many interesting new results in that domain.

References

[1] N Rowley, G R Satchler and P H Stelson, *Phys. Lett.* **B254**, 25 (1991)
[2] H A Aljuwair *et al*, *Phys. Rev.* **C30**, 1223 (1984)
[3] J X Wei, J R Leigh, D J Hinde, J O Newton, R C Lemmon, S Elfström, J X Chen and N Rowley, *Phys. Rev. Lett.* **67**, 3368 (1991)

J R Leigh, N Rowley, R C Lemmon, D J Hinde, J O Newton, J X Wei, J Mein, C R Morton, S Kuyucak and A T Kruppa, *Phys. Rev.* **C47**, R437 (1993)
[4] R C Lemmon, J R Leigh, J X Wei, C R Morton, D J Hinde, J O Newton, J C Mein, M Dasgupta and N Rowley, *Phys. Lett.* **B316**, 32 (1993)
[5] C R Morton, M Dasgupta, D J Hinde, J R Leigh, R C Lemmon, J P Lestone, J C Mein, J O Newton, H Timmers, N Rowley and A T Kruppa, *Phys. Rev. Lett.* **72**, 4074 (1994)
[6] A M Stefanini, D Ackermann, L Corradi, D R Napoli, C Petrache, P Spolaore, P Bednarczyk, H Q Zhang, S Beghini, G Montagnoli, L Mueller, F Scarlassara, G F Segato, F Sorame and N Rowley, *Phys. Rev. Lett.* **74**, 864 (1995)
[7] J C Mein *et al*, private communication
[8] M Dasgupta, D J Hinde, N Rowley and A M Stefanini, *Ann. Rev. Nucl. Part. Sci.* **48**, 401 (1998)
[9] P H Stelson, H J Kim, M Beckerman, D Shapira, and R L Robinson, *Phys. Rev.* **C41**, 1584 (1990)
[10] M Beckerman *et al*, *Phys. Rev. Lett.* **45**, 1472 (1980); *Phys. Rev.* **C23**, 1581 (1981)
[11] H Timmers, L Corradi, A M Stefanini, D Ackermann, J H He, S Beghini, G Montagnoli, F Scarlassara, G F Segato and N Rowley, *Phys. Lett.* **B399**, 35–39 (1997)
H Timmers, D Ackermann, S Beghini, L Corradi, J H He, G Montagnoli, F Scarlassara, A M Stefanini and N Rowley, *Nucl. Phys.* **A633**, 421–445 (1998)
[12] "Element 114 lumbers into view"; *Science* **283**, 474 (1999)
[13] N Rowley, H Timmers, J R Leigh, M Dasgupta, D J Hinde, J C Mein, C R Morton and J O Newton, *Phys. Lett.* **B373**, 23–29 (1996)
[14] H Timmers, J R Leigh, M Dasgupta, D J Hinde, R C Lemmon, J C Mein, C R Morton, J O Newton and N Rowley, *Nucl. Phys.* **A584**, 190 (1995)
[15] D J Hinde, M Dasgupta, J R Mein, J C Morton, J O Newton and H Timmers, *Phys. Rev.* **C53**, 1290 (1996)
[16] M Dasgupta *et al*, *Phys. Rev. Lett.* **82**, 1395 (1999) and contribution to this conference
[17] S Courtin *et al*, in progress
[18] V Fekou-Youmbi *et al*, *Nucl. Phys.* **A583**, 811 (1995)
[19] A Yoshida *et al*, *Nucl. Phys.* **A588**, 109c (1995)

Dynamics of low-energy heavy-ion fusion

A M STEFANINI
INFN-Laboratori Nazionali di Legnaro, I-35020 Legnaro, Padova, Italy

Abstract. Preliminary data on the fusion of ^{36}S + ^{96}Zr are reported; the excitation function near the barrier is intermediate between those of ^{40}Ca + ^{90,96}Zr. The peculiar role of the strong 3^- octupole vibration of ^{96}Zr is pointed out, in addition to the couplings to neutron transfer channels with positive Q-values. Recent data on ^{40}Ca + ^{124}Sn are also shown; for that system the fusion barrier distribution is wide without separated peaks, similar to the case of ^{40}Ca + ^{96}Zr. Simplified coupled-channel calculations have been performed, including surface vibrations and sequential neutron pick-up channels, with form factors that fit the single- and multi-nucleon transfer data for ^{40}Ca + ^{124}Sn. A good agreement with the data is found.

Keywords. Heavy ions; sub-barrier fusion; barrier distributions.

PACS No. 25.70.Jj

1. Introduction

There has been considerable interest (and discussion) in recent years about the possibility of extracting fusion barrier distributions [1] from the fusion excitation functions in the energy range encompassing the Coulomb barrier. This procedure has actually yielded detailed information on the fusion dynamics in several heavy-ion systems [2,3], more detailed than what is possible to get from a simple analysis of the excitation functions and from their comparison with the theoretical models.

Here I present some recent experimental results in this field, which our group has obtained at the Laboratori Nazionali di Legnaro of INFN. The measurements of fusion-evaporation cross sections were performed using the XTU tandem accelerator. ^{40}Ca, ^{36}S beams with intensities ~3–10 pnA; isotopically enriched targets were used, with thickness ~50–90 μg/cm^2, evaporated onto 15 μg/cm^2 carbon layers.

The evaporation residues (ER) were detected at 0° and at small angles by an energy time-of-flight telescope following an electrostatic beam deflector. Beam rejection factors $\sim 10^7$–10^8 were achieved. Absolute cross section normalization was ensured by four monitor detectors mounted in a ring perpendicular to the beam direction, each one at a scattering angle $\theta_{\text{lab}} = 22^0$, and by measuring the transmission of the beam deflector for ER (usually around 60–70%). Particular attention was devoted to the quality of the beam and to the statistical accuracy of the measurements, which was ~1% around and over the barrier. Excitation functions were measured at 0° only downwards in energy with 0.5 MeV steps (1.0 MeV for the highest energy points). Angular distributions of ER were measured at selected energies around and above the barriers in the range 0°–7° with 1° steps. See ref. [4] for more details.

2. Fusion with ^{90,96}Zr targets

The results of a detailed study of the two systems ^{40}Ca + ^{90,96}Zr were published recently [5]. Since the projectile ^{40}Ca is a magic nucleus, its influence on fusion was expected to be small, whereas both targets ^{90,96}Zr have a $Z = 40$ subshell closure. A main difference between the two reactions is in the neutron transfer Q-values which are very positive, in the case of ^{96}Zr only, up to the pickup of 8 neutrons. However, a further aspect was not considered fully in that work; while the low-lying quadrupole vibrations of ^{90}Zr and ^{96}Zr are found at similar excitation energies and are only moderately collective, ^{96}Zr has an octupole vibration significantly stronger and lower-lying than the corresponding state in ^{90}Zr.

Figure 1a shows the two measured excitation functions on a reduced energy scale. A very large relative enhancement is observed for ^{40}Ca + ^{96}Zr at low energies. The corresponding barrier distribution plotted in figure 1c has a flat and rather structureless shape extending to very low energies. It is qualitatively different from the distribution for ^{90}Zr (see figure 1b), which shows well defined peaks. The barrier structure and fusion excitation function of ^{40}Ca + ^{90}Zr were explained in terms of coupling to the low-lying inelastic excitations of ^{90}Zr (solid lines in figure 1a,b), but these couplings could not explain the fusion of ^{40}Ca + ^{96}Zr. Calculations [5] indicate that sequential neutron transfer is required to explain the observed distribution.

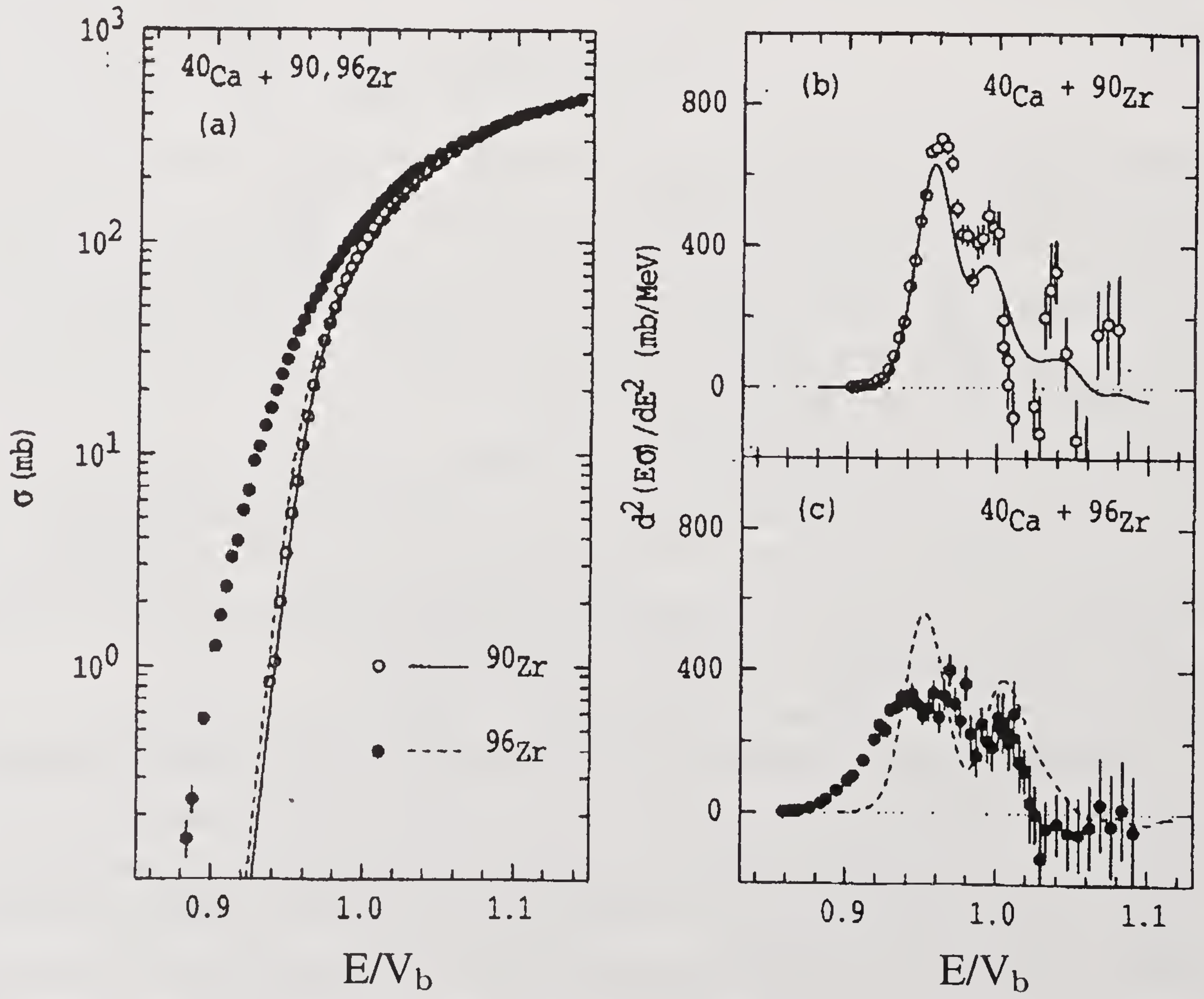

Figure 1. The fusion excitation functions and barrier distributions for ^{40}Ca + ^{90,96}Zr [5]. The CC calculations for ^{90}Zr (solid) and ^{96}Zr (dashed) including the inelastic excitations of the Zr nuclei are shown. Taken from [3].

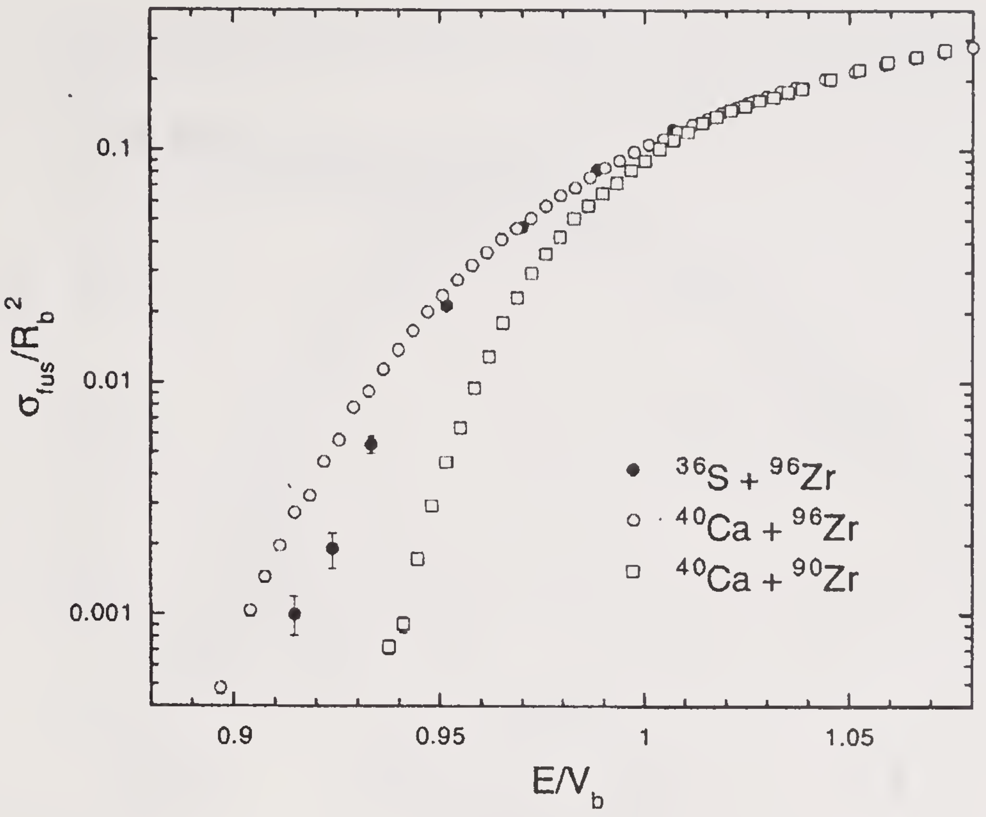

Figure 2. The fusion excitation functions for ^{36}S + ^{96}Zr and for ^{40}Ca + ^{90,96}Zr in a reduced scale.

In this context, it seemed important to us to try to assess experimentally the effect of the strong octupole vibration of ^{96}Zr on fusion. That is surely one reason for the relative enhancement of ^{40}Ca + ^{96}Zr compared to ^{40}Ca + ^{90}Zr, since, qualitatively speaking, one expects that the octupole shape strongly favours sub-barrier fusion. It is worthwhile pointing out, more is general, that there is little clear-cut available data in the literature about the influence of octupole vibrations on fusion, probably because either they are too high in energy, or their role is mixed up and surmounted by lower-lying quadrupole vibrations.

The case of ^{96}Zr is a promising one, since the 3^- state is relatively low and very strong ($\beta = 0.34$). The system ^{36}S + ^{96}Zr was considered, where, in comparison with ^{40}Ca + ^{96}Zr, we have a similar rigid projectile structure (the rather strong 3^- state of ^{40}Ca is high in energy, and its effect on fusion is anyway taken into account), but no transfer channels with positive or even slightly negative Q-values are available. Hence, we expect for ^{36}S + ^{96}Zr less sub-barrier fusion and, possibly, a barrier distribution with sharp and separated peaks, at variance with the case of ^{40}Ca + ^{96}Zr; the effect of the octupole coupling, if any, may be better isolated.

A preliminary experiment has been performed for ^{36}S + ^{96}Zr, and the measured cross sections are shown in figure 2, together with the previous results for the two Ca + Zr systems. The ^{36}S + ^{96}Zr cross sections are found to be intermediate between those of the other two systems, nearer to the ^{40}Ca + ^{96}Zr excitation function. A more detailed study of ^{36}S + ^{96}Zr will be performed at LNL soon, with small energy steps and high statistical accuracy, to enable us to extract the barrier distribution from the second derivative of the excitation function.

3. The case of ^{40}Ca + $^{124,(116)}$Sn

Large multinucleon transfer cross sections were measured for ^{40}Ca + ^{124}Sn [6] a couple of years ago, as well as, more recently, for ^{40}Ca + ^{96}Zr [7]. A proton-rich projectile (^{40}Ca)

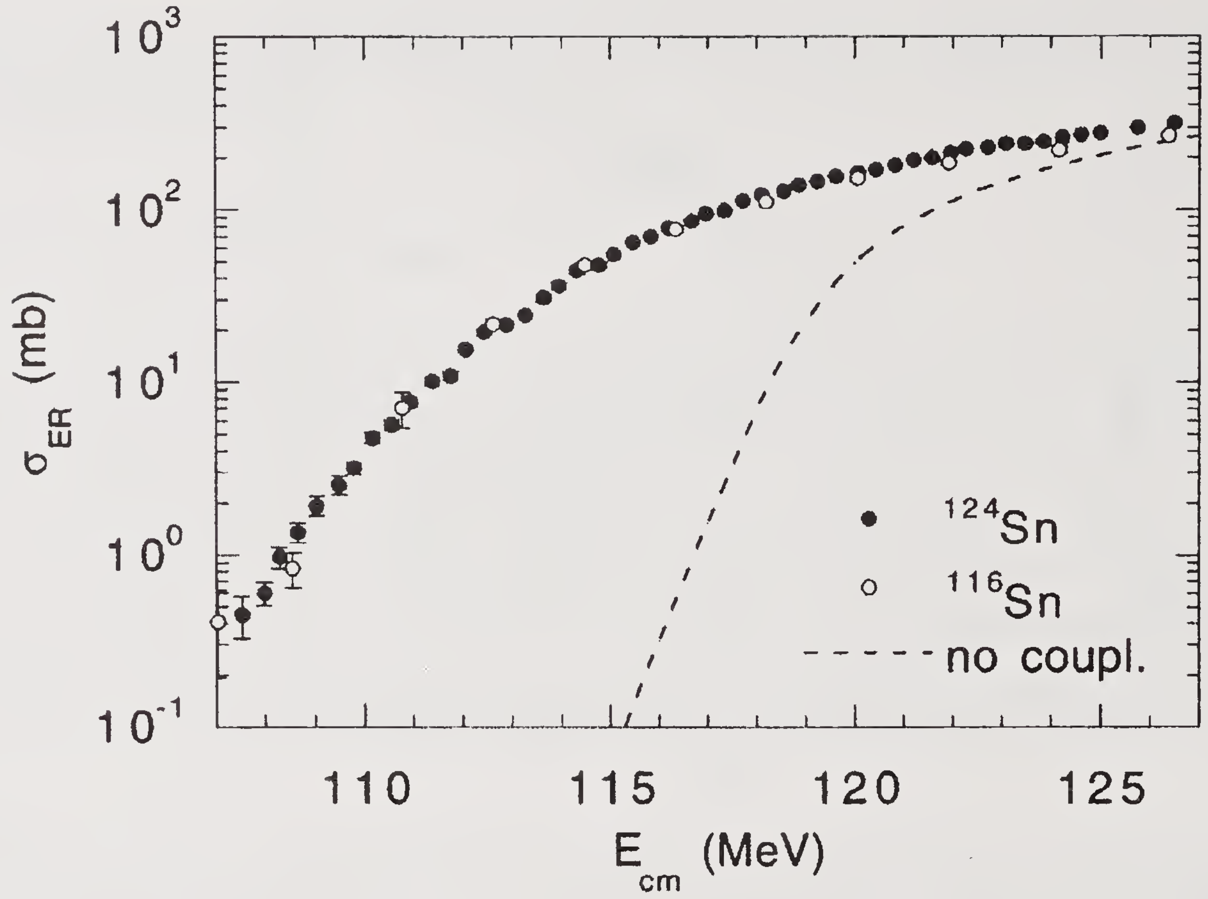

Figure 3. The fusion excitation functions for ^{40}Ca + $^{124,(116)}$Sn.

collides with neutron-rich targets, hence the Q-values for neutron pick-up channels are very positive in both cases, ranging from $\approx +5$ MeV to $\approx +12$ MeV for the transfer of up to 8 neutrons. It is interesting to point out that the angle- and Q-integrated cross sections for each individual transfer channel are very similar in the two systems.

The measurement of fusion-evaporation cross sections of ^{40}Ca + ^{124}Sn was recently performed at LNL, in the relevant energy range near the Coulomb barrier. The resulting evaporation residue (ER) cross sections are plotted in figure 3; since the fusion–fission cross sections are estimated to be very small (only a few mb at the highest energies), the data can be considered total fusion cross sections with little uncertainty. At selected energies, ER yields were also measured for the ^{40}Ca + ^{116}Sn systems. These are reported in figure 3 too, with a small shift of the energy to compensate for the Coulomb barrier difference between the two cases.

The two excitation functions overlap almost perfectly. We know that the nuclear structures of ^{124}Sn and ^{116}Sn are very similar; the Q-values for neutron pick-up in ^{40}Ca + ^{116}Sn are positive ($\approx$ 2–3 MeV), although not so large as in the reaction with ^{124}Sn. One may argue that either such transfer processes do not influence at all the fusion dynamics, or that their effect (if significant) is very similar in the two cases. An analogous situation was found in the study of ^{40}Ar + ^{112,116,122}Sn by Reisdorf *et al* [8]. It is possible, for ^{40}Ca + ^{124}Sn only, to extract the barrier distribution from the data. The case of ^{40}Ca + ^{116}Sn needs a more detailed experimental study, i.e. many more points around and below the barrier.

Since one has very similar Q-values for few- and multi-nucleon transfer channels in ^{40}Ca + ^{96}Zr, ^{124}Sn, it is interesting to compare their behaviour as far as fusion is concerned. Figure 4 shows the excitation functions in a reduced energy scale (top): the sub-barrier cross sections of ^{40}Ca + ^{96}Zr are significantly larger. The two barrier distributions are reported in the lower part of figure 4. As in the case of ^{40}Ca + ^{96}Zr, no defined peak is

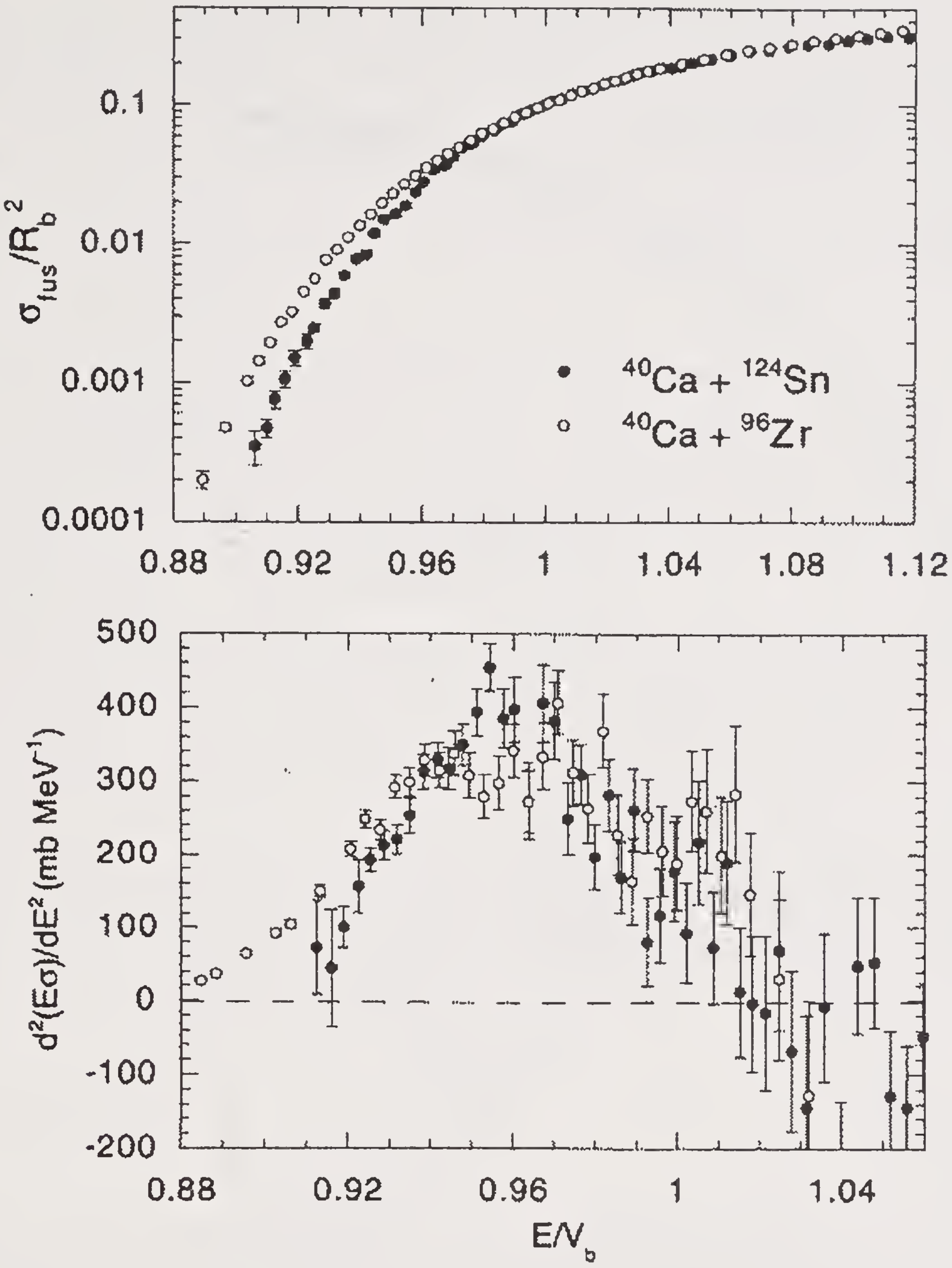

Figure 4. The reduced fusion excitation functions of ^{40}Ca + ^{124}Sn, ^{96}Zr (top), and the corresponding barrier distributions (down).

seen in the distribution for ^{40}Ca + ^{124}Sn and an overall bump-like shape is observed for both systems.

The distribution for ^{40}Ca + ^{96}Zr extends slightly farther down in energy. The underlying reason(s) are not clear at this level, and a consideration of the Q-value and angle-integrated transfer cross sections for the two systems does not help in this respect. Actually the mass and Z distributions of Ca-like ejectiles are very similar in the two systems, as stated above; the yields of corresponding nuclides rarely differ by more than a factor two. Hence, the mechanism leading to larger sub-barrier fusion cross sections in ^{40}Ca + ^{96}Zr might be looked for elsewhere. A possibility, supported by calculations, is the very strong octupole vibration of ^{96}Zr at ~1.8 MeV; the corresponding excitation in ^{124}Sn is much less collective and is found at ~2.6 MeV.

4. Analysis with simplified coupled-channel calculations

Simplified coupled-channels (CC) calculations have been performed for ^{40}Ca + ^{124}Sn with the code CCMPH [9], which allows for multi-phonon and multinucleon transfer modes to

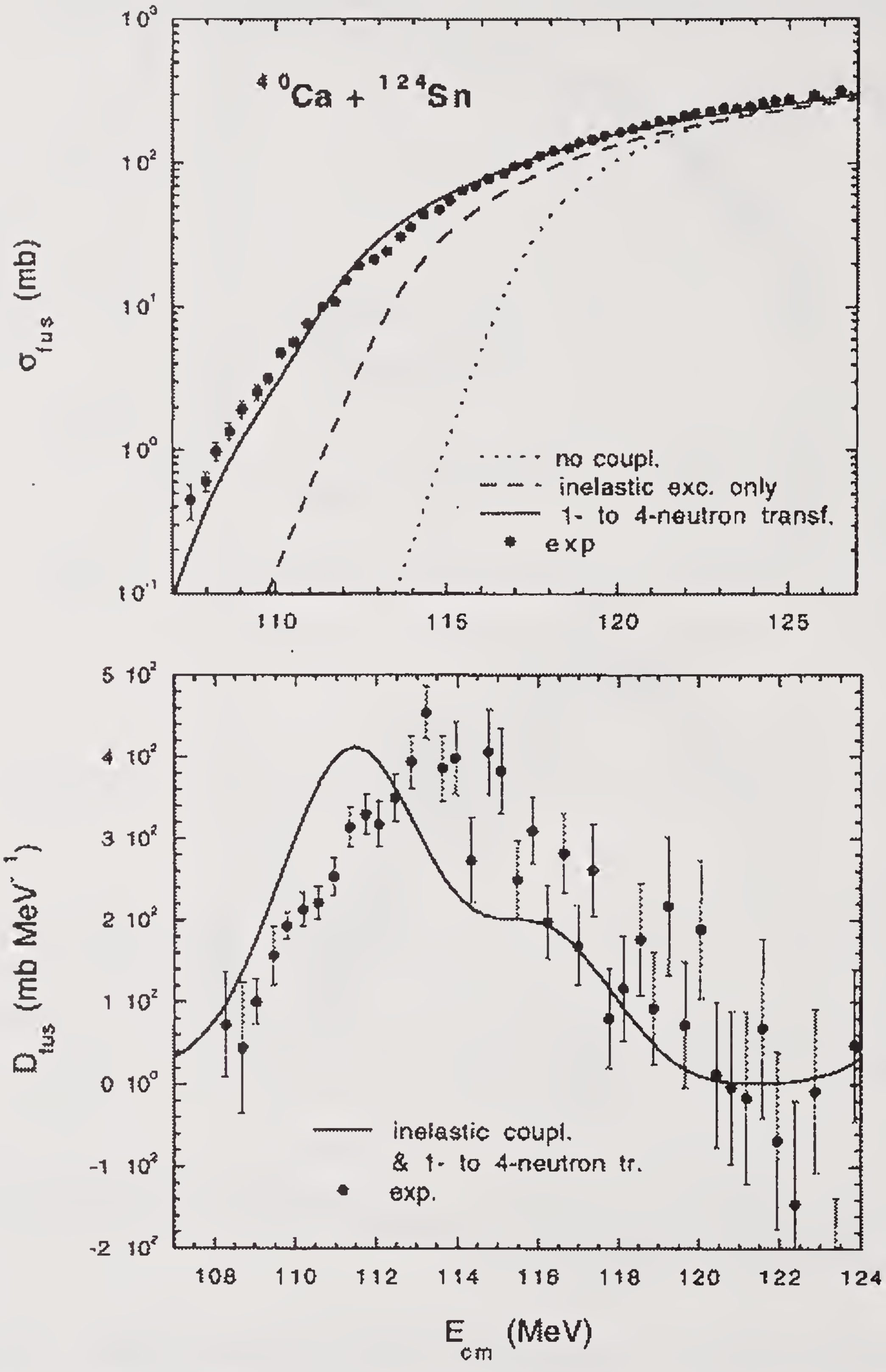

Figure 5. The fusion excitation function of ^{40}Ca + ^{124}Sn, (top), and the corresponding barrier distribution (down), compared with the results of coupled-channel calculations (see text).

be coupled in. As far as inelastic excitations are concerned, the lowest 2^+ and 3^- states of ^{124}Sn have been included, together with the strong octupole vibration of ^{40}Ca, although it lies rather high in energy. The Akyüz–Winther potential has been used, with a slightly larger diffusivity $a = 0.76$ fm. The mutual excitations of the Ca and Sn states have been considered too.

Sequential transfer of up to four neutrons has been included in the coupling scheme. The form factors for single-neutron pick-up are the same as used in ref. [6], which lead to a good agreement with the experimental transfer cross section and Q-value distribution. They were derived following Quesada *et al* [10] and include a set of transitions from six shell model states in ^{123}Sn ($1h_{11/2}, 2d_{3/2}, 3s_{1/2}, 2d_{5/2}, 1g_{7/2}, 1g_{9/2}$) to four states in

^{41}Ca $(1f_{5/2}, 2p_{1/2}, 2p_{3/2}, 1f_{7/2})$. Here the single form factors have been combined into one effective form factor, as a quadratic sum of the individual ones. This effective one-neutron form factor F_{1n} is close to 3 MeV at the barrier radius. For the $2n$, $3n$ and $4n$ pick-up channels, whose Q_{gs} are lage and positive, the prescription of Broglia *et al* [11] has been used, which leads to $F_{2n} = \sqrt{2} \times 3/2 F_{1n}$, $F_{3n} = \sqrt{3} \times 13/6 F_{1n}$ and $F_{4n} = 73/12 F_{1n}$. In the CCMPH calculations, zero Q-values (close to the optimum Q-values) were attributed to all of these channels.

The results of the CCMPH calculations are shown in figure 5. The fusion excitation function is in good agreement with the data, and it shows that large enhancements are produced both by inelastic excitations and by neutron transfer channels; the role of proton stripping channels should be investigated as well. However, the calculated barrier distribution looks like shifted in energy with respect to the 'experimental' one, although having an overall correct shape.

We see, anyway, that the complete and detailed sets of data obtained for ^{40}Ca + ^{124}Sn (and for other few cases as well) are suitable for a unified treatment of all the reaction channels. It seems particulary interesting to me the use of form factors that fit the experimental transfer data, for the coupled-channel calculation of fusion at low energies.

The simplified CC approach we have followed in the analysis of the present ^{40}Ca + ^{124}Sn system suffers from various approximations, and hence no defined conclusion should be drawn out of it. But I feel it is a step in the right direction, in order to better understand the dynamics of low-energy fusion.

Acknowledgements

The author is pleased to acknowledge the collaboration with his experimental colleagues D Ackermann, S Beghini, L Corradi, C J Lin, G Montagnoli, F Scarlassara, G F Segato and L F Zheng. He is also very grateful to G Pollarolo and N Rowley for many fruitful discussions.

References

[1] N Rowley, G R Satchler and P H Stelson, *Phys. Lett.* **B254**, 25 (1991)
[2] Proc. Int. Workshop on Heavy-Ion Collisions at Near-Barrier Energies, South Durras, NSW, Australia, March 17–21, 1997, *J. Phys. G: Nucl. Part. Phys.* **23** (1997)
[3] M Dasgupta, D J Hinde, N Rowley and A M Stefanini, *Ann. Rev. Nucl. Part. Sci.* (1998) in press
[4] A M Stefanini, D Ackermann, L Corradi, D R Napoli, C Petrache, P Spolaore, P Bednarczyk, H Q Zhang, S Beghini, G Montagnoli, L Müller, F Scarlassara, G F Segato, F Soramel and N Rowley, *Phys. Rev. Lett.* **74**, 864 (1995)
[5] H Timmers, D Ackermann, S Beghini, L Corradi, H J He, G Montagnoli, F Scarlassara, A M Stefanini and N Rowley, *Nucl. Phys.* **A633**, 421 (1998)
[6] L Corradi, J H He, D Ackermann, A M Stefanini, A Pisent, S Beghini, G Montagnoli, F Scarlassara, G F Segato, G Pollarolo, C H Dasso and A Winther, *Phys. Rev.* **C54**, 201 (1996)
[7] G Montagnoli, S Beghini, F Scarlassara, G F Segato, L Corradi, C J Lin and A M Stefanini, *J. Phys. G: Nucl. Part. Phys.* **23**, 1431 (1997)
[8] W Reisdorf, F P Hessberger, K D Hildenbrand, S Hofmann, G Münzenberg, K-H Schmidt, J H R Schneider, K Sümmerer, G Wirth, J V Kratz and K Schlitt, *Nucl. Phys.* **A438**, 212 (1985)

[9] M Dasgupta *et al*, *Nucl. Phys.* **A539**, 351 (1992); ANU Int. Rep. ANU P/1333 (1997)

[10] J M Quesada, G Pollarolo, R A Broglia and A Winther, *Nucl. Phys.* **A442**, 381 (1985)

[11] R A Broglia, C H Dasso, G Pollarolo and A Winther, *Phys. Rep.* **48**, 378 (1978)

Exploiting barrier distributions to investigate breakup effects in the fusion of ^{9}Be + ^{208}Pb

M DASGUPTA[1], D J HINDE[1], R D BUTT[1], A C BERRIMAN[1], C R MORTON[1],
J O NEWTON[1] and K HAGINO[2]
[1]Department of Nuclear Physics, Research School of Physical Sciences and Engineering, Australian National University, Canberra, ACT 0200, Australia
[2]Institute for Nuclear Theory, Department of Physics, University of Washington, Seattle, WA98915, USA

Abstract. The availability of precisely measured fusion excitation functions have allowed the determination of experimental fusion barrier distributions. This concept is utilised in ^{9}Be + ^{208}Pb reaction, to reliably predict the expected complete fusion cross-sections. However, the measured cross-sections are found to be only 68% of those predicted. The large cross-sections observed for incomplete fusion products support the interpretation that this suppression of fusion is caused by ^{9}Be breaking up into charged fragments before reaching the fusion barrier.

Keywords. Fusion; barrier distribution; breakup; incomplete fusion.

PACS No. 25.70.Jj

1. Introduction

It is now well accepted that fusion near the Coulomb barrier is strongly affected [1,2] by intrinsic degrees of freedom of the interacting nuclei, whose coupling with the relative motion effectively causes a splitting in energy of the single, uncoupled fusion barrier. This gives rise to a distribution of barrier heights [3], some higher and some lower in energy than the uncoupled barrier. The experimental effort towards obtaining precisely measured [4–8] fusion cross-sections has been extremely successful, with one of the main outcomes being the ability to extract an *experimental* fusion barrier distribution [9]. This, combined with improved theoretical models has led to a better, in some cases quantitative, understanding of the effects induced by target and projectile structure, as discussed by Rowley [10], Stefanini [11] and others [12] during this workshop.

We are now at a stage where we can start to exploit our knowledge of the near-barrier fusion process in order to explain properties of the compound nucleus and its decay. For example, this has helped in understanding the strong enhancement of the superdeformed band population in ^{135}Nd [13]. The renewed confidence in calculations of sub-barrier fusion angular momentum distributions has led to explanations [14] for the anomalously large fission fragment anisotropies observed in reactions with actinide nuclei in terms of the dynamics of the fusion process, rather than in terms of flaws in fusion models. Knowledge of the fusion process with stable beams is also the first step towards understanding fusion with unstable nuclei and it is this aspect that will be discussed in this paper.

The advent of radioactive beam facilities has enabled the study of unstable neutron-rich nuclei which have very weakly bound neutrons and exhibit characteristic features such as a neutron halo [15] extending to large radii, and a low energy threshold for breakup. The extended nuclear matter distribution is expected to lead [16] to a lower fusion barrier, and thus to an enhancement in fusion cross-sections [17] compared to those for tightly bound nuclei. The effect of couplings to channels which act as doorways to breakup is, however, controversial [18–21]. Any coupling will enhance the sub-barrier cross-sections, whereas breakup may result in capture of only a part of the projectile, thus suppressing complete fusion. Model predictions [18–20], however, differ in the relative magnitudes of enhancement and suppression. To investigate these aspects, fusion excitation functions for ^{9,11}Be + ^{238}U [22] and ^{9,10,11}Be + ^{209}Bi [23] were measured at energies around the barrier. The reactions with the stable ^{9}Be were included for comparison. The fusion cross-sections for ^{10,11}Be + ^{209}Bi at energies near and below the barrier were found to be similar to those for ^{9}Be, while above the barrier the ^{9}Be induced reaction gave the lowest fusion yield. It is not obvious whether this is due to differing enhancement or suppression for the stable and unstable projectiles.

To investigate the effect on fusion of couplings specific to unstable neutron-rich nuclei, it is necessary to reliably predict the cross-sections expected in their absence. Thus, in the above cases, definitive conclusions are difficult unless fusion with ^{9}Be is well understood. This requires knowledge of the energy of the average fusion barrier, and information on the couplings. Both these can be obtained from the distribution of fusion barriers extracted from a precisely measured fusion excitation function. The shape of the experimental barrier distribution is indicative of the couplings present and its centroid gives the average barrier position. Precise fusion excitation function measurements [24] for the reaction ^{9}Be + ^{208}Pb, with the aim of extracting the barrier distribution, were therefore made at the Australian National University. The experimental details are described in the next section. Section 3 discusses the identification of the products of complete fusion, followed by §4 where the result of the experimental determination of average barrier energy, along with the comparison with coupled channels calculations are presented. Section 5 presents the results of the incomplete fusion measurements, followed by a summary in §6.

2. The experiment

The experiments were performed with pulsed ^{9}Be beams (1ns on, 1μs off) in the energy range 35.0–51.0 MeV in 1 MeV steps, from the 14UD tandem accelerator at the Australian National University. Targets were of enriched ^{208}PbS, 340–400 μg/cm^2 in thickness, evaporated onto 15 μg/cm^2 C foils. Two monitor detectors, placed above and below the beam axis, measured the elastically scattered beam particles for normalization purposes. Recoiling heavy reaction products were stopped in aluminium catcher foils of thickness 360 μg/cm^2, placed immediately behind the target. The cross-sections for the reaction products or the evaporation residues were determined by measuring the α-particles emitted during their subsequent decay. The products were identified by their distinctive α-energies and half-lives (270 ns to 138 days). Alpha particles from short-lived activity (half-life $T_{1/2} \leq 26$ s) were measured *in situ* between the beam bursts, using an annular silicon surface barrier detector placed at a mean angle of 174° to the beam direction. These were measured at all beam energies using the same target. This eliminated uncertainties in the beam energy difference between data points which would result from the use of different targets. Fusion evaporation residues at energies higher than 47 MeV are long-lived ($T_{1/2} \geq$ 24 min). Their cross-sections were determined by using an un-irradiated target and catcher at each energy. Alpha particles from these products were measured using a silicon surface barrier detector situated below the annular counter, such that the target and catcher could be placed at a close geometry to the detector after the irradiation. The relative solid angles of the two detectors were determined using the $T_{1/2} =$ 24 min ^{212}Rn activity.

Fission following fusion was measured during the irradiations using two large area position sensitive multi-wire proportional counters (MWPCs), centred at 45° and −135° to the beam direction. Absolute cross-sections for evaporation residues and fission were determined by performing calibrations at sub-barrier energies in which elastically-scattered projectiles were detected in the two monitor detectors, the annular detector and the backward-angle MWPC.

3. Identification of the products of complete fusion

The compound nucleus ^{217}Rn formed following complete fusion of ^{9}Be with ^{208}Pb cools mainly by neutron evaporation. The measured cross-sections for $2n$, $3n$, $4n$ and $5n$ evaporation residues are shown in figure 1a. No proton evaporation residues were observed. In addition to the α-particles from the decay of Rn nuclei, α-particles from the decay of ^{210,211}Po and ^{212}Po nuclei were also observed as shown by hollow points and filled diamonds respectively in figure 1b. Po nuclei are formed as daughters of the Rn nuclei following their α-decay. However, the observed Po yields are much greater than expected from the Rn yields. The filled points show the ^{210,211,212}Po yields obtained after subtraction of the component resulting from the decay of the Po nuclei, formed as daughters of the Rn nuclei. The non-zero values of the Po yields are a clear indication that there is also a direct population mechanism. In principle the Po nuclei could originate from complete fusion followed by αxn evaporation. However the shapes of the excitation functions for these nuclei are distinctly different from those in figure 1a, and are not typical of fusion-evaporation.

To investigate the origin of the Po yield, the same compound nucleus ^{217}Rn was formed at similar excitation energies in the reaction ^{13}C + ^{204}Hg. The ^{211,212}Po α-decays, to which the measurement was most sensitive, had cross-sections of <5 mb, compared with a total of ~160 mb for the ^{9}Be + ^{208}Pb reaction. Furthermore, the fusion cross-sections determined from the sum of the xn evaporation and fission cross-sections agreed with the predictions of a coupled channels calculation and the Bass model [25], indicating that the xn evaporation yield essentially exhausts the total evaporation residue cross-section. Thus, the direct Po production observed in the ^{9}Be reaction cannot be due to complete fusion. It is attributed to incomplete fusion, and will be discussed in §5. The observed fission cross-sections were attributed to complete fusion of ^{9}Be + ^{208}Pb, since fission following incomplete fusion should be negligible due to the lower angular momentum and excitation energy brought in, and the higher fission barriers of the resulting compound nuclei.

Thus, the cross-section for complete fusion, defined as the capture of all the charge of the ^{9}Be projectile, was obtained by summing the Rn xn evaporation residue cross-sections and the fission cross-section at each energy.

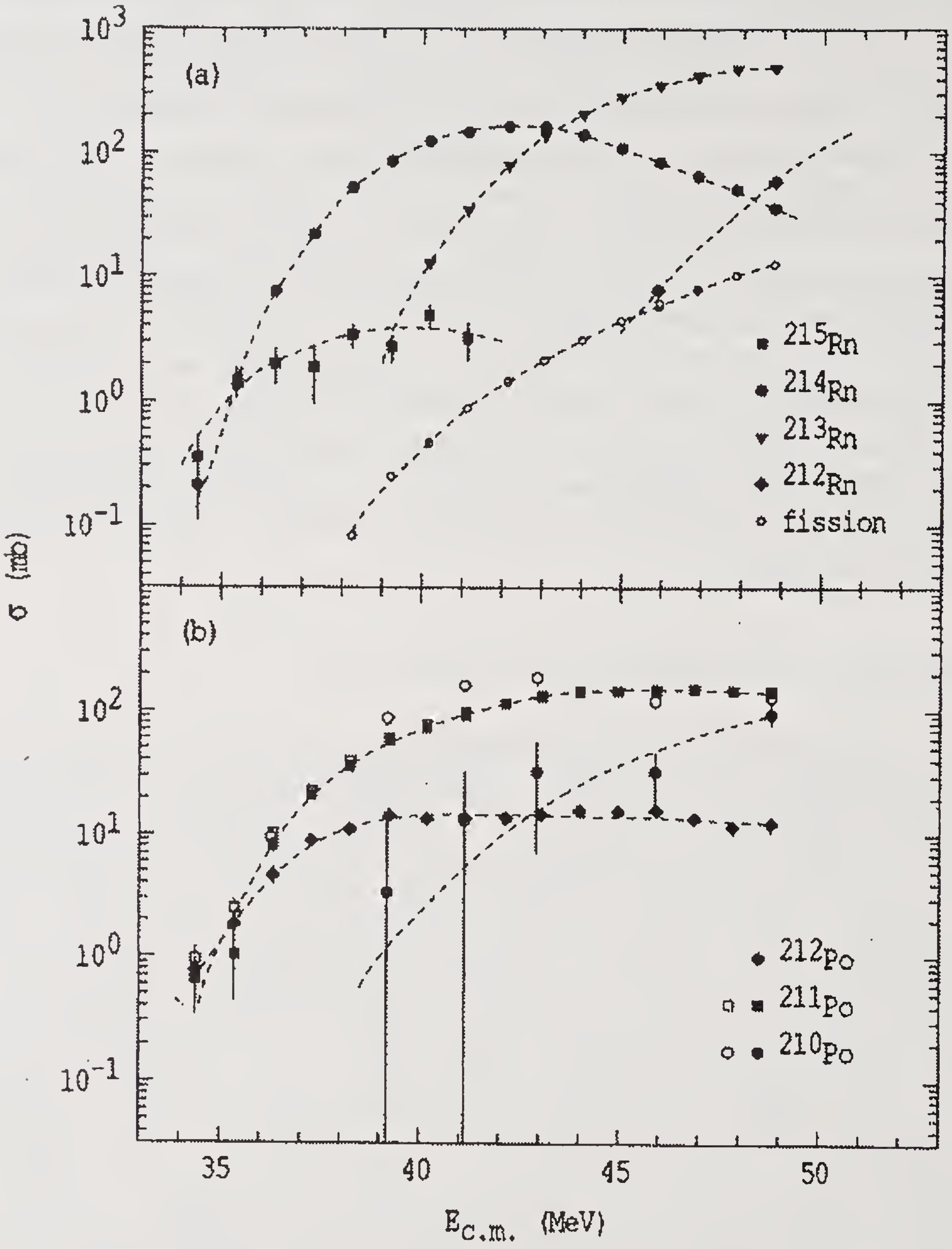

Figure 1. (**a**) The measured cross-sections for fission and the production of Rn isotopes. (**b**) The total (hollow points) and the direct (solid points) production of the Po isotopes as indicated. The dashed lines guide the eye.

4. Determination of the barrier height and comparison with calculations

The excitation function for complete fusion and the experimental barrier distribution $\mathrm{d}^2(E\sigma_{\mathrm{fus}})/\mathrm{d}E^2$ are shown by the filled circles in figure 2a and 2b, respectively. The barrier distribution has been evaluated using a point difference formula [6] with a c.m. energy step of 1.92 MeV. The average barrier position obtained from the experimental barrier distribution is 38.3±0.6 MeV. To predict the fusion cross-sections expected from the measured barrier distribution, realistic coupled channels calculations [26] were performed using a Woods–Saxon form for the nuclear potential chosen such that the average barrier energy of these calculations matched that measured. Couplings to the $5/2^-$ and $7/2^-$ states

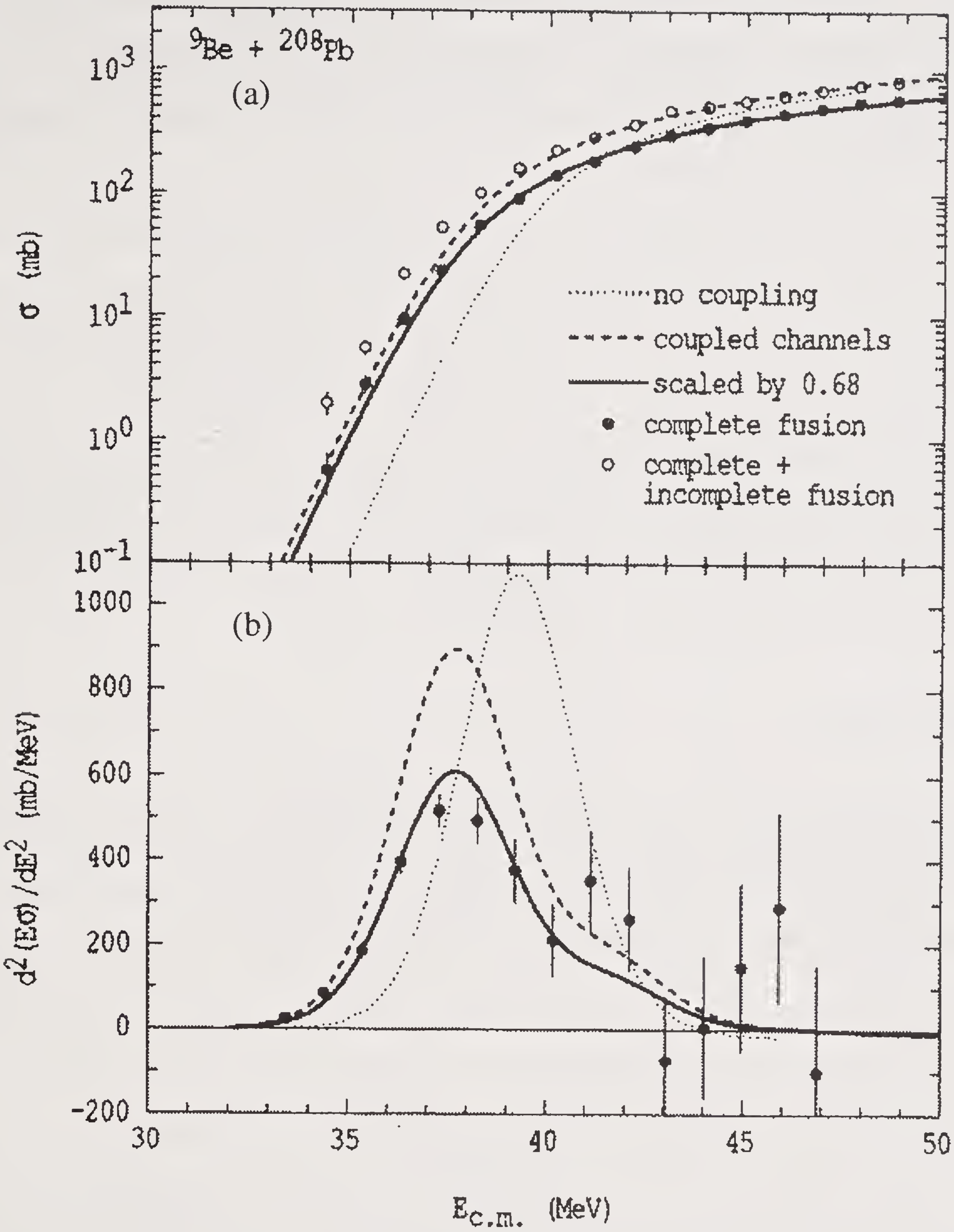

Figure 2. (**a**) The excitation function for complete fusion (filled circles) and (**b**) the barrier distribution for the reaction ^{9}Be + ^{208}Pb. The dotted line shows the calculation assuming a single barrier. The dashed line is the result of a coupled channels calculation (see text) which ignores breakup effects. The full line is the same calculation scaled by 0.68. The sum of measured complete and incomplete fusion cross-sections is given by the hollow circles.

of the $K^{\pi} = 3/2^{-}$ ground-state rotational band [27] in ^{9}Be, and to the 3^{-}, 5^{-} and the double octupole-phonon [28,29] states in ^{208}Pb, were included. Coupling strengths were obtained from the experimental ground state quadrupole moment [27] of ^{9}Be, and experimental deformation lengths [30] for one-phonon states in ^{208}Pb. Couplings to the double octupole-phonon states in ^{208}Pb were calculated in the harmonic limit.

The results of these calculations are shown in figure 2a and 2b by the dashed lines. They reproduce satisfactorily the asymmetric shape of the measured barrier distribution. The area under the calculated distribution is a measure of the geometrical cross-section πR^{2}, where R is the fusion barrier radius. The measured distribution shows a much smaller area than the calculation, despite the barrier energies being in agreement. This disagreement is necessarily reflected in the cross-sections as well, where the calculated values are considerably larger than those measured. This is in contrast to fusion with tightly bound projectiles [4–8], such as ^{16}O and ^{19}F, where calculations which correctly reproduce the average barrier position and the shape of the barrier distribution, and hence has the right potential parameters and couplings, give an extremely good fit to the cross-sections. The disagreement for ^{9}Be + ^{208}Pb, even though the barrier energies are correctly reproduced, suggests the presence of a mechanism hindering fusion. Agreement can be achieved if the calculated fusion cross-sections are scaled by 0.68, resulting in the full lines in figure 2a and 2b. This scaling factor will be model dependent at the lowest energies, as the calculations are sensitive to the types of coupling and their strength. However, at energies around and above the average barrier, the scaling factor is more robust, since changes in the couplings or potential shape within the constraints of the measured barrier distribution, does affect the calculations significantly. The suppression factor of 0.68 has an uncertainty of ±0.07 arising from the uncertainty in the mean barrier energy.

5. Incomplete fusion

The suppression of complete fusion discussed above, may be correlated with the large yields of ^{210,211,212}Po which, as mentioned in §3, are not the products of complete fusion. These can be formed if ^{9}Be breaks up into ^{4,5}He or two α particles and a neutron, and one of the charged fragments is captured by the ^{208}Pb. If all the fragments are captured then this process cannot be distinguished experimentally from fusion without breakup, and is included in the complete fusion yield. Incomplete fusion products following the breakup of ^{9}Be giving ^{6,7,8}Li were not observed; they are unfavoured due to large negative Q values. The large cross-sections for incomplete fusion, approximately half of those for complete fusion, demonstrate that ^{9}Be has a substantial probability of breaking up into charged fragments. The sum of the complete and incomplete fusion cross-sections is indicated by the hollow circles in figure 2a. It is interesting to note that they match the predictions of the un-scaled coupled channels fusion calculation, suggesting a direct relationship between the flux lost from fusion and the incomplete fusion yields. However, such a simple direct comparison is not strictly possible, since the cross-sections for incomplete fusion may include contributions from higher partial waves which may not have led to complete fusion.

The suppression of fusion observed in this experiment can be attributed to a reduction of flux at the fusion barrier radius due to breakup of the ^{9}Be projectiles. It would be interesting to investigate whether the breakup is dominated by the long range Coulomb or the short range nuclear interaction. Comparison of the present results with those existing for lighter targets [31–33] may give additional insights.

6. Discussion and summary

In studies of breakup effects for neutron-rich unstable nuclei, attention has been on the neutron separation energy [34], which for ^{11}Be is 0.50 MeV, compared with 1.67 MeV for ^{9}Be. This led to the expectation that breakup effects in ^{11}Be induced reactions would affect (suppress or enhance depending on the theoretical approach) fusion more strongly compared with those induced by ^{9}Be. However, the experimental data could not be explained on this basis. The present experiment demonstrates that breakup into charged fragments affects fusion very significantly. The two most favourable charged fragmentation channels for ^{9,11}Be are :

$$\begin{aligned} {}^{9}\mathrm{Be} &\rightarrow n + 2\alpha;\ \mathrm{Q} = -1.57\ \mathrm{MeV} \\ &\quad \alpha + {}^{5}\mathrm{He};\ \mathrm{Q} = -2.47\ \mathrm{MeV} \\ {}^{11}\mathrm{Be} &\rightarrow \alpha + {}^{6}\mathrm{He} + n;\ \mathrm{Q} = -7.91\ \mathrm{MeV} \\ &\quad \alpha + \alpha + 3n;\ \mathrm{Q} = -8.89\ \mathrm{MeV}, \end{aligned}$$

making ^{9}Be more unstable in this regard than ^{11}Be. Reactions with ^{9}Be therefore offer an excellent opportunity to study breakup and its effect on fusion, but they should not be taken as a stable standard against which to judge the breakup effects of unstable nuclei.

In summary, precise complete and incomplete fusion cross-sections have been measured [24] for ^{9}Be + ^{208}Pb near the Coulomb barrier. The barrier distribution for complete fusion shows conclusively that complete fusion of ^{9}Be is suppressed compared with the fusion of more tightly bound nuclei. The calculated fusion cross-sections need to be scaled by a factor 0.68 ± 0.07 in order to obtain a consistent representation of the measured fusion excitation function and barrier distribution. The loss of flux at the fusion barrier implied by this result can be related to the observed large cross-sections for Po nuclei, demonstrating that ^{9}Be has a large probability of breaking up into two helium nuclei, which suppresses the complete fusion yield. These measurements, in conjunction with breakup cross-sections and elastic scattering data, should encourage a complete theoretical description of fusion and breakup.

References

[1] M Beckerman, *Rep. Prog. Phys.* **51**, 1047 (1988) and references therein
[2] M Dasgupta *et al*, *Annu. Rev. Nucl. Part. Sci.* (in Press)
[3] C H Dasso *et al*, *Nucl. Phys.* **A405**, 381 (1982); **A407**, 221 (1983)
[4] J X Wei *et al*, *Phys. Rev. Lett.* **67**, 3368 (1991)
[5] C R Morton *et al*, *Phys. Rev. Lett.* **72**, 4074 (1994)
[6] J R Leigh *et al*, *Phys. Rev.* **C52**, 3151 (1995)
[7] A M Stefanini *et al*, *Phys. Rev. Lett.* **74**, 864 (1995)
[8] J D Bierman *et al*, *Phys. Rev. Lett.* **76**, 1587 (1996); *Phys. Rev.* **C54**, 3068 (1996)
[9] N Rowley *et al*, *Phys. Lett.* **B254**, 25 (1991)
[10] N Rowley, *Proc. Int. Workshop on Rare Nuclear Processes, November 1998, New Delhi* (to be published) (1999)
[11] A M Stefanini, *Proc. Int. Workshop on Rare nuclear Processes, November 1998, New Delhi* (to be published) (1999)
[12] Lagy T Baby *et al*, *Int. Workshop on Rare Nuclear Processes, November 1998, New Delhi* p2
[13] J M Nieminen *et al*, *Phys. Rev. Lett.* **78**, 3832 (1997)
[14] D J Hinde *et al*, *Phys. Rev. Lett.* **74**, 1295 (1995)
[15] P G Hansen *et al*, *Annu. Rev. Nucl. Part. Sci.* **45**, 591 (1995)
[16] C H Dasso and R Donangelo, *Phys. Lett.* **B276**, 1 (1991)
[17] N Takigawa and H Sagawa, *Phys. Lett.* **B265**, 23 (1991)

[18] M S Hussein *et al*, *Phys. Rev.* **C46**, 377 (1992); *Phys. Rev. Lett.* **72**, 2693 (1994); *Nucl. Phys.* **A588**, 85c (1995)
[19] C H Dasso *et al*, *Phys. Rev.* **C50**, R12 (1994); *Nucl. Phys.* **A597**, 473 (1996)
[20] N Takigawa *et al*, *Phys. Rev.* **C47**, R2470 (1993)
[21] C Signorini *et al*, *Eur. Phys. J.* **A2**, 227 (1998)
[22] V Fekou–Youimbi *et al*, *Nucl. Phys.* **A583**, 811c (1995)
[23] A Yoshida *et al*, *Phys. Lett.* **B389**, 457 (1996)
[24] M Dasgupta *et al*, *Phys. Rev. Lett.* (In press)
[25] R Bass, *Phys. Rev. Lett.* **39**, 265 (1977)
[26] K Hagino *et al*, *Phys. Rev. Lett.* **79**, 2014 (1997)
[27] J P Glickman *et al*, *Phys. Rev.* **C43**, 1740 (1991)
[28] Minfang Yeh *et al*, *Phys. Rev. Lett.* **76**, 1208 (1996)
[29] M Dasgupta *et al*, *J. Phys.* **G23**, 1491 (1997)
[30] M J Martin, *Nucl. Data Sheets* **47**, 797 (1986)
[31] J S Eck *et al*, *Phys. Rev.* **C27**, 1807 (1983)
[32] J Takahashi *et al*, *Phys. Rev. Lett.* **78**, 30 (1997)
[33] A Mukerjee and B Dasmahapatra, *Nucl. Phys.* **A614**, 238 (1997)
[34] C Signorini, *J. Phys.* **G23**, 1235 (1997)

Some aspects of heavy ion fusion–fission dynamics

D V SHETTY, R K CHOUDHURY*, B K NAYAK, D M NADKARNI and S S KAPOOR
Nuclear Physics Division, Bhabha Atomic Research Centre, Mumbai 400 085, India
Email: rkc@magnum.barc.ernet.in
*Corresponding author

Abstract. Study of heavy ion induced fusion–fission reactions at near and below barrier energies has attracted a great deal of attention in recent years, due to the observations of anomalous features in the fragment angular distributions for many target–projectile systems. Additionally there are also measurements of the fragment spin distributions and time-scales of the fusion–fission reactions, which have provided important information on the dynamics of these processes. In the present paper, the emphasis would be to highlight some of the recent experimental findings and their implications on the dynamics of the fusion–fission reactions in heavy ion collisions at near and above barrier energies.

Keywords. Heavy ions; fission; spin distribution of fission fragments; K-equilibration.

PACS No. **25.70.Jj**

1. Introduction

Studies of heavy ion induced fusion–fission reactions have provided valuable information on many of the dynamical features underlying these processes. The experimental observations of large scale damping of the collective modes in fission process leading to large dynamical delays in fission decay have led to extensive studies earlier in this field [1–4]. Recently, there have been observations of anomalous anisotropies in the angular distributions of the fission fragments in comparison to the standard saddle point statistical model (SSPSM) predictions in a large number of target-projectile systems. The anomaly is seen to be particularly prominent for heavy ion induced fission reactions using actinides such as Th, Np, U etc. as target nuclei, and many features such as entrance channel mass asymmetry effects at the above barrier energies, peak-like structures and ground state spin effects at sub-barrier energies have been reported. These results suggest the need to invoke new fission modes such as pre-equilibrium fission, quasi-fission etc, in addition to the fusion–fission reactions for these systems even at near barrier energies [5–8]. In a recent review [9], various aspects of the heavy ion fusion–fission reactions dealing with such issues have been discussed.

In pursuant of our earlier investigations on the fission dynamics in these heavy systems, recently we have carried out further work to study the spin distributions of fission fragments in the ^{12}C, ^{16}O, ^{19}F + ^{232}Th and ^{209}Bi reactions [10,11]. The present paper deals with one particular aspect of this work with regard to the fragment emission angle dependence of fragment spins in these systems. This study has convincingly resolved one of the long standing issues that the angular variation of the fragment spin and the fragment angular distribution could not be simultaneously explained within the SSPSM formalism using the same K-distribution [12–14]. From the analysis of the data obtained in the present measurements as well as those available from the literature on the emission angle dependence of the fragment spin, we show that the collective spin modes are suppressed for high K-states in the fission process. The following section gives the experimental details and data analysis procedure. Section 3 contains the discussions of the results and §4 gives the conclusions of the present work.

2. Experimental details and data analysis

The experiments were carried out using ^{12}C, ^{16}O and ^{19}F beams from the 14 MV BARC–TIFR pelletron accelerator at Mumbai. The fission fragments were detected using surface barrier detectors along 90° and 165° to the beam direction. The gamma rays were measured in coincidence with fission fragments with a gamma ray detector array consisting of 15 hexagonal BGO detectors (figure 1). The measured gamma ray multiplicities were analysed to extract the average fission fragment spins for fragment emission along 90° and 165° to the beam. Details of the experimental setup and the analysis procedure have been described in earlier references [10,11]. Figure 2 shows the average values of the fragment spins as a function of bombarding energy for the emission angles of 90° (solid circles) and 165° (hollow circles) with respect to the beam direction for ^{12}C, ^{16}O, ^{19}F + ^{232}Th and ^{209}Bi reactions measured in the present work. The average total fragment spins for fragments emitted along 90° to the beam are observed to be larger than for those emitted along 165° for all the systems. Also the angle dependence is observed to get weaker as one approaches the barrier energy V_{B}.

In the framework of the statistical model, the total fragment spin is given as [12,13]

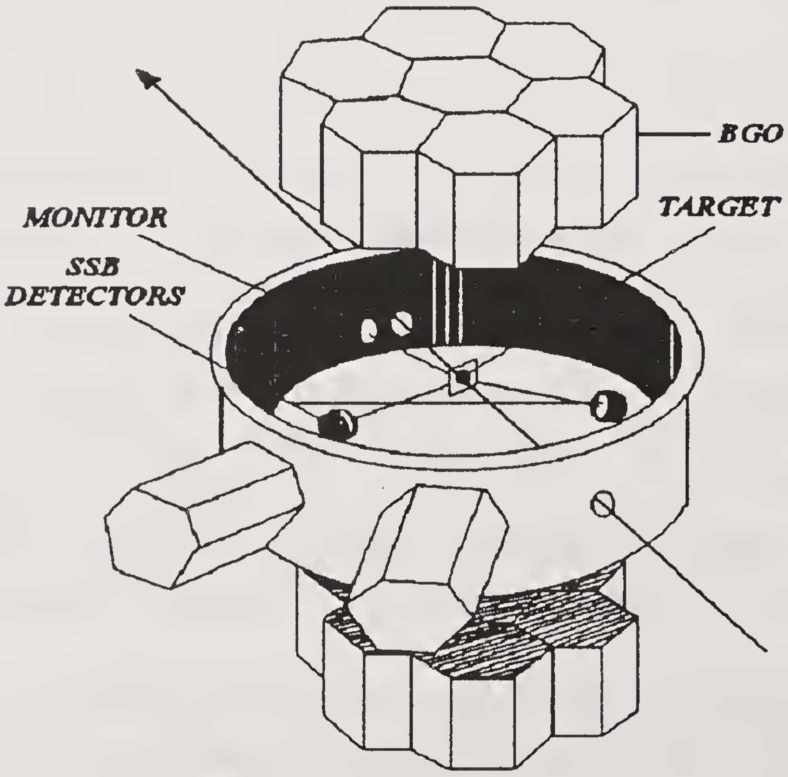

Figure 1. Schematic diagram of the experimental setup.

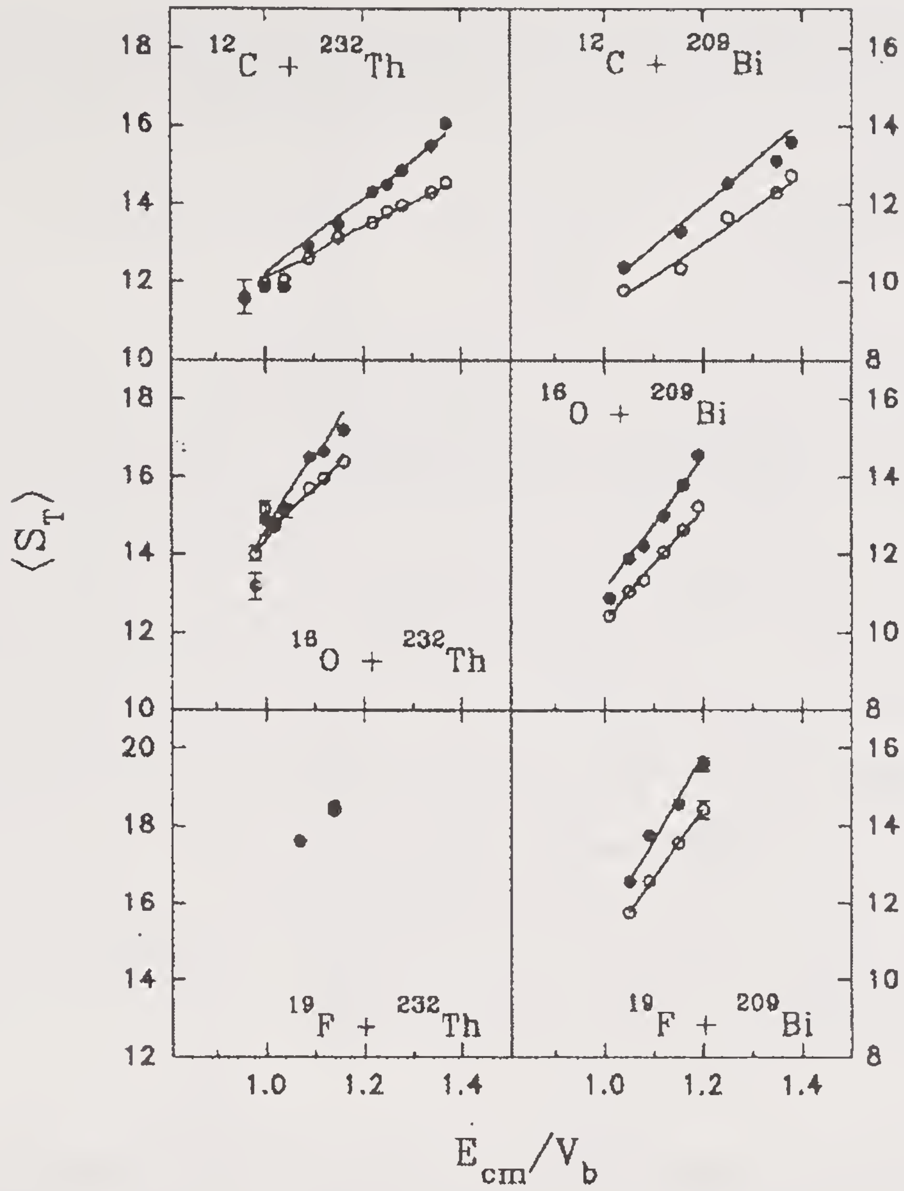

Figure 2. Fragment spin as a function of bombarding energy for emission angles of 90° (solid circle) and 165° (open circle). The solid lines are the modified statistical model calculations as discussed in the text.

$$\langle S_T^2(\theta)\rangle = \langle f^2 I_{CN}^2 + (1-f^2)K^2 + S_{\text{coll}}^2\rangle, \tag{1}$$

where the angular brackets in the above equation correspond to the average over K and I-distributions using the weight factor $W_{M,K}^I \propto \exp(-K^2/2K_0^2)$ and taking the compound nuclear I-distribution. The collective spin S_{coll} is assumed to be angle independent [10,12] and is given as $S_{\text{coll}} \propto A_{CN}^{5/6}T^{1/2} = kA_{CN}^{5/6}T^{1/2}$ where k is a proportionality constant and T is the temperature at the fission saddle point. The emission angle dependence of total fragment spin arises essentially due to the second term, which is governed by the K_0^2 parameter, i.e. the variance of the Gaussian distribution of K-states at the fission saddle point. For fragment emission along $\theta = 165°$ ($\theta \simeq 0°, K \simeq 0$), the above equation reduces to

$$\langle S_T^2(0°)\rangle = \langle f^2 I_{CN}^2 + (kA_{CN}^{5/6}T^{1/2})^2\rangle. \tag{2}$$

As discussed earlier [11–14], eq. (1) under the usual assumption of the constancy of collective spin magnitude S_{coll}, as a function of fragment emission angle fails to provide adequate description of the emission angle dependence of fragment spin. The calculated angular dependence of fragment spin is much too stronger compared to the experimental

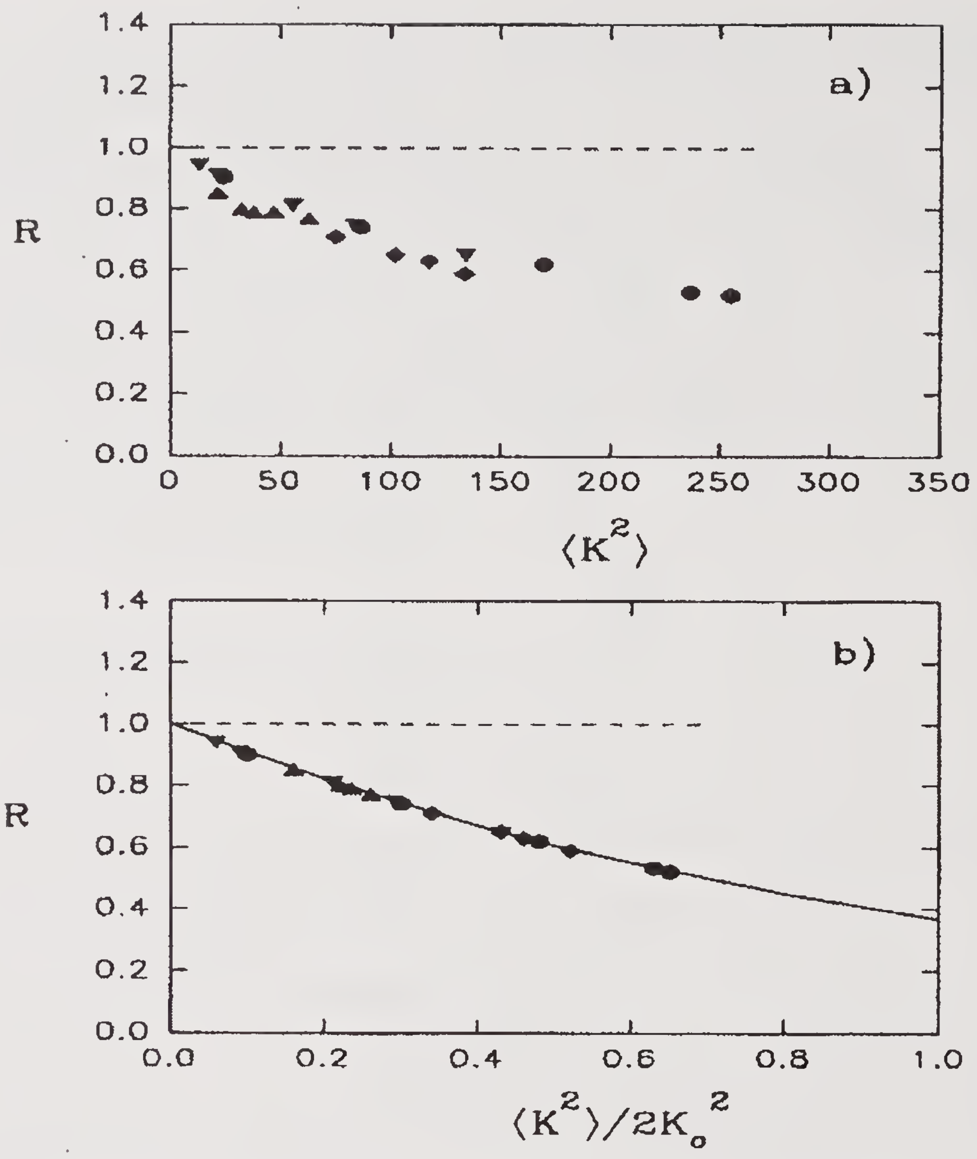

Figure 3. (**a**) The spin suppression factor R as a function of mean square spin in tilting mode $\langle K^2 \rangle$. The various symbols correspond to the different systems studied. (**b**) The spin suppression factor R as a function of the quantity $\langle K^2 \rangle / 2K_0^2$. The dashed lines correspond to the statistical model assumption of angle independent S_{coll}.

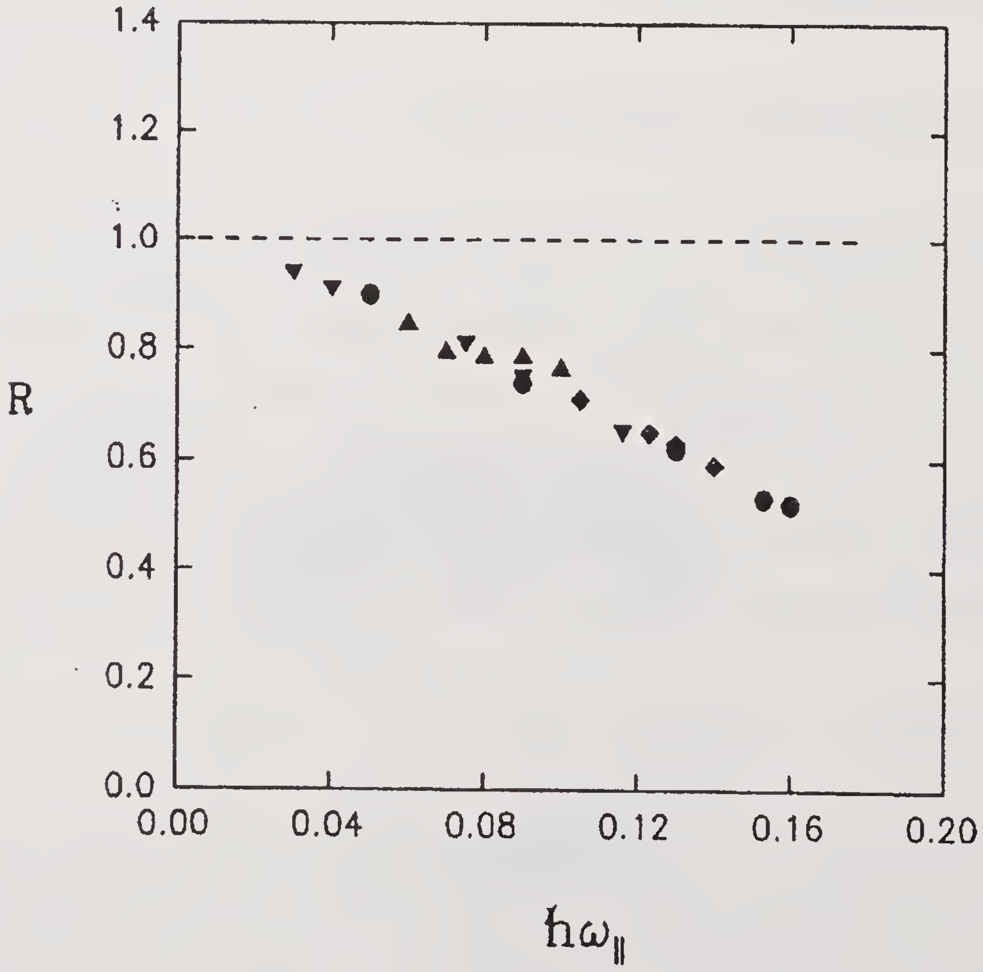

Figure 4. Spin suppression factor R as a function of rotational frequency $\omega_{||}$ of the tilting mode of spin excitation. The dashed line is the statistical model assumption.

results. In what follows, we show that all the available experimental data on the fragment spin versus emission angle require that $S_{\rm coll}$ depends on K, thereby implying that $S_{\rm coll}$ varies with emission angle θ. Under this assumption we write the total fragment spin as

$$\langle S_T^2(\theta)\rangle = \langle f^2 I_{CN}^2 + (1-f^2)K^2 + S_{\rm coll}^2(\theta)\rangle, \tag{3}$$

where $S_{\rm coll}(\theta)$ is angle dependent and can be written as $S_{\rm coll} = kA_{CN}^{5/6}T^{1/2}R(\theta)$, where $kA_{CN}^{5/6}T^{1/2}$ is the collective spin magnitude for fragment emission along 0° or 180° direction and $R(\theta)$ is the angle dependent reduction factor for emission along other angles. Of course, for fragment emission along $\theta \simeq 0°$, eq. (3) goes over to eq. (2).

The data from present measurements as well as from the earlier measurements were analysed as follows. The experimentally determined spins for fragment emission along $\theta = 165°$ direction were first analysed using eq. (2) to obtain the quantities f and k by a two variable least square fit using the above barrier data for all the systems. The average compound nucleus angular momentum $\langle I\rangle$, required for the calculation was taken from the coupled channel calculations which explain the fission excitation functions for all the systems. The spins measured for fragment emission at $\theta = 90°$ to the beam were then analysed using eq. (3). The values of $\langle K^2\rangle$ required in eq. (3) were deduced from the Gaussian K-distribution corresponding to the values of K_0^2, which are consistent with the measured fragment angular anisotropies [5,6,7,15–19] as given by

$$A = 1 + \frac{\langle I^2\rangle}{4K_0^2}. \tag{4}$$

Using the values of $\langle K^2\rangle$ and the deduced values of f and k from eq. (2), the values of $S_{\rm coll}(90°)$ could be deduced that explain the fragment spins at $\theta = 90°$. It was found that the $S_{\rm coll}(90°)$ values are lower than the $S_{\rm coll}(165°)$ values in all cases, as was reported earlier in ref. [11]. The collective spin for perpendicular emission of fragments is, thus, observed to be suppressed in comparison to the forward–backward emission. This suppression factor represented by $R = S_{\rm coll}(90°)/S_{\rm coll}(165°)$ is shown in figure 3(a) as a function of mean square spin in the tilting mode $\langle K^2\rangle$ for the various systems studied. It is seen that there exists a definite correlation between the suppression factor R and $\langle K^2\rangle$ for all the reactions. The correlation is observed to be even more systematic and universal when plotted as a function of the mean square spin in the tilting mode $\langle K^2\rangle$ normalised to the variance K_0^2 of the K-distribution at the saddle point as shown in figure 3(b). The observed correlation also implies that the collective spin is suppressed when the rotational frequency $\omega_{||} = \sqrt{\langle K^2\rangle}/J_{||}$ of the fissioning nuclei along the fission symmetry axis increases, as shown in figure 4. Higher the rotational frequency of the fissioning nucleus along the fission symmetry axis, more is the suppression of the statistical collective modes of the fissioning system. The statistical model predicts a constant magnitude for the value of $S_{\rm coll}$ as shown by the dashed lines in figures 3 and 4.

3. Discussion

From the above observed features in the variation of R with the tilting mode spin, as seen in figure 3, we have assumed a functional dependence of the form (shown by solid curve in figure 3(b)), $S_{\rm coll}(\theta) \propto \exp(-\langle K^2\rangle/2K_0^2)S_{\rm coll}(0°)$ to represent the suppression of

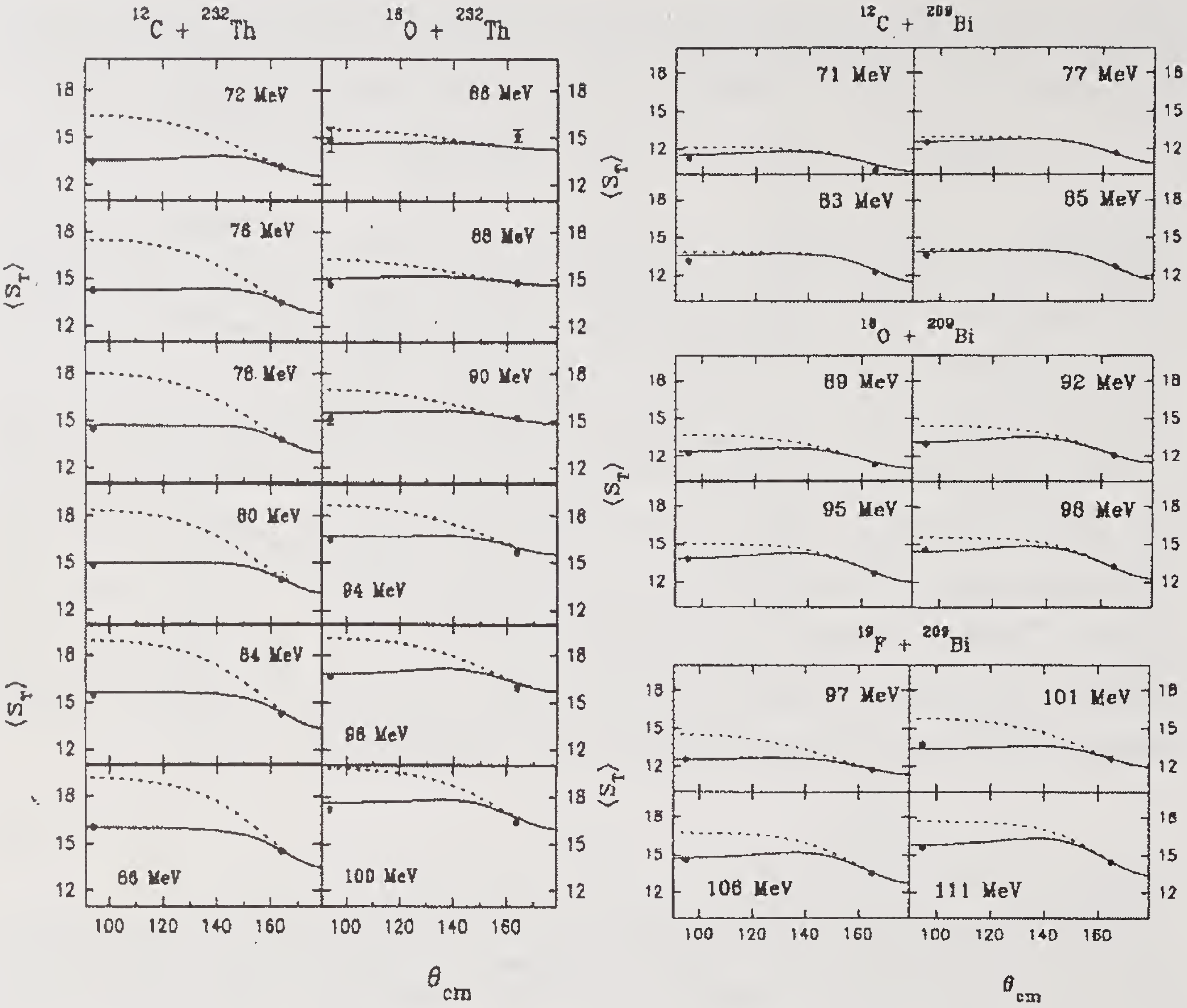

Figure 5. Total fragment spin as a function of emission angle. The dotted curves are the results of the statistical model calculations of Schmitt *et al* [12]. The solid curves correspond to the calculations assuming angle dependence of collective spin.

collective spin modes for high K-states. Using this functional form, we have calculated the average total fragment spin as a function of fragment emission angle for all the systems. The results of the calculations for the total fragment spin for fragment emission along 90° and 165° are shown in figure 2 for all the systems as a function of the bombarding energy. This is also shown as a function of emission angle for several bombarding energies in figure 5. The agreement between the calculated results and the experimental data is seen to be quite good. To test the predicted angle dependence of the present model, we carried out calculations for various other systems in 120 MeV ^{16}O induced reactions for which Schmitt *et al* [12] have carried out measurements of fragment spin at several different fragment emission angles. These results are shown in figure 6. It is seen that the angle dependence of fragment spins can be explained very well with the modified expression given by eq. (3).

The physical reason for the suppression of the collective spin modes for high K-states could be due to the fact that the spins in the individual fragments due to collective spin modes such as wriggling, bending and twisting are oppositely directed and the presence of the spin component due to the tilting mode (for which the individual fragments spins are

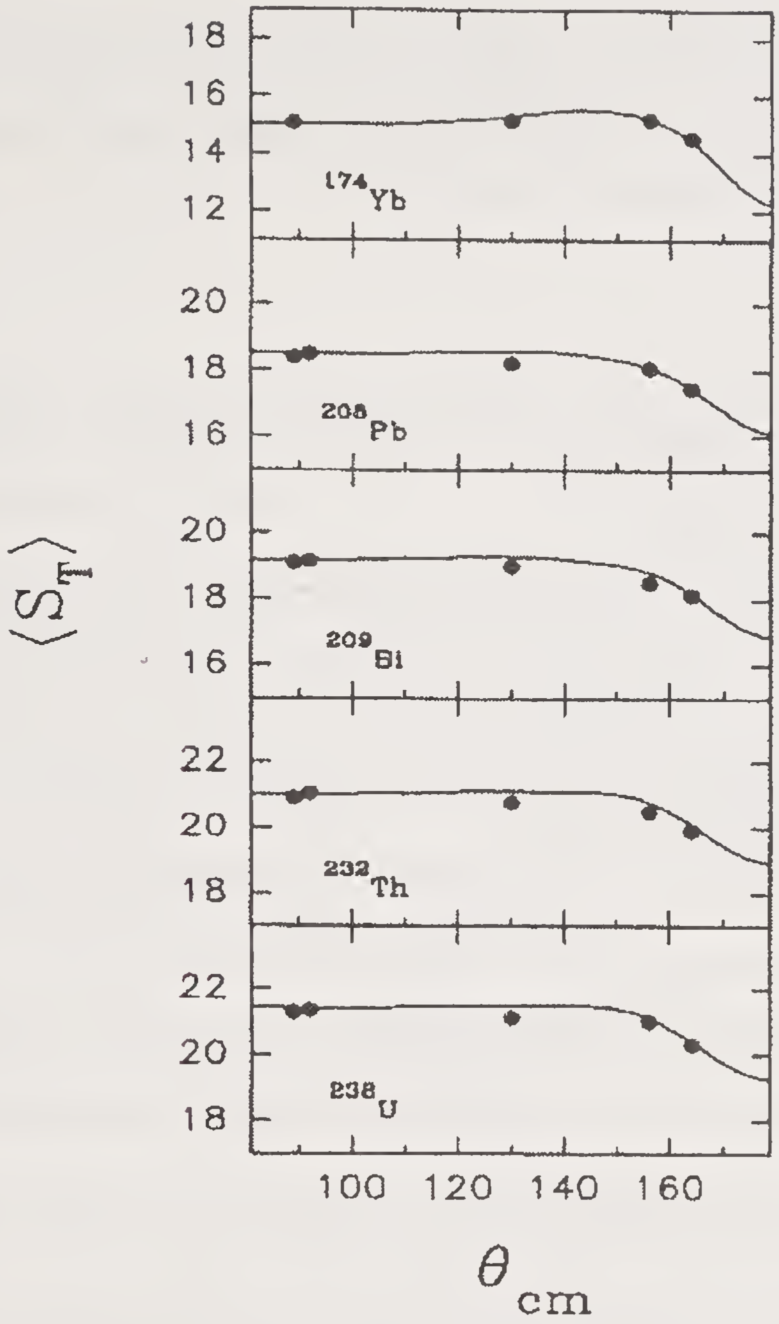

Figure 6. Modified statistical model calculations for 120 MeV ^{16}O induced reactions studied by Schmitt *et al* [12].

aligned in the same direction) results in individual fragments having unequal velocity fields in otherwise equally spinning fragments from the collective modes. This difference in the velocity field between the two fragments may act to retard the spinning motion in the two fragments. The suppression in the collective spin is then expected to depend on the amount of excess energy required to excite the tilting component. For $K = 0$, the collective spin is fully excited and is given by $S_{\text{coll}}(0°)$. For higher K values the collective spin modes are suppressed by an amount given by $S_{\text{coll}}(\theta, K) \propto \exp(-\Delta E/T) S_{\text{coll}}(K = 0)$, where ΔE is the energy required to excite the tilting mode and T is the temperature at the fission saddle point. The above results can thus be represented by means of a suppression factor R as a function of $\Delta E/T$. It thus follows that there exists a universal scaling of the collective spin suppression factor R on $\langle K^2 \rangle / 2K_0^2$ or on the rotational frequency $\omega_{||}$ along the fission axis as shown in figures 3 and 4.

4. Conclusion

The present work has shown that there exists a dynamical coupling of the tilting mode to the collective spin degrees of freedom. It is found that the collective spin modes in heavy ion induced fission reactions are fully excited only when the fragments are emitted along the beam direction ($K \simeq 0$) and there is a suppression of collective spins at other angles corresponding to higher K-states. The suppression of collective spins exhibits a universal behaviour with respect to the $\langle K^2\rangle/2K_0^2$ parameter or the rotational frequency of the fissioning nucleus along the fission symmetry axis.

References

[1] A Gavron *et al*, *Phys. Lett.* **B176**, 312 (1986)
[2] D J Hilscher *et al*, *Phys. Rev. Lett.* **62**, 1099 (1989)
[3] D J Hinde *et al*, *Phys. Rev.* **C45**, 1229 (1992)
[4] A Saxena, A Chatterjee, R K Choudhury, S S Kapoor and D M Nadkarni, *Phys. Rev.* **C49**, 932 (1994)
[5] J C Mein, D J Hinde, M Dasgupta, J R Leigh, J O Newton and H Timmers, *Phys. Rev.* **C55**, R995 (1997)
[6] J P Lestone, A A Sonzogni, M P Kelly and D J Prindle, *Phys. Rev.* **C55**, R16 (1997)
[7] V S Ramamurthy *et al*, *Phys. Rev. Lett.* **65**, 25 (1990)
[8] N Majumdar, P Bhattacharya, D C Biswas, R K Choudhury, D M Nadkarni and A Saxena, *Phys. Rev. Lett.* **77**, 5027 (1996)
[9] R K Choudhury, *Proc. INSA* **A64**, 67 (1998)
[10] D V Shetty, R K Choudhury, B K Nayak, D M Nadkarni and S S Kapoor, *Phys. Rev.* **C56**, 868 (1997)
[11] D V Shetty, R K Choudhury, B K Nayak, D M Nadkarni and S S Kapoor, *Phys. Rev.* **C58**, R616 (1998)
[12] R P Schmitt, L Cooke, H Dejbakhsh, D R Haenni, T Shutt, B K Srivastava and H Utsunomiya, *Nucl. Phys.* **A592**, 130 (1995)
[13] R P Schmitt, D R Haenni, L Cooke, H Dejbakhsh, G Mouchaty, T Shutt and H Utsunomiya, *Nucl. Phys.* **A487**, 370 (1988)
[14] R P Schmitt, L Cooke, H Dejbakhsh, D R Haenni, B K Srivastava, T Shutt and H Utsunomiya, *Proc. Int. Conf. on Fifty Years of Nuclear Fission* (1989) p. 713
[15] L Zuhua, H Zhang, J Xu, Y Qiao, X Qian and C Lin, *Phys. Rev.* **C54**, 761 (1997)
[16] R Vandenbosch *et al*, *Phys. Rev. Lett.* **56**, 1234 (1986)
[17] B B Back *et al*, *Phys. Rev.* **C32**, 195 (1985)
[18] E Vulgaris *et al*, *Phys. Rev.* **C33**, 2017 (1986)
[19] G V Ravi Prasad, A M Samant, A Shrivastava, A Navin, A Chatterjee, P Singh, S Kailas and V S Ramamurthy, *Phys. Rev.* **C57**, 971 (1998)

Transfer measurements for the Ti + Ni systems at near barrier energies

K M VARIER[1], A M VINODKUMAR[2], N V S V PRASAD[3],
P V MADHUSUDHANA RAO[4], D L SASTRY[4], LAGY T BABY[5],
M C RADHAKRISHNA[5], N G PUTTASWAMY[5], J J DAS[6], P SUGATHAN[6],
N MADHAVAN[6], A K SINHA[6] and D O KATARIA[7]
[1]Department of Physics, University of Calicut, Kerala 673 635, India
[2]Legnaro National Laboratory, I.N.F.N., Via Romea 4, Padova 35020, Italy
[3]I.K.S, Katholieke Universiteit Leuven, Belgium
[4]Department of Nuclear Physics, Andhra University, Visakhapatnam 530 003, India
[5]Department of Physics, University of Bangalore, Bangalore 560 056, India
[6]Nuclear Science Centre, P.B. No. 10502, New Delhi 110 067, India
[7]Mullard Space Science Laboratory, Holmbury St. Mary, Dorking, Surrey, RH5 6NT, UK

Abstract. Large enhancements have been observed in the sub-barrier fusion cross sections for Ti + Ni systems in our previous studies. Coupled channel calculations incorporating couplings to 2^+ and 3^- states failed to explain these enhancements completely. A possibilty of transfer channels contributing to the residual enhancements had been suggested. In order to investigate the role of relevant transfer channels, measurements of one- and two-nucleon transfer were carried out for ^{46,48}Ti + ^{64}Ni systems. The present paper gives the results of these studies.

Keywords. Transfer; sub-barrier fusion; kinematic coincidence.

PACS No. 25.70Jj

1. Introduction

Fusion and transfer are two important modes of interaction of heavy ions at energies near the Coulomb barrier. The fusion process at sub-barrier energies has usually been explained on the basis of the one dimensional barrier penetration model. However, in the early 80's, large enhancements in the fusion cross sections were observed by Beckerman and others [1] in the fusion of heavy ions at below barrier energies. This effect has been attributed to the coupling of the fusion channel to various other degrees of freedom. These include inelastic excitations, deformation of the projectile and the target, nucleon transfer etc. Coupled channel calculations including the contributions from the above channels have shown good agreement with the observed fusion enhancements [2]. A number of review articles have been published to date on the subject [3].

Few nucleon transfer reactions in the near and sub-barrier heavy ion collisions constitute a significant part of the reaction cross section. A full quantum mechanical description of the process becomes very tedious and involved. However, semiclassical methods are expected to be applicable. Also, efforts have been made to utilize the experimental transfer data along with the semiclassical approach for a reliable extraction of the transfer form factors. The form factors provide a quantitative input for taking into account the possible role of the transfer channels in the coupled channels approach for understanding the observed enhancements in the sub-barrier fusion observables like cross section, average spin etc.

The transfer measurements at the above barrier energies utilize the data forward of the grazing angle in order to extract the transfer probability as a function of the closest distance of approach. However, the transfer probabilities derived were found to be in disagreement with the theoretically derived values using the semiclassical approach. This is the so called slope anomaly [4]. An interpretation of this has been possible based on the interference of the Coulomb and nuclear branches of the deflection function [4]. In contrast to the above barrier data, the semiclassical methods have been found to describe the sub-barrier measurements quite successfully as contributions to the observed scattering process arise from the trajectories with impact parameters corresponding to the Coulomb branch only. Thus the sub-barrier measurements offer a completely unambiguous and reliable way of extracting the transfer form factors. Besides, the extraction of the transfer form factors from detailed experimental data for the multi-neutron and proton transfer data in the sub-barrier region should provide a simple and stringent test of the semiclassical concepts while describing the transfer process at large inter nuclear distances.

At the Nuclear Science Centre, New Delhi, we had carried out a few measurements [5,6] on the sub-barrier fusion of some Ti + Ni systems using the Pelletron accelerator and the Recoil Mass Separator HIRA installed there. These studies revolve around the quantitative test of the importance of the transfer channel coupling (especially the positive Q-value two neutron pick up for the reactions involving ^{64}Ni target, which are 2.58 MeV and 4.01 MeV respectively for ^{48}Ti and ^{46}Ti projectiles) which has been invoked in an empirical explanation of the observed isotopic dependence of the fusion enhancement [5,6]. To complement the fusion measurements, we have carried out transfer measurements also on the two systems ^{46,48}Ti + ^{64}Ni. In these measurements we have resorted to a kinematic coincidence technique for detecting the transfer products in order to overcome the problems associated with the M/q ambiguity at the focal plane of the HIRA. Such a technique was earlier seen to be helpful in this aspect [7]. In the following sections the details of these measurements and the important results obtained are given.

2. Experimental details

Experiments have been carried out using ^{46,48}Ti beams with energies ranging from 120 MeV to 142 MeV, obtained from the 16 MV Pelletron accelerator at the Nuclear Science Centre, New Delhi. Self-supporting ^{64}Ni targets with thickness of 240 μg/cm^2 were used. The recoiling target like nuclei at 20° enter the Recoil Mass Separator HIRA. These have been detected at the focal plane of the HIRA by a gas detector system [8] consisting of a front end multiwire proportional counter, position sensitive in two directions, backed by a $\Delta E - E$ gas ionization chamber. These are counted in coincidence with the corresponding low energy back scattered projectile-like particles detected in a Si surface barrier detector placed inside the scattering chamber at 91.5° and 94.2° respectively for ^{48}Ti and ^{46}Ti reactions. Impurity concentrations of neighbouring isotopes were estimated using the lowest beam energies.

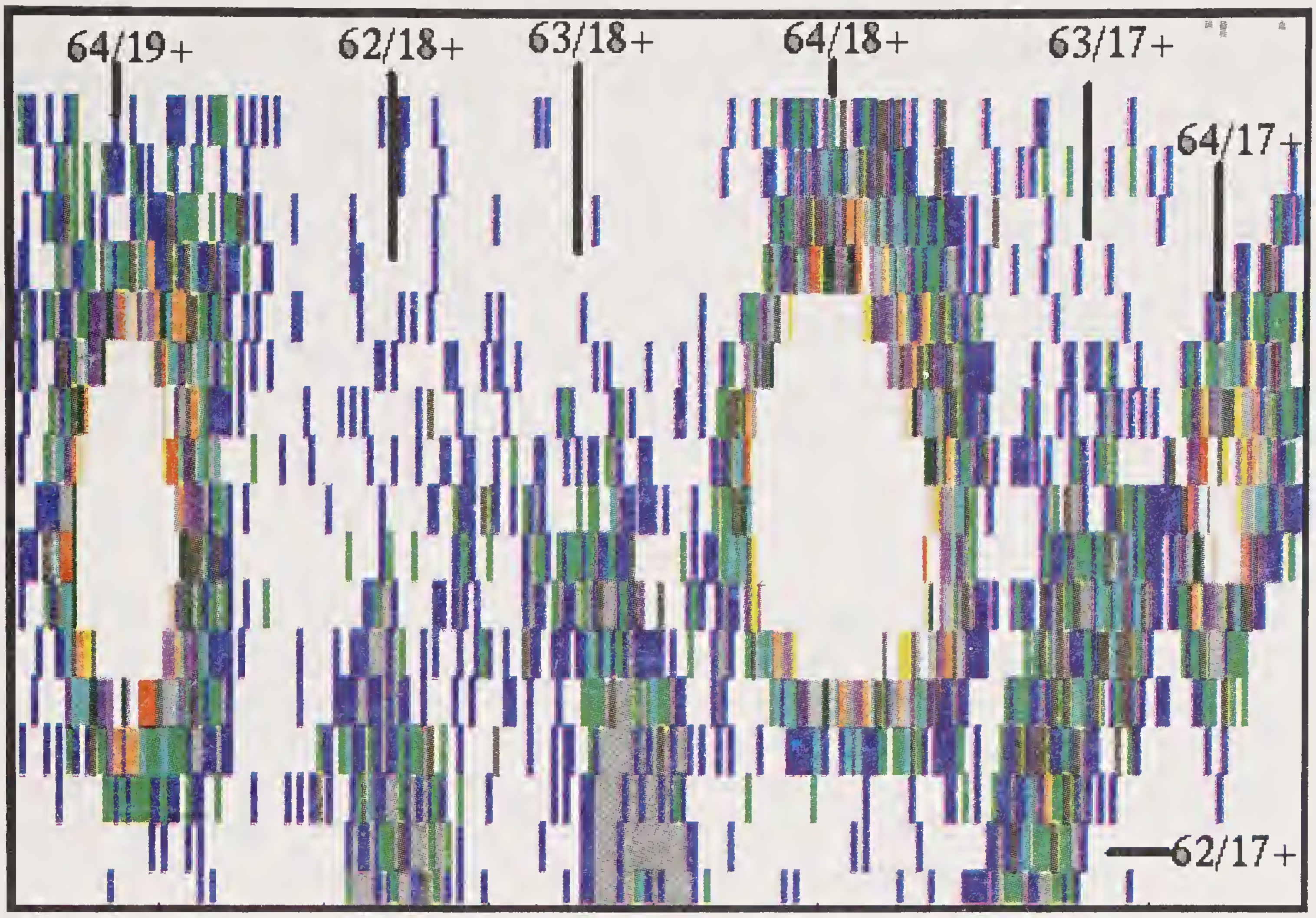

Figure 1. Two dimensional spectrum of HIRA focal plane position vs. time of flight.

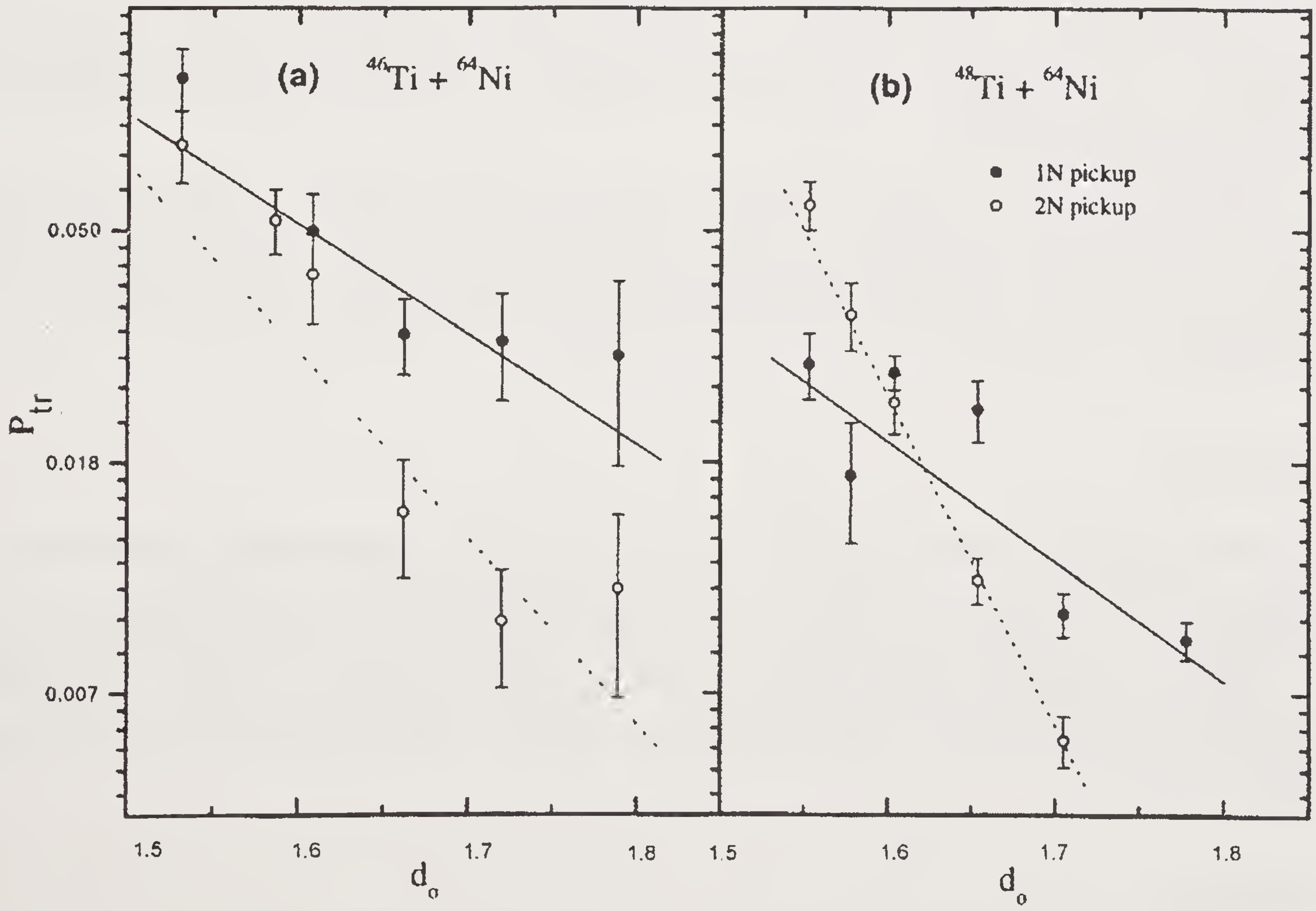

Figure 2. Transfer probability as function of reduced distance of closest approach.

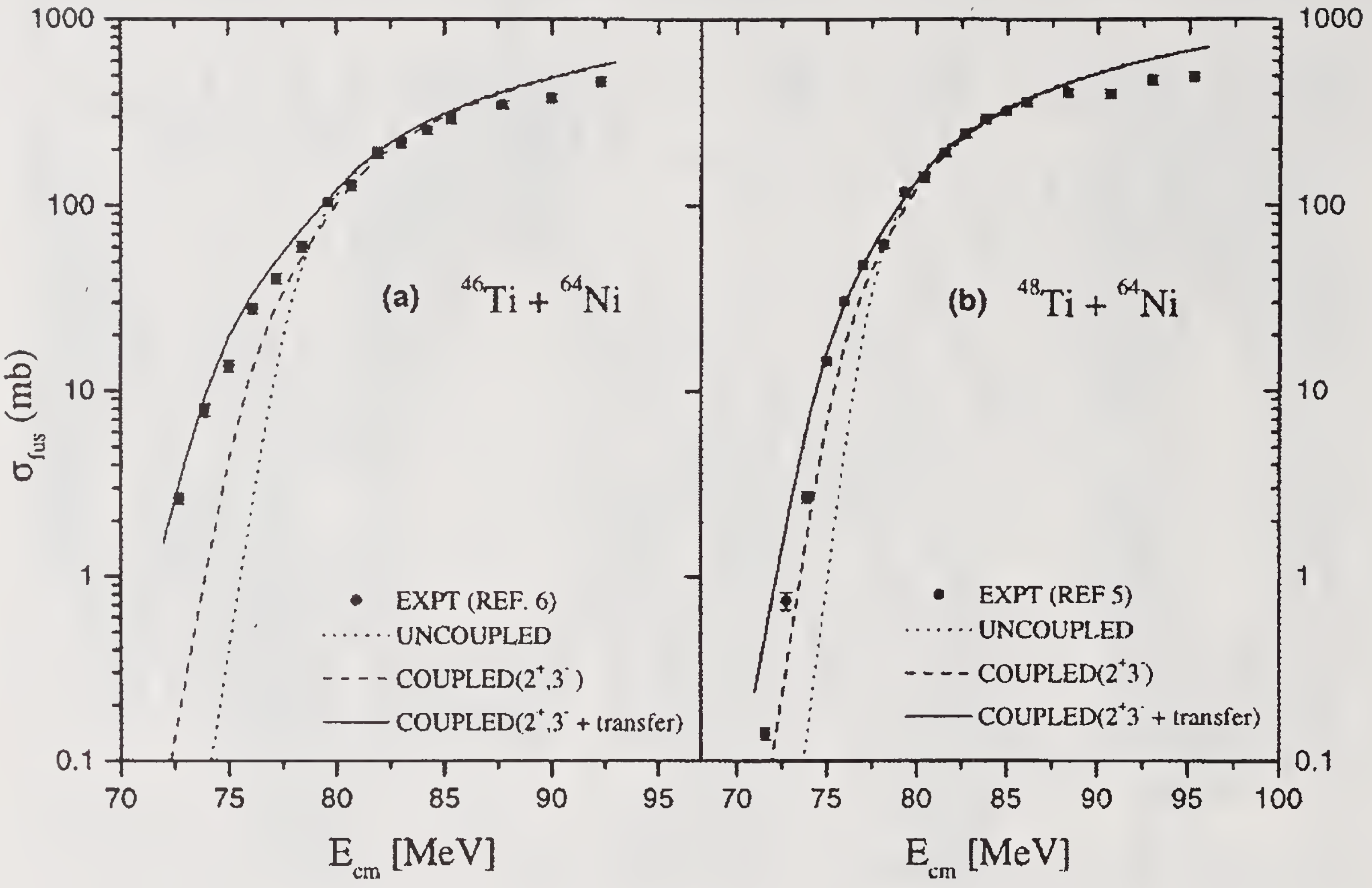

Figure 3. Experimental fusion excitation functions vis-a-vis coupled channels calculations.

The capability of the kinematic coincidence technique used in resolving the M/q ambiguity is demonstrated in figure 1 which shows a two dimensional plot of focal plane position vs. the flight time of the transfer products. The various M/q peaks are reasonably well separated in this plot.

Transfer probabilities for the one and two neutron transfer for both pick up and stripping have been extracted by taking the ratio of the cross section of a particular transfer channel to the sum of the cross sections for the transfer channels and the elastic channel. These have been plotted as function of the reduced distance of closest approach of the heavy ions in figure 2.

3. Results

The slope parameter was determined to be 0.34 and 0.93 respectively for the 1N and 2N channels of ^{48}Ti and 0.31 and 0.53 for the lighter Ti projectile from the plots in figure 2. The values of the slopes so obtained were used to extract the relevant transfer form factors and used in a coupled channel calculation. The results are shown in figure 3. Reasonable agreement was obtained with the experimental fusion excitation functions at near and sub-barrier energies.

References

[1] M Beckerman, M Salomaa, A Sperduto, J D Molitoris and A Di Rienzo, *Phys. Rev.* **C25**, 837, 885 (1982)

[2] C H Dasso, S Landowne and A Winther, *Nucl. Phys.* **A405**, 381 (1983); **A407**, 221 (1983)

[3] S G Steadman and M J Rhodes Brown, *Ann. Rev. Nucl. Part. Sci.* **36**, 649 (1986)
M Beckerman, *Rep. Prog. Nucl. Phys.* **51**, 1047 (1988)
W Reisdorf, *J. Phys.* **G20**, 1297 (1994)

[4] C V K Baba, V M Datar, K E G Löbner, A Navin and F J Schindler, *Phys. Lett.* **B338**, 147 (1994)

[5] A M Vinodkumar, K M Varier, N V S V Prasad, D L Sastry, A K Sinha, N Madhavan, P Sugathan, D O Kataria and J J Das, *Phys. Rev.* **C53**, 803 (1996)

[6] N V S V Prasad, A M Vinodkumar, A K Sinha, K M Varier, D L Sastry, N Madhavan, P Sugathan, D O Kataria and J J Das, *Nucl. Phys.* **A603**, 176 (1996)

[7] P P Shakkeeb *et al*, *Ann. Rep.* (Nuclear Science Centre, New Delhi, 1995)

[8] D O Kataria *et al*, *Nucl. Instrum. Methods* **A372**, 311 (1996)

Measurement of the ground state $2n$ pickup probability for ^{28}Si + ^{68}Zn and its role in sub-barrier fusion enhancement

VANDANA TRIPATHI[1], LAGY T BABY[1], P V MADHUSUDHANA RAO[2], S K HUI[3], R SINGH[4], J J DAS[1], P SUGATHAN[1], N MADHAVAN[1] and A K SINHA[1]
[1]Nuclear Science Centre, P.B. No. 10502, New Delhi 110 067, India
[2]Department of Nuclear Physics, Andhra University, Visakhapatnam 530 003, India
[3]Department of Physics, Calcutta University, Calcutta 700 009, India
[4]Department of Physics, Delhi University, New Delhi 110 007, India

Abstract. The ground state and excited state transfer yields for the 2-neutron pickup channel in the ^{28}Si + ^{68}Zn system have been measured explicitly. The recoil mass separator at the Nuclear Science Centre, New Delhi was used for the measurement. A NaI(Tl) detector was used for detecting the de-excitation γ's from the transfer products. The kinematic coincidence technique was employed for the transfer measurement. Simplified coupled channels calculations show that out of all transfer channels the major contribution to the sub-barrier enhancement comes from the ground state 2 neutron pickup channel with a ground state Q-value of + 1.83 MeV.

Keywords. Heavy-ion fusion; sub-barrier enhancement; ground state transfer; kinematic coincidence; simplified coupled channel calculation.

PACS Nos 25.70.Hi; 25.70.Jj

1. Introduction

Heavy-ion fusion cross-sections at below barrier energies are generally enhanced by orders of magnitude in comparison to the predictions of the one-dimensional quantum mechanical barrier penetration calculations [1]. The influence of additional quasi-elastic reactions on the barrier tunneling probability is believed to be responsible for the observed increase in flux going into the fusion channel as formulated in the coupled channels calculations [2,3]. The quasi-elastic channels considered explicitly are mostly limited to the inelastic excitations of the low lying levels. Such calculations reproduce the fusion cross-sections rather well in many cases [3]. However, the variation of the measured fusion cross-section within a given projectile target combination involving different isotopes especially at energies near the barrier is not easily understood by including inelastic channels alone in the coupled channel calculations. Such variations may arise from the influence of transfer channels which have distinctly different Q-values and probabilities for various isotopes. A correlated observation is the rather dramatic increase of transfer cross-sections (mainly neutron transfer) for heavier systems at energies near the barrier suggesting a correlation between fusion and nucleon transfer. It has been pointed out that nucleon transfer with positive ground state Q-value, Q_{gg}, favours fusion [4]. However even for the $2n$ pickup with large positive Q_{gg}, the ground state is very weakly populated as the $Q_{opt} \approx 0$. The main strength goes to states at higher excitation energies.

These observations call for experiments to measure the one and two nucleon transfer cross section with a resolution adequate to distinguish at least the ground state transfer events from the rest of the quasi-elastic transfer yield. These results can help in quantifying the role of positive Q-value transfer channels in the sub-barrier enhancement. We have attempted to measure the ground state and excited state transfer probabilities explicitly for the 2-neutron pickup reaction ^{68}Zn(^{28}Si ^{30}Si)^{66}Zn to study its influence on the sub-barrier fusion process. The above reaction has a positive ground state Q-value of 1.83 MeV and contributes significantly to the sub-barrier fusion cross-section enhancement [5,6]. We have combined the two techniques used for transfer measurement, that is identification of recoils using a recoil mass separator and the study of de-excitation γ rays in coincidence with the reaction products to estimate the ground state and quasi-elastic transfer yields.

2. Experiment

The experiment was performed at the Nuclear Science Centre, New Delhi using the ^{28}Si beam of energy 78 MeV from the 15UD Pelletron. The target used was 109 μg/cm^2 ^{68}Zn with 15 μg/cm^2 carbon backing. The ^{68}Zn target was 99.3% enriched (0.25% ^{66}Zn and 0.11% ^{67}Zn). The target-like reaction products, moving in the forward direction were separated out from the beam-like particles by the Heavy Ion Reaction Analyser (HIRA) and detected at the focal plane by a detector system consisting of a multi-wire proportional counter followed by an ionisation detector. HIRA was kept at 10 degree with respect to the beam for better beam rejection. The 'kinematic coincidence technique' was employed for the transfer measurement which involved detection of the kinematically correlated reaction products in coincidence. To detect the back scattered projectile-like particles a 8×47 mm^2 position sensitive detector (PSD) was placed at roughly 145 degree with respect to beam in the scattering chamber of HIRA at a distance of 80 mm from the target. The angle was optimised for maximum coincidence efficiency. A time-of-flight (TOF) arrangement was set up using the start signal from the PSD and stop from the focal plane timing. This was helpful in completely eliminating the beam background. Two monitors were kept at $\pm$ 25 degrees from the beam direction for beam monitoring. A $3'' \times 3''$ NaI(Tl) detector was put at a distance of 30 mm from the target. A 4 mm thick lead shielding was put around the detector to attenuate the X-rays and low energy γ rays. The timing signal from the γ detector was used to set up the coincidence between the prompt γ rays and the recoils at the focal plane.

3. Analysis

A typical projection of TOF vs focal plane position is shown in figure 1(a). The three peaks marked correspond to the elastic, $1n$- and $2n$-pickup channels. The pickup channels turn out to be mainly neutron channels from Q-value considerations. Elastically scattered recoils from the contaminants in the target (^{67}Zn and ^{66}Zn) also add to the transfer product yields from ^{68}Zn. An estimate of the contribution from these isotopes was obtained and

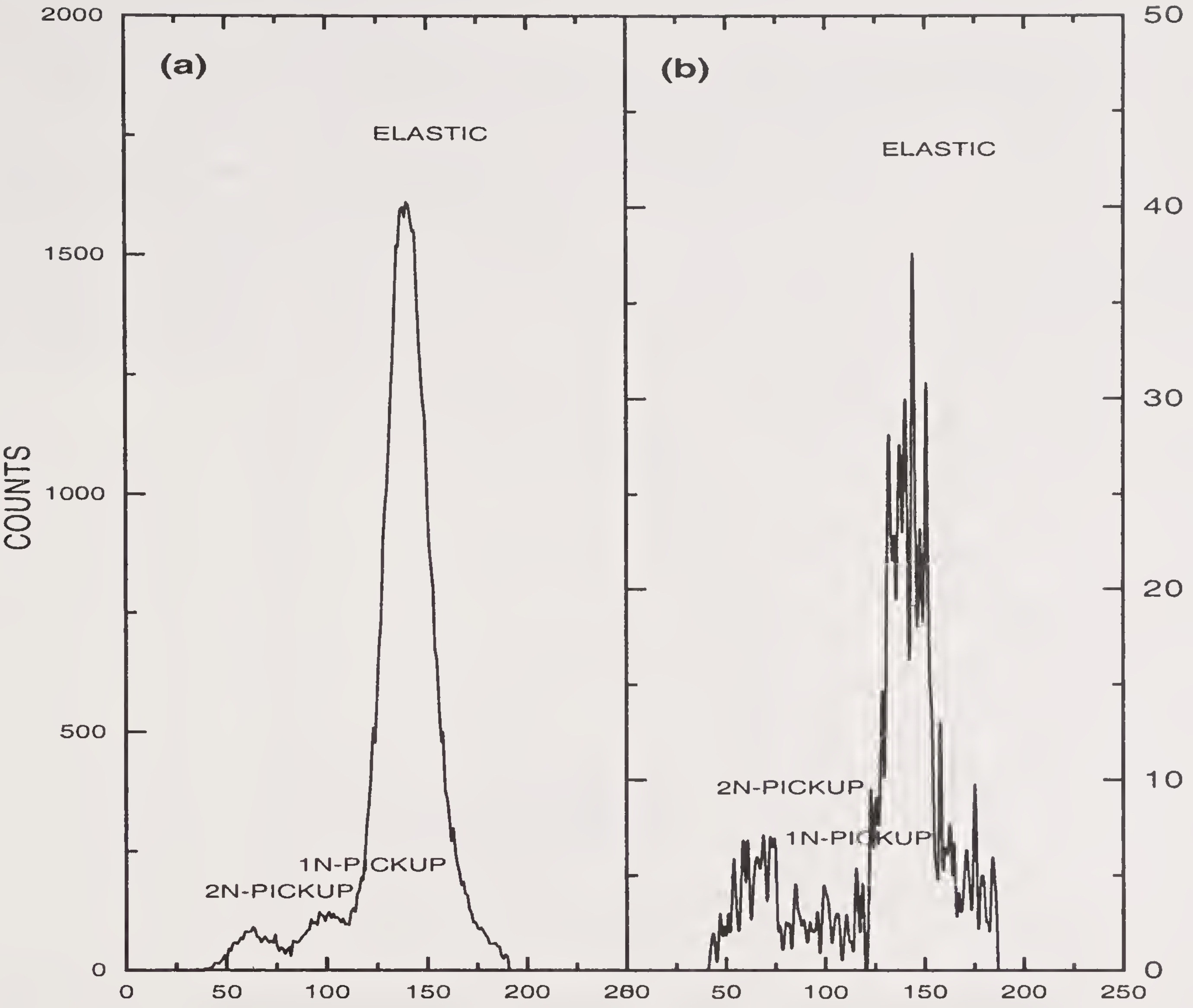

Figure 1. (**a**) Projected mass spectra at the focal plane of HIRA, (**b**) gated with the prompt timing between the recoils and the γ's. X axis is the position in both cases.

was subtracted from the transfer yields. Since HIRA detection efficiency is same for all channels and the solid angle factor being identical, the yields in the channels can be directly used for obtaining the transfer probabilities. The transfer probability for a particular transfer channel has been calculated as the ratio of the yield in that channel to the sum of the yields in elastic plus transfer channels. These correspond to the total quasi-elastic transfer probabilities for the $1n$- and $2n$- pickup.

The resolution of the NaI(Tl) was not good enough to resolve the individual gamma's. This was due to the high count rate which was essential for getting sufficient coincidence counts. So the prompt timing between the de-excitation gamma rays from the transfer products and the recoils was used to gate the TOF vs position plots. Figure 1(b) shows such a plot. The yields in the pickup channels after subtracting the background correspond to transfer to excited states. Corrections have been made for the excitation of the target impurities. After correcting for efficiency the transfer probability to the excited states was extracted as before .The ground state probability is given by the difference of the total and the quasi-elastic transfer probabilities. Table 1 gives the transfer probabilities for the $1n$ and $2n$ channels.

When the ground state and excited states can be treated separately [7], the total transfer probability will be the sum of ground state strength and strength to the excited states.

Table 1. Measured transfer probability for the $1n$ and $2n$ pickup channel at 78 MeV.

	$(P_{\mathrm{tr}})_{\mathrm{tot}}$	$(P_{\mathrm{tr}})_{\mathrm{ex.}}$	$(P_{\mathrm{tr}})_{\mathrm{gs}}$
+ $1n$	0.0580 ± 0.0006	-	-
+ $2n$	0.0450 ± 0.0006	0.041 ± 0.002	0.004 ± 0.002

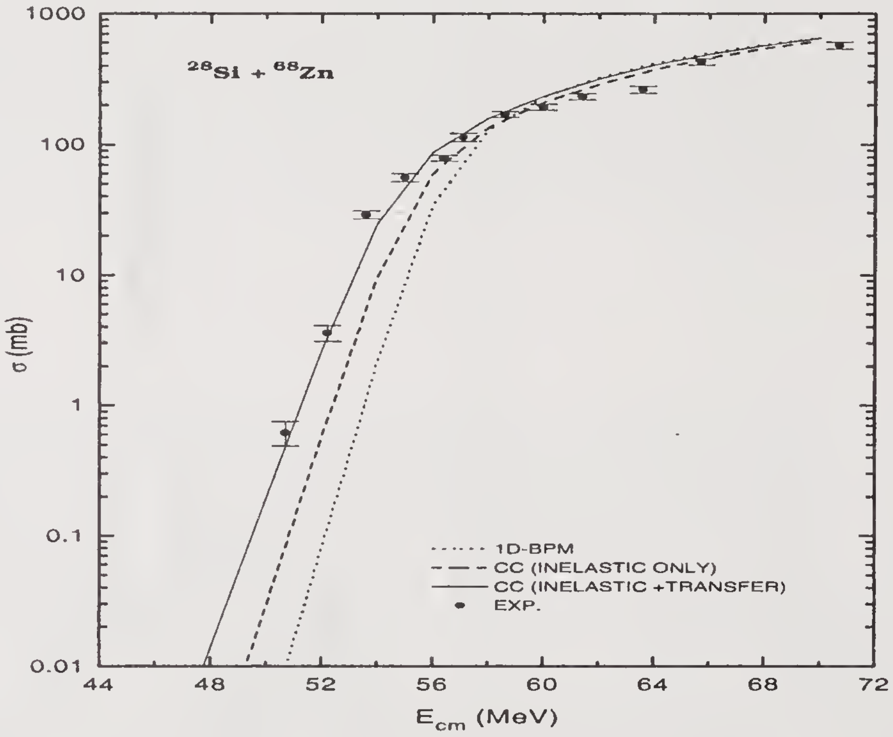

Figure 2. Simplified coupled channel calculations for the system ^{28}Si + ^{68}Zn.

Since the probabilities to both ground state and excited states are known experimentally for the $2n$ pickup channel, the form factors Fo and $\bar{F}$ [7] for the ground state and excited states respectively were calculated. For the $1n$ channel an average form factor was calculated. Coupled channels calculations were performed using a modified version of the code CCMOD [8]. The experimental fusion cross sections were taken from ref. [8]. A plot of the cross section vs energy is shown in figure 2. Inclusion of excitation of low lying 2^+, 3^- states of ^{28}Si and ^{68}Zn gives substantial enhancement but not enough to reproduce the data (figure 2). The negative Q-value transfer channels do not have any significant effect on the fusion result. The inclusion of $2n$ pickup to excited states of ^{30}Si and ^{66}Zn with an effective Q-value which is negative, does not improve the fit. Large asymptotic barrier shift of 2.52 MeV is obtained on coupling the ground state $2n$ transfer. This reproduces the below barrier data quite well (thick solid line in figure 2).

In summary, we have measured the ground state and quasi-elastic transfer strength for the reaction ^{68}Zn(^{28}Si ^{30}Si) ^{66}Zn. Simplified coupled channels calculations show that the major contribution to the sub-barrier enhancement apart from the inelastic couplings comes from the ground state 2 neutron transfer which has a positive Q-value, even though it is weakly populated. The results also point to the need for experiments to measure transfer yields to individual states, which will lead to a better understanding of sub-barrier fusion dynamics.

References

[1] M Beckerman, *Phys. Rep.* **129**, 145 (1985)
[2] H Esbensen, *NPA* **352**, 147 (1981)
[3] C H Dasso, S Landowne and A Winther, *NPA* **405**, 381 (1983); *NPA* **407**, 221 (1983)
[4] R A Broglia, C H Dasso, S Landowne and A Winther, *Phys. Rev.* **C27**, 2433 (1983)
[5] S Saha and Y K Agarwal, *Nucl. Phys.* **A601**, 251 (1996)
[6] D O Kataria *et al*, *Phys. Rev.* **C56**, 1902 (1997)
[7] Lagy T Baby *et al*, *Phys. Rev.* **C56**, 1936 (1997)
[8] M Dasgupta, A Navin, Y K Agarwal, C V K Baba, H C Jain, M L Jhingan and A Roy, *Nucl. Phys.* **A539**, 351 (1992)

Inclusive and exclusive measurements in the projectile breakup of ^{7}Li

T MADHUSOODHANAN[1], SAMIT MANDAL[2], M P SATHYAVATHIAMMA[1], RAMANI[1], N G PUTTASWAMY[1], T S MUDHOLE[3], A MANDAL[2], D K AVASTHI[2], R SHYAM[4] and S K DATTA[2]
[1]Department of Physics, Bangalore University, Bangalore 560 056, India
[2]Nuclear Science Centre, P.B. No 10502, New Delhi 110 067, India
[3]Department of Physics, Karnatak University, Dharwad 580 003, India
[4]Saha Institute of Nuclear Physics, Calcutta 700 064, India

Abstract. The inclusive and exclusive measurements were carried out for ^{7}Li projectile breakup on ^{27}Al target at 48 MeV. In the inclusive data we have observed a broad peak around the beam velocity for alphas and tritons. The exclusive data for alpha–triton coincidences show good agreement with the post-form DWBA theory of breakup reactions.

Keywords. Direct reactions; projectile breakup; post-form DWBA.

PACS Nos 25.10+s; 24.50+g; 25.70+z

1. Introduction

There has been considerable interest in the study of the emission of charged particles in a reaction between two complex nuclei. It is characterized by large cross-sections and unusual shapes of the energy spectra. In addition to the compound nucleus formation and emission of charged particles from the equilibrated system, the direct breakup of the projectile in the field of the target nucleus is found to be a dominant reaction channel [1–3]. A broad peak centered around the beam velocity is characteristic of the projectile breakup. The inclusive spectra are basically interpreted to originate from fragments in a spectator role, reflecting the momentum distribution of the clusters in the projectile before collision. Various simple models describe the shapes of the breakup spectra fairly well [4]. However these models account for only the elastic breakup mode and neglect the inelastic mode. Experimentally it is found that the inelastic channel contributes predominantly to the inclusive cross-section. A realistic approach is the DWBA breakup theory developed by Baur and coworkers. The theory is based on a one-step breakup mechanism and enables calculations of contributions from both the elastic and inelastic breakup modes [5].

A kinematically complete study of the ^{7}Li breakup is of considerable importance as it may lead to a better understanding of the breakup of the neutron rich ^{11}Li isotope and other isotopes which have a 'halo' structure [6]. Our motivation in this study is mainly to investigate the nuclear and Coulomb part of the breakup cross section.

2. Experimental details

A beam of 48 MeV ^{7}Li obtained from the Nuclear Science Centre, New Delhi was used in the experiment. A self supporting ^{27}Al foil of thickness 190 μg/cm^2 was used as target. The particle identification was achieved by using $\Delta E - E$ detector telescope. The experiment was carried out in the 1.5 m diameter general purpose scattering chamber (GPSC). Two telescopes were kept on each arm of the GPSC and one telescope was moved to different angles with the other fixed at 10°. The solid angle subtended by the solid state detector was 0.3 msr. The beam current on the target was around 10 pnA. A monitor detector was kept at 10° to view the beam. The data were also acquired using both solid state detectors (SSD) and a combination of a gas ionization chamber and a position sensitive strip detector (PSSD). The SSDs used were 100 μm Si for ΔE detector and 5 mm Si(Li) for the E detector. The 1 mm thick silicon PSSD with an active area of 50 mm × 50 mm was used as E detector. An ionization chamber with an active length of 10 cm, and operated at a field of 1 V/Torr/cm, was used as a ΔE detector for alpha particles. The coincidences between alpha particles and tritons were also recorded.

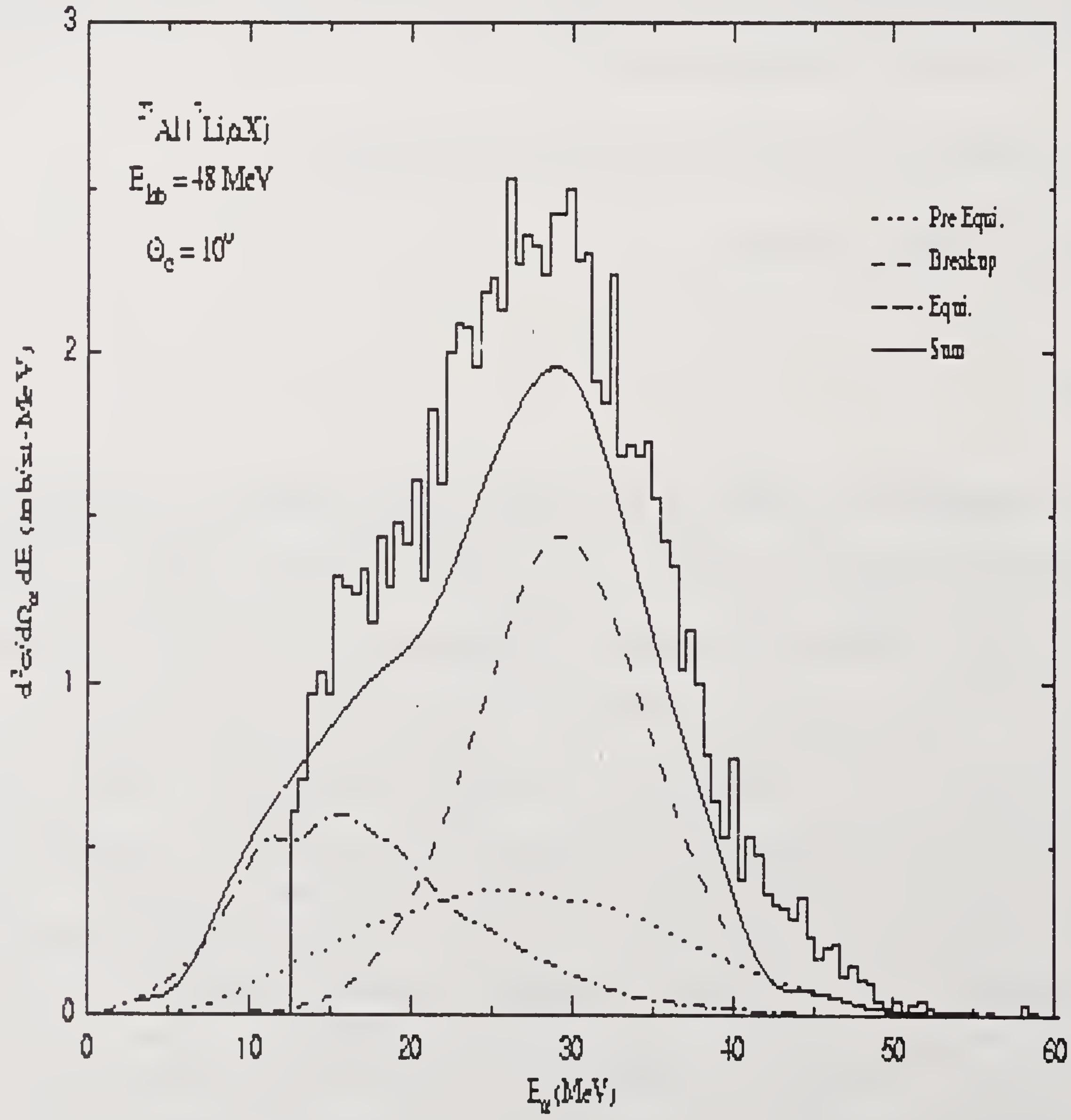

Figure 1. Experimental alpha energy (shown as histogram) spectrum obtained at 10° in the reaction ^{7}Li on ^{27}Al at 48 MeV.

3. Inclusive measurements and results

The differential energy spectra of the outgoing alphas and tritons were measured over a range of 8° to 38° in steps of 2°. A typical alpha spectrum at 10° is shown in figure 1. The broad bump corresponding to the beam velocity can be seen at the alpha energy of 27.4 MeV.

The breakup contribution was calculated in the framework of post-form DWBA theory. The inclusive breakup cross section for the reaction $a + A \to b + x + B$, with $c = B + x$, can be expressed as

$$\mathrm{d}\sigma^{\mathrm{incl}} = \frac{(2\pi)^4}{\hbar v_a} \sum_c |T^{\mathrm{DWBA}}_{a,bc}|^2 \delta(E - E_b - E_{Bc}) \mathrm{d}^3 q_b, \tag{1}$$

where v_a denotes the projectile velocity [5]. In this calculation for the breakup of ^{7}Li, a value of -100 MeV.fm$^{3/2}$ has been used for D_0. The prediction of the direct breakup theory is shown in figure 1 as dashed line. In order to take into account the high energy tail, the pre-equilibrium contribution has been estimated in the frame work of the coalescence model using a coalescence radius of 248 MeV/fm for alpha particles [7]; this is shown as dotted line. The low energy part of the spectrum is accounted for by the equilibrium emission of the particles. The energy distribution of those particles is calculated using the PACE code and the result is shown as dash-dotted curve. The sum of all these three contributions shown as solid line gives a reasonable fit to the experimental spectrum.

4. Exclusive measurements and results

For coincidence measurements one telescope was fixed at 10° and the other moved to different angles. The $E_\alpha + E_t$ spectrum showed a quasi-elastic peak around 45 MeV. This peak is used as a gate for extracting the exclusive spectra. It was noticed that there were no prominent peaks arising from the resonant breakup of ^{7}Li especially via the 4.63 MeV state. The energy integrated triple differential cross sections for alpha particles extracted at each angle are shown in figure 2.

These cross sections were compared with the direct fragmentation model (DFM) of breakup reactions formulated within the post-form DWBA [5]. In this model the incoming projectile is assumed to breakup instantaneously in the Coulomb and nuclear fields of the target nucleus. The triple differential cross section is given by

$$\frac{\mathrm{d}^3\sigma}{\mathrm{d}\Omega_b \mathrm{d}\Omega_x \mathrm{d}E_b} = \rho |T^{\mathrm{DWBA}}_{fi}|^2, \tag{2}$$

where ρ is the three-body density of states [5]. The optical potentials needed for the calculations are taken from the literature. The value of D_0 used in the evaluation of the matrix element is given in §3. In figure 2, the dashed (dotted) line represents the results of the calculation preformed with pure nuclear (pure Coulomb) interactions while the solid line is the full DWBA calculation. The theory is able to quantitatively describe the features of the data in the region where the angular seperation between the fragments is large. A similar agreement has been found for the case of energy integrated triton cross-sections.

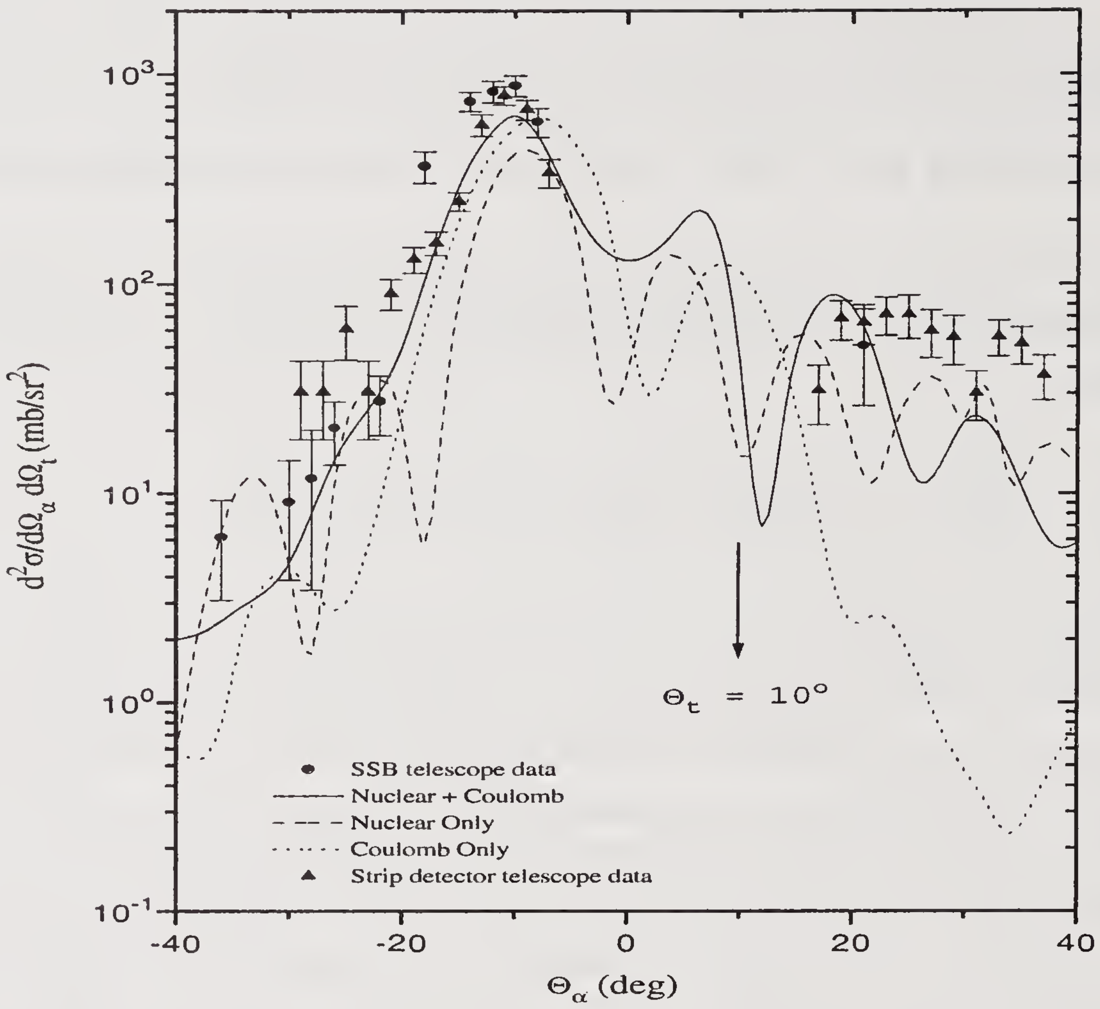

Figure 2. Energy integrated triple differential cross sections for alpha particles in the ^{7}Li breakup on ^{27}Al at 48 MeV. The triton detector was fixed at 10°.

Acknowledgement

The authors wish to thank the Pelletron staff of NSC for smooth running of the machine. The project has been partially supported by a research grant from the University Grants Commission.

References

[1] J Pampus, J Bisplinghoff, J Ernst, T Mayer-Kuckuk, J Rama Rao, G Baur, F Rosel and D Trautmann, *Nucl. Phys.* **A311**, 141 (1978)
[2] N Matsuoka, A Shimizu, K Hosono, T Saito, M Kondo, H Sakaguchi, A Goto and F Oklani, *Nucl. Phys.* **A337**, 269 (1980)
[3] B Neumann, H Rebel, J Buschmann, H J Gils, H Klewe-Nebenius and S Zagromski, *Nucl. Phys.* **A269**, 113 (1980)
[4] U Bechstedt, H Machner, G Baur, R Shyam, C Alderliesten, O Bousshid, A Djaloeis and P Jahn, *Nucl. Phys.* **A343**, 221 (1980)
[5] G Baur, R Rosel, D Trautmann and R Shyam, *Phys. Rep.* **111**, 333 (1984)
[6] Isao Tanihata, *J. Phys. G. Nucl. Part. Phys.* **22**, 157 (1996)
[7] H Machner, *Phys. Rep.* **127**, 309 (1985)

Asymmetric barrier model for heavy ion fusion and its relation to channel coupling

BASUDEB SAHU and C S SHASTRY*
Department of Physics, Ravenshaw College, Cuttack 753 003, India
*Department of Physics, North-Eastern Hill University, Shillong 793 022, India

Abstract. A new asymmetric parabolic effective fusion barrier model for heavy ion fusion is developed.

Keywords. Asymmetric parabolic barrier; heavy ion fusion.

PACS No. 25.70.Jj

1. Introduction

One expects that coupling effects in the mechanism of heavy ion (HI) fusion may dramatically change the shape of the barrier particularly in the region r interior to the Coulomb barrier position R_{B} such that there is a sharp fall of the potential in the interior region which results in an asymmetric barrier. Based on the exact transmission coefficient across an asymmetric parabolic barrier derived by Zafar Ahmed [1] and the ideas used earlier in our effective fusion barrier transmission model [2] we develop a new asymmetric parabolic effective fusion barrier model for heavy ion fusion. The expected change of shape of the barrier is represented by a variable curvature parameter ω_2 whereas the outer curvature ω_1 is kept unchanged.

2. Formulation

We explicitly use an asymmetric parabolic type barrier given by the potential

$$V(x) = \left(V_1 - \frac{1}{2}\mu\omega_1^2 x^2\right)\theta(x) + \left(V_2 - \frac{1}{2}\mu\omega_2^2 x^2\right)\theta(-x). \tag{1}$$

$\theta(x)$ is a step function such that $\theta(x) = 1, x > 0$ and $\theta(x) = 0, x \leq 0$. V_i and $\omega_i, i = 1, 2$ indicate the height and the curvature factors, respectively, and μ stands for the reduced mass. The potential barrier can be used to simulate the Coulomb barrier for any partial wave in the neighborhood of R_{B} which is taken to be at the origin in this particular expression (1). In a fusion calculation we set $V_1 = V_2 = V_{\mathrm{B}}$.

By defining $\alpha_i = (V_{\rm B} - E_{\rm cm})/\hbar\omega_i, i = 1,2$ and an asymmetric parameter $\eta = \sqrt{\omega_2/\omega_1}$ the transmission coefficient [1] at center of mass energy $E_{\rm cm}$ is given as

$$T(E_{\rm cm}) = \frac{1}{\frac{1}{4}\sqrt{1+{\rm e}^{2\pi\alpha_1}}\sqrt{1+{\rm e}^{2\pi\alpha_2}}\left[\eta\left(\frac{f_1}{f_2}\right)+\frac{1}{\eta}\left(\frac{f_2}{f_1}\right)\right]+\frac{1}{2}\left[{\rm e}^{\pi\alpha_1}\,{\rm e}^{\pi\alpha_2}+1\right]}, \tag{2}$$

where $f_1 = f(\alpha_1)$ and $f_2 = f(\alpha_2)$. The function $f(\alpha) = \left|\Gamma\left(\frac{1}{4}+i\frac{\alpha}{2}\right)/\Gamma\left(\frac{3}{4}+i\frac{\alpha}{2}\right)\right|$, can be approximated by $f_{\rm approx}(\alpha) = 1/\sqrt{\gamma}(1+1/8\gamma)$, where $\gamma = \sqrt{(1/16)+(\alpha^2/4)}$.

In order to consider the Coulomb barriers generated by different partial waves l, we need to replace the height $V_{\rm B}$ of the effective barrier by

$$V_{\rm B}^l = V_{\rm B} + \frac{\hbar^2}{2\mu}\frac{l(l+1)}{R_{\rm B}^2}.$$

The quantities $V_{\rm B}, R_{\rm B}$ and the outer region $(r > R_{\rm B})$ curvature factor ω_1 can be obtained using the following global formulae:

$$R_{\rm B} = r_0\left(A_1^{1/3} + A_2^{1/3}\right) + 2.72\,{\rm fm}, \quad V_{\rm B} = \frac{Z_1 Z_2 e^2}{R_{\rm B}}\left(1 - \frac{a}{R_{\rm B}}\right)$$

and

$$(\hbar\omega_1)^2 = \frac{Z_1 Z_2 e^2 \hbar^2}{\mu R_{\rm B}^2}\left(\frac{1}{a} - \frac{2}{R_{\rm B}}\right),$$

where $a = 0.63$ fm and $r_0 = 1.07$ fm, $A_j, Z_j, j = 1,2$ denote the mass number and proton number of the two colliding nuclei, respectively. We control the inner region $(r < R_{\rm B})$ curvature factor ω_2 by varying the parameter $\eta = \sqrt{\omega_2/\omega_1}$.

Using the above specifications we adopt the expression (2) to calculate transmission coefficient $T_l(E_{\rm cm})$ for different l's as a function of incident energy. This is then used to obtain the results for $\sigma_F^l, \sigma_F, \langle l\rangle$ and $D(E_{\rm cm})$ given by the formulae:

$$\sigma_F^l = \frac{\pi}{k^2}(2l+1)T_l, \quad \sigma_F = \sum_{l=0}^{\infty}\sigma_F^l,$$

$$\langle l\rangle = \frac{\sum_{l=0}^{\infty} l\sigma_F^l}{\sigma_F} \text{ and } D(E_{\rm cm}) = \frac{{\rm d}^2(E\sigma_F)}{{\rm d}E^2},$$

where $k = \sqrt{(2\mu/\hbar^2)E_{\rm cm}}$.

3. Results and discussion

In figure 1(a) and (b) (upper panel) we show by solid curve the variation of σ_F and $\langle l\rangle$, respectively, with energy for ^{40}Ca + ^{46,48,50}Ti systems. $E_{\rm lab}$ indicates energy in the laboratory frame. From these figures it is clear that fit to the experimental data is good. Values

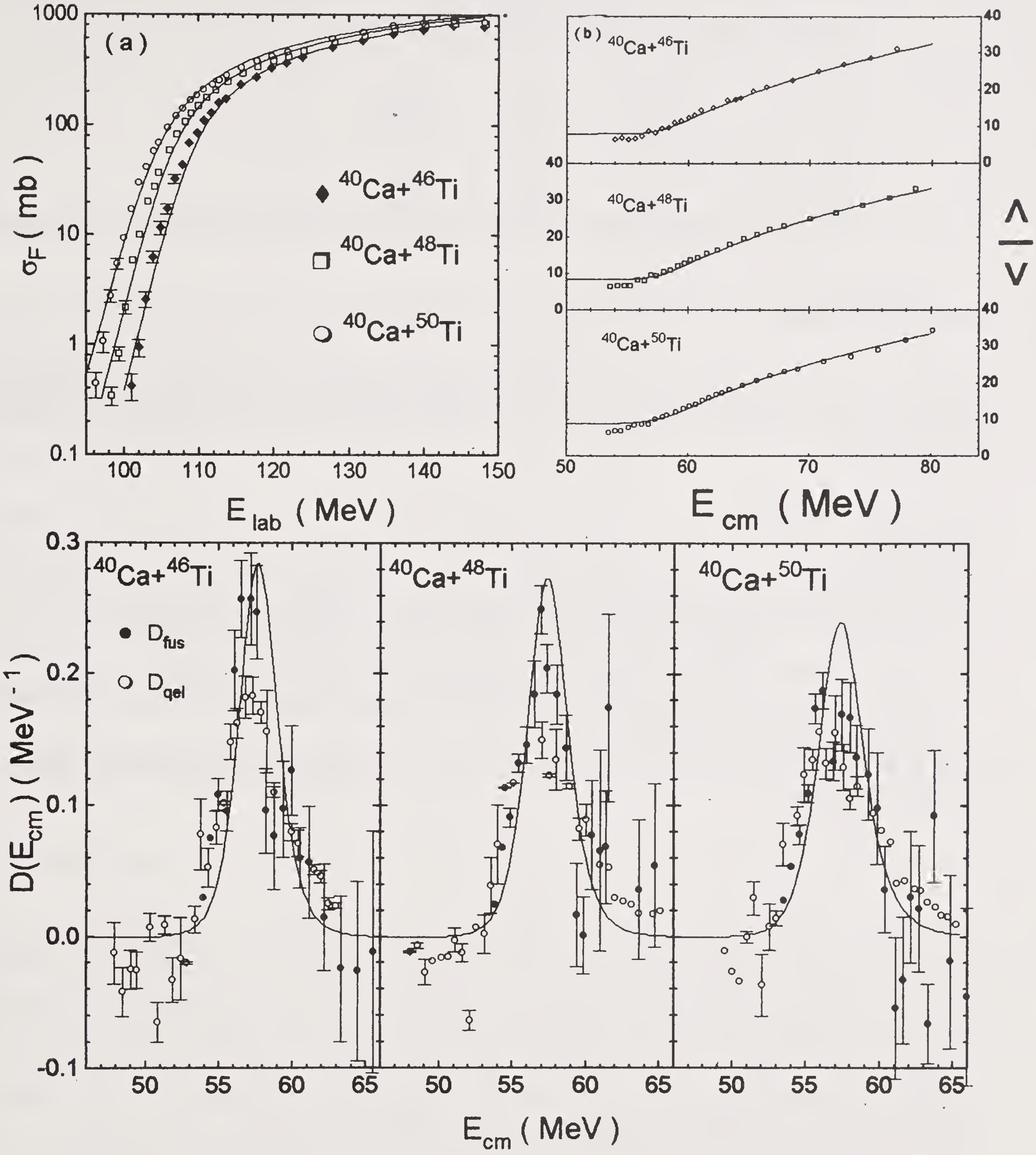

Figure 1. Upper panel shows the variation of (**a**) σ_F and (**b**) $\langle l \rangle$ with energy for ^{40}Ca + ^{46,48,50}Ti systems. Lower panel shows the variation of $D(E_{\rm cm})$ with $E_{\rm cm}$. Solid curves represent the results of present calculation. The experimental data are taken from ref. [4].

of $V_{\rm B}, R_{\rm B}, \hbar\omega_1$ and η used in the calculation for these systems are listed in table 1. In the lower panel of figure 1, we show the results for $D(E_{\rm cm})$ obtained by using point-difference formula used in ref. [3] for the ^{40}Ca + ^{46,48,50}Ti systems. The fit to the experimental data in these cases is impressive. If one examines D, the D variation curve becomes broader and shorter in height for larger η as in the case of ^{40}Ca + ^{50}Ti system (see table 1) where more channels are involved.

Table 1. Systems and s-wave barrier radius R_B, its height V_B, curvature factor $\hbar\omega_1$ and the asymmetry parameter η.

System	R_B (fm)	V_B (MeV)	$\hbar\omega_1$ (MeV)	η
^{40}Ca + ^{46}Ti	10.32	57.65	4.02	1.4
^{40}Ca + ^{48}Ti	10.37	57.36	3.96	1.5
^{40}Ca + ^{50}Ti	10.39	57.76	3.91	1.8

Acknowledgement

BS acknowledges support (Grant No.SP/S2/K14/96(PRU)) from DST, New Delhi and the facilities extended by North-Eastern Hill University, Shillong and Institute of Physics, Bhubaneswar.

References

[1] Zafar Ahmed, *J. Phys.* **A30**, 5243 (1997); Corrigenda: *J. Phys.* **A31**, 3115 (1998)
[2] B Sahu and C S Shastry *J. Phys.* **G15**, L149 (1989); **16**, 55 (1990); **22**, 1483 (1996)
B Sahu, I Jamir, E F P Lyngdoh and C S Shastry, *Phys. Rev.* **C57**, 1853 (1998)
[3] J X Wei, J R Leigh, D J Hinde, J O Newton, R C Lemmon, S Elfstrom, J X Chen and N Rowley, *Phys. Rev. Lett.* **67**, 3368 (1991)
[4] A A Sonzogni, J D Bierman, M P Kelly, J P Lestone, J F Liang and R Vandenbosch, *Phys. Rev.* **C57**, 722 (1998)

Nuclear orbiting and anomalies in nuclear reactions

A DE[1], A MITRA[2], A RAY[2], S R BANERJEE[2], M SENGUPTA[2], A CHATTERJEE[3], S KAILAS[3], H S PATEL[3], M G BETIGIRI[3] and S K DUTTA[4]
[1]Ranigung Girls' College, Dt. Burdwan, West Bengal, India
[2]Variable Energy Cyclotron Center, 1/AF, Bidhannagar, Calcutta 700 064, India
[3]Bhabha Atomic Research Centre, Trombay, Mumbai 400 085, India
[4]Nuclear Science Centre, P. B. No. 10502, New Delhi 110 067, India

Abstract. In this paper,we report our measurements of back-angle oxygen and carbon particle yields from ^{16}O + ^{89}Y, ^{12}C + ^{93}Nb reactions forming the same compound nucleus ^{105}Ag at the same excitation energy and spin distribution. We find anomalously large oxygen yield and entrance channel dependence at high excitation energies from ^{16}O + ^{89}Y reaction implying formation of a dinuclear orbiting complex. Possible connection between nuclear orbiting and fast fission is also discussed.

Keywords. Entrance channel dependence; orbiting.

PACS Nos 25.70; 24.10; 24.30; 24.60

1. Introduction

The concept of nuclear orbiting, although an old idea, is continuously being used under different names such as fast fission, dynamical fission, orbiting etc. to give qualitative explanations of different observed anomalies in nuclear reactions over a wide energy region and projectile–target combinations. Any dynamical picture of nuclear fusion must consider the evolution of an orbiting dinuclear complex into an equilibrated compound nucleus. In some situations, the dinuclear complex may only reach thermal equilibration, but never achieve shape equilibration. Such a dinuclear orbiting complex will have a large probability to break into entrance channel and should show strong entrance channel dependence over a large excitation energy region. Earlier works on back-angle study of target-like fragments [1–3] near $A = 40$ compound nucleus showed that ^{28}Si + ^{12}C, ^{24}Mg + ^{16}O etc. have strong entrance channel dependence and entrance channel yields. Studies of fusion–fission cross-sections from compound nuclei near $A = 100$ mass region also showed anomalies which could be interpreted as fast fission. Nagame *et al* [4] studied ^{37}Cl + ^{68}Zn and ^{16}O + ^{89}Y reactions using ^{37}Cl beam at 160 MeV and 177 MeV and ^{16}O beam at 140 MeV. They found that the observed mass, angular and total kinetic energy distributions of the fully energy damped symmetric mass division products are consistent with statistical liquid drop model. However the observed broad widths of mass and total kinetic energy cannot be accounted for within liquid drop model. The observation of broadening of the mass distributions with partial wave ℓ was interpreted as a signature of fast fission process which comes into play when the fission barriers vanish. However it was never clearly established whether the observation of broadening of mass and total kinetic energy distributions really imply a fast fission process where complete fusion does not take place. The objective of the present work is to look for orbiting effect in $A = 100$ mass region and establish a direct relationship between nuclear orbiting seen near $A = 40$ mass region and so called fast fission or dynamical fission effects reported near $A = 100$ mass region. An understanding of such relationship should give us new insight about the fundamental physics behind nuclear orbiting.

2. Experimental method and results

We form the same compound nucleus ^{105}Ag at the same excitation energy ($E_X = 76$ MeV) and with very similar spin distributions using two different reaction channels ^{16}O + ^{89}Y reaction at $E(^{16}\mathrm{O}) = 95.9$ MeV and ^{12}C + ^{93}Nb reaction at $E(^{12}\mathrm{C}) = 85.6$ MeV. The experiments were performed at BARC-TIFR Pelletron machine in Mumbai and Nuclear Science Center Pelletron machine in New Delhi. A 10 pna ^{16}O beam from BARC-TIFR Pelletron machine was used to bombard a 1 mg/cm^2 thick ^{89}Y foil. Four $\Delta E - E$ telescopes were placed between 140° to 170° to detect different fragments from alpha to oxygen. Similarly a 10 pna ^{12}C beam having 85.6 MeV energy was used to bombard a 1 mg/cm^2 thick ^{93}Nb foil and $\Delta E - E$ telescopes were placed at back-angles to detect different fragments. In this report, we shall discuss about oxygen and carbon particles emitted at back-angles. The data analysis for other fragments is still going on. The back-angle yields of oxygen and carbon particles were found to follow a 1/sin(θ) angular distribution in the centre of mass frame. The entrance channel dependence was studied from the ratio of back-angle oxygen to carbon yields as a function of exit channel energies for both ^{16}O + ^{89}Y and ^{12}C + ^{93}Nb reactions and a strong entrance channel dependence was seen in the strongly damped region. In figure 1, we plot the ratio of oxygen to carbon yields integrated over few MeV bins as a function of excitation energy for both ^{16}O + ^{89}Y and ^{12}C + ^{93}Nb reactions. We find that the two data sets overlap at low excitation energies, but differ greatly at high excitation energy. This result is very similar to what was found earlier for ^{28}Si + ^{12}C and ^{24}Mg + ^{16}O reactions. A comparison with ^{28}Si + ^{12}C and ^{24}Mg + ^{16}O reactions reveals that for the lighter systems the entrance channel dependence is dominant in the lower excitation energy region whereas for heavier system the entrance channel dependence is dominant in higher excitation energy region. We also find from figure 1 that the ratios of oxygen to carbon yields in different excitation energy bins for ^{12}C + ^{93}Nb system agree very well with compound nucleus CASCADE code predictions. Absolute yields of oxygen and carbon for ^{12}C + ^{93}Nb reaction also agree reasonably well with statistical model predictions. So we find that only the oxygen and carbon yields from ^{16}O + ^{89}Y reaction are anomalous and point to the formation of a long-lived dinuclear orbiting complex which is responsible for such large oxygen yield and entrance channel dependence.

3. Discussion

This work establishes very clearly the similarity between nuclear orbiting seen in certain lighter systems ($A = 40$ mass region) and fast fission seen near $A = 100$ mass region.

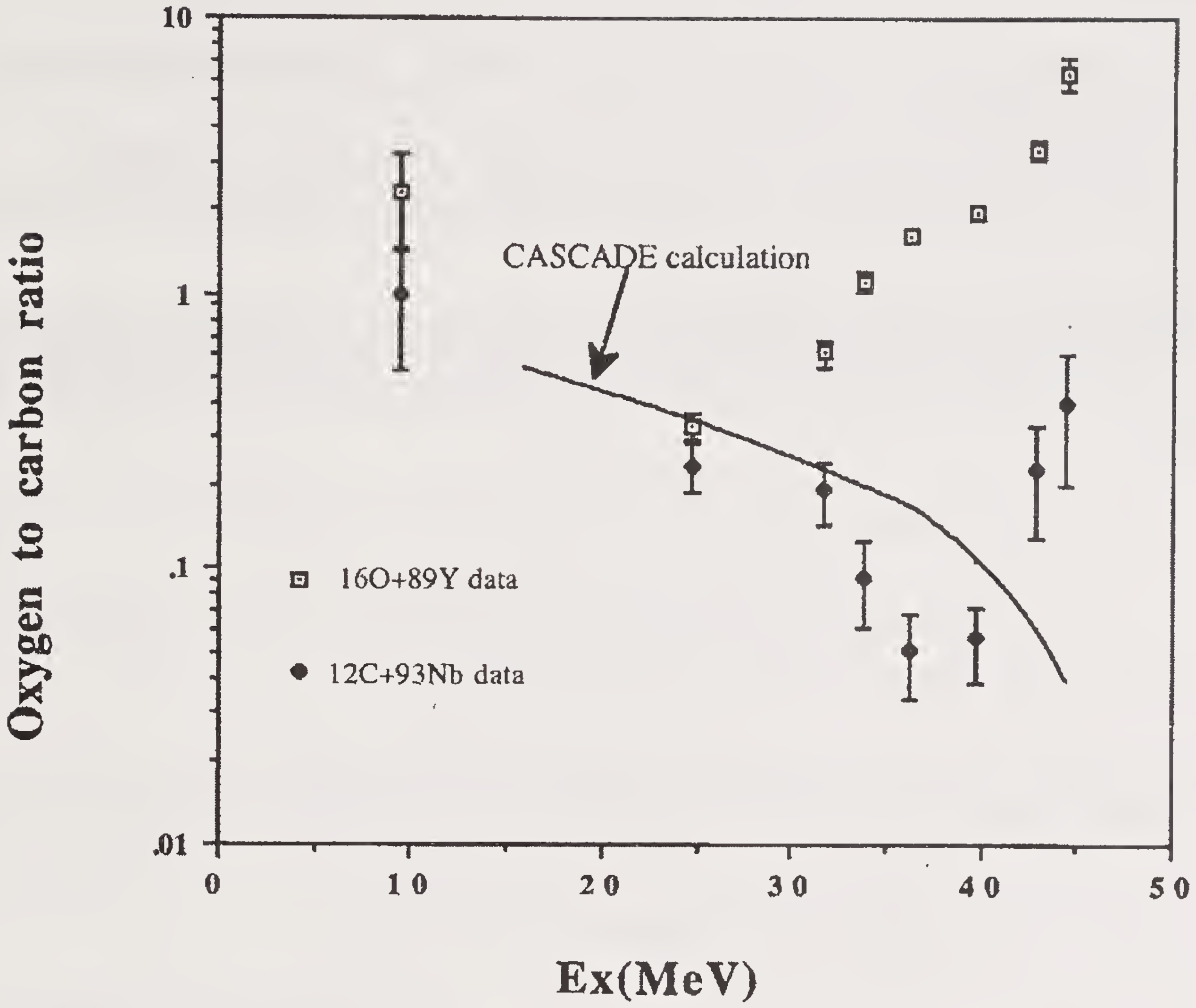

Figure 1. Ratio of oxygen to carbon yields versus excitation energy.

We also find that ^{12}C + ^{93}Nb system does not show any anomalous behaviour, but $^{16}O + ^{89}Y$ system shows orbiting type characteristics. So clearly all systems near $A = 100$ mass region do not show orbiting or fast fission type behaviour. It is very interesting to try to understand the fundamental reasons behind such dinuclear orbiting type behaviour and why this effect is seen selectively in certain systems only. Beck *et al* [5] proposed an explanation in terms of the number of open channels. Although Beck's explanations in terms of number of open channels seem to be adequate for systems around $A = 40$ mass region, it clearly cannot explain our observation of orbiting effect in $^{16}O + ^{89}Y$ system and the absence of such effect for $^{12}C + ^{93}Nb$ system. The numbers of open channels for both the systems are very large and much greater than those for $A = 40$ systems. So following Beck's arguments, the orbiting effect should not take place in such heavy mass regions. The number of open channels argument also cannot explain our earlier observations [6] regarding the lack of any orbiting effect for $^4He + ^{27}Al$ and $^4He + ^{40}Ca$ reactions.

We have not yet fully understood these effects and are now looking for an explanation in terms of nuclear structure physics.

Acknowledgement

We thank the staff of BARC-TIFR and NSC pelletron machines for smooth operation of their respective machines. We also thank Dr. Ajit Sinha for helping us in every respect during our experiment at NSC, Delhi.

References

[1] D Shapira, R Novotny, Y D Chan, K A Erb, J L C Ford Jr, J C Peng and J D Moses, *Phys. Lett.* **B114**, 111 (1982)
[2] D Shapira, J L C Ford Jr and J Gomez del Campo, *Phys. Rev.* **C26**, 2470 (1982)
[3] A Ray, S Gil, M Khandaker, D D Leach, D K Lock and R Vandenbosch, *Phys. Rev.* **C31**, 1573 (1985)
[4] Y Nagame *et al*, *Phys. Lett.* **B249**, 13 (1990)
[5] C Beck, Y Abe, N Aissaoui, B Djjeroud and F Haas, *Phys. Rev.* **C49**, 2618 (1994)
[6] A Ray, S R Banerjee, P Das, A Mitra, S K Basu and P Bhattacharyya, *Phys. Rev.* **C51**, R1604 (1995)

Quasielastic reactions around the Coulomb barrier in ^{16}O + ^{118}Sn

S SAHA, SAMIT K MANDAL, M B CHATTERJEE, B K SINHA and
S K DATTA*
Saha Institute of Nuclear Physics, 1/AF Bidhan Nagar, Calcutta 700 064, India
*Nuclear Science Centre, P O Box 10502, Aruna Asaf Ali Marg, New Delhi 110 067, India

Abstract. Measurement of elastic and quasielastic reaction cross sections were done in ^{16}O + ^{118}Sn system at two different energies above the barrier. Attempts are being made to understand the results in the framework of coupled reaction channel model.

Keywords. Quasielastic reactions; coupled channel; multinucleon transfer.

PACS Nos 25.70.-z; 25.70.Bc; 25.70.Hi

1. Introduction

Important role played by couplings between the different direct reactions and fusion channels have been of immense interest both from theoretical and experimental view points in recent years [1–5]. This is one of the areas where the scenario from the semiclassical and quantum theories are well understood, but experimental data in different systems are still lacking to test all the aspects of such theories. Some of the systems studied to probe the role of higher order couplings, multiphonon couplings, N/Z ratios, break-up channels, etc. have been presented in this workshop.

In order to investigate the interplay between the various reaction channels in heavy ion collision above the Coulomb barrier and the nature of the multinucleon transfer channels, we have carried out experiments in ^{16}O + ^{118}Sn system at two different energies above the Coulomb barrier. This system is particularly interesting because it was shown [6] that the enhancement of sub-barrier fusion (SBF) cross sections are small in this system, which have been attributed to smaller quasielastic transfer strengths and negative Q-values of the transfer channels. However, a comparison of the experimental fusion cross section data with the coupled reaction channel (CRC) calculation shows that (see figure 1) the smaller enhancement in SBF cross section can be well accounted for by inclusion of inelastic excitation channels alone in this system. The role played by the transfer channels are, therefore, not important. Our aim in this experiment is to investigate the role played by the transfer channels on the other direct reaction channels.

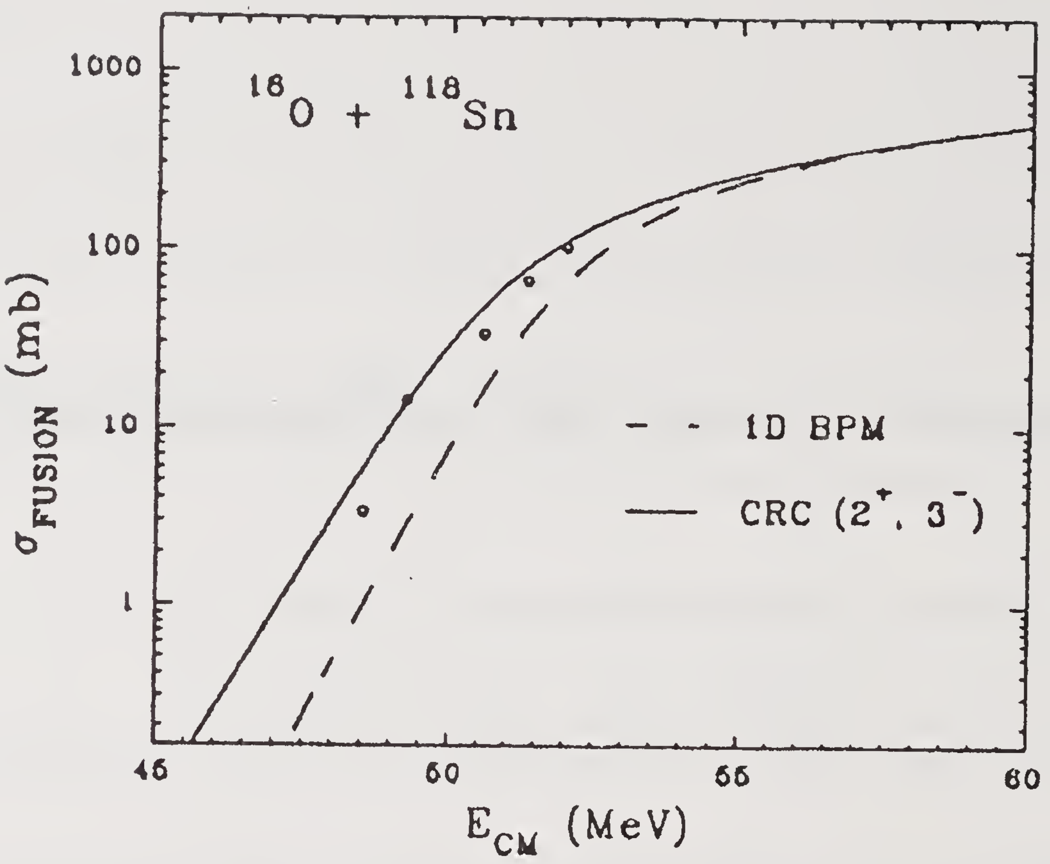

Figure 1. Comparison of experimental fusion cross section data with CRC and 1D BPM calculations in $^{16}O + ^{118}Sn$ system. The CRC calculation takes into account only the 2^+ and 3^- inelastic couplings.

2. Experiment

The experiments were done at the General Purpose Scattering Chamber Facility using ^{16}O beam at 70 MeV and 90 MeV energies from the 16UD Pelletron of the Nuclear Science Centre. ^{118}Sn targets (98% enrichment) were used. Angular distribution of the projectile-like reaction products were measured with one SSB detector time-of-flight (TOF) telescope. Excellent mass resolution ($\sim 2\%$) was achieved by cooling and overbiasing the SSB detectors to improve time resolution (better than 170 ps FWHM) of the TOF system. This was necessary to separate the one-neutron transfer channel in presence of high elastic yield. Two other SSB detectors were used to study the elastically and inelastically scattered particles.

The angular distributions were obtained from the experimental data for the different reaction channels. The elastic scattering data at two energies are shown in the figure 2(a). Optical model parameters were extracted from the elastic data. A short range volume imaginary potential was introduced *a priori* to account for the experimental fusion cross section data [6]. The results at two energies were found to agree reasonably well. A surface term in the imaginary potential was found to be necessary in this case to fit the data.

Quantum mechanical coupled channel calculations using the code FRESCO [2] including the inelastic and transfer couplings were done. Detailed observation based on these calculations will be described elsewhere [7]. The results for the 2^+ state in ^{118}Sn are shown in figure 2(b). Some of the results for the neutron transfer channels are shown in figure 3. It is observed that the elastic, inelastic and one-neutron transfer ($+1n$) data agree reasonably well with the FRESCO predictions. The data show reasonable agreement with the DWBA calculation as well, though the agreement is relatively better with coupled channel calculations.

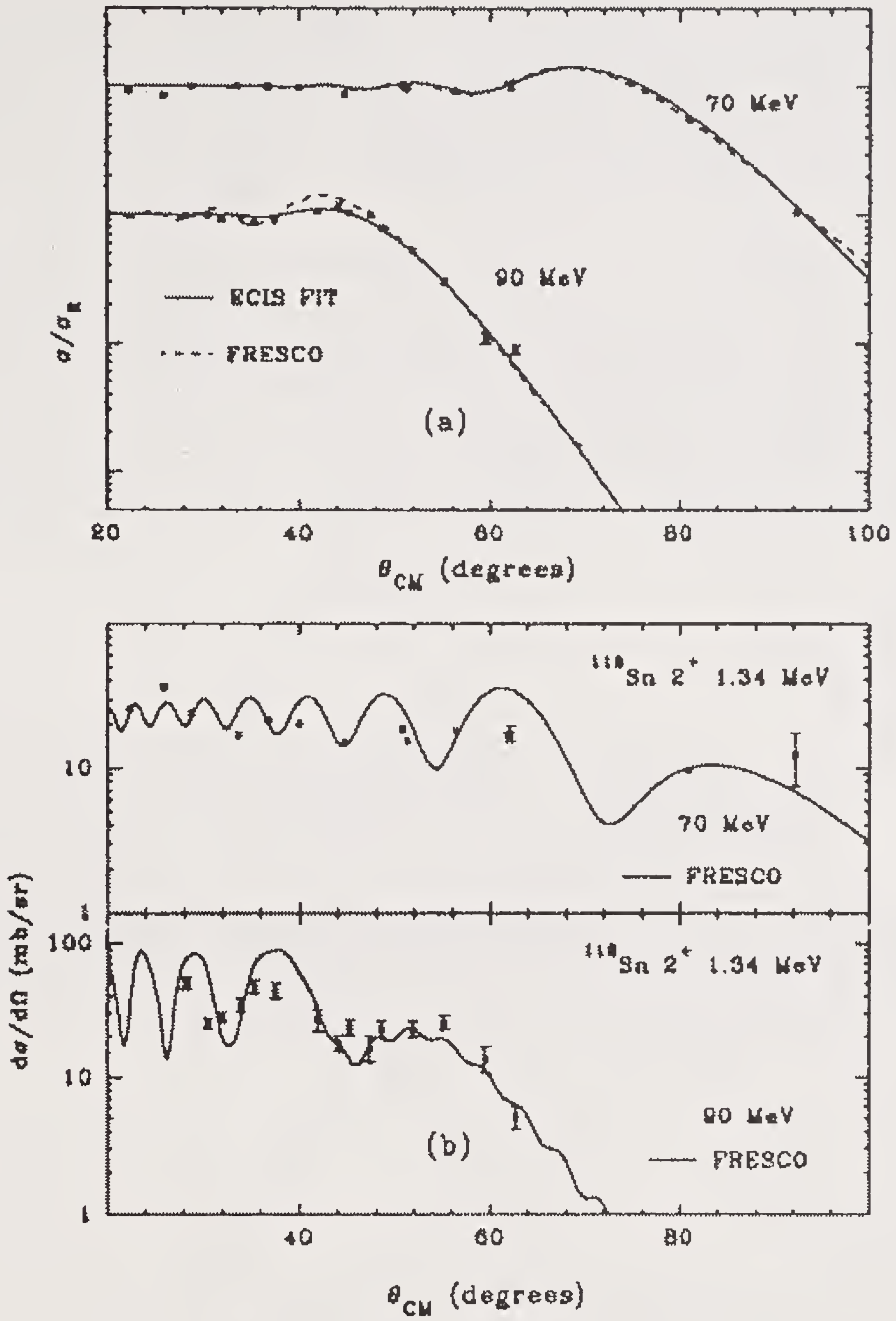

Figure 2. Angular distributions for elastic scattering and excitation of 2^+ state in ^{118}Sn. Results of fit to the elastic data and CRC calculation are shown in (a). Reasonable agreement between the data and the CRC results can be seen in both (a) and (b).

However, one-proton transfer ($-1p$) data do not agree well, particularly at forward angles at 90 MeV, but the measured angular distribution at 70 MeV agree reasonably well with the theoretical prediction (see figure 4). Furthermore, the nature of the multinucleon transfer (indicated by $+2n$, $-2p$, $-2p1n$, etc.) angular distributions show enhancement at forward angles, deviating from the typical bell-shaped nature.

Similar feature was also observed in the heavier systems studied by Corradi *et al* [5] in ^{40,48}Ca + ^{124}Sn systems, which was found to be consistent with the post-transfer neutron evaporation scenario. On the other hand, the deviation observed for the $-1p$ channel in

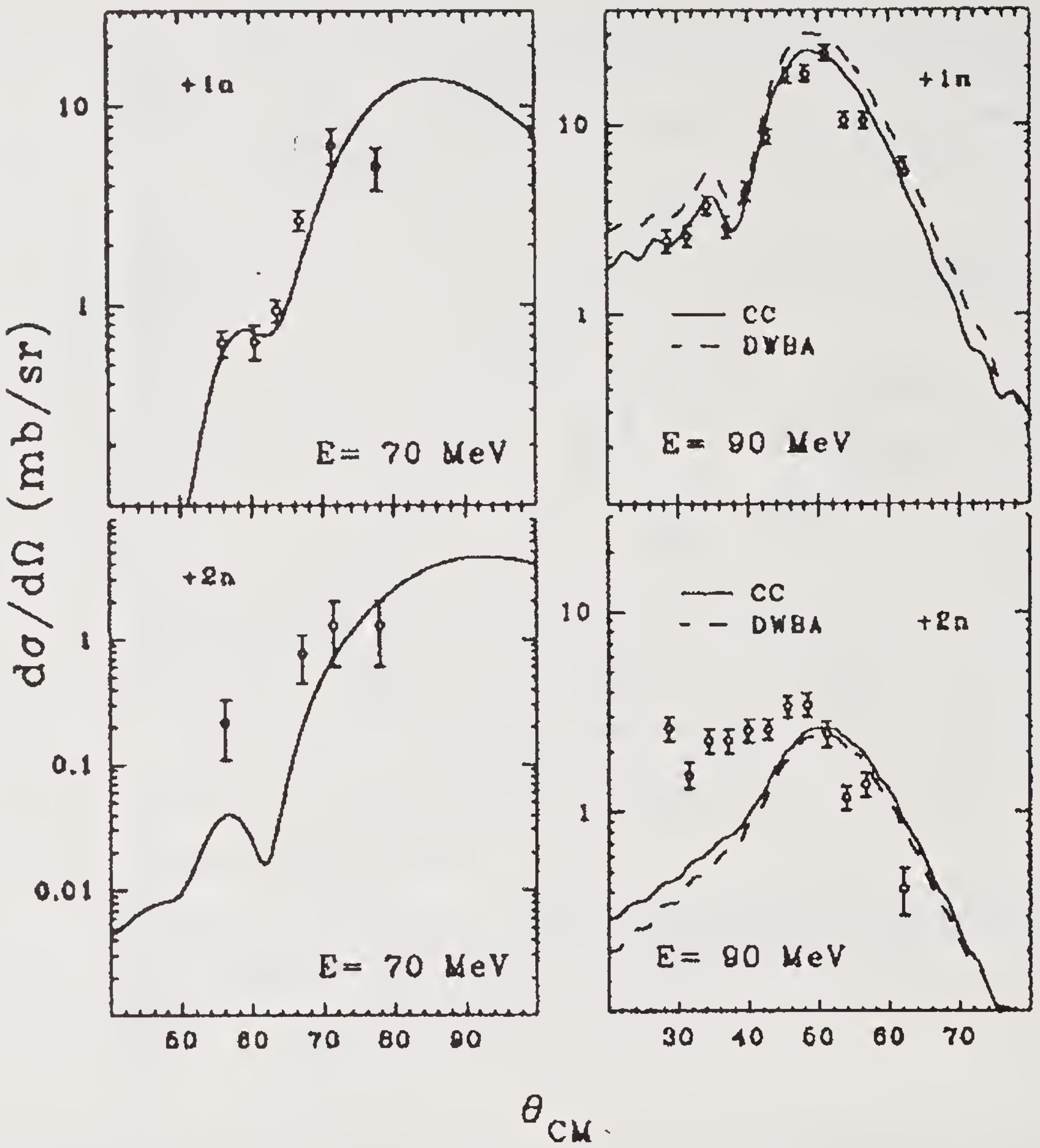

Figure 3. Angular distribution plots for the neutron transfer channels.

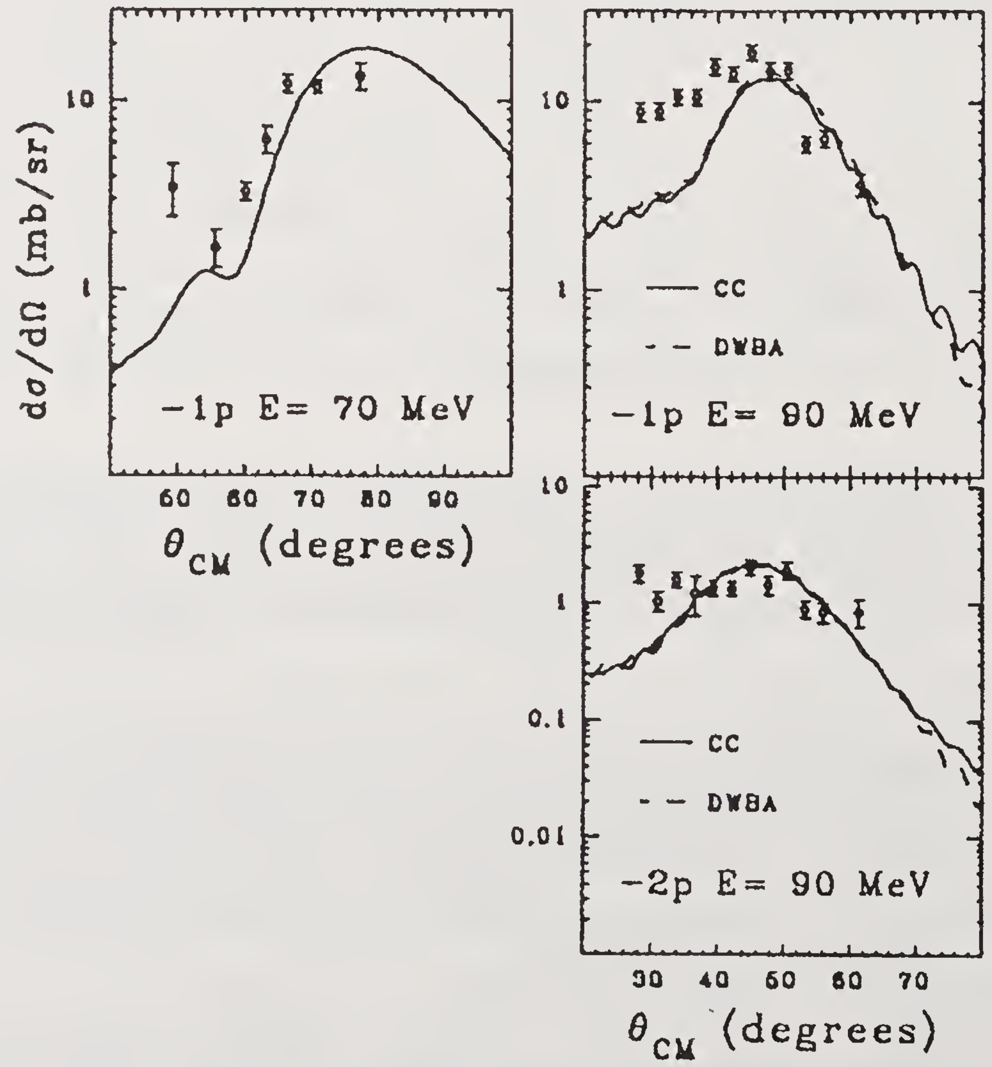

Figure 4. Angular distribution plots for the proton transfer channels.

^{16}O + ^{118}Sn system at 90 MeV is of a different nature, and possibly indicates a large contribution from low impact parameter region. This apparently indicates the onset of deep inelastic processes. The forward angle enhancement of the multinucleon transfer channels also follow the same nature, and is also correlated with significant energy loss as observed for the projectile-like particles. Further details of these observations will be published elsewhere [7].

In summary, the role of channel couplings on the nucleon transfer channels were studied in $^{16}O + {}^{118}Sn$ system. The role of couplings was found to be of lesser importance in this system, which is consistent with the observation made by Henning *et al* [6]. However, the angular distributions for the nucleon transfer channels indicate forward angle enhancement over the predictions based on direct reaction model, which indicates overlap of the direct and the deep inelastic reaction channels for the low impact parameter trajectories. Deep inelastic model based calculation is necessary to explain the apparent discrepancy in the forward angle data.

References

[1] M Beckerman, *Rep. Prog. Phys.* **51**, 1047 (1988)

[2] I J Thompson, *Comp. Phys. Comm.* **7**, 167 (1988)

[3] N Rowley, I J Thompson and M A Nagrajan, *Phys. Lett.* **B282**, 276 (1992)

[4] B Imanishi, S Misono and W von Oertzen, *Phys. Lett.* **B241**, 13 (1990)

[5] L Corradi, A M Stefanini, J H He, S Beghini, G Montagnoli, F Scarlassara, G F Segato, G Pollarolo and C H Dasso, *Phys. Rev.* **C56**, 938 (1997)

[6] W Henning, F L H Wolfs, J P Sciffer, and K E Rehm, *Phys. Rev. Lett.* **58**, 318 (1987)

[7] S Saha, Samit Mandal, M B Chatterji, B K Sinha and S K Datta, (to be published)

Coupled channels calculations for ^{18}O and ^{16}O break-up reaction

SAMIT K MANDAL* and R K BHOWMIK
Nuclear Science Centre, P.B. No. 10502, Aruna Asaf Ali Marg, New Delhi 110 067, India
*Present address: Saha Institute of Nuclear Physics, 1/AF, Bidhan Nagar, Calcutta 700 064, India

Abstract. α angular correlations were calculated using the coupled channels formalism for ^{16,18}O break-up reactions. Prominent Z dependency was observed in both the cases. ^{16}O break-up shows distinctively different behavior with different target materials.

Keywords. Break-up; coupled channels calculations.

PACS Nos 24.10.Eq; 25.70.Ef

1. Introduction

In a heavy-ion induced reaction the measurement of deexcited gamma-ray or particles in coincidence with the correlated particles is one of the powerful and elegant tools to investigate the nuclear dynamics and structure. It directly probes the different magnetic sub-state distribution and their probability of population since the different magnetic sub-state probability directly depends on the magnitude and phase of the transition amplitude. In general, for nuclear reactions induced by light-ions the excitations of different magnetic sub-states due to the long range forces are reasonably weak. Hence one can neglect the effects of the Coulomb contribution in their calculations. But in the heavy-ion induced reactions, low excitation energy allows large contributions from the Coulomb excitation and hence interference between the Coulomb and the nuclear interactions play a prominent role in the particle–gamma or particle–particle correlation.

This correlation is in general analysed in the framework of the DWBA which only includes the first order effects. Strong absorption model (SAM) is also used to extract the information from the correlation experiments [1]. This model has its own limitations due to several parametrizations. Therefore more sophisticated calculations are needed to extract the information accurately. The coupled channels calculations can be used to extract the information more accurately and it is possible to predict the significant region of the phase space where such type of reactions can be studied.

In the present paper we are reporting the theoretical calculations of the alpha decay of the states in ^{18}O through sequential break-up reaction ^{12}C(^{18}O, ^{18}O* $\to$ ^{14}Cα) at 82 MeV using coupled channels form factor. We predicted the possible nature of double differential cross section for α decay of states of ^{16}O in the sequential breakup reaction ^{12}C(^{16}O,

$^{16}\mathrm{O}^* \to ^{12}\mathrm{C}\alpha$) at different phase space. The calculations were also performed with different targets to investigate the effect of the Coulomb and nuclear contributions to the correlation.

2. Analysis and discussion

We have applied the coupled channels analysis to data described in ref. [1]. The coupled channels code FRESCO [2] was modified to calculate the angular correlations.

Consider a reaction,

$$A + a \to b^* + B \to c + C + B.$$

The angular correlation in the final system in terms of the m-state population $f_{JM}(\theta^*, \phi^*)$ of the intermediate state b^* is given by [3]

$$\frac{\mathrm{d}^2\sigma(\theta^*, \phi^*, \chi, \psi)}{\mathrm{d}\Omega^* \mathrm{d}\Omega_\Psi} = \frac{2J+1}{4\pi} \left| \sum_M f_{JM}(\theta^*, \phi^*)(-)^M \mathrm{e}^{-iM\psi} d^J_{M0}(\chi) \right|^2 .$$

Here ψ, χ for the decay particle C are measured with respect to the quantization axis used to calculate the form factor $f_{JM}(\theta^*, \phi^*)$. d^J_{M0} are the rotational matrix elements. The f_{JM} were calculated from the coupled channels formalism (see figure 1 of ref. [1] for the definition of angles). The form factor was f_{JM} calculated from the strong absorption model. The reduced electromagnetic excitation probabilities $B(E\lambda)$ for continuum state was estimated from the relations given below [for 2^+ (8.56 MeV) state of $^{16}\mathrm{O}$]

$$\frac{\mathrm{d}B(E\lambda)}{\mathrm{d}E_{\mathrm{cm}}} = \frac{\mu}{\pi^2\hbar^2} \frac{(2I_a+1)(2I_b+1)}{(2I_i+1)} \frac{\lambda(2\lambda+1)!!^2}{8\pi(\lambda+1)} \left(\frac{\hbar c}{E_\gamma}\right)^{(2L+1)} \mathrm{e}^{2\pi\eta} S_{E\lambda}(E_{\mathrm{cm}}),$$

where $S_{E\lambda}(E_{\mathrm{cm}})$ is the astrophysical S-factor.

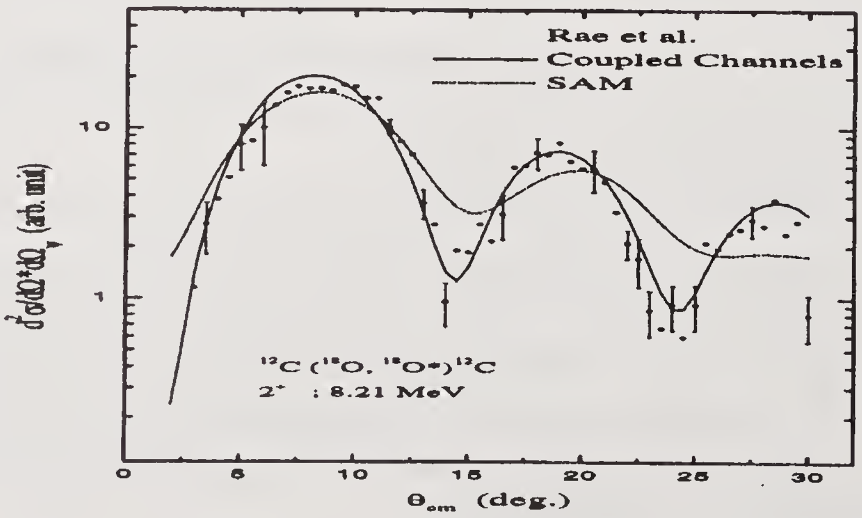

Figure 1. Double differential cross sections for α angular correlation. Solid line is the coupled channels and dotted line represents the SAM calculations (see text). Experimental cross sections are taken from ref. [1] at a constant emission angle $\psi = 72°$ for the α particle. θ_{cm} is the c.m. angle of the 8.21 MeV state in $^{18}\mathrm{O}^*$.

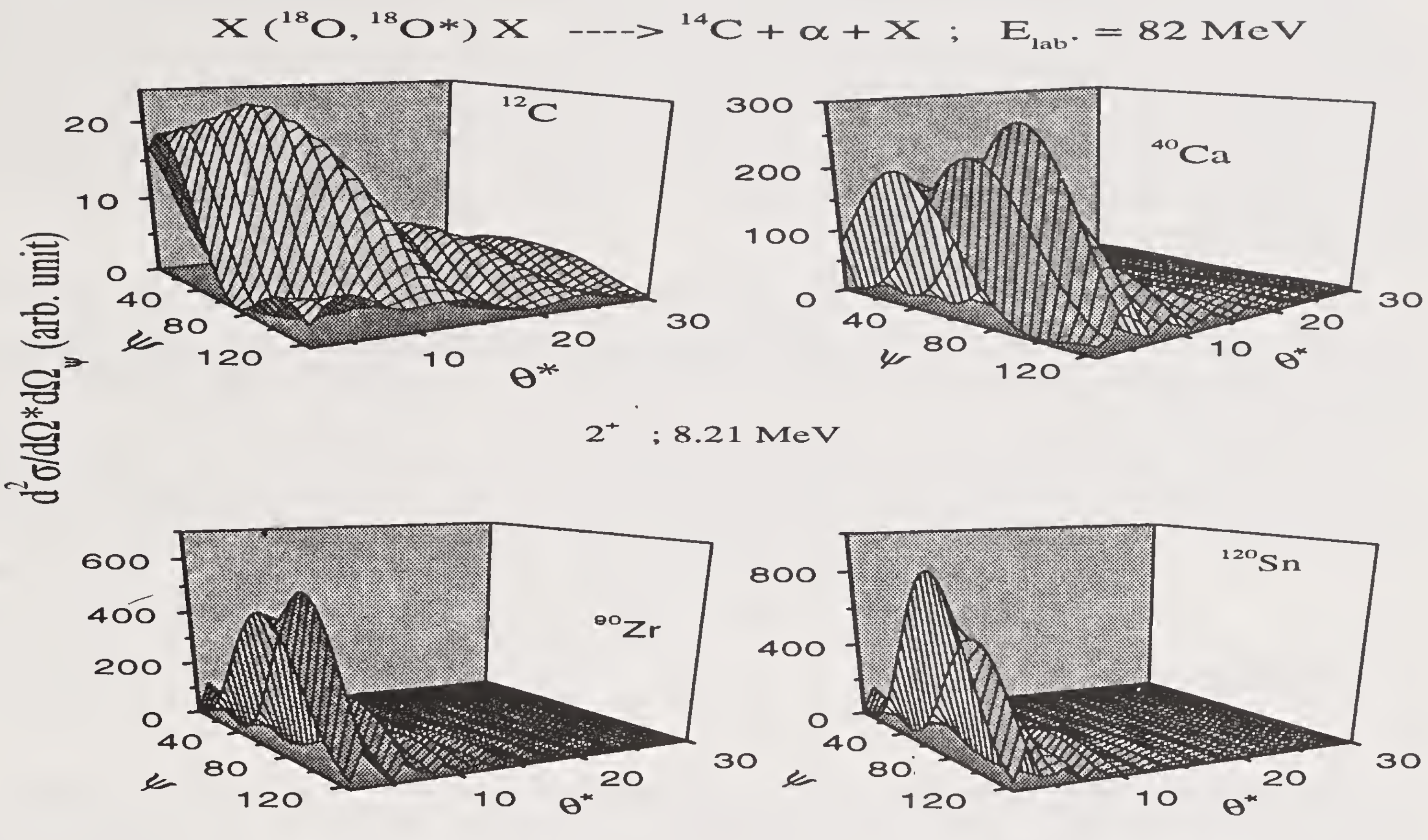

Figure 2. Three dimensional plots for the theoretical calculations with coupled channels form factor of α correlations for ^{18}O break-up in different target materials. θ^* is the c.m. angle of the intermediate state ^{18}O* and ψ the c.m. angle of emission of the α particle.

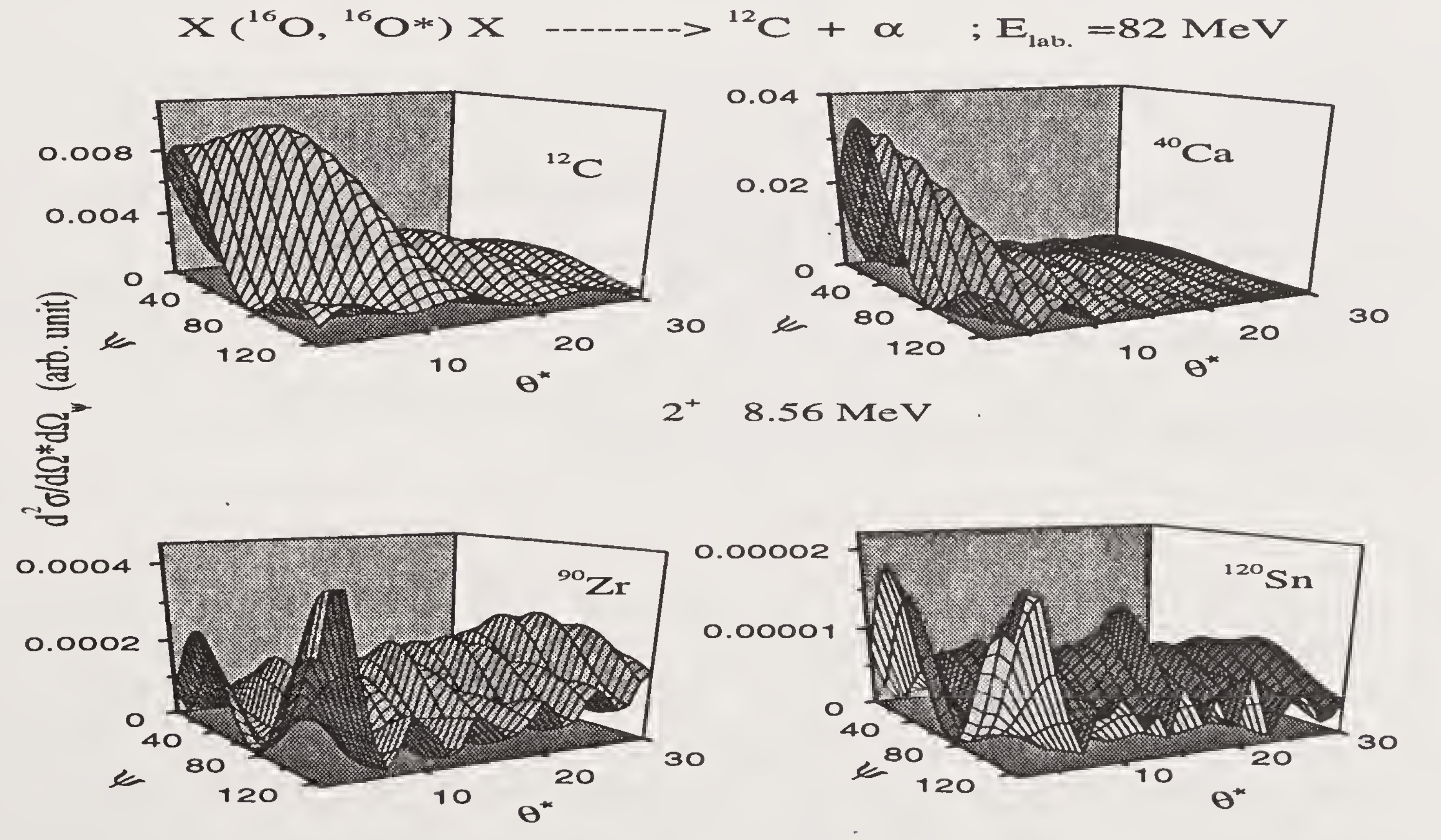

Figure 3. Three dimensional plots for the theoretical calculations with coupled channels form factor of α correlations for ^{16}O break-up in different target materials.

Using this formalism we explain the correlations for 8.21 MeV resonance for ^{18}O break-up into α and ^{14}C. The coupled channels calculations were performed by considering only two channels. The reduced electromagnetic excitation probability values were taken from the literature [4]. Figure 1 shows excellent agreement between theoretical calculations (straight line) with experiment. A SAM calculation (dotted line) was also performed with the parameter set given in ref. [1].

We have further calculated the correlations for 8.21 MeV resonances for ^{18}O break-up into α and ^{14}C, 8.56 MeV continuum state for ^{16}O break-up into α and ^{14}C for three different target elements ^{40}Ca, ^{90}Zr and ^{120}Sn (figures 2 and 3). Though calculations for both ^{16}O and ^{18}O show the prominent Z dependence, double differential cross section for α correlations of ^{16}O break-up behaves differently from ^{18}O with increasing Z [5]. This effect is most probably due to the two sd-shell neutrons present in the ^{18}O nuclei.

3. Conclusions

We have calculated the double differential cross section for α decay of 2^+ state of ^{18}O in the sequential breakup reaction $X(^{18}\mathrm{O}, {}^{18}\mathrm{O}^* \rightarrow {}^{14}\mathrm{C}\alpha)$ at 82 MeV with SAM and coupled channels form factor ($X = {}^{12}$C, ^{40}Ca, ^{90}Z, ^{120}Sn). Good agreement was observed with experimental results using the coupled channels form factor of the double differential cross section for α decay from the 8.21 MeV, 2^+-states of ^{18}O. We predicted the nature of double differential cross section for α decay from the 8.56 MeV, 2^+-states of ^{16}O in the sequential break-up reaction $^{12}\mathrm{C}(^{16}\mathrm{O}, {}^{16}\mathrm{O}^* \rightarrow {}^{12}\mathrm{C}\alpha)$ at 82 MeV using the coupled channels form factor. Further calculations and experiments are needed to extract more information about the dynamics of the reaction in the significant region of phase space for the above system.

References

[1] W D M Rae and R K Bhowmik, *Nucl. Phys.* **A420**, 320 (1984); **A427**, 142 (1984)

[2] I J Thompson, *Comp. Phys. Rep.* **7**, 167 (1988)

[3] F Poughen, P Roussel, M Bernas, F Diaf, B Fabbro, F Naulin, E Plagnol and G Rotbard, *Nucl. Phys.* **A325**, 481 (1979)

[4] D R Tilley, H R Weller, C M Cheves, R M Chasteler, *Nucl. Phys.* **A595**, 1 (1995)

[5] Samit Mandal and R K Bhowmik, under preparation

Fission fragment angular distributions in $^{16}O + ^{181}Ta$

BIVASH R BEHERA[1], SUBINIT ROY[2], P BASU[2], M K SHARAN[2], S JENA[1],
M SATPATHY[1], S K DATTA[4], L SATPATHY[3] and M L CHATTERJEE[2]
[1]Department of Physics, Utkal University, Bhubaneswar 751 004, India
[2]Saha Institute of Nuclear Physics, 1/AF, Bidhan Nagar, Calcutta 700 064, India
[3]Institute of Physics, Bhubaneswar 751 006, India
[4]Nuclear Science Centre, P.B. No. 10502, New Delhi 110 067, India

Abstract. Time of flight and energy of fission fragments were measured using pulsed beam. Fission fragment mass and energy integrated angular distributions were extracted. Fission fragment anisotropy was explained in the framework of saddle point model.

Keywords. Fusion–fission; quasifission; saddle-point model.

PACS Nos 25.70.Hi; 25.70.Jj

1. Introduction

Studies of HI induced fission angular distribution of fragments have shown a greater anisotropy than that expected on the basis of standard fission theory [1–2]. Wider mass distributions, forward backward asymmetry of mass distribution are also observed in some heavy systems [3]. These phenomena are attributed to many non-compound reaction process such as quasifission etc [3]. We have undertaken an experiment to understand reaction mechanism of fission through angular distribution and mass distribution measurements.

2. Experiment

The experiment was carried out at Nuclear Science Centre, New Delhi, using ^{16}O pulsed beam from 15UD pelletron. Beam of energy 92, 98 and 108 MeV was bombarded on tantalum target of thickness 205 $\mu g/cm^2$ and carbon backing 10 $\mu g/cm^2$ (thickness estimated by alpha transmission technique) in general purpose scattering chamber. Fission fragments were detected by number of 100 mm^2 partially depleted surface barrier detectors of thickness 200 to 300 micron operated in singles mode. Two additional detectors were kept at 10° on both side of beam axis inside the chamber to monitor Rutherford scattering for cross section normalization. For each event the detector measured energy and time of flight with respect to time structure of pulsed beam. The pulsed beam has repetition rate of 250 ns and width of 1.8 to 2 ns

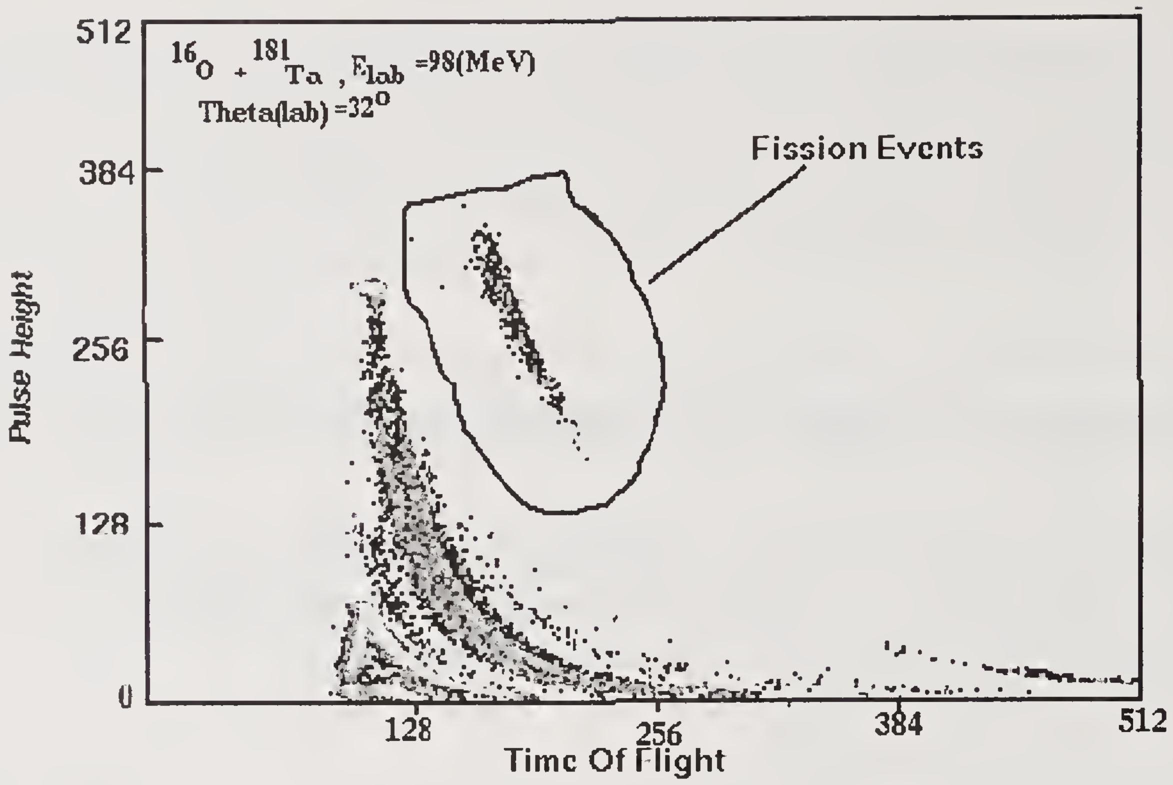

Figure 1. Two dimensional energy versus time of flight spectrum. Time of flight in arbitrary units.

(measured from width of elastic peak during the experiment). Start signal of the TAC was from detector and stop from RF of the accelerator. Absolute time scale of the events were determined from fast elastically scattered peak. The energy and time of flight signal were corrected for pulse height defect and plasma delay following the empirical formula of Ogihara [4]. Energy calibration of the detector was done from elastic scattering data at different energy and alpha and fission fragments emitted from ^{252}Cf source. Throughout the experiment there was good separation of fission events and other reaction products. For fission cross section calculation a gate was put on fission events at two dimensional scattered plot of energy versus time. At each angle cross section was normalized with yield of 10° monitor assuming it to be fully Rutherford. A typical two dimensional plot is shown in figure 1.

3. Results and discussion

The measured fission angular distributions were transformed from laboratory to center of mass frame by appropriate Jacobian obtained by using Viola systematics for symmetric fission [5]. The angular distributions in center of mass are fitted with sum of even order Legendre polynomials to extract the fission fragment anisotropy $W(180°)/W(90°)$. The angular distributions with fitting is shown in figure 2. Total fission cross sections are obtained by integrating the angular distribution data which is shown in figure 2. In the analysis of anisotropy saddle point model was used [6]. In the calculation of anisotropy by this model requires the value of the effective moment of inertia at the saddle point J_{eff} (l). The temperature T of the fissioning system at the transition state, and l distribution of the fissioning system. $J_{\mathrm{eff}}(l)$, the fission barrier $B_{\mathrm{f}}(l)$ and the ground state rotational energy $E_{\mathrm{rot}}(l)$ was calculated using the finite range model of Sierk [8]. The excitation energy at the saddle is calculated using the following equation:

$$E^{*} = E_{\mathrm{cm}} + Q - B_{\mathrm{f}}(l) - E_{\mathrm{rot}}(l) - E_{n}, \tag{1}$$

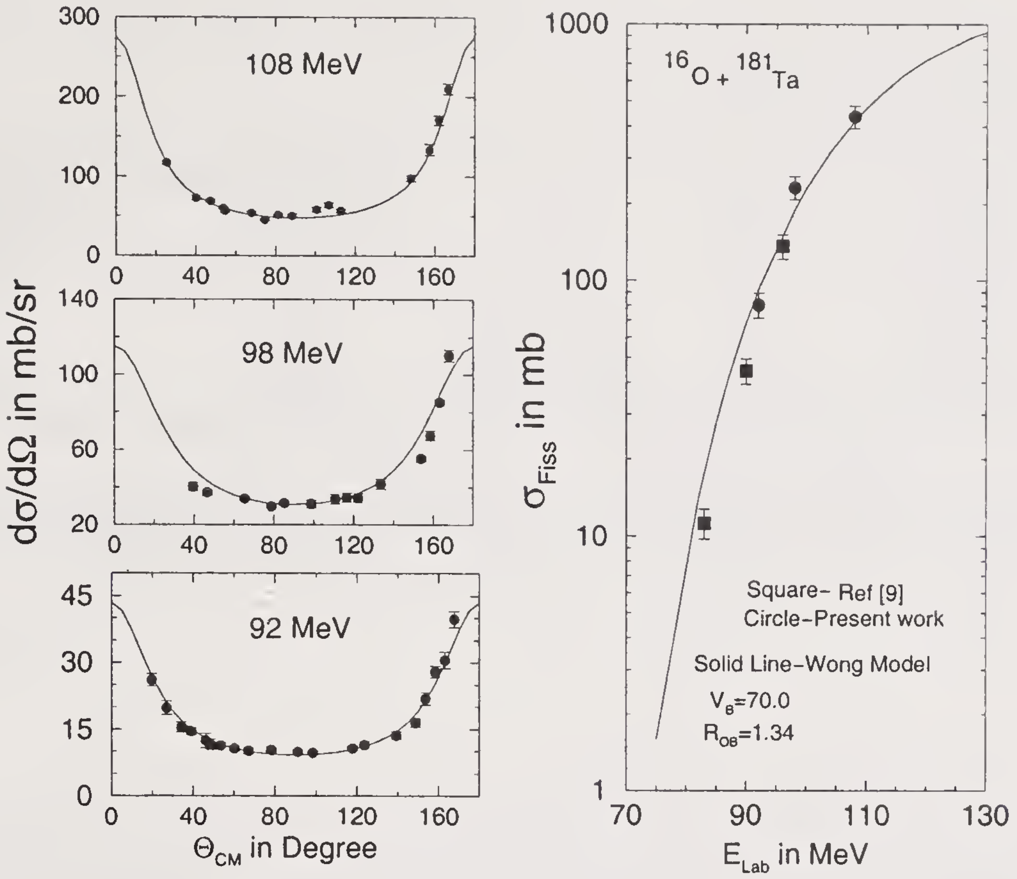

Figure 2. Left: Fission fragment angular distribution, solid lines are fit by even order legendre polynomials. Right: Fission excitation function.

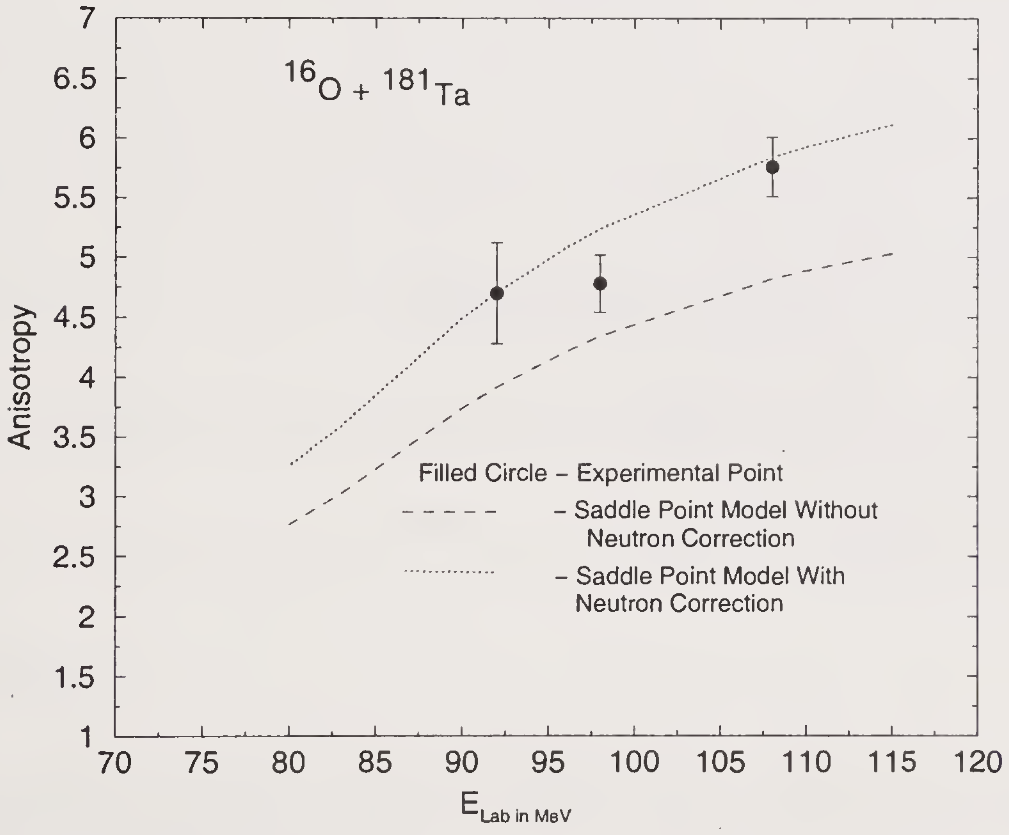

Figure 3. Fission fragment anisotropies for the system ^{16}O + ^{181}Ta.

where E_{cm} is the energy in the center of mass frame, Q is the Q value for forming the compound nucleus and E_n is the average energy removed by emission of the pre saddle neutrons. The saddle point temperature has been calculated using the relation $T = \sqrt{E^*/a}$, where a is the level density parameter. A value of $A/10$ MeV^{-1} was assumed for level density. In our system $\sigma_{\text{fission}} < \sigma_{\text{fusion}}$. The transmission coefficients $T(l)$ obtained from Wong model for fusion cross section [7] are multiplied by the fission probability $P_{\text{f}}(l)$ to obtain the l distributions for fission. $P_{\text{f}}(l)$ were obtained from statistical model code

Table 1. Summary of the results.

$E_{\rm beam}$ MeV	$\sigma_{\rm Fiss}$ (mb) expt.	$\sigma_{\rm Fiss}$ (mb) theory	A expt.	A (without neutron correction)	A (with neutron) correction)
108	437 ± 44	420	5.76±0.25	4.82	5.84
98	231 ± 41	189	4.78±0.24	4.34	5.22
92	80 ± 9	92	4.70±0.47	3.92	4.71

PACE2. We have used the values of prefission neutron multiplicity obtained from PACE2. The calculated anisotropies and measured anisotropies are shown in figure 3.

4. Conclusion

In the present paper analysis of fission fragment anisotropies and fission excitation function for the system ^{16}O + ^{181}Ta at energies above the barrier have been reported. The measured anisotropies are consistent with standard statistical model prediction. Mass distribution results will be reported elsewhere.

References

[1] B B Back, *Phys. Rev.* **C31**, 2104 (1985)
[2] B B Back *et al*, *Phys. Rev.* **C53**, 1734 (1996)
[3] Shen *et al*, *Phys. Rev.* **C36**, 115 (1987)
[4] M Ogihara *et al*, *Nucl. Instrum. Methods* **A251**, 313 (1986)
[5] V E Viola *et al*, *Phys. Rev.* **C31**, 1550 (1985)
[6] R Vandenbosch and J R Huizenga, *Nuclear Fission* (Academic Press, New York, 1973)
[7] C Y Wong, *Phys. Rev. Lett.* **31**, 766 (1973)
[8] A J Sierk, *Phys. Rev.* **C33**, 2039 (1986)
[9] F Videbaek *et al*, *Phys. Rev.* **C15**, 954 (1977)

A three body approach to study the structural properties of 2-n halo nuclei and the search for Efimov states

V S BHASIN
Department of Physics and Astrophysics, University of Delhi, Delhi 110 007, India

Abstract. The discovery of neutron rich isotopes of the lightest elements on the neutron drip line exhibiting a halo structure has opened up new vistas in research activities. The novel structural features associated with the halo phenomena have been the subject for extensive theoretical and experimental investigations in recent times. In this talk, I propose to present a broad overview of the recent developments in this field, bringing out the striking features which show that a large number of light nuclei near the neutron drip line are characterized by a clear separation between a 'normal' core nucleus and a loosely bound low density veil of neutrons. Specifically, the two neutron halos offer a natural premises, from a theoretical standpoint, to employ three body techniques for studying their detailed structural properties. A considerable part of the talk will be devoted to report and highlight the results on a number of light halo nuclei such as ^{11}Li, ^{14}Be, ^{19}B and ^{22}C on which we have been carrying out investigations employing a simple but realistic three body model. These three body systems which have been termed as 'Borromean' (i.e while three body systems are bound, the corresponding binary subsystems on the other hand are unbound) are characterized by large spacial extension and very low separation energy of the neutron. They are, therefore, ideally suited for exploring the possibility of the existence of Efimov states in two neutron halo nuclei. We have recently carried out the three body analyses to predict the possibility of the occurrence of such states on which experimental work at various laboratories is underway.

Keywords. Three body calculations; Efimov states; Borromean; halo nuclei.

PACS Nos 21.45.+v; 21.10.Dr; 21.60.Gx; 27.20.+n

1. Introduction

With the upcoming facilities for producing intense radioactive nuclear beams through high energy fragmentation alongwith the contemporary developments in the state of the art involving detectors and isotope separators, experiments have been carried out which have opened [1–4] a new rich field of nuclear physics: *the structure of nuclei near the driplines.* The chart of nuclides, in which the neutron number N is plotted against the proton number Z shows that stable nuclei form a diagonal band near $Z = N$ line. On either side of this 'valley of stability' lies a wider region of unstable nuclei. (These are nuclei that, if formed, will exist for a finite time before β-decaying to more stable forms.) The outer edges of this unstable region are known as the *proton and neutron driplines.*

Using the empirical mass formula for the binding energy:

$$B(N,Z) = b_v A - b_s A^{2/3} - \frac{1}{2} b_{\rm sym} \frac{(N-Z)^2}{A} - \frac{3}{5} \frac{Z^2 e^2}{R_c} \tag{1}$$

the minimization condition i.e,

$$\frac{\partial B}{\partial N}|_{A=\rm const} = 0$$

gives

$$(N-Z)_{\beta-\rm stable} = \frac{\frac{3}{5}\frac{e^2}{R_c}A - (M_n - M_p)}{2\frac{b_{\rm sym}}{A} + \frac{3}{5}\frac{e^2}{R_c}} \approx 6 \times 10^{-3} A^{5/3}. \tag{2}$$

The nuclei which satisfy this relationship gives rise to *the β-stability valley*. The neutron (proton) dripline which signify the limits of the nuclear periodic table with separation energies $S_n = 0$ ($S_p = 0$) are obtained through the conditions

$$\frac{\partial B}{\partial N}|_{Z\rm const} = 0 \quad \text{for the neutron dripline,}$$

$$\frac{\partial B}{\partial N}|_{N\rm const} = 0 \quad \text{for the proton dripline.}$$

These lines are located far off from the stability valley and there appears to be a large number of nuclei lying beyond the stability line.

Through several decades of studying the charge and matter distribution of stable nuclei, we have learnt *three characteristics of nuclear density* common to all nuclei.

1. The proportionality of the nuclear radius : $R \propto A^{1/3}$
   i.e $R = r_0 A^{1/3}$: $r_0 = 1.2 \times 10^{-15}$m.
2. Surface thickness of about 1 femtometer (the density over which the nuclear density drops about 70 percent to 30 percent of its maximum value).
3. An almost complete spatial overlap of the proton and neutron density distributions.

The pioneering experiments which were carried out to investigate the properties of these light neutron rich nuclei such as ^{8}He, ^{11}Li, ^{11}Be, ^{14}Be etc. seem to suggest that all the three rules mentioned above get violated. Thus, for instance, in the case of ^{11}Li, its rms radius is 3.16 fm – as large as that of ^{32}S; the surface thickness, or diffuseness is extremly large compared with that of the protons alone, which is more typical of a normal nuclear density distribution. Very weak binding of the outermost neutrons in the nucleus leads to neutron density distribution which extends well beyond the matter radius expected from systematics – indicating the formation of 'cloud' (quantum mechanical tunneling) commonly known as 'halo'. One can clearly see in the density distribution [5] a long tail formed by the last two neutrons. Such a description is indeed supported by the experimental observations of abnormally large total reaction and Coulomb dissociation cross-section, very sharply peaked angular distribution of the neutrons observed in coincidence with other fragments in the breakup reactions and sharp narrow structure observed in the momentum distribution of the fragments.

1.1 Excitation and structure of the halo nucleus

The discovery of the neutron halo has also brought to light new kinds of *excitation modes* in nuclei. Among the known collective nuclear excitations, the giant E1 excitation which results from the oscillation of the proton and neutron distributions against each other is the most pronounced nuclear excitation. In a nucleus with a neutron halo, one has a similar additional oscillation – that of the core against the halo. This excitation is known as the *soft E1 mode* because of the gradual decrease of the halo density at large distances, the restoring force is weak and the oscillation frequency is extremely low. In fact, several model calculations [6] predict the energy for this excitation to be about 1 MeV, much lower than the typical E1 giant resonance energy of around 20 MeV. Experimentally observed large dissociation cross-section of a halo nucleus like, ^{11}Li, by a high Z-target strongly suggests the existence of such a low frequency excitation mode.

Experiments also provide compelling evidence for halo clusterization of matter into a normal core nucleus and a loosely bound low density veil of neutrons around the core. For instance, the experimental measurements [7] on the magnetic dipole and dielectric quadrupole moments of ^{11}Li give values which are found to be close to those obtained for ^{9}Li. In addition the results [8] on charge changing reaction cross-section for ^{8,9,11}Li on C target strongly indicate that ^{11}Li is to be regarded as a three body system with ^{9}Li as core and the two neutrons orbiting around it.

The simplest halo is a two body system consisting of one neutron outside the nuclear core. It has been shown that if a neutron halo is defined as a divergent rms radius of the halo for the neutron separation energy, S_n, approaching zero, then a two body halo can occur only for s- and p-states. The conditions for the occurance of 2-n halo in three body systems such as in ^{11}Li where $S_{2n} > 0$ and $S_n(N-1) < 0$ are more restrictive. Nevertheless, it is quite clear that at such low energies the effective two body interaction is operative in low partial waves such as $l = 0$, 1 etc. To describe these binary interactions, the most natural choice, from an empirical standpoint, is the separable potentials which can be easily constructed from the two body data in a given partial wave. These potentials can then prove to be not only realistic enough to describe the binary system through analytic expressions but also turn out mathematically simple enough to solve the three body systems representing the 2-n halo nuclei. During the past few years we have been employing this approach [9,10] to study the structural properties of halo nuclei such as ^{11}Li, ^{14}Be, ^{19}B, ^{22}C and ^{20}C. Before I present the details to describe this approach and the results obtained on these systems, let me briefly mention some of the other theoretical approaches (with modifications in the standard ones) which have been put forth to account for the properties of the halo nuclei.

1.2 Other theoretical approaches

1.2.1. Shell model calculations: Here several difficulties appear; first shell model orbitals no longer provide a good starting point if the residual interaction is ignored – the valence particles in that case may not even be bound; second is the problem of treating the interaction in the nuclear exterior where many body effects may be small and the interaction is close to the ‘free’ particle case. Arima *et al* [11] employing the shell model, calculate the radii of neutron-rich p-shell nuclei and find rather difficult to correctly reproduce matter of ^{11}Li.

1.2.2. Self-consistent Hartree–Fock calculations (including relativistic mean field approach [12]): These attempts also fail to reproduce separation energies, rms radii, interaction cross-section for ^{11}Li, ^{6}He etc. However, as observed by Bertsch *et al* [13] only by adjusting the separation energy of the last neutron to the measured value is some agreement possible.

1.2.3. Three body approaches: A number of attempts using many variants of the three body approach have been made in the recent past and have been summarized in a review article by Zhukov *et al* [14] .

The object of the present work is to employ Faddeev's three body theory [15] using two body separable potentials to study the structural properties of $2n$-halo nuclei.

2. Faddeev's three body approach using separable potentials

In Faddeev's theory, the eigenfunction of the three-particle Hamiltonian with pair interaction is represented as a sum of three terms, viz,

$$\Psi = \psi^{(1)}(\vec{p}_{23}\,,\,\vec{p}_1) + \psi^{(2)}(\vec{p}_{31}\,,\,\vec{p}_2) + \psi^{(3)}(\vec{p}_{12}\,,\,\vec{p}_3) \tag{3}$$

for each of which there exists a coupled set of equations symbolically expressed as

$$\psi^{(i)} = \phi^{(i)} - G_0\, t_{jk}\,(\psi^{(j)} + \psi^{(k)}) \ \text{ for } i \neq j \neq k = 1,2,3. \tag{4}$$

In this equation t_{jk}'s are two-body t-matrices in the three-particle Hilbert space; $\phi^{(i)}$'s refer to the free states incorporating the appropriate boundary conditions for the three body scattering problems. In the case of bound state problem of our interest, the inhomogeneous terms do not appear and we have eventually the coupled integral equation in momentum space. The momenta appearing in the wave function (eq.(3)) are given by

$$\vec{p}_{ij} = \frac{m_j\vec{P}_i - m_i\vec{P}_j}{m_i + m_j}\,,\ \vec{p}_k = \frac{(m_i + m_j)\vec{P}_k - m_k(\vec{P}_i + \vec{P}_j)}{m_i + m_j + m_k}\,, \tag{5}$$

where $\vec{P}_1$, $\vec{P}_2$ represent the momenta of the two neutrons and $\vec{P}_3$ is the momentum of the core. In the three body c.m system $\vec{P}_1 + \vec{P}_2 + \vec{P}_3 = 0$, we have two independent momenta.

For the two body interaction, we assume separable potentials. The potential

$$V_{12} = -\frac{\lambda_n}{2\mu_{12}} g(p_{12}) g(p'_{12}), \qquad g(p) = \frac{1}{(p^2 + \beta^2)} \tag{6}$$

is known to reproduce the low energy scattering data for the $^1S_0$ $n - n$ state reasonably well with the help of adjustable parameters λ_n and β. For the n-core system, we assume that the core is spinless and the halo neutron exists in a low lying intruder s-orbit producing a virtual or a bound state with the core. With this restriction, we assume

$$V_{23} = -\frac{\lambda_c}{2\mu_{23}} f(p_{23}) f(p'_{23}),$$

$$V_{31} = -\frac{\lambda_c}{2\mu_{31}} f(p_{31}) f(p'_{31}),$$

$$f(p) = \frac{1}{(p^2 + \beta_1^2)}. \tag{7}$$

Here since we only know the bound state or the excitation energy of the system, this gives a certain amount of flexibility in the determination of the parameter β_1.

With this input, the solution of the three body wave-function can be analytically expressed as

$$\Psi(\vec{p}_{12}, \vec{p}_3; E) = D^{-1}(\vec{p}_{12}, \vec{p}_3; E)\,[g(p_{12})F(p_3) + f(p_{23})G(p_1) + f(p_{31})G(p_2)], \tag{8}$$

where the spectator function $F(p)$ and $G(p)$ satisfy the coupled integral equations:

$$[\lambda_n^{-1} - h_n(p)]F(p) = 2\int \mathrm{d}\vec{q}\, K_1(\vec{p}, \vec{q}; E) G(\vec{q}), \tag{9}$$

$$[\lambda_c^{-1} - h_c(p)]G(p) = 2\int \mathrm{d}\vec{q}\, K_2(\vec{p}, \vec{q}; E) F(\vec{q}) + \int \mathrm{d}\vec{q}\, K_3(\vec{p}, \vec{q}; E) G(\vec{q}), \tag{10}$$

where the kernels K_1, K_2, K_3 alongwith the other symbols are given in ref.[9].

3. Results and comparison with experimental data

The above formalism has been employed to study the properties of halo nuclei such as ^{11}Li, ^{14}Be, ^{19}B, ^{22}C and ^{20}C. The calculations to extract information on properties such as the binding energy, the momentum distribution of the core and of the halo neutron through the spectator functions as well as the root mean square separations of n–n and n-core pairs for ^{11}Li have been discussed in detail and compared with the experimental data in ref.[9]. Thus, for instance, the equations (9) and (10) which essentially reduce to one variable integral equations after performing the angular integrations, have been numerically solved as an eigenvalue problem in terms of the two body strength parameter λ_c by feeding the value of the three body binding energy E as input. The numerical values of λ_c so computed are then compared with those determined through the two body analysis. The results are compared in table 1.

Table 1.

B.E of ^{11}Li(MeV)	β/α	λ_n/α^3	β_1/α	λ_c/α^3	λ_c/α^3 from 3-body
0.34	5.8	18.6	5.0	10.32	12.92
	6.3	23.4	5.0	10.32	12.91
	5.8	18.6	5.5	14.00	17.01
0.20	5.8	18.6	5.0	10.32	12.39
	5.8	18.6	5.5	14.00	16.38

The solutions of the spectator functions $F(p)$ and $G(p)$ satisfying the integral eqs (9) and (10) describe the momentum distribution of the spectator particles i.e, of ^{9}Li and of the halo neutron within the nucleus. Experimentally, momentum distribution of ^{9}Li fragments following the break-up of ^{11}Li, i.e

$$^{11}\mathrm{Li} \;+ A_T \;\to\; ^9\mathrm{Li} \;+ X$$

has been studied by Orr *et al* [16] to observe the momentum distribution of ^{9}Li. Similarly, the experiments on the momentum distribution of neutrons through the reaction

$$^{11}\mathrm{Li} \;+ A_T \;\to\; ^9\mathrm{Li} \;+ n + X$$

using targets such as Be, C and Pb were carried out by Anne *et al* [17] to observe the momentum distribution of halo neutron in the nucleus. Figures (1) and (2) shown in ref. [9] compare reasonably well with the experimental findings.

From our 'master' three body equation (8), we can also make estimate of the correlations between the two halo neutrons and between a halo neutron and ^{9}Li core within the nucleus. In fact, the function

$$\phi_{nn} = D^{-1}(\vec{p}_{12}, \vec{p}_3; E)\, g(p_{12}) \tag{11}$$

and

$$\phi_{nc} = D^{-1}(\vec{p}_{12}, \vec{p}_3; E)\, f(p_{23}) \tag{12}$$

describe the correlation between the two neutrons and between the neutron and ^{9}Li.

Very recently kinematically complete measurements for Coulomb dissociation of ^{11}Li into $^9\mathrm{Li} + 2n$ have been carried out by Ieki *et al* [18]. The data for the correlation functions deduced from the relative momentum spectrum between two neutrons in coincidence with ^{9}Li has been compared in figure (3) of ref. [9]. Using these correlation functions we also compute the values of the root mean square radii $\bar{r}_{nn}$ and $\bar{r}_{nc}$ as a function of the three body binding energy. These are summarized in table 2.

With the help of these values, we then calculate the rms matter, $\bar{r}_{\mathrm{matter}}$, for ^{11}Li using the relation given in ref. [19].

$$\langle r^2 \rangle_{\mathrm{matter}} = \frac{A_c}{A} \langle r^2 \rangle_{\mathrm{core}} + \frac{1}{A} \langle \rho^2 \rangle\,, \tag{13}$$

where $\langle r^2 \rangle_{\mathrm{core}}$ is the mean square value of the radius of ^{9}Li and the radial variable $\rho^2 = x^2 + y^2$, $\vec{x} = \vec{r}_1 - \vec{r}_2/\sqrt{2}$ and $\vec{y} = \sqrt{(2A_c/A)}\,[(\vec{r}_1 + \vec{r}_2/2) - \vec{r}_3]$. Taking the value of $\sqrt{\langle r^2 \rangle_{\mathrm{core}}}$ for ^{9}Li to be 2.3 fm, we obtain the value of the matter radius to be 3.6 fm to be compared with the experimental value of 3.14 ± 0.06 fm.

Table 2.

B.E of ^{11}Li(MeV)	$\bar{r}_{nn}$	$\bar{r}_{nc}$
0.20	10.63	10.93
0.25	9.90	9.86
0.315	8.93	8.87

3.1 Efimov states in halo nuclei like ^{14}Be, ^{19}B, ^{22}C *and* ^{20}C

The above formalism has also been extended to address an intriguing question as to how far and under what conditions the two neutron halos characterized by large spatial extension and very low separation energy of the halo neutrons actually attain the Efimov limit so as to produce the Efimov states near the three body breakup threshold. Quantitatively, as pointed out by Efimov [20] , so long as

$$r_0\sqrt{|E|} \ll 1 \qquad \text{and} \qquad r_0 \ll a, \tag{14}$$

where r_0 is the range of the two body interaction, E is the energy of the three body system and a represents the scattering length of the virtual s-state of the two particles, the existence of resonating s-wave potentials results in the appearance of a three body long range interaction which goes as $1/R^2$ where $R^2 = r^2 + \rho^2$. The existence of such a long range force should respond by producing a large number of states particularly near and below the three body break up threshold. With this objective we investigated in ref. [10] the possibility for the occurence of the Efimov states in ^{14}Be assuming a possibility for the existence of a low lying s orbital state for the halo neutrons with ^{12}Be as core. The basic structure of the integral equations as given in ref. [9] is esssentially the same. However, for the purpose of studying the sensitive computational details of the Efimov effect, we transform these equations involving only dimensionless quantities as discussed in ref. [10]. In table 3 are shown the results of three body calculations of energies of ^{14}Be for the ground states and first two excited states (ϵ_0, ϵ_1 and ϵ_2) for different excitation energies of the $n{-}^{12}$Be system.

From table 3 we note that at 50 keV virtual state energy of $n{-}^{12}$Be system, the three body binding energy for ^{14}Be, as obtained from the set of integral equations, is 1350 keV which is in close agreement with the experimentally observed value. (Note that here the parameters of $n{-}^{12}$Be potential are taken as $\lambda_1 = 11.71\alpha^3$, $\beta_1 = 5.0\alpha$.) However, this two body potential does not reproduce any excited state for ^{14}Be system. As the virtual state energy of the $n{-}^{12}$Be system is lowered to 2 keV, the resulting three body system starts swelling and enters into the regime of Efimov effect. As a result we get two excited states besides the ground state energy of 1450 keV for the ^{14}Be system. The same trend appear to follow in the case of Borromean nuclei like ^{19}B and ^{22}C. Here we find that by employing the realistic two body potentials for $n{-}n$ and n-core systems, the three body equations can predict the three-body ground state energy in agreement with the experimental values. However, the input two body dynamics, does not allow the three body equation to admit any solution for the occurence of the excited states near the break-up threshold. It is only

Table 3.

$n{-}^{12}$Be energy (keV)	λ_1	a_s (fm)	ϵ_0 (keV)	ϵ_1 (keV)	ϵ_{02} (keV)
50	11.71	−21	1350		
5.8	12.32	−62	1408	0.1	
2	12.46	−105	1450	2.6	0.06
1	12.52	−149	1456	3.8	0.22
0.1	12.62	−483	1488	6.1	0.62
0.05	12.63	−658	1490	6.4	0.68
0.01	12.65	−1491	1490	6.9	0.72

by changing the parameters of the n-core potential so as to reduce the excitation energy to a few keV, that the Efimov region begins to develop and the excited states start appearing for the Borromean type halo nucleus.

The study of ^{20}C, which is not Borromean, has been found rather interesting. Here we consider $n-n-^{18}$C system, where n–^{18}C has an observed bound state energy of about 160 keV. In this case, with the two body potential for n–^{18}C, we find that our equations predict the ground state energy of 3.5 Mev in close agreement with the experimental value. In addition, we get the Efimov states for energies around 150 keV. Thus a realistic potential for a binary n–^{18}C system which reproduces the ground state energy in agreement with the experimentally observed value also predicts three excited states around 150 keV. This is a striking result which needs to be confirmed experimentally. This has led us to establish in quantitative terms general criteria for the occurrence of Efimov states in such halo nuclei [21].

4. Conclusion

The physics of the halo phenomena seems to be the *homefield* for *few body cluster models.* It is clear that to understand the structural properties of the $2n$ halo nuclei, one has to go beyond the meanfield approach to few body theoretical procedures such as the one laid down by *Faddeev three body theory.* By employing the separable potentials for the binary systems we solve the three body systems representing the $2n$ halo nuclei to compute their structural features. The present approach has the following *distinct advantages*;

1. It provides us direct information about the momentum distribution of single particles within the halo through the knowledge of the spectator function, which can be easily compared with the experimental data.
2. The information about the two body correlation function inside a halo nucleus can be obtained in a rather simple way from the solution of the three body wave-function.
3. It may be emphasized that since the three body observables are computed without resort to any approximation, any discrepancy between the observed and the calculated quantities should directly reflect on the inadequacy or limitation of the input two body potentials used.

To address the *deeper question* as to how these *new clustering features* emerge from the nuclear many body theory is a challenge (to theorists) for the future.

Acknowledgment

The financial grant from the UGC is gratefully acknowledged under the research project No.10-4/95(SR-I)

References

[1] P G Hansen, A S Jensen and B Jonson, *Ann. Rev. Nucl. Part. Sci.* **45**, 591 (1995)

[2] A C Mueller and B M Sherrill, *Ann. Rev. Nucl. Part. Sci.* **43**, 523 (1991)
[3] I Tanihata *et al*, *Phys. Lett.* **B160**, 380 (1985); **B206**, 592 (1988)
[4] T Kobayashi *et al*, *Phys. Rev. Lett.* **60**, 2599 (1988); see also *Phys. Lett.* **B232**, 51 (1989)
[5] Y Suzuki and Y Tosaka, *Nucl. Phys.* **A517**, 599 (1990)
G F Bertsch and J Foxwell, *Phys. Rev.* **C41**, 1300 (1990)
G F Bertsch and H Esbensen, *Ann. Phys.* **209**, 327 (1991)
[6] I Tanihata *et al*, *Phys. Lett.* **B160**, 380 (1985); see also *Nucl. Phys.* **A522**, 275C (1991)
[7] E Arnold *et al*, *Phys. Lett.* **B197**, 398 (1987); see also *Phys. Lett.* **B281**, 16 (1992)
[8] B Blank *et al*, *Z. Phys.* **A343**, 375 (1992)
[9] S Dasgupta, I Mazumdar and V S Bhasin, *Phys. Rev.* **C50**, R550 (1994)
[10] I Mazumdar and V S Bhasin, *Phys. Rev.* **C56**, R5 (1997)
[11] A Arima *et al*, *Nucl. Phys.* **A506**, 271 (1990)
[12] W Koepf *et al*, *Z. Phys.* **A340**, 119 (1991)
[13] G Bertsch and J Foxwell, *Phys. Rev.* **C42**, 758 (1990)
[14] M Zhukov *et al*, *Phys. Rep.* **231**, 151 (1993)
[15] L D Faddeev, *Sov. Phys. JETP* **12**, 1014 (1961)
[16] N A Orr *et al*, *Phys. Rev. Lett.* **69**, 2050 (1992)
[17] A Anne *et al*, *Phys. Lett.* **B250**, 19 (1990)
[18] K Ieki *et al*, *Phys. Rev. Lett.* **70**, 730 (1993)
[19] D V Fedorov, A S Jensen and K Riisager, *Phys. Lett.* **B312**, 1 (1993)
[20] V N Efimov, *Comments Nucl. Part. Phys.* **19**, 271 (1990)
[21] I Mazumdar, Vandana Arora and V S Bhasin, to be published

Rare cold nuclear processes – A review and some new results

RAJ K GUPTA
Physics Department, Panjab University, Chandigarh 160 014, India

Abstract. The rare nuclear processes of cluster radioactivity, cold fission and cold fusion, studied on the basis of the quantum mechanical fragmentation theory (QMFT), are reviewed. This theory was advanced as early as in 1974–75 by the author and collaborators, first at Frankfurt and then developed both at Frankfurt and Chandigarh. The QMFT predicted all the three phenomena to occur most probable as cold processes, *prior* to their experimental observations. The success of experiments with respect to the QMFT and some new results are presented as predictions of this theory for future experiments.

Keywords. Cluster radioactivity; cold fission; cold fusion.

PACS Nos 23.70.+j; 25.85.-w; 25.70.Pa

1. Introduction

Cluster radioactivity, cold fission and cold fusion of nuclei for synthesizing new heavy elements are rare nuclear processes. The interesting aspect of these processes is that they are not only rare but also occur more probable as cold phenomena. The rare nature of these processes stem from the fact that these processes are masked by other competing processes. Cluster radioactivity is masked by the larger number of α-decay events, cold fission by fragments of various other velocities (hot and/or bimodal fission) and cold fusion by their specific choice of target-projectile combinations, incident bombarding energies and angular momenta. The dynamical or quantum mechanical fragmentation theory (QMFT) predicted all the three phenomena to be most probable as cold processes. These predictions were made as early as in 1974–75, *prior* to their being observed experimentally. Note that the QMFT, being a quantum mechanical theory, does not preclude the other processes, like the hot fission or hot fusion, but predict them to be less probable, as is now observed to be the case. A complete study of these three processes and related new phenomena is given in a forthcoming new book [1] edited by the author and Walter Greiner.

Cluster radioactivity is the spontaneous emission of clusters heavier than α-particle and *without* being accompanied by any neutron emission. Thus, it is a cold process (zero excitation energy) since the energy released as Q-value is completely consumed by the kinetic energy alone of the two fragments (the cluster and daughter nuclei). Fission is also the spontaneous breaking of a nucleus into two fragments (for binary fission), heavier than the ones involved in cluster radioactivity, but *with* or *without* being accompanied by neutron emission. The neutronless fission or in terms of velocities the very high *total kinetic energy* (close to the Q-value) fission, called cold fission, was first observed in 1981/82 at Grenoble, using the recoil spectrometer Lohengrin, where the kinetic energies of the fragments were also measured along with their masses and charges [2,3]. The actual neutronless fission, an equivalent of cluster radioactivity, is observed more recently in 1994 at Oak Ridge, where the neutronless as well as high neutron multiplicity fissions are observed [4]. This establishes the cold and hot fission, as well as the bi-modal fission, first observed in 1986 as two different kinetic energy distributions [5]. The observed high neutron multiplicity fission in these experiments is also associated with hyper-deformation of the fission fragments at the scission configuration [6], since the total excitation energy (difference of Q-value and total kinetic energy) can go into not only the internal excitation of the fragments but also in their deformation degree of freedom. This hyper-deformation mode is apparently the low total kinetic energy or hot deformed fission, that was first observed in 1992 at ILL [7]. Finally, the real signatures of cold fusion were first seen in the 1994 experiments at GSI, Darmstadt, where enhanced fusion cross-sections were observed at lower excitation energies, or incident energies below the barrier [8–10]. Also, hot fusion experiments are carried out more recently which result in lower fusion cross-sections [11]. For example, ^{58}Fe + ^{208}Pb and ^{34}S + ^{238}U result in the same heavy nucleus $^{265,267}_{108}$Hs emitting one or five neutrons, respectively, but the first one is a cold reaction (18 MeV excitation energy) with 19 pb of fusion cross-section and the second one a hot reaction (50 MeV excitation energy) with only 2.5 pb of fusion cross-section. It is relevant to mention here that all the transactinides ($Z < 103$) are synthesized since 1975 using only, what can be termed as the cold fusion reactions on the basis of the QMFT. All these early experiments were made either at a single incident energy or at energies above the barrier. Thus, inspite of the use of cold fusion reactions, real signatures of cold fusion eluded detection till late 1994 when Hofmann *et al* [8] bombarded ^{208}Pb with ^{62,64}Ni at different incident energies, both above and below the barrier.

The QMFT is a unified description of all the three processes of (cold) fusion, fission and cluster radioactivity. The key result behind the three phenomena is the shell closure effect of one or both of the reaction partners for fusion or that of the decay products for fission and cluster radioactivity. Both experimentally and theoretically, for cold phenomena, one of the nucleus (or decay product) is always a *spherical* closed or nearly closed shell nucleus. Apparently, the significance of spherical closed shells raises the question of the role of *deformed* closed shells, which need to be investigated in future.

Section 2 gives briefly the essential aspects of the dynamical fragmentation theory, the QMFT. Applications of this theory to heavy ion reactions, specifically the synthesis of new heavy elements, the fission phenomenon and cluster radioactivity are reviewed in §3. This includes some new results obtained recently. Our conclusions are summarized in §4.

2. The dynamical fragmentation theory

The QMFT is based on two center shell model (TCSM), used as an average two-body potential in Strutinsky macro-microscopic method. The relevant dynamical collective coordinates are the mass and charge asymmetry coordinates

$$\eta = \frac{A_1 - A_2}{A_1 + A_2}(A = A_1 + A_2), \quad \eta_Z = \frac{Z_1 - Z_2}{Z_1 + Z_2}(Z = Z_1 + Z_2), \tag{1}$$

in addition to the commonly used coordinates of relative separation $\vec{R}$ of two nuclei (or fragments), their deformations β_i $(i = 1, 2)$ and neck parameter ε. Similarly, a neutron asymmetry coordinate can be introduced, but one need to treat only two of them as independent variables since the three are related. The limiting values of η are $0 \leq |\eta| \leq 1$ and thus allows a unified description of a few nucleon, multi-nucleon (or cluster) transfer, a large mass transfer, the complete fusion ($|\eta| = 1$) of nuclei and the symmetric ($\eta = 0$), asymmetric and super-asymmetric fission (equivalently the cluster radioactivity) of a nucleus or compound nucleus. The details are given in the review by Gupta and Greiner in [1].

For heavy-ion collisions, the time-dependent Schrödinger equation in η (taking motions in η and η_Z as weakly coupled)

$$H\Psi(\eta, t) = i\hbar\frac{\partial}{\partial t}\Psi(\eta, t), \tag{2}$$

is solved for $R(t)$ treated classically and the other coordinates β_1, β_2 and ε fixed by minimizing the collective potential in these coordinates. Equation (2) is solved for a number of heavy systems, showing a few nucleon to large mass transfer or no transfer at all for the initial η_i-values refering to outside or on the potential minima. This procedure, however, is very much computer-time consuming, but some simplifications have been possible.

The potentials $V(R, \eta)$ and $V(R, \eta_Z)$ show that the motions in both η and η_Z are much faster than the R-motion. This means that the potentials $V(R, \eta)$ and $V(R, \eta_Z)$ are nearly independent of the R-coordinate and hence R can be taken as a time-independent parameter. This reduces the time-dependent Schrödinger equation (2) to the stationary Schrödinger equation

$$\left\{-\frac{\hbar^2}{2\sqrt{B_{\eta\eta}}}\frac{\partial}{\partial\eta}\frac{1}{\sqrt{B\eta\eta}}\frac{\partial}{\partial\eta} + V_R(\eta)\right\}\Psi_R^{(\nu)}(\eta) = E_R^{(\nu)}\Psi_R^{(\nu)}(\eta), \tag{3}$$

where R is fixed at the post saddle point. This choice of R-value is justified by many good fits to both the fission and heavy-ion collision data and by an explicit, analytical solution of time-dependent Schrödinger equation in η_Z coordinate [1]. An interesting result of these calculations is that the yields ($\propto$ $|\Psi(\eta)^2$ or $|\Psi(\eta_Z)|^2$, respectively, for mass or charge distributions) are nearly insensitive to the detailed structure of the cranking masses $B_{\eta\eta}$, calculated consistently by using TCSM. In other words, the static potential $V(\eta)$ or $V(\eta_Z)$ contain all the important information of a fissioning or colliding system, given simply by the Coulomb interaction plus the sum of the ground state binding energies of two nuclei (at some critical distance R_c),

$$V(R_c, \eta, \eta_Z) = \frac{Z_1 Z_2 e^2}{R} - \sum_{i=1}^{2} B(A_i, Z_i, \beta_i) + V_{\mathrm{P}}. \tag{4}$$

The charges Z_1 and Z_2 are fixed by minimizing the potential in η_Z coordinate (which fixes β_i automatically) and then the proximity potential V_{P} is added to account for the additional attraction between nuclear surfaces. Equation (4), without V_{P}, formed the basis of our first calculation on *cold fusion* reaction valleys, which was later optimized by adding the requirements of smallest interaction barrier, largest interaction radius and non-necked (no saddle) nuclear shapes. Non-necked shapes are signatures of the cold fusion, and like the necked-in shapes are known to witness the preformation of fission fragments.

For cluster radioactivity, a model of coupled motion in $\vec{R}$ and η coordinates is developed by Malik and Gupta [17]. The decay constant λ or the decay half-life $T_{1/2}(= \ln 2/\lambda)$ is calculated as the product of cluster preformation probability P_0 (given by the solution of stationary Schrödinger equation (3)), the barrier impinging frequency ν_0 (obtained from the Q-value shared between two fragments) and the WKB barrier penetration probability P:

$$\lambda = P_0 \nu_0 P. \tag{5}$$

Further details can be seen in [1].

3. Applications

The QMFT is applied very successfully to many heavy ion reactions, the predictions of target-projectile combinations for cold synthesis of new and superheavy elements, the fission data and the exotic cluster decay process. In fact, both the phenomena of cold fission and cluster radioactivity were predicted on the basis of this theory, *prior* to their experimental observations, and the idea of cold fusion (for synthesis of new elements) was first introduced on the basis of this theory. The success of experiments in proving almost all the predictions of this theory are reviewed in ref. [1]. Here we discuss only one new result each for future experiments.

3.1 Cold fusion studies

Figure 1 shows a portion of the nuclear chart, depicting the superheavy elements beyond $Z = 103$, and the cold fusion reactions used. It is creditable to mention that all the reactions underlined in this figure were predicted on the basis of the QMFT about two decades back (see figure 2, only the even–even elements were studied [12]). Thus, the road to the centre of island of stability at $Z = 114$ seems opened. Two important points may, however, be mentioned. Firstly, the predicted neutron number $N = 184$ for the centre of island. What we have observed so far are the heavy nuclei in continuation of our earlier known chart of nuclei, near the β-stability line. Therefore, in order to reach the real island of stability predicted at $Z = 114$, $N = 184$, we have to overshoot it by means of radioactive nuclear beams. Secondly, some new relativistic mean field calculations [13] predict $Z = 120$, $N = 172$ or 184 as the major closed shells instead of $Z = 114$, $N = 184$. The QMFT predicts a possible synthesis of $Z = 120$ element by a cold fusion reaction ^{208}Pb + ^{98}Sr. The interesting point to note is that one of the reaction partners for cold fusion reactions is always the closed shell nucleus Pb.

3.2 Cold fission studies

The QMFT is known for its success to explain the symmetric as well as asymmetric mass distributions (the single-, double- and even triple-humped distributions), including the very-asymmetric case of fission valleys at large η-values, the super-asymmetric fission (an equivalent of cluster radioactivity), the charge distributions and the associated fine structure in them leading to proton odd–even effect, and the simultaneous occurrence of both the cold and normal (hot) fission modes, called the bi-modal fission.

Figure 3 illustrates the calculated isotonic and isotopic yields for fission of ^{236}U, compared with the experimental data [14]. Apparently, the calculations give experimental

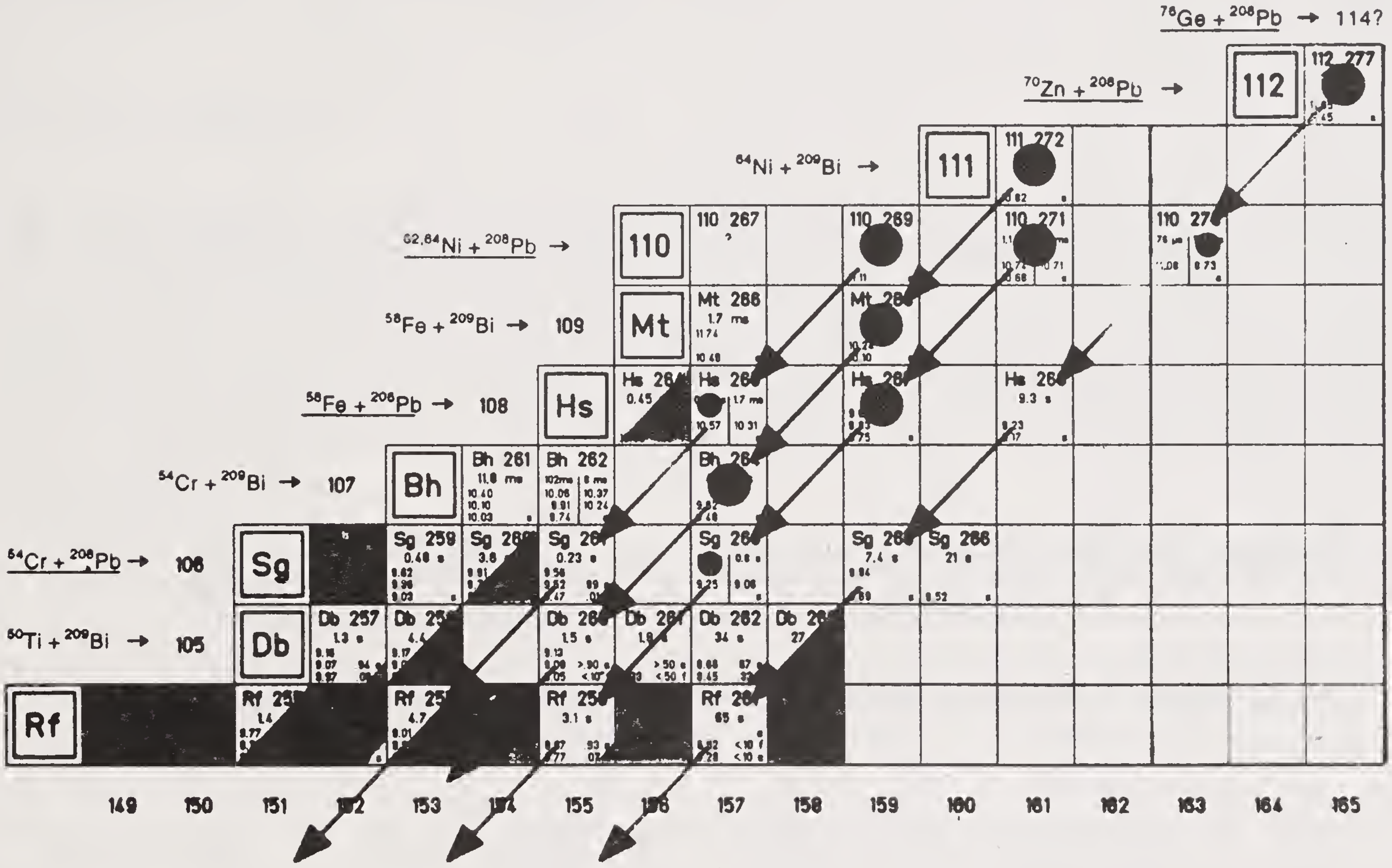
^{76}Ge + ^{208}Pb → 114?
^{70}Zn + ^{208}Pb →
^{64}Ni + ^{209}Bi →
^{62,64}Ni + ^{208}Pb →
^{58}Fe + ^{209}Bi → 109
^{58}Fe + ^{208}Pb → 108
^{54}Cr + ^{209}Bi → 107
^{54}Cr + ^{208}Pb → 106
^{50}Ti + ^{209}Bi → 105
112
111
110
Mt
Hs
Bh
Sg
Db
Rf
149
150
151
152
153
154
155
156
157
158
159
160
161
162
163
164
165

Figure 1. Nuclear chart (upper end only), along with the cold fusion reactions used to produce them (based on Münzenberg and Hofmann in [1]).

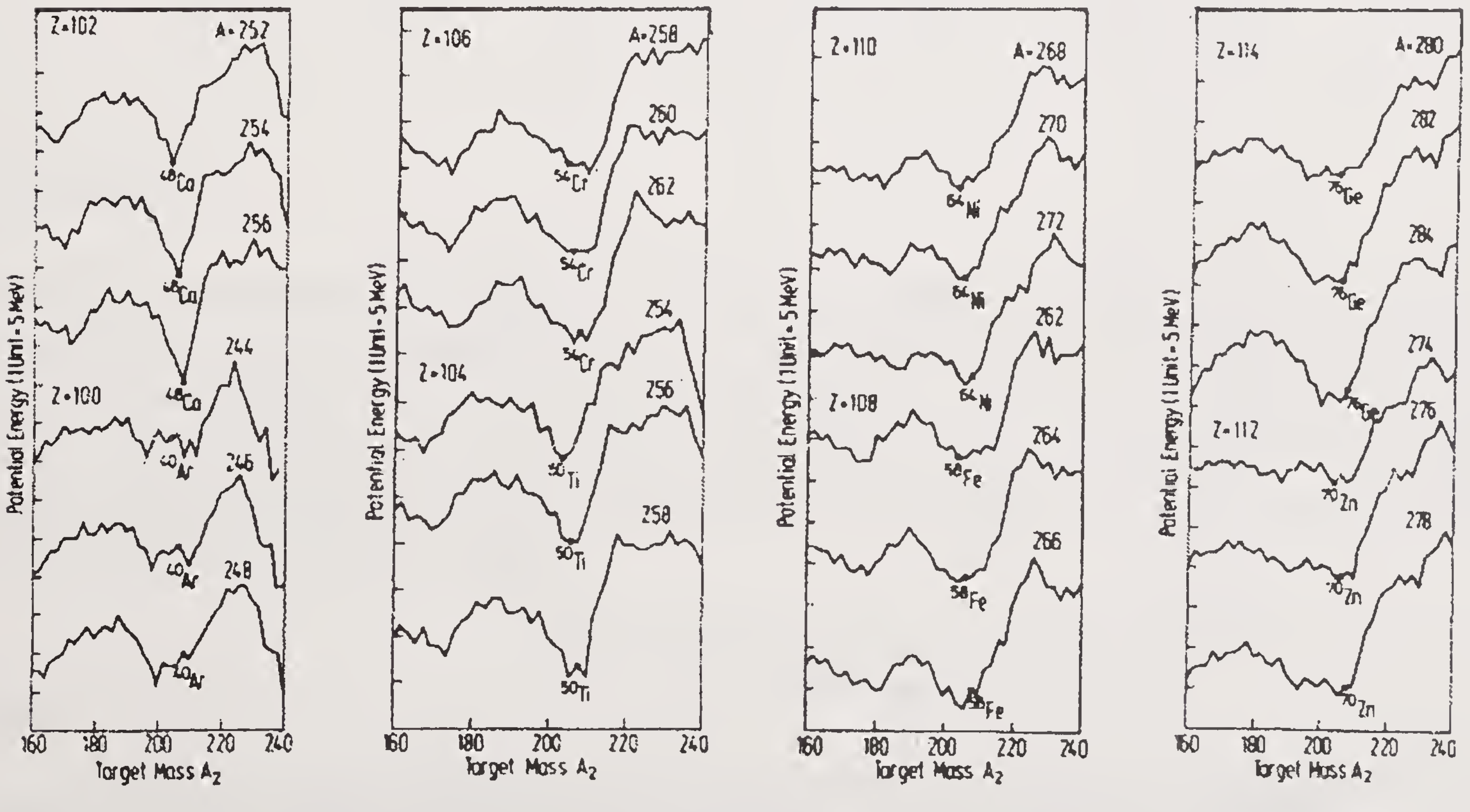

Figure 2. Calculated potential energy surfaces [12] using eq. (4).

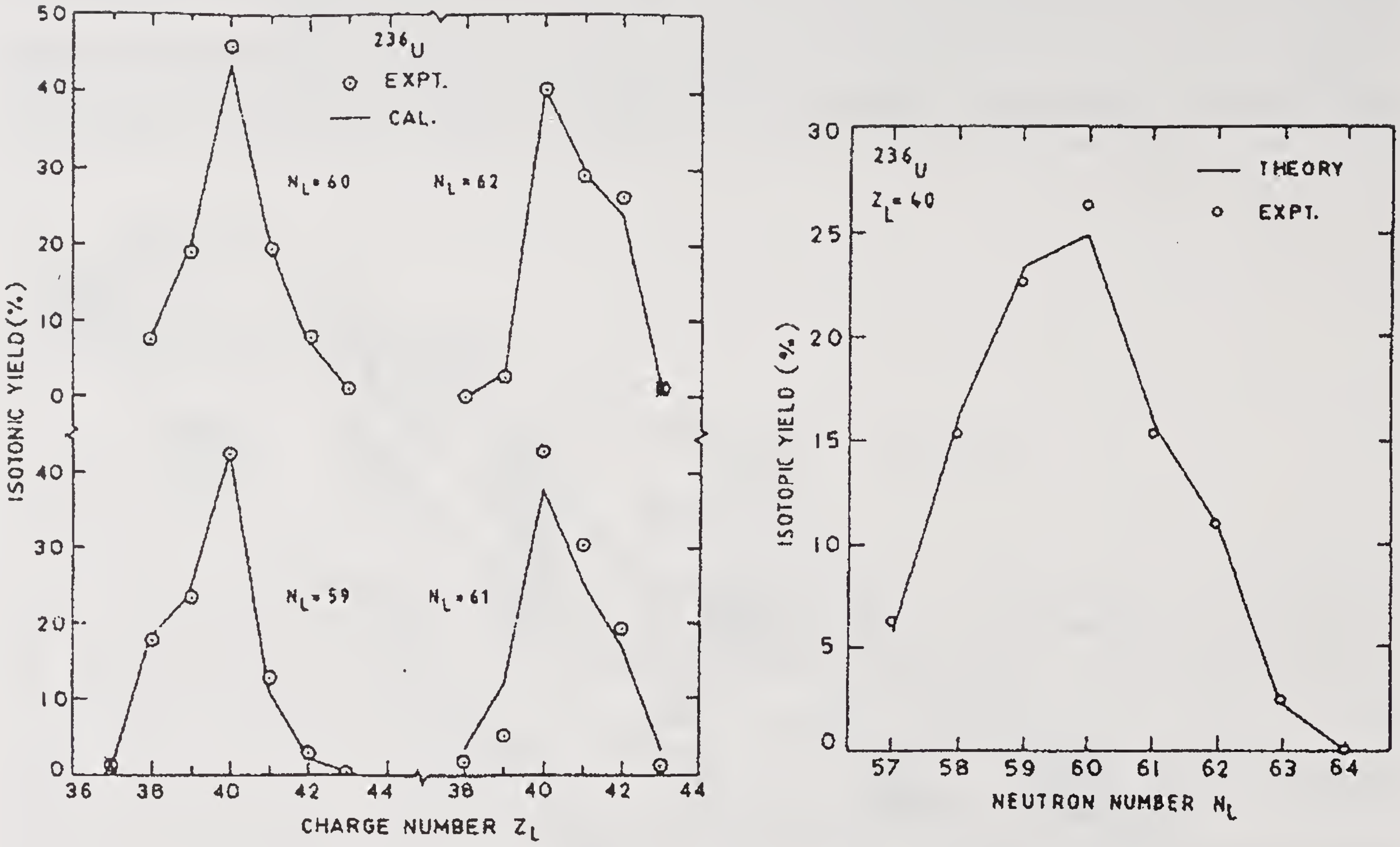

Figure 3. Percentage isotonic and isotopic yields for fission of ^{236}U.

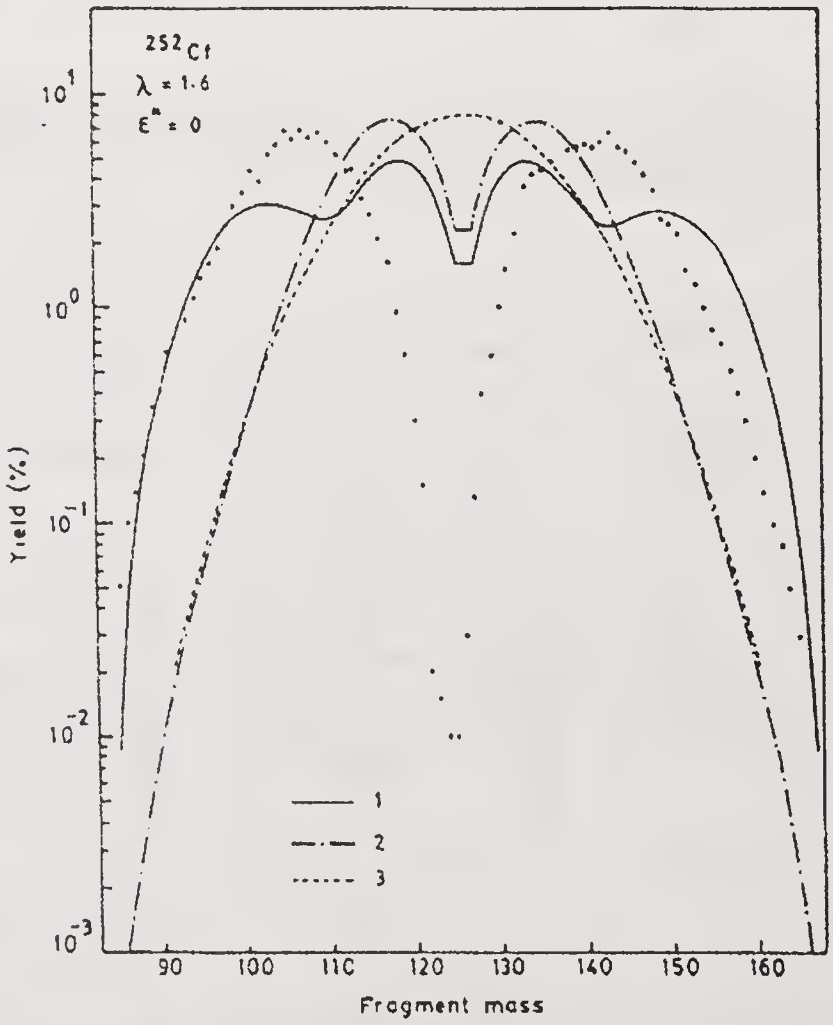

Figure 4. Fission yields of ^{252}Cf [15]. The experimental data is old. The recently observed peak at ^{132}Sn [16] was already given by the calculations.

results exactly. There is no parameter fitting in these calculations. Figure 4 gives the calculated fission yields for ^{252}Cf, [15]. The experimental data shown is the old data. The interesting result of this calculation is the appearance of a shoulder at ^{132}Sn, not there in the old data. This new mode of doubly magic ^{132}Sn fragment is now observed recently in the cold fission of ^{252}Cf [16]. Once again the closed shell effects (this time of ^{132}Sn) came into play and the theory preceded the experiments.

3.3 Cluster radioactivity

One of the important results of cluster radioactivity is that daughter nucleus is always observed to be the magic Pb or neighbouring nucleus. This has led us to predict the ^{100,132}Sn radioactivities and deformed (Os or W) daughter radioactivities (see e.g. Gupta in [1]). Table 1 presents the results of our calculation, based on the PCM of [17], for ^{249}Cf parent for which some preliminary experiments (Nice University preprint) indicate the possibility of ^{41}Sc cluster emission. Our calculations show that ^{249}Cf is not a very good parent for exotic cluster decays.

Table 1. Calculated cluster decay characteristics of ^{249}Cf. The only experimental information is the α-decay half-life log $T_{1/2}^{\alpha}$ (Expt.) = 10.04 s.

Cluster	Q-value (MeV)	Preformation probability P_0	Penetrability probability P	Decay constant λ (s^{-1})	Half-life $\log_{10} T_{1/2}$ (s)
^{4}He	6.30	8.23×10^{-01}	1.51×10^{-29}	2.92×10^{-08}	7.38
^{14}C	25.79	7.37×10^{-23}	3.51×10^{-43}	6.58×10^{-44}	43.02
^{30}Mg	69.77	5.51×10^{43}	2.41×10^{-38}	3.80×10^{-59}	58.26
^{42}S	109.42	2.07×10^{-34}	7.76×10^{-26}	4.84×10^{-38}	37.16
^{48}Ca	137.69	9.88×10^{-37}	1.14×10^{-22}	3.58×10^{-36}	36.29
^{50}Ca	136.69	5.53×10^{-38}	2.08×10^{-23}	3.56×10^{-39}	38.29
^{51}Ca	135.53	1.67×10^{-37}	3.56×10^{-24}	1.81×10^{-40}	39.58
^{52}Ca	132.66	1.89×10^{-38}	2.87×10^{-26}	1.62×10^{-43}	42.63

4. Summary

We have shown that the quantum mechanical fragmentation theory gives a unified description of the three rare processes, the cold fusion, cold fission and exotic cluster decay of nuclei. The unifying result is the closed shell effects of one or both the reaction partners or the outgoing fission or decay products. The process is most probable as cold since the shell effects are operative in full. As the system is heated, shell corrections reduce, so does the probability of their production.

References

[1] R K Gupta and W Greiner (eds), *Heavy Elements and Related New Phenomena* (World Scientific Pub., Singapore, 1999) vol. I and II (in press)

[2] U Quade *et al*, *Lecture Notes in Physics*, **158**, 40 (1981)

[3] F J Gönnenwein, *Int. Conf. on Nucl. Data for Basic and Applied Science* (Santa Fe, New Mexico, USA, 1985)
[4] G M Ter-Akopian *et al*, *Phys. Rev. Lett.* **73**, 1477 (1994)
[5] E K Hulet *et al*, *Phys. Rev. Lett.* **56**, 313 (1986)
[6] G M Ter-Akopian *et al*, *Phys. Rev. Lett.* **77**, 32 (1996)
[7] W Mollenkopf *et al*, *J. Phys. G: Nucl. Part. Phys.* **18**, L203 (1992)
[8] S Hofmann *et al*, *Z. Phys.* **A350**, 277 (1995)
[9] S Hofmann *et al*, *Z. Phys.* **A350**, 281 (1995)
[10] V Ninov *et al*, *Z. Phys.* **A356**, 11 (1996)
[11] Yu A Lazarev *et al*, *Phys. Rev. Lett.* **73**, 624 (1994)
[12] R K Gupta, C Pírvulescu, A Săndulescu and W Greiner, *Z. Phys.* **A283**, 217 (1977); *Sov. J. Nucl. Phys.* **28**, 160 (1978)
[13] R K Gupta, S K Patra and W Greiner, *Mod. Phys. Lett.* **A12**, 1727 (1997)
[14] W Lang, H-G Clerc, H Wohlfarth, H Schrader and K-H Schmidt, *Nucl. Phys.* **A345**, 34 (1980)
[15] S Kumar, R K Gupta and W Scheid, *Int. J. Mod. Phys.* **E3**, 195 (1994)
[16] F Gönnenwein, A Möller, M Cröni, M Hesse, M Wöstheinrich, H Faust, G Fioni and S Oberstedt, *Il. Nuovo Cimento* **A110**, 1089 (1977)
[17] S S Malik and R K Gupta, *Phys. Rev.* **C39**, 1992 (1989)

Astrophysical S-factors from asymptotic normalization coefficients

R E TRIBBLE, A AZHARI, H L CLARK, C A GAGLIARDI, Y-W LUI,
A M MUKHAMEDZHANOV, A SATTAROY, X TANG, L TRACHE, V BURJAN,
J CEJPEK*, V KROHA*, Š PISKOŘ*, J VINCOUR* and F CÂRSTOIU†
Cyclotron Institute, Texas A&M University, College Station, Texas 77843, USA
*Institute for Nuclear Physics, Czech Academy of Sciences, Prague-Řež, Czech Republic
†Institute for Atomic Physics, Bucharest, Romania

Abstract. S-factors for direct capture reactions can be found at astrophysical energies from asymptotic normalization coefficients which provide the normalization of the tail of the overlap function. For example the overlap for $^8\mathrm{B} \to {}^7\mathrm{Be} + p$ defines the S-factor for $^7\mathrm{Be}\,(p,\gamma)^8\mathrm{B}$. Peripheral transfer reactions offer a technique to determine these asymptotic normalization coefficients. As a test of the technique, the $^{16}\mathrm{O}(^3\mathrm{He}, d)^{17}\mathrm{F}$ reaction has been used to determine asymptotic normalization coefficients for transitions to the ground and first excited states of ^{17}F. The S-factors for $^{16}\mathrm{O}(p,\gamma)^{17}\mathrm{F}$ calculated from these $^{17}\mathrm{F} \to {}^{16}\mathrm{O} + p$ asymptotic normalization coefficients are found to be in very good agreement with recent measurements. Following the same technique, the $^{10}\mathrm{B}(^7\mathrm{Be}, {}^8\mathrm{B})^9\mathrm{Be}$ and $^{14}\mathrm{N}(^7\mathrm{Be}, {}^8\mathrm{B})^{13}\mathrm{C}$ reactions have been used to measure the asymptotic normalization coefficient for $^7\mathrm{Be}(p,\gamma)^8\mathrm{B}$. This result provides an indirect determination of $S_{17}(0)$.

Keywords. Nuclear astrophysics; S-factors.

PACS Nos 25.40.Lw; 21.10.Pc; 27.20.+n; 26.65.+t; 25.55.Hp; 26.20.+f

1. Introduction

Nuclear capture reactions such as (p,γ) and (α,γ), play a major role in defining our universe. Until recently, the only reliable method to determine a reaction rate that is dominated by direct capture has been to measure it at laboratory energies with a low energy particle beam and extrapolate the result to astrophysical energies. Often the reaction of interest involves a radioactive target which makes measurements quite difficult. Hence it is important to develop alternative techniques to determine rates. Coulomb dissociation may provide an indirect method for obtaining this information, but it has not yet been subjected to a suitable reliability test.

Direct capture reactions of astrophysical interest usually involve systems where the binding energy of the captured proton is low. Hence at stellar energies, the capture proceeds through the tail of the nuclear overlap function. The shape of the overlap function in this tail region is completely determined by the Coulomb interaction, so the amplitude of the overlap function alone dictates the rate of the capture reaction. The $^7\mathrm{Be}(p,\gamma)^8\mathrm{B}$ reaction is an excellent example of such a direct capture process. Indeed recent calculations of the normalization constant have been used to predict the capture rate [1,2]. But new measurements, both direct and indirect, are still needed as was underscored in a recent review of stellar reaction rates [3] which includes a detailed discussion of the uncertainties in our present knowledge of $S_{17}(0)$ and its importance to the solar neutrino problem.

The asymptotic normalization coefficient C for $A + p \leftrightarrow B$ specifies the amplitude of the single-proton tail of the wave function for nucleus B when the core A and the proton are separated by a distance large compared to the nuclear radius. In previous communications [1,4], we have pointed out that astrophysical S-factors for peripheral direct radiative capture reactions can be determined through measurements of asymptotic normalization coefficients (ANC) using traditional nuclear reactions such as peripheral nucleon transfer. Direct capture S-factors derived with this technique are most reliable at the lowest incident energies in the capture reaction, precisely where capture cross sections are smallest and most difficult to measure directly. Of course it is extremely important to test the reliability of the technique in order to know the precision with which it can be applied. Determining the S-factors for ^{16}O$(p,\gamma)^{17}$F from its ANC's has been recognized as a suitable test for this method [3] because the results can be compared to existing direct measurements of the cross sections [5,6]. Furthermore, the ^{16}O$(p,\gamma)^{17}$F reaction has substantial similarities to the ^{7}Be$(p,\gamma)^{8}$B reaction. Below we briefly discuss the results of a measurement of the ^{16}O(^{3}He,d)^{17}F reaction to determine the ANC's for the ground and first excited states in ^{17}F. From these ANC's we calculate S-factors for ^{16}O$(p,\gamma)^{17}$F and compare to experimental results. We then discuss our measurement of the ^{10}B(^{7}Be, ^{8}B)^{9}Be and ^{14}N(^{7}Be, ^{8}B)^{13}C reactions, the extraction of the ANC's for $^{8}\text{B} \rightarrow {}^{7}\text{Be} + p$ and our determination of $S_{17}(0)$.

2. A test case

The ^{16}O(^{3}He, d)^{17}F reaction was measured previously at a beam energy $E_{^3\mathrm{He}} = 25$ MeV [7]. We repeated the measurement at 29.75 MeV in order to obtain better angular coverage and to have a measurement at a second energy, both of which were necessary for extracting reliable ANC's. Data at laboratory scattering angles between 6.5° and 25° were obtained using Si solid state detectors and a ^{3}He beam, incident on a 134 μg/cm^{2} Mylar target, from the U-120M isochronous cyclotron of the Nuclear Physics Institute (NPI) of the Czech Academy of Sciences. Additional data at laboratory angles between 1° and 11° were obtained using the MDM magnetic spectrometer and a molecular $(^{3}\mathrm{He} - d)^{+}$ beam, incident on a 540 μg/cm^{2} Mylar target, from the Texas A&M University K500 superconducting cyclotron. Absolute cross sections were determined at the NPI using their detection system which has been well calibrated for (^{3}He, d) reaction studies. The data obtained at Texas A&M University were normalized to the data from the NPI measurement in the region where the two data sets overlapped. The angular distributions for the combined data sets are shown in figure 1. More details of the experiments can be found in [8].

For a peripheral transfer reaction, ANC's are extracted from the angular distributions by comparison to a DWBA calculation. Consider the proton transfer reaction $a + A \rightarrow c + B$, where $a = c + p$ and $B = A + p$. The experimental cross section is related to the DWBA cross section according to

$$\frac{\mathrm{d}\sigma}{\mathrm{d}\Omega} = \sum (C^{B}_{Ap})^{2} (C^{a}_{cp})^{2} R, \qquad (1)$$

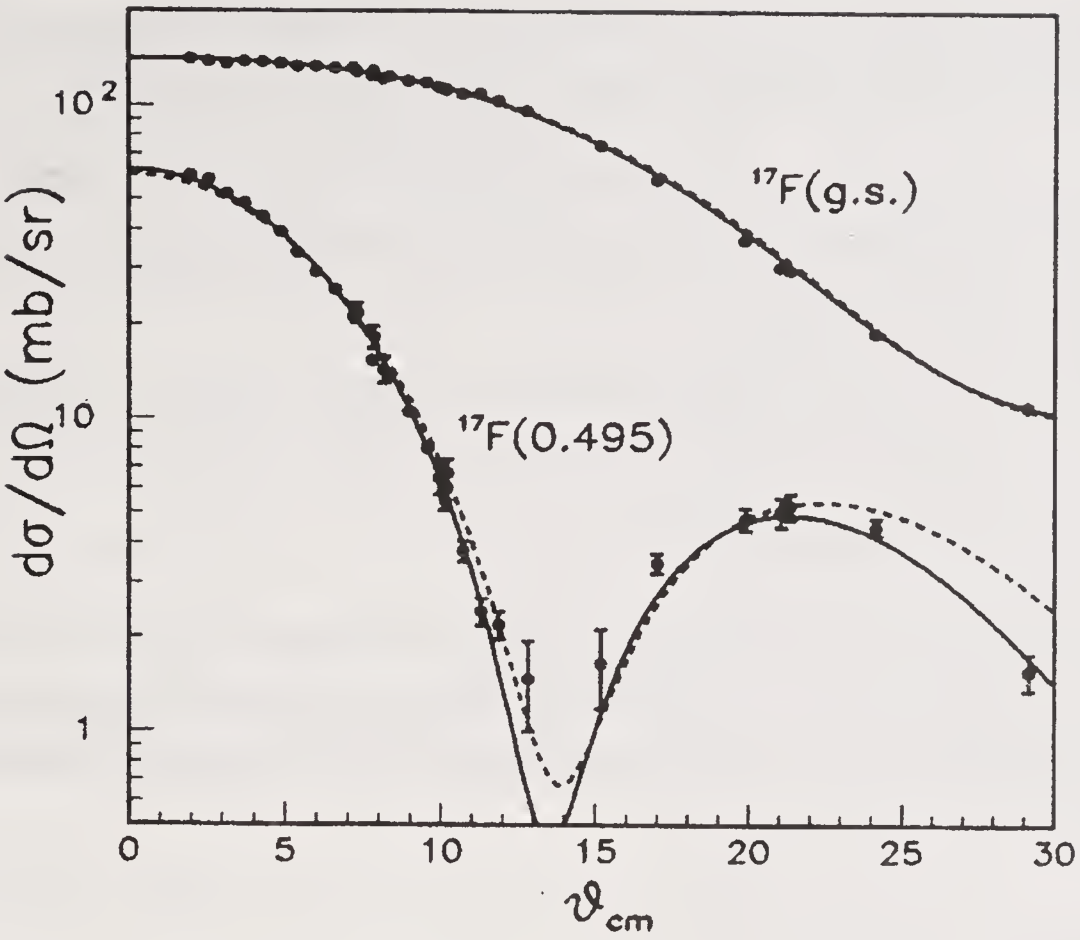

Figure 1. Angular distributions for the ground and first excited states of ^{17}F from the ^{16}O(^{3}He, d)^{17}F reaction. The curves are fits from DWBA calculations using two different optical potential sets.

where

$$R = \frac{\tilde{\sigma}^{\mathrm{DW}}}{b^2_{Ap} b^2_{cp}}. \tag{2}$$

$\tilde{\sigma}^{\mathrm{DW}}$ is the calculated DWBA cross section and the b's are the asymptotic normalization constants for the single particle orbitals used in the DWBA. The sum in eq. (1) is taken over the allowed angular momentum couplings, and the C's are the ANC's for $B \to A + p$ and $a \to c + p$. The normalization of the DWBA cross section by the ANC's for the single particle orbitals makes the extraction of the ANC for $B \to A + p$ essentially independent of the parameters used in the single particle potential wells (see [9,10] for additional details).

The DWBA calculations were carried out with the finite range code PTOLEMY [11], using the full transition operator. The single particle orbitals were calculated in Woods–Saxon potentials with r_0 in the range 1.15–1.35 fm and a_0 in the range 0.55–0.75 fm, and indicated that the calculated DWBA cross sections are insensitive to assumptions about the ^{17}F wave functions in the nuclear interior. A range of optical model parameter sets were studied for both the entrance and exit channels, as detailed in [8], and the resulting fits to the ground and excited state angular distributions using two different combinations of parameter sets are shown in figure 1. Normalizing the DWBA calculations to the data and dividing by the ANC's for the single particle orbital yields the product of the ANC's for the $^{17}\mathrm{F} \to {}^{16}\mathrm{O} + p$ and $^3\mathrm{He} \to d + p$ systems. Dividing this product by the known ANC for $^3\mathrm{He} \to d$+p [12,13] provides C^2 for $^{17}\mathrm{F} \to {}^{16}\mathrm{O} + p$. The dominant contribution to the uncertainties is due to the variation in the extracted ANC's with different optical model parameter sets. The fits shown in figure 1 are for the two combinations of parameter sets which give the largest variation in C^2. This difference was used to obtain the uncertainty in C^2 due to the choice of optical model parameters. Our final adopted ANC for the ground state is $C^2 = 1.08 \pm 0.10$ fm^{-1}. The uncertainty includes ± 4.8% from the absolute normalization and angle accuracies, plus the statistics of the fits, and ± 7.6% associated with the choice of optical model parameters and single particle orbital. Our final adopted ANC is $C^2 = 6490 \pm 680$ fm^{-1} for the excited state. The corresponding contributions to its uncertainty are ±5.4% and ±9.0%.

The relation of the ANC's to the direct capture rate at low energies is straightforward. The cross section for the direct capture reaction $A + p \to B + \gamma$ can be written as

$$\sigma = \lambda |\langle I^B_{Ap}(\mathbf{r})|\hat{O}(\mathbf{r})|\psi_i^{(+)}(\mathbf{r})\rangle|^2, \tag{3}$$

where λ contains kinematical factors, I^B_{Ap} is the overlap function for $B \to A + p$, $\hat{O}$ is the electromagnetic transition operator, and $\psi_i^{(+)}$ is the scattering wave in the incident channel. If the dominant contribution to the matrix element comes from outside the nuclear radius, the overlap function may be replaced by

$$I^B_{Ap}(r) \approx C \frac{W_{-\eta,l+1/2}(2\kappa r)}{r}, \tag{4}$$

where C defines the amplitude of the tail of the radial overlap function I^B_{Ap}, W is the Whittaker function, η is the Coulomb parameter for the bound state $B = A + p$, and κ

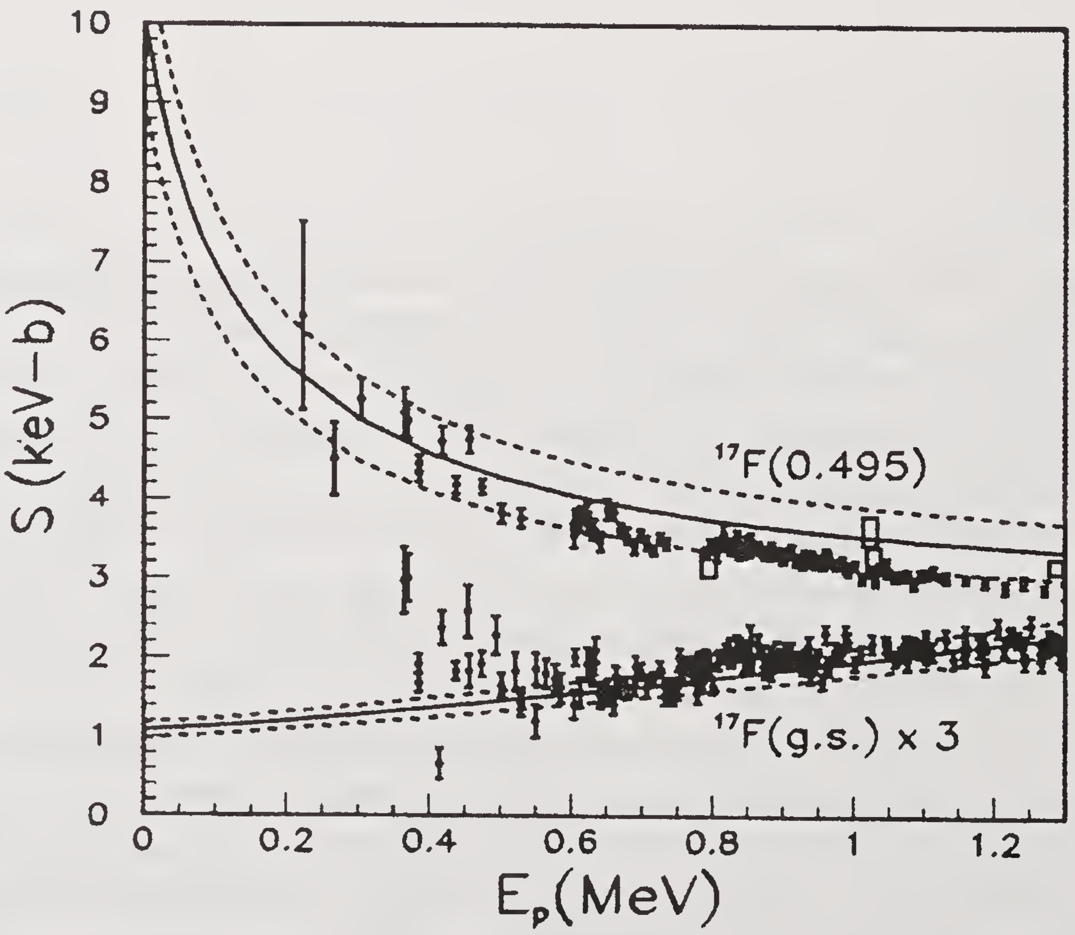

Figure 2. A comparison of the experimental S-factors to those determined from the ANC's found in ^{16}O(^{3}He, d)^{17}F. The solid data points are from [5], and the open boxes are from [6]. The solid lines indicate our calculated S-factors, and the dashed lines indicate the $\pm 1\sigma$ error bands. Note that the experimental ground state S-factor may be contaminated by background [15] at energies below 500 keV.

is the bound state wave number. For $^{16}O(p,\gamma)^{17}F$, the required C's are just the ANC's found above from the transfer reaction. Thus, the direct capture cross sections are directly proportional to the squares of these ANC's.

Following the prescription outlined above, the S-factors describing the capture to both the ground and first excited states for $^{16}O(p,\gamma)^{17}F$ were calculated, with no additional normalization constants, using the standard definition of S [14]. The results are shown in figure 2 compared to the two previous measurements of $^{16}O(p,\gamma)^{17}F$ [5,6]. Both E1 and E2 contributions have been included in the calculations, but the E1 components dominate the results. The theoretical uncertainty in the S-factors is less than 2% for energies below 1 MeV. Above 1 MeV the nuclear interaction begins to be important in the evaluation of the scattering wave function. The agreement between the measured S-factors and those calculated from our $^{17}F \rightarrow {}^{16}O + p$ ANC's is quite good, especially for energies below 1 MeV where the approximation of ignoring contributions from the nuclear interior should be very reliable and the optical potential uncertainties are negligible. Overall, the results verifying the technique is valid for determining S-factors to accuracies of at least 9%.

3. ANC for $^8B \rightarrow {}^7Be + p$

We have measured the (^{7}Be, ^{8}B) reaction on a 1.7 mg/cm^2 ^{10}B target and a 1.5 mg/cm^2 Melamine target in order to extract the ANC for $^8B \rightarrow {}^7Be + p$. The radioactive ^{7}Be beam was produced at 12 MeV/u by filtering reaction products from the $^1H(^7Li, {}^7Be)n$ reaction in the recoil spectrometer MARS, starting with a primary ^{7}Li beam at 18.6 MeV/A from the TAMU K500 cyclotron. The beam was incident on an H_2 cryogenic gas target, cooled by LN_2, which was kept at 1 atmosphere (absolute) pressure. Reaction products were measured by 5 cm × 5 cm Si detector telescopes consisting of a 100 μm ΔE strip detector, with 16 position sensitive strips, followed by a 1000 μm E counter. Two different detector configurations were used to take data. In one mode, two detector telescopes were mounted symmetrically about the beam axis as shown in figure 3. The angular coverage in this mode was from $\approx 4°$ to $\approx 18.5°$ in the laboratory frame for each telescope. In the second mode, a single detector telescope stack was placed at 0° and the beam was stopped just in front of the ΔE detector. The effective angular coverage in the lab for this mode was from $\approx 3.8°$ to $\approx 14°$.

A single 1000 μm Si strip detector was used for initial beam tuning. This detector, which was inserted at the target location, allowed us to optimize the beam shape and to normalize the ^{7}Be flux relative to a Faraday cup that measured the intensity of the primary ^{7}Li beam. Following optimization, the approximate ^{7}Be beam size was 6 mm × 3 mm (FWHM), the energy spread was $\approx$ 1.5 MeV, the full angular spread was $\Delta\theta \approx 28$ mrad and $\Delta\phi \approx 62$ mrad, and the purity was $\geq$ 99.5% ^{7}Be for the experiment with the ^{10}B target. The beam size and angular spread were improved for the experiment with the ^{14}N target to 4 mm × 3 mm (FWHM), $\Delta\theta \approx 28$ mrad and $\Delta\phi \approx 49$ mrad. Periodically during the data acquisition, the beam detector was inserted to check the stability of the secondary beam tune. The system was found to be quite stable over the course of the experiment with maximum changes in intensity observed to be less than 5%. The typical rate for ^{7}Be was $\approx$ 1.5 kHz/pnA of primary beam on the production target. Primary beam intensities of up to 80 pnA were obtained on the gas cell target during the experiments.

Preliminary results for the elastic scattering angular distributions from the two targets

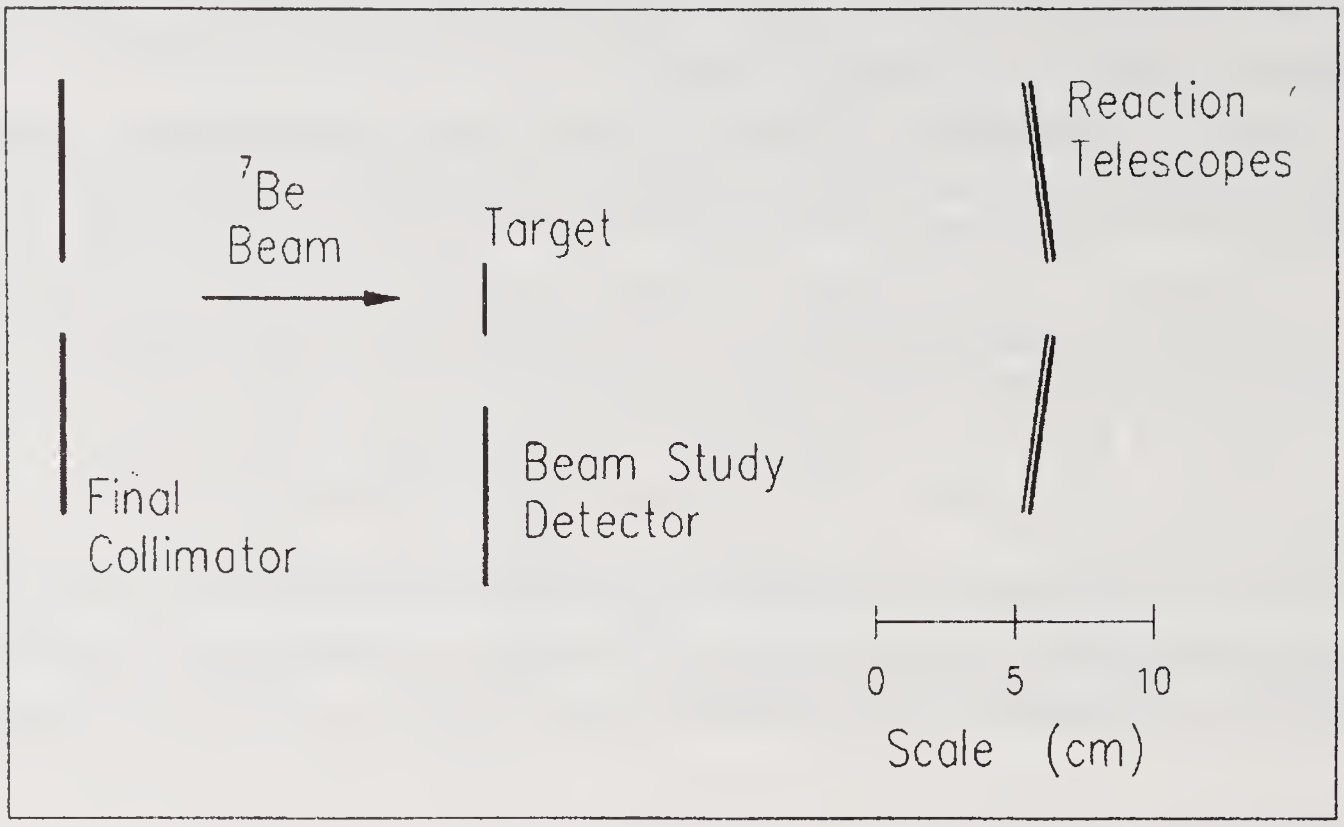

Figure 3. Detector geometry used for the (^{7}Be, ^{8}B) reaction studies.

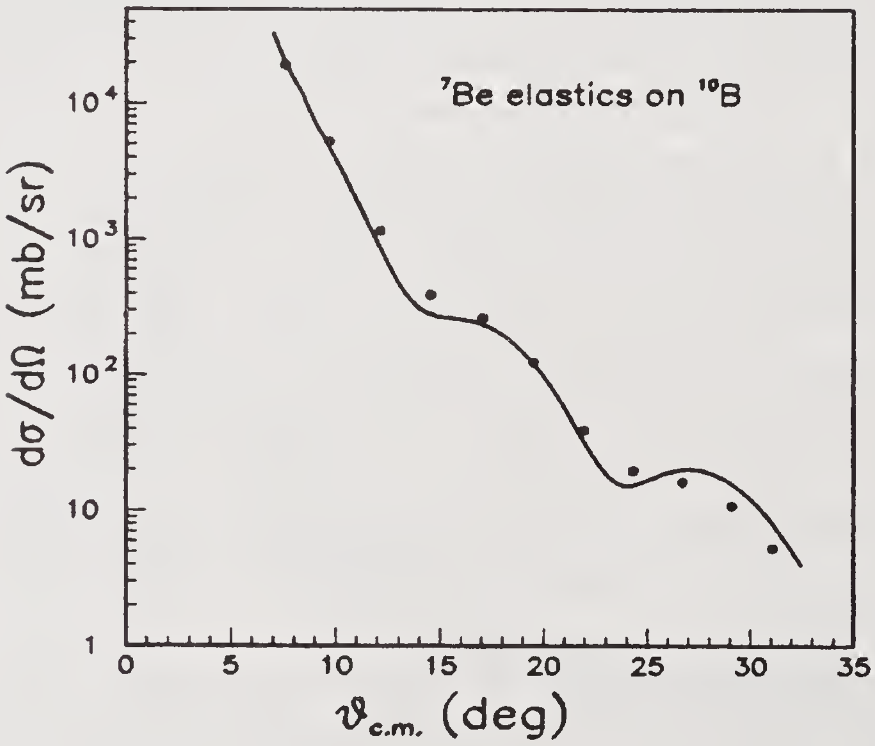

Figure 4. Angular distribution for elastic scattering from the ^{10}B target. The curve is from optical model calculations smoothed over the angular acceptance of each bin.

are shown in figures 4 and 5. For the ^{10}B target, the elastic scattering yield includes contributions from three target components, B (86%), C (10%) and O (4%), while the Melamine target includes N (67%) and C (28%). A Monte Carlo simulation described below was used to generate the solid angle factor for each angular bin and the smoothing needed for the calculation to account for the finite angular resolution of the beam. The absolute cross section is then fixed by the target thickness, number of incident ^{7}Be, the yield in each bin, and the solid angle. The curves shown with the elastic scattering were found from optical model calculations described below by adding together the cross section

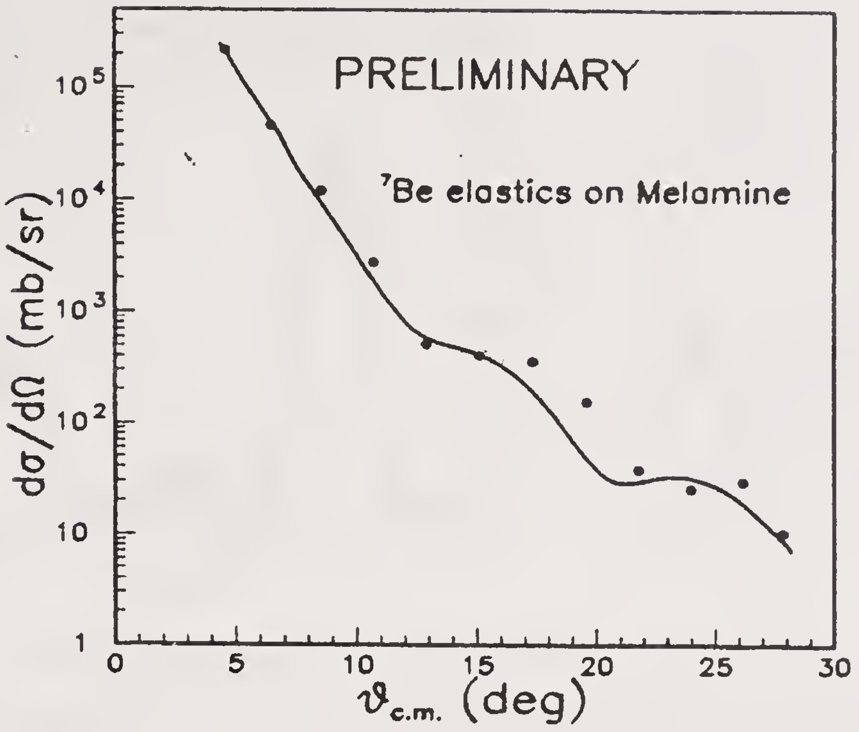

Figure 5. Angular distribution for elastic scattering from the Melamine target. The curve is from optical model calculations smoothed over the angular acceptance of each bin.

predictions for the target components in the laboratory frame and then transforming the result to the center of mass assuming kinematics appropriate for either the ^{10}B or ^{14}N targets.

The ^{8}B Q-value spectra, shown in figure 6, were obtained by assuming either a ^{10}B(^{7}Be, ^{8}B)^{9}Be or ^{14}N(^{7}Be, ^{8}B)^{13}C reaction and correcting the ^{8}B reaction products for kinematic energy shifts as a function of scattering angle. In the case of the ^{10}B target, the major contributions to the energy resolution seen in figure 6 are the beam energy spread, the target thickness and the nonuniformity of the target. The beam energy spread and differential energy loss in the target dominated the energy resolution for the Melamine target. Since the ground state of ^{9}Be is not cleanly separated from excited states, a Monte Carlo simulation of the experiment has been used to fix the line shape and determine cross sections. The simulation, which is fine tuned to reproduce the measured beam properties and the resolution observed in elastic scattering, includes the geometry of the experimental setup, reaction kinematics, nonuniform energy loss in the target and the size, angular spread and energy spread of the beam. The beam location and angle at the target are determined by symmetry requirements on ^{7}Be elastic scattering data. The three peaks shown in figure 6 for the ^{10}B target correspond to the excitation of the ground and second excited states of ^{9}Be and the ground state of ^{15}N from the ^{16}O contamination in the target. They were obtained by including the predicted angular distributions for the states in the Monte Carlo simulation and then extracting the associated Q-value spectrum. The normalization of the three peaks was done by a χ^2 minimization to the data. In the Melamine case, the ground state of ^{13}C is cleanly resolved from excited states making the normalization of the Q-value spectrum via the Monte Carlo simulation straight forward.

The ANC for $^8\text{B} \rightarrow {}^7\text{Be} + p$ was extracted based on the fit to the Q-value spectra and the ANCs for $^{10}\text{B} \rightarrow {}^9\text{Be} + p$ [9] and $^{14}\text{N} \rightarrow {}^{13}\text{C} + p$ [10] following the procedure outlined above in our test case. Two orbitals, $1p_{1/2}$ and $1p_{3/2}$, contribute to the transfer reaction but the $1p_{3/2}$ dominates in both cases. In calculating the angular distribution, we used

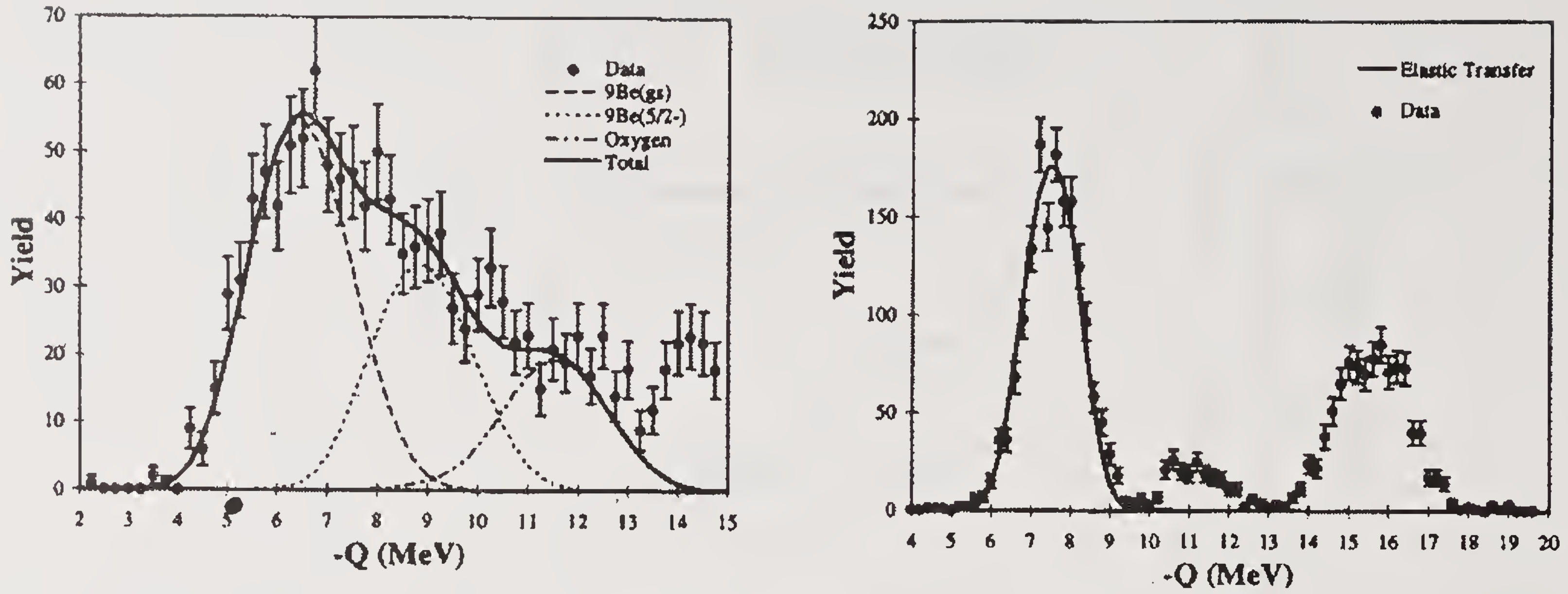

Figure 6. Q-value spectra for ^{8}B reaction products. The three peaks for the ^{10}B target correspond to the excitation of the ground state and second excited states of ^{9}Be and the ground state in ^{15}N from the ^{16}O contamination in the target. Data for the Melamine target show a clear isolation of the ground state for ^{13}C.

the ratio for the two orbitals as given by a microscopic description of the ^{8}B ground state [4]. No optical model parameters are available for either the entrance or exit channel in this reaction. As part of this program, we have obtained elastic scattering data on several beam–target combinations in this mass and energy range and have been developing appropriate optical model parameters that can be extended to ^{7}Be and ^{8}B projectiles [16]. Consequently we have chosen parameters obtained from renormalized microscopic folding potentials using the JLM effective NN interaction [17]. The surface region of these folding potentials was fit with volume Woods–Saxon forms and the parameters found for the entrance (exit) channel for the ^{10}B target were $V = 63.8(67.0)$ MeV, $W = 29.4(31.8)$ MeV, $R_V = 3.18(3.18)$ fm, $a_V = 0.85(0.876)$ fm, $R_I = 3.49(3.54)$ fm, $a_I = 0.95(0.99)$ fm. The corresponding values for ^{14}N were $V = 79.1(85.2)$ MeV, $W = 36.0(39.3)$ MeV, $R_V = 3.30(3.30)$ fm, $a_V = 0.88(0.91)$ fm, $R_I = 3.62(3.67)$ fm, $a_I = 0.98(1.02)$ fm. The entrance channel parameters were the same as those used in calculating the elastic scattering angular distributions for ^{7}Be on ^{10}B in figure 4 and on ^{14}N in figure 5. We have checked the sensitivity of the calculations by varying the normalization parameter. As in previous studies, the results are insensitive to bound state single particle well parameters in the DWBA calculations.

Angular distributions for the (^{7}Be, ^{8}B) reactions populating the ground states of ^{9}Be and ^{13}C were extracted using the same procedure as for the elastic scattering. The results are compared to DWBA calculations in figures 7 and 8. The normalization factors between the data and calculations were obtained from the fits to the respective Q-value spectra.

The astrophysical S-factor for ^{7}Be $(p,\gamma)^8$B has been determined from the ANC which includes a 10% uncertainty for optical model parameters, a 11% uncertainty for experimental fits and normalization of the absolute cross section and the uncertainty in the ANC's for $^{10}\mathrm{B} \to {}^9\mathrm{Be} + p$ and $^{14}\mathrm{N} \to {}^{13}\mathrm{C} + p$. The relative contribution of the two angular momentum couplings to the S-factor is straightforward to calculate and introduces a negligible additional uncertainty in our result [1,4]. The preliminary value that we find for the ^{10}B target is $S_{17}(0) = 17.2 \pm 2.6$ eV b and 18 ± 3 eV b for the ^{14}N target which are in good

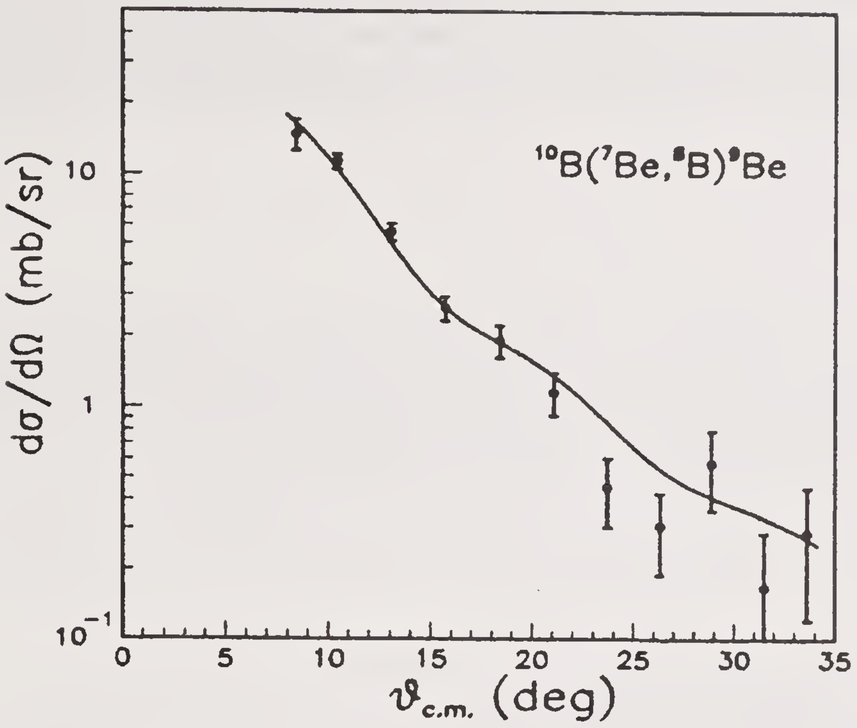

Figure 7. Angular distribution for ^8B populating the ground state of ^9Be from the ^{10}B target. The curve is from a DWBA calculation smoothed over the angular acceptance of each bin.

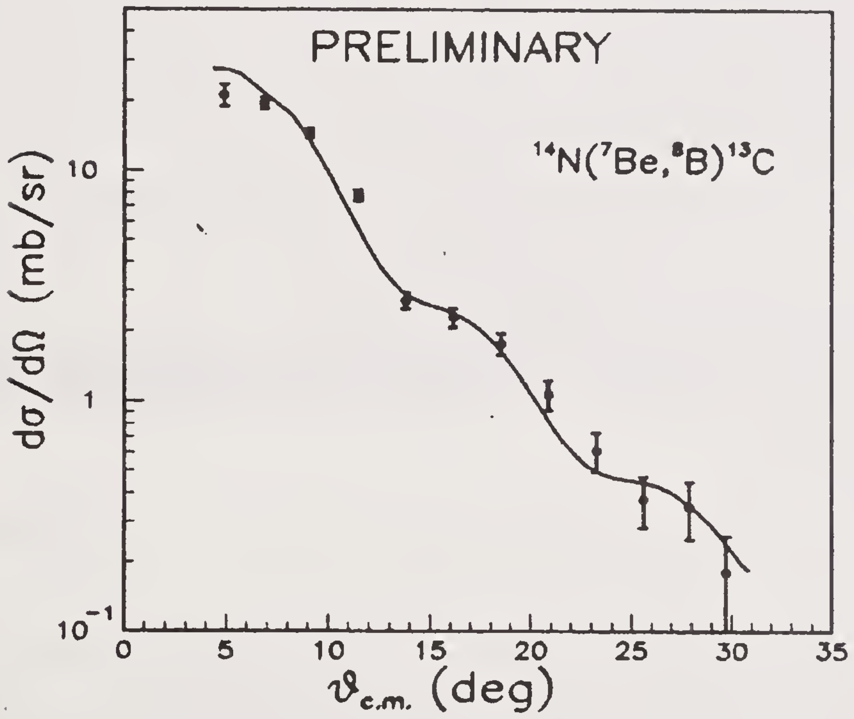

Figure 8. Angular distribution for ^8B populating the ground state of ^{13}C from the Melamine target. The curve is from a DWBA calculation smoothed over the angular acceptance of each bin.

agreement with the recommended value of 19^{+4}_{-2} eV b [3]. The simulation for the ^{14}N target has not been optimized so the result quoted for it and the uncertainty in the result are very preliminary.

One of the primary sources of uncertainty in the values quoted above for $S_{17}(0)$ is the optical model parameters that are used to predict the angular distribution. As indicated, we are working toward a set of global optical model parameters to be used for radioactive beams in this mass and energy region. Once this is complete, the calculations will be redone and a new ANC and hence $S_{17}(0)$ will be determined. The ANC's for $^{10}B \rightarrow {}^{9}Be + p$ and $^{14}N \rightarrow {}^{13}C + p$ represent the other major source of uncertainty. Measurements of these ANC's have been carried out using (^{3}He, d) reactions and the results should be forthcoming.

Acknowledgement

This work was supported in part by the U. S. Department of Energy under Grant number DE-FG05-93ER40773 and by the Robert A. Welch Foundation.

References

[1] H M Xu *et al*, *Phys. Rev. Lett.* **73**, 2027 (1994)
[2] L V Grigorenko *et al*, *Phys. Rev.* **C57**, R2099 (1998)
[3] E G Adelberger *et al*, *Rev. Mod. Phys.* **70**(**4**), 1265 (1998)
[4] A M Mukhamedzhanov and N K Timofeyuk, *JETP Lett.* **51**, 282 (1990)
[5] R Morlock *et al*, *Phys. Rev. Lett.* **79**, 3837 (1997)
[6] H C Chow, G M Griffith and T H Hall, *Can. J. Phys.* **53**, 1672 (1975)
[7] J Vernotte *et al*, *Nucl. Phys.* **A571**, 1 (1994)
[8] C A Gagliardi *et al*, *Phys. Rev.* (in press)
[9] A M Mukhamedzhanov *et al*, *Phys. Rev.* **C56**, 1302 (1997)
[10] L Trache *et al*, *Phys. Rev.* **C58**, 2715 (1998)
[11] M Rhoades-Brown, M McFarlane and S Pieper, *Phys. Rev.* **C21**, 2417 (1980); *Phys. Rev.* **C21**, 2436 (1980)
[12] M Kamimura and H Kameyama, *Nucl. Phys.* **A508**, 17c (1990)
[13] A M Mukhamedzhanov, R E Tribble and N K Timofeyuk, *Phys. Rev.* **C51**, 3472 (1995)
[14] J N Bahcall, *Neutrino Astrophysics* (Cambridge University Press, Cambridge, 1989)
[15] R Morlock, private communication
[16] L Trache *et al*, to be published
[17] J P Jeukenne, A Lejeune and C Mahaux, *Phys. Rev.* **C16**, 80 (1977)

Breakup of ^{8}B and the ^{7}Be(p, γ)^{8}B reaction*

R SHYAM and I J THOMPSON*
Saha Institute of Nuclear Physics, 1/AF, Bidhan Nagar, Calcutta 700 064, India
*Department of Physics, University of Surrey, Guildford, Surrey GU2 5XH, UK

Abstract. The calculated rate of events in some of the existing solar neutrino detectors is directly proportional to the rate of the ^{7}Be$(p,\gamma)^8$B reaction measured in the laboratory at low energies. However, the low-energy cross sections of this reaction are quite uncertain as various measurements differ from each other by 30–40%. The Coulomb dissociation process which reverses the radiative capture by the dissociation of ^{8}B in the Coulomb field of a target, provides an alternate way of accessing this reaction. While this method has several advantages (like large breakup cross sections and flexibility in the kinematics), the difficulties arise from the possible interference by the nuclear interactions, uncertainties in the contributions of the various multipoles and the higher order effects, which should be considered carefully. We review the progress made so far in the experimental measurements and theoretical analysis of the breakup of ^{8}B and discuss the current status of the low-energy cross sections (or the astrophysical S-factor) of the ^{7}Be$(p,\gamma)^8$B reaction extracted therefrom. The future directions of the experimental and theoretical investigations are also suggested.

Keywords. Coulomb and nuclear breakup of ^{8}B; radiative capture of p and ^{7}Be; astrophysical S-factors.

PACS Nos 25.70.De; 25.40.Lw; 96.60.Kx

1. Introduction

The ^{8}B isotope produced in the Sun via the radiative capture reaction ^{7}Be$(p,\gamma)^8$B is the principal source of the high energy neutrinos detected in the super-Kamiokande (SK) and ^{37}Cl detectors [1]. In fact the calculated rate of events in SK as well as SNO detectors [3] is directly proportional to the rate of this reaction measured in the laboratory at low energies ($\sim$ 20 keV) [3]. Unfortunately, the measured cross sections (at relative energies (E_{CM}) of [$p-{}^7$Be] $>$ 200 keV) disagree in absolute magnitude and the value extracted by extrapolating the data in the region of 20 keV differ from each other by 30–40%. This makes the rate of the reaction ^{7}Be$(p,\gamma)^8$B the most poorly known quantity in the entire nucleosynthesis chain leading to the formation of ^{8}B [4]. It may be noted that the rate of the ^{7}Be$(p,\gamma)^8$B reaction is usually given in terms of the zero-energy astrophysical S-factor, $S_{17}(0)$.

---

*Work supported by EPSRC, UK, grant nos J/95867 and L/94574.

The Coulomb dissociation (CD) method provides an alternative indirect way to determine the cross sections for the radiative capture reactions at low energies [5–9]. In this procedure it is assumed that the break-up reaction $a + Z \rightarrow (b + x) + Z$ proceeds entirely via the electromagnetic interaction; the two nuclei a and Z do not interact strongly. By further assuming that the electromagnetic excitation process is of first order, one can relate directly (see for e.g. refs [5,6]) the measured cross-sections of this reaction to those of the radiative capture reaction $b + x \rightarrow a + \gamma$. Thus, the astrophysical S-factors of the radiative capture processes can be determined from the study of break-up reactions under these conditions.

However, in the CD of ^{8}B, the contributions of $E2$ and $M1$ multipolarities can be disproportionately enhanced in certain kinematical regimes [10,11]. Furthermore, interference from the nuclear breakup processes may also be considerable in some regions. Therefore, a careful investigation [9,12] is necessary to isolate the conditions in which these terms have negligible effect on the calculated breakup cross sections.

Motobayshi *et al* [13] have performed the first measurements (to be referred as RIKEN-I) of the dissociation of ^{8}B into the ^{7}Be$-p$ low energy continuum in the field of ^{208}Pb with a radioactive ^{8}B beam of 46.5 MeV/nucleon energy. Assuming a pure E1 excitation, the Monte Carlo simulation of their data predicts a $S_{17}(0) = 16.7 \pm 3.2$ eV barn, which is considerably lower than the value of 22.4 ±2.0 eV barn used by Bahcall and Pinsonneault [2] in their standard solar model (SSM) calculations. This generated a lot of interest in the studies of the breakup reactions of ^{8}B. Since, under the kinematical conditions of the RIKEN-I experiment the $E2$ component of breakup may be disproportionately enhanced, attempts were made to determine this component by extending the angular range of the measurements in the RIKEN-I data in a repeat experiment [14] (to be referred as RIKEN-II) to larger angles which are expected to be more sensitive to this multipolarity. On the other hand, measurements of the breakup of ^{8}B were also carried out at sub-Coulomb beam energies [15] where $E2$ multipolarity is expected to dominate according to the semi-classical theory of the Coulomb excitation [16]. Measurements of the breakup of ^{8}B have also been performed at the relativistic energies of 250 MeV/nucleon at GSI, Darmstadt.

In this review, we present the latest status of the analysis of the available experimental data on the breakup of ^{8}B and of the extracted S_{17} value therefrom. Results obtained from both the semiclassical and full quantum mechanical calculations are discussed in the next two sections. Conclusions and the outlook is presented in §4.

2. Semiclassical calculations

2.1 RIKEN data, $E_{\rm beam} \sim 50$ MeV/nucleon

An analysis of the RIKEN-I data was presented in [7], where the breakup cross sections of ^{8}B corresponding to $E1$, $E2$ and $M1$ multipolarities were calculated within a semiclassical theory of Coulomb excitation, which included simultaneously the effects of Coulomb recoil and relativistic retardation. This was achieved by solving the general classical problem of the motion of two relativistic charged particles [17]. The role of the nuclear excitations was also investigated by performing full quantum mechanical calculation of the Coulomb, nuclear as well as of their interference terms, using a collective model prescription for the nuclear form factor. It was found that nuclear effects modify the pure Coulomb amplitudes very marginally in the entire kinematical regime of the RIKEN-I data.

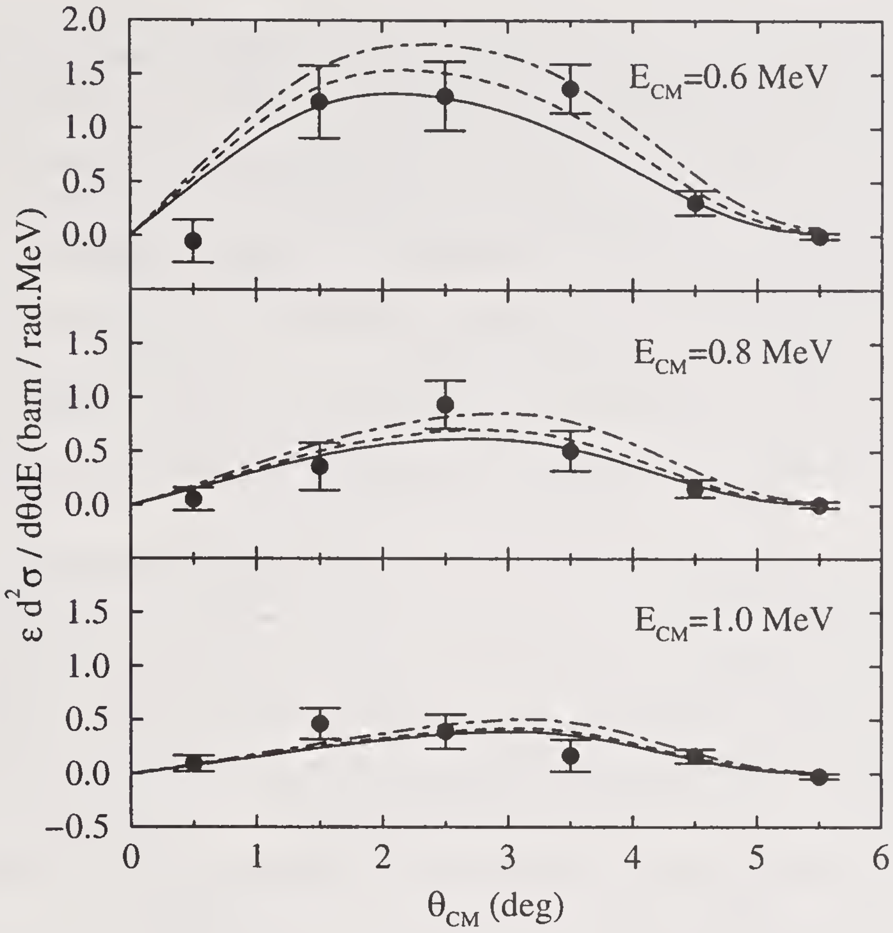

Figure 1. Comparison of experimental and theoretical Coulomb dissociation yields (cross section × detector efficiency) as a function of $\theta_{\rm cm}$ for the $E_{\rm cm}$ values of 0.6 MeV, 0.8 MeV and 1.0 MeV. Solid lines show the calculated pure $E1$ Coulomb dissociation cross sections obtained with best fit values of S factors as discussed in the text. The dashed and dashed dotted curves represent the sum of $E1$, $E2$ and $M1$ contributions with latter two components calculated with capture cross sections given in the models of TB [18] and KPK [19] respectively. The experimental data is taken from ref. [13].

The double differential cross-section for the Coulomb excitation of a projectile from its ground state to the continuum, with a definite multipolarity of order $\pi\lambda$ is given by [5–7]

$$\frac{{\rm d}^2\sigma}{{\rm d}\Omega{\rm d}E_\gamma} = \sum_{\pi\lambda} \frac{1}{E_\gamma}\frac{{\rm d}n_{\pi\lambda}}{{\rm d}\Omega}\sigma_\gamma^{\pi\lambda}(E_\gamma), \tag{1}$$

where $\sigma_\gamma^{\pi\lambda}(E_\gamma)$ is the cross-section for the photodisintegration process $\gamma + a \to b + x$, with photon energy E_γ, and multipolarity $\pi = E$ (electric) or M (magnetic), and $\lambda = 1, 2, \ldots$ (order), which is related to that of the radiative capture process $\sigma(b + x \to a + \gamma)$ through the theorem of detailed balance. In terms of the astrophysical S-factor, $S(E_{\rm cm})$, we can write

$$\sigma(b + x \to a + \gamma) = \frac{S(E_{\rm cm})}{E_{\rm cm}} \exp(-2\pi\eta(E_{\rm cm})), \tag{2}$$

where $\eta = (Z_b Z_x e^2/\hbar v)$, with v, Z_b and Z_x being the relative center of mass velocity, and charges of the fragments b and x respectively.

In most cases, only one or two multipolarities dominate the radiative capture as well as the Coulomb dissociation cross sections. In eq. (1) $n_{\pi\lambda}(E_\gamma)$ represents the number of equivalent (virtual) photons provided by the Coulomb field of the target to the projectile, which is calculated by the method discussed in refs [7,17] . $S(E_{\rm cm})$, can be directly determined from the measured Coulomb dissociation cross-sections using eqs (1) and (2).

In figure 1, we show the comparison of the calculated [7] Coulomb dissociation double differential cross sections with the corresponding data of ref. [13] as a function of the scattering angle $\theta_{\rm cm}$ of the excited ^{8}B (center of mass of the ^{7}Be+p system) for three values of the $E_{\rm cm}$. The calculated $E1$, $E2$ and $M1$ cross sections are folded with an efficiency matrix provided to us by the RIKEN group. The solid lines in figure 1 show the calculated $E1$ cross sections obtained with S-factors (S_{17}) that provide best fit to the data (determined by χ^2 minimization procedure). These are (17.58 ± 2.26) eV barn, (14.07 ± 2.67) eV barn and (15.59 ± 3.49) eV barn at $E_{\rm cm} = 0.6$ MeV, 0.8 MeV and 1.0 MeV respectively. By using a direct extrapolation procedure, the best fit '$E1$ only' S_{17} factors, give a $S_{17}(0) = (15.5 \pm 2.80)$ eV barn.

The contributions of the $E2$ and $M1$ excitations are calculated by using the radiative capture cross sections $\sigma(p+{}^7\text{Be}\rightarrow{}^8\text{B}+\gamma)$, given by the models of Typel and Baur (TB) [18] and Kim, Park and Kim (KPK) [19]. We have used as input the corresponding S factors averaged over energy bins of experimental uncertainty in the relative energy of the fragments. In figure 1, the dashed (dashed dotted) line shows the $E1$ (with best fit S_{17}) + $E2 + M1$ cross sections, with $E2$ and $M1$ components calculated with TB (KPK) capture cross sections. It is clear that the magnitude of the $E2$ contributions to the RIKEN-I data depend significantly on the nuclear structure model used to calculate the corresponding capture cross sections, and it is difficult to draw any definite conclusion about the extent of its role in the RIKEN-I data from this analysis. The $M1$ component contributes insignificantly and unlike the $E2$ component it is not as model dependent.

Since at larger scattering angles, the angular distributions of the Coulomb breakup of ^{8}B are expected to be more sensitive to the $E2$ component, the RIKEN group has repeated their experiment [14] where the angular range of the data was extended up to 9°. In figure 2, we show a comparison of the calculated Coulomb dissociation cross sections for the double differential cross sections with the RIKEN-II data. In these calculations the capture cross sections have been taken from Esbensen and Bertsch [20], which predicts a $S_{17}(0) = 18.5$ eV barn. Since we have not used any arbitrary normalization constant in the theoretical calculations shown in this figure, RIKEN-II data seems to be consistent with a slightly larger value of $S_{17}(0)$ as compared to RIKEN-I. We also note that while the $E2$ component contributes significantly to the total cross sections at all the angles in the energy bin 2000–2250 keV, it is dominant beyond 6° in the lower energy range of E_{CM}. However, at larger angles the nuclear breakup effects are also expected to be more important. Therefore, it would be necessary to include these effects before drawing any conclusion about the role of $E2$ multipolarity in this data.

In ref. [14], an analysis of the data was performed within the distorted wave Born-approximation including the nuclear effects, where it was concluded that the $E2$ component and the nuclear breakup effects are considerably smaller. However, they use a collective model prescription to calculate the inelastic nuclear form factor (see eg. [7]). Due to a long tail in the ^{8}B g.s wave function this procedure is unlikely to be accurate. Furthermore, Coulomb breakup is calculated by a point-like projectile approximation (PLPA) in these studies (and also in the semiclassical calculations presented above), and its range of validity is yet to be determined for this projectile.

It is therefore, necessary to perform a full quantum mechanical analysis of the RIKEN-II data in order to check the validity of various assumptions of the Coulomb dissociation method. This will be presented in §3.

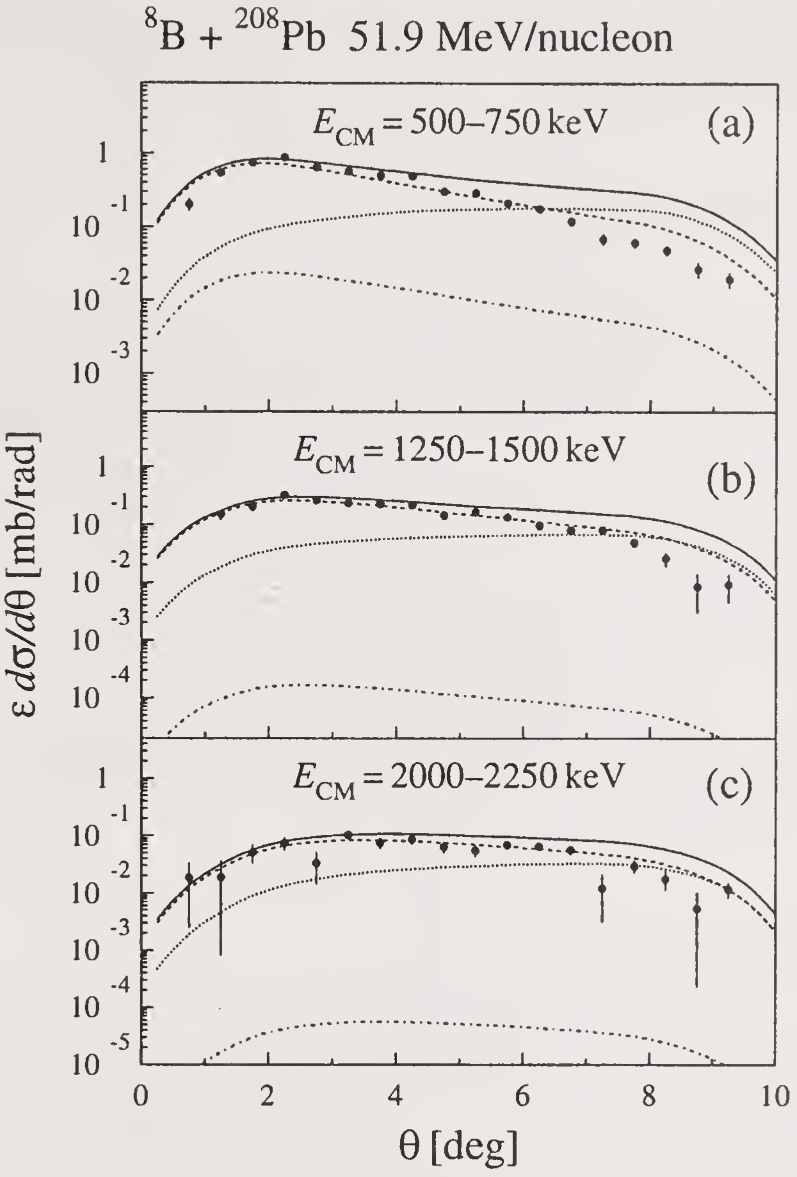

Figure 2. $E1$ (dashed line), $E2$ (dotted line), and $M1$ (dashed-dotted line) components of the Coulomb dissociation cross section $\epsilon d\sigma/d\theta$ as a function of the scattering angle in the dissociation of ^{8}B on ^{208}Pb target at the beam energy of 51.9 MeV/nucleon. The solid line shows their sum. Results for relative energy bins of (**a**) 500–750 keV, (**b**) 1250–1500 keV and (**c**) 2000–2250 keV are shown. ϵ is the detector efficiency. The experimental data and ϵ are taken from ref. [14].

2.2 Notre Dame data, $E_{\text{beam}} = 25.8$ MeV

The Notre Dame group has measured the breakup of ^{8}B on the ^{58}Ni target at the beam energy of 25.8 MeV, well below the Coulomb barrier, where the $E2$ component is expected to dominate the CD process [15]. However, the reliable extraction of the $E2$ component from this data, where only the integrated cross section of the ^{7}Be fragment is measured, is still doubtful. The analysis of the data reported in ref. [15] used the Alder–Winter's semiclassical theory of Coulomb excitation, where the final state is treated as a two-body system, thus assuming that the measured angles of ^{7}Be were equal to those of the ^{7}Be-p center of mass. The inadequacy of this assumption has been demonstrated in [8]. Furthermore, the total breakup cross section reported in this experiment could not be reproduced within the Alder–Winther theory even if a wide variety of structure models of ^{8}B were used [21]. Therefore, the uncertainty about the magnitude of the $E2$ cross section calculated with various structure models of ^{8}B is not eliminated by the Notre Dame measurements [15].

Furthermore, the importance of the nuclear breakup effects in the kinematical regime of the Notre Dame experiment has been emphasized in ref. [22]. Therefore, there is a need to reanalyse this data using a quantum mechanical theory where the nuclear excitations and the three-body kinematics are taken into account.

3. Full quantum mechanical calculations

A one-step prior-form DWBA analysis of the ^{8}B breakup data has been reported in [9] at both low and high energies in order to check the validity of various assumptions of the Coulomb dissociation method. The breakup process is described as a single proton excitation of the projectile from its ground state to a range of states in the continuum, which is discretized by the method of continuum bins. Excitations to states corresponding to the relative energy (of the $p-{}^7$Be system) up to 3.0 MeV and relative partial waves up to 3 have been taken into account. The point-like projectile approximation as well as collective model prescription for the nuclear form factor have been avoided, by determining the nuclear and Coulomb parts by a single-folding method where the relevant fragment-target interactions are folded by the projectile wave functions in the ground and continuum states.

3.1 ^{8}B *breakup at* $\sim$ *50 MeV, RIKEN data*

In figure 3a, $E1$ and $E2$ components of the angular distributions for the $^8\mathrm{B} + {}^{208}\mathrm{Pb} \rightarrow {}^8\mathrm{B}^* + {}^{208}\mathrm{Pb}$ reaction measured by the Kikuchi *et al* [14] at the beam energy of 415 MeV are shown, for the pure Coulomb excitation case. The dashed, dotted and solid lines represent $E1$, $E2$ and $E1 + E2$ cross sections respectively which are obtained by the single-folding procedure. Also shown in this figure are the corresponding results obtained by PLPA (curves with solid circles). We note that PLPA becomes inaccurate beyond 4° in this case. Moreover, the $E2$ component of the pure Coulomb excitation becomes increasingly important also after this angle.

In figure 3b, the cross sections obtained by summing coherently the Coulomb and nuclear amplitudes (to be referred as *total* in the following) are shown. The dashed and dotted lines show the dipole and quadrupole cross sections respectively, while the solid line represents their sum. It can be noted that nuclear effects modify the pure Coulomb $E1$ cross sections substantially after $\sim 4°$, and the $E2$ cross sections in the entire angular range. However, since the $E2$ components are quite small at angles $\leq 4°$, the difference between pure Coulomb and *total* dipole + quadrupole cross sections is appreciable only after this angle.

Therefore, at RIKEN energies, the PLPA breaks down beyond 4°, where the Coulomb-nuclear interference effects as well as the quadrupole component of breakup is substantial. Hence, the Coulomb dissociation method as used in ref. [7] to extract $S_{17}(0)$ from the measurements of the angular distributions in the breakup of ^{8}B on heavy target at RIKEN energies ($\sim$ 50 MeV/nucleon), is reliable only when data is taken at angles below 4°.

In figure 4a, b and c the comparison of calculations [9] for $\epsilon \cdot \mathrm{d}\sigma/\mathrm{d}\theta$ with the experimental data of Kikuchi *et al* [14] is shown as a function of the scattering angle $\theta_{^8\mathrm{B}^*}$ of the excited ^{8}B (center of mass of the ^{7}Be+p system) for three relative energy bins. The efficiency (ϵ) matrix as well as angular and energy averaging were the same as those discussed in ref. [14]. The dashed and dotted lines are the pure Coulomb $E1$+$E2$ and

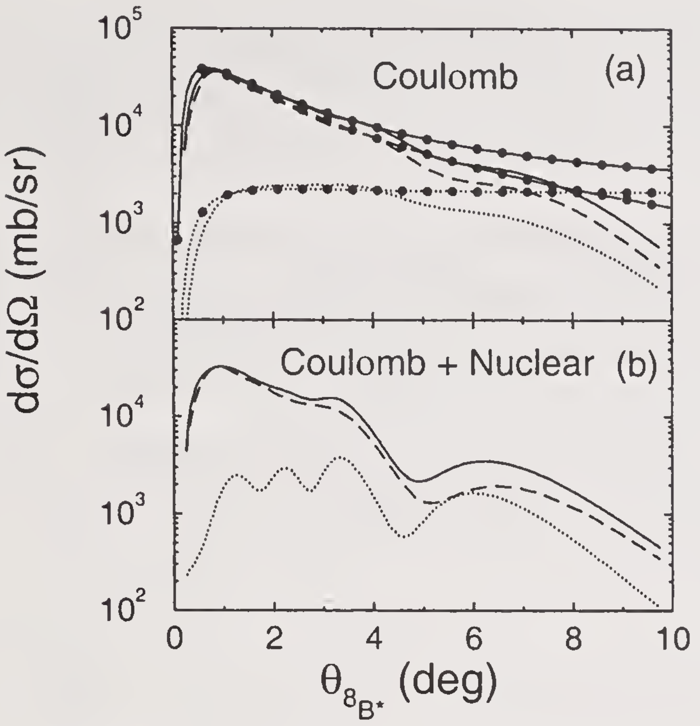

Figure 3. Angular distribution for ^{8}B+^{208}Pb $\rightarrow$ ^{8}B*(^{7}Be+p)+ ^{208}Pb reaction at the beam energy of 415 MeV. (**a**) Results for pure Coulomb excitation, the dashed and dotted curves represent the $E1$ and $E2$ cross sections while their sum is depicted by the solid line. Also shown here are the results obtained with a point-like projectile approximation (Alder–Winther theory), where dashed and dotted lines with solid circles show the corresponding $E1$ and $E2$ cross sections while the solid line with solid circles represents their sum. (**b**) Coherent sum of Coulomb and nuclear excitation calculations; the dashed and dotted lines show the dipole and quadrupole components while the solid line is their sum.

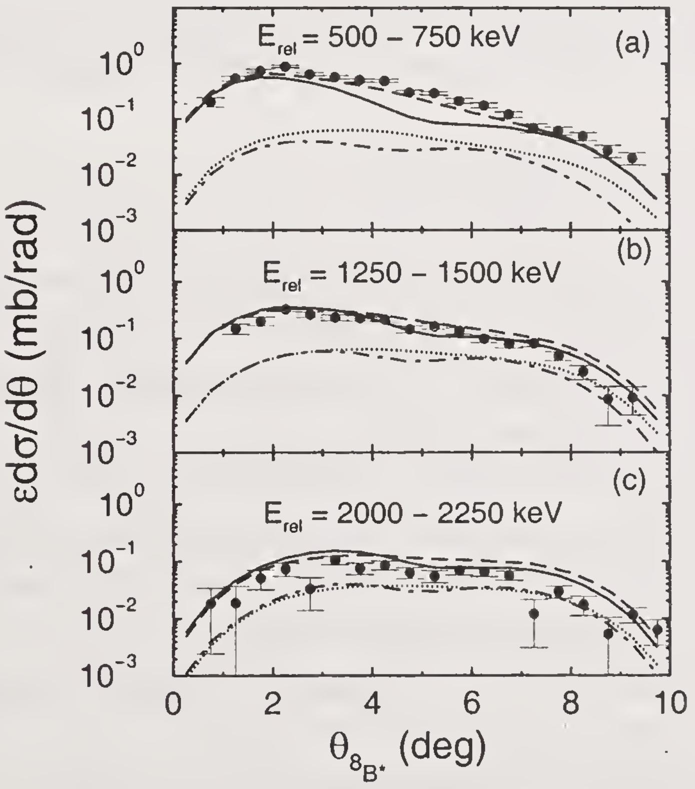

Figure 4. Comparison of experimental and theoretical cross section $\epsilon\, d\sigma/d\theta$ as a function of the scattering angle $\theta_{8_{B^*}}$ for ^{8}B+^{208}Pb $\rightarrow$ ^{8}B*(^{7}Be+p)+ ^{208}Pb reaction at the beam energy of 415 MeV. Results for three relative energy bins of (**a**) 500–750 keV, (**b**) 1250–1500 keV, (**c**) 2000–2250 keV are shown. ϵ is the detector efficiency. Solid lines show the calculated total Coulomb plus nuclear dissociation cross sections while the dashed lines represents the corresponding pure Coulomb dissociation result. Pure quadrupole Coulomb and Coulomb + nuclear cross sections are shown by dotted and dashed-dotted lines. The experimental data and the detector efficiencies are taken from [14].

$E2$ cross sections respectively while the solid and dashed lines are the corresponding *total* cross sections. We note that the calculations are in fair agreement with the experimental data. No arbitrary normalization constant has been used in the results reported in this figure.

The quadrupole component of breakup is significant at almost all the angles in the relative energy bin 2.0–2.25 MeV (c), and at angles beyond 5° in the energy bin 1.25–1.50 MeV (b). On the other hand, its contribution is inconsequential in the energy bin 0.5–0.75 MeV (a). This result is in somewhat disagreement with that reported in ref. [14], where this component is reported to be small everywhere below 1.75 MeV relative energy. Although these authors also perform a quantum mechanical calculation within DWBA, their treatment of the continuum state is very different from that of ref. [9]. Moreover they use a collective model prescription for the Coulomb and nuclear form factors, which has a limited applicability for ^{8}B breakup. Bertulani and Gai [12] have also reported smaller quadrupole component in their analysis of this data. These authors do not include the nuclear effects in the $E1$ excitations and make use of the eikonal approximation to calculate the quadrupole nuclear excitation amplitudes. Moreover, the Coulomb excitation amplitudes have been calculated with the PLPA which have been found to be invalid at higher angles (see figure 3). It is also noted in figure 3 that Coulomb-nuclear interference effects reduce the $E1$ cross sections at larger angles.

Some authors have studied the importance of the higher order effects in the Coulomb breakup of ^{8}B [24,25,20,26]. At RIKEN energies these effects play only a minor role for this reaction in the kinematical regime of forward angles and low relative energies [24,20,26]. Therefore, the conclusions arrived in ref. [9] about the RIKEN data are unlikely to be affected much by the higher order breakup effects. However, the multi-step breakup could play an important role at Notre Dame energies, which is discussed in [23].

3.2 ^{8}B *breakup at sub-Coulomb energies; Notre Dame data*

In figure 5a and b, the calculated angular distributions [9] of ^{7}Be and ^{8}B* respectively in a ^{8}B induced breakup reaction on ^{58}Ni target are shown, at the beam energy of 25.8 MeV. Pure Coulomb and pure nuclear breakup cross sections are represented by the dashed and dashed-dotted curves respectively. The *total* cross sections are represented by the solid lines. In these calculations also the procedure of single-folding the respective fragment-target interactions with ^{8}B ground and continuum state wave functions have been used. One can see that the angular distributions of ^{7}Be and ^{8}B* are distinctly different from each other. While pure Coulomb and *total* breakup cross sections show a forward peak in case of ^{7}Be (which is typical of the angular distribution of fragments emitted in breakup reactions), those of ^{8}B* tend to zero as angle goes to zero. The latter is the manifestation of the adiabatic cut-off typical of the Coulomb-excitation process. In both the cases the nuclear effects are small below 20° and there is a Coulomb-nuclear interference minimum between 25°–60°. However the magnitude of various cross sections are smaller in figure 5a. Furthermore, the nuclear-dominated peak occurs at different angles in figures 5a ($\simeq 55°$) and 5b ($\simeq 70°$). As discussed in [8], the angles of ^{7}Be can be related to those of ^{8}B*. A given $\theta_{^7\mathrm{Be}}$ gets contributions from a range of generally larger $\theta_{^8\mathrm{B}^*}$. This could explain the shifting of the peaks of various curves to lower angles in figure 5a as compared to the corresponding ones in figure 5b. This underlines the importance of three-body kinematics in describing the inclusive breakup reactions.

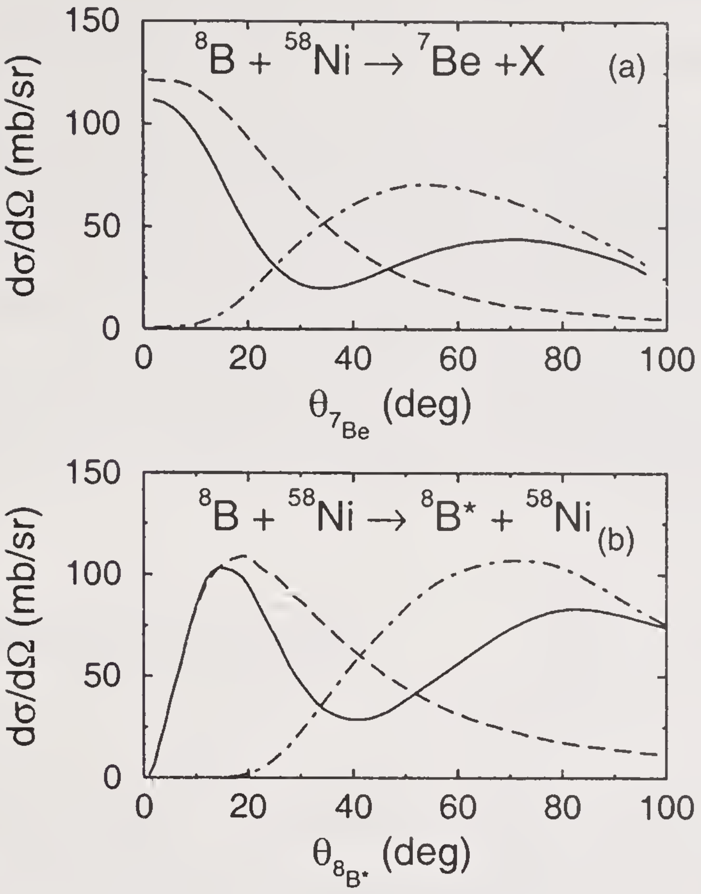

Figure 5. (**a**) Angular distribution of the ^{7}Be fragment emitted in the breakup reaction of ^{8}B on ^{58}Ni target at the beam energy of 25.8 MeV. The dashed and dashed-dotted lines show the pure Coulomb and pure nuclear breakup cross sections respectively while their coherent some is represented by the solid line. (**b**) Angular distribution of $^8B^*$ in the Coulomb excitation of ^{8}B on ^{58}Ni at the beam energy of 25.8 MeV. The dashed and dashed-dotted lines show the cross sections for pure Coulomb and pure nuclear excitation respectively, while the solid line represents their coherent sum.

The ratio of the experimental integrated breakup cross section of ^{7}Be (obtained by integrating the breakup yields in the angular range, (45 ± 6)°, of the experimental setup) to Rutherford elastic scattering of ^{8}B is reported to be $(8.1 \pm 0.8^{+2.0}_{-0.5}) \times 10^{-3}$ [15]. It is not possible to get this cross section by directly integrating the angular distributions shown in figure 4b in this angular range as the corresponding angles belong to $^8B^*$ and not to ^{7}Be. However, in the three-body case (figure 5a), this can be done in a straight-forward way. This gives a value of 7.0×10^{-3} which is in close agreement with the experimental data. Thus, previous failures to explain the experimental value may be attributed to the neglect of both the Coulomb-nuclear interference effects and the three-body kinematics.

In figure 6, the range of the validity of the point-like projectile approximation (PLPA) and the role of the Coulomb-nuclear interference effects on the cross sections of dipole and quadrupole components is investigated. In figure 6a the results for pure Coulomb breakup are shown. Dipole and quadrupole components of the cross section obtained by the single-folding procedure are shown by solid and dashed lines respectively, while those obtained with the PLPA by solid and dashed lines with solid circles. It can be noted that PLPA is not valid for angles beyond 20°. The condition that the impact parameter of the collision is larger than the sum of the projectile and target radii ($b > R_a + R_t$), assumed in applying the Alder–Winther theory, is no longer valid because there is a long tail in the ^{8}B ground state wave function. We also note that the quadrupole component is affected more by the PLPA as compared to the dipole. The big difference in the dipole and quadrupole cross sections seen in the PLPA results beyond 20° (where the quadrupole component is much

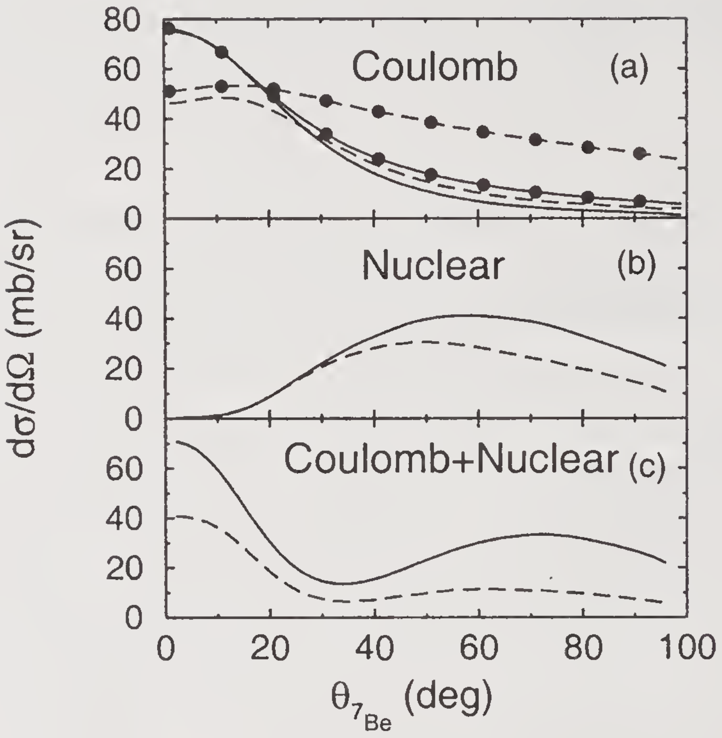

Figure 6. Dipole (solid lines) and quadrupole (dashed lines) components of the angular distributions of the ^{7}Be fragment emitted in the breakup reaction of ^{8}B on ^{58}Ni target at the beam energy of 25.8 MeV. (**a**) Pure Coulomb breakup; also shown here are the $E1$ (solid lines with solid circles) and $E2$ (dashed lines with solid circles) cross sections obtained with point-like projectile and target approximation (Alder–Winther theory), (**b**) pure nuclear breakup and (**c**) Coulomb plus nuclear breakup where the corresponding amplitudes are coherently summed.

bigger than the dipole), almost disappears in the corresponding cross sections obtained by single-folding procedure. Nevertheless, the quadrupole cross sections still remain larger than those of the dipole beyond 30° in the latter case.

In connection with PLPA, it should be made clear that p + target and the ^{7}Be + target potentials do take into account the finite size of the ^{7}Be and target nuclei. This effect, however, is only important when two nuclei are very close to each other and is masked by the nuclear effects which would be important at those impact parameters.

Dipole and quadrupole cross sections for pure nuclear breakup are shown in figure 6b. The cross sections obtained by summing coherently the amplitudes of $E1$ and $E2$ components of pure Coulomb and pure nuclear breakup are shown in figure 6c. We notice that the Coulomb-nuclear interference effects make the contributions of the dipole component of the *total* cross section larger than those of quadrupole one at all the angles. This result is quite remarkable as it implies that the $E2$ component of the total break up cross section in the ^{8}B induced reaction on ^{58}Ni target is not dominant even at the sub-Coulomb beam energies. Therefore, there is hardly any hope of determining the $E2$ component of ^{8}B breakup by Notre Dame type of experiment [15].

This underlines the need for more refined experiments to determine the $E2$ component. It is clear from figure 6c that the measurements of the angular distributions may provide useful information about the $E2$ component as it is different from that of the $E1$ multipolarity. On the other hand, the angular distributions of the fragments, calculated within a semiclassical theory without making the approximation of isotropic angular distributions in the projectile rest frame, have been shown to have large $E1$–$E2$ interference effects [20]. They lead to asymmetries in the momentum distributions of the fragments, whose measurements may enable one to put constraints on the $E2$ component [27]. However, for better accuracy of this method, improved calculations including the nuclear effects may be necessary.

These results for the nuclear effects in the angular distribution of $^{8}B^{*}$ are approximately similar to those reported in [28], where Coulomb and nuclear form factors are calculated by folding the proton-target mean-field (parameterized by a Woods–Saxon function) by the ground and discretized continuum state ^{8}B wave functions. These authors calculate various cross sections by integrating a fixed projectile-target optical potential along a semiclassical trajectory. However, since the three-body kinematics for the final state has not been considered by them, a direct comparison between their calculations and the data of [15] is not possible.

4. Summary and conclusions

The Coulomb dissociation method provides a useful tool to calculate the cross sections of the difficult-to-measure time-reversed processes (i.e. radiative capture reactions) of astrophysical interest. Application of this method in determining the low-energy cross sections of the $^{7}Be(p,\gamma)^{8}B$, which is of considerable interest in the context of the solar neutrino problem, has yielded some interesting results since the first pioneering experiment performed at RIKEN on the $^{8}B + {}^{208}Pb \to {}^{8}B^{*} + {}^{208}Pb$ at beam energies around 50 MeV/nucleon. Detailed theoretical analysis (within the one-step distorted wave Born approximation) reveal that RIKEN-I and RIKEN-II data are almost free from the nuclear effects and are dominated by the $E1$ component for ^{7}Be-p relative energies < 0.75 MeV at very forward angles ($\leq 4^{\circ}$). The study of the breakup of ^{8}B in this kinematical regime is, therefore, better suited for the extraction of a reliable $S_{17}(0)$ for the capture reaction $^{7}Be(p,\gamma)^{8}B$ at low relative energies.

For the breakup reaction at low energy the Coulomb-nuclear interference effects are quite important. A very striking feature of this effect is that it makes the $E1$ component of the *total* cross section of the breakup reaction $^{8}B + {}^{58}Ni \to {}^{7}Be + X$ (at the beam energy of 25.8 MeV), larger than the corresponding $E2$ component at all the angles. This renders untenable the main objective of the Notre Dame experiment of determining the $E2$ component in the breakup of ^{8}B at low beam energies. The dominance of the $E2$ component for this reaction at this energy, seen in the semi-classical Alder–Winther theory of Coulomb excitation has led to this expectation. However, we note that even in pure Coulomb dissociation process, with finite size of the projectile taken into account, the $E2$ components is almost equal to that of $E1$ in the relevant angular range.

It can be said that the feasibility of the Coulomb dissociation method in determining the $S_{17}(0)$ from the breakup reactions of ^{8}B has been established by identifying the kinematical regime where the assumptions of this method are well fulfilled. We now have all the theoretical tools to analyse such experiments, and it may soon become possible to extract a reliable value of S_{17} by means of the Coulomb dissociation method.

References

[1] J N Bahcall, *Neutrino Astrophysics* (Cambridge University Press, New York, 1989)
[2] J N Bahcall and M H Pinsonneault, *Rev. Mod. Phys.* **69**, 781 (1995)
[3] J N Bahcall, *Nucl. Phys.* **A631**, 29 (1998)
[4] E G Adelberger *et al*, *Rev. Mod. Phys.* **70**, 1265 (1998)
[5] G Baur and H Rebel, *J. Phys.* **G20**, 1 (1994)

[6] G Baur and H Rebel, *Ann. Rev. Nuc. Part. Sci.* **46**, 321 (1997)

[7] R Shyam, I J Thompson and A K Dutt–Majumder, *Phys. Lett.* **B371**, 1 (1996)

[8] R Shyam and I J Thompson, *Phys. Lett.* **B415**, 315 (1997)

[9] R Shyam and I J Thompson, *Phys. Rev.* **C59**, 2465 (1999)

[10] K Langanke and T D Shoppa, *Phys. Rev.* **C49**, R1771 (1994); **51**, 2844(E) (1995); **52**, 1709 (1995)

[11] M Gai and C A Bertulani, *Phys. Rev.* **C52**, 1706 (1995)

[12] C A Bertulani and M Gai, *Nucl. Phys.* **A636**, 227 (1998)

[13] T Motobayashi *et al*, *Phys. Rev. Lett.* **73**, 2680 (1994)

[14] T Kikuchi *et al*, *Phys. Lett.* **B391**, 261 (1997)

[15] Johanes von Schwarzenberg *et al*, *Phys. Rev.* **C53**, R2598 (1996)

[16] K Alder and A Winther, *Electromagnetic Excitation* (North-Holland, Amsterdam, 1975)

[17] A N F Alexio and C A Bertulani, *Nucl. Phys.* **A505**, 448 (1989)

[18] S Typel and G Baur, *Phys. Rev.* **C50**, 2104 (1994)

[19] K H Kim, M H Park and B T Kim, *Phys. Rev.* **C35**, 363 (1987)

[20] H Esbensen and G F Bertsch, *Nucl. Phys.* **A600**, 37 (1996)

[21] F M Nunes, R Shyam and I J Thompson, *J. Phys.* **G24**, 1575 (1998)

[22] F M Nunes and I J Thompson, *Phys. Rev.* **C57**, R2818 (1998)

[23] F M Nunes and I J Thompson, *Phys. Rev.* **C59**, 2652 (1999)

[24] S Typel and G Baur, *Phys. Rev.* **C50**, 2104 (1994)

[25] H Esbensen, G F Bertsch and C A Bertulani, *Nucl. Phys.* **A581**, 107 (1995)

[26] S Typel, H Wolter and G Baur, *Nucl. Phys.* **A617**, 147 (1997)

[27] B Davids *et al*, *Phys. Rev. Lett.* **81**, 2209 (1998)

[28] C H Dasso, S M Lenzi and A Vitturi, *Nucl. Phys.* **A639**, 635 (1999)

Perspectives from above and beyond the proton drip-line

P J WOODS
Department of Physics and Astronomy, University of Edinburgh, Edinburgh EH9 3JZ, UK

Abstract. This paper will review the dramatic increase in our knowledge of one and two proton unbound nuclei [1] such as recoil decay tagging [2] are revealing unique insights into the structure of nuclei beyond the proton drip-line. These studies of excited states provide complementary information to proton radioactivity studies, particularly regarding the role of deformation [3]. Radioactive beams are being used to study two-proton unbound resonances and to study explosive nuclear astrophysical reactions in the region of the proton drip-line.

Keywords. Proton drip-line; recoil decay tagging; one and two proton emission; radioactive beams; nuclear astrophysics.

PACS Nos 23.50.+z; 21.10.Dr

References

[1] P J Woods and C N Davids, *Ann. Rev. Nucl. Part. Sci.* **47**, 541 (1997)
[2] E S Paul *et al*, *Phys. Rev.* **C51**, 78 (1995)
[3] C N Davids *et al*, *Phys. Rev. Lett.* **80**, 1849 (1998)

Mass measurements of relativistic projectile fragments in the storage ring ESR

T RADON[1], H GEISSEL[1], F ATTALLAH[1], K BECKERT[1], F BOSCH[1], A DOLINSKIY[1], H EICKHOFF[1], M FALCH[2], B FRANCZAK[1], B FRANZKE[1], Y FUJITA[3], M HAUSMANN[1], M HELLSTRÖM[1], F HERFURTH[1], TH KERSCHER[2], O KLEPPER[1], H-J KLUGE[1], C KOZHUHAROV[1], YU LITVINOV[4], K E G LÖBNER[2], G MÜNZENBERG[1], F NOLDEN[1], YU NOVIKOV[4], Z PATYK[5], W QUINT[1], H REICH[1], C SCHEIDENBERGER[1], B SCHLITT[1], J STADLMANN[6], M STECK[1], K SÜMMERER[1], L VERMEEREN[1], M WINKLER[1], TH WINKLER[1] and H WOLLNIK[6]

[1] Gesellschaft für Schwerionenforschung mbH, Planckstraße 1, D-64291 Darmstadt, Germany
[2] Sektion für Physik, LMU München, Am Coulombwall, D-85748 Garching, Germany
[3] Department of Physics, Osaka University, Toyonaka, Osaka 560, Japan
[4] St. Petersburg Nuclear Physics Institute, Gatchina 188350, Russia
[5] Soltan Institute for Nuclear Studies, 00-681 Warsaw, Poland
[6] II. Physikalisches Institut, JLU Gießen, Heinrich-Buff-Ring 16, D-35392 Gießen, Germany

Abstract. Two experimental methods of measuring masses of exotic nuclei in the storage ring ESR are presented. Bismuth and nickel fragments were produced via projectile fragmentation, separated and investigated with the combination of the fragment separator FRS and the ESR: (i) Direct mass measurements of relativistic projectile fragments were performed using Schottky mass spectrometry (SMS), i.e., exotic nuclei were stored and cooled in the ESR. Applying electron cooling, the relative velocity spread of circulating low intensity beams can be reduced below 10^{-6}. Under this condition a mass resolving power of up to $m/\Delta m = 6.5 \cdot 10^5$ (FWHM) was achieved in a recent measurement. Previously unknown masses of more than 100 neutron-deficient isotopes have been measured in the range of $60 \leq Z \leq 84$. Using known Q_α values the area of known masses could be extended to more exotic nuclei and to higher proton numbers. The results are compared with mass models and extrapolations of experimental values. In a second experiment with ^{209}Bi projectiles the area of the measured masses was extended to lower proton numbers. Due to various improvements at the ESR the precision of the measurements could be raised. (ii) Exotic nuclei with half-lives shorter than the time needed for SMS (present limit: $T_{1/2} \approx 5$ sec) can be investigated by time-of-flight measurements whereby the ESR is operated in the isochronous mode. This novel experimental technique has been successfully applied in first measurements with nickel and neon fragments where a mass resolving power of $m/\Delta m = 1.5 \cdot 10^5$ (FWHM) was achieved.

Keywords. Mass measurements; storage ring; Schottky spectroscopy; isochronous mode.

PACS No. 21.10.Dr; 27.80.+w; 29.20.Dh

1. Introduction

The mass of a nucleus is its most fundamental property as it reflects all forces between the nucleons. By now only 1600 atomic masses are known whereas the existence of more than 2500 nuclei is established. Nuclei with known masses can be found in or near the valley of β-stability (see figure 1).

However, the study of masses far off stability, where nuclear models have large uncertainties, will contribute more to an improved knowledge of nuclear binding and structure. Here the masses of nuclei are most important for the understanding of astrophysical processes (r-, s-, rp-path). Recent review articles [1–3] present the progress of atomic mass measurements.

The unique combination of the fragment separator FRS [4] and the experimental storage ring ESR [5] gives excellent conditions to perform mass measurements of relativistic exotic nuclei. We performed measurements on the neutron deficient part of the lead region [6,7]. This area was mainly chosen due to the possiblity to connect members of α-chains linked by precise Q_α values to the backbone of known masses [6] in order to cover nuclei at the proton dripline. Another motivation was to measure masses of refractory elements ($72 \leq Z \leq 78$) which cannot be produced by ISOL-techniques. Including α-chains we were able to cover a large number of elements reaching from proton numbers of about 60 up to uranium. An overview of the mass surface covered by our mass measurements with ^{209}Bi projectiles is shown in figure 2. The isotopes with known masses before our experiments as well as those which were measured in 1995 and 1997 for the first time are indicated in the chart of nuclides 6. In the experiment performed in 1997 we extended the measured

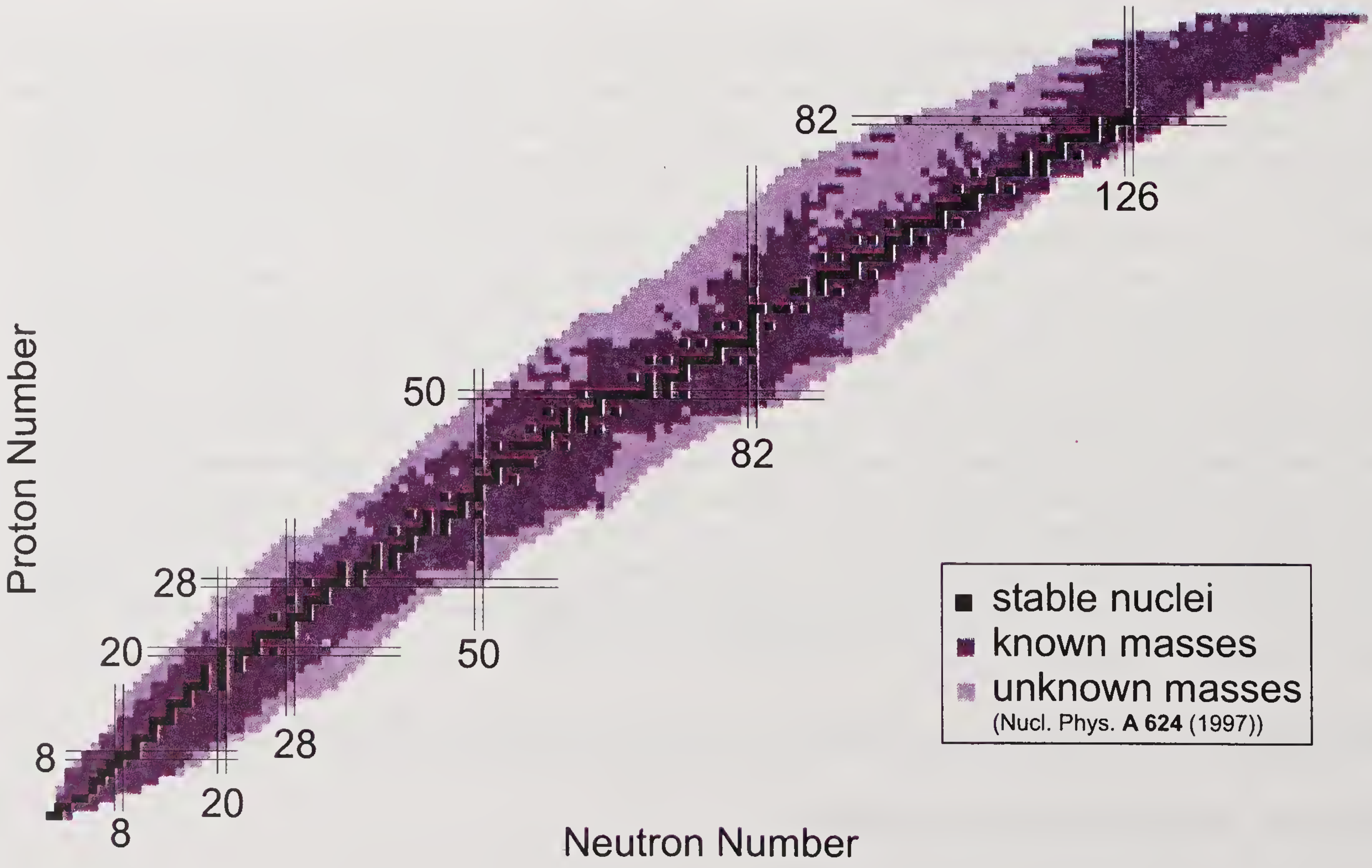

Figure 1. Chart of nuclei showing known and unknown masses up to $Z = 94$.

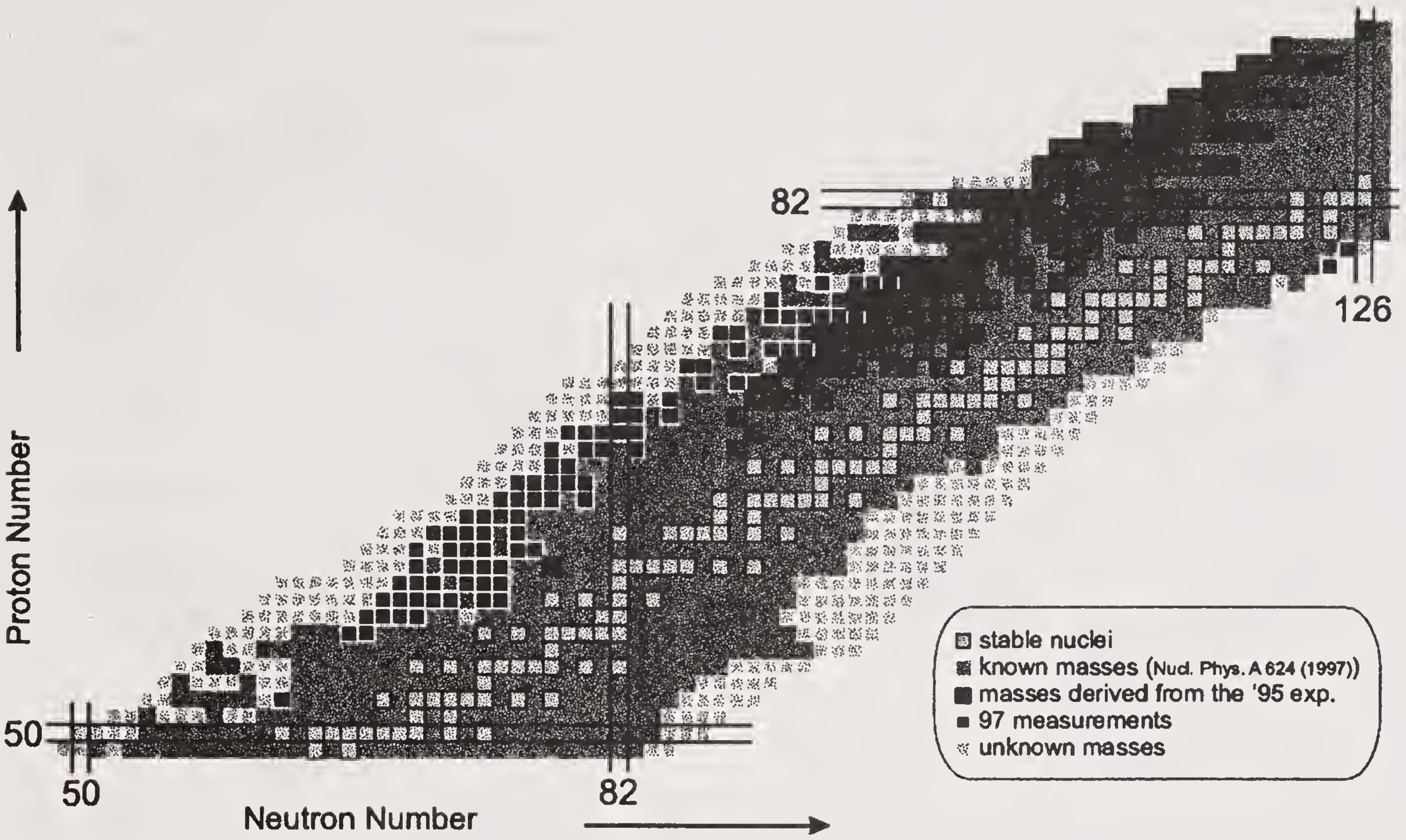

Figure 2. Range of FRS-ESR mass measurements covered in experiments with ^{209}Bi projectile fragments in 1995 and 1997. In the latter experiment we extended the measured mass surface down to cesium and also to neutron-rich fragments near the shell closures at $Z = 82$ and $N = 126$. The marked areas of our studies represent the previously unknown masses only [7].

mass surface to smaller Z values down to tin and also to neutron-rich fragments near the shell closures at $Z = 82$ and $N = 126$.

2. Two ways of mass measurements at the SIS-FRS-ESR facility

Stable beams of relativistic heavy ions provided by the synchrotron SIS [8] are converted into exotic nuclei by nuclear collisions in the production target at the entrance of the spectrometer FRS. The FRS [9] separates the fragments in flight and injects them into the ESR for precise mass determination, performed by measuring the revolution frequency of the stored ions. The ESR is equipped with an electron cooler [10] and can store ions in the range of $(0.5 \leq B\rho \leq 10)$ Tm . The storage time of the circulating nuclei (τ_{st}) is limited by atomic collisions with atoms of the residual gas (pressure $\leq 10^{-10}$ mbar) and with the electrons of the cooler. τ_{st} can range from hours up to days depending on the velocity and the charge state of the stored ions. The phase-space density of the stored ions can be drastically reduced by electron cooling, e.g., the relative velocity spread of a low-intensity cooled beam can be less than 10^{-6}.

Two methods are employed to perform precise mass measurements of stored ions circulating in the ESR: (i) Mass spectrometry using cooled ion beams [6,11]. (ii) Mass spectrometry of hot fragments operating the ESR in the isochronous mode. Both principles can be easily understood by the first-order relation between the mass m, the revolution frequency f, and the velocity v (see figure 3).

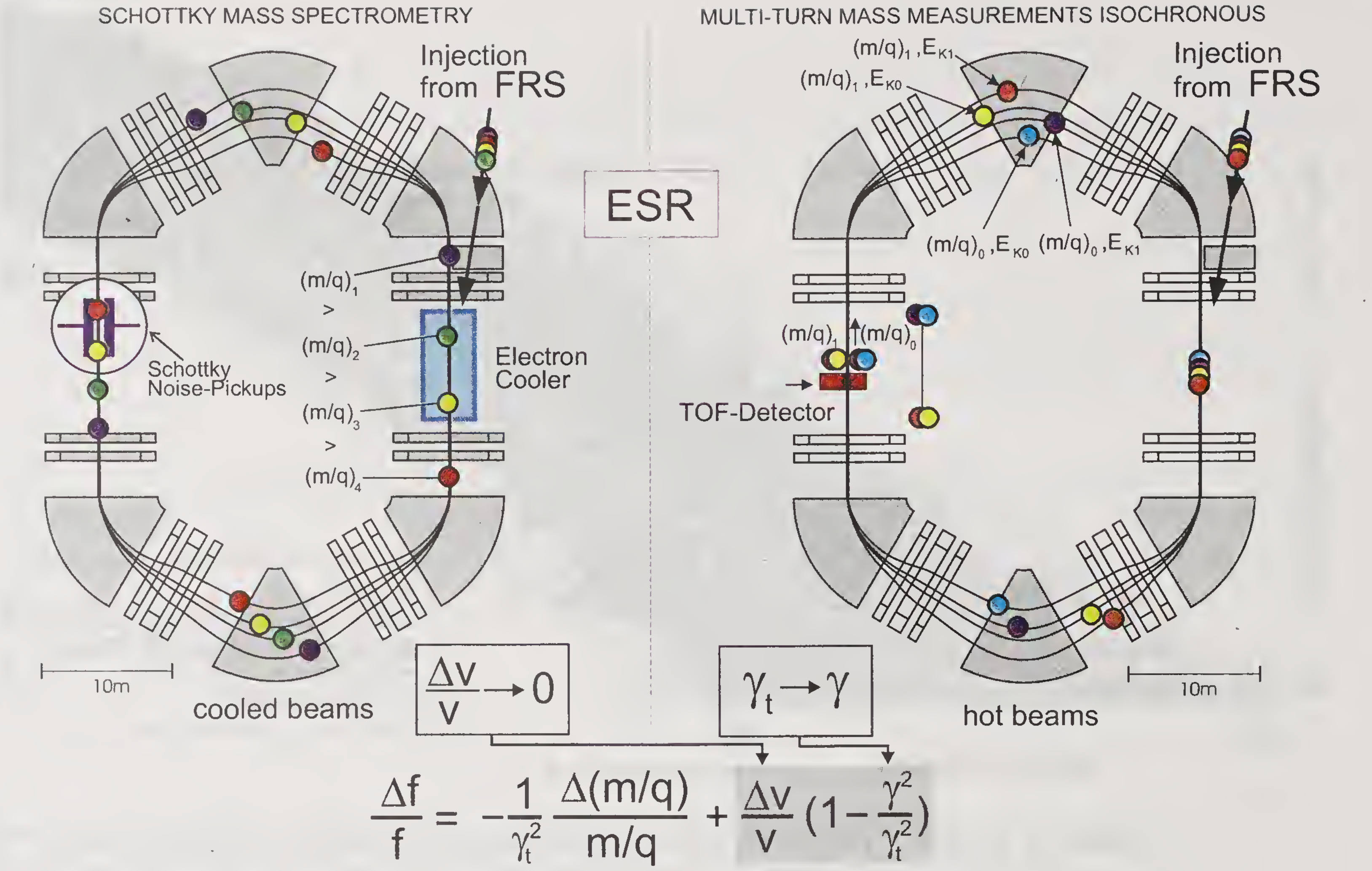

$$\frac{\Delta f}{f} = -\frac{1}{\gamma_t^2}\frac{\Delta(m/q)}{m/q} + \frac{\Delta v}{v}\left(1-\frac{\gamma^2}{\gamma_t^2}\right)$$

Figure 3. The mass resolution in a storage ring is given by the precision achieved for the frequency and velocity determination. γ is the relativistic Lorentz-factor and γ_t represents the reduced transition energy which characterizes the ion-optical mode of the ring. From this formula it is obvious that either cooling $\Delta v/v \rightarrow 0$ or the isochronous condition, $\gamma \rightarrow \gamma_t$, are the basis of precise mass measurements.

3. Schottky mass measurements with cooled fragments

A production target of 8 g/cm^2 beryllium was placed at the entrance of the FRS. The target was especially chosen to inject a large number of elements and isotopes at the same time in the ESR. The incident energy was 930 MeV/u in the case of ^{209}Bi and 750 MeV/u in the case of ^{58}Ni-projectiles. These energies were selected to operate the electron cooler in the range of 200 kV for the terminal voltage. The fragments were separated with the FRS by pure magnetic rigidity ($B\rho$) analysis during the major part of the mass measurements. In this case up to 60 different fragments were injected into the ESR by a single bunch of projectiles from SIS. In the ESR the ions were stored and cooled and detected via Schottky spectrometry.

Schottky spectroscopy is a widely used tool for beam diagnosis in circular accelerators and storage rings. The induced signals of the stored circulating ions in non-destructive Schottky noise-pickups (see left part of figure 3) are recorded and analysed.

Already in our pilot experiments with cooled projectile fragments [4,12] we have applied Schottky diagnostics and since then we have gradually developed this technique for the requirements of precision mass spectrometry [6,13,11]. The stored and cooled ions circulate in the ESR with revolution frequencies of about 1.9 MHz. In the experiments we used the Schottky-noise signal of the 16th and the 32nd harmonic of the revolution frequencies. This high-frequency band has to be reduced by an admixture of an external oscillator frequency to match the working range of 100 kHz of the Fourier-analyser system. A data-acquisition system digitizes the Schottky signals with a sampling rate of 256 kHz. The frequency bandwidth of 100 kHz covers most of the $B\rho$ acceptance of the stored beam in the ESR. The energy of our secondary beams ($E_{\rm sec} \approx 350$ MeV) allowed an optimum performance of the electron cooler and, in addition, presented the opportunity to measure the masses of bismuth fragments in bare, H-like, and He-like charge states. The mass measurement in different charge states yields not only redundant data for the same isotope, but is also an excellent feature for the calibration: Exotic neutron deficient nuclei having small magnetic rigidities and unknown masses appear in the Schottky spectra e.g. in He-like charge states in the neighborhood of isotopes with known masses in bare charge states located nearer to the β stability-line. The uncertainty of the rest mass of the electron and its binding energies are known with an error which is completely negligible compared to our present errors for the nuclear masses [6] being in the order of 10^{-6}.

3.1 Results of the first Schottky mass measurements with bismuth-projectiles

After having demonstrated that the results obtained with our novel experimental methods for direct mass measurements agree well with already known light masses [4,12], a large number of isotopes with unknown masses has been measured (figure 4).

The masses were evaluated by application of a maximum likelihood method. The relation of the mass-over-charge ratio as a function of the revolution frequency was fitted by a first-order polynomial connecting the known masses as references [14]. The unknown masses were determined by searching the maximum of the probability density for all data. The total error of the new masses is in the range of 100 to 200 keV, where a systematic error of about 95 keV has been included. The systematic error has been evaluated by a comparison with previously well-known masses. The good accuracy of our measured data is a solid basis for a better understanding of nuclear forces.

Figure 4 shows one proton separation energies for nuclei in the sub-uranium region. For several elements (Bi to Pa) we can derive mass values for nuclei with negative proton separation energies, i.e. the proton dripline could be located here. For other nuclei (Au to Ho) the location of the dripline can now be interpolated more precisely. The fact that we did not derive negative proton separation energies for even nuclei shows that the proton pairing energy plays an important role for dripline nuclei. Figure 5 shows that the proton pairing energy increases in direction towards the dripline. It is also worthwhile to mention that some of the neutron deficient mercury isotopes show an increase in their pairing energies compared to the neighboring isotopes (see also figure 4: large odd-even staggering for these isotopes). This may be an indication for shape coexistence in these nuclei [16].

In the last decades a large number of mass models have been proposed and developed [15]. They are based on different assumptions and can roughly be divided into three categories. They belong either to pure microscopic models, which start from the nucleon–nucleon interaction, or they belong to the macroscopic–microscopic models which use the liquid drop model with shell corrections or they are based on special mass relations combining the masses for adjacent nuclei. Here it is only the intention to give representative examples of different approaches to mass formulae. The most crucial test for the reliability of a mass model is its predictive capability in new regions that were not considered when the theory was formulated.

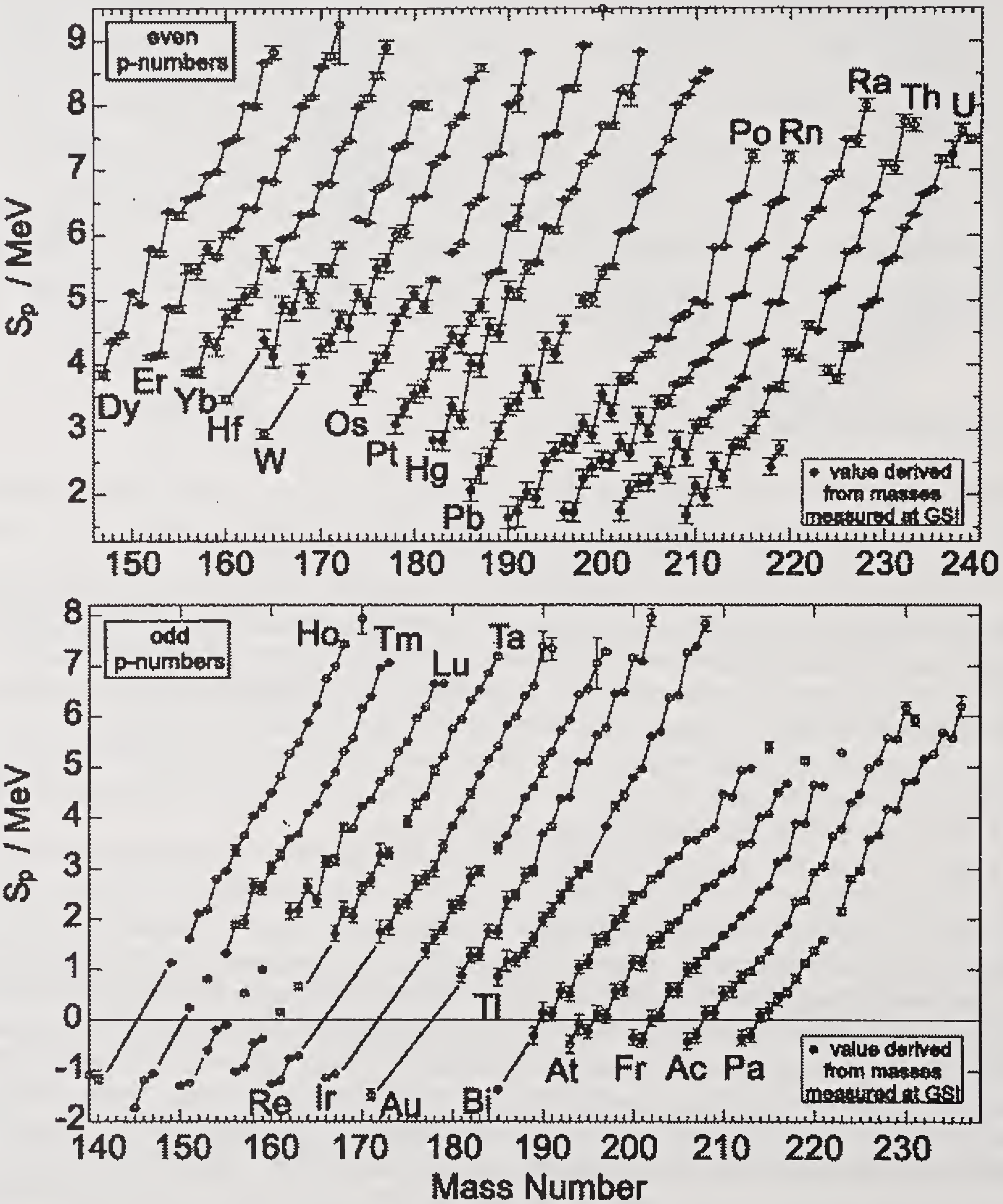

Figure 4. One proton separation energies for even (upper panel) and odd (lower panel) proton numbers. Masses derived from measurements at GSI are marked by a filled symbol.

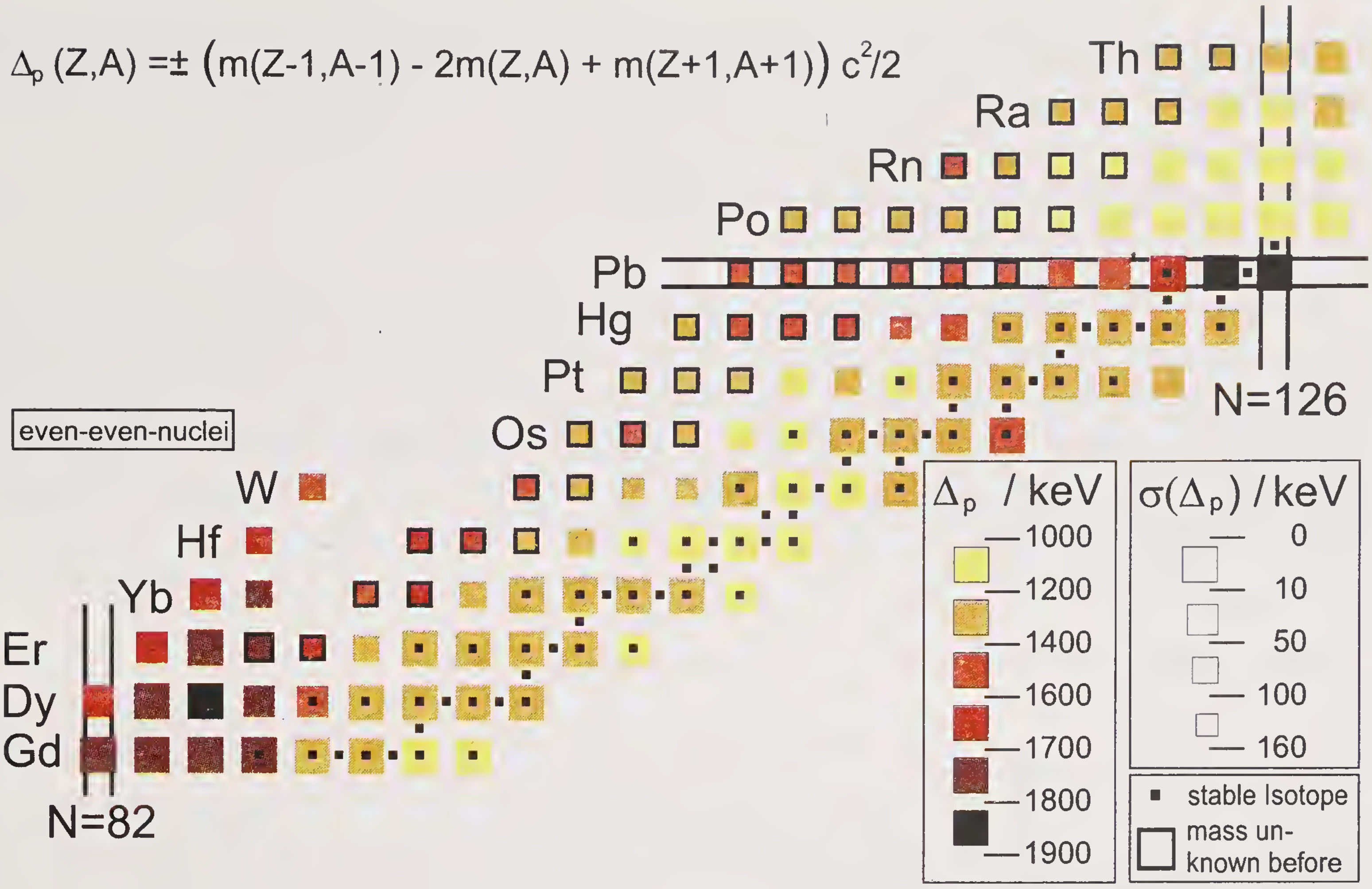

Figure 5. Proton pairing energies for even–even nuclei. The strength of the proton pairing energy Δ_p is given by the color of the squares representing one nucleus and the error $\sigma(\Delta_p)$ is given by the size of the squares. Masses derived from measurements at GSI are marked with a frame. The formula used is not valid to show pairing energies for the lead isotopes, as it also exhibits the larger shell effect here.

Table 1. Mass models compared to our measured data (previously unknown values only). A χ^2-test (eq.(1)) and a root mean square deviation (eq.(2)) from our data were calculated to compare with various types of models.

Mass formula	Category	χ^2	σ_{rms}
Aboussir, Pearson *et al* [17]	microscopic (global)	60.5	773
Duflo–Zucker [18]	microscopic (global)	42.0	650
Möller–Nix [19]	macro-microscopic	40.3	644
Spanier–Johansson [20]	liquid drop with corr. (global) contributions (local)	143.5	1190
Jänecke–Masson [21]	mass relations (local)	20.5	467
Audi-Wapstra *et al* [14]	least-squares adjustment	1.8	137

Using our new mass values we can check the predictive power of various mass formulae tested by the following χ^2-criterion.

$$\chi^2 = \frac{1}{n-1}\sum_{i=1}^{n}\frac{(M_{\mathrm{exp}} - M_{\mathrm{th}})_i^2}{(\Delta M_{\mathrm{exp}})_i^2}, \tag{1}$$

where n is the number of the compared nuclei. M_{exp} and M_{th} represent the measured masses and the theoretically determined masses respectively.

To compare a model to experimental data disregarding error bars the classical rms deviation is used:

$$\sigma_{\rm rms}^2 = \frac{1}{n-1}\sum_{i=1}^{n}(M_{\rm exp} - M_{\rm th})_i^2. \tag{2}$$

Table 1 shows various mass models and mass extrapolations including their predictive power for our 193 previously unknown masses according to eqs (1) and (2). One may easily see from table 1 that these mass models do not predict new masses with a precision needed for a good understanding of the mass surface and to accurately predict the positions of driplines. The extrapolations of Audi and Waptsra [14] however give a satisfactory result for our recently measured masses.

3.2 Experimental improvements for Schottky mass measurements

A number of important improvements could be achieved in our recent experiment in 1997. The performance of the ESR cooler was considerably improved yielding a much stronger cooling force and better stability which led to shorter cooling times and, therefore, gave access to isotopes with shorter half-lives. The maximum voltage of the cooler could also be improved so that we were able to access nuclei with lower proton numbers compared to the 1995 measurements using the same projectile. Furthermore, a better stabilization of the power supplies and an improved magnetic field homogeneity of the ESR magnets helped to significantly improve the resolving power in the mass spectra.

In figure 6 we present Schottky frequency spectra for bismuth and nickel fragments characterized by a mass resolving power of $6.5 \cdot 10^5$ which is about a factor of two better than in our experiment performed in 1995 [6]. It should be mentioned that the half-life

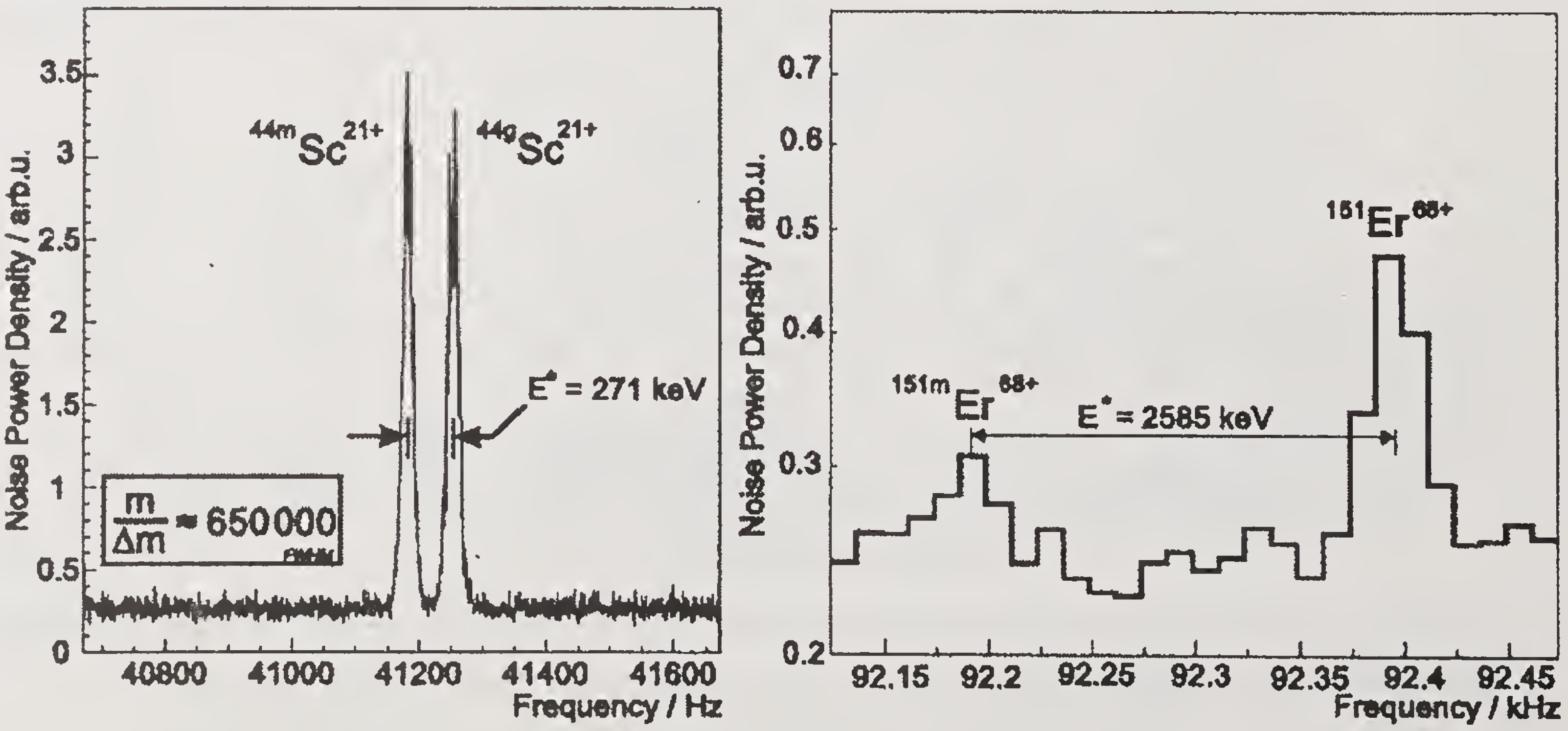

Figure 6. Mass resolved Schottky frequency spectra of bare ^{44g,m}Sc ions (ground and isomeric states separated by 271 keV, left panel) of bare ^{151g,m}Er ions (ground and isomeric states separated by 2585 keV, right panel) [7].

of neutral ^{151m}Er atoms is 0.58 s, however, in our case with bare nuclei the half-life is prolonged by roughly a factor of 21. In the experiment performed in 1997 we used ^{58}Ni and ^{209}Bi projectiles and set the magnetic fields of the FRS and ESR and the cooler voltage corresponding to a constant $B\rho$ value of 6.5 Tm. The advantage of this procedure was that we only had to adjust the ESR once to the FRS which turned out to be a crucial part in the measurements performed in 1995. The scaling of the incident energy (750–900 MeV/u) was a faster procedure to fill the ESR with the desired exotic nuclei.

A new data acquisition system was taken into operation which represented further experimental improvements. The digitized signals of the Schottky pick-up were sequentially recorded on tape giving a time stamp of every event. Fast Fourier transformation of this time-correlated data can be performed off-line in order to obtain the revolution frequencies of the stored ions as well as the half-life information of the radioactive species. Furthermore, time-drifts of the experimental conditions can be corrected in the off-line analysis.

4. Isochronous mass measurements with projectile fragments

There are still regions on the chart of nuclei where Schottky mass spectrometry can still contribute to an improved knowledge of nuclear masses using e.g. stochastic cooling [22], but the most exotic nuclei have too short half-lives for this experimental technique. Exotic nuclei with half-lives shorter than the time needed for cooling and recording can be investigated by time-of-flight techniques in the ESR. Here the ESR is operated in the isochronous mode [23,24]. In this case, the magnetic fields of the ESR are set such that the revolution frequency of an ion species becomes independent of its velocity spread (see right panel of figure 3). This novel experimental technique has been successfully applied in first measurements with nickel [24] and neon fragments. The ESR lattice was tuned to γ_t=1.37 corresponding to a kinetic energy of 345 MeV/u for the stored ions. γ_t is mainly determined by the dispersion function inside the dipole magnets. First frequency spectra were recorded in the isochronous mode using projectile fragments created by a ^{58}Ni beam. The relative velocity spread of these stored ions was about 10^{-3}. Although the momentum acceptance inside the ESR is strongly reduced in the isochronous mode, as compared to the standard operation, the measured m/q acceptance still reached 1.2%. Already in this pilot experiment we achieved a remarkable mass resolving power of $m/\Delta m = 1.5 \cdot 10^5$ (FWHM) as demonstrated by resolving ^{56}Ni and ^{52}Fe fragments (see [7]). Mass uncertainties for nickel-fragments were found to be in the order of 30–60 keV. In another experiment with a ^{22}Ne-beam cooling was applied in addition to measure the revolution frequency of the fragments circulating in the isochronous lattice of the ESR. As a consequence very small linewidths of the frequency peaks were derived which led to mass accuracies below 10 keV for Ne-fragments. Applying cooling to isochronous beams gives the possibility to nicely map γ_t as a function of the pathlength. It was found that a linear mass calibration can be used over a large frequency range. In the off-line analysis the measured dependence of the frequency on the velocity could be well understood and was reproduced by ion-optical model calculations. New ion-optical calculations suggest strong improvements for the isochronous mode which will be tested in coming experiments [25]. For the future it is planned to perform direct mass measurements of ^{238}U fission fragments ($T_{1/2} < 1$ s) using the isochronous method.

References

[1] H-J Kluge, in [15]

[2] G Audi, O Bersillon, J Blachot and A H Wapstra, *Nucl. Phys.* **A624**, 1 (1997)

[3] W Mittig, A Lepine-Szily and N A Orr, *Ann. Rev. Nucl. Sci.* **47**, 27 (1997)

[4] H Geissel *et al*, *Phys. Rev. Lett.* **68**, 3412 (1992)

[5] B Franzke *et al*, *Nucl. Instrum. Methods* **B24/25**, 18 (1987)

[6] T Radon, Th Kerscher and B Schlitt *et al*, *Phys. Rev. Lett.* **78**, 4701 (1997)

[7] H Geissel and T Radon *et al*, Experiments with Stored Relativistic Exotic Nuclei in CP455, *ENAM 98: Exotic Nuclei and Atomic Masses* edited by B M Sherril, D J Morrisey, and Cary N Davids (The American Institute of Physics, 1-56396-804-5/98, 1998)

[8] K Blasche and B Franczak, *Proc. of the third European Part. Acc. Conf., Berlin* edited by H Henke, H Homeyer and Ch Petit-Jean-Genaz (Gif-sur-Yvette: Editions Fronitière, 1992) p. 9

[9] H Geissel, *et al*, *Nucl. Instrum. Methods* **B70**, 286 (1992)

[10] M Steck *et al*, *Phys. Rev. Lett.* **77**, 3803 (1996)

[11] B Schlitt *et al*, *Hyp. Int.* **99**, 117 (1996); *Nucl. Phys.* **A626**, 315c (1997)

[12] H Irnich, H Geissel and F Nolden *et al*, *Phys. Rev. Lett.* **75**, 4182 (1995)

[13] B Franzke *et al*, *Phys. Scr.* **T59**, 176 (1995)

[14] G Audi and A H Wapstra, *Nucl. Phys.* **A595**, 409 (1995)

[15] D Guillemaud-Mueller (ed.) *Proceedings of ENAM95* (Gif-sur-Yvette: Editions Fronitière, ISBN 2-86332-186-2, 3, 1995)

[16] G Ulm *et al*, *Z. Phys.* **A325**, 247 (1986)

[17] Y Aboussir, J M Pearson, A K Dutta and F Tondeur, *Atomic Data Nucl. Data Tables* **61**, 127 (1995)

[18] J Duflo and A P Zuker, *Phys. Rev.* **C52**, 23 (1995)

[19] P Möller, J R Nix, W D Myers and W J Swiatecki, *Atomic Data Nucl. Data Tables* **59**, 185 (1995)

[20] L Spanier and S E Johannson, *Atomic Data Nucl. Data Tables* **93**, 259 (1988)

[21] J Jännecke and P J Masson, *Atomic Data Nucl. Data Tables* **39**, 265 (1988)

[22] F Nolden, B Franzke and A Schwinn, GSI-Report 98-1 171 (1998)

[23] H Wollnik *et al*, GSI-Report 86-1 372 (1986)

[24] M Hausmann *et al*, GSI-Report 98-1 170 (1998)

[25] M Hausmann *et al*, *Proc. of the 6th European Particle Accelerator Conference* edited by S Myers, L Liljeby, Ch Petit-Jean-Genaz, J Poole and K-G Rensfeldt (Institute of Physics Publishing, Bristol, 1998) pp. 511–513

The analysis of reactions leading to synthesis of super heavy elements within the dinuclear system concept

E A CHEREPANOV
Flerov Laboratory of Nuclear Reactions, Joint Institute for Nuclear Research, 141980 Dubna, Moscow Region, Russia
Email: cher@jinr.ru

Abstract. The dinuclear system concept of complete fusion of nuclei has been applied to the analysis of superheavy elements synthesis. The optimal excitation energy of compound nuclei and production cross sections in the cold synthesis of heavy elements with charge $Z = 102 - 112$ have been calculated. The possibility of synthesizing the element with magic number $Z = 114$ in cold and hot fusion reactions has been considered.

Keywords. Fusion; fission; superheavy elements; quasi-fission; deexcitation.

PACS Nos 24.75+i; 25.85.-w; 25.85.Jg; 27.90.+b

1. Introduction

The application of heavy ions of large mass is necessary for the decision of problems of the synthesis of new elements. Especially important in planning the experiments on the synthesis of new elements is to know the cross section of complete fusion. The cross sections of complete fusion in reactions with heavy ions up to values $Z_p \cdot Z_t = 1600$ are well described by the existing theoretical models. For $Z_p \cdot Z_t > 1600$ values the cross section of complete fusion dramatically fell.

There are different models for the description of complete fusion of massive nuclei. Most popular of them is the macroscopic dynamical model of Swiatecki [1]. However, a lot of experimental data for reactions of cold synthesis cannot be explained even qualitatively within the framework of this model. For instance, new elements with $Z = 107 - 112$ were produced in GSI using targets close to Pb (see, for example, ref. [2]). In these reactions the maxima of the excitation functions for the evaporation of one neutron lie below the Bass barrier. Complete fusion for these reactions in framework MDM required a large excess (several tens of MeV) of the collision kinetic energy above the entrance Coulomb barrier B_{Bass}. In Japan, an approach is being developed on the basis of the fluctuation–dissipation model (see, for example ref. [3]), for the description of the fusion of heavy symmetric systems leading to the formation of transfermium nuclei. Estimation of the formation cross sections of SHE in standard statistical model taking into account the limitations on fusion from empirical systematics were made in ref. [4].

In all listed models, as it seems, there is no systematic comparison with the existing experimental data. Such a comparison could give significant weight to the theoretical predictions. In FLNR (JINR) a new approach has been developed for the description of complete fusion of massive nuclei based on dinuclear system (DNS) concept [6]. In the present work an attempt is undertaken to describe the existing data on cold synthesis of new elements on the basis of the DNS concept. We analysed various ('cold' and 'hot') reactions leading to the synthesis of the new element with charge number 114.

2. Description of the theoretical approach

2.1 Basic assumptions of the DNS-concept

The motivation of the DNS-concept and its comparison with MDM have already been presented in [5,6]. Therefore, here we point out only the basic assumptions used in the analysis of the SHE-synthesis reactions. According to the DNS-concept the complete fusion process proceeds in the following way. On the capture stage, after full dissipation of the collision kinetic energy, a dinuclear system is being formed (well known from deep inelastic transfer reactions). Complete fusion is an evolution process in which the nucleons of one nucleus sequentially are transferred to the second nucleus. The main characteristic of the DNS, determining its evolution, is the potential energy of the system $V(Z, L)$, which calculated according to the equation:

$$V(Z,L) = B_1 + B_2 + V(R^*, L) - [B_{\mathrm{CN}} + V_{\mathrm{rot}}^{\mathrm{CN}}(R^*, L)], \tag{1}$$

where B_1, B_2 and B_{CN} are the nuclear binding energies of the DNS nuclei and the compound nucleus, and Z is the atomic number of one of the nuclei in the DNS, L is the spin of the system. The value of $V(Z, L)$ was normalized to the energy of rotating compound nucleus by $B_{\mathrm{CN}} + V_{\mathrm{rot}}^{\mathrm{CN}}(R^*, L)$. The nucleus–nucleus potential $V(R, L)$ incorporates the nuclear, Coulomb and centrifugal potentials:

$$V(R,L) = V_n(R) + V_c(R) + V_{\mathrm{rot}}(R, L), \tag{2}$$

where R is the distance between the centers of the nuclei in the DNS.

In calculating $V(R, L)$, the DNS was assumed to have the shape of two slightly overlapping nuclei. R^* is the value of R, at which the DNS is to be found at the bottom of the 'pocket' in the potential $V(R, L)$. The nuclear potential $V_n(R)$ was calculated using the double folding method (see details in ref. [7]). The centrifugal potential was calculated for the case of the rigid rotor moment of inertia.

2.2 Peculiarities in the complete fusion of two massive nuclei within the DNS concept

Figure 1 presents the potential energy of the DNS, curve $V(Z, L = 0)$ exhibits two minima: the first one $Z = 0$ corresponding to complete fusion and the second one $Z = Z_{\mathrm{CN}}/2 = (Z_p + Z_t)/2$ corresponding to the formation of a symmetric DNS. During the evolution DNS can decay into two nuclei. viz. quasi-fission takes place.

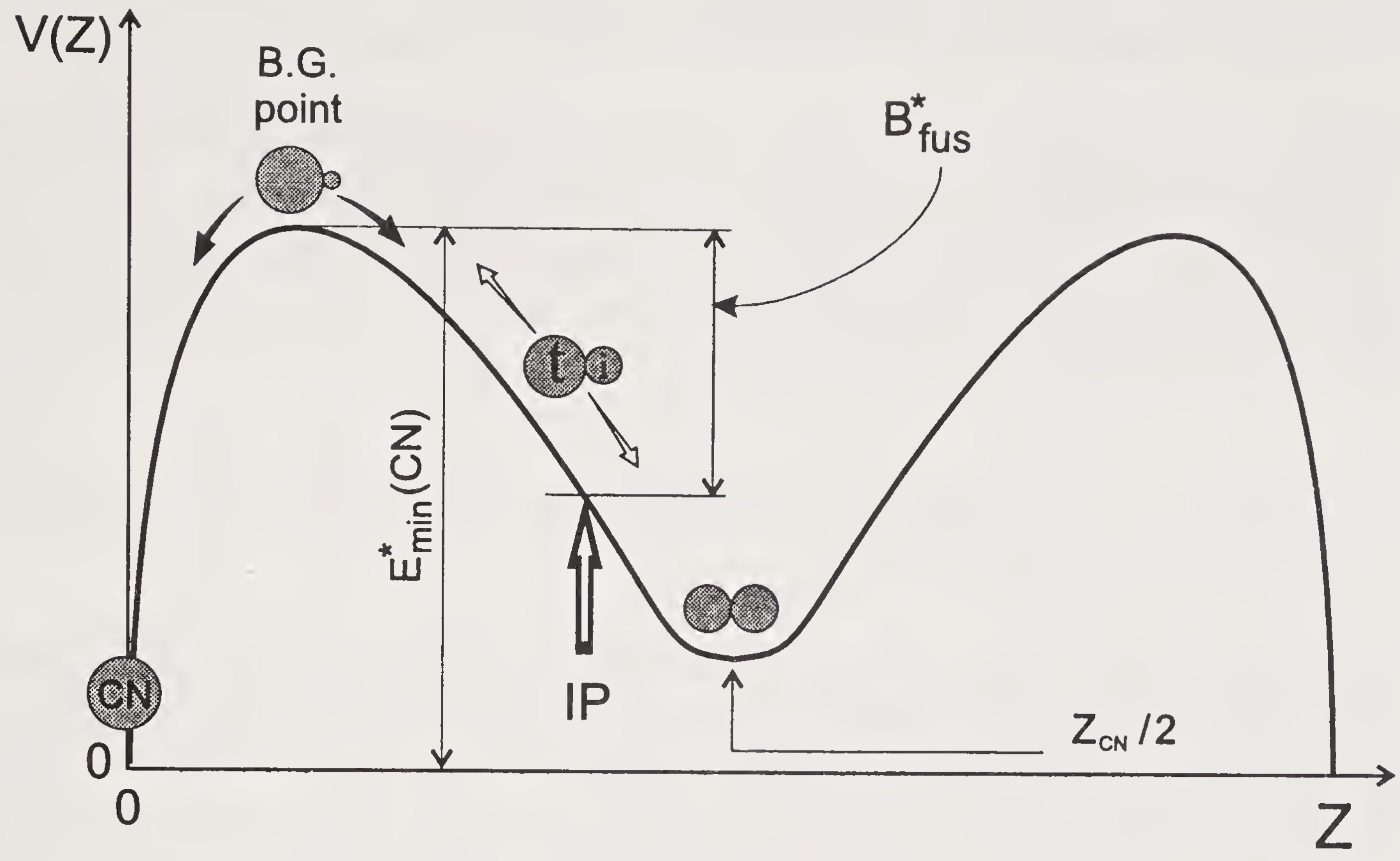

Figure 1. Schematic illustration of driving potential as a function of atomic number of the DNS nuclei. The possible moving of DNS and reaction input point are indicated with arrows.

The synthesis of super heavy elements (SHE) is usually performed at projectile energies leading to excitation energies of the compound nucleus as low as possible. This ensures higher survival probability of the compound nucleus during its deexcitation. As can be seen from figure 1, the main 'heating' of the compound nucleus takes place during the descent of the DNS from the BG point. It is at this evolution stage that the greater part of the system's potential energy is transformed into thermal excitation. However, whether the DNS will reach the state of a compound nucleus or will undergo quasi-fission is determined already when approaching the BG point. At the same time, exactly at this evolution stage the DNS excitation energy is lowest. Thus, one can say that during the most important step to complete fusion, the DNS is in a cold state. This peculiarity in the evolution of the DNS in SHE-synthesis reactions required using real masses in calculating the potential energy $V(Z, L)$ in eq. (1). The deformation of the DNS nuclei formed during its evolution to the compound nucleus was taken into consideration. The deformation of the heavy nucleus was taken in the ground state, the deformation of the light nucleus – in the 2^+ state.

If the injection point of the reaction is situated to the right of the maximum in $V(Z, L = 0)$ (the Businaro–Gallone (BG) point), the initial DNS may follow either of the two possible evolution paths: to a larger or smaller charge asymmetry. On the contrary, on the way to the compound nucleus the DNS has to overcome the potential barrier, B^*_{fus}, which is equal to the difference in $V(Z, L)$ at the BG point and at the injection point of the reaction. The appearance of the inner fusion barrier B^*_{fus} [6] is due to the endothermic character of the process of nucleon rearrangement in the massive DNS, which leads the system in the direction of the compound nucleus. The energy necessary for this rearrangement is supplied from the DNS excitation energy E. The formation of the compound nucleus is not possible, if the DNS excitation energy is less than the value of B^*_{fus}.

2.3 Optimal energy for synthesis of SHE

Figure 2 demonstrates excitation energies at maximum of experimental and theoretical excitation functions of compound nuclei of elements with charge numbers Z from 102–114 produced in cold fusion (HI,1n) reactions. The curve indicates the value $E^*_{\min(\mathrm{CN})}$ calculated on the Bass barrier [9]. From figure 2 one can see that our calculated values of E^*_{1n} are close to the experimental data.

2.4 The role of quasi-fission in the reactions of synthesis of SHE: Competition between complete fusion and quasi-fission

Another important characteristic of the fusion of massive nuclei, which manifests itself only in the DNS-concept, is the competition between complete fusion and quasi-fission. Due to the statistical character of the exchange of nucleons between the DNS nuclei, a certain probability exists that either the system reaches and overcomes the BG point, which leads to the formation of a compound nucleus, or the dinuclear system decay into two nuclei (undergoes quasi-fission). The more symmetric the reaction, the higher the inner fusion barrier B^*_{fus} which has to be overcome by the DNS on its way to the compound nucleus and, also, the stronger is the quasi-fission channel.

In most known models of the complete fusion of nuclei, the formation cross section of compound nuclei σ_{fus} is not different from the capture cross section σ_{c}. In our approach the fusion cross section σ_{fus} is a part of the capture cross section σ_{c}

$$\sigma_{\mathrm{fus}} = \sigma_{\mathrm{c}} \cdot P_{\mathrm{CN}} = \pi \lambda_0^2 \sum_{l=0}^{l_{\mathrm{cr}}} (2l+1) T(l, E_{\mathrm{cm}}) \cdot P_{\mathrm{CN}}. \tag{3}$$

Here λ_0 is the de Broglie wavelength of the relative motion of interacting nuclei, E_{cm} is the bombarding energy in the center-of-mass system, $T(l, E_{\mathrm{cm}})$ is the penetration coefficient of the lth partial wave through the potential barrier. $T(l, E_{\mathrm{cm}})$ is approximated by the

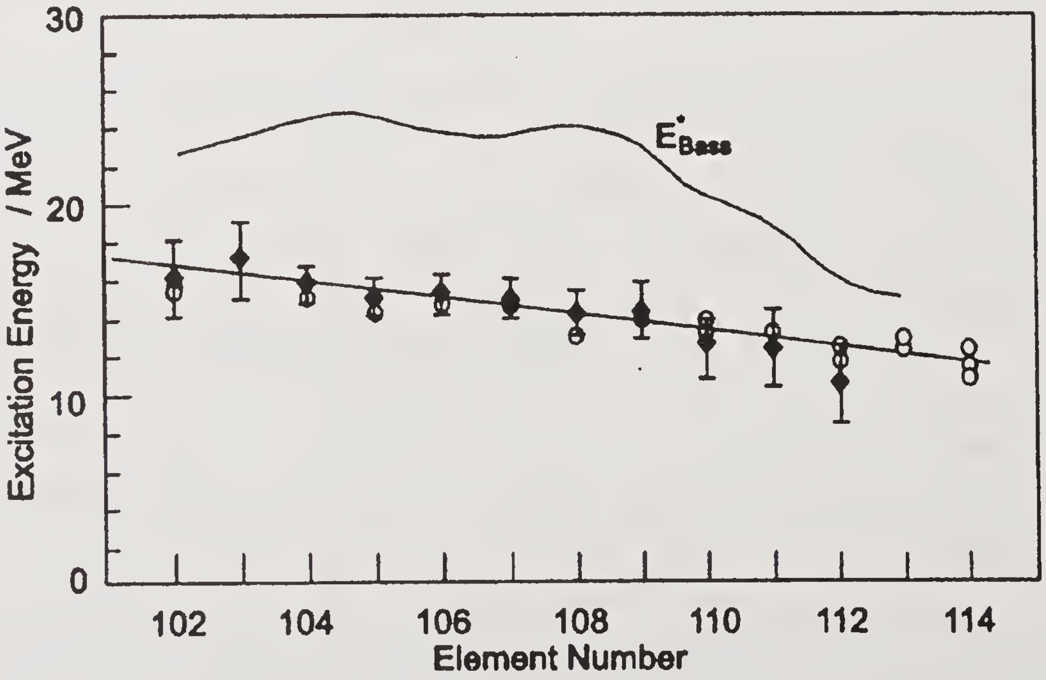

Figure 2. Excitation energies at the maximum of the excitation functions of (HI,1n) reactions leading to nuclei with Z = 102–114, ○ – theoretical (see table 1) and ● – experimental data [8].

Table 1. Results of our calculations for cold fusion reactions. The references on experimental values for reactions with $Z_{\mathrm{CN}} = 104$–112 (see in Review [2] and references therein).

Reactions	E^*_{th} MeV	E^*_{exp} MeV	P_{CN}	$\sigma^{\mathrm{th}}_{1n}$ mb	$\sigma^{\mathrm{exp}}_{1n}$ mb	Ref.
$^{48}\mathrm{Ca}+^{208}\mathrm{Pb} = {}^{256}102$	15.6	16.0	$2.9 \cdot 10^{-1}$	$5.8 \cdot 10^{-4}$	$(1.3^{+0.4}_{-0.4})10^{-4}$	[20]
$^{48}\mathrm{Ca}+^{206}\mathrm{Pb} = {}^{254}102$	16.1	24.0	$3.3 \cdot 10^{-1}$	$1.9 \cdot 10^{-4}$	$(6.0^{+1.6}_{-1.6})10^{-5}$	[21]
$^{50}\mathrm{Ti}+^{208}\mathrm{Pb} = {}^{258}104$	15.2	15.0	$7.7 \cdot 10^{-2}$	$2.8 \cdot 10^{-5}$	$(1.0^{+0.13}_{-0.13})10^{-5}$	[2]
$^{50}\mathrm{Ti}+^{209}\mathrm{Bi} = {}^{259}105$	14.7	15.0	$7.9 \cdot 10^{-3}$	$2.1 \cdot 10^{-6}$	$(4.5^{+0.9}_{-0.9})10^{-6}$	[2]
$^{54}\mathrm{Cr}+^{208}\mathrm{Pb} = {}^{262}106$	14.5	15.0	$5.5 \cdot 10^{-4}$	$3.4 \cdot 10^{-7}$	$(5.0^{+1.4}_{-1.4})10^{-7}$	[2]
$^{54}\mathrm{Cr}+^{209}\mathrm{Bi} = {}^{263}107$	14.4		$3.2 \cdot 10^{-4}$	$1.6 \cdot 10^{-7}$	$(2.0^{+1.3}_{-1.2})10^{-7}$	[2]
$^{58}\mathrm{Fe}+^{208}\mathrm{Pb} = {}^{266}108$	12.9	14.0	$8.8 \cdot 10^{-5}$	$1.3 \cdot 10^{-7}$	$(6.7^{+0.75}_{-0.75})10^{-8}$	[2]
$^{58}\mathrm{Fe}+^{209}\mathrm{Bi} = {}^{267}109$	14.0	14.0	$2.9 \cdot 10^{-5}$	$1.8 \cdot 10^{-8}$	$(7.5^{+5.0}_{-3.5})10^{-9}$	[2]
$^{62}\mathrm{Ni}+^{208}\mathrm{Pb} = {}^{270}110$	13.9	13.8	$7.7 \cdot 10^{-6}$	$5.5 \cdot 10^{-9}$	$(3.5^{+2.7}_{-1.8})10^{-9}$	[2]
$^{64}\mathrm{Ni}+^{208}\mathrm{Pb} = {}^{272}110$	13.1	12.2	$2.5 \cdot 10^{-5}$	$2.4 \cdot 10^{-8}$	$(1.5^{+0.9}_{-0.6})10^{-8}$	[2]
$^{64}\mathrm{Ni}+^{209}\mathrm{Bi} = {}^{273}111$	13.2	13.5	$1.4 \cdot 10^{-5}$	$1.2 \cdot 10^{-8}$	$(3.5^{+4.6}_{-2.3})10^{-9}$	[2]
$^{70}\mathrm{Zn}+^{208}\mathrm{Pb} = {}^{278}112$	11.8	10.0	$7.3 \cdot 10^{-6}$	$1.4 \cdot 10^{-9}$	$(1.0^{+1.3}_{-0.7})10^{-9}$	[2]
$^{68}\mathrm{Zn}+^{208}\mathrm{Pb} = {}^{276}112$	12.3	10–12	$1.4 \cdot 10^{-5}$	$2.2 \cdot 10^{-9}$	$< 1.3 \cdot 10^{-9}$	[2]
$^{70}\mathrm{Zn}+^{209}\mathrm{Bi} = {}^{279}113$	12.7	10–12	$1.3 \cdot 10^{-6}$	$6.4 \cdot 10^{-10}$	$< 6.0 \cdot 10^{-10}$	[22]
$^{68}\mathrm{Zn}+^{209}\mathrm{Bi} = {}^{277}113$	12.8		$2.6 \cdot 10^{-6}$	$1.1 \cdot 10^{-9}$		
$^{76}\mathrm{Ge}+^{208}\mathrm{Pb} = {}^{284}114$	10.8		$3.3 \cdot 10^{-8}$	$1.2 \cdot 10^{-10}$		
$^{74}\mathrm{Ge}+^{208}\mathrm{Pb} = {}^{282}114$	10.8		$1.1 \cdot 10^{-7}$	$1.2 \cdot 10^{-10}$		
$^{72}\mathrm{Ge}+^{208}\mathrm{Pb} = {}^{280}114$	11.6		$3.5 \cdot 10^{-7}$	$9.5 \cdot 10^{-11}$		
$^{70}\mathrm{Ge}+^{208}\mathrm{Pb} = {}^{278}114$	12.4		$3.8 \cdot 10^{-7}$	$1.9 \cdot 10^{-11}$		

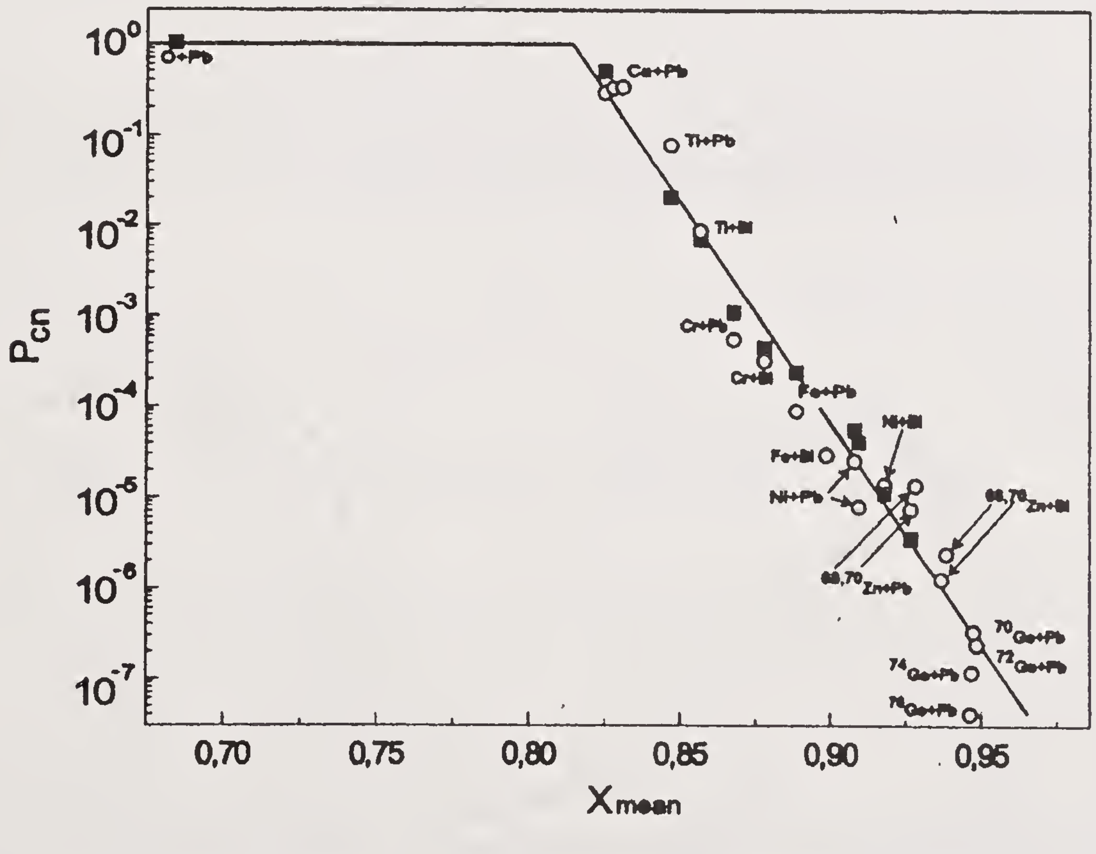

Figure 3. Probability of compound nucleus formation for different reactions as a function of the fissility parameter x_{mean}. Solid squares (■) represent the P_{CN} values extracted from experimental data [12], open circles (○) represent our calculations based on the model describing the competition between complete fusion and quasi-fission [6].

penetration factor of a parabolic barrier. P_{CN} is the probability of forming a compound nucleus in competition with quasi-fission [6]. In figure 3 are shown the values of P_{CN}, calculated for different reactions with ^{208}Pb and ^{209}Bi targets.

The ratio of repulsive Coulomb forces and the attractive nuclear forces governs the moving of two nuclei into one. For a monosystem this ratio is given by the fissility parameter x. For two touching sphere configuration, taking into account that the proton and neutron ratio between the two partners is equilibrated very quickly ($\approx 10^{-22}$ sec), a modified parameter x_{mean} describing the ratio of Coulomb and nuclear forces has been defined according to [13] and [14].

2.5 Capture cross section

The capture cross section σ_{c} makes up a part of the total inelastic cross section

$$\sigma_{\mathrm{c}}/\sigma_R = \frac{\sum_{l=0}^{l_{kr}}(2l+1)T(l,E)}{\sum_{l=0}^{\infty}(2l+1)T(l,E)}. \tag{4}$$

The l_{kr} is the critical angular moment, at which the capture of a heavy ion occurs and an excited DNS is formed. The value of l_{kr} was taken from empirical systematics of the ratio $\sigma_{\mathrm{c}}/\sigma_R$ [10]. In the figure 4 one can see the experimental data and our calculations σ_{c} for two type of reactions: with a ^{208}Pb target (left) and a ^{238}U target (right). The rather good agreement between the calculations and the experimental data is obvious.

2.6 Survival probability

The production cross section for evaporation residues with emission of x neutrons from heavy compound nuclei can be written in the following form as

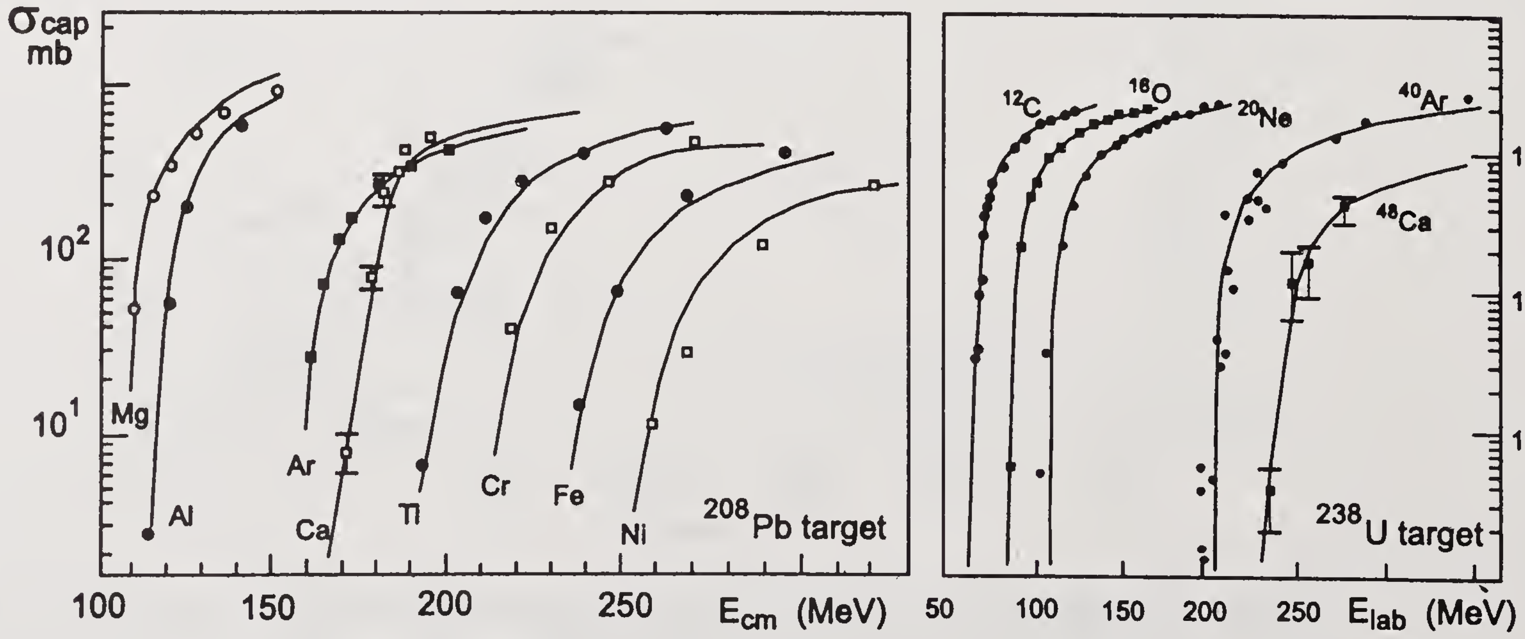

Figure 4. Capture cross sections for two targets Pb (left) and U (right) as a function of bombardment energy and different heavy ions. Points are experimental data, curves are result of calculations.

$$\sigma_{xn}(E^*) \approx \sigma_{\text{fus}} \cdot P_{xn}(E^*) \cdot W_{\text{sur}}(E^*), \tag{5}$$

where σ_{fus} is the compound nucleus formation cross section; E^* the excitation energy of compound nucleus; P_{xn} is the probability of evaporation of exactly x neutrons from the excited compound nuclei [11]; W_{sur} is the probability of survival of the heavy ($\Gamma_n/\Gamma_{\text{tot}} \approx \Gamma_n/\Gamma_f$) compound nucleus during its deexcitation

$$W_{\text{sur}}(E^*) = \prod_{k=1}^{x} \left(\frac{\Gamma_n(E_k^*)}{\Gamma_f(E_k^*)}\right)_k, \tag{6}$$

where x is the number of evaporated neutrons, k the index of the evaporation step. For the partial widths of neutron emission and fission the following expressions have been used [9]:

$$\Gamma_n(E^*, L) \approx \frac{(2s+\mu)}{(\pi\hbar)^2 \rho_m(U)} \int_0^{U-B_n} \sigma_{\text{inv}}(E_n)\rho_d(U - B_n - E_n)E_n \mathrm{d}E_n, \tag{7}$$

$$\Gamma_f(E^*, L) \approx (2\pi\rho_m(U))^{-1} \int_0^{U_s-B_f} \rho_s(U_s - B_f - \varepsilon)\mathrm{d}\varepsilon, \tag{8}$$

where U is the thermal energy of the mother nucleus, s the spin of the emitted particle and μ is the reduced mass of the system (particle neutron plus daughter nucleus). The symbols m and d indicate the mother and the daughter nuclei, respectively. The inverse cross section σ_{inv} is calculated within the model described in [10]..

In expression (8) the thermal energy U_s and the rotational energy E_r^s are connected at the saddle point by the relation $U_s = E^* - E_r^s$. This form of the width Γ_f takes into account the change of the fission barrier of the rotating nucleus so far as $B_f(I) = B_f(0) - (E_r - E_r^s)$ (see details in [15]).

To describe the level density as a function of the excitation energy, the well known Fermi-gas expression (see, for example, book [16])

$$\rho(E^*) = \frac{\sqrt{\pi}}{12} \frac{1}{a^{1/4}(E^* - \delta)^{5/4}} \exp[S(E^*)] \tag{9}$$

has been used. In (9) the dependence of the nucleus entropy S on the excitation energy E^* is determined by the relation: $S = 2at$, using the connection of the temperature with the excitation energy of the nucleus $E^* = at^2$, here δ is correction accounting for even-odd effects [18]. The parameter of the level density $a = \pi^2 g_0/6$ is expressed through the density of single particle states near the Fermi energy $g_0 = f(E_f) =$ constant. The decrease of the influence of shell effects on the level density with increasing excitation energy is taken into account by the phenomenological expression [16]:

$$a(E^*) = \tilde{a}[1 + f(E^*)\Delta W/E^*]. \tag{10}$$

Here $f(E^*) = 1 - \exp(-\gamma E^*)$, ΔW is the shell correction in the nuclear mass formula, $\tilde{a} = A(\alpha + \beta A)$ is the Fermi-gas value of the level density parameter, A is the mass

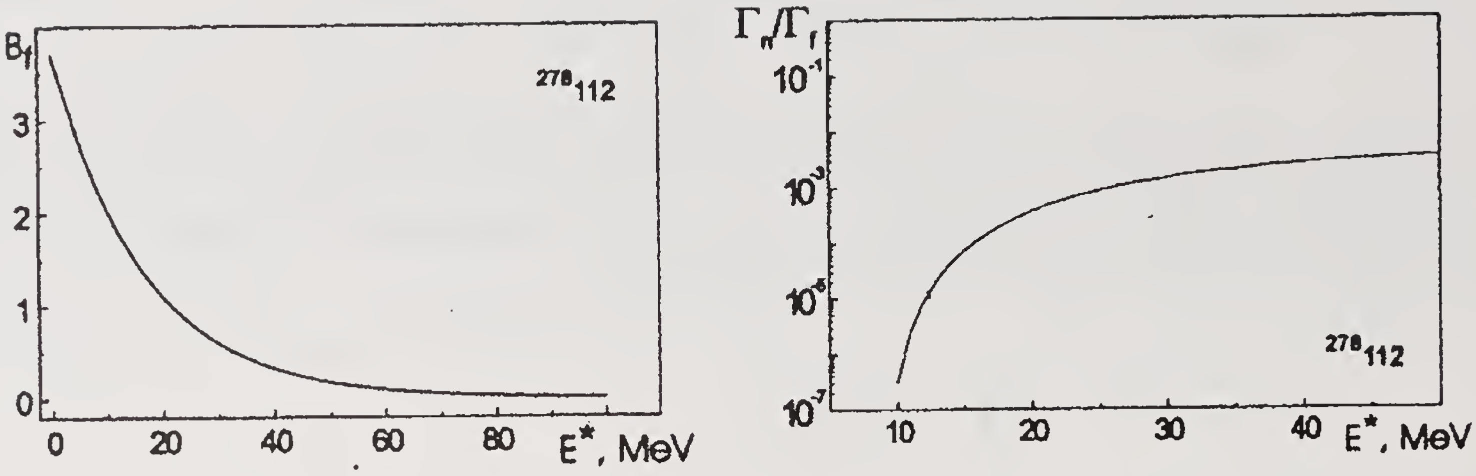

Figure 5. Fission barrier and Γ_n/Γ_f values for element 112 as a function of excitation energy.

number of nucleus. The empirical values of the parameters $\alpha = 0.134$ MeV^{-1}, $\beta = -1.21 \cdot 10^{-4}$ MeV^{-1}, $\gamma = 0.061$ MeV $^{-1}$ have been obtained in ref. [18] from the analysis of the data on the level density taking into account the contribution of the collective states to the total level density.

The fission barrier B_f is a sum of liquid drop $B_f^{\rm LD}$ and shell correction ΔW parts $B_f = B_f^{\rm LD} + \Delta W$. To calculate $W_{\rm sur}$, we need the fission barrier of compound nuclei. For transfermium region of compound nuclei the $B_f^{\rm LD}$ is very small. To include effect of washing of shell corrections we used the next equation $B_f(E^*) = \Delta W \cdot \exp(-\gamma E^*)$. For our calculation we used the value of $B_f(E^* = 0) = B_f^{\rm stat}$ from ref. [17].

In figure 5 one can see that the dependence of the fission barrier and ratio Γ_n/Γ_f on E^* in region of maximum of excitation functions for (HI,1n) reactions (10 – 20 MeV) is very strong.

3. The analysis of reactions used for the synthesis of the transfermium and superheavy elements

3.1 *Reactions of cold fusion*

The 'cold' method of synthesis of heavy elements where evaporation of one neutron has higher probability, named 'cold fusion' (was proposed in Dubna by Oganessian [19]), was successfully used to produce new transfermium elements up to $Z = 112$.

One can see from figure 6 that our approach allows rather good description of the experimental data on cold fusion (HI,1n) reactions.

3.2 *Hot fusion reactions*

As one can see from figure 6, that σ_{1n} of reactions which leads to synthesis of the superheavy element with magic number $Z = 114$ with Pb target is less than 1 pb.

Therefore we analysed another reaction ^{48}Ca + ^{244}Pu = ^{292}114, which was chosen for the synthesis of element 114 in FLNR (Dubna) (see, for example, ref. [23]). There are experimental data in which a ^{48}Ca-beam was used to bombard targets of Pb, Th, U. For the

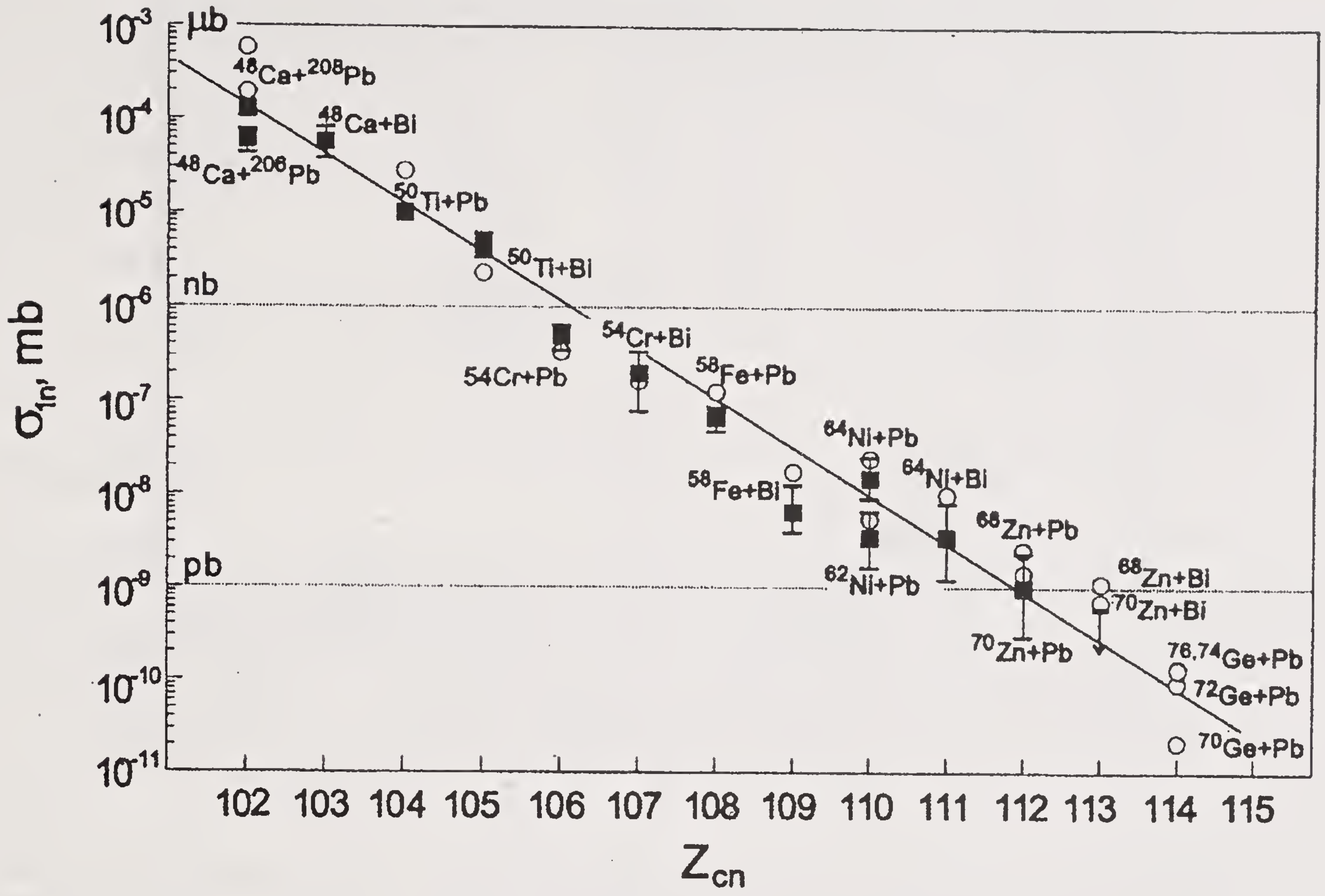

Figure 6. Experimental data (black squares) and theoretical calculations (open circles) for synthesis of elements from 102 to 114 in cold fusion reactions (HI,$1n$), the combinations are noted in the figure. The line has been drawn to guide the eyes. The references on experimental data σ_{1n} are given in table 1.

reaction ^{48}Ca + ^{208}Pb = ^{256}102 measurements of the excitation functions for the evaporation of 1, 2, 3, 4 neutrons, as well as the fusion–fission cross section [20], which for heavy compound nuclei coincides with the fusion cross section, have been measured. Therefore it seemed very interesting to analyse these reactions in the framework of the DNS concept.

In figure 7 one can see calculations based on the DNS-concept for two reactions. For the ^{48}Ca + ^{208}Pb = ^{256}102 reaction (left panel) our calculation rather well describes the experimental data for evaporation residue cross sections. For the ^{48}Ca + ^{232}Th = ^{280}110 reaction (right panel), for which only σ_{3n} has been measured, our calculation is not in disagreement with the experimental point.

As one can see from figure 8 our calculations for the ^{48}Ca + ^{238}U = ^{286}112 reaction agree with the experimental values. The right panel of figure 8 shows our estimations for the cross sections for the ^{48}Ca + ^{244}Pu = ^{292}114 reaction.

Comparing our estimations (see figure 6) for the ^{76,74,72,70}Ge + ^{208}Pb = ^{284,282,270,278}114 reaction with these for the reaction ^{48}Ca + ^{244}Pu = ^{292}114 (see figure 8), it follows that the latter one is more preferable.

There exist also other estimations of cross section for the combination ^{48}Ca + ^{244}Pu = ^{292}114 (see table 2). One can see that our estimation is in rather good agreement with value of cross sections from ref. [4].

Now in the FLNR an experiment is running to produce the isotope of element 114, in the reaction ^{48}Ca + ^{244}Pu = ^{292}114. This experiment is very important, since it would give a possibility to reach the island of stability, about which physicists of the whole world dream for more than 30 years.

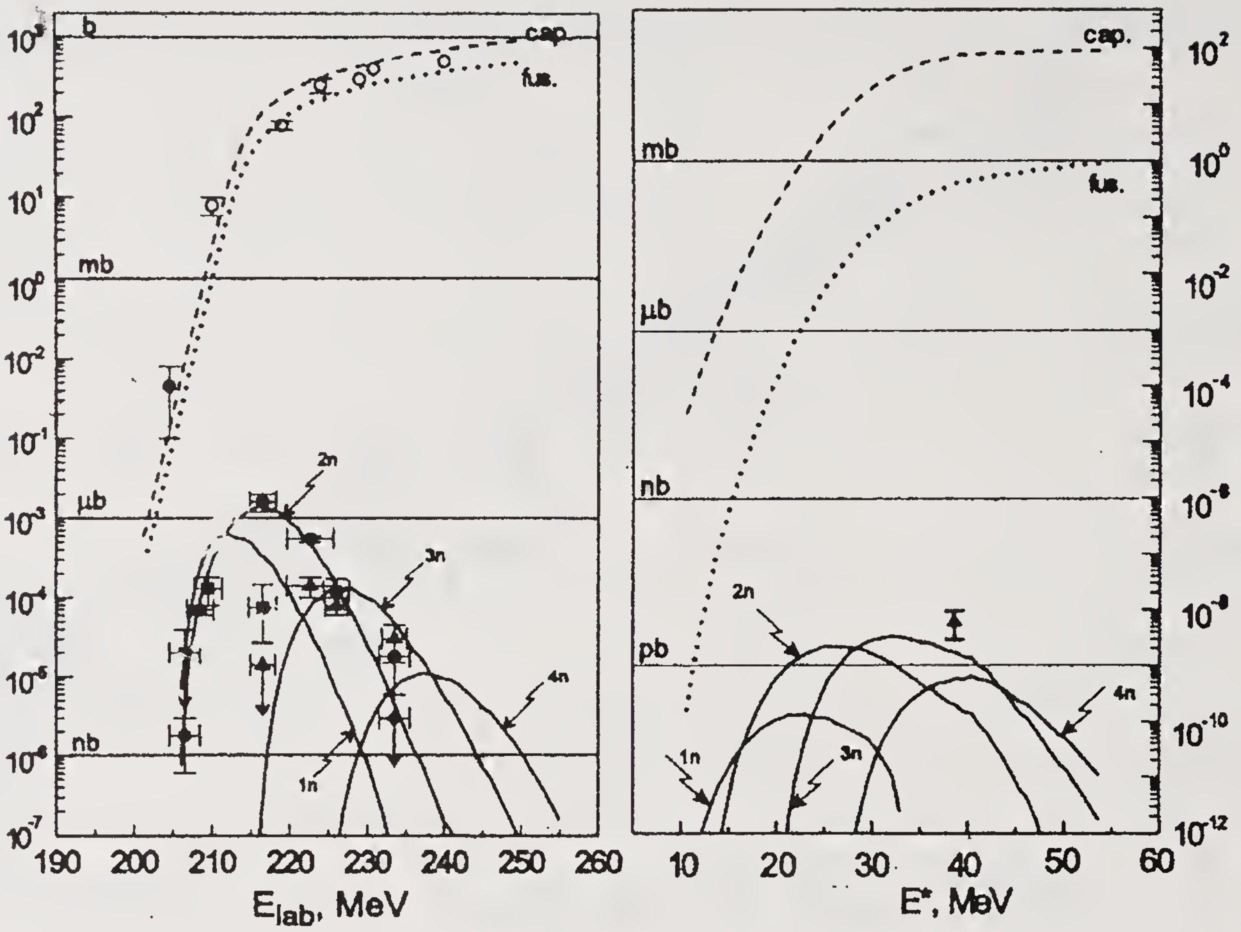

Figure 7. Results for the two reactions ^{48}Ca + ^{208}Pb = ^{256}102 (left) and ^{48}Ca + ^{232}Th = ^{280}110 (right). (○) denote the experimental values of fusion–fission cross sections [20], solid points (●) experimental values of σ_{xn} [20], the experimental value σ_{3n} for the right reaction was taken from ref. [24], curves are the result of our estimations: dashed curves are calculations for σ_c, dotted curves are for σ_{fus}, and solid curves are for σ_{xn}.

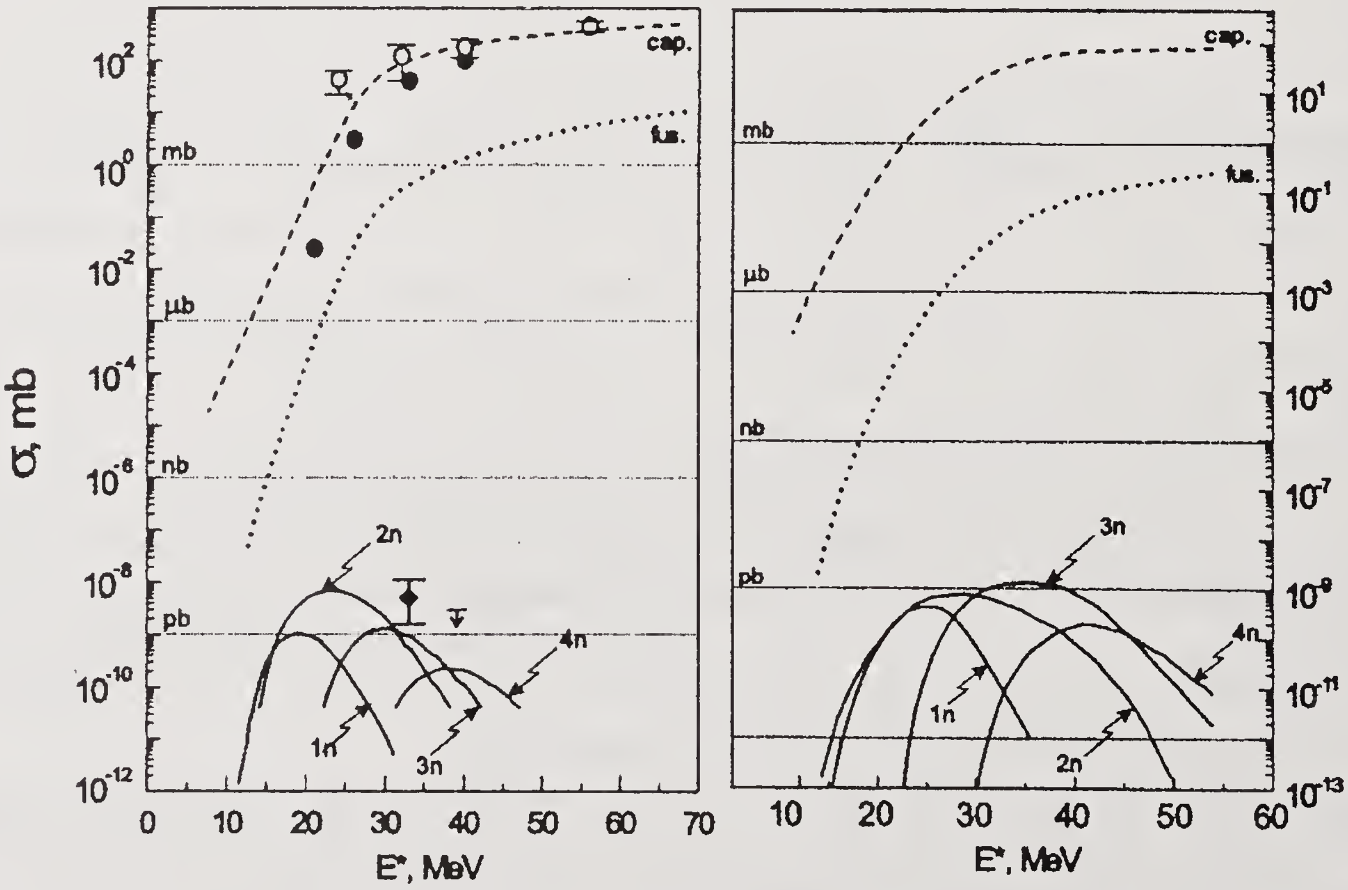

Figure 8. Cross sections for the reactions ^{48}Ca + ^{238}U (left) and ^{48}Ca + ^{244}Pu (right) leading to compound nuclei with $Z = 112$ and $Z = 114$, respectively. On the left, open and solid circles are capture cross sections from refs [25] and [26] correspondingly. Experimental data for σ_{xn} was taken from [27]. Different curves are theoretical calculations (explanation see in the caption of figure 7).

Table 2. Results of different estimations (maximal quantities) for cross section values for ^{48}Ca + ^{244}Pu = $^{292-xn}114$ reaction.

Channel	E^*	Value	Ref.
σ_{3n}	35 MeV	3.5 pb	[4]
σ_{3n}	26 MeV	100 pb	[28]
$\sigma_{\rm ER}$	37 MeV	10 pb	[29]
σ_{3n}	32 MeV	20 pb	[23]
σ_{3n}	35 MeV	1.5 pb	Present work

4. Conclusions

The DNS concept was used in the analysis of existing experimental data on reactions leading to the synthesis of elements 102 and 112. The attempt to synthesize element 114 was also analysed. The method applied in this article describes well a wide set of experimental data on reactions of cold synthesis (reactions with evaporation of one neutron (HI,1n)) concerning the maxima of the excitation functions (figure 2), and their absolute values (figure 6). The DNS concept allows to carry out calculations of the inner fusion barrier $B^*_{\rm fus}$ for synthesis reactions, which in turn gives an estimation of the threshold ΔE for complete fusion. The DNS concept allows to estimate competition between complete fusion and dominant quasi-fission in SHE synthesis reactions, which gives the probability $P_{\rm cn}$ of forming a compound nucleus after capture. In 'cold' fusion reactions, the quasi-fission is the main factor determining the decrease of SHE-production cross sections when increasing the atomic number of the synthesized SHE. It was shown that the reaction ^{48}Ca + ^{244}Pu = $^{292}114$ for the synthesis of element 114, suggested in FLNR [23], is more preferable compared with the reaction of a Ge-beam on a Pb-target.

Acknowledgements

The author thanks Professors Yu Ts Oganessian and M G Itkis for support and constant attention to the given work and Prof. A Sobiczewski and Drs A V Antonenko, A K Nasirov and R Kalpakchieva for useful discussions and interest. I am indebted to Prof. V V Volkov and Dr G G Adamian, for help, fruitful discussions, valuable remarks and useful suggestions during the whole period of preparing of this article. I express my special gratitude to Dr B I Pustylnik for the long-term cooperation and fruitful discussions on the mechanism of interaction of heavy nuclei and decay of the excited compound nucleus.

References

[1] W J Swiatecki, *Phys. Scr.* **24**, 113 (1981)
S Bjornholm and W J Swiatecki, *Nucl. Phys.* **A391**, 471 (1982)
[2] S Hofmann, *Rep. Prog. Phys.* **61**, 639–689 (1998)
[3] Y Abe, Y Aritomo, T Wada and M Ohta, *J. Phys. Nucl. Part. Phys.* **23**(**10**), 1275–1284 (1997)
[4] B I Pustylnik, *VI Int. School-Seminar Heavy Ion Physics, 22–27 September* (Dubna, Russia, Word Scientific), pp. 431–433

[5] V V Volkov, *Izvestiya AN USSR ser. fiz.* **50**, 1879 (1986)

[6] A V Antonenko, E A Cherepanov, A K Nasirov, V P Permjakov and V V Volkov, *Phys. Lett.* **B319**, 425 (1993); *Phys. Rev.* **C51**, 2635 (1995)
G G Adamian, N V Antonenko, W Scheid and V V Volkov, *Nucl. Phys.* **A627**, 361–378 (1997)

[7] G G Adamian, N V Antonenko, R V Jolos, S P Ivanova and O I Melnikova, *Int. J. Mod. Phys.* **E5**, 191–216 (1996)

[8] A G Popeko, *Proc. 174 WE-Heraeus-Seminar 'New Ideas on Clustering in Nuc. and Atomic Phys.', Rauischholzhausen, Germany*, June 9-13, 1997, p. 1137–1142

[9] R Bass, *Nuclear Reactions with Heavy Ions* (Springer, New York, 1980)

[10] E A Cherepanov, *Proc. Int. Symp. on In Beam Nuclear Spectroscopy* (Debrecen, Hungary, May 14–18, 1984) p. 499–506

[11] T Sikkeland, *Phys. Rev.* **169**, 1232 (1968)

[12] P Armbruster, GSI–Preprint–98–96, 1998

[13] H Gaggeler, T Sikkeland, G Wirth, W Bruchle, W Bogl, G Franz, G Herrmann, J V Kratz, M Schaedel, K Summerer and W Weber, *Z. Phys.* **A316**, 291 (1984)

[14] K-H Schmidt and W Morawek, *Rep. Prog. Phys.* **54**, 949–1003 (1991)

[15] M Blann and F Plasil, *Phys. Rev. Lett.* **29**, 303 (1972)

[16] A V Ignatyuk, *Statistical properties of excited nuclei* (Energoizdat, Moskva, 1983)

[17] R Smolanczuk, J Skalski and A Sobiczewski, *Phys. Rev.* **C52**, 1871 (1995)

[18] E A Cherepanov and A S Iljinov, *Nucleonika* **25**, 611–621 (1980)

[19] Yu Ts Oganessian, *Lecture Notes in Phys.* (Springer, Heidelberg, 1975) vol. 33, p. 221

[20] A V Yeremin, V I Chepigin, M G Itkis, A P Kabachenko, S P Korotkov, O N Malyshev, Yu Ts Oganessian, A G Popeko, J Ronac, R N Sagaidak, M L Chelnokov, V A Gorshkov and A Yu Lavrentev, *Rapid Comm. JINR* **6**, (92)-98

[21] Yu Ts Oganessian, V K Utyonkov, Yu V Lobanov, F S Abdulin, A N Polyakov, I V Shirokovsky, Yu S Tsyganov, S Iliev, V G Subbotin, A M Sukhov, G V Buklanov, A N Mezencev, O V Ivanov, K Subotik, R W Lougheed, K J Moody, M A Stoyer, M J Stoyer and J F Wild, *Proc VI Int Conf. on Dynamical Aspects on Nuclear Fission* (Slovak Repablic, Casta-Paperchichka, October 19–23, 1998)

[22] F P Hessberger, S Hofmann, V Ninov, P Armbruster, H Folger, A Lavrentev, M E Leino, G Muenzenberg, A G Popeko, S Saro and A N Yeremin, *Proc. VI Int. Conf. on Dynamical Aspects on Nuclear Fission* (Slovak Repablic, Casta-Paperchichka, October 19–23, 1998)

[23] Yu Ts Oganessian, *Proc. Int. Conf. Structure of Vacuum and Elementary Matter* (Wilderness, South Africa, March 10–16, 1996) p. 11–24

[24] Yu Ts Oganessian and A V Yeremin, *Proc. VI Int. Conf. on Dynamical Aspects on Nuclear Fission* (Slovak Repablic, Casta-Paperchichka, October 19–23, 1998)

[25] M G Itkis, Yu Ts Oganessian, E M Kozulin, N A Kondratiev, L Krupa, I V Pokrovsky, A N Polyakov, V A Ponamarenko, A Ya Rusanov and V I Vakatov, Submitted to *Nuovo Cimento.*

[26] W Q Shen, J Albinski, A Gobbim, S Gralla, K D Hildenbrand, N Herrmann, J Kuzminski, W F J Muller, H Stelzer and J Toke, *Phys. Rev.* **C36**, 115–142 (1987)

[27] Yu Ts Oganessian, A V Yeremin, G G Gulbekian, S L Bogomolov, V I Chepigin, B N Gikal, V A Gorshkov, M G Itkis, A P Kabachenko, V B Kutner, A Yu Lavrentev, O N Malyshev, A G Popeko, J Rohas, R N Sagaidak, S Hofmann, G Muenzenberg, M Veselsky, S Saro, N Iwasa and K Morita, preprint JINR E7-98-212, 1998 (submitted to *Europian Phys. J.*)

[28] G Giardina, A D'Arrigo and R Sturiale, *Proc. VIII Int. Conf. on Nuclear Reactions Mechanisms* (Varenna, June 9–14, 1997) p. 435–443

[29] T Wada, Private communication

Proton radioactivity – spherical and deformed*

C N DAVIDS[a], P J WOODS[b], D SEWERYNIAK[a,c], A A SONZOGNI[a],
J C BATCHELDER[d], C R BINGHAM[e], T DAVINSON[b], D J HENDERSON[a],
R J IRVINE[b], G L POLI[f], J UUSITALO[a] and W B WALTERS[c]
[a]Argonne National Laboratory, Argonne, IL, USA
[b]University of Edinburgh, Edinburgh, UK
[c]University of Maryland, College Park, MD, USA
[d]UNIRIB, Oak Ridge Associated Universities, Oak Ridge, TN, USA
[e]University of Tennessee, Knoxville, TN, USA
[f]University of Milano, Milano, Italy

Abstract. The proton drip line defines one of the fundamental limits to nuclear stability. Nuclei lying beyond this line are energetically unbound to the emission of a constituent proton from their ground states.

For near-spherical nuclei in the region of the drip line between $Z = 69$ (Tm) and $Z = 81$ (Tl), proton decay transition rates have been shown to be well reproduced by WKB calculations using spectroscopic factors derived from a low-seniority shell model calculation [2]. Another approach using spectroscopic factors obtained from the independent quasiparticle approximation has also proved successful in this region [3]. These interpretations have allowed the extraction of nuclear structure information from nuclei well beyond the proton drip line.

The rare-earth proton emitters ^{141}Ho and ^{131}Eu have recently been observed [4], and their decay rates can only be explained by assuming large deformation for these nuclei. In addition to providing information on the wavefunctions and deformations of these nuclei, these results offer the opportunity to study the phenomenon of quantum mechanical tunneling through a deformed potential barrier.

Keywords. Proton drip line; proton radioactivity; spherical proton emitters; deformed proton emitters.

PACS Nos 23.50.+z; 21.10.Dr; 25.70.Gh

References

[1] P J Woods and C N Davids, *Ann. Rev. Nucl. Part. Sci.* **47**, 541 (1997)
[2] C N Davids *et al*, *Phys. Rev.* **C55**, 2255 (1997)
[3] S Åberg, P B Semmes and W Nazarewicz, *Phys. Rev.* **C56**, 1762 (1997)
[4] C N Davids *et al*, *Phys. Rev. Lett.* **80**, 1849 (1998)

---

*Work supported by the U.S. Department of Energy, Nuclear Physics Division, under contract W-31-109-ENG-38.

A rare nuclear decay process: The internal conversion between bound atomic states

J F CHEMIN[1], T CARREYRE[3], M AICHE[1], F ATTALLAH[1], G BOGAERT[1], J P GRANDIN[1], M HARSTON[1], W E MEYERHOF[2] and J N SCHEURER[4]
[1]Centre d'Etudes Nucleaires de Bordeaux-Gradignan, 33175 Gradignan, France
[2]Centre de Spectroscopie Nucleaire et de Spectroscopie de Masse, 91405 Orsay, France
[3]Department of Physics, Stanford University, Stanford, California 94305
[4]Grand Accelerateur National d'Ions Lourds, 14021 Caen, France

Abstract. We shall report on the recently observed dependence of the lifetime of the first excited state in ^{125}Te on the ionic charge state. Then we shall give an interpretation of the dependence of the half-life in terms of a new type of nuclear internal conversion without emission of the electron into the continuum of electron energies. We have named this process internal conversion between bound atomic states or BIC. The resonant character of the BIC will be established and the main parameters governing the decay process will be discussed [1–3].

Finally the results of a recent experiment performed at the GANIL accelerator attempting to measure directly the value of the internal conversion coefficient associated with BIC in ^{125}Te ions with charge states ranging between 44+ and 48+ will be given.

In conclusion we shall discuss the relation between the BIC and nuclear excitation by electron transition, NEET, in the excitation of some nuclear isomeric states.

Keywords. Nuclear decay; internal conversion.

PACS Nos 23.20.Nx; 21.10.Tg

References

[1] F Attallah *et al*, *Phys. Rev. Lett.* **75**, 1715 (1995)
[2] F F Karpeshin, M R Harston, F Attallah, J F Chemin, J N Scheurer, I M Band and M B Tvzhaskovaskaya, *Phys. Rev.* **C53**, 1640 (1996)
[3] F Attallah *et al*, *Phys. Rev.* **C55**, 1665 (1997)

Cubic potential models for cluster radioactivity

G SHANMUGAM
Department of Physics, Manonmaniam Sundaranar University, Tirunelveli 627 012, India

Abstract. Cluster radioactivity is a process by which nuclei equal and heavier than the α-particle is emitted spontaneously. The clusters usually emitted in this process are the α-particle, carbon, oxygen, neon, magnesium, silicon etc. When the mass of the cluster becomes comparable with the mass of the daughter, symmetric fission takes place. Thus the cluster radioactivity is an intermediate process between the well known α-decay and the spontaneous fission. In earlier years such cluster radioactivity was found mostly in actinide nuclei like radium, uranium etc. Very recently it has been predicted that such decays are possible in a new region around ^{114}Ba. There has been an exciting experimental detection of the emission of ^{12}C from ^{114}Ba leading to ^{102}Sn, which is attracting a lot of attention recently.

To study the phenomenon of cluster radioactivity there are various theoretical models in vogue. The existing models generally fall under two categories: the unified fission model (UFM) and the preformed cluster model (PCM). The physics of the UFM and the PCM are completely different. The UFM considers cluster radioactivity simply as a barrier penetration phenomenon in between the fission and the α-decay without worrying about the cluster being or not being preformed in the parent nucleus. In the PCM clusters are assumed to be preborn in a parent nucleus before they could penetrate the potential barrier with a given Q-value. The basic assumption of the UFM is that heavy clusters as well as the α-particle have equal probability of being preformed. In PCM, clusters of different sizes have different probabilities of their being preformed in the parent nucleus.

We have developed three fission models during the last decade using the cubic potential for the pre-scission region. The use of these models in the study of cluster radioactivity in both the actinide and barium regions will be discussed in this talk in comparison with the other existing theories.

Keywords. Cluster radioactivity; fission models.

PACS Nos 23.70.+j; 23.90.+w

Fission experiments with secondary beams

J BENLLIURE[a], S STEINHÄUSER[b], C BÖCKSTIEGEL[b], A GREWE[b], H-G CLERC[b], A HEINZ[a], M DE JONG[b], A R JUNGHANS[a], J MÜLLER[b], K-H SCHMIDT[a] and M PFÜTZNER[c]
[a]Gesellschaft für Schwerionenforschung m. b. H., Planckstrasse 1, 64291 Darmstadt, Germany
[b]Institut für Kernphysik, Technische Universität Darmstadt, Schlossgartenstrasse 9, 64289 Darmstadt, Germany
[c]Institute of Experimental Physics, University of Warsaw, Ul Hoza 69, 00-381 Warszawa, Poland

Abstract. Nuclear fission from excitation energies around 11 MeV was studied at GSI, Darmstadt for 76 neutron-deficient actinides and pre-actinides by use of relativistic secondary beams. The characteristics of multimodal fission of nuclei around ^{226}Th are systematically investigated and related to the influence of shell effects on the potential-energy and on the level density between saddle point and scission. A systematic view on the large number of elemental yields measured gave rise to a new interpretation of the enhanced production of even elements in nuclear fission and allowed for a new understanding of pair breaking in fission.

Keywords. Nuclear reactions; radioactive beams; nuclear fission; shell effects.

PACS Nos 24.75+i; 25.85.-w; 25.85.Jg; 27.90.+b

1. Introduction

Nuclear fission provides unique information on the reordering of nucleons in a large-scale collective motion. The signatures of shell structure and pairing correlations show up in fission from low excitation energies. They have general implications on the influence of shell structure on nuclear dynamics and on the viscosity of cold nuclear matter. The use of secondary beams gives access to a large new field of fissioning systems by overcoming restrictions of conventional experimental techniques. In this contribution, the large body of data acquired in a recent experiment is presented and the resulting progress in the understanding of the fission dynamics is sketched.

2. Experiment

The secondary-beam facility of GSI, Darmstadt offers unique possibilities to provide secondary beams of neutron-deficient actinides and pre-actinides produced by fragmentation of relativistic ^{238}U projectiles. Within the limits given by the primary-beam intensity and

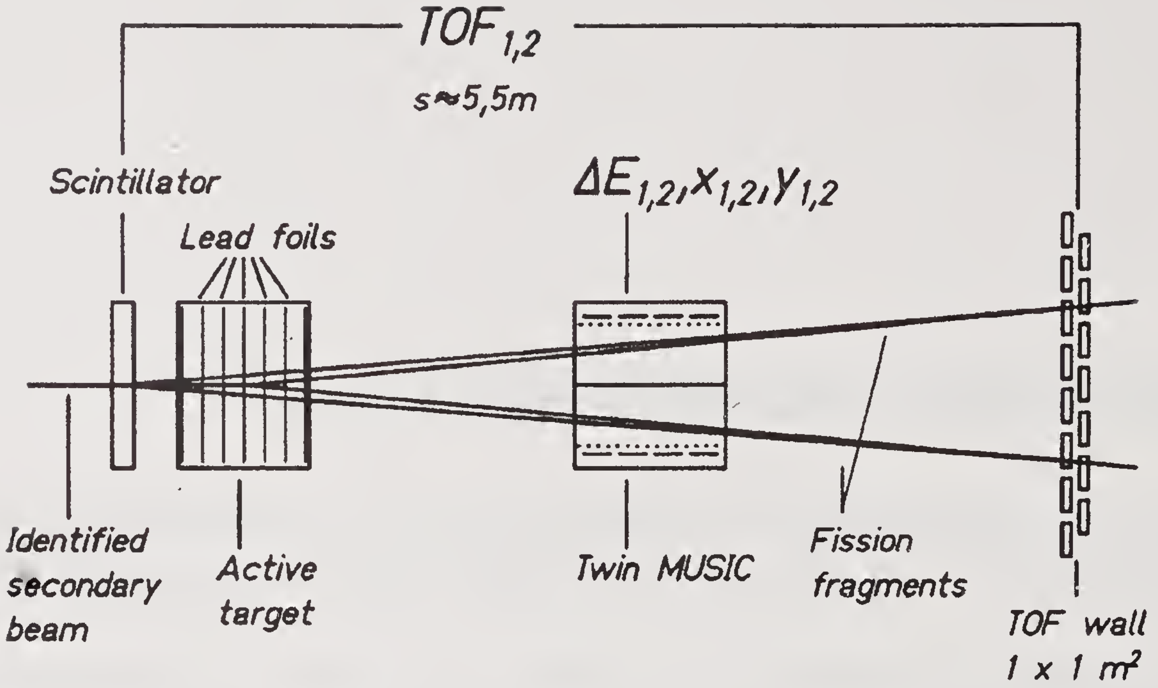

Figure 1. Schematical drawing of the set up for the fission experiment mounted behind the fragment separator.

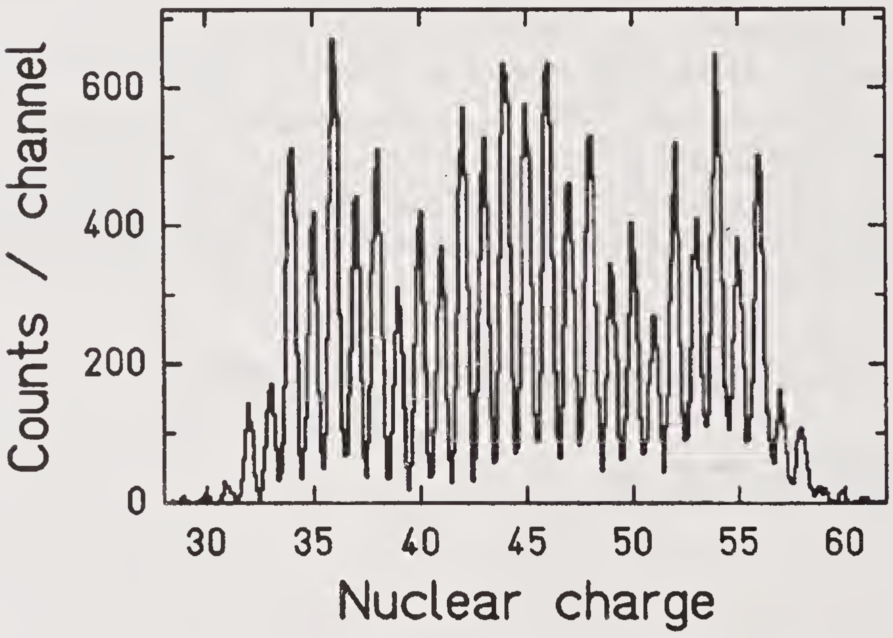

Figure 2. Nuclear-charge response of the twin MUSIC with velocity correction applied as obtained for the fission fragments after electromagnetic excitation of ^{226}Th projectiles.

the fragmentation cross sections [1,2], nuclear charge and mass number of the secondary projectiles can freely be selected by tuning the fragment separator [3].

Fission from the desired excitation-energy range slightly above the fission barrier was induced by electromagnetic interactions in a heavy target material. In the next section we give a detailed description of this excitation mechanism.

The experimental setup behind the fragment separator is sketched in figure 1. As secondary target we used a stack of lead foils with a total thickness of 3 g/cm^2 mounted in a gas-filled chamber which acts as a subdivided ionization chamber (active target). With this device it is possible to discriminate fission induced in the lead foils against fission induced in other layers, e.g. the scintillator. The average energy of the secondary projectiles in the lead target was about 430 A MeV. The differential energy loss of each fission fragment was measured separately with a horizontally subdivided twin ionization chamber. In order to correct the energy loss for the velocity dependence, the time-of-flight of the fission fragments was measured by means of a (1m × 1m) scintillator wall. Figure 2 shows the nuclear-charge response of the experimental set up for fission fragments after electromagnetic-induced fission of ^{226}Th. Due to the high center-of-mass energies, an excellent charge resolution is achieved. Events stemming from reactions at lower impact parameters were suppressed. For details of the analysis procedure see refs [4,5].

3. Excitation mechanism

The electromagnetic excitation in-flight in the secondary target is one of the most important ingredients of the experiment, ideally adapted to the kinematic properties and to the low intensities of the secondary beams. It populates states in the vicinity of the fission barrier with large cross section of a few barns. Although the excitation energy acquired is not precisely known for a single event, the excitation-energy distribution can be calculated with rather good precision. The electromagnetic field of a lead target nucleus, seen by the projectile, can be represented by a flux of equivalent photons of different energies and multipolarities according to ref. [6]. The projectiles are excited according to the energy-dependent photo absorption cross section which is dominated by the giant dipole resonance with small contributions of the giant quadrupole resonances. First-chance fission represents the main source of fission, but also fission after evaporation of one or two particles (mostly neutrons) occurs with a probability of about 20%. This leads to a reduction of the excitation energy at fission. The excitation-energy distribution at fission after electromagnetic excitation of ^{234}U in the passage of a lead target at 430 A MeV is shown in figure 3 (for details of the calculation see ref. [4]). The calculated excitation-energy distributions of the other nuclei investigated are similar.

4. Results and discussion

In the present experiment, the elemental yields and the total kinetic energies of long isotopic chains from ^{205}At to ^{234}U have been determined. The elemental yields are shown in figures 4 and 5. The transition from symmetric fission in the lighter systems to asymmetric

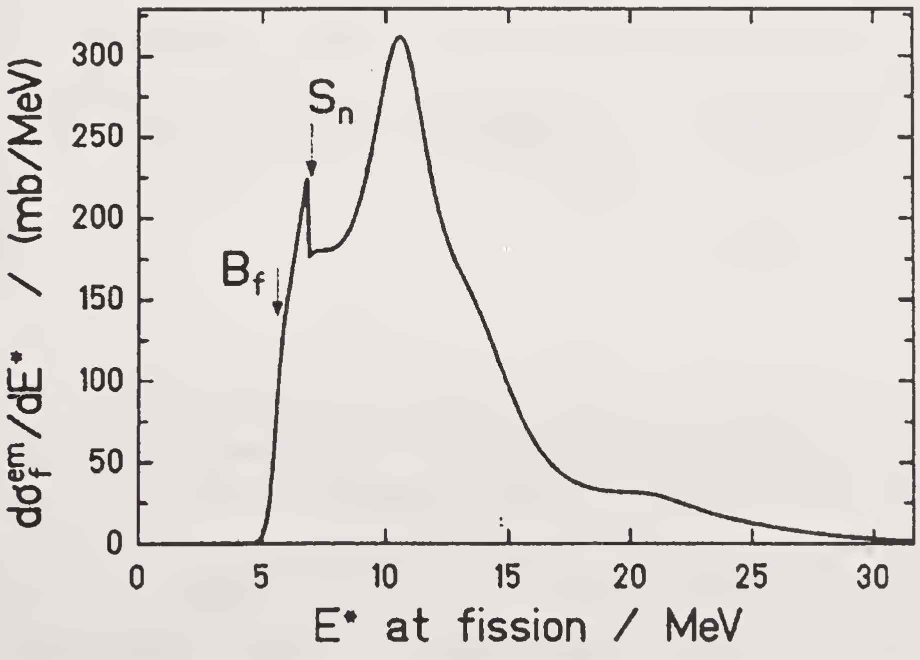

Figure 3. Calculated distribution of excitation-energies at fission after electromagnetic excitation of ^{234}U projectiles at 430 A MeV in a lead target.

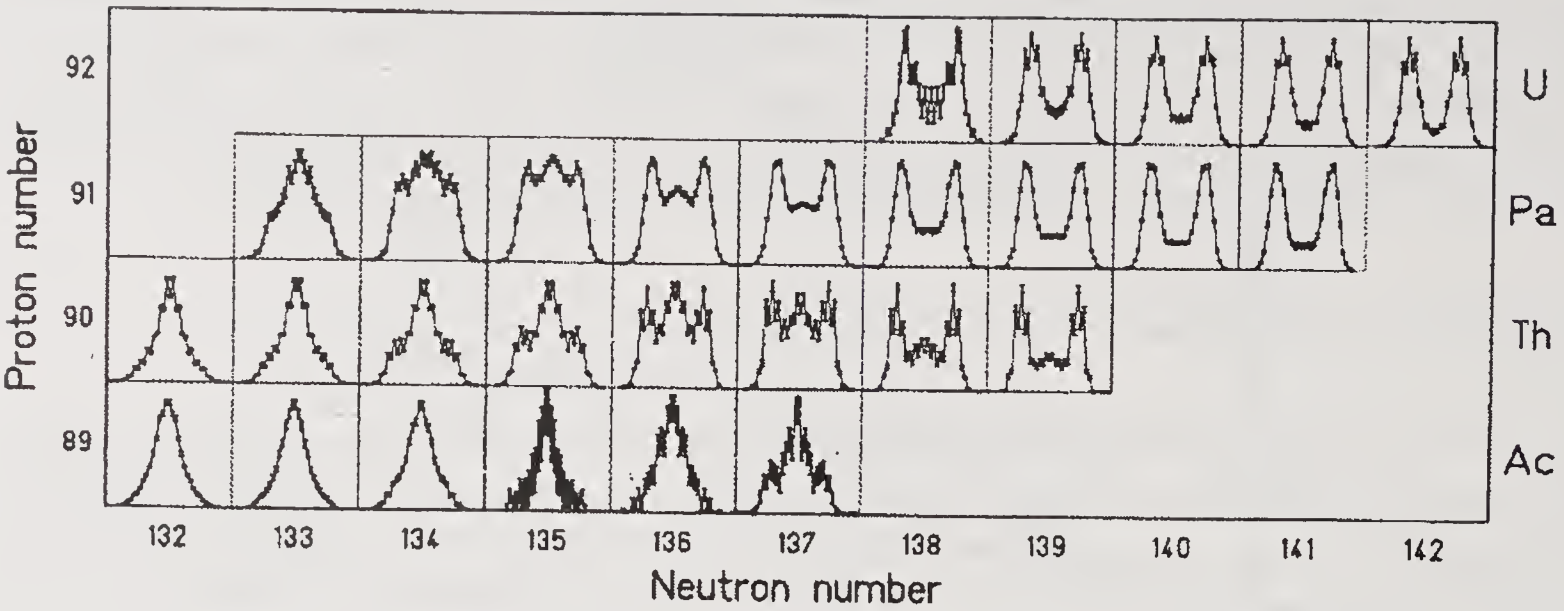

Figure 4. Measured fission-fragment charge distributions from ^{221}Ac to ^{234}U are shown on a chart of the nuclides.

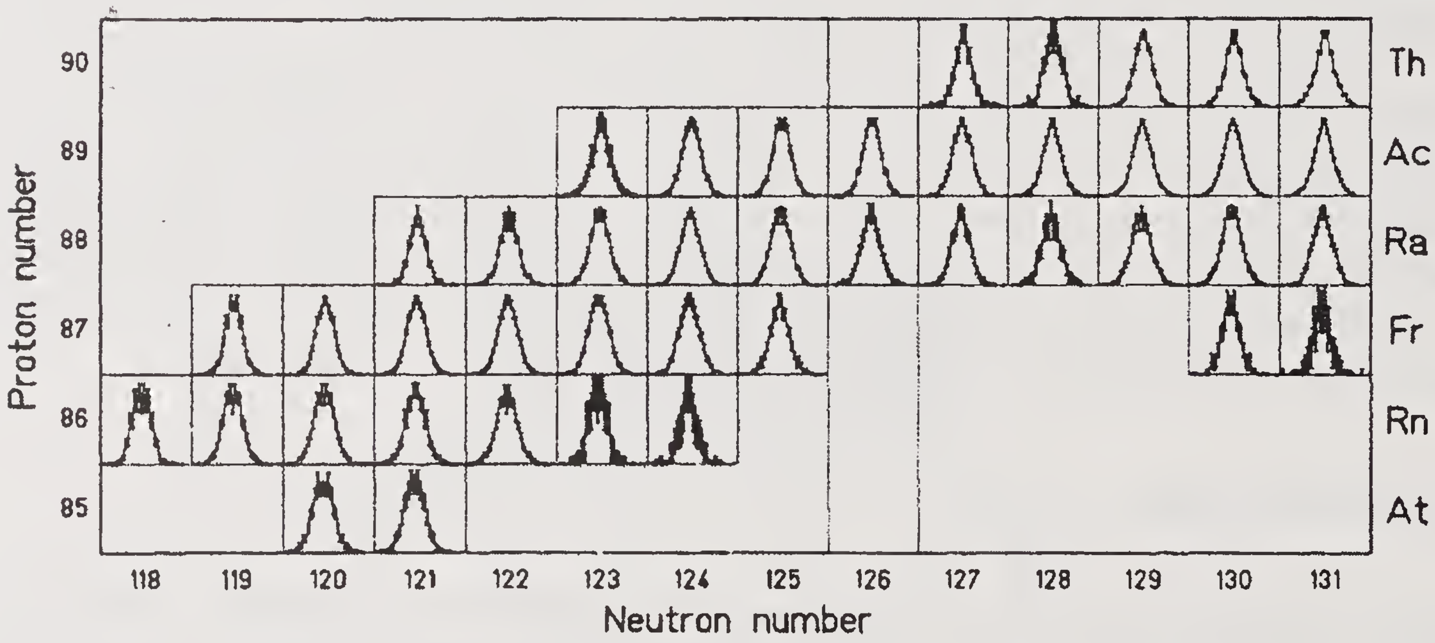

Figure 5. Measured fission-fragment charge distributions from ^{205}At to ^{221}Th are shown on a chart of the nuclides.

fission in the heavier systems is systematically covered. In the transitional region, around ^{226}Th, triple-humped distributions appear, revealing comparable intensities for symmetric and asymmetric fission. In particular, for uranium and thorium isotopes strong even-odd effects are observed.

4.1 Fission channels

Turkevich and Niday [7] already noticed that different components which they named as fission modes appear in the fission-fragment yields and in the kinetic-energy distributions. Later, models were proposed to deduce the fission characteristics from the properties of the scission configuration alone, e.g. ref. [8]. However, these neglect the dynamic evolution of the system from saddle to scission which seems to be very important [9–11]. The concept of independent fission channels has been developed [12,13] according to which the fissioning system follows specific valleys in the potential energy in the direction of elongation. Several properties (e.g. average mass or charge split, mass or charge width, mean total kinetic energy) could be related to calculated properties of the highly deformed fissioning system. However, the mechanisms which determine the fission-fragment yields are not sufficiently well understood to allow for quantitative predictions. Therefore, the intensities of the fission channels are usually deduced from experiment.

The systematic survey on fissioning systems with strongly varying charge distributions (see figures 4 and 5) will provide a new test case for the concept of independent fission channels. Moreover, it will enable a more systematic view on how the intensities of the fission channels vary as a function of the nuclear composition. At first glance, two fission components appear in the measured charge distributions, a symmetric and an asymmetric one. The weights of these two fission components were quantitatively determined by fitting three Gaussian curves to the charge-yield distributions. The widths (standard deviation) of the symmetric and the asymmetric components were found to be close to 4.0 charge units and 2.2 charge units, respectively, for all nuclei for which they could be extracted. In cases where either one of the components was too weak, the corresponding value from this systematics was used. The ratio of symmetric to asymmetric fission was then determined by the ratio of the areas of the Gaussians describing the data. The result of this procedure is shown in figure 6. The transition is rather smooth and the weights of the two fission components scale with the mass of the fissioning nucleus.

The data on elemental yields support the idea, stated by Itkis *et al* [14,15], that the weights of the fission channels are principally determined by an interplay of the neutron shells at $N = 82$ and $N = 86$ with the liquid-drop potential. A quantitative description of this idea has been formulated by Benlliure *et al* [16] by relating the charge distributions to the density of transition states in the vicinity of the outer fission barrier. From the model calculations (figure 6) we can conclude that the transition from the asymmetric to the symmetric components is mainly determined by the variation in the stiffness of the liquid-drop potential.

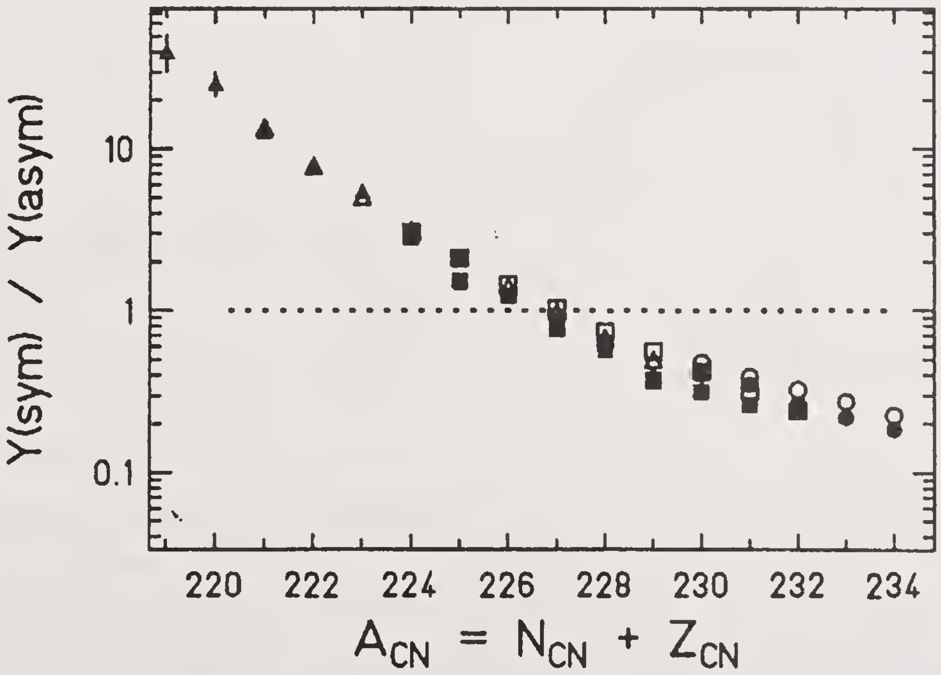

Figure 6. Intensity ratios of the symmetric and the asymmetric fission components in the transitional region as a function of mass number. The full triangles (squares, circles) correspond to thorium (protactinium, uranium) isotopes. The open symbols correspond to model calculations (see text).

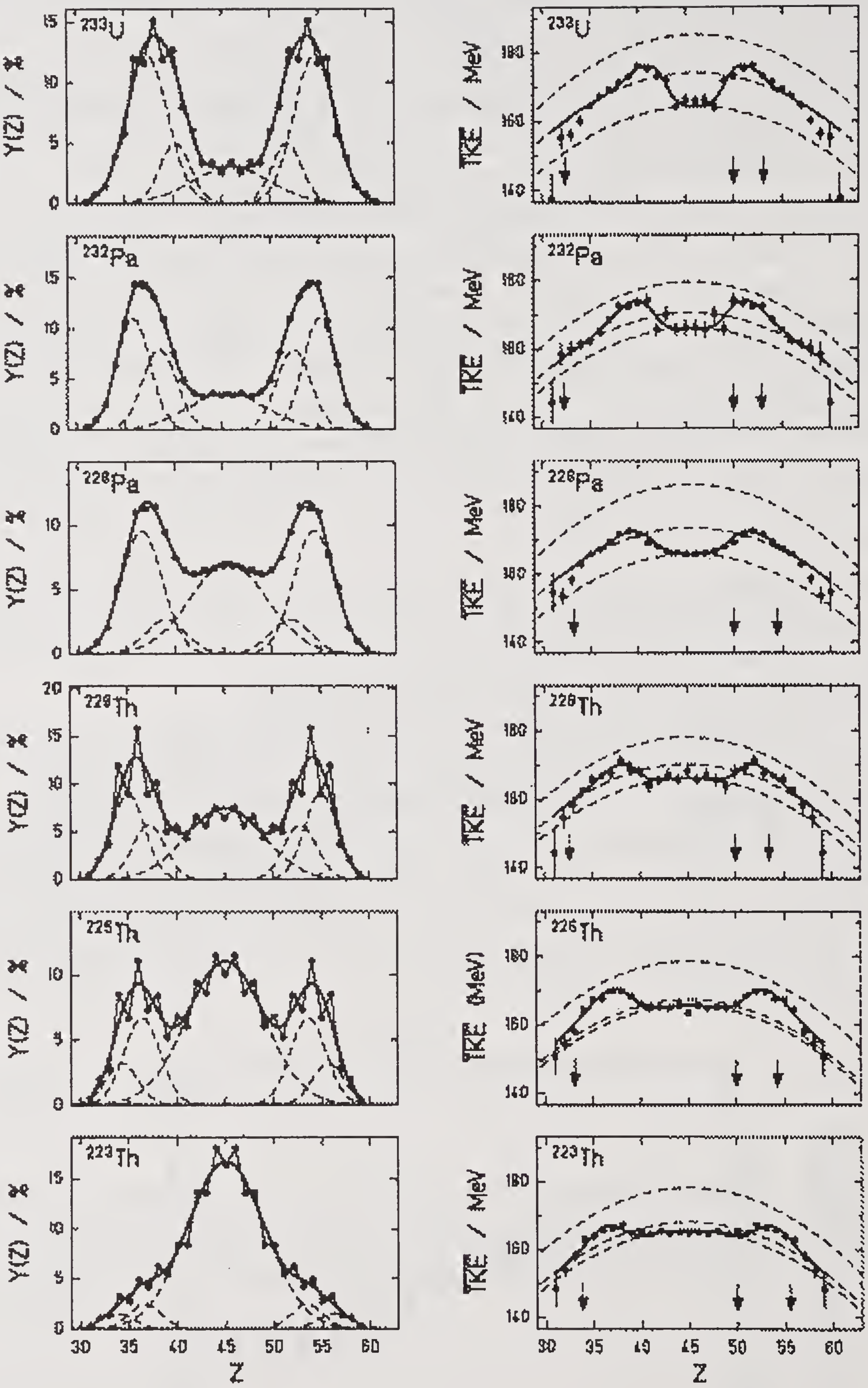

Figure 7. Measured elemental yields (left part) and average total kinetic energies (right part) as a function of the nuclear charge measured for fission fragments of several fissioning nuclei. Only statistical errors are given. The total kinetic energies are subject to an additional systematic uncertainty of 2%, common to all data [5]. Arrows indicate the positions of neutron ($N = 50, 82$) and proton shells ($Z = 50$). The positions of the neutron shells are calculated from the proton numbers by assuming an unchanged charge density (UCD). The full lines show descriptions with the model of independent fission channels. The contributions of the individual channels are depicted by dashed lines (see text for details).

4.2 Influence of shell structure

In detail, the charge-yield distributions and the total kinetic energies of ^{233}U, ^{232}Pa, ^{228}Pa, ^{228}Th, ^{226}Th, and ^{223}Th are shown in figure 7. The gross structural effects observed in the charge yields are different from those showing up in the total kinetic energies. From ^{233}U to ^{223}Th, the weight of the asymmetric fission component decreases strongly, while the enhancement of the total kinetic energies near $Z = 52$ to 54 is preserved. In a simultaneous fit to elemental yields and total kinetic energies, it was possible to reproduce these data with the assumption of independent fission channels. A description with two fission channels only, which well reproduces the nuclear-charge yields, represents the measured TKE values only poorly. A satisfactory description was obtained with three channels, 'standard I' at $N = 82$, 'standard II' around $N = 88$ in the heavy fragment, and 'superlong' at symmetry, using the notations introduced by Brosa *et al* [13]. Each channel was represented by a Gaussian distribution in the yields and a specific scission-point configuration. In order to consider the trivial variation of the total kinetic energy as a function of mass and charge split, the Coulomb repulsion V_{C} in the scission-point configuration was parametrized by the following expression, introduced in ref. [8]:

$$V_{\mathrm{C}} = \frac{Z_1 \cdot Z_2 \cdot e^2}{r_0 \left(A_1^{1/3} \left[1 + \frac{2\beta_1}{3} \right] + A_2^{1/3} \left[1 + \frac{2\beta_2}{3} \right] \right) + d}. \tag{1}$$

Z_i, A_i and β are nuclear-charge numbers, mass numbers and deformations of the fission fragments respectively, $r_0 = 1.16$ fm is the nuclear-radius constant, and e the elementary charge. The mass numbers were related to the charge numbers by the UCD assumption. The deformation parameters were fixed at $\beta = 0.6$ as predicted by the liquid-drop model, see ref. [8]. The 'tip distance' d was determined from a fitting procedure, requiring that the measured TKE values are best reproduced by V_{C}. Since the fit can only yield one parameter of eq. (1), the elongation of the system, parametrized by the tip distance d, also effectively represents variations in the deformation of the fragments.

For each fission channel, position, width, and height of the Gaussian representing the nuclear-charge yields as well as the tip distance of the scission configuration were treated as free parameters. The width of the superlong channel had to be kept constant for the fit to converge. The yields are formulated as the sum and the total kinetic energies as the weighted average of the different components. Unfortunately, the dispersion of the total kinetic energy could not be deduced in the secondary beam experiment due to the limited resolution. Therefore, the relative weights of the two asymmetric fission channels could only be determined with rather large error bars.

As a remarkable result, we found that the superlong channel which appears at symmetry becomes more compact for the lighter systems as can be seen in figure 8. This finding indicates that this channel is influenced by shell effects, too, although the charge distribution can be represented by a simple Gaussian. The variation of the tip distance in the symmetric channel can be related to the properties of the shell around $N = 64$ which tends to become less deformed with decreasing neutron number (see e.g. refs [8,17]. Moreover, the symmetric channel appears to be much narrower than observed previously in heavier systems.

In figure 9 it is shown the evolution of the positions in charge and neutron number of both asymmetric fission channels (standard I and standard II) as a function of the mass

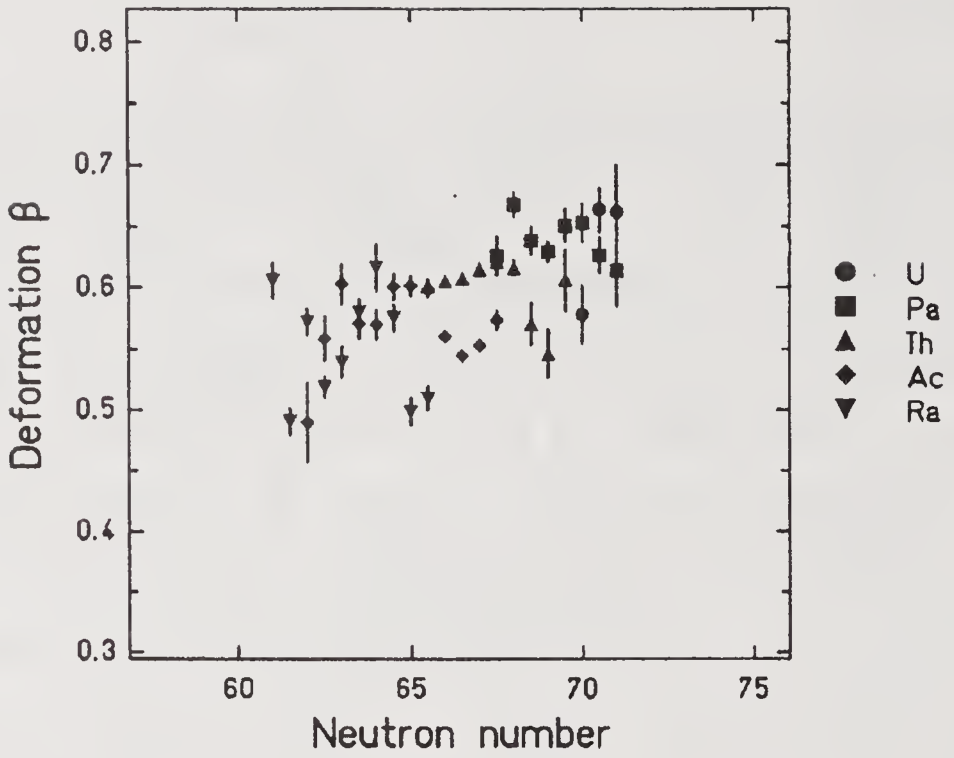

Figure 8. Evolution of deformation in the symmetric fission component obtained from the fits as a function of the neutron number of the fission fragments estimated assuming UCD.

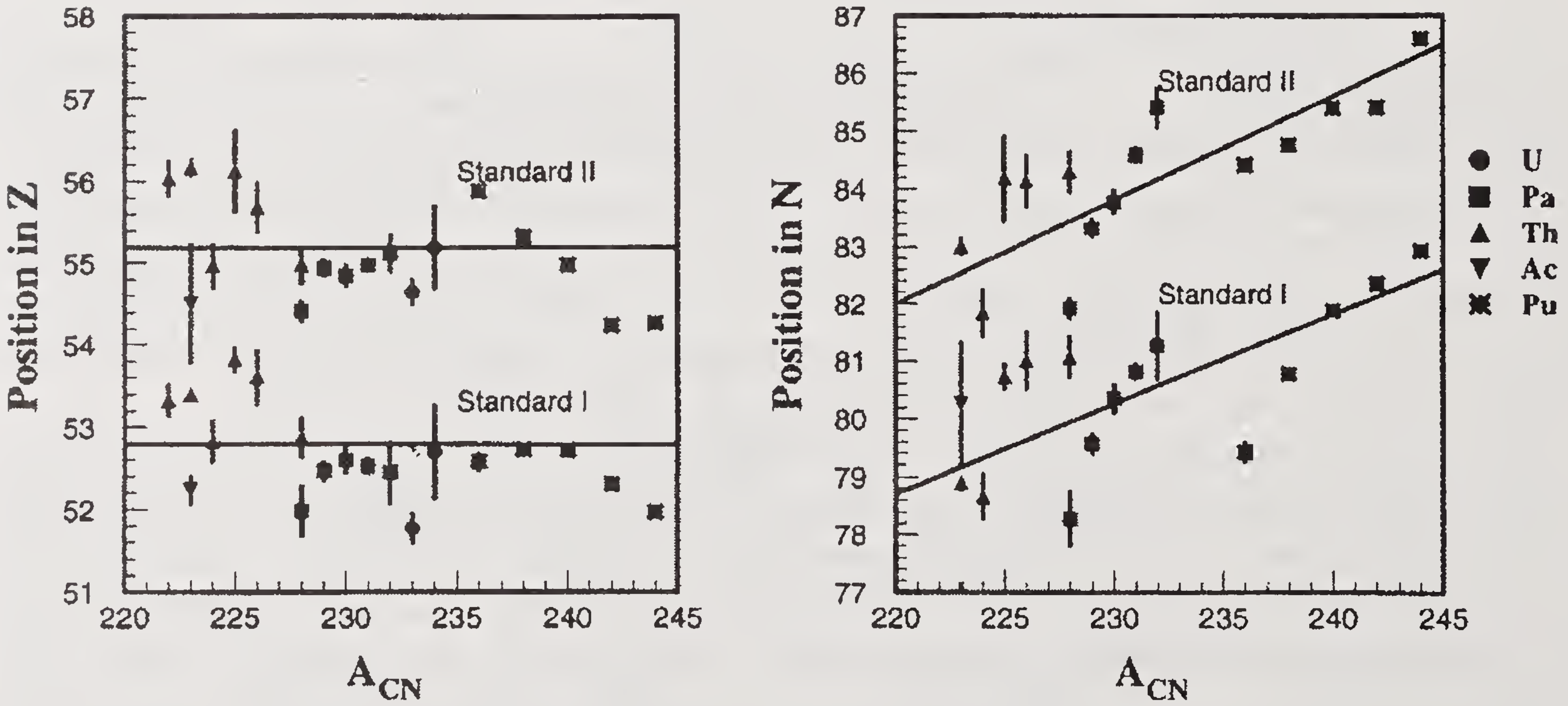

Figure 9. Position in nuclear charge and neutron number of the two asymmetric fission modes (standard I and standard II) as a function of the mass of the fissioning system. The data corresponding to the plutonium isotopes were taken from ref. [18]. The position in neutron number was estimated from the position in nuclear charge by the UCD assumption.

of the fissioning nucleus. We observe a constant position in charge corresponding to the values $Z = 53$ (standard I) and $Z = 55$ (standard II), while the positions in neutron number change with the mass of the fissioning nucleus. Since the two most important asymmetric fission channels (standard I and standard II) are usually associated [8] with the spherical $N = 82$ shell and the deformed $N = 88$ shell, respectively, this is a remarkable result.

From the good simultaneous description of nuclear-charge yields and total kinetic energies as demonstrated by figure 7 we conclude that the concept of independent fission channels has passed an important test although the parameters of the fission channels can not be directly related to the known properties of the nuclear shells. It allows for the strong variations of the yields while keeping the TKE distributions almost unchanged. However, we would also like to add a critical remark. In accordance with the usual treatment, the most probable scission-point configuration, parametrized by the tip distance d, was fixed at one value for each fission channel and not allowed to vary as a function of charge split. This might be a severe oversimplification. It is known that the energetically most favourable deformation in a deformed shell region varies with the number of nucleons [8,17]. Therefore a corresponding variation of the mean elongation at the scission point as a function of the charge split is to be expected. This would imply a variation of the most probable tip distance d even inside one fission channel. Besides the symmetric channel, this also concerns the standard II fission channel related to the $N = 88$ deformed shell. Therefore, part of the increase of the TKE values in the asymmetric component towards symmetry, which is attributed to the compact standard I channel in our description, may rather be imputed to a variation of the scission configuration in the standard II channel to more compact shapes. This would strongly affect all parameters of the two asymmetric fission channels.

5. Conclusion

A new experimental technique was applied to measure elemental yields and total kinetic energies after low-energy fission of short-lived radioactive nuclei. The beautiful data nicely demonstrate the decisive influence of nuclear structure on the fission process in a particular interesting transitional region around ^{227}Th. In contrast to the total kinetic energies, the element distributions were found to vary strongly, essentially as a function of mass number of the fissioning system. This behaviour could well be reproduced by the model of independent fission channels. The weights of the asymmetric fission channels decrease with decreasing mass of the fissioning nucleus, but the scission-point configurations remain unchanged. The scission-point configuration of the symmetric fission channel, however, evolves to more compact shapes for the lighter fissioning nuclei, where symmetric splits correspond to smaller nucleon numbers. This clearly reveals the influence of shell effects also in the symmetric channel. The analysis of both asymmetric channels (standard I and standard II) show that these two fission channels can not be explained by the influence of the shells $N = 82$ and $N = 88$.

References

[1] H-G Clerc, M deJong, T Brohm, M Dornik, A Grewe, E Hanel t, A Heinz, A R Junghans, C Röhl, S Steinhäuser, B Voss, C Ziegler, K-H Schmidt, S Czajkowski, H Geissel, H Irnich, A Magel, G Münzenberg, F Nickel, A Piechacyek, C Scheidenberger, W Schwab, K Sümmerer, W Trinder, M Pfützner, B Blank, A Ignatyuk and G Kudyaev, *Nucl. Phys.* **A590**, 785 (1995)

[2] A R Junghans, M de Jong, H-G Clerc, A V Ignatyuk, G A Kudyaev and K-H Schmidt, *Nucl. Phys.* **A629**, 635 (1998)

[3] H Geissel, P Armbruster, K-H Behr, A Brünle, K Burkard, M Chen, H Folger, B Franczak, H Keller, O Klepper, B Langenbeck, F Nickel, F Pfeng, M Pfützner, E Roeckl, K Rykaczewski,

I Schall, D Schardt, C Scheidenberger, K-H Schmidt, A Schröter, T Schwab, K Sümmerer, M Weber, G Münzenberg, T Brohm, H-G Clerc, M Fauerbach, J-J Gaimard, A Grewe, E Hanelt, B Knödler, M Steiner, B Voss, J Weckenmann, C Ziegler, A Magel, H Wollnik, J P Dufour, Y Fujita, D J Vieira and B Sherrill, *Nucl. Instrum. Methods* **B70**, 286 (1992)

[4] A Grewe, S Andriamonje, C Böckstiegel, T Brohm, H-G Clerc, S Czajkowski, E Hanelt, A Heinz, M G Itkis, M de Jong, M S Pravikoff, K-H Schmidt, W Schwab, S Steinhäuser, K Sümmerer and B Voss, *Nucl. Phys.* **A614**, 400 (1997)

[5] C Böckstiegel, S Steinhäuser, J Benlliure, H-G Clerc, A Grewe, A Heinz, M de Jong, A R Junghans, J Müller and K-H Schmidt, *Phys. Lett.* **B398**, 259 (1997)

[6] B Baur and C A Bertulani, *Phys. Rev.* **C34**, 1654 (1986)

[7] A Turkevich and J B Niday, *Phys. Rev.* **84**, 52 (1951)

[8] B D Wilkins, E P Steinberg and R R Chasman, *Phys. Rev.* **C14**, 1832 (1976)

[9] P Möller and S G Nilsson, *Phys. Lett.* **B31**, 283 (1970)

[10] G A Kudyaev, Yu B Ostapenko and G N Smirenkin, *Sov. J. Nucl. Phys.* **45**, 951 (1987)

[11] H Kudo, H Muramatsu, H Nakahara, K Miyano and I Kohno, *Phys. Rev.* **C25**, 3011 (1982)

[12] V V Pashkevich, *Nucl. Phys.* **A169**, 275 (1971)

[13] U Brosa, S Grossmann and A Müller, *Phys. Rep.* **197**, 167 (1990)

[14] M G Itkis, Yu Ts Oganessian, G Chubarian, V N Okolovich and G N Smirenkin, in *Nuclear Fission and Fission-Product Spectroscopy* edited by H Faust and G Fioni (ILL Grenoble, 1994) pp. 77

[15] M G Itkis, V N Okolovich, A Yu Rusanov and G N Smirenkin, *Sov. J. Part. Nucl.* **19**, 301 (1988)

[16] J Benlliure, A Grewe, M de Jong, K-H Schmidt and S Zhdanov, *Nucl. Phys.* **A628**, 458 (1998)

[17] I Ragnarsson and R K Sheline, *Phys. Scr.* **29**, 385 (1984)

[18] L Dematté, C Wagemans, R Barthélémy, P D'hondt and A Deruytter, *Nucl. Phys.* **A617**, 331 (1997)

Statistical fluctuations in hot rotating nuclei

M RAJASEKARAN and D CALEB CHANTHI RAJ*
Department of Nuclear Physics, University of Madras, Guindy Campus, Chennai 600 025, India
*Department of Physics, S.R.M. Engineering College, Kattankulathur, Chennai 603 203, India

Abstract. Thermal fluctuations in angular momentum due to excitation is investigated. Shape changes or structural rearrangement are observed as a consequence of fluctuation in second moment of spin. The uncertainty in angular momentum is considerably enhanced due to thermal fluctuation and is strongly dependent on spin and structural changes.

Keywords. Spin cut off parameter; nuclear structure.

PACS No. **21.10.M**

1. Introduction

The two important properties of nuclear level density are its dependence on spin and energy. The dependence of level density upon total angular momentum I for a system of non-interacting fermions is given approximately by [1,2]

$$\rho(E^*, I) = \rho(E^*, I = 0)(2I + 1)\exp[-I(I + 1)/2\sigma^2]. \tag{1}$$

In the above expression, energy dependence is mostly contained in the term $\rho(E^*, I = 0)$ and the spin dependence is the spin cut-off parameter σ^2.

Our knowledge about σ^2, the quantity which characterises the spin distribution in excited nuclei, comes mainly from isomer ratio measurements [3–5] and angular distribution of particles emitted in compound nuclear reactions [6,7].

Theoretically, the value of the spin cut-off parameter σ^2 is given [8,9] by the relation $\sigma^2 = JT/\hbar^2$, where J is the nuclear moment of inertia and T the nuclear temperature.

The present situation with regard to the determination of the important parameter σ is not very satisfactory, though attempts have been made earlier to determine σ^2 by different methods [10–13]. The purpose of the present work is to derive an expression for σ^2, which is also the second moment of spin, from statistical cranked theory and study the dependence of shell effects, angular momentum and excitation energy on σ^2 . The second moment so calculated, provides a more illustrative method of analysing the shape evolution with spin. Calculations of second moment, neutron separation energy, proton separation energy etc., as a function of spin are done for ^{56}Fe, ^{90}Zr and ^{158}Er. We find that σ^2 fluctuates with spin. The fluctuation is accompanied by shape changes.

2. Method

The grand partition function [14,15] for the hot rotating nuclei in terms of the routhian is given by

$$\ln Q = \Sigma_i \ln[1+\exp(\alpha_z + \omega m_i^z - \beta\epsilon_i^z)] + \Sigma_i \ln[1+\exp(\alpha_n + \omega m_i^n - \beta\epsilon_i^n)], \quad (2)$$

where the Lagrangian multiplier α_z, α_n and ω conserve the number of proton, neutrons and total angular momentum of the system. $\epsilon_i^z(\omega)$ and $\epsilon_i^n(\omega)$ are the routhians for protons and neutrons and m_i^z and m_i^n their respective spin projections, for a given temperature $T = 1/\beta$. ω, in eq. (2) refers to rotational frequency.

It can be shown, as in ref. [16], that the nth derivative of $\ln Q(\alpha,\beta,\omega)$ with respect to the Lagrangian multipliers (α,β,ω) which conserve the particle number, energy and angular momentum respectively, yields the corresponding nth moment of the observables E, N and I.

Explicitly the second moment of the angular momentum, σ^2, is given by

$$\begin{aligned}\partial^2 \ln Q/\partial\omega^2 &= \langle I\rangle^2 - \langle I^2\rangle \\ &= \sigma^2 \end{aligned} \quad (3)$$

with similar equations for fluctuation in energy and particle number.

The relevant equations, in terms of routhians $\epsilon_i(\omega)$ and spin projections m_i are

$$\langle N\rangle = \Sigma_i[1+\exp(-\alpha_n - \omega m_i^n + \beta\epsilon_i^n)]^{-1} = \Sigma_i n_i^n, \quad (4)$$

$$\langle Z\rangle = \Sigma_i[1+\exp(-\alpha_z - \omega m_i^z + \beta\epsilon_i^z)]^{-1} = \Sigma_i n_i^z, \quad (5)$$

$$\langle E\rangle = \Sigma_i n_i^n \epsilon_i^z + \Sigma_i n_i^n \epsilon_i^n. \quad (6)$$

The total angular momentum for the system is given by

$$\langle I\rangle = \Sigma_i n_i^z m_i^z + \Sigma_i n_i^n m_i^n. \quad (7)$$

The eigenvalues ϵ_i and m_i are obtained by diagonalizing the Nilsson Hamiltonian in cylindrical basis [14,15]. In the above equations, superficies z, n refer to single particle values and Lagrangian multipliers corresponding to protons and neutrons.

The simultaneous equations (4), (5) and (7) are solved for α_z, α_n and ω, for a given T, N, Z and I.

From eqs (2), (3) and (7), we have

$$\sigma_I^2 = \Sigma_i m_i^2 (1-n_i)n_i. \quad (8)$$

In equation (8), $(1-n_i)n_i$ refers to the number fluctuation. Other relevant equations of importance are calculated as follows.

The excitation energy E^* is given by

$$E^* = E - E_0, \quad (9)$$

with the ground state energy

$$E_0 = \Sigma_{i=1}^{Z} \epsilon_i^z + \Sigma_{i=1}^{N} \epsilon_i^n, \quad (10)$$

where the summation is only up to the Fermi level of protons and neutrons.

The entropy of the system is then obtained as

$$S = \partial(T ln Q)/\partial T = S_z + S_n, \tag{11}$$

where

$$\begin{aligned} S_z &= -\Sigma_i[n_i^z \ln\ n_i^z + (1-n_i^z)\ \ln(1-n_i^z)], \\ S_n &= -\Sigma_i[n_i^n \ln\ n_i^n + (1-n_i^n)\ \ln(1-n_i^n)]. \end{aligned} \tag{12}$$

The free energy of the system is given by

$$E_{\text{free}} = E - TS. \tag{13}$$

The deformation parameters δ is varied from 0 to 0.6 and γ varied from 0 to 60. All necessary statistical quantities discussed above are calculated at each deformation. The calculations are performed for different angular momenta and temperature. For each T and I, the free energy is minimised with respect to δ and γ and the relevant parameters are obtained.

3. Results and discussion

Calculations and results are presented here for hot rotating nuclei, ^{56}Fe, ^{90}Zr and ^{158}Er. Our calculations show that at $T = 0.5$ MeV, ^{56}Fe, at ground state is prolate in shape. With the onset of rotation, the nucleus becomes spherical at $I = 2\hbar$ and remains so till $16\hbar$. At $I = 18\hbar$, the nucleus changes to oblate shape. At $T = 1.75$ MeV, however, the nucleus remains spherical from $I = 0$ to $40\hbar$. ^{158}Er is prolate in shape. However the nucleus

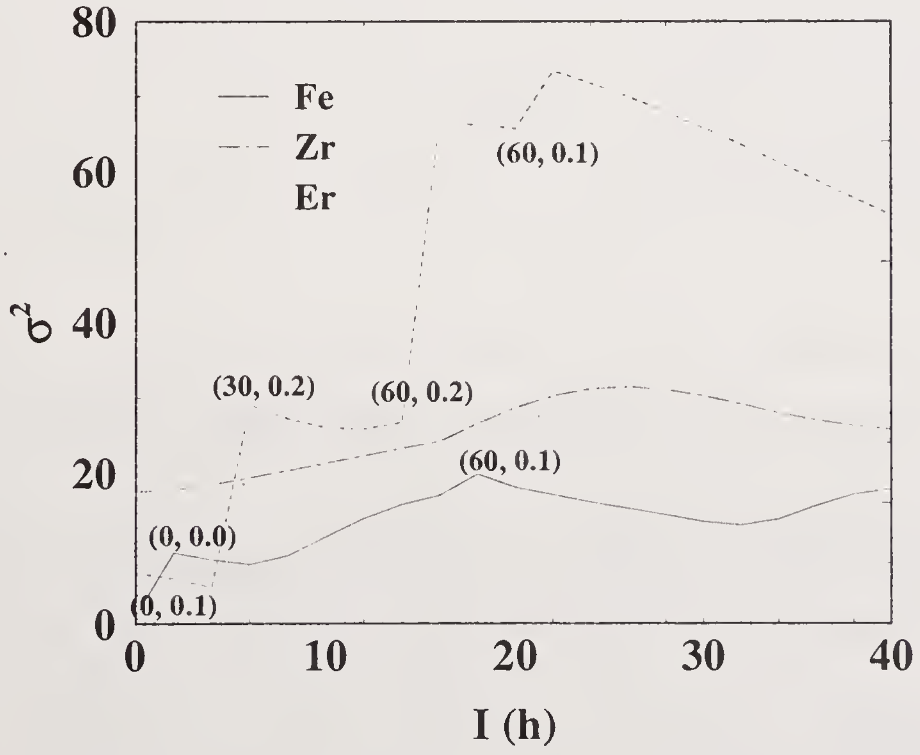

Figure 1. σ^2 vs I at $T = 0.5$ MeV for ^{56}Fe, ^{90}Zr and ^{158}Er, energy minimised with respect to deformation. Numbers within parenthesis represent γ and ϵ.

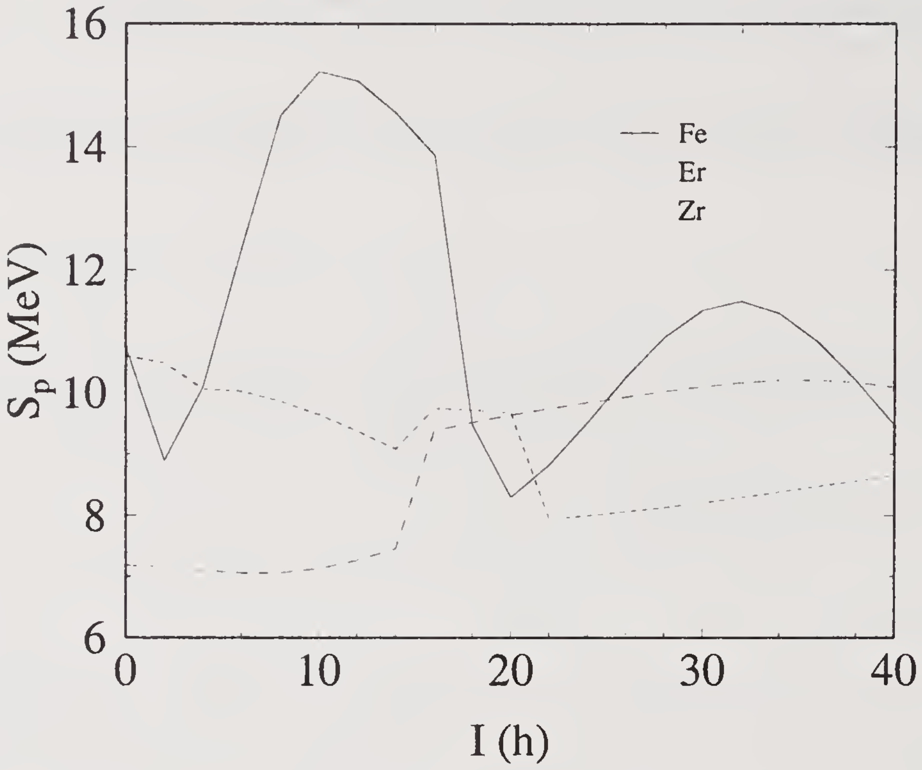

Figure 2. S_p vs I at $T = 0.5$ MeV, energy minimised with respect to deformation.

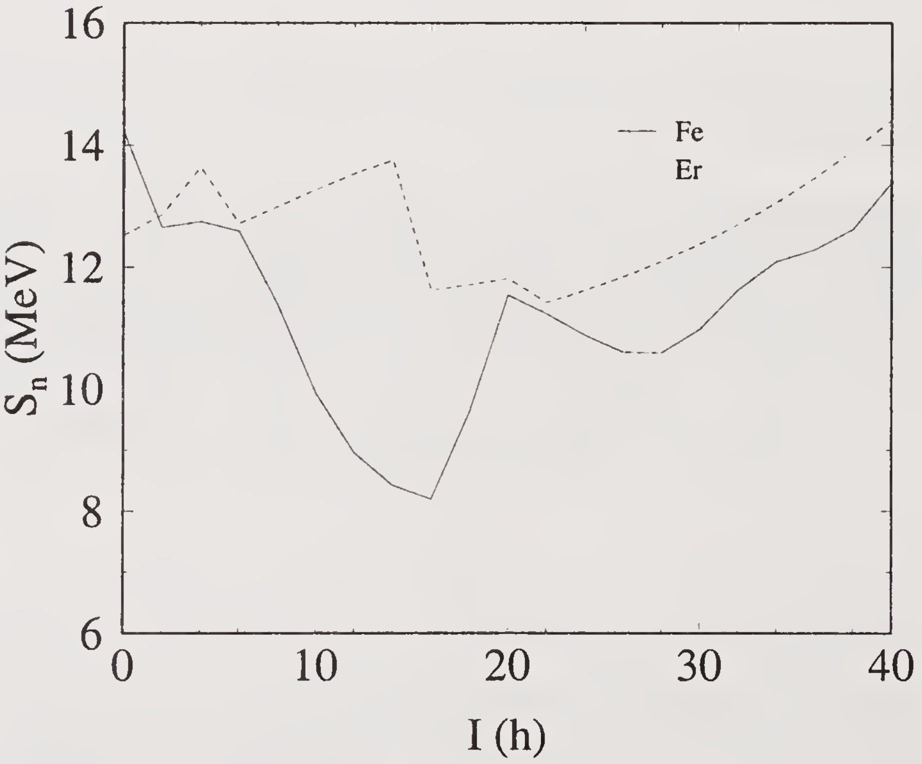

Figure 3. S_n vs I.

becomes triaxial at $I = 6\hbar$ and remains so till $14\hbar$. At $16\hbar$, there is a shape transition to oblate.

Figure 1 shows the second moment of spin as a function of I, for these nuclei. The aforementioned shape changes can be explicitly seen from the figure, by their corresponding changes in σ^2 at that I value. The deformation changes are marked in figure.

We also plot in figures 2 and 3, proton and neutron separation energies vs. angular momentum I. It is now possible to infer from figures 2 and 3, that change in shape of the nucleus can be attributed to proton or neutron. If, at a particular I, there is a sizeable change in S_p, it would imply that shape change was due to proton and that the change in shape is due to neutron, if there is a change in S_n. Earlier Rajasekaran *et al* used

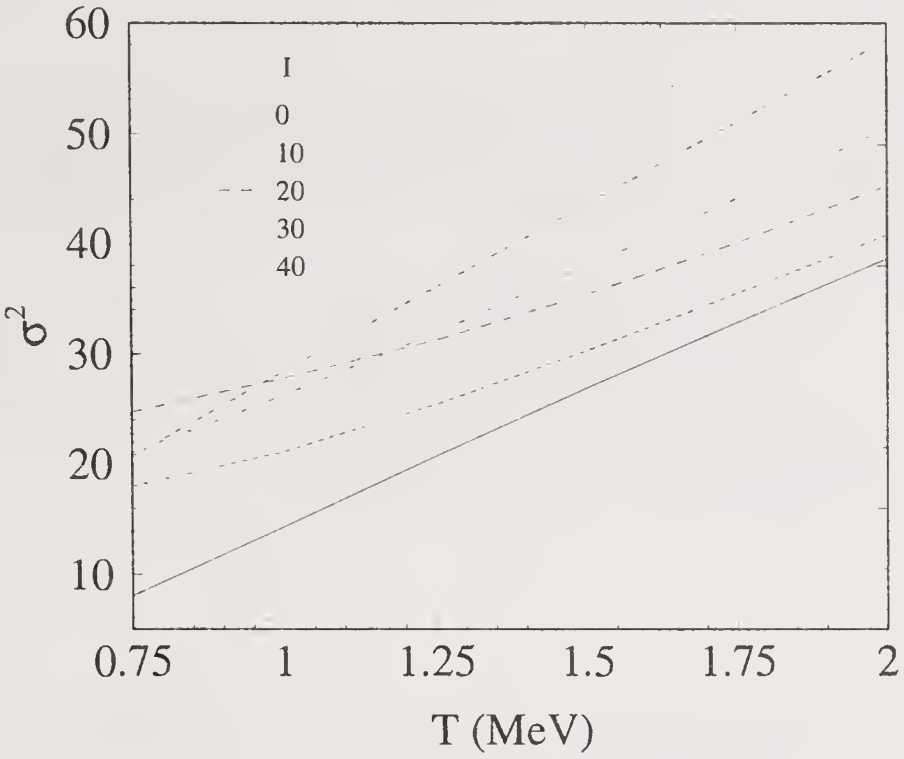

Figure 4. σ^2 vs T for a given deformation and angular momentum.

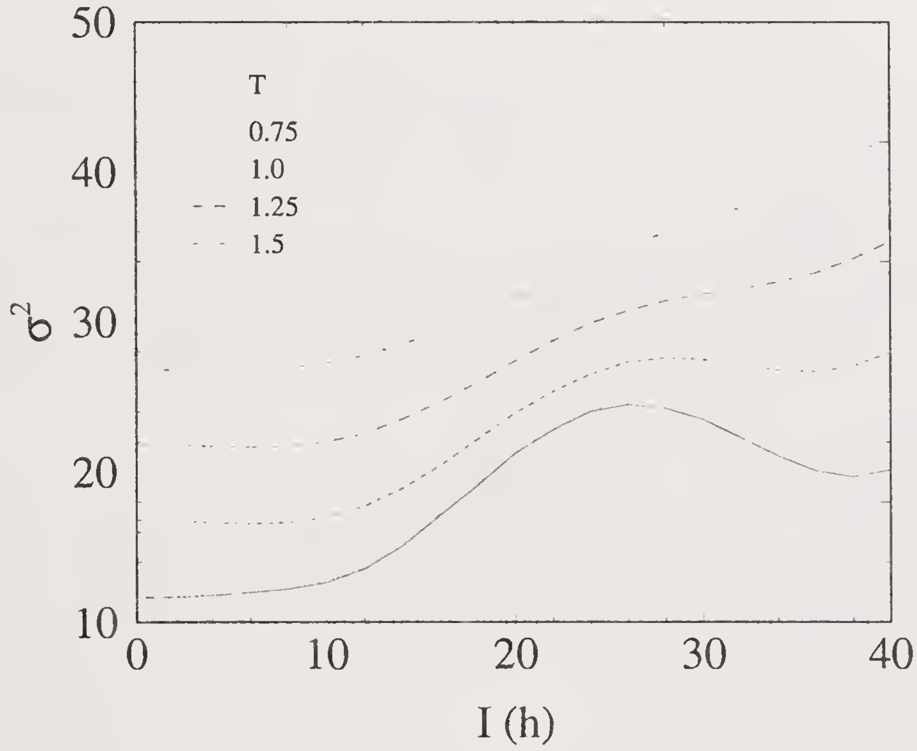

Figure 5. σ^2 vs I for a given deformation, plotted for different temperatures (^{158}Er, $\delta = 0$).

the statistical theory to study the effect of spin and structural changes on one neutron emission [17] in ^{92}Zr(^{64}Ni, $1n$)^{155}Er reaction.

The fluctuations in σ^2 and shape is observed only at low temperatures. At high temperatures, the second moment of spin gets smoothened and the shape of the nucleus also does not change. The shell effects which play a decisive role in deciding the shape of the nucleus is predominant only at low temperatures and since at high temperatures, the shell effects gets washed out, the σ^2 plot is smooth and there is no change in the shape of the nucleus. When $T = 0$ MeV, however, the term $(1 - n_i)n_i$, in eq. (8) becomes 0, since $n = 1$ or 0. Consequently, the second moment vanishes in this limit.

Figure 4 shows that for a given angular momentum state, σ^2 increases as temperature T increases. This is because, at higher temperatures, smoothening of occupation probabilities take place, resulting in the increase of σ^2.

The effect of shell structure on σ^2 can be clearly seen in figure 5. At low temperatures ($T = 0.75$ MeV), we see a hump at $I = 26\hbar$. This hump is due to shell structure in the nucleus. But as temperature increases, the hump in the σ^2 curve gets stretched at the same I. At $T = 1.5$ MeV, it gets totally vanished.

Further a drop in σ^2 implies a sharp spin distribution function and less of uncertainty in the determination of spin. In the case of determination of spin by multiplicity measurement which may be good for a clean rotation, that is, spin perpendicular to symmetry axis, it could be better if the second moment of $\langle M \rangle$ is also measured.

Acknowledgement

Our sincere thanks to Dr. R Premanand for his enormous help at various stages of this work. This work is partially supported by the University Grants Commission, under the Committee on Strengthening of Infrastructure in Science Technology program and S.R.M. Engineering College.

References

[1] H A Bethe, *Rev. Mod. Phys.* **9**, 69 (1937)
[2] T Ericson, *Adv. Phys.* **9**, 425 (1960)
[3] R Vandenbosch and J R Huizenga, *Phys. Rev.* **120**, 1313 (1960)
[4] M Bormann, H H Bissem, E Magiera and R Warnemude, *Nucl. Phys.* **A157**, 481 (1970)
[5] A C Douglas and N MacDonald, *Nucl. Phys.* **13**, 382 (1959)
[6] T Ericson and V Strutinsky, *Nucl. Phys.* **8**, 284 (1958)
[7] T Ericson and V Strutinsky, *Nucl. Phys.* **9**, 363 (1958)
[8] J R Huizenga and L G Moretto, *Ann. Rev. Nucl. Sci.* **22**, 427 (1972)
[9] J R Huizenga and R Vandenbosch, *Phys. Rev.* **120**, 1305 (1960)
[10] C C Lu Vaz and J R Huizenga, *Nucl. Phys.* **A197**, 321 (1972)
[11] A L Goodman, *Nucl. Phys.* **A369**, 365 (1981)
[12] A L Goodman, *Nucl. Phys.* **A370**, 90 (1981)
[13] A L Goodman, *Nucl. Phys.* **A352**, 45 (1981)
[14] M Rajasekaran, T R Rajasekaran, N Arunachalam and V Devanathan, *Phys. Rev.* **C37**, 307 (1988)
[15] M Rajasekaran, N Arunachalam, T R Rajasekaran and V Devanathan, *Phys. Rev.* **C36**, 1860 (1987)
[16] M Rajasekaran and V Devanathan, *Phys. Lett.* **B113**, 433 (1982)
[17] M Rajasekaran, T R Rajasekaran, N Arunachalam and V Devanathan, *Phys. Rev. Lett.* **61**, 2077 (1988)

List of Participants

Y K Agarwal Tata Institute of Fundamental Research, Homi Bhabha Road, Mumbai 400 005, India

Amita Department of Physics, University of Roorkee, Roorkee 247 667, India
(amitarph@rurkiu.ernet.in)

P Arumugam Department of Physics, Manonmanian Sundaranar University, Tirunelveli 627 012, India

K Asokan Nuclear Science Centre, New Delhi 110 017, India
(asokan@nsc.ernet.in)

C V K Baba 2 D Pallavi Apartments, House No 8-3-169/113, Siddharthanagar, Hyderabad, India
(cvkbaba@satyam.net.in)

Lagy T Baby Nuclear Science Centre, New Delhi 110 067, India
(lagy@nsc.ernet.in)

G M Carmel Vigila Bai Department of Physics, Manonmanian Sundaranar University, Tirunelveli 627 012, India

B R Behera Utkal University, Bhubaneswar 751 004, India

G Alpheus Benjamin Department of Physics, Manonmanian Sundaranar University, Tirunelveli 627 012, India

Jose Anaya Benlliure Plackstrasse 1, 64291-Darmstadt, Germany
(Jbenlliure@exp602.gsi.de)

Ionela Berceanu National Institute of Nuclear Physics and Engineering "Horia Hulubei", Post Box MG-6, RO-76900, Bucharest, Romania
(berceanu@dracula.ifa.ro)

Vidya Sagar Bhasin Department of Physics, University of Delhi, Delhi 110 007, India

Rupayan Bhattacharya Gurudas College, 1/1 Suren Sarkar Road, Calcutta 700 054, India

R K Bhowmik Nuclear Science Centre, New Delhi 110 067, India
(ranjan@nsc.ernet.in)

B Bindukumar School of Studies in Physics, Vikram University, Ujjain 456 010, India

Cyril Broude Weizmann Institute of Science, Rehovot, Israel 76100
(fnbroude@weizmann.weizmann.ac.il)

Oscar Angel Capurro Department of Fisica-Laboratono TANDAR-Commission National de Energra Atomica, Avenida del Liberator 8250, Postal Code 1429, City Buenos Aires, Republica Argentina
(CAPURRO@tandar.cnea.edu.ar)

R Srinivasa Chakrawarthy Institute fur kernphysik, Universitat zu Koln, 77, Zulpicher str, D-50937 Koln, Germany
(chakra@ikp.uni-koeln.de)

Jean Francois Chemin 15, Allee de la Sanguine CESTAS 33610, France
(chemin@cenbg.in2p3.fr)

Evgueni Cherepanov Laboratory of Nuclear Reactions, Joint Institute for Nuclear Research, 141980, Dubna, Moscow Region, Russia
(Cher@jinr.dubna.su)

Kamal Girishchandra Chhaya Department of Physics, Saurashtra University, H-67, Sarita Vihar Soc., Opp. Ruda-2, Rajkot 360 005, India

Surya Narayan Chintalapudi Inter University Consortium for DAE Facilities, III/LB-8, Bidhan Nagar, Calcutta 700 091, India
(snc@gamma.iuc.res.in)

R K Choudhury Nuclear Physics Division, Bhabha Atomic Research Centre, Mumbai 400 085, India
(rkc@magnum.barc.ernet.in)

J J Das Nuclear Science Centre, New Delhi 110 067, India
(jjdas@nsc.ernet.in)

Pragya Das Physics Department, Indian Institute of Technology, Powai, Mumbai 400 076, India

Mahananda Dasgupta Department of Nuclear Physics, RS Phys SE, Australian National University, ACT 0200, Canberra, Australia
(mdg103@nuc.anu.edu.au)

S K Datta Nuclear Science Centre, New Delhi 110 067, India
(skd@nsc.ernet.in)

Cary N Davids Physics Division, Argonne National Laboratory, 9700 South Cass Avenue, Argonne, Illinois 60439, USA
(davids@anlphy.phy.anl.gov)

Shashi Kumar Dhiman Department of Physics, Himachal Pradesh University, Shimla 171 005, India

Emilian Dragulescu National Institute of Nuclear Physics and Engineering "Horia Hulubei", P.O. Box MG-6, R-76900, City, Bucharest, Romania
(edrag@roifa.ifa.ro)

Manisha Dudeja Physics Department, University of Roorkee, Roorkee 247 667, India

Peter Egelhof GSI Darmstadt, Planckstr.1, 64291 Darmstadt, Germany
(egelhof@vscn.gsi.de /egelhof@axp101.gsi.de)

Sandip Sitaram Ghugre Inter University Consortium for DAE Facilities, III/LB-8, Bidhan Nagar, Calcutta 700 091, India

Giorgio Giardina Physics Department, University of Messina, Salita Sperone, 31-98166 Messina, Italy
(giardina@nucleo.unime.it)

Indra Mani Govil Department of Physics, Panjab University, Chandigarh 160 014, India
(govil%phys@puniv.chd.nic.in)

Hari Om Gupta C/o Prof Raghuvir Singh, Department of Physics and Astrophysics, Delhi University, Delhi 110 007, India

S L Gupta Department of Physics and Astrophysics, University of Delhi, Delhi 110 007, India

Sunita Gupta Department of Physics, Aligarh Muslim University, Aligarh 202 002, India
(wct01sg@amu.up.nic.in)

Raj K Gupta Physics Department, Panjab University, Chandigarh 160 014, India
(rkgupta%phys@puniv.chd.nic.in)

Susanta Kumar Hui Department of Physics, Calcutta University, Calcutta 700 009, India

V Ison Department of Physics, University of Calicut, Calicut 673 635, India

Mohammad Ismail Variable Energy Cyclotron Centre, Sector-I/AF, Salt Lake City, Calcutta 700 064, India

Ashok Kumar Jain Department of Physics, University of Roorkee, Roorkee 247 667, India
(akjph@rurkiu.ernet.in)

B K Jain Nuclear Physics Division, Bhabha Atomic Research Centre, Mumbai 400 085, India
(bkjain@magnum.barc.ernet.in)

Hem Chand Jain Tata Institute of Fundamental Research, Homi Bhabha Road, Mumbai 400 005, India
(hcjain@tifr.res.in)

Akhil Jhingan Nuclear Science Centre, New Delhi 110 067, India
(akhil@nsc.ernet.in)

Pankaj Joshi Nuclear Science Centre, New Delhi 110 067, India
(pankaj@nsc.ernet.in)

Swaminathan Kailas Nuclear Physics Division, Bhabha Atomic Research Centre, Mumbai 400 085, India

S S Kapoor Nuclear Physics Division, Bhabha Atomic Research Centre, Mumbai 400 085, India

Swapneel Ramakant Kore Department of Physics, University of Mumbai, Tilak Bhavan, Kalina Campus, Santacruz (E), Mumbai 400 098, India

Ram Chandra Govindrao Kulkarni Department of Physics, Saurashtra University, Rajkot 360 005, India

S Santhosh Kumar Department of Physics, Manonmanian Sundaranar University, Tirunelveli 627 012, India
(munphys@imsc.ernet.in)

Rakesh Kumar Nuclear Science Centre, New Delhi 110 067, India

T Madhusoodhanan Department of Physics, Bangalore University, Bangalore 560 056, India

P V Madhusudana Rao Department of Nuclear Physics, Andhra University, Visakhapatnam 530 003, India
(auphy@nsc.ernet.in)

Ramendra Nath Majumdar Vivekananda College, Calcutta 700 063, India

Samit Kumar Mandal Saha Institute of Nuclear Physics, 1/AF, Bidhan Nagar, Calcutta 700 064, India

D Mehta Department of Physics and Astrophysics, University of Delhi, Delhi 110 007, India

G K Mehta Nuclear Science Centre, New Delhi 110 067, India
(gkm@nsc.ernet.in)

Nihar Ranjan Mishra Department of Nuclear Physics, Andhra University, Visakhapatnam 530 003, India

Gopal Mukherjee Nuclear Science Centre, New Delhi 110 067, India
(gopal@nsc.ernet.in)

Anjali Mukherjee Saha Institute of Nuclear Physics, 1/AF Bidhan Nagar, Calcutta 700 064, India

S Mukherjee School of Studies in Physics, Vikram University, Ujjain 456 010, India

S Muralithar Nuclear Science Centre, New Delhi 110 067, India
(murali@nsc.ernet.in)

V Nanal Department of Nuclear and Atomic Physics, Tata Institute of Fundamental Research, Homi Bhabha Road, Mumbai 400 005, India
(nanal@tifr.res.in)

B S Narasingh Department of Nuclear and Atomic Physics, Tata Institute of Fundamental Research, Homi Bhabha Road, Mumbai 400 005, India
(bsns@tifr.res.in)

Madhavan Narayanasamy Nuclear Science Centre, New Delhi 110 067, India
(madhavan@nsc.ernet.in)

Subir Nath Nuclear Science Centre, New Delhi 110 067, India
(subir@nsc.ernet.in)

Basanta Kumar Nayak Bhabha Atomic Research Centre, Mumbai 400 085, India

R Palit Department of Nuclear and Atomic Physics, Tata Institute of Fundamental Research, Homi Bhabha Road, Mumbai 400 005, India
(palit@tifr.res.in)

S C Pancholi Department of Physics and Astrophysics, University of Delhi, Delhi 110 007, India

Shriprakash Bandulal Patel Department of Physics, University of Mumbai, Tilak Bhavan, Kalina Campus, Santacruz (E), Mumbai 400 098, India

N S Pattabhiraman Inter University Consortium for DAE Facilities, III/LB-8, Bidhan Nagar, Calcutta 700 091, India

R G Pillay Department of Nuclear and Atomic Physics, Tata Institute of Fundamental Research, Homi Bhabha Road, Mumbai 400 005, India
(pillay@tifr.res.in)

Giovanni Pollarolo Dipartimento di Fisica Teorica, Universita' di Torino, e INFN Sezione di Torino, Via P. Giuria 1, 10125-Torino, Italy
(NANNI@to.infn.it)

Amalia Pop National Institute for Physics and Nuclear Engineering "Horia Hulubei", Department of Experimental Fundamental Physics, Str. Atomistilor No. 1, R.O. 76900, P.O. Box MG-6, Bucharest-Magurele, Romania
(a_pop@roifa.ifa.ro)

Rajeshwari Prasad Department of Physics, Aligarh Muslim University, Aligarh 202 002, India

Rajeev K Puri Physics Department, Panjab University, Chandigarh 160 014, India

M C Radhakrishna Department of Physics, Bangalore University, Bangalore 560 056, India

Torsten Radon Gesellschaft fuer Schwerionenforschung, Planckstrasse 1, D-64291 Darmstadt, Germany
(T.Radon@gsi.de)

Chaleb Chanthi Raj Department of Nuclear Physics, University of Madras, Chennai 600 025, India

M Rajasekharan Department of Nuclear Physics, University of Madras, Chennai 600 025, India
(munphys@imsc.ernet.in)

V S Ramamurthy Department of Science and Technology, Technology Bhawan, New Delhi 110 016, India

V Ramasubramanian Department of Physics, Manonmanian Sundaranar University, Tirunelveli 627 012, India
(bio@md3.vsnl.net.in)

Amlan Ray Variable Energy Cyclotron Centre, Sector-I/AF, Salt Lake City, Calcutta 700 064, India

Neil Rowley Institut de Recherches Subatomiques, 23 rue du Loess BP 28-67037 Strasbourg Cedex 2, France
(Neil.Rowley@IReS.in2p3.fr)

Satyajit Saha Saha Institute of Nuclear Physics, 1/AF, Bidhan Nagar, Calcutta 700 064, India

Maitreyee Saha Sarkar Saha Institute of Nuclear Physics, 1/AF Bidhan Nagar, Calcutta 700 064, India

Basudeb Sahu Department of Physics, Ravenshaw College, Cuttack 753 003, India

Sukhendusekhar Sarkar Ananda Mohan College, 102/1, Raja Rammohan Sarani, Calcutta 700 009, India

Richard P Schmitt Cyclotron Institute, Texas A&M University, College Station, Texas 77843, USA
(schmitt@leper.tamu.edu)

V Selvam Department of Physics, Manonmanian Sundaranar University, Tirunelveli 627 012, India

G Shanmugam Department of Physics, Manonmanian Sundaranar University, Tirunelveli 627 012, India
(bio@md3.vsnl.net.in)

Manoj Kumar Sharma Department of Physics, Aligarh Muslim University, Aligarh 202 002, India

J K Sharma Department of Physics, Himachal Pradesh University, Simla 171 005, India

Manoj K Sharma Physics Department, Panjab University, Chandigarh 160 014, India
(manoj%phys@puniv.chd.nic.in)

Anil Kumar Sharma School of Studies in Physics, Vikram University, Ujjain 456 010, India

Radhey Shyam Saha Institute of Nuclear Physics, 1/AF Bidhan Nagar, Calcutta 700 064, India
(shyam@tnp.saha.ernet.in)

Bhanu Prakash Singh Department of Physics, Aligarh Muslim University, Aligarh 202 002, India

Raghuvir Singh Department of Physics and Astrophysics, University of Delhi, Delhi 110 007, India

Nirmal Singh Department of Physics, Panjab University, Chandigarh 160 014, India
(nsingh%phys@puniv.chd.nic.in)

Rajesh Pratap Singh Nuclear Science Centre, New Delhi 110 067, India

Ajit Kumar Sinha Nuclear Science Centre, New Delhi 110 067, India
(aks@nsc.ernet.in)

Aradhana Krishna Bihari Lal Srivastava Nuclear Physics Division, Bhabha Atomic Research Centre, Mumbai 400 085, India

Alberto M Stefanini INFN-Laboratori Naz Di Legnaro, Via Romea 4, Legnaro, I-35020, Padova, Italy
(ALBERTO@lnl.infn.it)

Bala Subramanium C/o Dr. R K Gupta, Panjab University, Chandigarh 160 014, India

Pullanhiotan Sugathan Nuclear Science Centre, New Delhi 110 067, India
(sugathan@nsc.ernet.in)

Alejandro Szanto de Toledo University of Sao Paulo, Institute de Fisica, Dept. de Fisica Nuclear, C.P. 66318, CEP 05315-970-Sao Paulo, Brazil
(szanto@if.usp.br)

Renju George Thomas Nuclear Physics Division, Bhabha Atomic Research Centre, Mumbai 400 085, India

P N Trehan (Retired) Punjab University, Chandigarh 160 014, India

Robert E Tribble Cyclotron Institute, Texas A&M University, College Station, TX 77843, USA
(tribble@comp.tamu.edu)

Vandana Tripathi Nuclear Science Centre, New Delhi 110 067, India

K M Varier Department of Physics, University of Calicut, Calicut 673 635, India
(kmv@unical.ac.in)

Raghav Varma Department of Physics, Indian Institute of Technology, Mumbai 400 005, India

Vijay Kiran Vemuri C/o Dr. B Krishnarajulu, Department of Physics, Osmania University, Hyderabad 500 007, India

Giuseppe Viesti Physics Department, University of Padova and INFN, Via Marzolo 8, 35131 Padova, Italy
(giuseppe.viesti@pd.infn.it)

Vireshkumar Inter University Consortium for DAE Facilities, III/LB-8, Bidhan Nagar, Calcutta 700 091, India

Philip J Woods Department of Physics and Astronomy, Edinburgh University, Kings Buildings, Mayfield Road, Edinburgh, EH9 3JZ, UK
(pjw@ph.ed.ac.uk)

Brij Kumar Yogi, Physics Department, GC Kota, MDSU, Ajmer 324 009, India

Some glimpses of the Workshop . . .

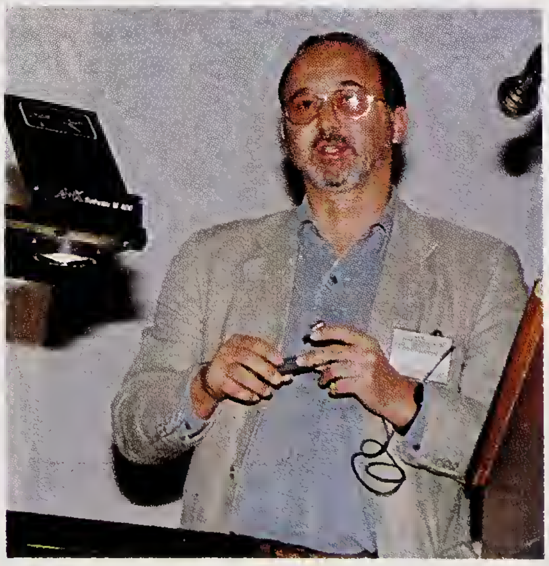

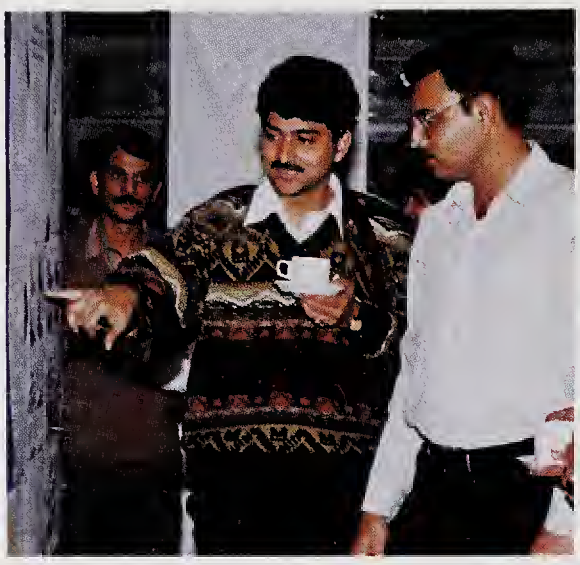

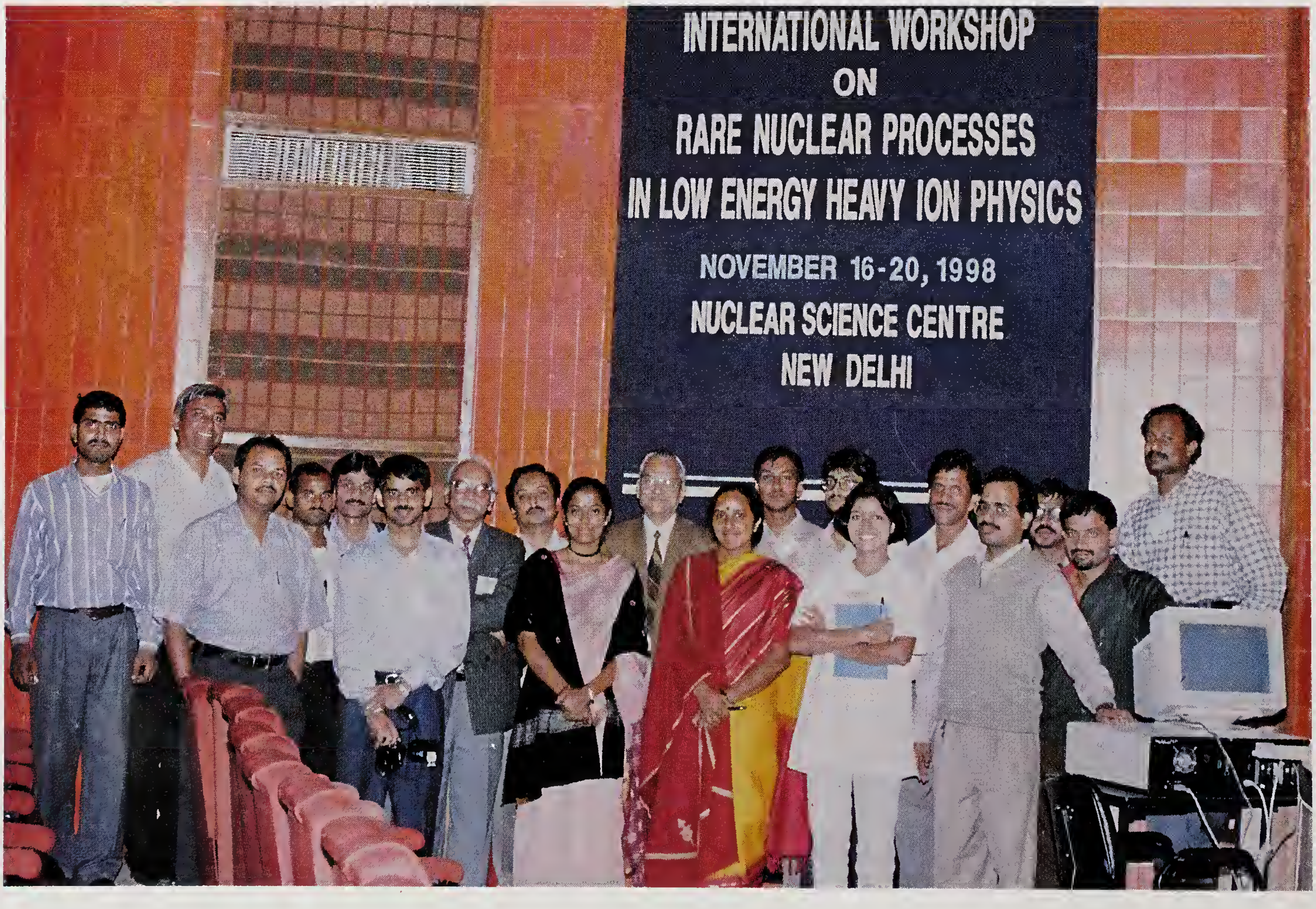
INTERNATIONAL WORKSHOP
ON
RARE NUCLEAR PROCESSES
IN LOW ENERGY HEAVY ION PHYSICS
NOVEMBER 16-20, 1998
NUCLEAR SCIENCE CENTRE
NEW DELHI